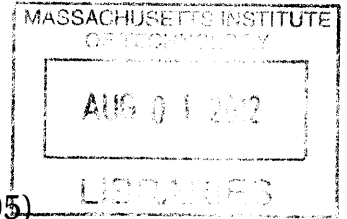


**Study of High Transverse Momentum Charged Particle
Suppression in Heavy Ion Collisions at LHC**

ARCHIVES



by

Andre Sungho Yoon

B.S., University of Illinois at Urbana-Champaign (2005)

Submitted to the Department of Physics
in partial fulfillment of the requirements for the degree of


Doctor of Philosophy


at the

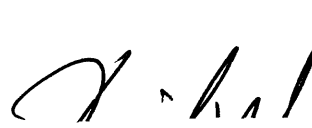
MASSACHUSETTS INSTITUTE OF TECHNOLOGY

June 2012

© Massachusetts Institute of Technology 2012. All rights reserved.

Author 
Department of Physics
May 16, 2012

Certified by 
Wit Busza
Francis Friedman Professor of Physics
Thesis Supervisor

Accepted by 
Krishna Rajagopal
Associate Department Head for Education

Study of High Transverse Momentum Charged Particle Suppression in Heavy Ion Collisions at LHC

by

Andre Sungho Yoon

Submitted to the Department of Physics
on May 16, 2012, in partial fulfillment of the
requirements for the degree of
Doctor of Philosophy

Abstract

The charged particle spectrum at large transverse momentum (p_T), dominated by hadrons originating from parton fragmentation, is an important observable for studying the properties of the hot, dense medium produced in high-energy heavy-ion collisions. The study of the modifications of the p_T spectrum in PbPb compared to pp collisions at the same collision energy can shed light on the detailed mechanism by which hard partons lose energy traversing the medium. In this thesis, the transverse momentum spectra of charged particles in pp and PbPb collisions at $\sqrt{s_{NN}} = 2.76$ TeV measured up to $p_T = 100$ GeV/c with the CMS experiment at the Large Hadron Collider (LHC) are presented. In the transverse momentum range $p_T = 5$ –10 GeV/c, the charged particle yield in the most central PbPb collisions is suppressed by up to a factor of 7 compared to the pp yield scaled by the number of incoherent nucleon-nucleon collisions. At higher p_T , this suppression is significantly reduced, approaching roughly a factor of 2 for particles with p_T in the range $p_T = 40$ –100 GeV/c. A simple modeling of the parton energy loss applied to the PYTHIA Monte-Carlo (MC) reveals that the charged particle spectrum with the pQCD-motivated fractional parton energy loss can describe the shape of the measured suppression well in the range $p_T = 5$ –100 GeV/c.

Thesis Supervisor: Wit Busza

Title: Francis Friedman Professor of Physics

This work is dedicated to my father, Chung Yoon.

Contents

1. Introduction	9
2. Motivation	11
2.1. Quantum Chromodynamics	11
2.1.1. Asymptotic Freedom and Confinement	13
2.2. QCD Phase Diagram	15
2.3. Relativistic Heavy Ion Collisions	18
2.3.1. Evolution of Hot and Dense Matter	20
2.3.2. Energy Density	21
2.4. Jet Quenching	22
2.4.1. Energy Loss Mechanisms	23
2.4.2. High-energy Parton Propagation in Medium	23
2.4.3. Nuclear Modification Factor R_{AA}	29
2.5. Goal of this Thesis	33
3. The CMS Experiment	35
3.1. Large Hadron Collider	35
3.2. CMS Detector	37
3.2.1. Tracker	37
3.2.2. Electromagnetic Calorimeter (ECAL)	42
3.2.3. Hadron Calorimeter (HCAL)	43
3.2.4. Muon Systems	44
3.2.5. Beam Scintillating Counter (BSC)	46
3.2.6. Beam Pick-Up Timing Experiment (BPTX)	46
3.2.7. CMS Trigger and Data Acquisition System (TriDAS)	47
3.2.8. Simulations	48
4. Event Characterization	49
4.0.9. Collision Trigger	49
4.0.10. Collision Geometry	51
4.0.11. Vertex Reconstruction	55
5. Particle Reconstruction	59
5.1. Generation of Seeds	59
5.1.1. Hit Reconstruction	59
5.1.2. Pair and Triplet Seed Generation	60
5.2. Trajectory building	62

5.2.1.	Final track fit and Iterations	63
5.2.2.	Track Selections	63
5.3.	Track reconstruction in PbPb collisions	65
5.3.1.	Tracking Environment in PbPb Collisions	65
5.3.2.	Heavy-ion Tracking	67
5.3.3.	Higher Tracking Iterations	67
5.3.4.	Track-calorimeter Matching	68
5.3.5.	Tracking Performance in PbPb	71
6.	Obtaining Charged Particle Spectra	75
6.0.6.	Correction to Raw Spectra	76
6.0.7.	Systematic Uncertainties	83
7.	Results and Discussions	89
7.0.8.	Charged Particle Spectra in pp at $\sqrt{s} = 0.9, 2.76$ and 7 TeV	89
7.0.9.	x_T scaling and Interpolation	91
7.0.10.	Charged Particles Spectra in PbPb and R_{AA}	96
8.	Model Studies	103
8.1.	Modeling Cronin Effect	103
8.2.	Constraining Energy Loss Models	105
8.2.1.	Convolution Method	105
8.2.2.	Energy Loss Scenarios	106
8.2.3.	Modeled R_{AA}	107
8.2.4.	R_{AA} and v_2 Correlation	111
9.	Conclusions	115
A.	QCD Lagrangian	117
B.	Track Quality Distributions	119
C.	Tabulated Results	125
	Bibliography	147

1. Introduction

One can ask a naïve question, “what will happen if one puts ordinary matter under extreme conditions of temperature and density?” Answering this seemingly naive question necessitates the understanding of nature of fundamental building blocks of nuclear matter¹ and the force that governs them. Quantum Chromodynamics (QCD) is a theory of the strong interaction that describes the interaction of the fundamental building block of nuclear matter, quarks and the force mediator, gluons [1, 2]. (see Chap 2.1)

Due to the properties of the strong interaction, the nuclear matter exists in wildly different matter phases at different conditions of temperature and density. At sufficiently high temperature, however, a universal matter phase is known to occur, where quarks are no longer bound in hadrons (e.g., proton or neutron) unlike ordinary nuclear matter we see around us, but rather roam freely in a “soup” of quarks and gluons [3–5]. This new state of matter is known as Quark-Gluon-Plasma (QGP), a term first introduced in Ref. [5]. (see Chap 2.2)

While this new state of matter is postulated to have existed shortly after the creation of universe known as Big Bang or in the core of neutron star [3], verifying the existence of it has long been sought after. A similar condition of temperature and density as in the universe few μs after the Big Bang can be created experimentally in a collision of heavy atomic nuclei such as gold (Au) or lead (Pb) nucleus at a nearly speed of light, where nuclear matter is squeezed into a very small region of space ($\sim \mathcal{O}(10) \text{ fm}^3$) for a very short period of time ($\sim \mathcal{O}(1) \text{ fm}/c$). The resulting matter created in such collisions, which we call “medium” hereafter, can be studied via the detection and the analyses of the final state particles that stream out of the collisions. Many intriguing properties of the medium produced in the collisions of various nucleus species in a wide range of center-of-mass energies have been known to this date based on the studies carried out with the experimental programs at different accelerator facilities. (see Chap 2.3)

One of the most interesting phenomena, which was observed at Relativistic Heavy Ion Collider (RHIC) for the first time and served as an early indication of the strong medium effect and therefore as a signature of the new state of matter, is “jet quenching”. Jet quenching refers to the loss of energy of highly energetic quark or gluon, or indistinguishably called parton, due to their interaction with hot and dense system created in heavy-ion collisions. As a consequence of jet quenching, the momentum spectrum of parton and their final state products, i.e., charged particles, is known to be modified in the presence of the medium. The modification of the spectrum is typically quantified by dividing the transverse momentum (p_T) spectrum of charged particles in

¹The nuclear matter refers to any system of interacting nucleons or their building blocks, quarks and gluons

1. Introduction

heavy-ion collision by the transverse momentum spectrum of charged particles in a reference nucleon-nucleon collision at the same center-of-mass energy after accounting for multiple nucleon-nucleon collisions that can occur in the case of heavy-ion collisions, and this factor is known as nuclear modification factor (R_{AA})². While numerous theoretical model predictions can describe the R_{AA} measurements at RHIC, the extension of the theoretical model predictions at higher center-of-mass energy varies greatly in particular for high momentum particles, exhibiting large theoretical uncertainty. (see Chap. 2.4)

In the winter of 2010, after an intense period of running with proton beams, the Large Hadron Collider (LHC) at the European Organization for Nuclear Research (CERN) delivered the first Pb ion beams and their collisions at the highest center-of-mass energy ever achieved in an accelerator, which is approximately 14 times larger than the center-of-mass energy achieved at RHIC. During the two four-week runs in 2010 and 2011, the LHC delivered over a billion heavy-ion collisions. The CMS experiment, one of the four major experiments at the LHC, collected those collisions data with very high efficiency, allowing detailed studies of the produced medium. (see Chap 3)

The measurement of R_{AA} in the PbPb collisions at the LHC has been performed based on the data collected by the CMS detector. The measurement involves the “reconstruction” of the detected particles with the CMS tracking system and the detailed analysis of the reconstructed particles in well defined sets of collision events. In order to identify individual particle unambiguously and estimate its momentum precisely in the much higher particle density environment presented in heavy-ion collisions than in pp collisions, the tracking reconstruction algorithms and the track selection criteria were modified from the default ones used for pp collisions and thoroughly tested. The information from the CMS calorimeters was additionally used to suppress the spurious high- p_T tracks. (see Chap. 4, 5, and 6)

This thesis presents the measurement of the nuclear modification factor R_{AA} in PbPb collisions at a center-of-mass energy of $\sqrt{s_{NN}} = 2.76$ TeV and the studies of jet quenching based on the comparisons of the measurements to numerous theoretical model predictions as well as to simple modelings of the parton energy loss applied to the PYTHIA Monte-Carlo (MC) [6]. (see Chap. 7, 8, and 9)

²see Eq. 2.14 in Sec 2.4.3 for the formula of R_{AA}

2. Motivation

From the studies of heavy-ion collisions, we hope to better understand the nature of strong interaction in the domain of extreme temperature and density, that maybe realized in the early universe ($\sim \mathcal{O}(10^{-5})$ s after the big bang¹) or in the core of neutron star [3]. The QCD provides the theoretical framework for studying heavy-ion collisions. However, its applicability is rather limited as it is notoriously difficult to solve QCD Lagrangian for a many-body, strongly interacting system. A series of different approaches that are using the perturbation theory (pQCD), the lattice gauge theory (LQCD), or the duality known as Anti-de Sitter/Conformal-Field-Theory (AdS/CFT) correspondence are employed to overcome such difficulty and explain some of the observed phenomena. Observation of jet quenching phenomenon in heavy-ion collision at collider energies is an important ‘tool’ to study QCD medium and the nature of QCD energy loss mechanisms since the quantification of jet quenching via an observable such as nuclear modification factor R_{AA} allows a direct comparison with theoretical predictions that are made based on the pQCD or the AdS/CFT calculations of parton energy loss in the QCD medium.

2.1. Quantum Chromodynamics

Quantum Chromodynamics (QCD) is a theory of the strong interaction, one of the four fundamental forces in the Standard Model of particle physics, that describes the interaction of the fundamental building block of hadronic matter, quarks and the force mediator, gluons [1]. There are six known types so-called ‘flavors’ of quarks with three different ‘color’ charges². This is the force that is responsible for the binding of nucleons inside nuclei via exchange of gluon, manifested as pion exchange. The QCD Lagrangian, a function that summarizes the dynamics of strong interaction for quark and gluon, is given by [8, 9],

$$\mathcal{L}_{QCD} = -\frac{1}{4} F_{\mu\nu}^{(a)} F^{(a)\mu\nu} + i \sum_q \bar{\psi}_{qi} (\gamma^\mu (D_\mu)_j^i - m_q \delta_j^i) \psi_q^j, \quad (2.1)$$

The detailed explanation of each term in Eq 2.1 can be found in Appendix A and in the references in Ref. [2]. Here, a brief explanation of what each term in the Lagrangian

¹This estimation is based on the extrapolation of the present conditions to the early universe using a relation between the size of observable universe, R , a time after the big bang, t , and temperature, T from the Friedmann equation; $R \propto T^{-1} \propto t^{1/2}$ in a relativistic phase and $R \propto t^{2/3}$ during non-relativistic phase [7].

²The six flavors are u, d, c, s, t and the charges are R (red), B (blue), and G (green).

2. Motivation

implies in the dynamics is given. The first term consisting of gluon field tensors ($F_{\mu\nu}^{(a)}$) in the Lagrangian describes the dynamics of gluons including self-interactions (e.g. gluon-gluon) and the second term consisting of quark fields describes the motion of free quark and their interaction with gluons, as shown in Fig. 2.1

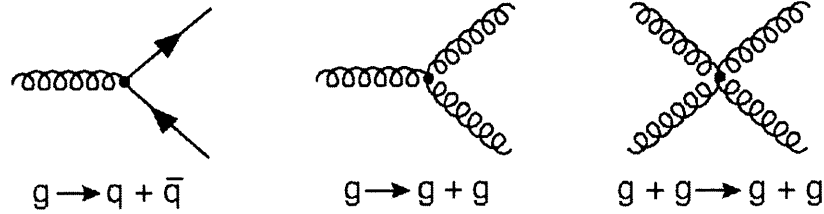


Figure 2.1.: Feynman diagrams of quark-gluon and gluon-gluon interaction vertices.

What distinguishes QCD from Quantum Electrodynamics (QED), a quantum theory of the electromagnetic interaction, is that the gluon field tensor ($F_{\mu\nu}^{(a)}$) contains a non-vanishing term, known as SU(3) structure constants which are expressed as a commutation relation. For that reason, QCD is called a non-Abelian (i.e., non-commutative) gauge theory. Unlike in QED where photon, a force carrier of the electromagnetic interaction, interacts with only charged particles, and therefore no direct photon-photon interactions exist, in QCD there exist gluon-gluon interactions as a direct consequence of this non-zero structure constant. Another crucial aspect that distinguishes QCD from QED is the existence of different kinds of charges, known as ‘color’ charges. The concept of color charge was first introduced in order to cure a situation where three quarks (identical quantum states) coexist in a composite particle (hadron) known as Δ^{++} , which seemingly violates the Pauli exclusion principle without an additional quantum state³.

By assigning different colors (R , G , and B) to each quark in Δ^{++} , the violation of the Pauli exclusion principle could be avoided. While it’s not related with the color we see in nature, it was named ‘color’ in analogy to the white color (‘colorless’ hadron) that can be created from the combination of red, blue, and green (red, blue, and green quarks). Each color also has anti-color just as there exists an anti-quark, anti-particle of a quark. While a quark carries one of the three colors, gluons carry mixture of color and anti-color which allows nine possible color and anti-color combinations with a color singlet ruled out by the lack of long range gluon interaction⁴. This notion of color was later supported experimentally from the comparison of the measured cross-sections

³The quarks inside Δ^{++} have the same spin state ($\uparrow\uparrow$) with $1/2$ each, same flavors (uuu), and symmetric spatial wavefunction (inferred from the positive parity of Δ^{++} , thereby having symmetric wavefunction, which is forbidden by the Pauli exclusion principle requiring the fermion wavefunction to be anti-symmetric).

⁴If the single gluon existed, the interaction between color singlets, e.g., proton and proton, would have a long range (infinite because gluon is massless) component, which we do not observe in the singlet interactions [10]

between $e^+e^- \rightarrow \mu^+\mu^-$ and $e^+e^- \rightarrow q\bar{q} \rightarrow \text{hadrons}$ [1], which is directly sensitive to the number of colors.

2.1.1. Asymptotic Freedom and Confinement

Different interactions in nature are characterized by their strength of interaction because it plays an important role in dynamics. The strength of interaction in turn is characterized by the coupling constant (α). For example, the electromagnetic interaction is characterized by the coupling constant known as a fine structure constant⁵. On the contrary to what name, ‘constant’, suggests, the fine structure constant is indeed not constant. Rather it varies as a function of energy scale, equivalently as a function of length scale or momentum transfer (Q). This running coupling constant is a general phenomenon in quantum field theory due to quantum fluctuation which makes vacuum as a polarized medium. As a consequence of the polarization, the effective charge, which is a sum of the charge of interest (i.e. test charge) and the induced charge, appears to be dependent on the distance scale. In QED, the vacuum polarization leads to the ‘screenings’ of electric charge. Therefore, the effective charge appears weaker at a larger distance. On the other hand, in QCD because of the gluon self couplings, the polarization leads to the ‘anti-screening’ of charge (color) and so the effective charge appears stronger at a larger distance. In the opposite direction, the effective charge becomes weaker and weaker at a shorter distance. QCD reveals that the strong interaction approaches asymptotically free gauge theory with vanishing coupling constant. In other words, $\alpha_{\text{strong}}(Q) \rightarrow 0$ as $Q \rightarrow \infty$. This is called the asymptotic freedom, which is unique for the non-Abelian gauge theories [11, 12].

While the absolute size of α_s is not predicted in QCD, the energy dependence can be precisely determined through the renormalization⁶ [12];

$$\alpha_s(Q^2) = \frac{\alpha_s(\mu^2)}{1 + \frac{\alpha_s(\mu^2)}{12\pi}(33 - 2n_f)\log\frac{Q^2}{\mu^2}} \quad (2.2)$$

where n_f is the number of quark flavor and μ is an arbitrary momentum or energy scale introduced in the renormalization⁷. It is noted that QCD is asymptotically free and possess the aforementioned feature of anti-screening only if n_f is less than 16 (\because it requires $33 - 2n_f > 0$) as it can be seen from the denominator of Eq. 2.2. In fact, there are only six known flavors. It can also be seen from the equation that as Q^2 becomes larger, $\alpha_s(Q^2)$ decreases asymptotically. The asymptotic freedom has been extensively tested in various measurements [12, 13], which is nicely summarized in Fig. 2.2.

As mentioned in Chap. 1, QCD have been remarkably successful in describing vari-

⁵ $\alpha = e^2/4\pi\epsilon_0\hbar c \sim 1/137$

⁶The renormalization in field theory is a procedure to re-normalize un-renormalized constants that appear in Lagrangian such that the observable quantities is kept finite when the ultraviolet cut-off is removed [11]

⁷It is nature to identify the renormalization scale with the physics energy scale of the process of interest, $\mu^2 = Q^2$

2. Motivation

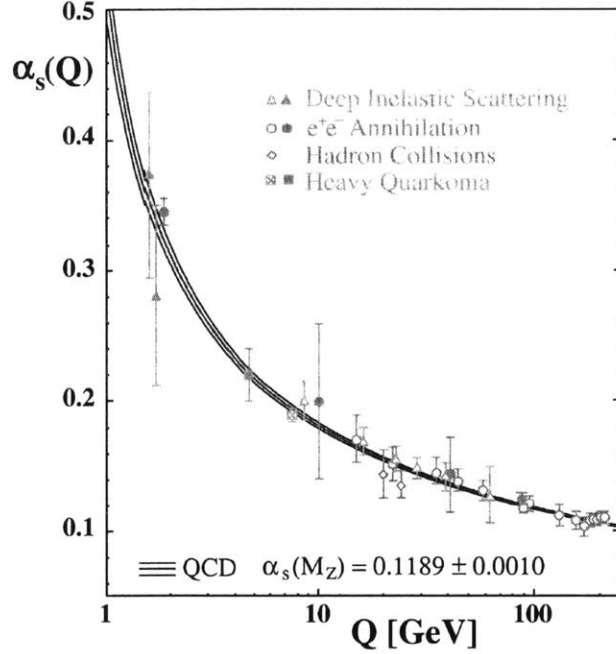


Figure 2.2.: Summary of the measurements of $\alpha_s(Q)$ in comparison with the QCD predictions shown as a function of the energy scale Q [12]. Also shown is the α_s at a fixed, standard energy scale of Z boson mass, i.e., $Q = M_Z$.

ous phenomena of strong interactions. However, interestingly, an individual quark or gluon, basic ‘building block’ of QCD, has never been detected in nature. But rather, it has been observed only within the colorless bound state⁸. The ‘colorless’ means a state of the bound state is a color singlet under rotation in color state. This phenomenon is hypothesized under a name ‘color confinement’. While a rigorous theoretical description of the color confinement is lacking, it is made plausible by the asymptotic freedom; because of the running coupling constant, the force between two quarks increases as the distance between them increases, which requires an infinite amount of energy to separate the quarks completely⁹. Experimentally, when two quarks are separated by a large amount of energy (e.g. in a hard-scattering of two quarks in particle collisions), what one sees instead is a spray of colorless bound states collimated in space. This is so called ‘jet’. And this materialization of quark or gluon into jet is called fragmentation or hadronization [14]. The fragmentation is understood on a semi-empirical ground as the transformation of the field energy created between the separating quarks at some point when the creation of quark and anti-quark pair is more favorable energetically

⁸The simplest colorless bound state configuration of quarks are either three quarks (so-called baryon) or quark and anti-quark (as symmetric superposition of red+anti-red, blue+anti-blue, and green+anti-green (so-called meson) [14].

⁹The potential energy between two quarks, q and \bar{q} , for example, is phenomenologically known to be linear with a separation distance, i.e. $V(r) \sim r$

than keeping the color flux in the field growing.

2.2. QCD Phase Diagram

Thermodynamically distinct phase of matter is often presented in the form of a phase diagram. A phase diagram of the nuclear matter exhibits a rich structure with distinct phases at a different combination of temperature and density due to the properties of strong interaction. However, the detailed phase structure is not well established either experimentally and theoretically, and thus it is subject to extensive studies. When crossing boundary between different phases, a phase transition is expected to occur. The phase transition in general is characterized by the order of the derivative (i.e., n^{th} -order) of one or more state variables (e.g., Gibbs free energy) with respect to some thermodynamic variables such as temperature and pressure¹⁰.

QCD Phase Diagram

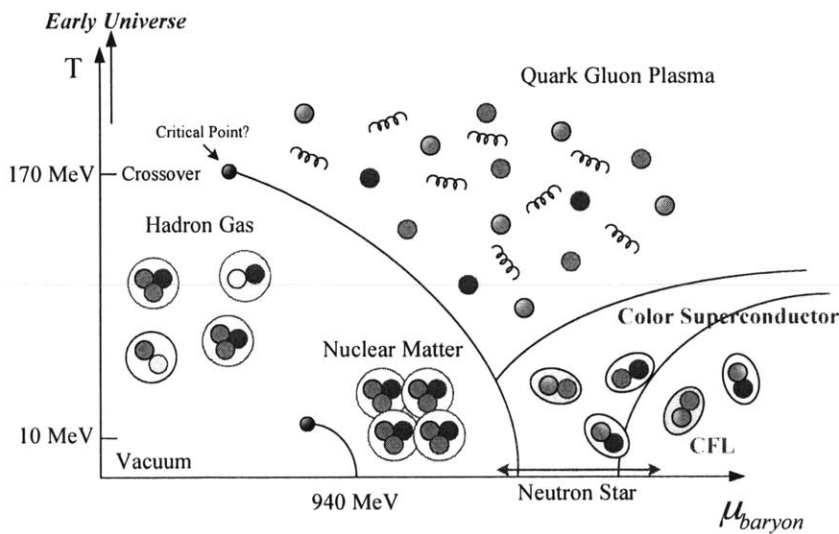


Figure 2.3.: Schematic phase diagram of nuclear matter as a function of temperature and baryon chemical potential [15]. (see text)

A schematic diagram in Fig. 2.3 shows our current understanding of nuclear matter phase as a function of temperature T (y -axis) and baryon chemical potential μ_B

¹⁰The first-order phase transitions are discontinuous in entropy and volume, which are both first derivative of the Gibbs free energy, for example, $G(p, T) = U + pV - TS$, where U is the internal energy, p is pressure, V is volume, T is the temperature and S is the entropy. The phase transition between liquid and vapour below a critical temperature is first-order. Second-order phase transitions are continuous in the first derivative, but exhibit discontinuity in a second derivative.

2. Motivation

(x -axis). The baryon chemical potential is defined as the Gibbs energy¹¹ required to add or remove a baryon at fixed pressure and temperature and is proportional to the net baryon density, which is defined as baryon density subtracted by anti-baryon density. Figure 2.3 is based on a body of experimental and theoretical results, including various model calculations, perturbative calculations in asymptotic regimes, and lattice calculation from the first principle. While the exact locations of distinct phases in the diagram and boundaries between them are uncertain and therefore subjects to further studies, semi-quantitative thermodynamic description of the phase diagram can be made.

As well known from the matter surrounding us, at low temperature quarks and gluons are bound in hadrons, mostly nucleons around us, e.g., proton and neutron, which are in turn bound together forming nuclei under normal conditions. Staying below the temperature of the order of the nuclear binding energy ($\approx 1-10$ MeV), a first-order phase transition of ‘liquid’ nuclear matter into a gas of individual nucleons takes place when the baryon chemical potential increases [16]. This gaseous state is referred to as hadronic gas. The phase transition ends at a critical point at the temperature around 10 MeV, which is indicated in the bottom-middle of Fig. 2.3.

As the net baryon densities increases (i.e., along the x -axis) staying close to $T \sim 0$ (i.e., staying with ‘cold’ nuclear matter), the aforementioned hadronic phase experiences a first-order phase transition to color superconducting phases [17], where a degenerate Fermi liquid of quark, with a condensate of Cooper pair¹² near the Fermi surface is formed. It is possible since the strong interaction becomes weaker, allowing the quarks near the Fermi surface almost free, and the interaction in some quark interaction channels is attractive [19]. Depending on how many colors and quark flavors can effectively form the Cooper pair, the color superconducting phase is divided into two distinctive phases, two-flavor superconducting phase (so-called ‘2SC’ phase) and Color-Flavor Locked (CFL) phase. In the 2SC phase, only two out of three colors as well as two out of the three ‘light’ flavors (u and d quark)¹³ are involved in the forming of the Cooper pair. At even higher baryon density ($\mu_B \gg m_s$), where QCD coupling becomes even weaker, the CFL phase starts to be dominant resulting in the CFL quark matter. The Cooper pair in this regime is formed from all three colors and the three flavors (u, d , and s). While the two phases may be realized in the core of neutron stars with interesting phenomenological consequences [19, 21], it is not yet found experimentally whether the core of the neutron star is dense enough to create such phases. A detailed review of the color superconducting phase can be found from Ref. [19].

Now moving along the y -axis (i.e., changing the temperature), regardless of the

¹¹It is similarly defined for the internal energy (U) with a fixed entropy and volume, and for the enthalpy (H) with a fixed entropy and pressure instead.

¹²The Cooper pair is two electrons (or fermions in general) that are bound by net attractive force (e.g., via an exchange of phonon, the quanta of lattice vibration energy). While an electron is a fermion, the pair of electron behaves as a boson and therefore can form a condensate that leads to superconductivity in a certain condition [18].

¹³ c, b, t quarks do not play a major role at the density scale of interest because of their much larger masses [20].

baryon chemical potential, there exists a universal matter phase at sufficiently high temperature, known as Quark-Gluon Plasma (QGP)¹⁴ [3–5]. QGP phase is the phase where the quarks are liberated from hadrons, known as color deconfinement and freely moving in an extended volume. The transition to the QGP phase can occur with or without the first-order phase transition depending on μ_B , which is indicated by the solid line and by ‘Crossover’, respectively, in Fig. 2.3. The crossover implies there is no ordered transition with smooth changes of state variables. The end of the first-order phase transition or the crossover is marked by a point in the phase diagram, known as a critical point. While the existence of the crossover region close to $\mu_B \sim 0$ and the critical point in turn is supported by the rigorous Lattice-QCD (LQCD) calculations [23, 24]¹⁵, the precise location of critical point being very dependent on the model assumptions is yet uncertain [25].

The energy density and the temperature that are required for the QGP phase transition along the x -axis (i.e., $\mu_B = 0$) are estimated to be, $\epsilon_c \simeq 700 \text{ GeV/fm}^3$ and $T_c \approx 140\text{--}200 \text{ MeV}$, respectively, based on the aforementioned LQCD calculations [23, 26–28] as well as on the more recent calculation [29]. Figure 2.4 shows such result in Ref. [26, 27] in the form of the energy density as a function of temperature. It clearly shows energy density increases rapidly around $T \simeq 170 \text{ MeV}$, indicating that the relevant number of degree of freedom increases due to the liberation of quark and gluon from hadrons. The y -axis is expressed as a fraction of T^4 to compare with Stefan-Boltzmann prediction¹⁶. Well above T_c , the energy density flattens out reaching the energy density only about 20% below the energy density in Stefan-Boltzmann (SB) limit (i.e., non-interacting gas of massless quark and gluon). It is noted that the attainable temperature at the RHIC is already above T_c and at the LHC it is at least three times higher than the calculated critical temperature needed for the QGP phase transition, as marked in Fig. 2.4.

While the energy density attainable at RHIC and LHC being 20% lower than the SB limit is somewhat contradictory to the naïve expectation of non-interacting system of quarks and gluons due to the asymptotically vanishing interaction at a short distance scale, there exist firm evidences that the system created in the heavy-ion collisions exhibits significant interaction among its constituents, one of the most important discoveries at RHIC, which will be elaborated in the forthcoming section (Sec. 2.3). Moreover, the non-perturbative calculations of the energy density based on the AdS/CFT correspondence [30, 31], albeit with an assumption of large number of quark flavors (referred to as large- N limit), shows quantitatively similar trend supporting the lattice-based calculations.

¹⁴It has also been called with different terms such as strongly-coupled QGP (sQGP) [22], weakly-coupled QGP (wQGP), or Quark Gluon Liquid, referring to specific properties of this new state of matter.

¹⁵Lattice-QCD calculations solve the QCD Lagrangian after discretizing it on a discrete Euclidean space-time lattice, thereby overcoming a difficulty of numerical calculation of the QCD Lagrangian in strongly interacting regime [20]. Yet, it requires formidable computational power for the calculations.

¹⁶Stefan-Boltzmann prediction of $\epsilon_{SB} = 3P_{SB}$, where $P_{SB} = N_{d.o.f} \times (\pi^2/90) T^4$. For a system with only pions ($\mu_B \sim 0$) of three charges neglecting their mass, $\epsilon/T^4 \sim 3 \times 3 \times (\pi^2/90) \sim 1$. For QGP with three light quark flavors, $\epsilon/T^4 = (\epsilon_{\text{gluon}} + (7/8) \times \epsilon_{\text{quark}})/T^4 = (\pi^2/90) \times (2_{\text{spin}} \times 8_{\text{colors}} + (7/8) \times 2_{\text{spin}} \times 2_{q\bar{q}} \times 3_{\text{colors}} \times 3_{\text{flavors}}) \sim 12$, as shown in Fig. 2.4. The factor of 7/8 appeared to account for a different statistics between Fermion and Boson.

2. Motivation

At a finite non-zero baryon chemical potential in the finite temperature regime, the first-order transition is expected with the critical temperature decreasing as the baryon chemical potential increases. This is the regime where a numerical calculation of the QCD Lagrangian is notoriously difficult, so it is more rigorously studied based on effective theories with model calculations as well as the ‘low’ energy heavy-ion collision experiments [20].

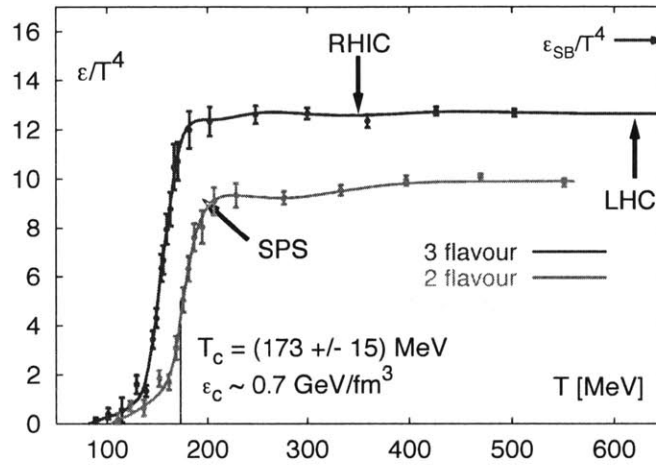


Figure 2.4.: LQCD calculation of ϵ/T^4 as a function of T with different number of quark flavors up to three (u, d, s) with equal mass and two equal and one heavier mass scenarios [26, 27]. Also shown is the energy density estimated based on the Bjorken formula [32] (see also Sec. 2.3.2) in the initial stage of heavy-ion collisions at the SPS, RHIC, and LHC.

2.3. Relativistic Heavy Ion Collisions

Extremely hot and dense nuclear matter can be created in head-on collisions of heavy ions, with large amount of energy concentrated in a small volume for a very short period of time from the near simultaneous collision of many nucleons. In a head-on collision of Pb ions at the LHC, for example, up to about 1900 nucleon-nucleon collisions [33] can take place with $\sim \mathcal{O}(1)$ TeV energy concentrated in a central region [34]. Collisions of heavy ions followed by the detailed analysis of detected signals being the most useful tool to study experimentally the nuclear matter in the domain of extreme temperature and density have been pursued for more than two decades¹⁷. A wealth of interesting

¹⁷The Alternating Gradient Synchrotron (AGS) at Brookhaven studied the collisions of ‘light nuclei’ such as sulphur (^{32}S) and silicon (^{28}S) from $\sqrt{s_{\text{NN}}} = 2.5$ to 4.3 GeV. The AGS is currently used as an injector for the RHIC. The Super Proton Synchrotron (SPS) at CERN studied the collisions of sulphur (^{32}S) as well as lead (^{208}Pb) from $\sqrt{s_{\text{NN}}} = 8$ to 17.3 GeV.

2.3. Relativistic Heavy Ion Collisions

and intriguing results have been produced from the analyses of the heavy ion collisions, relating various observables with the properties of the produced matter in heavy ion collisions [35, 36]

Before the advent of the Large Hadron Collider (LHC), the highest energy heavy ion collisions was achieved at Brookhaven's Relativistic Heavy Ion Collider (RHIC), where billions of d+Au, Cu+Cu, and Au+Au collisions have been recorded at energies up to $\sqrt{s_{NN}} = 200$ GeV¹⁸ [37]. At RHIC, a series of measurements were made supporting unambiguously that the initial energy density reached in the collision is considerably higher than the critical energy density¹⁹ [39, 40]. At the same time, intriguing evidences that the constituents of the produced matter with large density interact strongly in contrast to a naive expectation of weakly interacting system with small coupling constant were found. The evidence are based on the interpretations of two interesting observations, 'azimuthal anisotropy' and 'jet quenching'.

The azimuthal anisotropy refers to the anisotropy of produced particles in the azimuthal direction with respect to the reaction plane, which was defined by the line between the center of nuclei (i.e., impact parameter, b) and the direction of incoming nuclei (i.e., beam direction, z). In the off-center collisions of incoming nuclei (i.e., $0 < b < 2R_{\text{nuclei}}$), the overlap region has an asymmetric shape, often referred to as an 'almond shape', causing anisotropic origin of particle productions in space. If the quarks and gluons behave collectively with strong interaction between them, the pressure gradient can be built during the system expansion²⁰ resulting in an anisotropic azimuthal distribution of the out-going particles. The magnitude of the azimuthal anisotropy is characterized by the amplitude of the second term, known as v_2 or 'elliptic flow', in the Fourier expansion of the azimuthal distribution of final-state out-going particles, $dN/d\phi$. Non-zero, in fact, unexpectedly large azimuthal anisotropy observed in the RHIC data indicates that the quarks and gluons inside the medium indeed interact strongly to the extent that the systems resembles more closely a liquid than an weakly interacting ideal gas. A detailed comparison with ideal hydrodynamic calculations also reveals that the local thermal equilibrium (i.e., thermalization) should take place in a very short time scale (< 1 fm/c)²¹ implying that the thermalization is achieved in a very early stage of the evolution [42–44]. Furthermore, an observation that v_2 of meson and baryon scale with the number of constituent quarks, $n_q = 2$ and 3, for meson and baryon, respectively, further supports the interpretation that the system behaves collectively with the partonic degree of freedoms rather than with hadronic degree of freedoms [45, 46].

¹⁸NN refers to the Nucleon-Nucleon and it means, for example, 200 GeV center-of-mass energy per nucleon pair, i.e., $\sqrt{s_{NN}}$ multiplied by the the number of nucleons in a nucleus gives the total center-of-mass energy in nucleus-nucleus collision.

¹⁹Also, the initial temperature is estimated based on the measurement of the enhanced direct photon yield to be between 300-600 MeV [38], which is higher than the critical temperature.

²⁰The system expands and cools down quickly as a consequence of the large excess of pressure built in the medium with respect to the surrounding, i.e., vacuum.

²¹It is further supported by the calculation made based on the gauge/gravity duality (i.e., AdS/CFT) description of the strongly coupled system [41]. 1 fm/c corresponds to 3.336×10^{-24} sec.

2. Motivation

The observation of jet quenching in the RHIC data supports the idea of strongly interacting medium, but it provides different insight to the medium produced in heavy ion collisions, which is discussed in more details in the following section 2.4. A thorough overview of the experimental and theoretical results in heavy ion collisions made at RHIC can be found from the proceedings of the ‘Quark Matter’ conference series [47–51] and from the ‘White Papers’ from the four RHIC experiments [52–55].

The highest collision of heavy ion was recently achieved in 2010 at the LHC with 2.76 TeV center-of-mass energy per nucleon pair. The collision of Pb ions at such high energy allows to probe the produced matter at unprecedentedly high energy density, which is generally accepted to be far beyond the critical temperature of the QGP phase transition as shown in Fig. 2.4. The abundant production of particles with large momentum transfer involved such as quarks or gluons, various resonances (J/ψ , ψ' , Υ and so on), Z^0 , W^\pm and photon-jet events, known as ‘hard-probe’ in particular allows to study various properties of the medium in a ‘tomographic’ manner [56], potentially opening a new era in the history of heavy ion physics.

2.3.1. Evolution of Hot and Dense Matter

The space-time evolution of the produced medium can be viewed with different characteristic stages that follow subsequently in time. The picture for the evolution of hot and dense matter that follows is based on reasoning and theoretical model calculations but only partly based on experimental observations because experimentally only the final state products are studied, which may or may not carry the information about the different stages of the evolution. Therefore, the picture below is largely model-dependent.

Before a collision, the two incoming nuclei are envisaged as two highly squeezed ‘pancakes’ due to Lorentz contraction when viewed from a lab reference frame. At the instance of collision, near-simultaneous collisions of many nucleons take place with a chance of large momentum transfer between two partons inside the nucleons, ‘hard-scattering’. The resulting system with the squeezed nuclear matter over an extended volume begins to expand and cool down rapidly as a result of the pressure gradient established between the system created and the surrounding vacuum. During the expansion, the constituents²² interact through elastic or inelastic (re-)scattering.

During the expansion the system evolves from the partonic matter (QGP) to the hadronic matter. In this evolution, there are two characteristic stages, known as ‘freeze-out’. One is chemical freeze-out and the other one is thermal freeze-out [57], as shown as a dotted line between the QGP phase and the hadron phase and as solid line at the end of the evolution in Fig. 2.5, respectively. When the system cools down to a some temperature below T_c , hadrons begin to form out of ‘soup’ of the quarks and gluons. This is known as chemical freeze-out. The chemical freeze-out marks the end of all the inelastic interaction and the fixation of hadron abundances. The system now consisting of the hadronic gas further cools down and at some point when the interaction rate be-

²²The constituents can be either partons, hadrons, or mixtures of them, depending on the stage of the evolution.

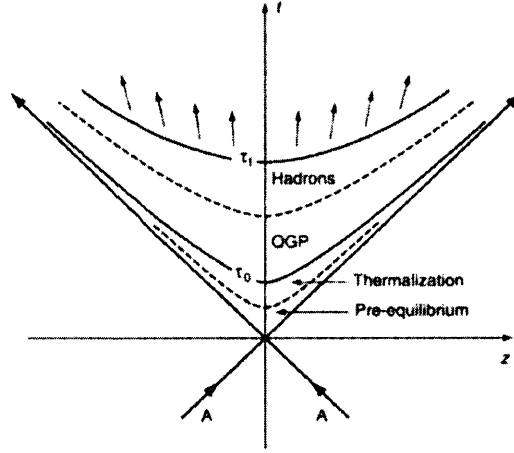


Figure 2.5.: Schematic light-cone diagram of the (longitudinal) evolution of hot and dense system created in the collision of heavy ions [36]. The hyperbolic lines represent the contours of constant proper time τ .

tween the hadrons is not high enough to maintain the thermalization, the momentum of each hadron is fixed and the hadrons stream away freely, which is in the end being detected by an experimental apparatus. This is known as thermal (or kinetic) freeze-out. From the studies of the abundances of produced hadron species in heavy-ion collisions, whose relative abundance is well described by a simple statistical model, a temperature and a baryon chemical potential at the point of chemical freeze-out can be measured for a given center-of-mass energy [20, 36].

2.3.2. Energy Density

The energy density achieved in heavy ion collision at a given time, t , in the central mid-rapidity region (i.e., 90 degree with respect to the beam direction) can be estimated based on the approach by Bjorken [32] as

$$\epsilon_{Bj}(t) \approx \frac{d\langle E_T \rangle}{dy} \times \left(\frac{1}{2t_0 \mathcal{A}} \right) \left(= \frac{\text{total energy contained in a volume}}{\text{volume}} \right) \quad (2.3)$$

where $d\langle E_T \rangle/dy$ is the traverse energy per unit rapidity in the mid-rapidity region, \mathcal{A} is the transverse area of the incident nuclei, and t_0 is the formation time, i.e., time elapsed until the thermalized deconfined matter is formed. At the LHC, for example, where $d\langle E_T \rangle/dy$ is measured as 2.1 TeV in the mid-rapidity for the events with near-head-on collisions [34] and \mathcal{A} can be estimated by $\pi \times (R_{\text{nuclei}})^2 = \pi \times (7\text{fm})^2$, with an assumption for the formation time of $t_0 \sim 1.0 \text{ fm}/c$, it is estimated to be about $7 \text{ GeV}/\text{fm}^3$, which is approximately three to four times larger than the energy density that can be estimated

2. Motivation

for RHIC²³. While this approach is considered as lower limit as it is based on a simple assumption that the volume is approximated as a cylinder with transverse area equal to that of a gold nucleus with a length growing as a function of time during the expansion. Also it doesn't take into accounts effects from longitudinal evolution. Nonetheless, it is already about 10 times higher than the expected critical energy density ($\epsilon_c \sim 0.7$ GeV/fm³) for the deconfinement of the quarks and gluons.

2.4. Jet Quenching

Jet quenching refers to a phenomenon that out-going quarks or gluons (i.e., partons) produced from a hard-scattering of incoming partons lose its energy due to the interaction with hot, dense medium created in heavy-ion collisions. It is called jet quenching because the collimated spray of hadrons, i.e., jet, is expected to be attenuated or disappeared as a consequence of the energy loss of out-going parton. The idea of jet quenching was first introduced in the early eighties [61–63] and a distinctive evidence of jet quenching was found at the RHIC. The observation has been considered as one of the most important discoveries at the RHIC to date.

Study of jet quenching phenomenology is one of the most useful tools to probe hot, dense medium because the energy loss of parton traversing the medium, $\Delta E = E_{\text{final}} - E_{\text{initial}}$ provides a fundamental information on the properties of the medium [8, 64, 65]. For the hadrons with momentum greater than $\mathcal{O}(1)$ GeV/c, originated from the fragmentation of hard-scattered parton, it involves large momentum transfer (Q^2 , where Q^2 is defined as four-momentum squared known as virtuality) in the hard-scattering of incoming partons. It implies that hard-scattered partons are produced in a very short time scale, $t \sim \mathcal{O}(1/Q)$, and therefore they have enough time to traverse, interacting with the produced medium. The jet quenching can be seen in an analogous way from a charged particle with a known charge and energy passing through matter, where the energy loss (or the rate of energy loss per unit path length, $-dE/dx$) depends on the properties of the matter such as the electron density, the mean excitation potential of the target material and so on²⁴ [8]. Because of this possibility of probing inside and extracting information about the medium via the attenuation pattern of highly energetic parton passing through the medium, the jet quenching is often referred to as ‘tomography’ of heavy-ion collisions.

²³More precise estimation of the energy density can be made. See Ref. [55, 58–60]

²⁴For the moderately relativistic heavy charged particles, for example, the average energy loss per path length can be described by the Bethe–Block formula, $-(dE/dx) \propto K z^2 \frac{Z}{A} \frac{1}{\beta^2}$, where Z is the atomic number of absorber, A is the atomic mass of the absorber, z is the charge number of incident particle, and β is the fractional speed of the incident particle, i.e., v/c . A detailed description of the formula can be found in the section, “Passage of particle through matter” from Ref. [8]

2.4.1. Energy Loss Mechanisms

The total energy loss of a quark or a gluon traversing a medium is the sum of the energy losses due to two dominant mechanisms [64], collisional energy loss and radiative energy loss (i.e. $\Delta E = \Delta E_{\text{coll}} + \Delta E_{\text{rad}}$), which is illustrated with diagrams in Fig. 2.6 for a quark of energy E traversing the medium. It is noted that the collisional energy loss is elastic (i.e., scattering without particle production), but the radiative energy loss is inelastic (i.e., scattering with a production of new particles)

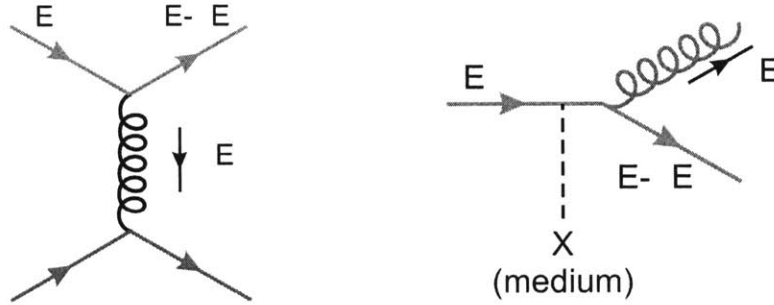


Figure 2.6.: Schematic diagram of collisional and radiative energy loss for a quark with energy E traversing a medium [64]. Note the second diagram takes place in the absence of any medium as well (c.f. the QCD radiation probability which follows the Dokshitzer-Gribov-Lipatov-Altarelli-Parisi (DGALP) evolution equation [8] in vacuum.)

While the energy loss due to the electromagnetic interaction (QED) can also be understood as the sum of the collisional and radiative energy, the energy loss due strong interaction (QCD) is more sophisticated because of the properties of strong interaction such as the running coupling constant (i.e., $\alpha_s(Q)$), the difference of the interaction strength between quark and gluon²⁵, and above all, the presence of gluon self coupling, a direct consequence of non-Abelian nature of QCD interaction.

2.4.2. High-energy Parton Propagation in Medium

2.4.2.1. Collisional Energy Loss in QCD

The collisional energy loss of the quark or gluon due to their interaction with the constituents quark or gluons that comprise the medium, often referred to as thermal quarks or gluons, can be captured in a relatively simple expression of differential cross section formula given [61, 66] by

²⁵The relative strengths of the different quark and gluon interaction vertices are proportional to the 'color factors'; $\alpha_s C_F (q \rightarrow qg)$, $\alpha_s C_A (g \rightarrow gg)$, $\alpha_s T_F (g \rightarrow q\bar{q})$, where $C_A = N_c$, $C_F = (N_c^2 - 1)/2N_c$, and $T_F = 1/2$, as determined from $SU(N_c)$ color group. With three colors, i.e., $N_c = 3$, $C_A = 3$, $C_F = 4/3$, and $T_F = 1/2$ [8].

2. Motivation

$$\frac{d\sigma}{dq^2} \simeq C_i \frac{2\pi\alpha_s^2}{(q^2)^2} \quad (2.4)$$

where the constant, C_i , are 9/4, 1, 4/9, respectively for gg , gq , and qq , and q^2 is the (four) momentum transfer squared. The energy loss per path length in the medium can be obtained by integrating the above cross section over all possible momentum transfer range between the incident quark or gluon with the medium [66],

$$-\frac{dE}{dx} \simeq \frac{4\pi\alpha_s^2 T^2}{3} \left(1 + \frac{N_c}{6}\right) \ln \frac{cE}{\alpha_s T} \quad (2.5)$$

where c is a constant of $\mathcal{O}(1)$ and T is the temperature of the medium. With an energy density and the temperature relation, i.e., $\epsilon \propto T^4$ ²⁶, it can be seen that the collisional energy loss is proportional to the square root of the medium energy density, $dE/dx \sim \alpha_s^2 \sqrt{\epsilon}$, as first pointed out by Bjorken [61], hinting that by measuring the energy loss the initial parton (energy) density can be probed.

For a quark with 20 GeV energy propagating the medium with the temperature $T = 250$ MeV, for example, the collisional energy loss per path length is estimated based on Eq. 2.5 as 0.2–0.3 GeV/fm [67, 68]. Assuming a medium of size $L \sim 10$ fm, the collisional energy loss amounts to about 2–3 GeV, which is only about 10% loss of the initial energy. The collisional energy loss of a quark as a function of initial energy E for individual processes including the additional contributions²⁷ that were not included in the original calculation is calculated in Ref. [69], and is shown in Fig 2.7. One can see from Fig. 2.7 that dE/dx for the 20 GeV quark is estimated to be 0.8 GeV/fm, which is larger than the original estimatin, and attributed to the inclusion of the additional processes with larger $\alpha_s = 0.3$ used in the calculation [69].

As illustrated, the collisional energy loss is small ($dE/dx \simeq \mathcal{O}(1)$ GeV/fm)²⁸ and usually considered as negligible contribution in the calculations of parton energy loss in medium, overtaken by the radiative energy loss (see Sec. 2.4.2.2). However, more detailed studies [69, 71–74] of the collisional energy loss mechanism revealed that the size of the collisional energy loss can be bigger than originally estimated in Ref [61] (as already seen in Fig. 2.7), resulting in a comparable energy loss with the radiative one in a certain kinematic region. The importance of the collisional energy loss for heavier quarks (c , b), in particular, is found highly relevant for the estimation of the total energy loss in medium.

2.4.2.2. Radiative Energy Loss in QCD

The radiative energy loss is mainly caused by gluon radiation induced by multiple scattering of a quark or a gluon traversing the medium, known as medium-induced gluon

²⁶It is estimated in the leading order coupling constant as $\epsilon = (8/15)\pi^2 T^4 (1 + 21N_c/32)$ [61, 66]

²⁷While in the original calculation [61], only the t channel processes are considered (only Compton-like scattering), u and s channels (QCD Mollerand and Bhaba scatterings) are included in this work.

²⁸Note that it can be compared to the energy loss of highly energetic quark propagating hadronic matter, which is estimated to be around the same order [70].

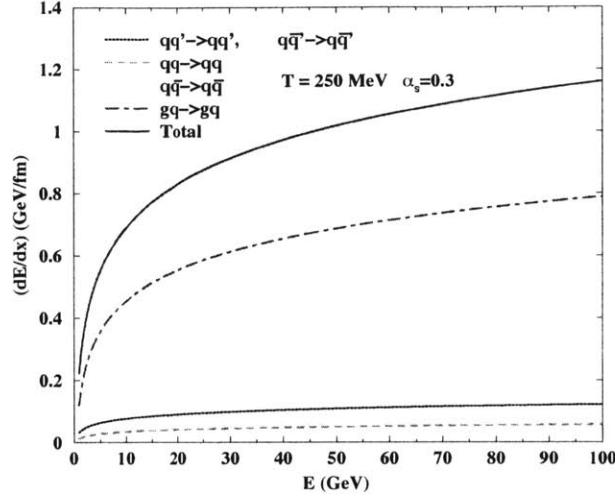


Figure 2.7.: The collisional energy loss of a quark propagating a medium of temperature $T = 250$ MeV with an initial energy E [69]. The prime (') denotes different quark flavors.

radiation (or gluon Bremsstrahlung), and this energy loss mechanism is known to be more efficient than the collisional energy loss in reducing the energy of propagating parton, and therefore can dominate the total energy loss in the high energy regime [66, 75]. Considering a very energetic quark of energy E traversing the medium with a size L , the energy loss due to the medium induced gluon radiation can be obtained with several assumptions and approximations as follows. A thorough review of the radiative energy loss can be found in Ref. [66, 76].

First, the medium is modelled as a collection of independent and static scattering centers as schematically show in Fig. 2.8. The loss of parton energy amounts to the energy carried away by the radiated gluon. The radiated gluon is assumed to suffers the subsequent multiple scatterings in a coherent manner (i.e., many scattering centers acting as a single one) due to the interaction with the medium with the mean free path (λ_g , the subscript g is dropped hereafter), which depends on the density of scattering center in the medium (ρ) and the scattering cross section (σ) via $\lambda = 1/\rho\sigma$. As a useful variable that characterises the medium, μ is introduced as the Debye screening mass (an inverse of Debye screening length²⁹). It also characterizes the typical momentum exchange with the medium. With the assumption of independent scattering center, the mean free path λ of the propagating parton is considered much larger than the Debye screening length (i.e., the inverse of the Debye screening mass μ), that is, $\mu^{-1} \ll \lambda$.

In each collision on a scattering center, the gluon receives momentum of k_{\perp} in the transverse direction, which is typically about the same as μ . After N_{coh} (coherent) scat-

²⁹The Debye length is a characteristic length scale over which a long range interaction (Coulomb potential) is effectively screened.

2. Motivation

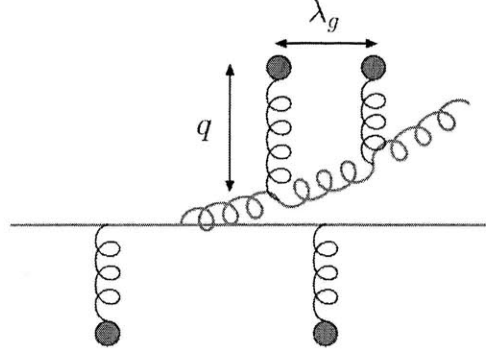


Figure 2.8.: A schematic of a typical gluon radiation diagrams in the presence of the medium (courtesy of M. van Leeuwen). The blue circle represents the scattering center and the red wiggled-line represents the radiated gluon.

terings, therefore, the gluon acquires a total momentum k_T in the transverse direction with respect to the direction the parton is propagating to

$$\langle k_T^2 \rangle \simeq N_{coh} \mu^2 \quad (2.6)$$

with $N_{coh} = l_{coh} / \lambda$, where l_{coh} is the path length travelled by the propagating parton during the emission of the gluon. The emission of gluon involves a formation time (t_{coh}), which is the minimum time needed for a quanta to be resolved from the incident parton, i.e., to become an independent quanta. The formation (or coherence) time in the gluon reference frame t_{coh}^{gluon} can be expressed as $t_{coh}^{gluon} \sim 1/k_T$ ³⁰. When the energy of the emitted gluon is w , this means the formation time, and therefore the coherence length in the lab reference frame can be expressed with the small angle approximation, i.e., $\theta \sim k_T/w$ as

$$t_{coh} = l_{coh} \simeq \frac{2w}{\langle k_T^2 \rangle} \quad (2.7)$$

Using Eq. 2.6 it can be rewritten as

$$l_{coh} = \sqrt{\frac{2w\lambda}{\mu^2}} \quad (2.8)$$

The average momentum transferred squared μ^2 from the medium to the gluon per mean free path is conveniently defined as

$$\hat{q} \equiv \frac{\mu^2}{\lambda} \quad (2.9)$$

³⁰ $E t \sim \hbar$

which is commonly used in characterizing the ‘stopping power’ of medium and known as a transport coefficient, pronounced as ‘que-hat’. Therefore, in a thick medium where $\lambda < l_{coh} < L$ (i.e., $\lambda \ll L$) known as Landau-Pomeranchuk-Migdal (LPM) regime, the gluons will be emitted up to a characteristic energy ω_c , which is defined as the radiated energy when $l_{coh} = L$

$$\omega_c \equiv \frac{1}{2} \frac{\mu^2 L^2}{\lambda} = \frac{1}{2} \hat{q} L^2 \quad (2.10)$$

Finally, the energy spectrum of radiated gluon per path length estimated in the LPM regime as

$$\omega \frac{dI}{d\omega dx} \simeq \alpha_s C_R \sqrt{\frac{\mu^2}{\omega \lambda}} = \alpha_s C_R \sqrt{\frac{\hat{q}}{\omega}} \quad (2.11)$$

where C_R is C_F for a quark and C_A for a gluon³¹. Over the entire path length L ,

$$\omega \frac{dI}{d\omega} \simeq \alpha_s C_R \sqrt{\frac{\hat{q}}{\omega}} L = \alpha_s C_R \sqrt{\frac{\hat{q} L^2}{\omega}} = \alpha_s C_R \sqrt{\frac{2\omega_c}{\omega}} \quad (2.12)$$

Now the average medium-induced energy loss can be obtained by integrating the energy spectrum up to the characteristic energy scale ω_c

$$\langle \Delta E \rangle = \int_0^{\omega_c} \omega \frac{dI}{d\omega} d\omega \simeq \alpha_s C_R \omega_c \propto \alpha_s C_R \hat{q} L^2 \quad (2.13)$$

As can be seen from this equation, the energy loss is larger by a factor of 9/4 for a gluon than for a quark traversing the medium because of the color factor C_R . It is interesting to see that the average energy loss due to the medium induced gluon radiation in this LPM regime is proportional to L^2 . Note that in the same LPM regime, the radiative energy loss in QED is proportional to L [64]. From the L^2 dependence, it can be inferred that $dE/dx \propto L$, which can be also derived directly by integrating Eq. 2.11 over ω in the range $0 < \omega < E$ [66]. While this linear L dependency in dE/dx (quadratic dependence in ΔE , equivalently) is not immediately intuitive, it can be understood as follows.

The hard momentum transfer involves ‘close’ collision, which can be treated ‘microscopically’ and the resulting energy loss per path length should not be dependent on the size of the medium (only the total energy loss does) since the involved scale is much smaller than the size of the medium. On the other hand, the soft momentum transfer involves ‘distant’ collisions from many scattering centres acting coherently as a single one³². It implies that the energy of the softly emitted gluon per path length travelled

³¹There are several steps involved in Eq. 2.11. First, $\omega \frac{dI}{d\omega dx} \simeq \frac{1}{l_{coh}} \frac{\omega dI}{d\omega}$ because the scattering centers act as a single scattering center. Second, $\omega \frac{dI}{d\omega} \simeq \frac{\alpha_s}{\pi} C_R$ for the single scattering spectrum in the soft ω limit [77].

³²The de Broglie wave length of the exchanged particle is comparable to the inter-scattering spacing,

2. Motivation

is dependent on the maximum coherent scattering length, i.e., the size of a medium L because the gluon can radiate up to the characteristic energy ω_c , which is essentially determined by the size of the medium. Knowing $dE/dx \propto L, L^2$ dependence of the total energy loss ΔE is evident. The argument, of course, is valid only in the regime where the mean free path is much smaller than the size of the medium with many coherent scattering taking place before exiting the medium, i.e., LPM regime.

Also interesting is that the energy loss in the above formalism is independent of the initial parton energy E , as found in Ref. [78–80]. It is noted, however, depending on the way the medium-induced gluon radiation is formulated, (logarithmic) E dependency is retained in different models [81–83]. The radiative energy loss of a quark as well as a gluon as a function of initial energy E is calculated in Ref. [69] using the formula found in Ref [84], which has the logarithmic E dependence. The result is shown for ΔE in Fig 2.9 in comparison to the collisional energy loss in the same initial energy range. It can be clearly seen that for $E > 10$ GeV, the radiative energy loss is a dominant source of the total energy loss in medium for both quark and gluon.

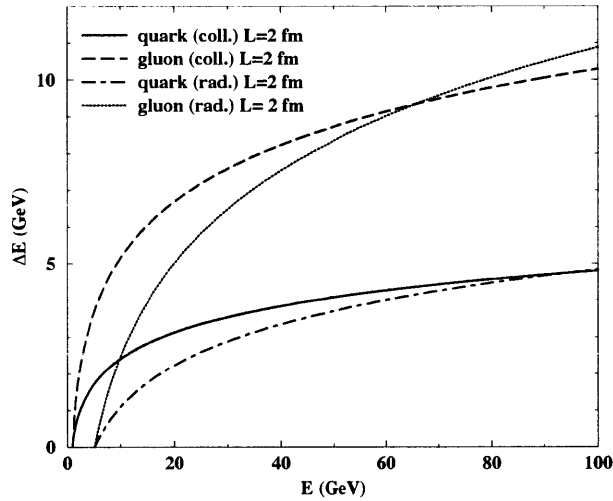


Figure 2.9.: The radiative energy loss of a quark and a gluon propagating a medium with an initial energy E [69].

While non-trivial simplifications with various approximations are involved in the aforementioned formalisms of the medium induced gluon radiation, it is regarded as an important piece for the understanding of jet quenching phenomenology in the field of heavy-ion physics [85].

therefore instead of the individual scattering, the total scatter should be considered for the energy loss.

2.4.3. Nuclear Modification Factor R_{AA}

One of the interesting phenomenological consequences of jet quenching is the modified energy spectrum of jet and in turn of charged particles, dominated by hadrons originating from parton fragmentation. The modified charged particle spectrum can be quantified by comparing the charged particle spectrum in nucleus-nucleus (AA) to the charged particle spectrum in nucleon-nucleon (NN) collision, often referred to as ‘baseline spectrum’. It is typically expressed in terms of the nuclear modification factor, known as R_{AA} , as a function of transverse momentum (p_T) of produced particles,

$$R_{AA}(p_T) = \frac{d^2 N_{ch}^{AA} / dp_T d\eta}{\langle T_{AA} \rangle d^2 \sigma_{ch}^{NN} / dp_T d\eta} \left(\approx \frac{\text{“hot, dense QCD medium”}}{\text{“QCD vacuum”}} \right) \quad (2.14)$$

where N_{ch}^{AA} and σ_{ch}^{NN} represent the charged particle yield per event in nucleus-nucleus collisions and the charged particle cross section in nucleon-nucleon collisions, respectively. In order to compare the yield of high- p_T charged particles produced in AA and NN collisions, a scaling factor, the nuclear overlap function T_{AA} , is needed to provide a proper normalization at a given impact parameter in AA collisions. This factor is computed as the ratio between the number of binary nucleon-nucleon collisions N_{coll} , calculated from the Glauber model of the nuclear collision geometry [86], and the inelastic nucleon-nucleon (NN) cross section $\sigma_{inel}^{NN} = 64 \pm 5$ mb at $\sqrt{s} = 2.76$ TeV [8]. This normalization scheme, based on the assumption of independent point-like scattering, is known as binary collision scaling or N_{coll} scaling (see Sec 4.0.10.1 for more detailed discussion).

As illustrated inside the parentheses in Eq. 2.14, R_{AA} can be understood as a measure of the final state effect of the hot, dense medium on the produced particles via the comparison to the baseline where no final state effect is present. In the absence of initial- and/or final-state effects on the p_T spectrum in AA collisions, R_{AA} at high p_T is unity by construction with the binary collision scaling.

From the measurement of nuclear modification factor in a control experiment with the collisions of nucleon(s)-nucleus such as pAu or deuteron-gold (dAu), the size of initial-state effect on the R_{AA} measurement can be inferred. Figure 2.10(a) shows one of the R_{AA} measurements made for π^0 and η in dAu collisions at RHIC [87], where the sizeable and strong centrality-dependent suppression observed in AuAu collisions cannot be seen. Based on the measurement, the size of the initial-state effect can be inferred to be smaller than 10%, which is also estimated in the pQCD calculation as discussed in Ref. [64].

While similar experimental observation has not been made at the LHC energy yet³³, the recent measurements [88–90] made by the CMS collaboration on the nuclear modification factor of ‘colorless’ probes such as Z^0 , W and the isolated photon convincingly suggest that no sizeable initial-state effect is present in the PbPb collisions at $\sqrt{s_{NN}} = 200$ GeV. It also establishes the binary scaling within the quoted systematic uncertainty. Figure 2.10 shows a collection of the Z^0 , W and isolated photon R_{AA} measurements as

³³A dedicated pPb run period at LHC is planned to be in the late 2012.

2. Motivation

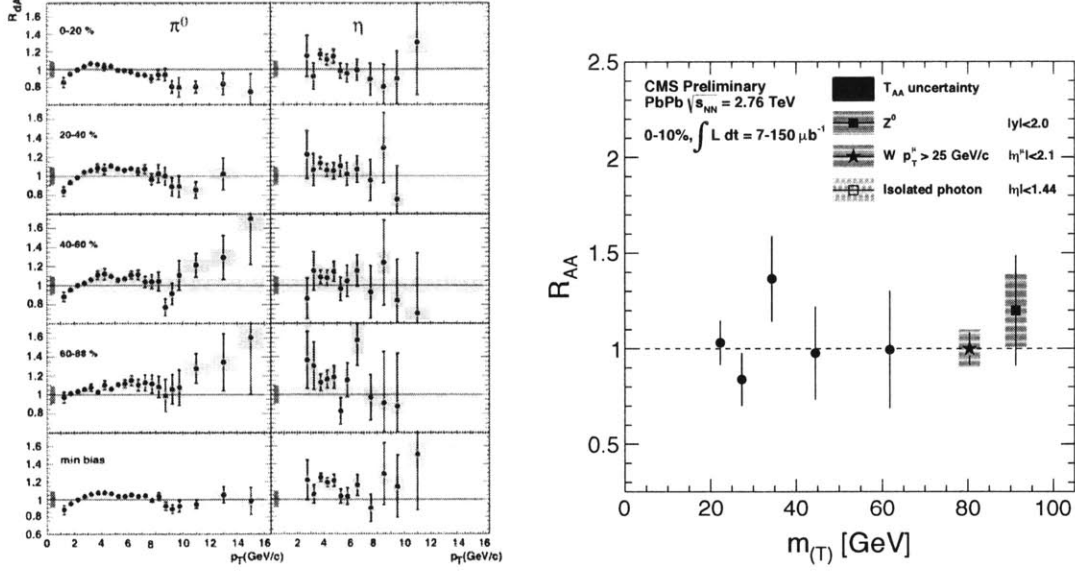


Figure 2.10.: (Left) R_{AA} of π^0 and η in dAu collisions at RHIC [87]. (Right) R_{AA} of the ‘colorless’ probes: Z^0 , W and isolated photon.

a function of m_T , which is defined as $\sqrt{m_{Z^0, W}^2 + p_T^2}$ and used in this plot to compare on an equal footing of hard-scattering scale.

As briefly mentioned in the beginning of this chapter, the quantification of jet quenching via R_{AA} allows comparisons with various theoretical predictions made based on pQCD or AdS/CFT calculations of parton energy loss in a medium. From such comparisons, certain properties of the medium such as an average transport coefficient (\hat{q}) or the initial gluon density dN_g/dy of the expanding medium can be extracted. For example, the average transport coefficient (\hat{q}) or the initial gluon density dN_g/dy are linked to the measured suppression factor via Eq. 2.13 and the GLV modeling [83] of jet quenching, respectively,

$$\langle \Delta E \rangle \propto \alpha_s \langle \hat{q} \rangle L^2 \quad \text{or} \quad \langle \Delta E \rangle \propto \alpha_s^3 C_R \frac{1}{A_\perp} \frac{dN_g}{dy} L \quad (2.15)$$

where A_\perp is the transverse area of the medium before expansion

The use of fast moving parton and its products for the study of jet quenching as a ‘well-calibrated probe’ relies on firm theoretical and experimental grounds of particle production at large momenta. In fact, a direct comparison of various model predictions with the charged particle R_{AA} measurement is possible only when hard-scattered parton production cross section with their probability of fragmenting into charged particle in nucleon-nucleon collision at the same center-of-mass energy of nucleus-nucleus collision is known. In the following sections, a brief review on the theoretical and experimental aspects of the high momentum particle production and the status of R_{AA}

measurements are given.

2.4.3.1. Hadron Productions at Large Transverse Momenta

Hadron production of high transverse momenta particles ($p_T \geq 2 \text{ GeV}/c$), which originates from the fragmentation of hard-scattered partons [91], is theoretically well understood and experimentally well verified. The fragmentation of hard-scattered partons into hadrons is described by the probability of finding a hadron carrying a specific fraction of the parton momentum, known as the fragmentation function (FF). In hadronic collisions, a full description also requires knowledge of the distribution of the initial partons within the colliding hadrons, known as the parton distribution function (PDF). The measurement of the inclusive charged particle p_T spectrum at large transverse momentum, therefore, measures in essence the convolution of three pieces: the hard-parton scattering cross section, the PDFs and the FFs.

Theoretically, in the QCD factorization scheme of hadron-hadron collisions [91, 92], the invariant cross section for inclusive high- p_T hadron production is given by:

$$E_c \frac{d^3\sigma(AB \rightarrow CX)}{d^3p_c} = \frac{1}{\pi} \sum \int_0^1 dx_a \int_0^1 dx_b q_a^A(x_a; Q^2) q_b^B(x_b; Q^2) \frac{1}{z} D_c^c(z; Q^2) \frac{d\hat{\sigma}(ab \rightarrow cd)}{d\hat{t}} \quad (2.16)$$

where the parton distribution function $q_a^A(x_a)$ describes the number density of constituents a within hadron A with longitudinal momentum fraction x_a (in the range $x_a \rightarrow x_a + dx_a$). The fragmentation function $D_c^c(z)$ represents the probability that parton c hadronizes into C carrying a fraction z of the parton energy. Q^2 is the characteristic energy scale of the hard scattering. The LO cross section for the hard scattering of partons a and b at short distance is denoted by $\hat{\sigma}$. The summation is over all partons a , b , c , and d . The hadronization of parton d is implicit in the summation. A direct calculation of Eq. 2.16 is possible up to a certain order in α_s provided that $q_a^A(x_a)$ and $D_c^c(z)$ are given. The formulation of the inclusive cross section in the factorized QCD can be illustrated as,

$$\sigma_{had} = PDF_{a/A} \otimes PDF_{b/B} \otimes \hat{\sigma}(\text{hard parton scattering}) \otimes FF \quad (2.17)$$

On the experimental side, the inclusive charged particle p_T spectra have been measured in pp and $p\bar{p}$ over a wide range of center-of-mass energies from 31 GeV to 1.96 TeV [93–97], and recently at 2.36 TeV at LHC [98, 99]. While p_T range of the previous measurements were limited below 50 GeV/ c , the latest measurements presented and discussed in this thesis extended the p_T reach up to about 200 GeV/ c at $\sqrt{s} = 7 \text{ TeV}$, confirming the validity of factorized QCD for the inclusive hadron production at the highest collider energy to date.

2. Motivation

2.4.3.2. Modified Hadron Spectrum in Heavy Ion Collisions

One of the most exciting results from RHIC was the observation [52–55] of the modified (i.e., suppressed) hadron spectrum in AuAu collisions at $\sqrt{s_{NN}} = 200$ GeV compared to the hadron spectrum in pp collisions at the same center-of-mass energy. The yield of $p_T \sim 5\text{--}10$ GeV/c charged particles was observed to be suppressed in the head-on collisions of heavy-ion by up to a factor of five compared to that in pp collisions (i.e. $R_{AA} \approx 0.2$), indicating that there is strong final state medium effect on the produced particles.

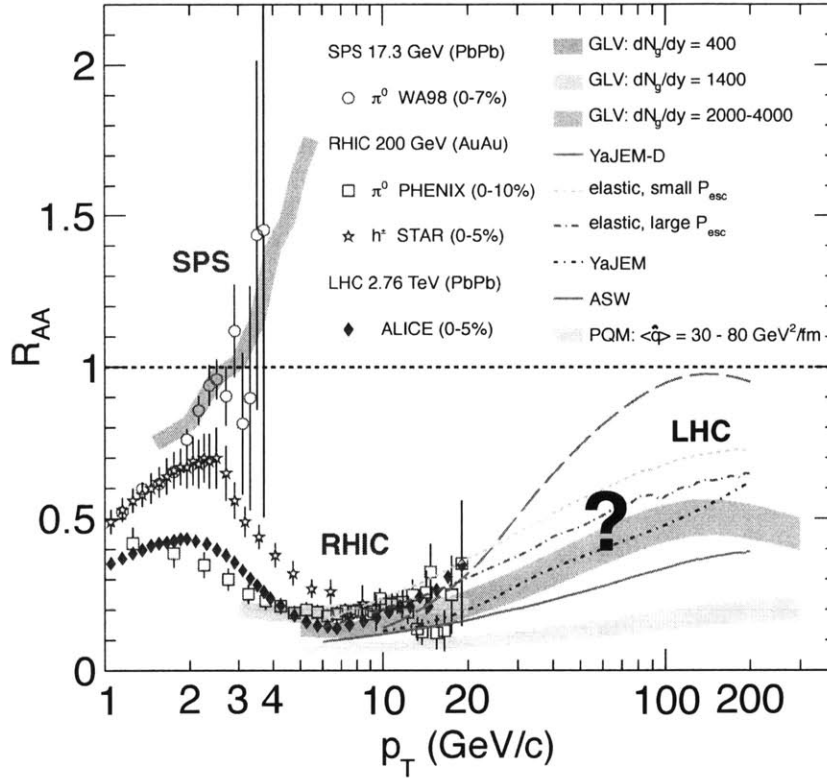


Figure 2.11.: Measurements of the nuclear modification factor R_{AA} in central heavy-ion collisions at three different center-of-mass energies, as a function of p_T , for neutral pions (π^0), charged hadrons (h^\pm), and charged particles [100–104], compared to several theoretical predictions [105–110].

Figure 2.11(a) shows the measurements of R_{AA} at the RHIC not only for hadrons but also for neutral pion π^0 , the latter being less suppressed below $p_T \approx 8$ GeV/c [103, 104] likely due to parton recombination processes that enhance proton production and thus the overall yield of charged hadrons [111]. Also shown is the measurement of R_{AA} for π^0 at $\sqrt{s_{NN}} = 17.3$ GeV at the SPS, where no strong modification is observed, indicating that the final state medium effect is far less stringent, if any, in the low energy PbPb collisions. The rising trends of R_{AA} seen in the low- p_T region ($p_T < 3$ GeV/c) at different center-of-mass energies is interpreted as the consequence of the enhancement

of hadron yield in nucleon-nucleus (NA) or AA collisions compared to NN collisions, known as ‘Cronin effect’ [112, 113]. This enhancement, which is seen more prominently from the measurements in the lower energy NA collisions [112–114], is known to be caused by the multiple scattering of incoming or outgoing parton and/or of the produced hadrons³⁴. The theoretical predictions of GLV made for the two center-of-mass energy [106, 107] seem to be in good quantitative agreements with the measurements.

At LHC, the charged particle production is found to be about 50% more suppressed below $p_T \approx 10$ GeV/ c , and has the same quantitative suppression value as for neutral pions measured by PHENIX [103]. At higher p_T limited below 20 GeV/ c a similar level of suppression is observed but with an indication of a fast rise (i.e., less suppression) toward the higher momentum region, as shown in Fig. 2.11(a). While the various theoretical model predictions made for the LHC energies (2.76 TeV and 5.5 TeV) have similar level of suppression below 20 GeV/ c and predict the generally rising behavior of R_{AA} , the magnitude of the predicted slope varies greatly between models, depending on the assumptions for the jet-quenching mechanism. Therefore, a measurement up to higher p_T range can clearly help in constraining the quenching parameters used in these models and improve the understanding of parton energy loss in a hot and dense medium.

2.5. Goal of this Thesis

This thesis presents the measurement of phase-space-invariant differential yield, $E d^3 N_{ch}/dp^3$, of primary charged particles in pp and PbPb collisions at $\sqrt{s_{NN}} = 2.76$ TeV and the measurement of nuclear modification factor, R_{AA} , up to $p_T = 100$ GeV/ c . As mentioned earlier, the R_{AA} measurement presented in this thesis should further help in containing the quenching parameters used in various models and improve the understanding of parton energy loss in a hot and dense medium. Comparisons with various model predictions as well as a simple parton energy loss model applied to the PYTHIA MC will be made and discussed.

Also presented is the measurement of phase-space-invariant yield in a lower (0.9 TeV) and a higher (7 TeV) center-of-mass energy pp collisions. From the measured yields at different pp collision energies, the energy-independent scaling behaviour of the inclusive charged particle production known as x_T scaling is studied. To test the scaling, the spectra at 2.76 TeV will be interpolated based on the measurements at different center-of-mass energies using the x_T scaling. The interpolated spectrum will be compared to the measured spectrum. Together with the comparisons to pQCD predictions, the measurements establish the firm experimental ground on the inclusive production of high p_T charged particle over a wide kinematic range at a various collision energies and serve as the well-calibrated probe of the jet quenching measurement.

A key technique used in the spectra analyses is to use the data sampled by the trigger based on the presence of jet in events, so-called jet-trigger. This technique not only al-

³⁴The exact mechanism of the Cronin effect is yet to be understood [115]. In the parton recombination model, for example, the Cronin effect is also described by the parton recombination at the hadronisation rather than the multiple scattering [115].

2. Motivation

lows to enhance the p_T reach of the measurements but also helps to minimize the number of mis-identified tracks in the samples through an implicit use of the calorimeter information, which will be discussed in details in Chap. 4. One of the main challenges in the analysis was to develop the reconstruction algorithms with a set of track quality selections that gives very low rate of mis-identified tracks while maintaining high track reconstruction efficiency in the most dense track environment in PbPb collisions. A detailed discussion will also follow in Chap. 5.

3. The CMS Experiment

The results presented in this thesis are based on the analyses of the pp and PbPb collisions data collected during the period of 2010–2011 by the Compact Muon Solenoid (CMS) experiment, one of the four experiments at the Large Hadron Collider (LHC). After an intense period of commissioning and a short period of pp collisions at center-of-mass energies of 0.9 and 2.36 TeV in 2009 [116], the LHC delivered pp collisions at different center-of-mass energies of 0.9, 2.76 and 7 TeV and PbPb collisions at a center-of-mass energy per nucleon pair of 2.76 TeV, the latter being the highest heavy ion collisions ever achieved in an accelerator. The LHC is scheduled to continue running until the end of 2012 and have a shut-down to prepare for running at a designed center-of-mass energy of 14 TeV in pp and 5.5 TeV in PbPb [117].

3.1. Large Hadron Collider

The Large Hadron Collider (LHC) is a two-ring-superconducting hadron accelerator with a circumference of 26.7 km installed between 45–170 m beneath the ground [118]. The LHC is categorized as a superconducting synchrotron, i.e., it is cyclic at a fixed radius of circulation with the electric field (to accelerate the hadrons or nucleus) and the magnetic field (to keep them in a fixed radius) synchronized with the beams. The LHC was designed to deliver beams of proton (or Pb ions) and collide them with a center-of-mass energy up to 14 TeV (or 5.5 TeV per nucleon pair ¹), equivalently 2.24 (8.8) in micro-joules (μj). The layout of the LHC with CERN accelerator complex is shown in Fig. 3.1. The LHC consists of eight arcs and eight straight sections (not shown in the layout) [118]. The arc is 2.45 km long and it contains the superconducting dipole magnets used for bending, which operates at the nominal magnetic field of 8.33 T [119]. The straight section is 545 m long and it serves as an experimental or utility sections. The two multi-purpose detectors, ATLAS and CMS, are located in the intersections where high luminosity ² beams are delivered and crossed. Two other detectors, ALICE and LHCb, dedicated for heavy ion physics and B-physics are located in the intersections, where relatively lower luminosity beam are delivered and crossed.

¹The center-of-mass energy per nucleon pair in heavy ion collisions is calculated as the center-of-mass energy in pp scaled by the charge-to-mass ratio of the ions, i.e., A/Z for the same magnetic rigidity of the LHC. e.g., for Pb ions, an equivalent center-of-mass energy per nucleon is $14 \text{ TeV} \times (82/208) = 5.5 \text{ TeV}$

²In accelerator physics, the luminosity, often denoted as \mathcal{L} , is defined as the number of particles per unit area pre unit time multiplied by the opacity of the target, which is an important quantity not only for the characterization of the accelerator performance but also for the cross section measurement of a certain interaction.

3. The CMS Experiment

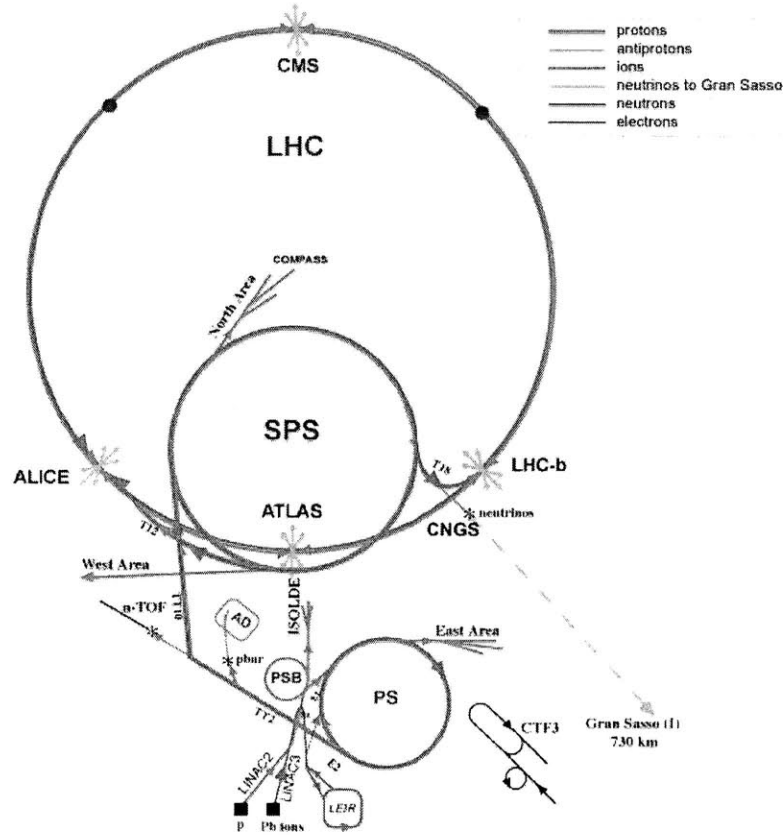


Figure 3.1.: Schematic layout of the CERN accelerator complex [120]

The circulation of the beams inside the LHC rings follows the injection chain in the CERN accelerator complex [121, 122]: First, protons are obtained from the source of hydrogen gas after removing electrons through a cathode chamber inside the Duoplasmatron [123]. Second, the protons from the LINAC2 are injected at an energy of 50 MeV into the PS Booster (PSB), where the protons are boosted to an energy of 1.4 GeV. Third, the protons are sent to the Proton Synchrotron (PS) and to the Super Proton Synchrotron (SPS) sequentially to achieve an energy of 450 GeV. Lastly, they are sent to the two rings of the LHC for final acceleration to boost to an energy of 7 TeV per proton per beam. The injection chain of Pb ions is similar to that of pp except the initial phase of the acceleration before the PS. The Pb ions are generated from the source of heated (temperature around 550°C) purified lead vapour, which are ionized subsequently by an electric current in the LINAC3. The lead ions with different charge states are sent through a carbon foil to select mostly Pb^{54+} . Pb^{54+} ions are accumulated and accelerated in the Low Energy Ion Ring (LEIR), which are sent to the PS and SPS subsequently, where they are sent through a second foil to fully strip electrons to produce a beam of Pb^{82+} ions [121, 122].

3.2. CMS Detector

The Compact Muon Solenoid (CMS) is a multi-purpose detector designed to operate in the highest particle density environments created in pp and PbPb collisions at the center-of-mass energy up to 14 TeV and 5.5 TeV per nucleon pair at luminosities up to $10^{34} \text{ cm}^{-2}\text{s}^{-1}$ and $10^{27} \text{ cm}^{-2}\text{s}^{-1}$, respectively [124]. The CMS, installed about 100 m beneath the ground, has an overall dimension of 21.6 m in length, 14.6 m in diameter, and a total weight of 12500t. The overall layout of the CMS detector is shown in Fig. 3.2. The central feature of the CMS apparatus is a superconducting solenoid of 6 m internal diameter, providing an axial magnetic field of 3.8 T. Immersed in the magnetic field are the pixel tracker, the silicon strip tracker (SST), the lead tungstate crystal electromagnetic calorimeter (ECAL), and the brass/scintillator hadron calorimeter (HCAL). Muons are measured in gas ionisation detectors embedded in the steel return yoke. The CMS experiment uses a right-handed coordinate system, with the origin at the nominal interaction point, the x -axis pointing to the center of the LHC ring, the y -axis pointing up perpendicular to the plane of the LHC, and the z -axis along the counterclockwise beam direction. The azimuthal angle (ϕ) is measured in the (x, y) plane.

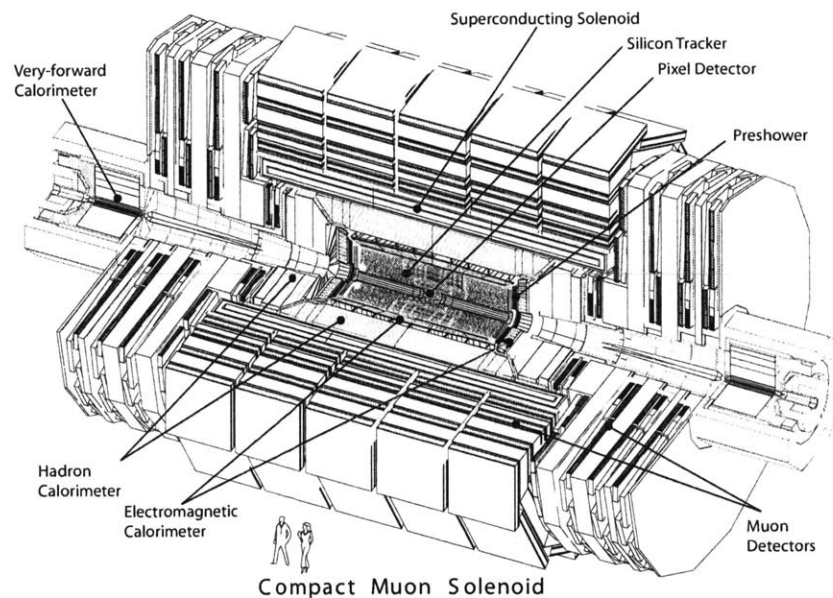


Figure 3.2.: Overall layout of the CMS detector [124]

3.2.1. Tracker

The CMS tracker was designed to measure the trajectories of charged particles originated from pp and PbPb collisions within the nominal pseudorapidity range $|\eta| < 2.4$ inside a 3.8 T axial magnetic field. It is also capable of measuring the precise positions

3. The CMS Experiment

of the primary vertex (i.e., collision points) and the secondary vertex within $10\text{--}20\ \mu\text{m}$ resolution. It consists of two main components: silicon pixel detector and silicon strip detector (SST). The detailed descriptions of each component are found in the following sections, Sec. 3.2.1.1 and Sec. 3.2.1.2.

The overall layout of the CMS tracker is shown in Fig 3.3. The silicon pixel detector covers 4 to 15 cm in radius and 49 cm on either side of the nominal collision points along the LHC beam line. The silicon strip detector covers 25 to 110 cm in radius and 280 cm on either side of the nominal collision points along the LHC beam line. Further dissection of the CMS tracker as shown in Fig 3.3 is as follows. The three cylindrical layers of the pixel detector modules are located at a radii of 4.4, 7.3 and 10.2 cm with two disks of the pixel detector modules on each side of the three layers. From the inside out, the next four layers of the silicon strip detectors modules (Tracker Inner Barrel, TIB) with three disks (Tracker Inner Disk, TID) on each side are located between 20–55 cm in radius, surrounded by six layers of the silicon strip modules (Tracker Outer Barrel, TOB). The Tracker EndCap (TEC), consisting of nine layers, are located on each side of the TIB and TOB in between 22.5 and 113.5 cm in radius as shown in Fig 3.3.

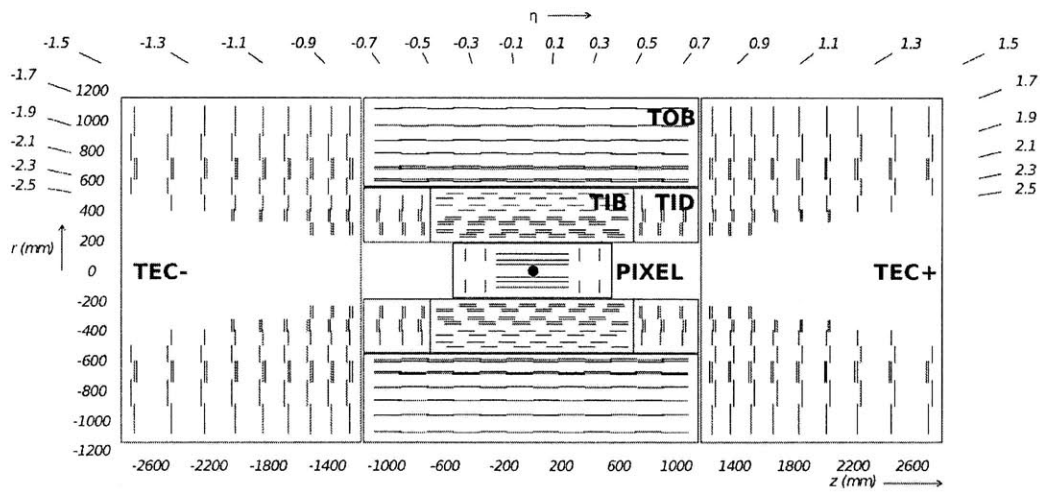


Figure 3.3.: Overall layout of the CMS tracker [124]. A detector module is represented a line with double line indicating modules mounted back-to-back. Also shown is the η coverage of each detector module.

With the axial magnetic field generated by the super-conducting solenoid, the tracker is designed to provide an impact parameter resolution of about $100\ \mu\text{m}$ and a transverse momentum resolution of about 0.7% (5.0%) for 1 (1000) GeV/c charged particles at normal incidence ($\eta = 0$) [125]. The tracker was aligned as described in Ref. [126] using cosmic ray data prior to the LHC commissioning. The precision achieved for the positions of the detector modules with respect to particle trajectories is $3\text{--}4\ \mu\text{m}$ in the barrel.

3.2.1.1. Silicon Pixel Detector

The pixel detector consists of three 53.3 cm-long barrel layers and two endcap disks on each side of the barrel section. The innermost barrel layer has a radius of 4.4 cm, while for the second and third layers the radii are 7.3 cm and 10.2 cm, respectively as discussed in 3.2.1. There's a total of 66 million active pixels with an area of about 1 m². The pixel detector provides up to three precise measurement points, 'hits', with efficient η coverage depending on the number of hits³.

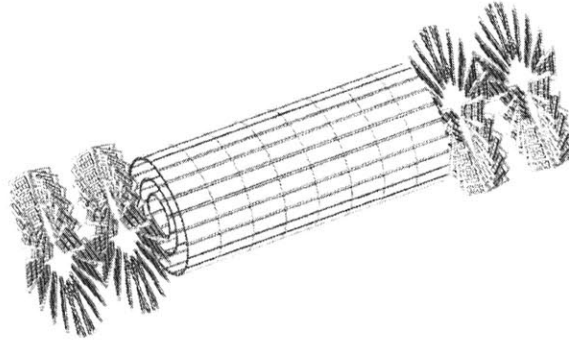


Figure 3.4.: Schematic view of the CMS pixel system. The forward pixel detectors (FPix) are in turbine-like geometry tilted by 20° [127].

The active pixel has a dimension of $100 \times 150 \mu\text{m}^2$, which allows similar resolution in $r-\phi$ and z directions⁴.

Subsystem	No. layers (or disks)	Direction	Resolution
Barrel Pixel (BPix)	3 layers	$r-\phi \times z$	$15 \sim 20 \mu\text{m}^2$
Forward Pixel (FPix)	2 disks	$r-\phi \times r$	$15 \sim 20 \mu\text{m}^2$

Table 3.1.: Resolution of the pixel system

The sensor adopted for the pixel is n^+ implant on n^- substrate detector, known as 'n-on-n concept' (n^+ pixelated implants on n-bulk), which allows operation even at very high particle density⁵. When a charged particle passes through the biased sensor, electrons are created due to ionization and at the same time holes are created in opposite

³With three-hits, the efficient geometrical acceptance covers $|\eta| < 2.2$. With two-hits only, the efficient geometrical acceptance covers $|\eta| < 2.5$.

⁴For a dimension of p (i.e., pitch of p), the position resolution arising from geometrical consideration can be estimated as $\sigma_x \approx p/\sqrt{12}$ with $\langle \Delta x^2 \rangle = (1/p) \int_{-p/2}^{p/2} x^2 dx = p^2/12$

⁵In this design, even after the charge sign inversion due to a radiation damage, the highest electrical field is formed closest to the collection electronodes. Therefore, the sensor can still operate efficiently as far as the pixels are isolated from each other [128].

3. The CMS Experiment

directions. The electrons are collected and amplified by the readout chip (ROC) creating a measurement point, i.e., hit [128]. How the position of individual hit is determined will be discussed in Chap. 5. Figure 3.5 shows the photos of four pixel cells in the barrel and in the forward. Details on the inter-pixel isolation techniques that are used for manufacturing the pixel sensors can be found in Ref. [124].

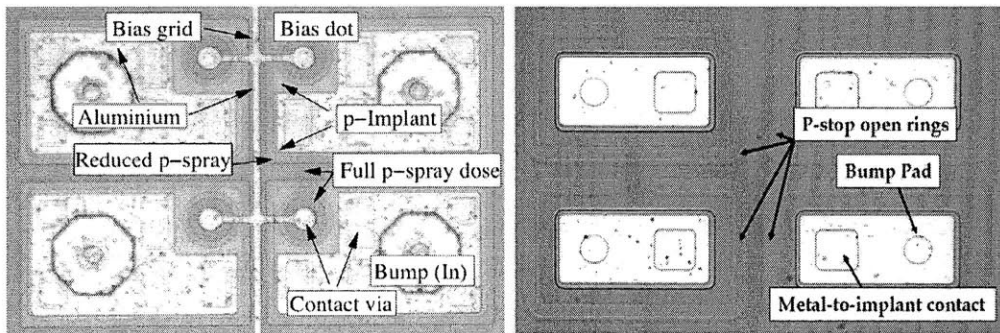


Figure 3.5.: Photos of four pixel cells used in the barrel (left) and in the forward (right) [124]

Sensor signals are read out by ROCs bump bonded to the sensors. The main purpose of the read-out chip is to amplify and buffer the charge signals from the sensors. Only signals above an adjustable threshold are read out, which is known as zero-suppression (ZS). While the readout of the sensor signals is processed, lower level trigger (L1) verification is done, rejecting signals without corresponding L1 trigger. The signals readout by the ROCs are digitized and formatted in the pixel front end driver (pxFED), which is eventually sent to one of the units known as event builder in the CMS data acquisition (CMS DAQ) system.

Due to the strong magnetic field present in the CMS tracker, the electrons created in the pixel are Lorentz drifted in the azimuthal direction enhancing the charge sharing over more than one pixel and therefore allowing to enhance the position resolution⁶. With the Lorentz-drift-enhanced position determination, a spatial resolution is in the range 15–20 μm is achieved [124]. The forward detectors are tilted by 20° in a turbine-like geometry to create the Lorentz drift and therefore to enhance charge sharing.

3.2.1.2. Silicon Strip Tracker (SST)

The silicon strip detector consists of the detector modules grouped into several subsystems, TIB, TID, TOB, and TEC, depending on the r and z positions, as discussed at the beginning of the section 3.2.1. There is a total of 9.3 M active elements (i.e., the number of read-out channels) in 24244 sensors with an effective area reaching 198 m².

⁶While the position resolution for a single pixel is given by $p/\sqrt{12}$, when there's more than one pixel sharing the charges, the position can be interpolated giving a better position resolution.

Figure 3.6 shows the layout of the silicon strip detector viewed in the plane perpendicular to the beam direction. The first two layers of the TIB and TOB, highlighted in blue, are double-sided.

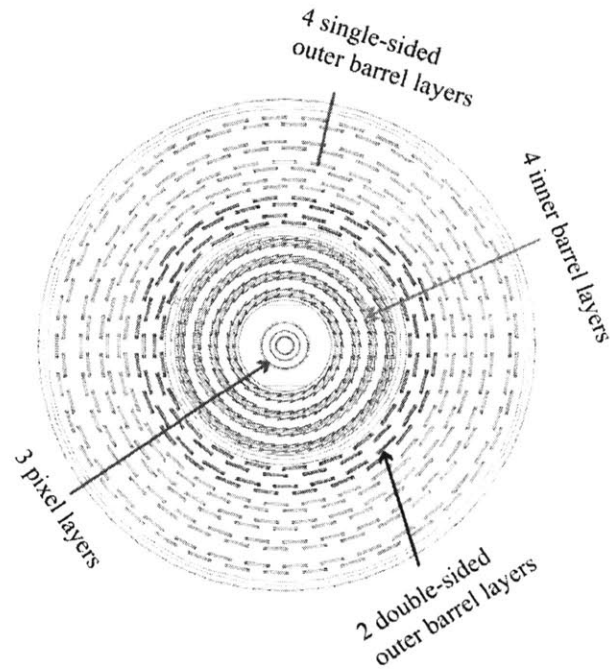


Figure 3.6.: Schematic of the SST viewed in the plane perpendicular to the beam direction [129].

The sensor elements in the SST use single sided AC-coupled⁷ p-on-n type silicon micro-strip sensor [124, 131]. The typical cell size is $10 \text{ cm} \times 80 \mu\text{m}$ with extended pitch in the outer region ($55 \text{ cm} < r < 110 \text{ cm}$). While the inner tracker subsystems use the thinner sensor with the thickness of $320 \mu\text{m}$, the outer tracker subsystems use the sensor with the thickness of $500 \mu\text{m}$. The first two layers in TIB and TOB, as indicated as double lines in Fig 3.3 (also in Fig. 3.6), use the single module mounted back-to-back, known as ‘stereo module’, with the second module (farther in r) rotated by 100 mrad with respect to the first module, which allows a measurement in the orthogonal direction. Also, the first two rings of TID and the first two and the fifth ring of the TEC are equipped with stereo modules. Table. 3.2 shows the the number of sensor elements, the thickness of the strip and the mean pitch in each subsystem [124, 132],

Sensor signals from the silicon sensors are read out by a custom integrated circuit called APV25 [133], where the signal amplification, the signal shaping, and the transmission to the Front End Driver (FED) designated to the strip tracker via optical fibres. The APV25 has a total of 128 read-out channels and operates at a voltage of 1.25 and 2.5

⁷It means the sensor is equipped with integrated capacitors, which allows the AC coupling of the signals from the strip to the read-out electronics [130].

3. The CMS Experiment

Subsystem	No. layers	thickness (μm)	mean pitch (μm)	Direction	Resolution
TIB	4	320	80(2)/120(2)	$r-\phi(z)$	23-34(23) μm
TOB	6	500	183(4)/122(2)	$r-\phi(z)$	35-52(52) μm
TID	3	320	100–141	ϕ	91-100 μrad
TEC (inner)	4	320	97–184	ϕ	45-100 μrad
TEC (outer)	3	500	97–184	ϕ	45-100 μrad

Table 3.2.: Specification of each subsystem in the SST. For the barrel systems, the mean pitch is shown separately for inner and outer rings with the number of layers. (e.g., for TIB, first two layers have $80\mu\text{m}$ and the second two layers have $120\mu\text{m}$.)

V. For a trigger latency up to $4\mu\text{s}$, the APV25 can hold data to buffer. The FED receives data from 96 optical fibers with two APV25 (256 channels equivalently) assigned to each fiber. The received optical signal is converted to electric signal and subsequently digitized, which in turn is used for the pedestal and the common mode noise subtractions.

3.2.1.3. Superconducting Solenoid Magnet

The superconducting solenoid magnet with a main purpose to achieve an excellent momentum resolution, generates an axial magnetic field of 3.8 T ⁸ inside 6-m diameter and 12.5-m length solenoid with a returned flux outside of the solenoid. The entire tracker system and the calorimeter are located inside the magnet and the muon detector systems are located outside. The coil of the solenoid magnet are made from the four layers of superconducting cable NbTi conductor [124]. The solenoid is contained in a cryostat where an operation temperature of 4 K is maintained.

3.2.2. Electromagnetic Calorimeter (ECAL)

The Electromagnetic Calorimeter (ECAL) in CMS uses the lead tungstate (PbWO_4) crystals with almost 4π coverage over the pseudorapidity range $|\eta| < 3.0$. Figure 3.7 shows the schematic layout of the CMS ECAL [134]. The ECAL consists of a barrel part, Ecal Barrel (EB) and two endcap parts, Ecal Endcap (EE) and ECAL preshower, the latter being a sampling calorimeter with two layers of the silicon strip sensor placed in between the lead absorber. The EB covers the pseudorapidity range $|\eta| < 1.479$ and it is divided in the azimuthal direction into 18 sectors so-called Supermodules, each of which contains 1700 crystals. The EE covers the pseudorapidity range $1.479 < |\eta| < 3.0$ and it is divided vertically into a smaller unit called ‘Dee’, each of the Dee is further divided into a smaller subunit of 5×5 crystals called ‘Supercrystals’, as shown in Fig. 3.7. Lastly, the ECAL preshower, placed in front of the EE, covers the pseudorapidity range $1.653 < |\eta| < 2.6$. While the preshower was designed specifically for the identification of neutral pion, it also helps the separation between π^0 and photon.

⁸While the designed field strength was 4.0 T , the operational field strength achieved during 2009–2011 running was 3.8 T .

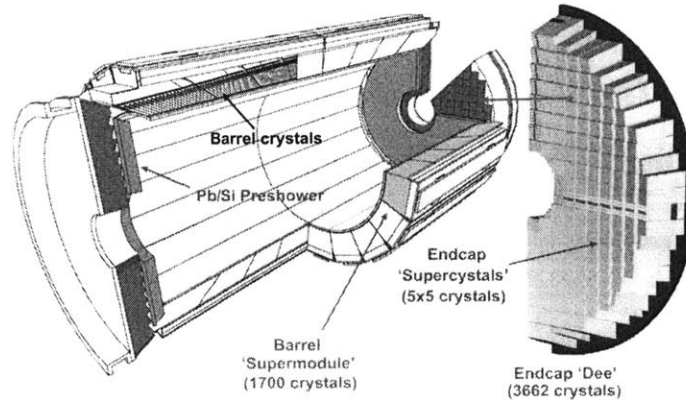


Figure 3.7.: Schematic layout of the ECAL system [134].

The PbWO_4 was chosen for the ECAL because of the high density (8.28 g/cm^3), the short radiation length⁹ ($X_0 = 0.89 \text{ cm}$), and the small Molière radius (2.2 cm), which allows to design a compact system with a fine granularity [124]. The crystal in the barrel has a x - y dimension of $22(26) \text{ mm} \times 22(26) \text{ mm}$ at the front (rear) face of the crystal (equivalently, 0.0174×0.0174 in $\eta - \phi$) with a length of 230 mm, which corresponds to $25.8X_0$. In the endcap, the crystal has a x - y dimension of $28.62(30) \text{ mm} \times 28.62(30) \text{ mm}$ at the front (rear) face of the crystal with a length of 220 mm, which corresponds to $24.7X_0$. For the detection and the amplification of scintillation light from the PbWO_4 , different choices of the photodetectors are used for the barrel and the endcap because of different magnetic field strength and the radiation level [124]. The barrel uses the custom-designed Avalanche Photo Diodes (APDs) and the endcap uses again the custom-designed Vacuum Photo Triodes (VPTs). The use of the APD is largely driven by the requirement for the operation in the presence of strong magnetic field and high radiation levels [135].

A typical energy resolution is given by the following parametrization, $(\sigma/E)^2 = (2.8\%/\sqrt{E})^2 + (0.12/E)^2 + (0.30\%)^2$, where the total resolution is the sum of three contributions, namely, stochastic term, noise term, and constant term from left in the right hand side, each of which was measured with the electron test beam in 2004 [124].

3.2.3. Hadron Calorimeter (HCAL)

The Hadron Calorimeter (HCAL) in CMS is a brass/scintillator sampling hadron calorimeter located outside of the ECAL. The HCAL consists of the barrel (HB) and the endcap (HE) hadron calorimeters surrounded by the solenoid magnet, the outer (HO) hadron calorimeters located outside of the solenoid magnet, and the forward (HF) hadron calorimeter at high η . Figure 3.8 shows the schematic longitudinal view of the CMS

⁹The radiation length of a material is a characteristic length scale of the energy loss rate of an electron traversing the material due to electromagnetic radiation [134].

3. The CMS Experiment

detector.

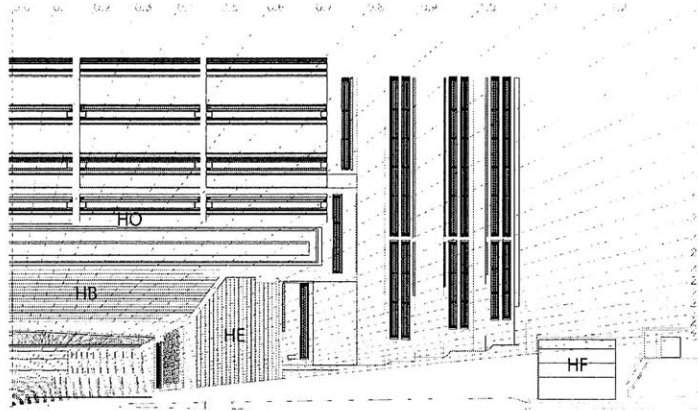


Figure 3.8.: Schematic longitudinal view of the CMS detector with the HCAL subsystems, HB, HE, and HO shown with their η (dotted-lines) coverages.

The HB covers the pseudorapidity range $|\eta| < 1.3$ and it is divided in z direction into two parts, HB+ and HB-, with the 36 identical wedges aligned parallel to the beam axis. The wedges are made of flat brass absorber plates. Each wedge occupies 20° in the azimuthal direction and is segmented into four azimuthal sector. Together with the plastic scintillator divided into 16 η sectors, HB has the granularity of $(\Delta\eta, \Delta\phi) = (0.087, 0.087)$.

The HO covers the similar rapidity range as the HB does, i.e., $|\eta| < 1.3$. Being located outside of the solenoid, it utilizes the solenoid coil as an additional absorber material and ensures that the hadronic shower is sampled with enough interaction lengths¹⁰. There is a single layer of the HO scintillator at a radial distance of 4.07 m except in the middle (i.e., $\eta = 0$), where there is two layers of the HO scintillator since at $\eta = 0$, the absorber depths is minimum. The HE covers the pseudorapidity range $1.3 < |\eta| < 3.0$. The granularity of the HE is $(\Delta\eta, \Delta\phi) = (0.17, 0.17)$. Lastly, the HF covers the pseudorapidity range $4.5 < |\eta| < 5.0$ and has the granularity of $(\Delta\eta, \Delta\phi) = (0.175, 0.175)$.

The scintillation light, converted by WaveLength-Shifting (WLS) fibers, is detected by photo-detectors known as Hybrid Photo-Diodes (HPD). The detected (analogue) signal is then converted to a digital signal by a charge-integrating ADC ASIC called QIE (Charge Integration and Encode) [124].

3.2.4. Muon Systems

The CMS muon system comprises three sub-detector components with a primary goal to provide robust and precise measurements of muons as well as triggering information [124]. The three subsystems are the Drift Tube (DT) chambers, the Cathode Strip

¹⁰The interaction length, usually noted as λ , is defined as the mean path length.

Chambers (CSC) and the Resistive Plate Chambers (RPC). The layout of the muon system is shown in Fig. 3.9, where the location of each sub-detector component with the respective η coverage is shown.

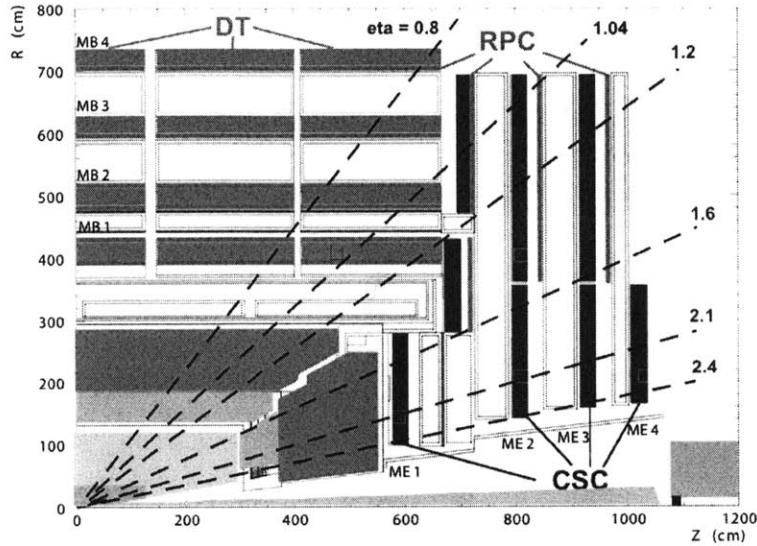


Figure 3.9.: Schematic longitudinal view of the CMS detector with the muon subsystems, DT, CSC, and RPC shown with their η (dotted-lines) coverages [136].

The DTs, located radially outside of the calorimeter system, cover the barrel region with the pseudo-rapidity range $|\eta| < 1.3$. The DTs are gaseous detector with a $50 \mu\text{m}$ diameter wire in the middle of the DT cell acting as an anode. The DTs are used as tracking detector with the single position resolution of about $200 \mu\text{m}$ and the global position resolution in $r - \phi$ of $100 \mu\text{m}$. The CSCs located in the endcap cover the pseudo-rapidity up to $|\eta| < 2.4$. The CSCs are multiwire proportional chamber with each CSC comprised of 7 trapezoidal panels with 6 gas gaps. It is capable of providing up to 6 space coordinates¹¹ with the position resolution of $100\text{--}200 \mu\text{m}$ and the angular resolution of order of 10 mrad [136]. The RPCs are located in the barrel region as well as in the endcap region, in-between the DTs and the CSCs as shown in Fig. 3.9, covering the full pseudo-rapidity range $|\eta| < 2.4$. The RPCs are gaseous parallel-plate detectors with double-gap structure operated in avalanche mode [124]. The double gap structure allows to operate at lower gas gain with an effective efficiency higher than the single gap structure [124]. It provides a fast ($t \ll 25 \text{ ns}$) response with good timing resolution of 1.5 ns but with coarser position resolution around 1.5 cm in $r - \phi$. The momentum resolution achieved standalone (i.e., only the muon system) is approximately 10 (25%) at 100 (1000 GeV). When combined with the CMS tracking system (global), the achieved momentum resolution is about 1 (10%) at 100 (1000 GeV).

¹¹The precise position is made based on the charge distribution induced on the cathode strips.

3. The CMS Experiment

3.2.5. Beam Scintillating Counter (BSC)

The Beam Scintillating Counter (BSC) is a set of 16 scintillator tiles located at a distance of 10.86 m from the nominal interaction point (IP), one on each side, and covers the $|\eta|$ range from 3.23 to 4.65 [137, 138]. As shown in Fig 3.10, it is mounted to the front of the HF and consists of a ring-shape scintillator segmented into eight sectors and four pedal-shape scintillators splitted vertically into two. The BSC with a primary purpose to provide information on the relative rates of collisions and beam backgrounds is capable of measuring hit and coincidence rates with a time resolution of 3 ns and an average minimum ionising particle (MIP) detection efficiency of 95.7% [137].

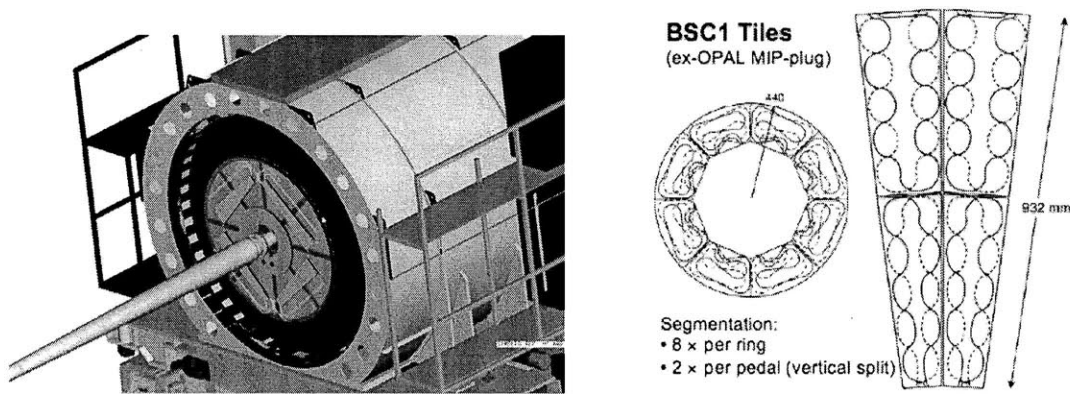


Figure 3.10.: Schematic layout and the illustration of the segmentation of the BSC detector system [138]

It is made of plastic *polyvinyl-toluene* (PVT) scintillation tiles with Wavelength shifting fibres (WLS) and the photomultiplier (PM) tubes for the readout of the output light from the WLS fibres. During the 2010 and 2011 pp and PbPb runs, the BSC was heavily used for the selection of 'good' collision events and the rejection of beam background, which will be further discussed in the following chapter (Chap. 4). The BSC is a part of CMS Beam Conditions and Radiation Monitoring System (BRM) system, which provides monitoring information on the beam condition and radiation field in and around the CMS detector [124, 139]. Other sub-system parts of the BRM systems includes BCM, BPTX, and PLT [124].

3.2.6. Beam Pick-Up Timing Experiment (BPTX)

The Beam Pick-Up Timing Experiment (BTPX), located at a distance of 175 m from the nominal IP, one on each side, is designed to provide information on the time structure of the LHC beam [124, 140]. It is a system of two electrostatic pick-up device with a good timing resolution (<200 ps) [124]. When proton or lead-ion beams pass through the device, induced charges are created into electrodes and gives accurate beam timing and position information. The BPTX measurements are used as an input to the global

decision of the CMS detector system for event selections as it provides information on the presence of beams in the opposite direction. When the relative phase of the BPTX signals from each side is provided, the interaction point in the z direction can also be calculated. The BPTX was also heavily used for the selection of ‘good’ collision events and the rejection of beam background along with the BSC during the pp and PbPb runs, which will be further discussed in Chap. 4.

3.2.7. CMS Trigger and Data Acquisition System (TriDAS)

The trigger system in the CMS consists of two levels, a custom hardware trigger, the Level-1 Trigger (L1) and a software trigger, the High Level Trigger (HLT) [141]. The CMS Data Acquisition (DAQ) system is designed to read out the detectors and record data at the LHC bunch crossing frequency of up to 40 MHz. The rate of the event recording (i.e., HLT output rate) for the offline processing and analysis is $\mathcal{O}(10^2)$ Hz. The architecture of the CMS DAQ system is shown in Fig 3.11.

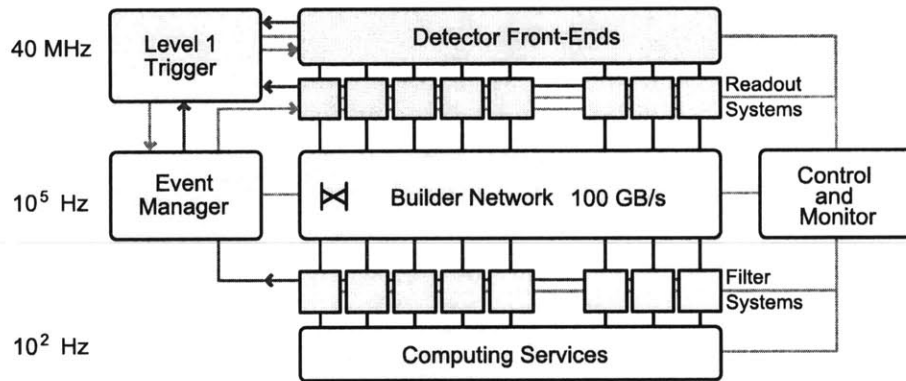


Figure 3.11.: Schematic of the CMS DAQ system architecture [136].

The CMS TriDAS is described in detail in Ref. [142]. While the collision rate in PbPb runs is much lower than in pp runs¹², because of the larger data volume per event ($\mathcal{O}(10)$ MByte as opposed to $\mathcal{O}(1)$ MByte) as well as the larger computing time involved in the HLT processing¹³, intense commissioning of the CMS TriDAS for the PbPb runs in 2010 and 2011 were done.

¹²In pp, the collisions rate reaches 600 MHz with approximately 20 inelastic collisions per crossing (known as ‘pile-up’) at nominal instantaneous luminosity of $10^{34} \text{cm}^{-2} \text{s}^{-1}$.

¹³During the 2011 PbPb runs, the full Heavy Ion tracking algorithm (see Sec. 5) was ran in the HLT in addition to the signal zero-suppression algorithms, which required on average $\mathcal{O}(1)$ minute.

3. *The CMS Experiment*

3.2.8. Simulations

The Monte-Carlo (MC) simulation of the CMS detector response is made in the CMS Simulation Software (CMSSW) based on the simulation package GEANT4 [143]. The full-scale MC event generation and the simulation of the detector response of the generated particle as well as the reconstruction based on the response are all performed within the CMSSW software framework [144] in the same manner as it is done for ‘real’ data. The analysis of the reconstructed objects (i.e., tracks, vertices, calorimeter energy, and etc) is also usually done in the framework. All the source codes that can be used in the CMSSW framework as well as the technical reference manual is available for browsing, searching and downloading in the following URLs.

- <http://cmssw.cvs.cern.ch/cgi-bin/cmssw.cgi/CMSSW/>
- <http://cmslxr.fnal.gov/lxr/>
- <http://cmssdt.cern.ch/SDT/doxygen/index.php>

4. Event Characterization

While the rate of Pb beam crossing in the CMS detector reaches 8 MHz with an interaction probability of $\mathcal{O}(10^{-4} - 10^{-3})$, only those events with actual PbPb collisions are selected by collisions triggers with given trigger efficiencies and recorded in tape. Further offline selections are performed to select a clean sample of collisions events for analyses. The selected and reconstructed events are classified depending on their collisions geometry and vertex position.

4.0.9. Collision Trigger

An identification of inelastic collision event is made based on the information from various sub-detector systems. Since the collision requires the presence of two beams crossing inside the CMS, a coincidence of the signals from both side of the BPTX detector (i.e., $z+$ and $z-$) is minimally required. While the requirement of the BPTX signals ensures the presence of the beams in the $z+$ and $z-$ directions with a given efficiency, the presence of the beams does not always ensure the collisions of two Pb ions. This is because the interaction probability for a given beam crossing is much lower than unity, $\mathcal{O}(10^{-3})$, and also there exist interactions between the beam and the gas inside the beam pipe, resulting in ‘beam-halo’, ‘beam-gas’, and ‘beam-scraping’ events. For the identification (or rejection) of collisions (or non-collision) events, the presence of signals from either or both sides of the forward detectors such as the HF or the BSC, or the presence of at least one reconstructed trajectory of charged particle (i.e., track) and the trajectory–vertex compatibility are required in the tracker. This set of requirements ensures the presence of activities in the CMS detector as a signature of collision, and therefore the presence of collision. A so-called ‘trigger’ is a custom-hardware or software unit that makes a decision based on single or multiple signals readout from the various sub-detectors. It will be discussed further in the following sections, Sec. 4.0.9.1 and Sec. 4.0.9.2.

The analyses presented in this thesis use two types of triggers, a minimum bias (Min-Bias) trigger and jet-triggers. The minimum bias trigger is a trigger that is designed to select a large fraction of total inelastic cross sections of PbPb with a least possible bias as the name suggests. The MB trigger was highly prescaled in the 2010 and 2011 data taking (i.e., only a small fraction, 0.01–0.1%, of all the available MB events are recorded) to fit in the storage limit while other ‘object’ triggers that trigger on a particular object, such as high energetic jet, photon, or muon are either not-prescaled or prescaled by a smaller factor, depending on the energy thresholds. The jet-trigger is one of the object triggers that is designed to select events with jet having the jet energy above a certain

4. Event Characterization

jet energy threshold. The jet-triggers are used in the analyses presented in this thesis in order to extend the statistical reach of the spectra in the highly prescaled MB sample.

4.0.9.1. Minimum Bias Selection

A clean sample of minimum bias events from PbPb collisions was collected, based on a trigger requiring a coincidence between signals in the opposite sides of either the HF or the BSCs. To ensure a pure sample of inelastic hadronic collision events, additional offline selections were performed. These include a beam-halo veto, based on the BSC timing, an offline requirement of at least 3 towers on each HF with an energy deposit of more than 3 GeV per tower, a reconstructed vertex, based on at least two pixel tracks with $p_T > 75$ MeV/c, and a rejection of beam-scraping events, based on the compatibility of pixel cluster shapes with the reconstructed primary vertex.

The distribution of first layer pixel hits versus total energy deposited in the HF is shown in Fig. 4.1 both before and after all event selections are applied. The combination of the above selections is sufficient to clean up the sample from non-diagonal contributions (beam-gas, beam-halo, beam-scraping, UPC).

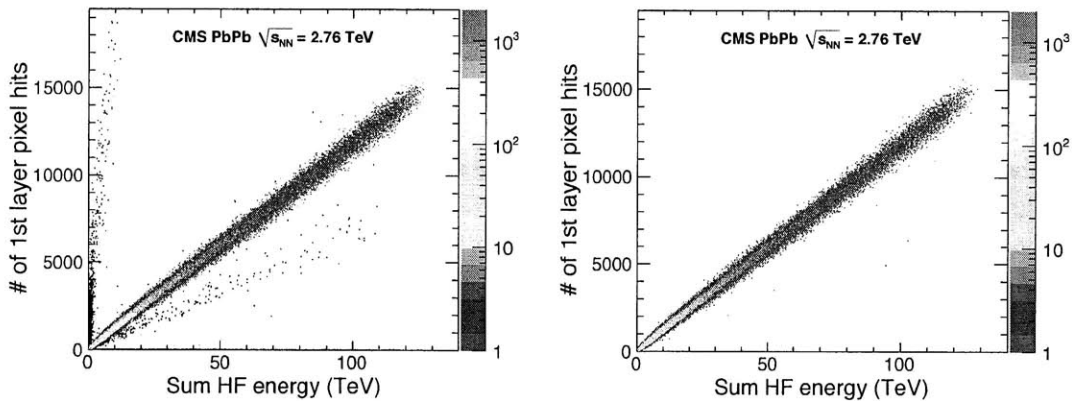


Figure 4.1.: (Left panel) Correlation for 60k minimum bias events in one collision run between the number of pixel hits and the total energy deposited by the HF. Good collisions (colored points) have a tight correlation, while events firing the BSC halo bits, displaying beam-scraping event-like features, or lacking a valid reconstructed vertex are off-diagonal (black points). (Right panel) The same correlation for only those events passing all selection cuts described in the text.

The determination of the overall selection efficiency for selecting hadronic inelastic collision is discussed in Sec 4.0.10.2.

4.0.9.2. Jet Events Selection

An identification of an event with jet requires an online jet finding, and energy and position reconstruction. The jet-triggers are based on the calorimeter-based jet reconstruction in heavy ion collisions, which is performed with an iterative cone algorithm modified to subtract the soft underlying event on an event-by-event basis [145]. Details on the jet reconstruction and background subtraction technique can be found in Refs. [145, 146]. The offline jet reconstruction is done using the same jet finding algorithm but with more sophisticated tower cleaning as well as more accurate jet energy correction.

Figure 4.2 shows the efficiency curve for one of the jet-triggers at the HLT level, named as HLT_HIJet50U, where the efficiency is defined as the ratio of the number of triggered events over the number of minimum bias events as a function of the transverse energy (E_T) of leading jet, i.e., most energetic jet that is found in each event.

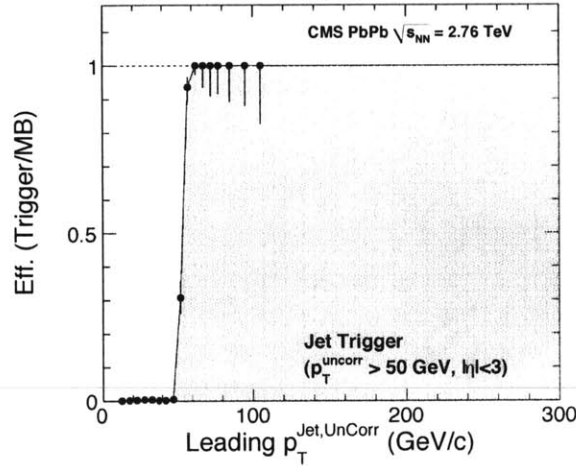


Figure 4.2.: Trigger efficiency of HLT jet-trigger with (un-corrected) energy threshold of 50 GeV.

As seen in Fig. 4.2, the efficiency becomes fully efficient above 80 GeV or so, which is higher than the threshold used in the event selection. This is because the offline reconstruction uses more sophisticated tower cleaning and more accurate jet energy correction as well as the narrower η range than in the online reconstruction.

4.0.10. Collision Geometry

In heavy-ion physics, the geometrical aspects of heavy-ion collision is highly relevant for the characterization of the colliding system, and consequently for the characterization of the produced medium and their final state particles that are being detected. Thus, the properties of produced medium in heavy-ion collisions is frequently studied as a function of collision geometry.

4. Event Characterization

The high energy heavy ion collision can be viewed as the collision of two extended objects with varying impact parameter, b , defined as the distance between the centers of the two nuclei that is perpendicular to the direction of the projectile motion ¹ as illustrated in Fig. 4.3. The collisions of heavy-ion that can occur in a broad range of impact parameter ² are divided up in percentile of total inelastic cross section, known as collision ‘centrality’. For example, 0–5% centrality means 5% of the total (inelastic) cross section that are thought to represent the most head-on collision. While the collision impact parameter having a femtoscopic length scale is not a directly measurable quantity, it can be estimated from the modelling of heavy ion collision geometry and associating it with measurable quantities such as $dN/d\eta$, energy deposited in the forward detector, and etc with a basic assumption that the impact parameter b is monotonically related to the number of particles that are produced. Such modelling also allows to determine so-called centrality variables such as the number of nucleons that ‘participate’ in collisions (N_{part}) and the number of binary nucleon-nucleon collisions (N_{coll}) as well as the impact parameter (b).

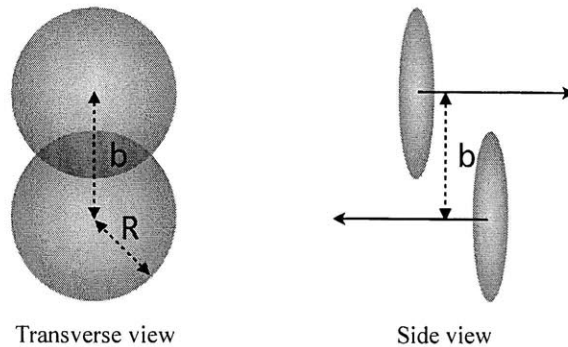


Figure 4.3.: Illustration of high energy nucleus-nucleus collision viewed transversely (left) and sideways (right).

4.0.10.1. Glauber Model and Centrality Variables

A Glauber model [147] is most commonly used in the description of the nuclear reactions, and is used for determining the aforementioned centrality variables in relativistic heavy ion physics. It is a semi-classical model of multiple-scattering of nucleons in nuclear target, which treats a nucleus-nucleus collision as independent collisions of the

¹The size of de Broglie wavelength of nucleus moving nearly at a speed of light is much smaller than the size of nucleus, therefore the geometry of nucleus is a relevant degree of freedom in characterizing collisions. For example, for ^{208}Pb with a center-of-mass energy of 2.76 TeV, de Broglie wavelength is calculated as $\lambda = 2\pi\hbar/p \approx 2\pi \times 197\text{MeV} \cdot \text{fm}/2760 \text{ GeV}$, which is much smaller than the size of Pb nucleus, $R \approx 7\text{fm}$.

²Approximating the nucleus as a hard sphere, the impact parameter range is $0 < b < 2R$, where R is a radius of the heavy-ion

nucleons that are distributed inside a nucleus according to a smooth density distribution. In this model, two nuclei are arranged with a random impact parameter, and the interaction probabilities between two nucleons from each nuclei are calculated based on the known nucleon-nucleon inelastic cross section at a given center-of-mass energy [147, 148]. The nucleon density is usually parametrized by a ‘Wood-Saxon’ distribution [148],

$$\rho(r) = \frac{\rho_0}{1 + \exp(\frac{r-R}{d})}, \quad (4.1)$$

where ρ_0 is the charge density in the center of the nuclei, R is the radius of nuclei, and d is the characteristic length scale known as ‘skin depth’. For example, for a lead ion ^{208}Pb , $R \approx 7$ fm and the skin depth of $d = 0.54$ ³.

The Glauber model assumes that at sufficiently high energy the trajectory of each nucleon with sufficient momentum remains un-deflected as two nuclei pass through each other with an interaction probability given by an inelastic nucleon-nucleon (NN) cross section, $\sigma_{\text{inel}}^{\text{NN}}$. With this assumption, which holds as a good approximation at high energy [36], the total nucleus-nucleus (AA) cross section can be expressed analytically in terms of the inelastic NN cross section [150]. While detailed derivations can be found in the respective references, quoting the net result, the total inelastic PbPb cross section at $\sqrt{s} = 2.76$ TeV is given by $\sigma_{\text{inel}}^{\text{AA}} = 7660$ mb [150] with $\sigma_{\text{inel}}^{\text{NN}} = 64$ mb. Also, the minimum bias cross section for the hard-process (i.e., process that involves relatively large momentum transfer) is approximately given by $\sigma_{\text{hard}}^{\text{AA}} = A \times A \times \sigma_{\text{hard}}^{\text{NN}}$ [150].

4.0.10.2. Centrality Determination

Determination of the aforementioned centrality variables involves two steps: 1. defining centrality class (often referred to as ‘bin’) for a measured distribution that varies monotonically with particle multiplicity (e.g., $dN/d\eta$, energy deposited in the forward detector, and etc) and a distribution calculated from phenomenological Glauber calculation. 2. associating (mapping) the measured distribution and the calculated distribution in a given centrality bin. A cartoon in Figure 4.4 shows how a measured quantity, charged particle multiplicity in this example, is related to the collision geometry and corresponding centrality variables.

In order to define centrality boundaries and therefore centrality bins in fractions of total inelastic cross section, as shown as dotted lines in Fig. 4.4, it is important to use a clean sample of minimum bias events with a well known (trigger) selection efficiency. The trigger efficiency is estimated based on the simulated minimum bias PbPb events from the heavy ion MC event generator such as HYDJET [151] with realistic detector conditions. It is determined for a given multiplicity M as the fraction of MC events with M that pass the same offline and online event selections applied in the data, i.e., $\epsilon(M) = N_{\text{sel}}^{\text{MC}}(M)/N^{\text{MC}}(M)$. The systematic uncertainty of the estimation is determined

³The radius is calculated based on a empirical formula, $R = 1.19A^{1/3} - 1.61A^{-1/3}$ and a skin depth $d = 0.54$ fm as given in [149].

4. Event Characterization

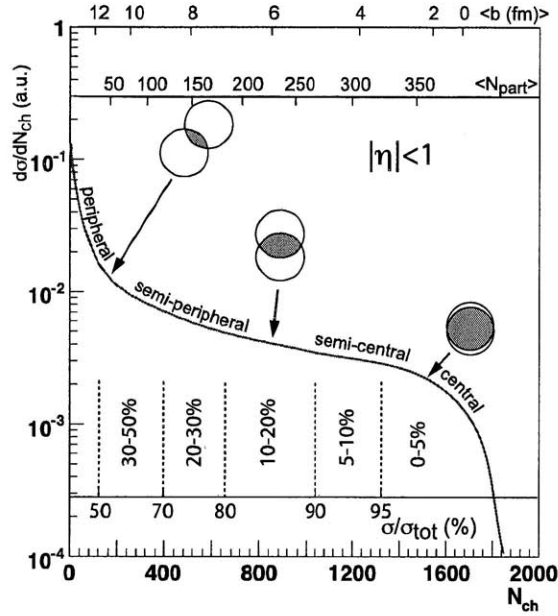


Figure 4.4.: A cartoon that illustrates how a measured charged particle multiplicity is related to the collision geometry and centrality variables [148].

by varying the MC parameters that affect the multiplicity and overall normalization with the range of each parameter chosen from the comparison of the multiplicity distribution in the data and MC. The overall efficiency for selecting hadronic inelastic collisions is estimated in this way to be $(97 \pm 3)\%$. It is noted that the sizeable inefficiency indeed comes from the events in the peripheral bin where the particle multiplicity is low (close to that of pp collision in the most peripheral event) compared to the multiplicity in the central events, as one can expect from the fact that the selection efficiency is generally dependent on the particle multiplicity in particular in the tail of the low multiplicity distribution.

In the analyses presented in this thesis, the collision event centrality is determined from the event-by-event total energy deposition in both HF calorimeters. The distribution of this observable in minimum bias events from the 2010 data sample, shown in Fig. 4.5, is used to divide the event sample into 40 centrality bins, each corresponding to 2.5% of the total inelastic cross section. Figure 4.5 shows the distribution of events according to centrality bin, which is flat by construction for the minimum bias selection, except in the most peripheral events where the trigger and offline event selection are no longer fully efficient. Figure 4.5 also shows the distributions of the total HF energy and of the cross-section fraction for the events selected by single-jet triggers with calibrated transverse energy thresholds of $E_T = 65$ GeV (Jet65) and 80 GeV (Jet80) from the 2011 data samples. The events are analysed in six centrality bins: 0–5% (most central), 5–10%, 10–30%, 30–50%, 50–70%, and 70–90% (most peripheral).

The mean and r.m.s. of the N_{part} , N_{coll} , and T_{AA} distributions evaluated using fully sim-

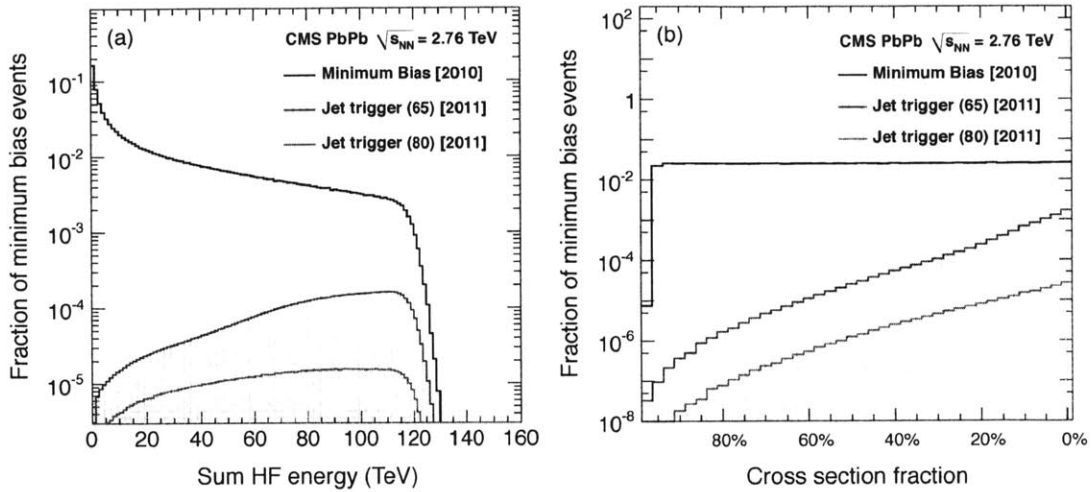


Figure 4.5.: (a) Probability distribution of the total HF energy for minimum bias events (black line), Jet65-triggered (blue-shaded region), and Jet80-triggered (red-shaded region) events. (b) Distribution of the events in bins of fractional cross section for minimum bias (black line), Jet65-triggered (blue-shaded region), and Jet80-triggered (red-shaded region) events.

ulated and reconstructed MC events based on the Glauber model of the incoming nuclei and studies of bin-to-bin smearing, caused by finite resolution effects [152], along with their corresponding systematic uncertainties, are listed in Table 4.1 for the six centrality bins used in this analysis. The uncertainties on the centrality variables are derived from the propagation of the uncertainties on the event selection efficiency and on the parameters of the Glauber model, the former being dominant in peripheral bins [33].

4.0.11. Vertex Reconstruction

When a collision occurs, there exists a position in space from which all the primary particles produced in the collision originate. This position in space is known as ‘vertex’ and it is important to know a rather precise vertex position in each event since it is used as a starting point for the reconstruction of charged particle trajectories. Also, the presence of reconstructed vertex in a given beam crossing is used to decide whether a collision takes place or not (see Sec. 4.0.9). In the PbPb bunch crossing a chance of having more than one collisions and therefore more than one vertices was low because of low interaction probability intended in the beam condition during 2010 and 2011 runs. In the pp bunch crossing, on the other hand, the probability was much higher resulting in the number of collisions per bunch crossing to reach up to 20 during the high-luminosity runs.

The reconstruction of vertex position in PbPb collision at CMS is done as follows. First, a rough estimate of the position in z -direction is obtained by stepping through

4. Event Characterization

Table 4.1.: Centrality Tables

Centrality bin	$\langle N_{\text{part}} \rangle$	r.m.s.	$\langle N_{\text{coll}} \rangle$	r.m.s.	$\langle T_{\text{AA}} \rangle$ (mb ⁻¹)	r.m.s.
0–5%	381 ± 2	19.2	1660 ± 130	166	25.9 ± 1.06	2.60
5–10%	329 ± 3	22.5	1310 ± 110	168	20.5 ± 0.94	2.62
10–30%	224 ± 4	45.9	745 ± 67	240	11.6 ± 0.67	3.75
30–50%	108 ± 4	27.1	251 ± 28	101	3.92 ± 0.37	1.58
50–70%	42.0 ± 3.5	14.4	62.8 ± 9.4	33.4	0.98 ± 0.14	0.52
70–90%	11.4 ± 1.5	5.73	10.8 ± 2.0	7.29	0.17 ± 0.03	0.11
50–90%	26.7 ± 2.5	18.84	36.9 ± 5.7	35.5	0.58 ± 0.09	0.56

from -30 to 30 cm and determining the compatibility of the pixel cluster lengths with the vertex hypothesis, as illustrated in Fig. 4.6. The maximum in the number of com-

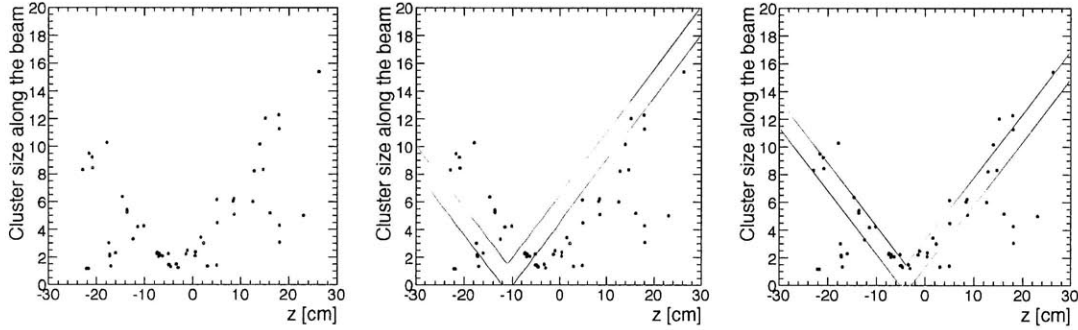


Figure 4.6.: Distributions of pixel cluster size along the beam as a function of z with the red lines to illustrate at which z position the highest number of compatible pixel clusters are found. In this event, the most compatible z position is found to be around -4 cm.

patible hits is called the ‘cluster vertex’. For the precise determination of the position not only in the z direction, but also in x and y directions, the hits in the pixel tracking system are used. Starting from a tracking region around this cluster vertex, groups of the three “hits” in the subsequent pixel layers (pixel triplet) that are compatible with a trajectory assumption are generated. The η – ϕ extent of the tracking region is restricted in events with many pixel hits as the quality of the vertex reconstruction does not improve significantly for more than ~ 50 tracks, limiting the time to perform the pixel triplet generation in a reasonable time scale ($t \ll 1$ min per event). From the generated pixel triplets, the median peak position is found. The pixel triplet tracks from the previous step that are compatible with the beam-spot position in x – y position and this median vertex position in z are passed to a full 3-d vertex fitter.

The beam-spot is the luminous region produced by the colliding beams at CMS, which is measured in an average over many events. The width of the “beam-spot” in the CMS interaction region during the nominal run is expected to be about $16\mu\text{m}$ and vary approximately within 20% during a beam lifetime, $\mathcal{O}(10)$ hours. The beam-spot position is used as a precise estimate of the interaction region in $x - y$ direction, which provides a constraint for the vertex reconstruction as well as the track reconstruction (see Sec 5). The beam-spot measurement is done with the so called $d_0\text{-}\phi$ algorithm [153, 154], which is based on a fast χ^2 fit of the parametrized track impact parameter distribution as a function of ϕ , i.e., $d_0(\phi)$.

In the cases where there are sufficiently many tracks for the fit to succeed, the 3-d vertex is used. For very low multiplicity events where the fit fails, it chooses the 1-d median vertex for the z position and the beam spot for the transverse position. Figure 4.7 shows a comparison of the reconstructed z -vertex distribution between the data and the HYDJET simulated MC events for different centrality bins. It shows nicely that the distribution in the data and MC are in a good agreement throughout the centrality bins.

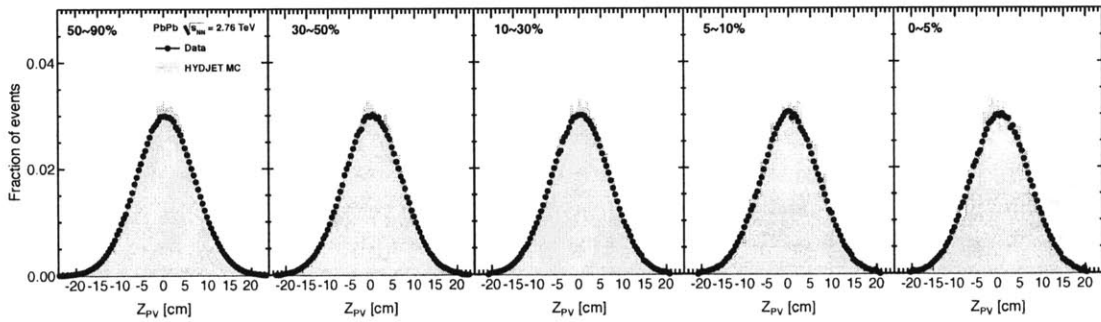


Figure 4.7.: rz distributions of reconstructed vertices in data and MC for different centrality bins

The resolution of vertex reconstruction in (x, y, z) are determined by a data-driven method. All the tracks in a single event are randomly divided into two sub-events. The vertex reconstruction is performed separately based on the tracks in each sub-event and the difference of the x, y, z positions between the two resulting vertices are related to a vertex resolution in each direction. The vertex resolution in each direction determined in this way is shown in Figs. 4.8 as a function of the number of associated tracks N_{trk} (i.e., tracks that are found to be compatible with a vertex) and compared to the resolution obtained from the comparison of generator level (i.e., “true”) and reconstructed vertex position in the HYDJET and AMPT MC samples. The pull distribution, defined as the residuals divided by sum in quadrature of the uncertainty, $|V_z^1 - V_z^2| / \sqrt{\sigma_1^2 + \sigma_2^2}$ with V_z representing the z vertex position, are also shown in the right panel. While the resolution stays almost independent of the number of associated tracks around $50\mu\text{m}$ in the transverse direction and $30\mu\text{m}$ in the z direction for $N_{trk} > 10$, below 10 associated tracks, there’s a strong N_{trk} dependence in all directions, implying the vertex resolution

4. Event Characterization

in more peripheral event is poorer.

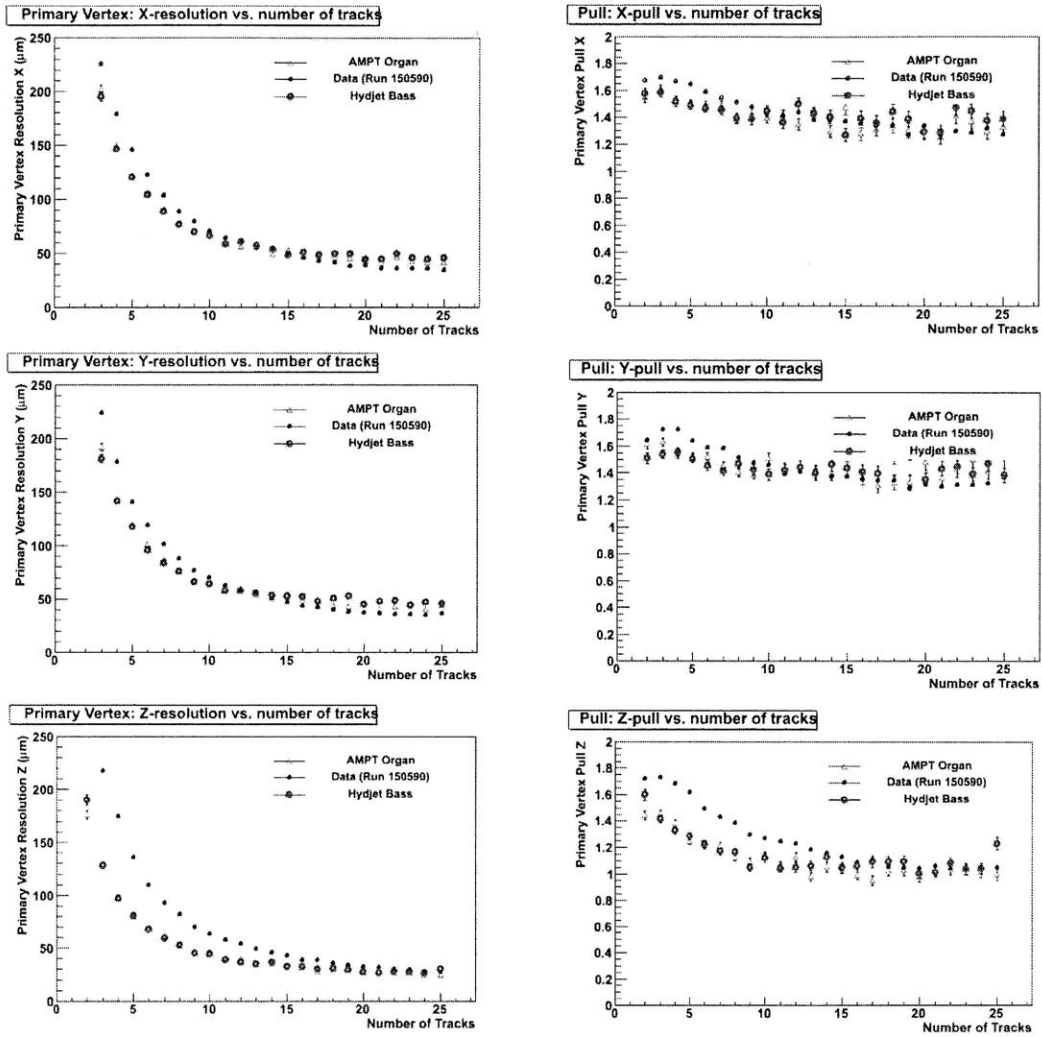


Figure 4.8.: Vertex resolution and pull size in x, y, z directions as a function of the number of associated tracks.

5. Particle Reconstruction

The reconstruction of charged particles is performed based on hits (i.e., measurement points) in the silicon pixel and strip detectors. The standard CMS track reconstruction algorithm used in pp collision, known as the combinatorial track finder, consists of three steps with multiple iterations of each step [155, 156]. Final track selections, which are tuned to achieve high track reconstruction efficiency with low fraction of mis-identified tracks ('fake'), are followed for the measurements of charged particle momentum spectra. While the reconstruction of charged particles in PbPb collisions is based on the standard CMS pp tracking, it is slightly modified to cope with the challenges presented by the much higher hit density in central PbPb collisions. It also uses additional information based on the energy deposition in the CMS calorimeters to achieve high tracking efficiency while keeping the fake fraction low even in the most dense track environment in the central PbPb collisions.

5.1. Generation of Seeds

The first step in the standard CMS track reconstruction is to generate "seed" by grouping two (pairs) or three (triplets) reconstructed hits in the pixel barrel and endcap detectors with constraints from a beam spot or a vertex position [157], which are reconstructed as described in Sec. 4.0.11. Prior to the seed generation, the spatial positions of hits each track leaves in the pixel and the silicon detectors are 'reconstructed' and used as input for the track reconstruction as described in the sections that follow.

5.1.1. Hit Reconstruction

The reconstruction of hits, so-called 'local reconstruction', transforms the digitized hit information into the reconstructed hits in the local coordinate system¹ of the sensors in the tracker and is done in two steps. First, a set of adjacent pixels or strips above threshold² are grouped to form a 'cluster', known as clustering [158, 159]. With a finite width of the pixel and silicon sensor, an incoming particle does not always enter and leave the same sensor, rather it drifts inside the sensor resulting in a charge sharing over more than one silicon sensor. The drift is enhanced in the presence of the magnetic field due

¹In the local coordinate system, x -axis is defined as a direction perpendicular to the beam axis, y -axis is defined as a direction parallel to the beam axis, and z -axis is defined as a direction that is always perpendicular to the silicon module [158]

²The average effective thresholds in the pixel detector are approximately $3500e$ in the barrel and $3000e$ in the endcap, where e is the magnitude of the electron charge [125].

5. Particle Reconstruction

to the Lorentz force. Figure 5.1 shows the cluster charge distributions measured in the pixel barrel and in the endcap from the 0.9 TeV minimum bias data and fully simulated PYTHIA MC samples. The comparison between the data and MC shows a good agreement except the data distribution is slightly wider possibly due to the gain variation in pixel [125].

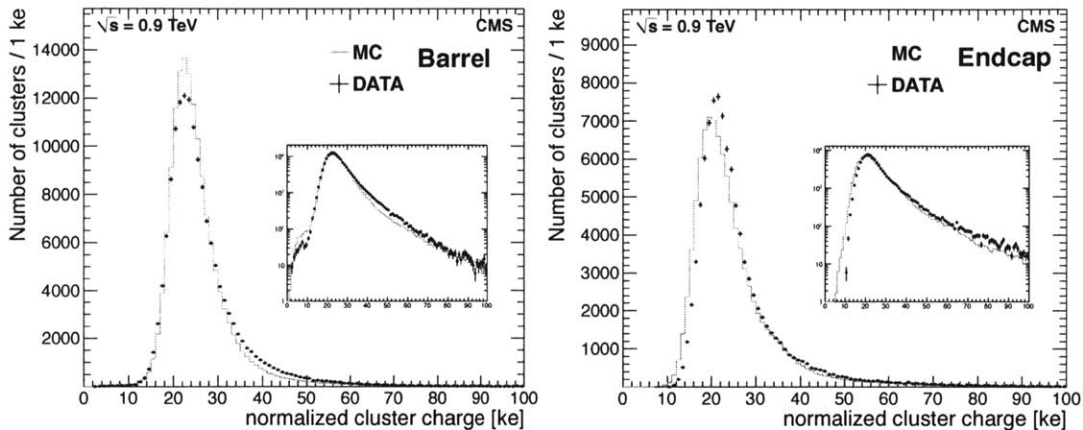


Figure 5.1.: Distribution of the cluster charge in the pixel barrel (left) and in the endcap (right) [125]. The same figure with the semi-log scale is shown in the inset.

For a given cluster, the hit position is evaluated with the projected impact angles of the track onto the local coordinate system. With the size of charges deposited in the sensor at the incidence and at the departure, along with the information of the shared charge width determined from the projected angles, the hit position in the $x - y$ direction is computed³ along with the corresponding position uncertainty based on a parametrization of the error as a function of the cluster size and the angles or the root-mean-square values of the hit residual in the absence of the angles information [158]. If only one sensor has been hit, the middle of the sensor in the local x and y directions will be the position coordinate.

5.1.2. Pair and Triplet Seed Generation

From various combinations of hits in the two subsequent pixel layers in the barrel and endcap (e.g., 1st and 2nd layers, 1st and 3rd layers, 2nd and 3rd layers, and etc), hit pairs are formed. Figure 5.2 and Fig. 5.3 shows all possible layer and disk combinations of pixel hits used for finding pixel pairs and pixel triplets, respectively. Starting from the outer layer, a second hit in the inner layer is searched, constrained by the vertex (or beam-spot) position and the outer layer hit position and guided by the analytical prediction for its position. The pixel triplet is formed by adding one more hit to a given pixel pair.

³It's basically the geometric center of the cluster with the adjustment due to the weighting with the size of charges and a correction due to the Lorentz shift [158]

From the found pixel pair and triplets, corresponding seeds are generated with the track parameters and its uncertainties estimated using the equations of an ideal helix passing through two hits with the beam-spot or vertex position in case of pixel pair and three hits in case of pixel triplet, from which the radius of the curvature R is extracted and the momentum $p_T(\text{GeV}/c) \simeq 0.003BR[\text{T}][\text{cm}]$ is estimated.

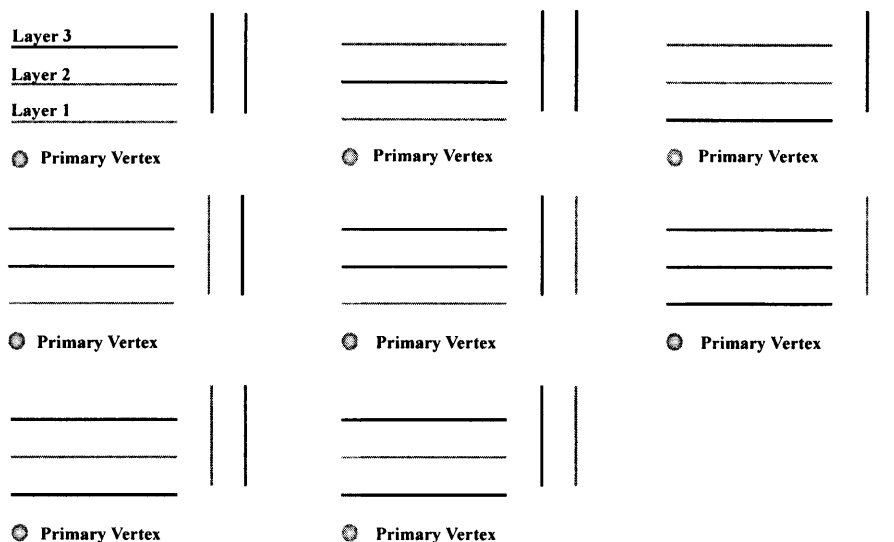


Figure 5.2.: Possible pixel layer and disk combinations for finding pixel pairs.

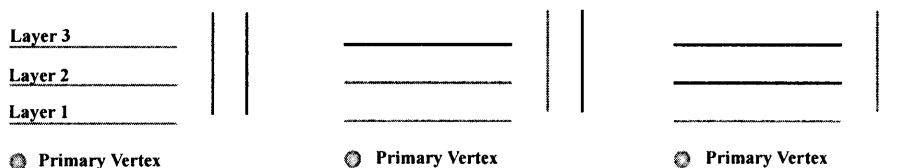


Figure 5.3.: Possible pixel layer and disk combinations for finding pixel triplets.

5.1.2.1. Track Parameters

In the CMS track reconstruction [156], the five parameters are used to describe a trajectory of track. The five parameters are the coordinates in the transverse plane (d_0) and in the longitudinal plane (z_0), the azimuthal angle of the momentum vector (φ), the (cotangent of) polar angle ($\cot(\vartheta)$), and the transverse momentum p_T , defined at the point of closest approach of track to the beam axis, i.e., the impact point. With this parametrization, the helix equation of motion of a track in the presence of a magnetic field parallel to the z -axis is given by [156, 160]

5. Particle Reconstruction

$$x(\varphi) = x_r + d_0 \sin \varphi_p - \frac{p_T}{qB_z} (\sin \varphi - \sin \varphi_p) \quad (5.1)$$

$$y(\varphi) = y_r - d_0 \sin \varphi_p + \frac{p_T}{qB_z} (\cos \varphi - \cos \varphi_p) \quad (5.2)$$

$$z(\varphi) = z_r + z_0 - \frac{p_T}{qB_z} (\varphi - \varphi_p) \cot(\vartheta) \quad (5.3)$$

,where $\vec{r}_r = (x_r, y_r, z_r)$ is the reference point, q is the magnitude of the charge, and B_z is the z -component of the magnetic field.

5.2. Trajectory building

The seed found in the first step is then propagated outward using a combinatorial Kalman filter ⁴ algorithm in search of compatible hits [162], which is equivalent to a global least square minimization [163]. The propagation is done by extrapolating the first estimate of track parameters obtained from the seed to subsequent layer according to equations of motion of a charged particle in a constant magnetic field (i.e., helix motion). The propagation accounts for multiple scattering and energy loss in the traversed material. To find compatible hits, a compatible pixel or strip layer is first determined. A detector layer is considered compatible if the position of the extrapolated trajectory on the detector layer is within $n \times \sigma$ of the position uncertainty on the layer with n ranges between 3 to 5 configurably. For each compatible detector layer, compatible hits (or measurements) are found based on the χ^2 residual between the measured positions and the predicted position from the the initial seed.

A compatible hit is added to the trajectory and the track parameters and the respective uncertainties are updated accordingly. When there's more than one compatible hit are found, multiple trajectories are created for each compatible hit in parallel (i.e., combinatorial). If there's no hit found in a certain compatible layer, a trajectory is still propagated further treating it as 'invalid' hit in order to maximize the track finding efficiency. This procedure of trajectory building is repeated until there's no further compatible hit is found or the outermost layer of the tracker is reached. Once all the possible trajectories are built from the seeds, cleaning step is applied to remove potentially duplicate tracks. Duplicate tracks are created when the same trajectory is built twice from two different seeds or more than one trajectory are built from a single seed. Based on a shared hit fraction defined as $f_{shared} = N_{shared}^{hit} / \min(N_1^{hit}, N_2^{hit})$, the track with the least number of hits is removed. This cleaning is repeated for all the possible combination of the built trajectories.

⁴The Kalman filter is in general a set of mathematical equations used to estimate the states of dynamic system recursively (i.e., the state is updated with the inclusion of new measurements) in a way that the a global least square error is minimized. The update of the state is done recursively with the inclusion of new measurement, i.e. repetition of (*prediction* \rightarrow *measurement* \rightarrow *filtering*) [161].

5.2.1. Final track fit and Iterations

Lastly, the collection of hits in each trajectory built from the previous steps is fitted with a least χ^2 in the form of Kalman filter for the final and optimized estimation of the track parameters. The aforementioned steps with the track selections described in the following section are performed up to six iterations with different combinations of the seed types (e.g., pixel pair, pixel triplet, or pixel pair+pixel triplet) and the (seeding) track selection criteria for seeding tracks, which are progressively looser, which is known as ‘iterative tracking’. At each iteration, those hits that are unambiguously belonging to the tracks found in previous iteration are removed to avoid creating duplicate tracks. While the first two iteration (0th and 1st) suffice to find the vast majority of primary tracks, the next iterations (2nd and 3rd) and the final two iterations (4th and 5th) are designed to find tracks with displaced vertex position and tracks with no pixel hits, respectively [164]. Detailed settings of each iteration can be found in Table 5.1 (Sec. 5.2.2).

For a given track trajectory, the momentum \vec{p} is estimated as follows. The momentum components, projected onto $\rho - \phi$ and $\rho - z$, are determined first. perpendicular and parallel to the beam axis. From the measured p_T , the size of the momentum ($|\vec{p}|$) is determined from $p = p_T / \cos \lambda = 0.3BR / \cos \lambda$. p_i can be determined at a given point. The uncertainty for the momentum estimation is directly translated from the uncertainty of the R determination with a given number of measurements.

5.2.2. Track Selections

In order to minimize fake tracks retaining high track reconstruction efficiency, a set of quality selections is made for the reconstructed tracks (i.e., ‘quality cuts’). The tracks that satisfy the standard (tightest) quality selections made in CMS is called *highPurity* tracks. This criterion, described in Ref. [154], consists of numerous selections on the properties of the tracks, including the normalised χ^2 , the compatibility with the beam-line and primary vertices, the number of valid hits, and etc. A list of quality variables used in the selection is listed below.

- Number of valid hits: N_{hits}^{valid}
- Number of detector layers with measurements: N_{layers}
- Fit chi-square and normalized fit chi-square: χ^2 ($\chi^2/N_{d.o.f}$)
- Distance of closest approach in $x - y$ direction: d_0 (or d_{xy})
- Corresponding error of d_0 : $\sigma(d_0)$
- Distance of closest approach in the longitudinal direction: d_z
- Corresponding error of d_z : $\sigma(d_z)$
- Relative p_T error: $\sigma(p_T)/p_T$

5. Particle Reconstruction

,and the combined variables such as $d_{0,z}/\sqrt{\sigma(d_{0,z}^2)+\sigma(v_{0,z})}$ are also used as it is proven to be more discriminant between the genuine and fake tracks. The variables related to the distance of closest approach of track at the point of impact, (i.e., transverse and longitudinal impact parameter), which is calculated with respect to the vertex position, are referred to as ‘vertex compatibility’. The aforementioned iterative tracking uses different settings in each iterations, which can be found in Table 5.1. The parameters are slightly different as they are tuned in each software (CMSSW) version, which can be found from the CMS Iterative Tracking page [165].

Iteration	Seeding Layers	p_T cut (GeV/c)	d_0 cut (cm)	d_z cut (cm)
0	pixel triplets	0.5	0.2	15.9
1	pixel pairs	0.9	0.2	0.2*
2	pixel triplets	0.2	0.2	17.5
3	pixel pairs	0.35	1.2	7.0
4	TIB 1+2 and TID/TEC ring 1+2	0.5	2.2	10.0
5	TOB 1+2 and TEC ring 5	0.8	5.2	10.0

Table 5.1.: Setting for each iteration in the iterative tracking. The p_T cut and impact parameter cuts are applied during the seeding. d_z is calculated with respect to the center of the CMS detector except the 1st iteration where it’s calculated with respect to the reconstructed vertex, noted by the symbol *.

For the measurement of charged particle p_T spectra in pp collision, in order to minimise the contribution from misidentified tracks and tracks with poor momentum resolution following quality cuts are additionally applied to the *highPurity* tracks: the requirement of at least five hits on the track ($N_{hist}^{valid} \geq 5$), the normalized χ^2 per degree of freedom divided by the number of tracker layers used in the fit less than a maximum value which varies from 0.48 and 0.07 depending on η and p_T , ($0.48 \geq (\chi^2/N_{d.o.f})/N_{layers} \geq 0.07$) and a relative momentum uncertainty of less than 20% ($\sigma(p_T)/p_T \geq 0.2$). Furthermore, to reject non-primary tracks (i.e., the products of weak decays and secondary interactions with detector material), selections are placed on the impact parameter of the tracks with respect to the primary vertex position. Specifically, the transverse and longitudinal impact parameters are required to be less than 0.2cm and also less than 3 times the sum in quadrature of the uncertainties on the impact parameter and the corresponding vertex position, $d_{0,z}/\sqrt{\sigma(d_{0,z}^2)+\sigma(v_{0,z})}$, where $\sigma(v_{0,z})$ is the uncertainty in the vertex position in the transverse and longitudinal direction. In the case of multiple quality reconstructed vertices in the minimum bias event samples, tracks that pass the impact parameter selections with respect to any vertex are used in the analysis. The number of events, by which the track p_T distribution is normalised, is then scaled by a factor to account for the event pileup fraction.

5.3. Track reconstruction in PbPb collisions

Due much higher track density environment in central PbPb collisions compared to pp collisions of the measurements, the default pp tracking reconstruction described in the previous sections does not work optimally in terms of reconstruction time, often causing abnormal termination of CPU during the execution of the reconstruction algorithms. Moreover, it generates large fraction of fake tracks due to high combinatorial backgrounds in central PbPb collisions. For the reconstruction of charged particles in PbPb collisions, therefore, some criteria in the pp tracking reconstruction have been fine-tuned to cope with the challenges presented by the higher track density. Also, the ‘heavy-ion tracking’ is comprised of three iterations instead of six ⁵. For the final track selection, calorimeter information is additionally used as a handle for discriminating the genuine and fake tracks.

5.3.1. Tracking Environment in PbPb Collisions

With the near simultaneous collisions of many nucleons that can occur in heavy-ion collision, much higher number of charged particles are produced in PbPb collisions than in pp collisions. The charged particle multiplicity reaches about 1600 per unit pseudo-rapidity in the most central (0–5%) collisions compared to about 5 charged particles in the minimum bias events at the same center-of-mass energy ⁶. Therefore, it poses a large number of hits and combinatorial background to deal with in the heavy-ion tracking. Figure 5.4 shows the average occupancy of the tracker barrel, defined as a fraction of the total number of strip modules that are ‘activated’ (i.e., signal above threshold), made for the minimum bias pp collision and the HYDJET MC simulation in 0–5% central event. The average occupancy for the minimum bias PbPb collision stays below about 10%.

The high occupancy environment affects the pixel and the strip detector hardware and readout electronics, which is detailed in the following section. In order to deal with the high track hit density posed by the larger track multiplicity, the heavy-ion tracking algorithms are tuned to have in general tighter settings with limited number of tracking iterations. While the default heavy-ion tracking is done in a single tracking iteration based on the pixel triplet seeding, the higher iterations (2nd and 3rd) are used as well for analyses that use high p_T tracks as object including the analysis presented in this thesis.

5.3.1.1. High Occupancy Effects in Hardware and Readout

While the occupancy in the pixel system is rather low (at a few % level) due to high granularity of the system, the readout chain with finite buffer size can still be highly affected leading to data losses. The readout chip (ROC) or the FED input with finite

⁵In heavy-ion tracking, the iteration starts from 1st instead of 0th by convention.

⁶The number of charged particles per pseudo-rapidity, $dN/d\eta|_{\eta \approx 0}$ in the most central collision (0–5%) of PbPb collisions at $\sqrt{s_{NN}} = 2.76$ TeV is measured as 1612 ± 55 [166] while it is estimated to be 3.8~4.8 based on the extrapolation [166] of the measurements [167, 168] at $\sqrt{2.36}$ TeV.

5. Particle Reconstruction

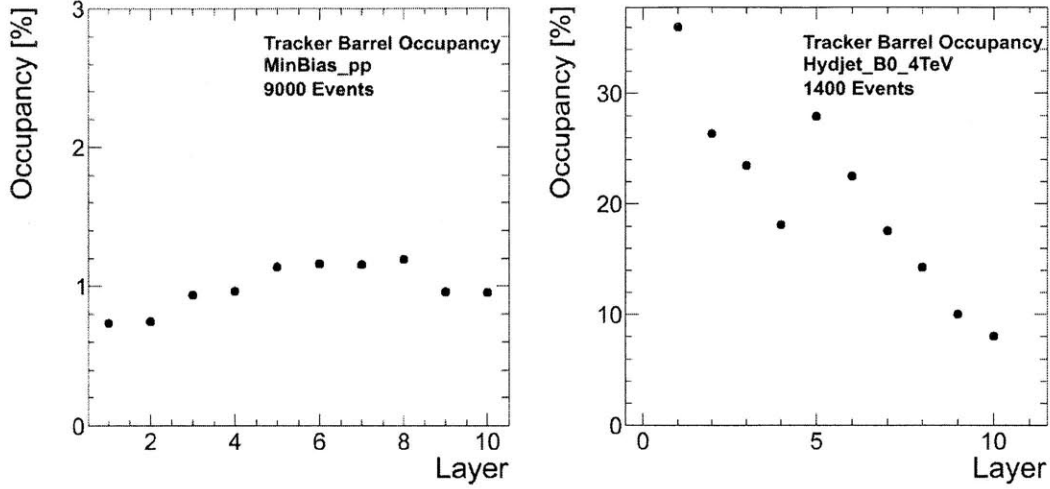


Figure 5.4.: Tracker occupancy in pp minimum bias event (Left). Tracker occupancy in PbPb 0–5% event (Right).

buffer sizes ⁷ can be overflowed where there is a large number of hits in a central PbPb event [169], in particular when there are subsequent events with high multiplicity (i.e. subsequent central events). To prevent such buffer-overflow and the breakdown of the readout chain, $\mathcal{O}(10\mu s)$ of hold-off was introduced in the pixel firmware. While the loss of data due to the hold-off was negligible during the 2010 PbPb run, during the 2011 run when the interaction frequency was higher, up to a few % of dead-time of the detector readout was caused because of the hold-off.

As seen from Fig 5.4, the occupancy in the silicon strip tracker (SST) system in PbPb collisions is sizeable compared to that of pp collisions. The high detector occupancy can directly affect the track reconstruction efficiency via potential hit losses caused by incorrectly identified noise or pedestal thresholds that are dependent on the detector occupancy [169]; The analogue data transferred from each APV (see Sec 3.2.1.2) in the SST go through pedestal subtraction, Common Mode Noise (CMN) subtraction and FED zero-suppression based on the Zero-Suppression (ZS) algorithm implemented in the firmware, transferring only useful signal information. If the ZS algorithm identify the related thresholds incorrectly, it can lead to a potential hit loss and in turn the track reconstruction efficiency. Figure 5.5 shows an example distribution of the ADC counts in each strip in the 7 APV modules. From the dotted black line to the solid red line, it illustrates how big he size of the pedestal and the CMN are. The strips ADC counts that are highlighted as yellow represent the incorrectly identified baseline that can potentially lead to hit losses.

During the 2010 PbPb run, the ZS algorithm was not performed in the detector readout chain, known as tracker Virgin Raw (VR) mode, since the default ZS algorithm used in pp collisions was not optimized for identifying thresholds in the high occupancy. As a

⁷For each double-columns (DCOLs), consisting of 160 pixels, up to 31 hits can be buffered before it is reset. As for the FED, 1000 pixel per readout link that connects a ROC to the FED can be buffered [169].

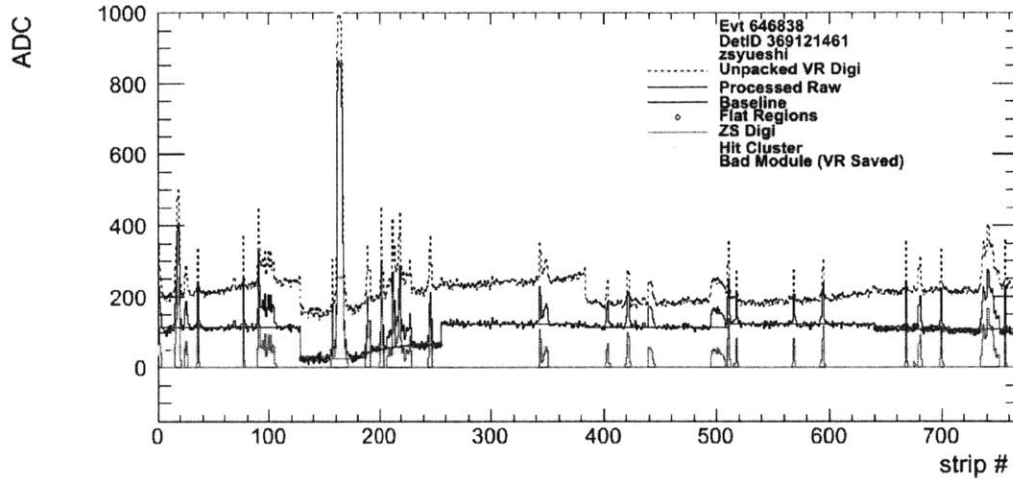


Figure 5.5.: Distribution of the ADC counts for each strip and the illustration of the Zero-Suppression

consequence of running in the VR mode, the data volume of about 20 MB per event (10 times larger than that of pp collision data) regardless of event centrality had to be handled until the ZS algorithm specifically developed for heavy-ion collisions was finally performed in the offline data reconstructions. During the 2011 PbPb run, on the other hand, the ZS algorithm, which was improved based on the 2010 data, was performed in the High Level Trigger (HLT) system, allowing smaller data volume to be handled and to be stored in the storage.

5.3.2. Heavy-ion Tracking

First, prior to track reconstruction, the three-dimensional primary vertex position is fitted from a collection of pixel triplet tracks reconstructed from a region around the beam spot as described in Sec. 4.0.11. Next, to reduce the random combinatorial background, track candidates are only built from triplet seeds. The seeds from a restricted region within 2 mm of the primary vertex are constructed with a minimum p_T of 0.9 GeV/c. Further selections are made before propagating the seed trajectories through the strip tracker to build fully reconstructed tracks. The selections include a 'loose' requirement of the track fit χ^2 less than 1000, the distance of closest approach (d_0) of track in the transverse direction less than 0.3 cm, and lastly the maximum distance of closest approach of track in the longitudinal direction (d_z) less than 6 times the corresponding error ($\sigma(d_z)$).

5.3.3. Higher Tracking Iterations

To improve the track reconstruction efficiency, two more iterations of the tracking are performed after removing hits unambiguously belonging to the tracks found in the first

5. Particle Reconstruction

iteration. In the second and third iterations, more efficient pp-based pixel pair and triplet seedings are used, respectively. While using the pp-based pixel pair seeding in the first iteration would have resulted in the larger number of seeds due to the combinatorial, using it in the higher iteration results in the number of seeds that can be further reconstructed within the available CPU and memory budget because the number of hits remaining after the first iteration is highly reduced. A set of ‘tight’ quality cuts are applied on the tracks found in the 2nd and 3rd iterations before they are merged with the tracks from the first-iteration to ensure that the additional tracks from the higher iterations have high purity (i.e., high real-to-fake track ratio) The selection includes the requirement of at least fourteen hits on the track ($N \geq 14$), the normalized χ^2 per degree of freedom divided by the number of tracker layers used in the fit less than 0.15 ($(\chi^2/N_{d.o.f})/N_{layers} \leq 0.15$), a relative momentum uncertainty of less than 5% ($\sigma(p_T)/p_T \leq 0.05$), and aforementioned vertex compatibility less than three ($d_{0,z}/\sqrt{\sigma(d_{0,z}^2) + \sigma(v_{0,z})} \leq 3$).

5.3.4. Track-calorimeter Matching

Lastly, the calorimeter (ECAL and HCAL) information is used to improve tracking efficiency at high p_T ($\gtrsim 30$ GeV/c) by requiring looser quality criteria for tracks that are determined to be calorimeter compatible. This is possible because genuine tracks with high p_T are expected to leave large energy deposits in the calorimeter. Figure 5.6 shows the correlation between the energy deposited in the calorimeter systems, ECAL, HCAL, and both ECAL and HCAL with the momentum of individual track separately for the real (colored) tracks and the fake (empty box) tracks. The red line illustrates that a large fraction of the fake tracks can be rejected without loss of the real track at a given momentum.

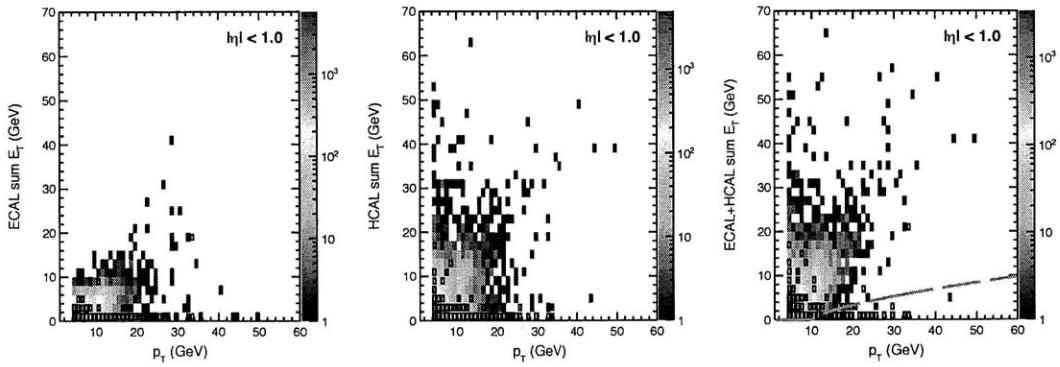


Figure 5.6.: Correlation between the calorimeter energy deposit and the track momentum.

Tracks are matched to the closest calorimeter cell in (η, ϕ) , where ϕ is the azimuthal angle of the track. A track is determined to be compatible with the matched calorimeter cell if the sum of the transverse energy measured by the electromagnetic and hadronic

calorimeter cells is above a minimum fraction (30%) of the track transverse momentum in addition to a requirement of the closest distance in (η, ϕ) smaller than a p_T dependent cut which varies from ~ 0 to 0.087 ⁸

5.3.4.1. Track Selections

A set of quality cuts is applied on the all iterations combined tracks. If a certain track is calorimeter compatible, looser set of selections are performed. On the other hand, in case of calorimeter-incompatible tracks, ‘tight’ quality criteria are imposed. To summarize the quality cuts that are applied on the tracks differentially for the two cases,

- ‘Loose’ selections for calorimeter-compatible tracks
 - $N_{hits}^{valid} \geq 10$
 - $\sigma(p_T)/p_T \leq 0.1$
 - $(\chi^2/N_{d.o.f})/N_{layers} \leq 0.15$
 - $d_{0,z}/\sqrt{\sigma(d_{0,z}^2) + \sigma(v_{0,z})} \leq 8$
- ‘Tight’ selections for calorimeter-incompatible tracks
 - $N_{hits}^{valid} \geq 13$
 - $\sigma(p_T)/p_T \leq 0.05$
 - $(\chi^2/N_{d.o.f})/N_{layers} \leq 0.15$
 - $d_{0,z}/\sqrt{\sigma(d_{0,z}^2) + \sigma(v_{0,z})} \leq 3$

Since the tracks from the 2nd and 3rd iterations are selected with event tighter selections, the quality cuts did not reject any tracks from the higher iterations. The distributions of the tracks qualities are shown for the the final tracks that passed the aforementioned quality selections between the data and MC in Fig 5.7. Two different versions (39X and 44X) of the MC are shown for the simulations of the detector with realistic detector condition in 2010 and 2011, respectively. The later MC simulation is further divided into two different *HYDJET* ‘tunes’, later being tuned to the various results obtained based on the 2010 data [170]. The difference between the two is negligible. The same quality distributions shown in bins of p_T and centrality can be found in Appendix B. Overall, the simulated and reconstructed *HYDJET* MC describes the reconstructed data reasonably well, justifying the use of the *HYDJET* MC as the tracking inefficiency corrections.

⁸The exact p_T dependent cut is given by $0.087/(1.0+0.1\exp(-0.28(p_T-20)))$, which is determined from calorimeter-matching cut study.

5. Particle Reconstruction

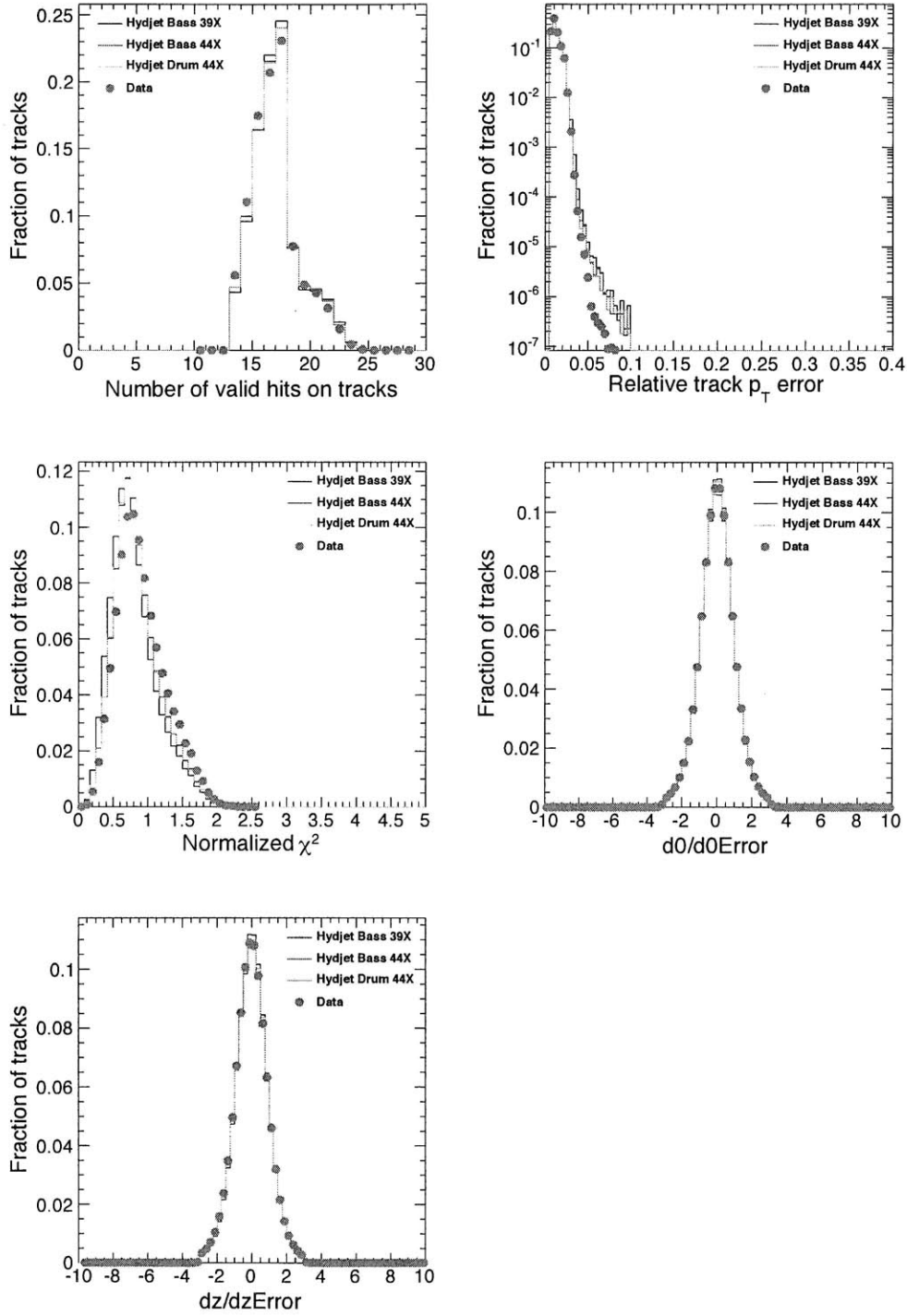
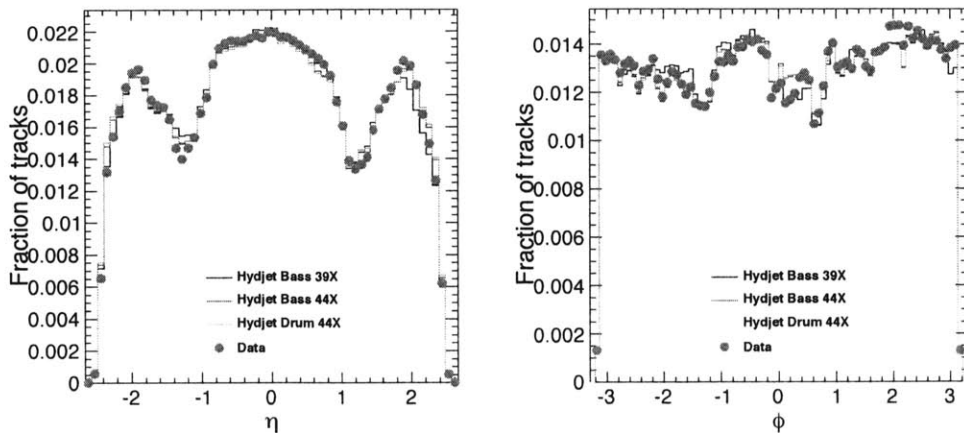


Figure 5.7.: Track quality distributions. From the top left, it is N_{hits}^{valid} , $\sigma(p_T)/p_T$, $(\chi^2/N_{d.o.f})/N_{layers}$, $d_0/\sqrt{\sigma(d_0^2)+\sigma(v_0)}$, and $d_z/\sqrt{\sigma(d_z^2)+\sigma(v_z)}$.

Figure 5.8.: Track η and ϕ distribution between data and MC.

5.3.5. Tracking Performance in PbPb

The tracking performance of the tracks that are selected in the previous section is evaluated based on simulated minimum bias PbPb events from the *HYDJET* [151] generator and from the *HYDJET* sample mixed at the level of simulated hits with QCD events generated with different setting of the hard-scattering scale $\hat{p}_T=30, 50, 80, 110, \text{ and } 170$ GeV/c) from *PYQUEN* [151], a generator for the simulation of rescattering as well as radiative and collisional energy loss of hard partons in heavy-ion collisions. The latter samples, which by construction produce hard-scattering (i.e., jet) in every event, are needed since the minimum bias sample alone requires numerous number of event generation to achieve a similar statistical reach of high p_T particles in the data due to steeply falling nature of high p_T particle production probability. The performance includes the geometrical acceptance of the detector (A), the efficiency of the reconstruction algorithm (ϵ), the fraction of the tracks for which a single charged particle is reconstructed as more than one track, known as ‘multiple’ reconstruction fraction (M), the fraction of tracks corresponding to non-primary charged particles, known as secondary fraction (S), and the fraction of misidentified tracks that do not correspond to any charged particle, known as ‘fake’ fraction (F). Figure 5.9 shows the global tracking efficiency (i.e., the algorithmic efficiency times the geometrical acceptance) and the fake rate of the selected tracks as a function of p_T for tracks with $|\eta| < 1$, evaluated from various MC sample. Figure 5.10 shows the secondary and multiple reconstruction fractions as a function of p_T for tracks with $|\eta| < 1$, evaluated from the sample (i.e., *HYDJET* embedded dijet sample with hard-scattering scales of 170 GeV/c) with the highest statistics up to 100 GeV/c.

5. Particle Reconstruction

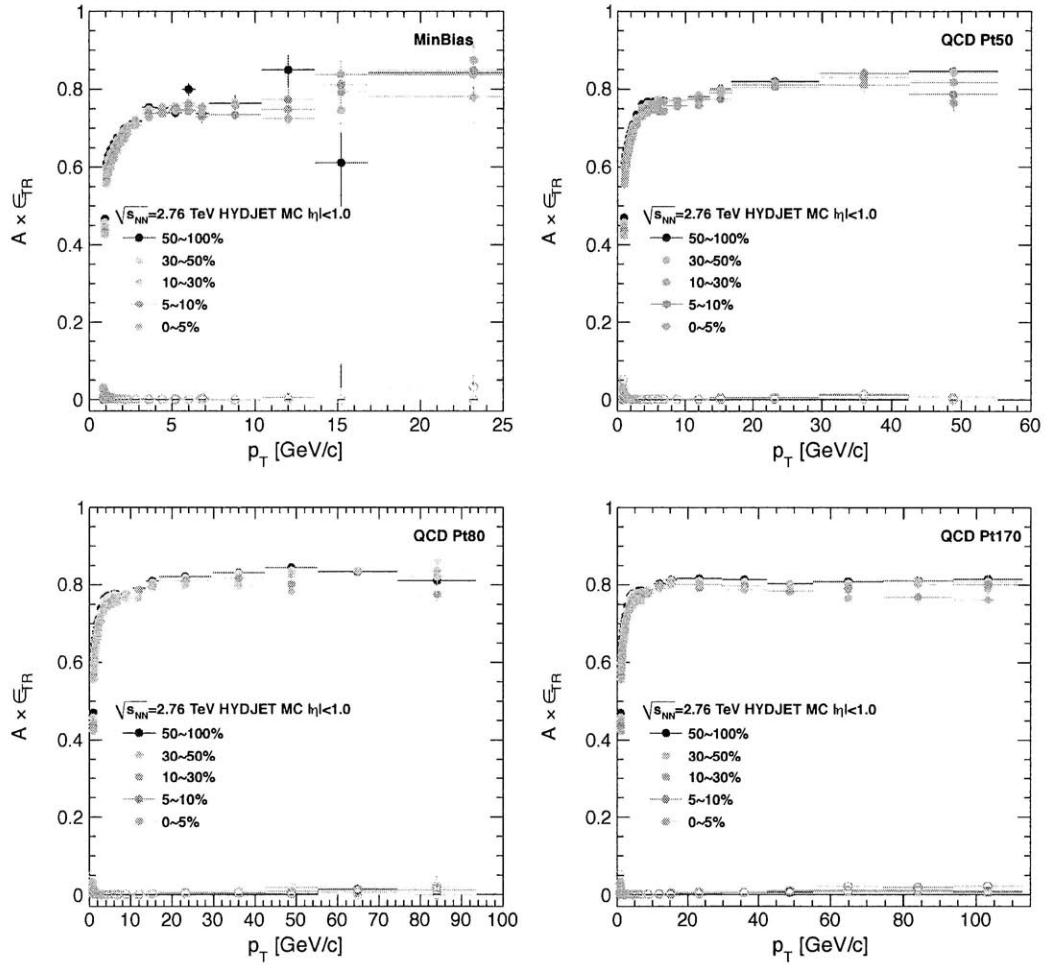


Figure 5.9.: Global tracking efficiency and fake rate evaluated from MinBias sample and HYDJET embedded dijet sample with hard-scattering scales of 50, 80, 170 GeV/c.

5.3. Track reconstruction in PbPb collisions

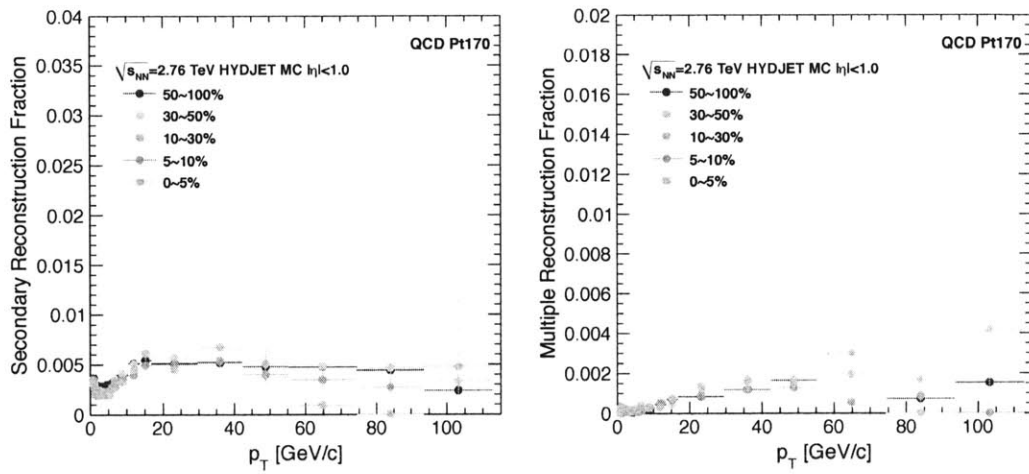


Figure 5.10.: Secondary fraction and multiple reconstruction fraction evaluated from the HYDJET embedded dijet sample with hard-scattering scales of 170 GeV/c.

6. Obtaining Charged Particle Spectra

The primary charged particle momentum spectra in the form of ‘invariant yield’ can be constructed based on the measured number of charged particle tracks in a given momentum and pseudorapidity bins. The invariant yield is defined as

$$E \frac{d^3 N_{ch}}{d^3 p} = E \frac{d^3 N_{ch}}{d p_x d p_y d p_z} \quad (6.1)$$

, which describes the number of primary charged particles (N_{ch}), defined to include decay products of particles with proper lifetimes less than 1 cm, per event in a given momentum phase space, $\vec{p} = (\vec{p}, \vec{p} + d\vec{p})$, similarly as introduced in Eq. 2.16 in Sec. 2.4.3.1. Since the average distribution of produced single-particle is symmetric in the azimuthal direction, the invariant yield can be integrated over the azimuthal direction after recasting Eq. 6.1 into the cylindrical coordinate.

$$E \frac{d^3 N_{ch}}{d^3 p} = \frac{E}{p_T} \frac{d^3 N_{ch}}{d p_T d \phi d p_z} = \frac{E}{2\pi p_T} \frac{d^2 N_{ch}}{d p_T d p_z} \quad (6.2)$$

Now, using the expressions $E = m_T \cosh(y)$ and $p_z = m_T \sinh(y)$, the invariant yield formula can be expressed as a function of rapidity (y), which can be further rewritten in terms of pseudorapidity (η) with the approximation for relativistic particles ($E \gg m$).

$$E \frac{d^3 N_{ch}}{d^3 p} = \frac{1}{p_T} \frac{d^3 N_{ch}}{d p_T d \phi d y} \approx \frac{1}{p_T} \frac{d^3 N_{ch}}{d p_T d \phi d \eta} \quad (6.3)$$

Since the analysis is done on the inclusive high- p_T particle production without the identification of particle species, η is measured instead of y . It can be seen clearly from Eq. 6.3 that the formula is indeed invariant under the Lorentz transformation ($\hat{y} = y + \text{const.} \therefore d\hat{y} = dy$) since the rapidity transforms additively.

Knowing the time-integrated luminosity of the analysed data sample, $\int \mathcal{L} dt$, the invariant differential cross section can be obtained by normalizing the corresponding yield by the integrated luminosity,

$$E \frac{d^3 \sigma_{ch}}{d^3 p} = \frac{1}{\int \mathcal{L} dt} \times E \frac{d^3 N_{ch}}{d^3 p} \quad (6.4)$$

, where the luminosity is measured using the HF detector as described in Ref. [171, 172].

6. Obtaining Charged Particle Spectra

6.0.6. Correction to Raw Spectra

To arrive at the final invariant yield for a given centrality bin, a number of corrections are applied to the raw charged spectra according to the following equation:

$$E \frac{d^3 N_{ch}}{d^3 p}(p_T, \eta) = \frac{\sum_{E_T^{jet}} N_{track}^{raw}(E_T^{jet}, p_T, \eta) \cdot w_{tr}(p_T, \eta, E_T^{jet})}{2\pi p_T \cdot \delta p_T \cdot \delta \eta \cdot N^{selected}} \quad (6.5)$$

,where N_{track}^{raw} is the raw number of tracks in a bin with transverse momentum width Δp_T and pseudorapidity width $\Delta \eta$, E_T^{jet} is the transverse energy of nearby jet ¹ and $N^{selected}$ is the number of selected events. A track weight w_{tr} is applied as a function of pseudorapidity, transverse momentum, transverse energy of nearby jet, and event centrality, variables that the tracking performance are most dependent on, and it is given by

$$w_{tr}(p_T, \eta, E_T^{jet}) = \frac{(1-F) \cdot (1-S)}{A \cdot \epsilon^{tr} \cdot (1+D)} \quad (6.6)$$

accounting for the geometrical acceptance (A), the algorithmic efficiency (ϵ), the multiple reconstruction fraction (M), the secondary fraction (S), and the fake fraction (F), as introduced in 5.3.5.

Figure 6.1 shows comparisons between the reconstructed (i.e., simulated with the detector response and track finding algorithms performed) and corrected (i.e, weighted by w_{tr}) MC spectra and the generator-level MC “truth” (i.e, input) spectra for the same selected events in different centrality bins, referred to as “closure test” plot, for the pure MB sample, the MB and QCD mixed events sample, respectively. It demonstrates that the truth spectra can be rebuilt from the reconstructed spectra by correcting for the known tracking inefficiency. The latter mixed samples are used to check wider momentum range.

6.0.6.1. Trigger Matching

The reconstructed and tracking inefficiency corrected p_T spectrum in the minimum-bias events and in the jet-triggered events are combined after normalizing each spectrum by “equivalent number of MB events”. The equivalent number of MB events means that the number of event that would have required in the MB sample to reach a same kinematic (i.e., p_T) reach in a given jet trigger. For the MB sample, it’s simply the number of events in the sample (after correcting for a possible trigger inefficiency). For the jet-triggered sample, it can be calculated by scaling the number of events in a well defined jet E_T range with the scaling factor obtained from the ratio of all MB events to the number of events in the same jet E_T range in the MB sample. The jet E_T range is chosen such that the lower boundary sits well above the jet E_T , above which the jet-triggering is fully efficient (i.e, every event with jet having $E_T \geq E'_T$ is triggered therefore recorded by

¹The nearby jet is defined for a given track as a jet that is closest in (η, ϕ) , i.e., $\Delta R = \sqrt{(\Delta \eta)^2 + (\Delta \phi)^2}$. If no jet is found within ΔR of 0.8, it’s categorized as no nearby jet, assigning 0 to the nearby jet energy.

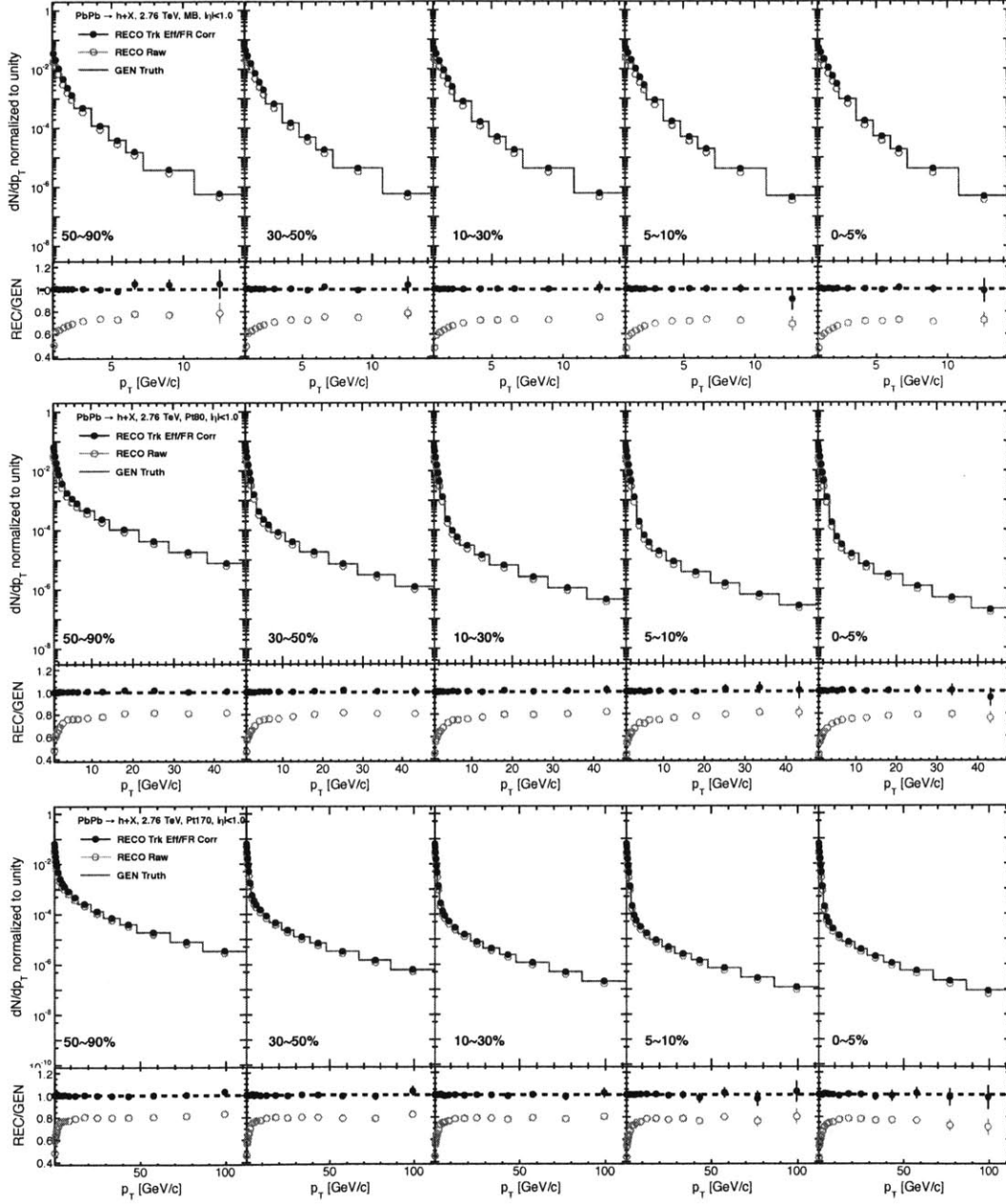


Figure 6.1.: Closure test of MC-based tracking corrections applied to reconstructed MC (HYDJET), MC (HYDJET + PYTHIA QCD $\hat{p}_T > 80$ and 170 GeV/c) events and compared to the generator-level truth for different centralities

6. Obtaining Charged Particle Spectra

the jet-trigger) in order to avoid the inefficiency in the jet-trigger. Also, the jet E_T is chosen in the range where there exists sufficient statistics in the MB sample to ensure the determination of the scaling factor is not statistically limited. Figure 6.2(a) shows the distributions of the corrected transverse energy of leading jets normalised by the number of selected minimum bias events N_{MB}^{Evt} and the efficiency turn-on curves for the jet triggers with uncorrected energy thresholds of 65 and 80 GeV. The respective triggers become fully efficient above about 80 and 100 GeV.

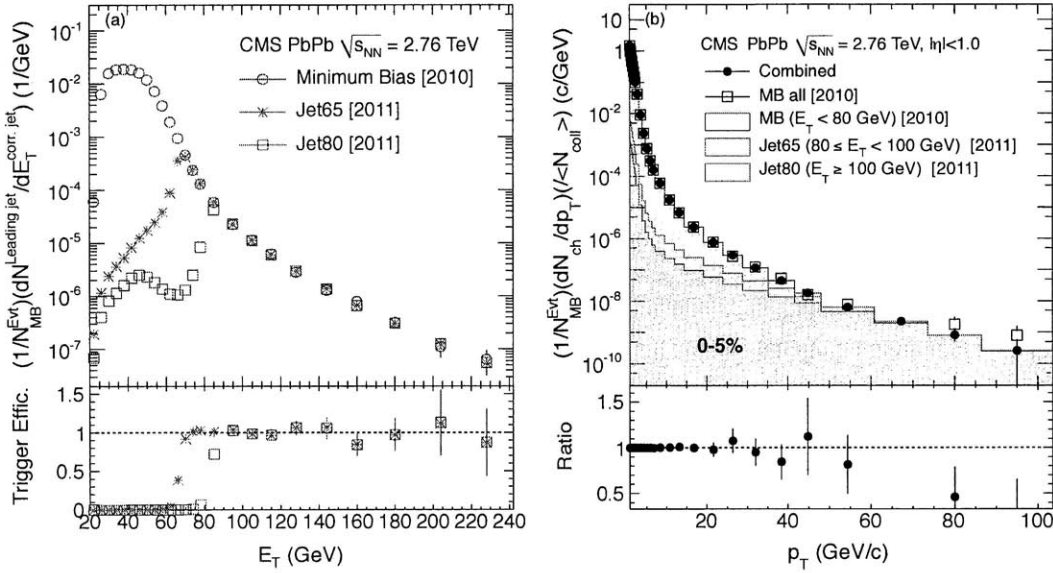


Figure 6.2.: (a) E_T distributions and the efficiency turn-on (b) Combined charged particle dN/dp_T with each trigger contribution explicitly shown

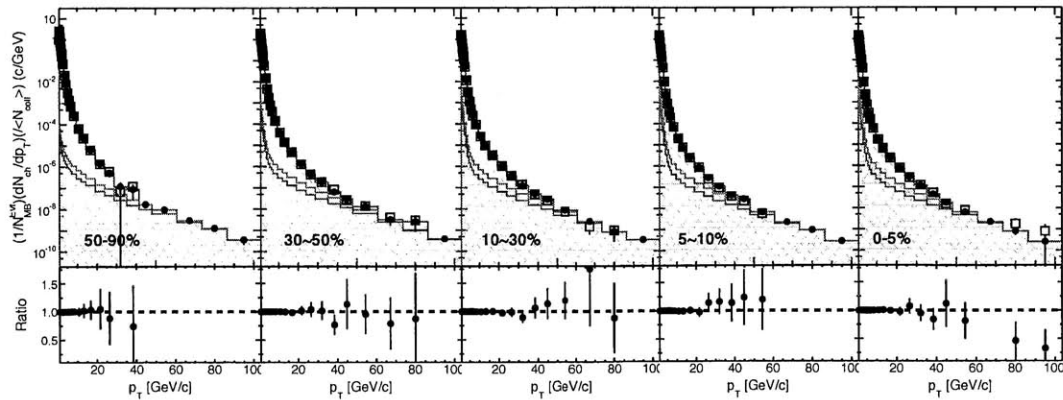


Figure 6.3.: The same plot as in Fig 6.2(b) made for other centrality bins as well.

In this analysis, the range is chosen to be $80 < E_T < 100$ GeV for the jet-trigger (JET65) with a trigger threshold of 65 GeV, and the equivalent number of MB events (N_{MB}^{Jet65}) for

this trigger is calculated as

$$N_{MB}^{Jet65} = N^{Jet65}[80 < E_T < 100] \times (N^{MB} / N^{MB}[80 < E_T < 100]) \quad (6.7)$$

The same calculation is carried out for the second jet-trigger used in this analysis, i.e. JET80, with the range $E_T \geq 100$ GeV. Once the reconstructed p_T spectra in the MB, the JET65, and the JET80 in the given non-overlapping jet E_T ranges are corrected for the tracking inefficiency as prescribed in the previous section, each spectrum is normalized by the “equivalent number of MB events” and simply added to construct a full spectrum from all three trigger samples with the maximum possible kinematic reach in the entire data samples.

To test whether this matching of different triggers gives a smooth spectrum that would have been built from the MB sample alone if there were no prescale, the spectrum from the full MB sample without any jet E_T cut is compared with the combined spectrum. While the test is limited by the MB statistics, it provides an essential test in the region where the contribution of the MB sample is overtaken by the contribution of the jet-trigger samples. Figure 6.2(b) shows the result of the test where the contribution of each trigger to the total spectrum is shown explicitly as a function of track p_T for the 0–5% most central events. The same combined distributions with each trigger contribution for other centrality bins are shown in Fig. 6.3.

6.0.6.2. Momentum Resolution and Binning

Due to finite resolution in determining the transverse momentum of reconstructed track, the tracking inefficiency corrected spectrum needs to be further corrected for the finite momentum resolution, which is determined by comparing the generator-level p_T with the reconstructed p_T in the aforementioned MC samples. Figure 6.4 shows the 2D scatter distribution of the reconstructed p_T on the y -axis and the truth p_T on the x -axis. It can be seen that at a given truth p_T , the reconstructed p_T is distributed around the truth p_T with a finite resolution. The momentum resolution, defined as the mean of the difference between the truth p_T and the reconstructed p_T divided by the reconstructed p_T , i.e., $\sigma(p_T^{rec} - p_T^{gen}) / p_T^{rec}$, is determined from the 2D scatter plot by determining the mean of the difference as a function of the reconstructed p_T .

The momentum resolution determined in this way from various MC samples are shown in Fig. 6.5(a) along with the momentum resolution in pp and a simple power-law fit. The momentum resolution is shown to rise from a minimum of around 1% at 10 GeV/c to around 5% at 150 GeV/c. It is almost identical to the momentum resolution in pp tracking. The same momentum resolutions determined from one of the mixed sample, plotted in different centrality bins, are shown in Fig. 6.5(b), which shows no centrality dependence.

In general, the combination of a finite momentum resolution and a steeply falling spectrum results in an overestimation of the spectrum in all p_T bins above the most probable value². The correction factor for this overestimation is derived by comparing a known

²This can be understood as follows. In a steeply falling spectrum, for a given p_T there's more tracks at a

6. Obtaining Charged Particle Spectra

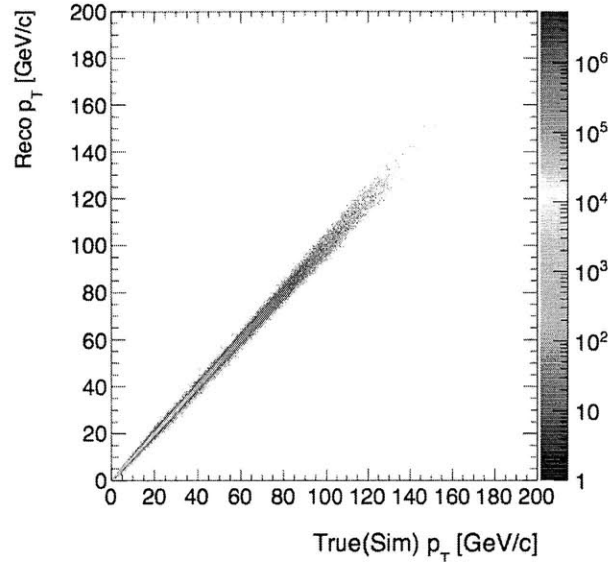


Figure 6.4.: 2D scatter plot of reconstructed track p_T versus simulated track p_T from the MB mixed with QCD sample with a hard-scattering scale of 170 GeV/c.

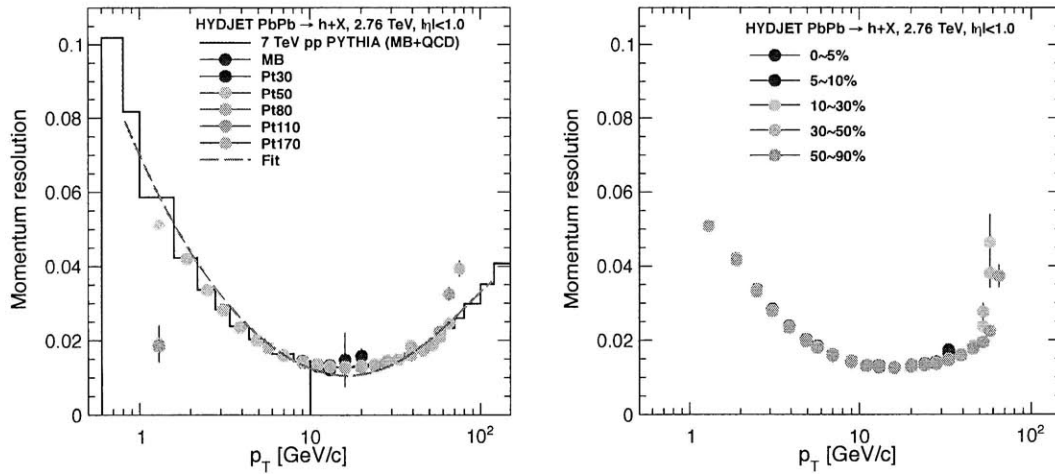


Figure 6.5.: (Right) Momentum resolution $(p_T^{reco} - p_T^{true})/p_T^{reco}$ determined from various MC samples: minimum bias, hard-scattering scales of 30, 50, 80, 110, and 170 GeV (Left) Momentum resolution determined from MC sample with the hard-scattering scale of 170 GeV for different centralities.

spectrum before and after the smearing. As it can be seen from Fig 6.6, the scale of the necessary correction ranges from 0.5% to 3% (see Fig. 6.6).

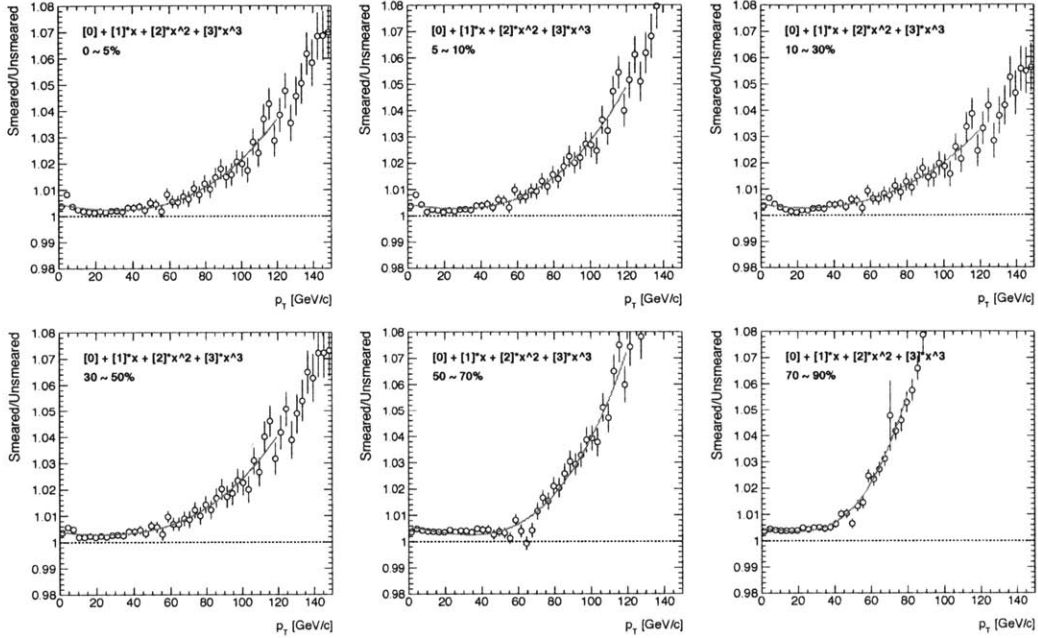


Figure 6.6.: The ratio of the momentum resolution smeared dN/dp_T to dN/dp_T before smearing in different centrality bins with a four-component power-law fitted to the ratio.

Furthermore, the use of finite bin width (Δp_T) in sampling (i.e., “histogramming”) tracks, which varies depending on the momentum ranges, results in an overestimate of the value quoted at the center of the bin since in a steeply falling spectrum the mean of the track momentum in each momentum bin is located close to the lower edge of the bin and not identical to the center of the bin. This can be corrected with a MC-based response matrix and an initial assumption of the spectra shape (from uncorrected data). In practice, the two effects (momentum resolution and binning) are treated with the same correction that is applied by fitting the functional form of the differential yield, smearing it with the MC-based momentum resolution, re-binning it into the bins of the final invariant yield, and comparing back to the original fitted form. The magnitude of the final correction is shown for just the binning effect and for the combined effects in Fig. 6.7.

For the original narrow bins in which the track distributions are first histogrammed (corresponding to the open circles in Fig. 6.7), the combined effect ranges from about 0.5 - 3.5% in the p_T range we access in the analysis. For clarity of the final presentation,

lower adjacent p_T , i.e. $p_T - \Delta p_T$ than at a higher adjacent p_T , i.e. $p_T + \Delta p_T$, therefore, at a given p_T , the smearing results in more tracks ending up in the same p_T than without smearing.

6. Obtaining Charged Particle Spectra

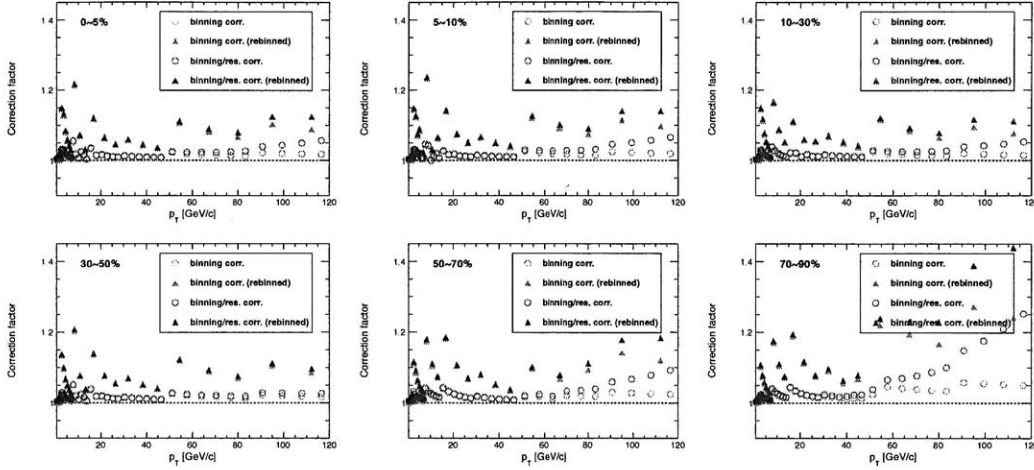


Figure 6.7.: Magnitude of binning correction alone (open red circles) and binning + momentum smearing corrections (open blue circles) in the original narrow bins of the analysis (i.e. before re-binning) After re-binning, the same quantities are shown as filled triangles.

and to minimize the statistical errors on the last points, many of these narrow bins are combined for the final results. For the wide bins, the correction necessary to take the average value in a p_T bin and convert to the true value at the center of the p_T -bin can be as large as 15%. However, Fig. 6.8(a) shows that this procedure is under control.

A key ingredient in the aforementioned corrections was the fitting of the tracking inefficiency corrected dN/dp_T spectrum, which is slightly more complicated than in the case of pp spectrum since the shape of the PbPb spectrum can hardly be described by a monotonic power-law shape. Rather, it can be described by a combination of exponential and power-law shape depending on the momentum ranges. The following procedures are performed to find a fit function that can describe the shape of the spectra in each centrality bin with reasonably small residual.

- Fit three different regions of the spectrum separately with an overlap between the fits (power-law and exponential combined)
- Three different p_T regions are defined (without an overlap in p_T) based on the distance between the fits.
- Combine the three fit functions with a third-order polynomial smoothing for the joint regions.
- Final fit function is obtained based on the smoothly combined function.

An example result of the fitting is shown in Fig. 6.8(b).

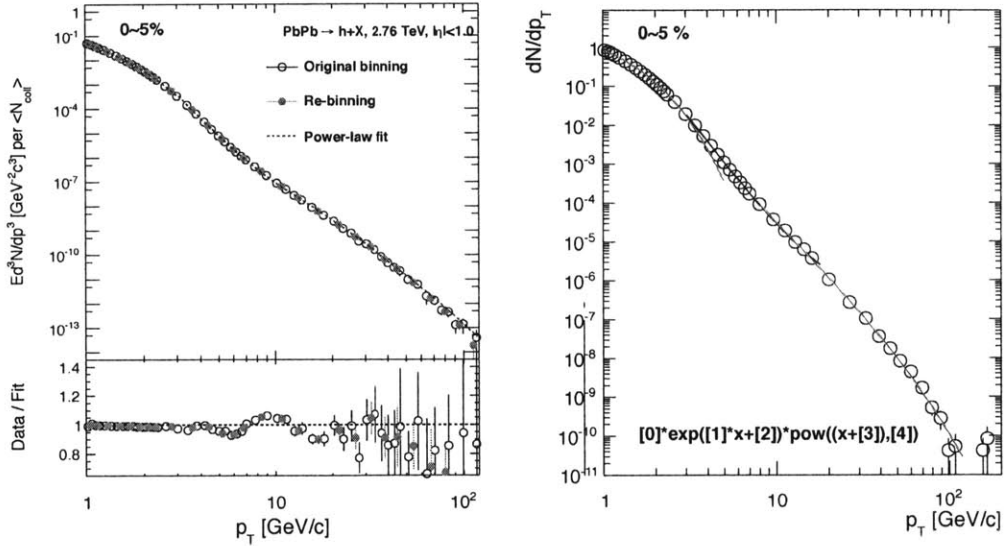


Figure 6.8.: The fully corrected (including binning correction) differential invariant yield in the original narrow bins (open circles) and in the final wider bins (solid circles) is compared to a common fit. The bottom panel shows the ratio of the yield to the fit.

6.0.7. Systematic Uncertainties

The systematic uncertainties assigned to each correction is shown in Fig. 6.9 as a function of p_T in two centrality bins and summarized in the table 6.1, along with the systematic uncertainties in the pp spectra measurement [173]. Except for the uncertainty related to the overall normalization, i.e., N_{coll} determination, the largest source of uncertainty comes from the track reconstruction. The uncertainty assigned to the track reconstruction and the other corrections are discussed below.

Before applying the tight quality selections on the reconstructed tracks, the charged particle reconstruction efficiency is studied by inserting simulated pion tracks or *PYQUEN* dijet events into two different background samples: (i) simulated minimum bias *HYDJET* events by mixing *GEANT4* [143] detector hits, and (ii) PbPb data events by combining the raw digitized detector signals. The efficiencies estimated by these two methods agree within 3.0–5.7% in the range $1 < p_T < 100$ GeV/c. Due to limitations in the data-mixing technique, the two cannot be compared on an equal footing after applying all of the quality cuts, in particular those involving the consistency of a track with the primary vertex. However, it is possible to ensure that the distributions on which the selections are made (i.e., the χ^2 of the track fit, the distance of closest approach between track and vertex, the number of hits in the silicon pixel and strip detectors) are consistent between the data and the MC simulations, both as a function of p_T and event centrality. To this end, an additional series of checks is performed by varying the

6. Obtaining Charged Particle Spectra

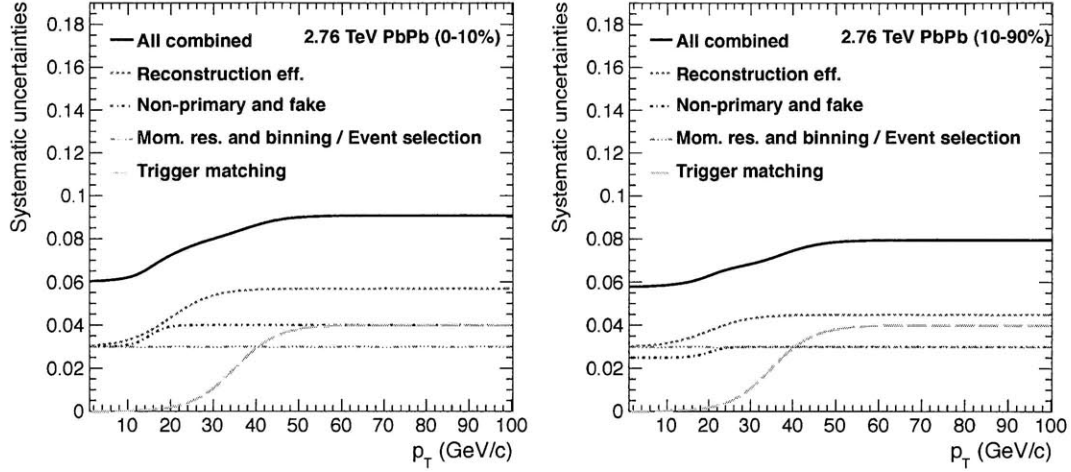


Figure 6.9.: The systematic uncertainties assigned to each corrections and the combined one.

requirements imposed during the track selection and in the determination of the corresponding MC-based corrections. The resulting variations in the corrected results are within the quoted systematic uncertainties.

The fraction of misidentified tracks estimated from simulated events for each leading-jet E_T sample as a function of track p_T is checked against an estimate from data that uses the sidebands of the impact parameter distributions. Studies of simulated events reveal that, at low p_T and in peripheral events (e.g., 50–90%), the sidebands are dominated by secondaries and products of weak decays because of their displaced vertex positions. However, in central events (e.g., 0–5%) and at high p_T they are mostly misidentified tracks. The fake fraction in 0–50% centrality range is estimated by fitting the distribution with signal and background shape and by extrapolating the sideband region under the peak from correctly reconstructed primary tracks. Figure 6.11 shows the estimated fake fraction in comparison with the distributions of the fake rate and their mean estimated based on the MC samples. Based on varying the functional form of the sideband extrapolation under the peak from correctly reconstructed primary tracks, a 2.5–4.0% systematic uncertainty is quoted for the fraction of misidentified tracks remaining after all selection cuts.

An additional check is performed for tracks with p_T above 10 GeV/ c to correlate the reconstructed track momentum with the energy deposited in the ECAL and HCAL. The fraction of high- p_T tracks with a typically small amount of energy deposited in the calorimeters is consistent with the quoted uncertainty on the misidentification rate.

The tendency for finite bin widths and finite transverse-momentum resolution to deform a steeply falling p_T spectrum is corrected for in the analysis of the pp spectrum. The higher occupancy in PbPb events than in pp events has negligible effect on the momentum resolution. The resulting 3.0% systematic uncertainty is dominated by the

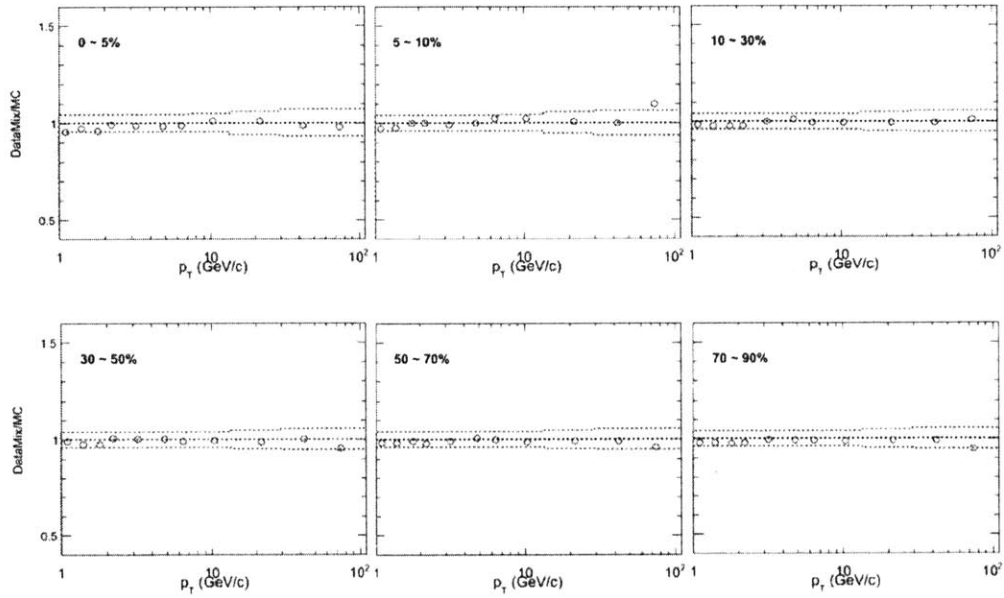


Figure 6.10.: Comparison between the tracking efficiency obtained based on the MC sample mixed with real data and the tracking efficiency obtained based on the pure MC sample.

uncertain shape of the momentum spectrum at high p_T . For the R_{AA} and R_{CP} measurements, a 2.0% systematic uncertainty is quoted after subtracting the correlated uncertainty between the PbPb and pp p_T spectra, or between the central and peripheral PbPb p_T spectra. For the normalization of the pp collision, 6.0% luminosity uncertainty is quoted based on the HF-based luminosity determination [171] and the absolute luminosity calibration, known as Van der Meer scans [172].

A summary of all the contributions to the systematic uncertainty affecting the PbPb and pp p_T spectra, and the resulting R_{AA} and R_{CP} values, is given in Table 6.1.

6. Obtaining Charged Particle Spectra

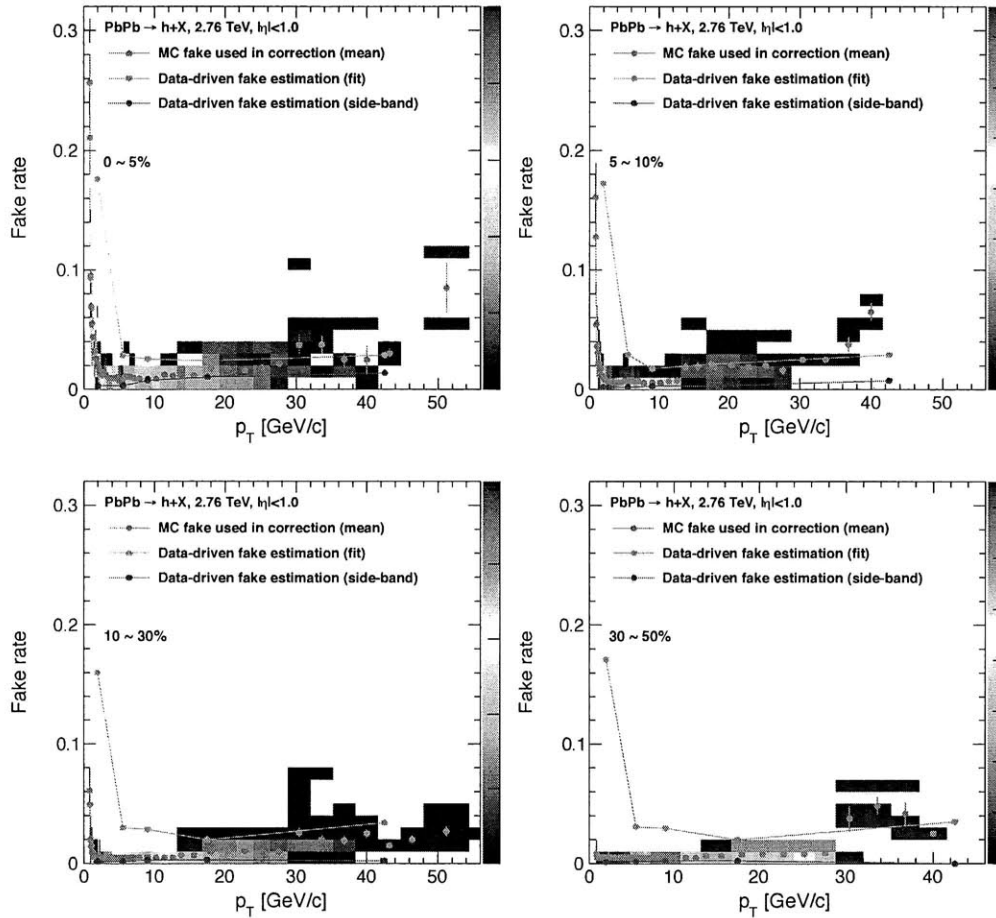


Figure 6.11.: Fake estimation based on the sideband method in comparison to the fake rate estimated based on the MC samples.

7. Results and Discussions

As discussed earlier in Sec. 2.4.3.1, it is important to establish our firm understanding of the high- p_T particle productions in nucleon-nucleon collision first for the study of the medium produced in nucleus-nucleus collision using the produced high- p_T particle as a probe. It is particularly important at LHC because we explore the new energy regime, which is about 14 times larger than the highest energy achieved previously. Using the analysis methods described in the previous chapter, the charged particle spectra in pp at $\sqrt{s} = 0.9, 2.76$ and 7 TeV have been measured and compared to the pQCD calculations. Also based on the measurements, a known scaling behaviour of the p_T spectra at different collisions energy, x_T scaling, is tested. The measurement in pp collisions at $\sqrt{s} = 2.76$ TeV¹ is used as a reference spectrum to quantify the high- p_T particle suppression observed in the p_T spectra in PbPb collision at $\sqrt{s_{NN}} = 2.76$ TeV that have been measured using the analysis methods described in the previous chapter as well. The observed suppression in R_{AA} is then compared to various theoretical model predictions.

7.0.8. Charged Particle Spectra in pp at $\sqrt{s} = 0.9, 2.76$ and 7 TeV

The invariant differential yields for charged particles within $|\eta| < 2.4$ for 0.9 and 7 TeV and $|\eta| < 1.0$ for 2.76 TeV² are obtained after applying various corrections [173]. The measurement at 0.9 and 7 TeV are shown for a limited p_T range in Figs. 7.1(a) and 7.1(b) in order to quantify the agreement with previous CMS measurements at $\sqrt{s} = 0.9$ and 7 TeV [98, 174]. At each energy, both CMS measurements are divided by a Tsallis fit [175] to the earlier measurement and the ratios compared in the lower panels. For the earlier measurements, the error bars indicate the statistical plus systematic uncertainties added in quadrature. The bands around the new measurements represent all contributions to the systematic uncertainty, except the contribution from the common event selection [173]. Statistical uncertainties are negligible on the new measurements in this p_T range. Below $p_T = 4$ GeV/ c for the 0.9 TeV sample and below $p_T = 6$ GeV/ c at $\sqrt{s} = 7$ TeV, which are the limits of the previously published CMS spectra, the new results are in

¹While the measurements at 0.9 and 7 TeV were made well before the 2010 PbPb data taking, the analysis of 2.76 TeV data was done only after the analysis of the 2010 PbPb data. Therefore, the first R_{AA} measurement was made, in the lack of the 2.76 TeV measurement, with a 2.76 TeV reference spectrum, which was interpolated based on the x_T scaling established by the 0.9 and 7 TeV measurements along with the existing measurements at different center-of-mass energies. Later, it was found that the interpolated spectrum is in a very good agreement with the measured spectrum.

²The measurements at 0.9 and 7 TeV have been made for the full pseudo-rapidity coverage of the CMS tracking system $|\eta| < 2.4$, but the measurement at 2.76 TeV have been focused on the narrower pseudo-rapidity coverage $|\eta| < 1.0$ in order to compare with the spectra in PbPb, which have been measured for $|\eta| < 1.0$.

7. Results and Discussions

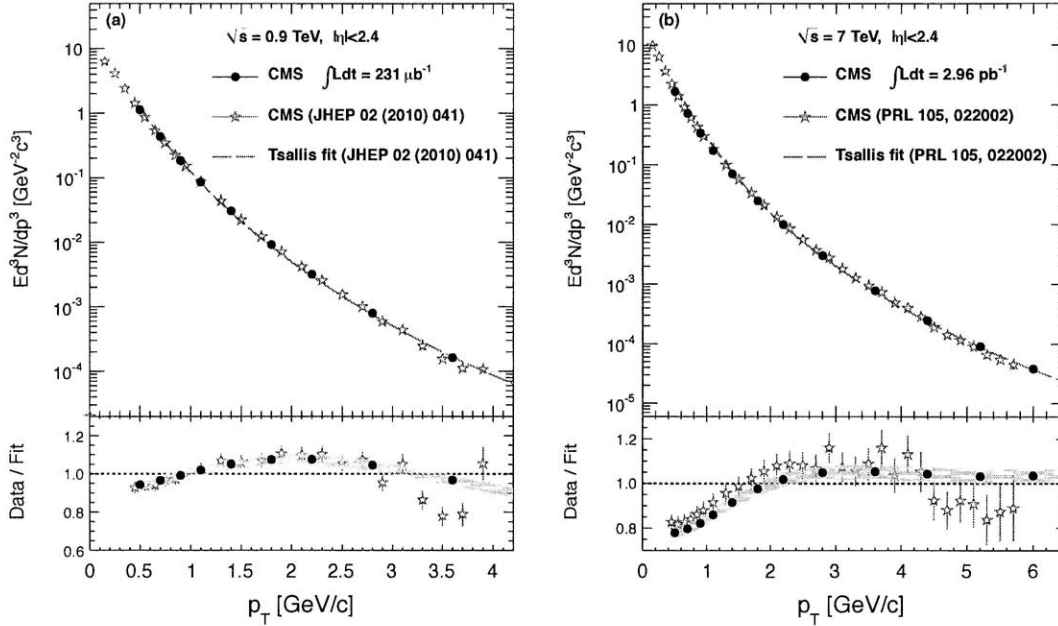


Figure 7.1.: Upper panel: the invariant charged particle differential yield from the present analysis (solid circles) and the previous CMS measurements (stars) at $\sqrt{s} = 0.9$ TeV (Left) and 7 TeV (Right) over the limited p_T range of the earlier result. Lower panel: the ratio of the new (solid circles) and previous (stars) CMS results to a Tsallis fit of the earlier measurement.

reasonable agreement with the earlier measurements. However, the measured spectra do deviate from the Tsallis fits in the earlier papers by as much as 20% at low p_T . The origin of the small difference between the two CMS measurements at $\sqrt{s} = 7$ TeV is attributed to the different tracking algorithms used in the two measurements, as well as the different `PYTHIA` tunes used to determine the tracking corrections.

In the upper plots of Figs. 7.2, the charged particle differential transverse momentum yields are displayed for $\sqrt{s} = 0.9$ and 7.0 TeV. It is shown separately for $\sqrt{s} = 2.76$ TeV in Fig. 7.3. The distribution for the 7 TeV covers the p_T range up to 200 GeV/c, the largest range ever measured in a colliding beam experiment. Also shown in the figures are various generator-level MC predictions for the yields [6, 176–178]. The lower plots of Figs. 7.2 show the ratios of the data to the various MC predictions. As already observed in Ref. [174], there is a deficit of $p_T < 1$ GeV/c particles in the predicted 7 TeV spectra for several of the popular `PYTHIA` tunes. Whereas for the whole p_T range above 1 GeV/c, `PYTHIA8` is the most consistent with the new 7 TeV result (within 10%), the lower energy measurements are described better by `PROQ20`. While these comparisons provide an important constraint on the different generator parameters responsible for sizable variations among the tunes, it is difficult to extract quantitatively what physics aspects of the particular tune gives a better agreement with the data due to large

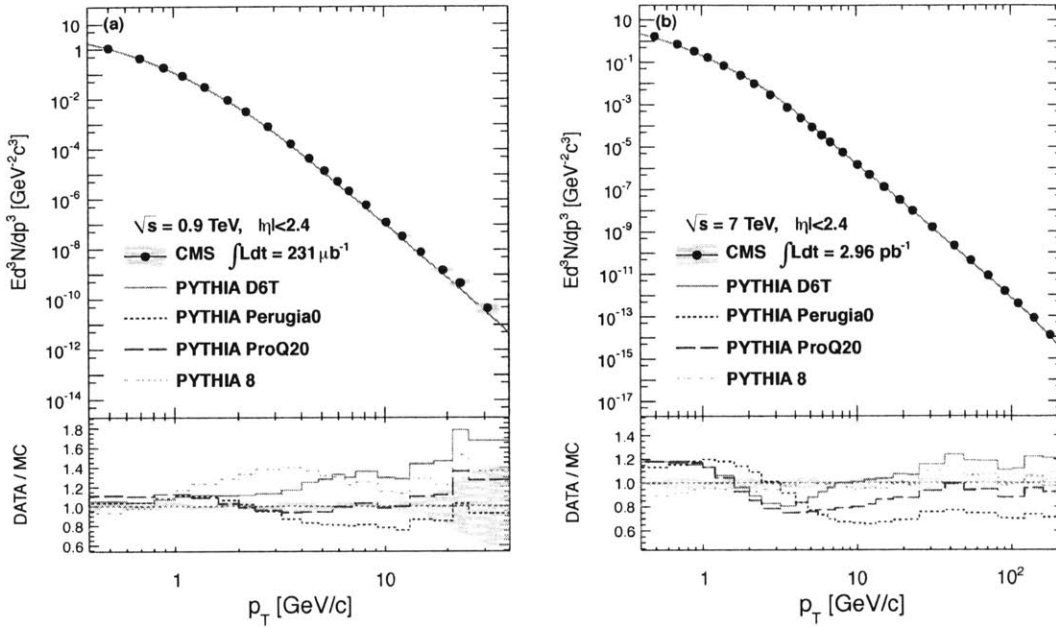


Figure 7.2.: Upper panel: the invariant charged particle differential yield at $\sqrt{s} = 0.9$ TeV (Left), and 7 TeV (Right) compared with the predictions of four tunes of the PYTHIA MC generator. Lower panel: the ratio of the new CMS measurement to the four PYTHIA tunes. Tabulated result can be found in Table C.1 and C.2.

number of parameters ($\mathcal{O}(10) > N_{para}$) with different ranges involved among the different tunes. Thus, it is subject to further systematic studies, for example, as it is done in Ref. [177, 179].

7.0.9. x_T scaling and Interpolation

As discussed in Ref. [180, 181], a robust prediction of pQCD hard-processes is the power-law scaling of the inclusive charged particle invariant differential cross section with the variable $x_T \equiv 2p_T/\sqrt{s}$:

$$E \frac{d^3\sigma}{dp^3} = F(x_T)/p_T^{n(x_T, \sqrt{s})} = F'(x_T)/\sqrt{s}^{n(x_T, \sqrt{s})}, \quad (7.1)$$

where F and F' are independent of \sqrt{s} , and the slow evolution of the power-law exponent n with x_T and \sqrt{s} ($n \simeq 5-6$) is due to the running of α_s and changes in the parton distribution and fragmentation functions.

In the upper plot of Fig. 7.4(a), the 0.9 and 7 TeV pp measurements from this analysis are compared to the empirical scaling observed from measurements over a range of lower $p\bar{p}$ collision energies by plotting $\sqrt{s}^n E d^3\sigma/dp^3$ as a function of the scaling pa-

7. Results and Discussions

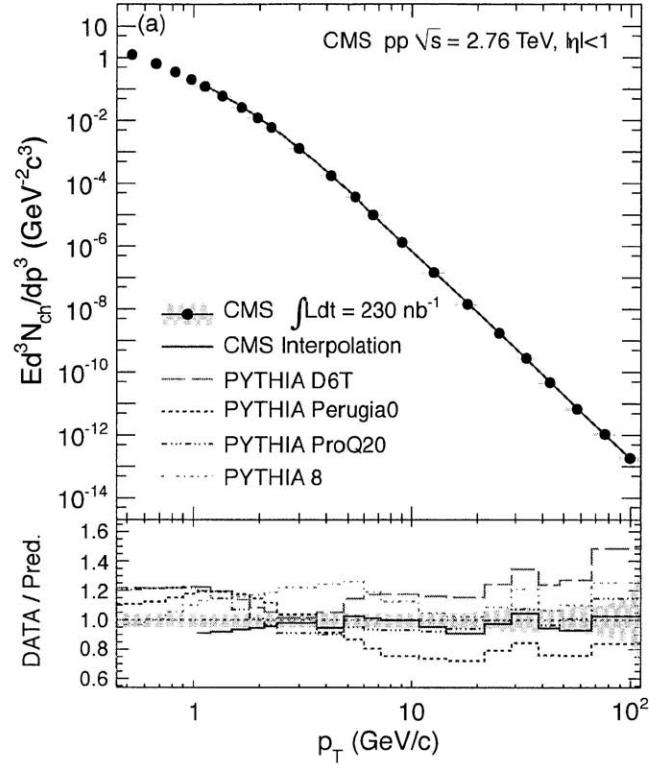


Figure 7.3.: Upper panel: the invariant charged particle differential yield at $\sqrt{s} = 2.76$ TeV for $|\eta| < 1.0$ compared with the predictions of four tunes of the PYTHIA MC generator. Lower panel: the ratio of the new CMS measurement to the four PYTHIA tunes as well as to the interpolated spectra, which is explained in Sec. 7.0.9. Tabulated result can be found in Table C.3.

parameter x_T . For the purpose of reporting the CMS results as differential cross sections, the integrated luminosities for the analysed data samples were measured according to the descriptions in Ref. [171, 172]. Also, to compare with the published results from the CDF experiment at $\sqrt{s} = 0.63, 1.8,$ and 1.96 TeV, the pseudorapidity range has been restricted to $|\eta| < 1.0$ with the number of positive and negative charged particles averaged³. Whereas an exponent $n = 5.5$ was found in Ref. [181] from a global fit to only the previous $p\bar{p}$ measurements from $\sqrt{s} = 0.2$ to 1.96 TeV, the x_T scaling presented in this paper is optimised for use in an interpolation between the CDF and CMS measurements from $\sqrt{s} = 0.9$ to 7 TeV. Within this range, the best scaling is achieved with an exponent of $n = 4.9 \pm 0.1$. This is consistent with the predictions of next-to-leading-order (NLO) calculations, where the scaling is also found to be optimised for this value of the exponent [181]. Similarly in Fig. 7.4, the same quantity without averaging the positive

³ $\left(\frac{N^+ + N^-}{2}\right) = \frac{N}{2}$ with $N_+ = N_-$

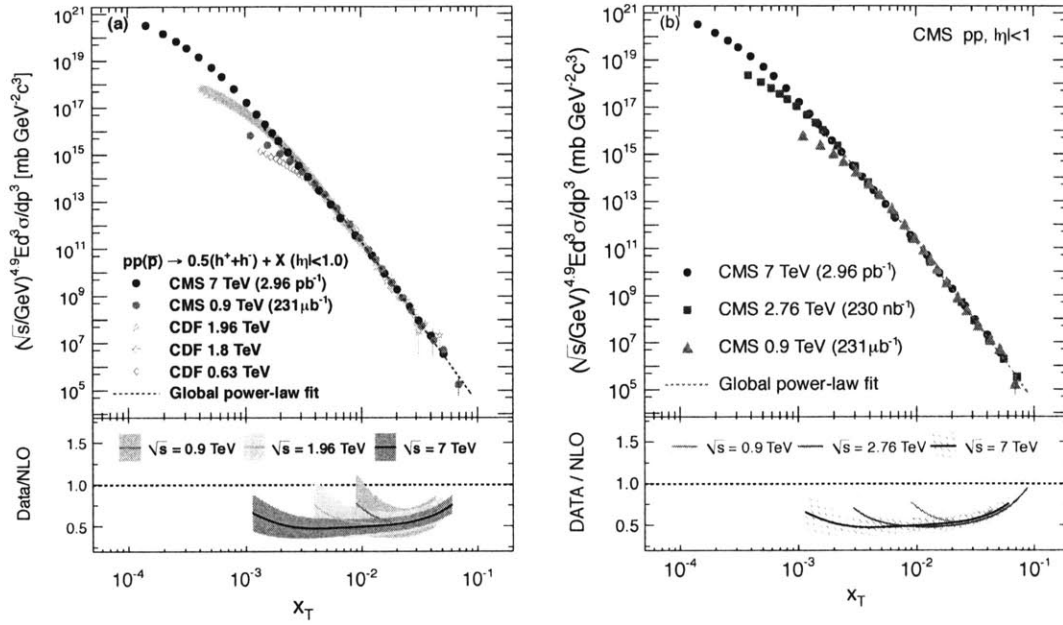


Figure 7.4.: (a) Inclusive charged particle invariant differential cross sections, scaled by $\sqrt{s}^{4.9}$, for $|\eta| < 1.0$ as a function of x_T for the measurements at various center-of-mass energies with the ratios of differential cross sections measured at 0.9, 1.96, and 7 TeV to those predicted by NLO calculations for factorisation scales ranging from 0.5–2.0 p_T in the lower panel. (b) The same cross sections for CMS data only including the measurement at 2.76 TeV with the NLO calculations in the lower lower panel. Tabulated result can be found in Table C.6.

and negative charged particles is shown for the CMS measurements only including 2.76 TeV result. The scaling behavior can be clearly seen from the CMS measurements only. From the lower panel of Fig. 7.4(a) and 7.4, it is apparent that the NLO calculations over-predict the measured cross sections by almost a factor of two at all collision energies. This is in spite of the relatively good agreement in the inclusive jet spectrum [182, 183], which suggests that the fragmentation functions are not well tuned for LHC energies.

The CMS results are consistent over the accessible x_T range with the empirical x_T scaling given by Eq. (7.1) established at lower energies. The global power-law fit shown in the lower panel of Figs. 7.4 is of the form $F'(x_T) = p_0 \cdot [1 + (x_T/p_1)]^{p_2}$, where p_0 , p_1 , and p_2 are free parameters, and the region below $p_T = 3.5$ GeV/c has been excluded to avoid complications from soft-particle production. Considering the somewhat naïve power-law function and the expected non-scaling effects [184], the measurements are in reasonable agreement with the global power-law fit result (within roughly 50%) over its full x_T range.

As mentioned briefly in the beginning of this chapter, when the first R_{AA} measurement

7. Results and Discussions

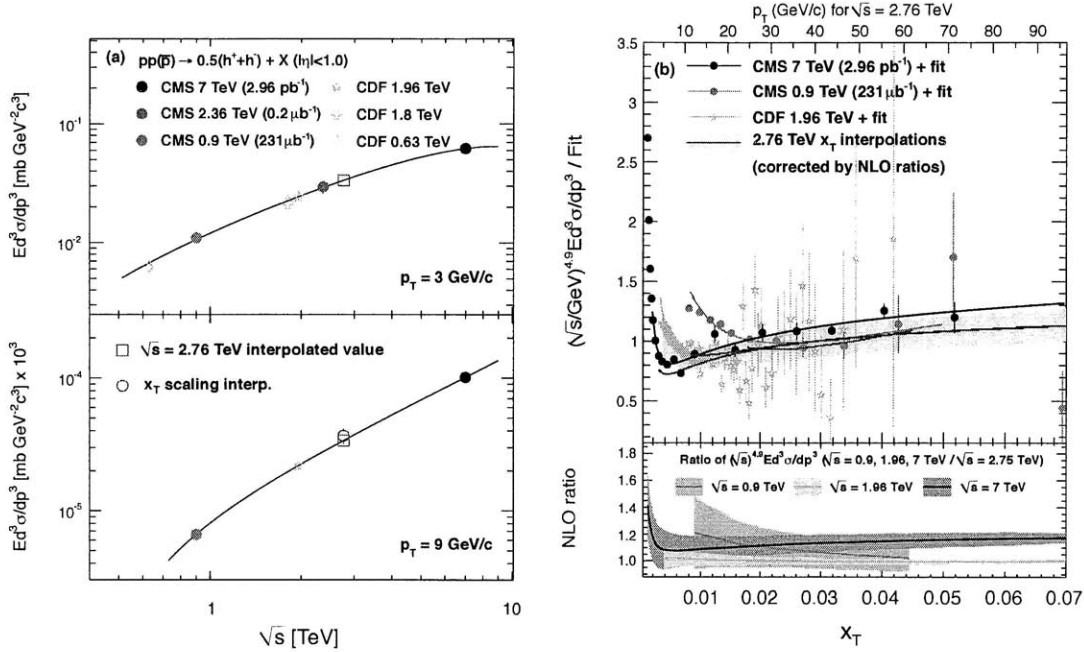


Figure 7.5.: (a) Interpolations between measured charged particle differential cross sections at different \sqrt{s} for the two example values of $p_T = 3$ and 9 GeV/c. (b) Upper panel: ratios of the scaled differential cross sections to the global power-law x_T fit described in the text (coloured markers) and fits to these ratios (similarly coloured thin lines). The upper axis translates x_T to p_T for $\sqrt{s} = 2.76$ TeV. Lower panel: ratios of the NLO-calculated cross sections at three different energies, scaled by $\sqrt{s}^{4.9}$, to the cross section calculated at $\sqrt{s} = 2.75$ TeV.

was carried out, the 2.76 TeV measured spectra was not available. So, in the lack of the measured reference spectrum, a reference spectrum was constructed based on the combined technique of so-called ‘direct’ cross section interpolation and the x_T scaling as described in the following section.

7.0.9.1. Interpolation of 2.76 TeV Spectrum

In order to construct a predicted reference charged particle differential cross section at $\sqrt{s} = 2.76$ TeV for comparison with the measured PbPb heavy-ion spectrum, two different techniques are used in partially overlapping transverse momentum regimes. In the high- p_T range from 5.0–200 GeV/c, where approximate x_T scaling is expected to hold, the estimated 2.76 TeV cross section is derived from a common x_T -scaling curve, based on the CDF and CMS measurements shown in Fig. 7.4(a). In the low- p_T range from 1.0–20 GeV/c, it is possible to interpolate directly between the several measured cross section values as a function of \sqrt{s} at each fixed p_T value.

As discussed in the previous section, the upper panel of Fig. 7.4(a) shows the residual difference from perfect x_T scaling with exponent $n = 4.9$ for the 0.9 and 7 TeV CMS measurements and for the 1.96 TeV CDF measurement [97, 185]. The \sqrt{s} and x_T dependence of the residuals are not unexpected, since this behaviour is predicted by NLO calculations. This can be seen in the lower panel of Fig. 7.5(b), which shows the predicted deviation from perfect x_T scaling for calculated NLO cross sections at several collision energies with respect to a reference centre-of-mass energy of 2.75 TeV [181]. The width of the bands represents the variation of the factorisation scale by a factor of two. The calculations were performed using the CTEQ66 parton distribution functions [186], DSS fragmentation [187], and a factorisation scale $\mu = p_T$ [181]. Taking the magnitude of the x_T -scaling violation from NLO (ranging from 0–20%), each of the three measurements in data (i.e., 0.9, 1.96, and 7 TeV) can be corrected separately to arrive at an expectation for the 2.76 TeV cross section. The three independent interpolations based on NLO-corrected x_T scaling are shown as solid blue lines in the upper panel of Fig. 7.5(b).

The combined ‘best estimate’ (shown as a shaded band) has an associated uncertainty that covers the deviations of up to 12% observed by varying the factorisation scale from $\mu = 0.5 p_T$ to $\mu = 2.0 p_T$ for each of the three collision energies. The error band is expanded below $p_T \approx 8$ GeV/ c to include the full difference between the 1.96 and 7 TeV results, since the evolution of the spectra below this value —corresponding to $x_T = 0.0023$ (7 TeV), 0.0082 (1.96 TeV), and 0.018 (0.9 TeV) — is no longer consistently described by x_T scaling and the NLO-based corrections. In addition to the 12% contribution from the uncertainty on the NLO-based correction, the final uncertainty on the interpolated cross section has an additional component to account for possible correlations in the luminosity uncertainty between the three measurements. This term, taken as equal to the smallest individual uncertainty (4%), is added in quadrature.

The direct interpolation of cross sections at a fixed value of p_T is done using CDF measurements at $\sqrt{s} = 0.63, 1.8$ and 1.96 TeV [96, 97, 185], the new CMS measurements at $\sqrt{s} = 0.9$ and 7 TeV, as well as an earlier result at $\sqrt{s} = 2.36$ TeV [98]. The latter measurement is converted to a differential cross section assuming the total inelastic cross section of 60.5 mb from PYTHIA. At each energy, an empirical fit to the p_T distribution is first constructed to provide a continuous estimation independent of different binning. Then, in arbitrarily small p_T bins, these empirical fits are evaluated and the evolution of the cross section with \sqrt{s} is parametrised by a second-order polynomial. Two examples of these fits are shown in Fig. 7.5(a) for $p_T = 3$ and 9 GeV/ c . Second-order polynomial fits to the measured data are shown by the solid lines. The open squares show the resulting interpolated cross sections for $\sqrt{s} = 2.76$ TeV. The open circle on the lower panel represents the corresponding estimate from the x_T -scaling approach in the overlap region where both can be estimated. The uncertainty on the value of the fit evaluated at $\sqrt{s} = 2.76$ TeV is taken from the covariance matrix of the fit terms, with an additional 4% added in quadrature to account conservatively for any correlation in the luminosity uncertainty between the different measurements.

To arrive at a single interpolated spectrum over the full p_T range, a linear combination of the two techniques is used with weights that vary linearly across the overlap range from $p_T = 5$ GeV/ c (only direct interpolation at fixed p_T) to $p_T = 20$ GeV/ c (only x_T scaling

7. Results and Discussions

with NLO-based residual correction). In the p_T range where the two techniques overlap, the different methods agree to within their respective systematic uncertainties. (The fixed- p_T interpolation value is typically around 8% lower than the x_T interpolation.) The resulting predicted 2.76 TeV differential cross section is shown in the upper panel of Fig. 7.3 along with the 2.76 TeV measurement. It can be clearly seen from the lower panel, where the ratio of the measured spectrum to the interpolated spectrum is shown, that the agreement is very good except for the low p_T below 2 GeV/c or so, indicating that the direct cross section interpolation does not work as well as in the intermediate p_T range ($2 < p_T < 10$ GeV/c)

The measurements of charged particle spectra up to high- p_T at different center of mass energies and their comparisons with the PYTHIA and the next-to-leading order (NLO) pQCD calculations show that the production of high- p_T charged particle is well understood in the pQCD framework even at the highest center-of-mass collision energies achieved in an accelerator-based experiment. This leads to a conclusion that the use of high- p_T particle production continues to be a useful tool to study the jet quenching phenomenology in the TeV-scale collisions energies, via studying the fate of well calibrated high- p_T particles produced in heavy-ion collisions.

7.0.10. Charged Particles Spectra in PbPb and R_{AA}

After applying various corrections described in the previous chapter, the invariant differential yields for charged particles within $|\eta| < 1.0$ in PbPb collisions at $\sqrt{s_{NN}} = 2.76$ TeV are obtained. The PbPb spectrum is shown for six centrality bins and compared to the measured pp reference spectrum at the same center-of-mass energy, scaled by the nuclear overlap function, in Fig. 7.6. For easier viewing, several sets of points have been scaled by the arbitrary factors given in the figure. The statistical uncertainty is smaller than the marker size for most of the points. In the lower panel of the figure, the average relative systematic uncertainties of the PbPb differential yields for the 0–10% and 10–90% centrality intervals are shown as a function of p_T . By comparing the PbPb measurements to the dashed lines representing the scaled pp reference spectrum, it is clear that the charged particle spectrum is strongly suppressed in central PbPb events compared to pp, with the most pronounced suppression at around 5–10 GeV/c.

The nuclear modification factor R_{AA} , as already defined in Sec. 2.4.3 as

$$R_{AA}(p_T) = \frac{d^2 N_{ch}^{AA} / dp_T d\eta}{\langle T_{AA} \rangle d^2 \sigma_{ch}^{NN} / dp_T d\eta}, \quad (7.2)$$

is constructed according to Eq. 7.2 by dividing the PbPb p_T spectrum for each centrality range by the scaled pp reference spectrum (i.e., the filled points by the dashed lines in Fig. 7.6). It is presented as a function of p_T in Fig. 7.7 for each of the six centrality bins. The yellow boxes around the points show the systematic uncertainties, including those from the pp reference spectrum, listed in Table 6.1. An additional systematic uncertainty from the T_{AA} normalization, common to all points and also listed in Table 6.1 is displayed as the shaded band around unity in each plot. The statistical un-

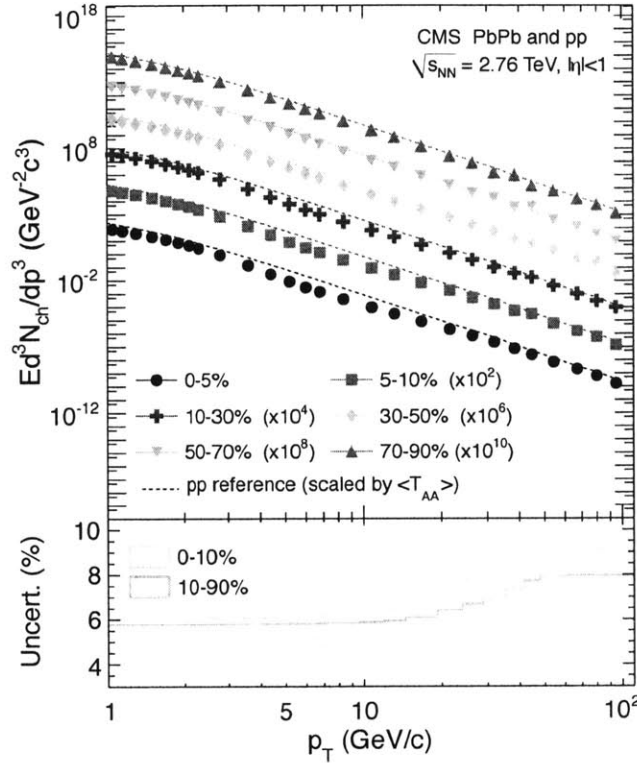


Figure 7.6.: Upper panel: Invariant charged particle differential yield in PbPb collisions at 2.76 TeV in bins of collision centrality (symbols), compared to that of pp at 2.76 TeV, normalized by the corresponding pp invariant cross sections scaled by the nuclear overlap function (dashed lines). Tabulated results can be found in Table C.7– C.12.

certainties do not increase monotonically as a function of p_T , as seen most prominently in the peripheral bins, as a consequence of combining the highly prescaled minimum bias sample with the two unprescaled jet triggers, as discussed in the previous chapter (Sec. 6.0.6.1). In the most peripheral events (70–90%), a moderate suppression of about a factor of 2 ($R_{AA} \approx 0.6$) is observed at low p_T , with R_{AA} rising slightly with increasing transverse momentum. The suppression becomes more pronounced in the more central collisions, as expected from the increasingly dense final-state system and longer average path-lengths traversed by hard-scattered partons before fragmenting into final hadrons. In the 0–5% centrality bin, R_{AA} reaches a minimum value of about 0.13 at $p_T = 6\text{--}7$ GeV/c. At higher p_T , the value of R_{AA} rises and levels off above 40 GeV/c at approximately 0.5. A rising R_{AA} may simply reflect the flattening of the unquenched nucleon-nucleon spectrum at high p_T if one assumes a constant fractional energy loss, although the magnitude of the rise varies among the different theoretical models.

7. Results and Discussions

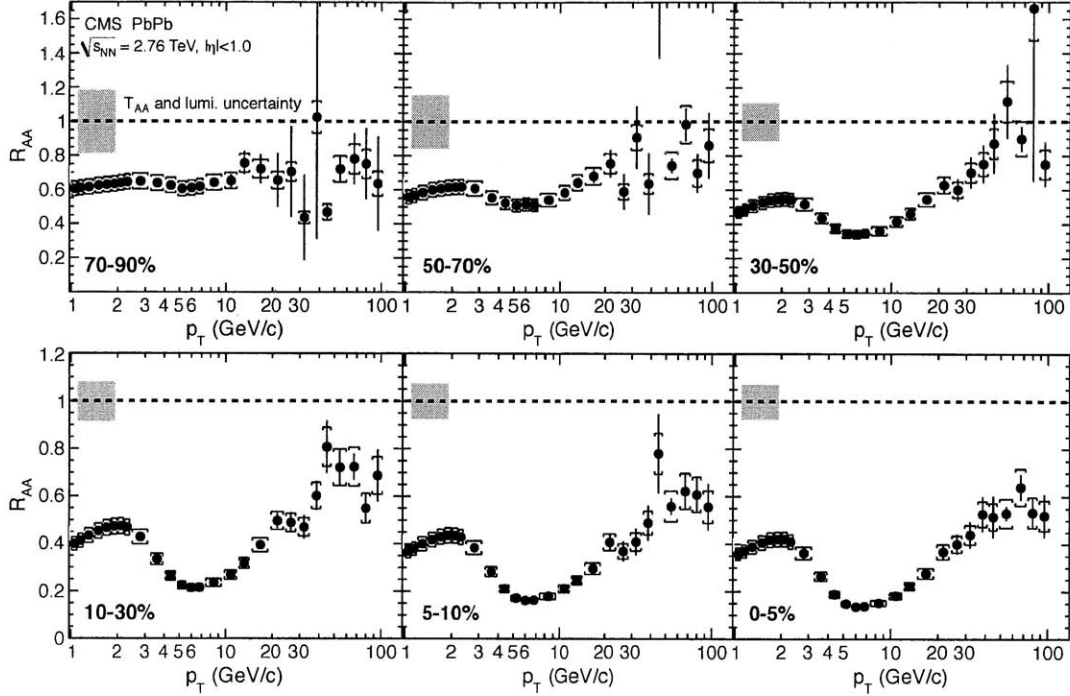


Figure 7.7.: Nuclear modification factor R_{AA} (filled circles) as a function of p_T for six PbPb centralities. The error bars represent the statistical uncertainties and the yellow boxes represent the p_T -dependent systematic uncertainties. An additional systematic uncertainty from the normalization of T_{AA} and the pp integrated luminosity, common to all points, is shown as the shaded band around unity in each plot. Tabulated results can be found in Table C.13–C.18.

In addition to R_{AA} , the centrality dependence of the PbPb spectrum can also be examined through the T_{AA} -scaled ratio of spectra in central and peripheral bins (R_{CP}),

$$R_{CP}(p_T) = \frac{(d^2 N_{ch}^{AA}/d p_T d \eta)/N_{coll} [\text{central}]}{(d^2 N_{ch}^{AA}/d p_T d \eta)/N_{coll} [\text{peripheral}]} \quad (7.3)$$

R_{CP} , which essentially compares the spectra in different centrality bins, is constructed according to Eq. (7.3) by dividing the PbPb p_T spectrum for the four centrality ranges (0–5, 5–10, 10–30, 30–50%) by PbPb p_T spectrum in 50–90% centrality bin. The peripheral interval used for the normalization is chosen as the combined 50–90% centrality bin to improve the statistical precision at high p_T . Since R_{CP} does not use a pp reference spectrum as the denominator, this approach removes the 4.4–9.0% systematic uncertainty from the pp reference, albeit with rather larger overall normalization uncertainties propagated from the N_{coll} uncertainty in 50–90%. The resulting values of R_{CP} for the

four most central bins are shown in Fig. 7.8. The statistical uncertainty of R_{CP} does not increase monotonically with p_T for the same reasons as mentioned for R_{AA} . As in the measurement of R_{AA} , the R_{CP} results show that the p_T spectra in central PbPb collisions are significantly suppressed compared to peripheral collisions.

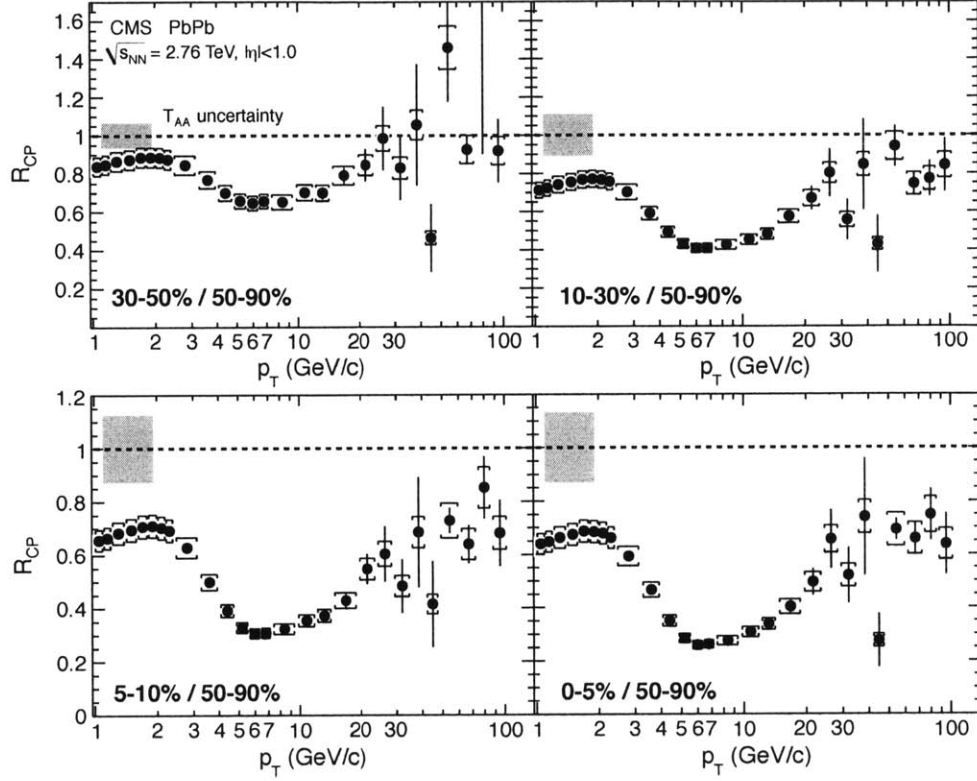


Figure 7.8.: T_{AA} -scaled ratio of p_T spectra in central and peripheral bins, R_{CP} , as a function of p_T for four PbPb centralities. The error bars represent the statistical uncertainties and the yellow boxes the p_T -dependent systematic uncertainties. An additional systematic uncertainty from the normalization of T_{AA} , common to all points, is shown as the shaded band around unity in each plot. Tabulated results can be found in Table C.19– C.22.

The evolution of the nuclear modification factor with center-of-mass energy, from the SPS [101, 102] to RHIC [103, 104] and then to the LHC [100], as shown earlier in Fig. 2.11(a) of Sec. 2.4.3, is now presented in Fig. 7.9 with the new CMS measurement discussed so far. In this figure, one can compare the result presented in this thesis to to the ALICE result [100], made earlier at the same center-of-mass energy, limited in p_T reach below 20 GeV/c. Note that the pp spectrum measured by CMS at $\sqrt{s} = 2.76$ TeV is roughly 5–15% higher than the ALICE spectrum obtained by interpolating their 0.9 and 7 TeV spectra [100]. The two R_{AA} results are in agreement within their respective

7. Results and Discussions

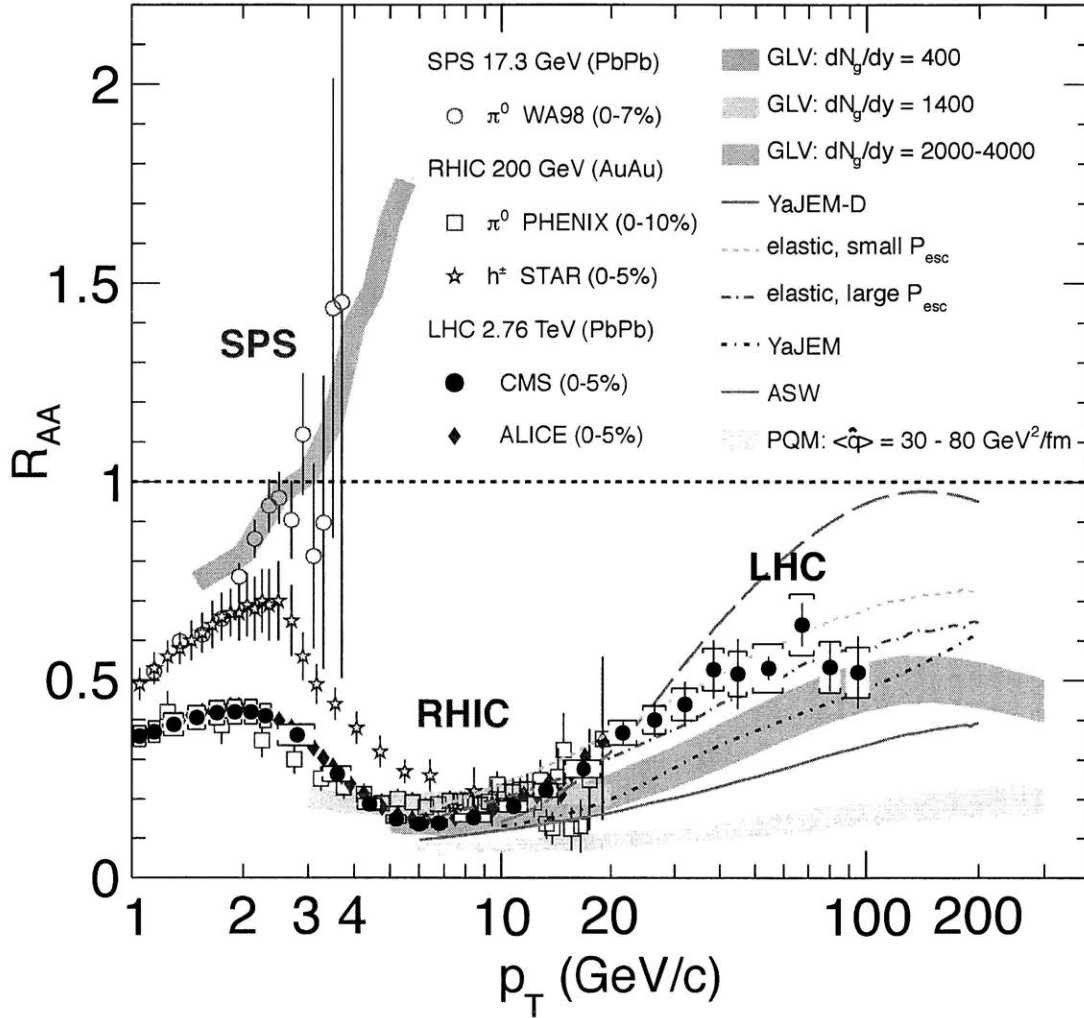


Figure 7.9.: Measurements of the nuclear modification factor R_{AA} in central heavy-ion collisions at three different center-of-mass energies, as a function of p_T , for neutral pions (π^0), charged hadrons (h^\pm), and charged particles [100–104], including the measurement presented here compared to several theoretical predictions [105–110] (see text).

statistical and systematic uncertainties.

The high- p_T measurement of R_{AA} from this analysis, up to $p_T = 100$ GeV/ c , is now compared with the measurements of R_{AA} in central heavy-ion collisions at three different energies and compared to a number of theoretical predictions, as first shown in Fig 2.11(a) without the measurement presented in this thesis. The result with the measurement is shown in Fig. 7.9. The theoretical predictions include those that are made for the LHC design energy of $\sqrt{s_{NN}} = 5.5$ TeV (PQM [105] with medium transport-coefficient $\langle \hat{q} \rangle = 30\text{--}80$ GeV²/fm and GLV [106, 107] for various values of the medium gluon pseudorapidity density dN_g/dy) and for the actual collision energy of $\sqrt{s_{NN}} = 2.76$ TeV (ASW [108, 109] and YaJEM [110] including a model for elastic energy loss parameterized with the P_{esc} variable). While most models predict the generally rising behavior of R_{AA} that is observed in the data at high p_T , the magnitude of the predicted slope varies greatly between models, depending on the assumptions for the jet-quenching mechanism. As it can be seen in the figure, the large theoretical model uncertainty can already be reduced, illuminating some of the model predictions. While a through description of each models shown in Fig 7.9 can be found in the respective references [105–110] and in a review paper [64], the key features of some of the theoretical model predictions and possible implications of the comparison are discussed in the following section.

7.0.10.1. Model Comparisons

As seen in Fig 7.9, there exist various theoretical models for the predictions of the nuclear modification factors. While many of them describe the measurements at lower energies rather successfully with one or few parameters tuned to the measurements. it is not straightforward to make detailed comparisons between the models because the calculations are made with models of wildly varying details about the energy loss mechanism as well as about the medium itself⁴ [64].

There is an effort in the theory community (TECHQM Collaboration [188]) to address this issue by creating an ideal situation where a quark of known energy propagating a static medium and comparing the size of energy losses (known as ‘QGP brick’ problem) with a goal to compare different models more quantitatively on an equal footing [189]. Here, a brief explanation of several models shown in the figure is given.

ASW: The ASW (Arment, Salgado, and Wiedemann) model of parton energy loss [108], which is based on the ‘quenching weight’ calculations for the multiple soft scattering approximation implemented in the modified fragmentation function⁵ was tuned with \hat{q} as an overall scaling parameter to the RHIC measurements. In Fig 7.9, R_{AA} is calculated in Ref. [110] with a realistic medium-density profile, which is based on the relativistic-hydrodynamic simulation.

⁴For example, different models choose different α_s , either as a running constant or as a fixed value. Another example is that while some model assume static medium, other models use (hydrodynamically) expanding medium.

⁵This means the vacuum fragmentation function is modified, $D^{medium}(z; Q^2) = P_E(\epsilon; \hat{q}) \otimes D^{vacuum}(z; Q^2)$, in Eq. 2.16 for the calculation of high p_T particle production, where $\epsilon = \Delta E/E$.

7. Results and Discussions

GLV: The GLV (Gyulassy, Lévai, and Vitev) model [106, 107] calculates the parton energy loss due to the medium induced radiation assuming that the produced medium is modelled by N well-separated, almost static color screened Yukawa potentials (known as opacity) in a dense deconfined medium. Unlike in the ASW model, the free parameter is the initial gluon density dN^g/dy instead of \hat{q} . In Fig. 7.9, the calculations are made for the initial gluon density of 400, 1400, and 2000-4000, respectively for $\sqrt{s_{NN}} = 17.3$ (SPS), 200 (RHIC), and 5500 (LHC) GeV. It is noted that the initial gluon density quoted for the SPS and RHIC are the initial gluon density needed to describe the $\pi^0 R_{AA}$ measurements [64].

YaJEM: The YaJEM (Yet another Jet Energy-loss Model) [110] is a Monte-Carlo implementation that calculates the medium-induced radiation of parton propagating the medium with modified splitting probability via a virtuality gain. YaJEM-D is a variation of the YaJEM that uses a dynamic minimum virtuality scale, which is dependent on the initial energy and the path length. The YaJEM-D has stronger path length dependence as a consequence.

PQM: The Parton Quenching Model is a PYTHIA-based Monte-Carlo implementation of the energy loss calculation using constrained quenching weights in BDMPS (Baier-Dokshitzer-Mueller-Peigné-Schiff) framework [78] in a realistic description of collisions geometry [105, 190]. The PQM uses \hat{q} as a free parameter. The result shown for in Fig. 7.9 is based on the extrapolated \hat{q} from the RHIC tuning (i.e., $\langle \hat{q} \rangle \simeq 14 \text{ GeV}^2/\text{fm}$). As can be seen from Fig. 7.9, the PQM model prediction highly under-estimates the measured R_{AA} . This could be attributed to that the extrapolated \hat{q} is largely over-predicted and/or that E dependence of the parton energy loss due to gluon radiation in the eikonal limit of very large parton initial energy, i.e., no E dependency, is not proper.

8. Model Studies

To gain more insight on the characteristic shape the measured R_{AA} exhibits and the possible implications on the parton energy loss, a simple ‘toy’ model study is performed using the PYTHIA MC. The low- p_T region ($p_T < 3$ GeV/ c) of the PbPb p_T spectra is modeled by smearing the pp p_T spectra, which mimics the Cronin effect (see Sec. 2.4.3.2). The high- p_T region above 5 GeV/ c is modeled by applying energy loss to the jet (or parton) generated by the PYTHIA MC before fragmenting into charged particles. A set of different energy loss models are used, and the resulting spectra that are modified and their ratio to the original, unmodified spectra, ‘ R_{AA} ’¹, in turn are compared. While there is no assumption and modeling of heavy-ion geometry made in this toy model study, the centrality dependence of parton energy loss is studied by comparing the PYTHIA-based model R_{AA} to the measured R_{AA} with one free parameter tuned for different centrality bins, which can be linked to the system size dependence and the path length dependence of parton energy loss once the collision geometry is properly modeled.

8.1. Modeling Cronin Effect

As described in Sec. 2.4.3.2, the observed Cronin effect is thought to be caused by the momentum broadening of incoming or outgoing parton and/or of the produced hadrons. This effect is simply mimicked by applying transverse momentum broadening with Gaussian shape to all charged particles produced in the PYTHIA MC sample. After dividing the resulting p_T distribution by the original p_T distribution, the ratio is compared to the measured R_{AA} in 0–5% centrality bin to see how much charged particle p_T broadening is needed to describe the rising trend of the R_{AA} below 3 GeV/ c .

For this study and the rest of studies that follow, we adopt PROQ20 tune for the PYTHIA generation among other tunes that are available because it is most consistent (within $\sim 10\%$) with the measured charged particle spectra in pp at $\sqrt{s} = 2.76$ TeV (see Fig. 7.3). It is also consistent within about 20% with the measurements at 0.9 and 7 TeV over the entire p_T ranges. To maintain similar statistics over the entire kinematic reach at $\sqrt{s} = 2.76$ TeV collisions, QCD samples are generated in bins of hard-scattering scale, i.e., $\hat{p}_T = 0\text{--}5, 5\text{--}10, 10\text{--}20, 20\text{--}30$, and so on. The different \hat{p}_T bin samples are then combined after properly weighting each sample by its corresponding cross section.

¹This ratio is not exactly the R_{AA} as defined in Eq. 2.14 as the numerator is not from PbPb collisions but rather from modified pp PYTHIA collision, i.e., no multiple NN collisions. Nonetheless, this ratio $(dN/dp_T)_{\text{modified}}/(dN/dp_T)_{\text{unmodified}}$ can be seen as the ratio of modified spectrum to the unmodified spectrum, which resembles the meaning of R_{AA} .

8. Model Studies

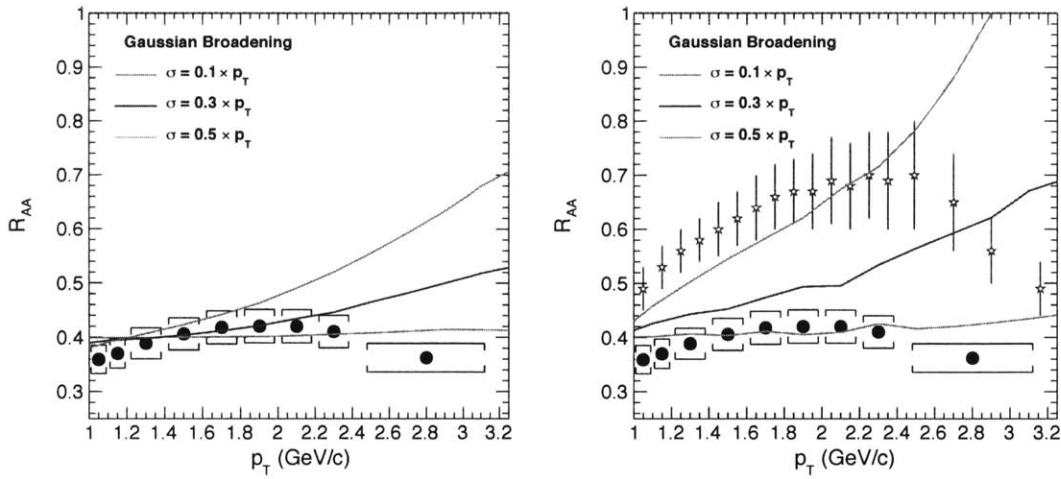


Figure 8.1.: R_{AA} in 0–5% bin compared to the PYTHIA-based modeled ‘ R_{AA} ’ with different choices of the Gaussian broadening parameter for $\sqrt{s_{NN}} = 2.76$ TeV (Left) and for $\sqrt{s_{NN}} = 0.2$ TeV (Right).

Figure 8.1(a) shows the result with the width of Gaussian broadening given by $\mathcal{C} \times p_T$, where \mathcal{C} is a constant and p_T is the transverse momentum of individual charged particle. The constant (‘free parameter’) is chosen such that resulting model- R_{AA} is close to the measured one. For the illustration, the constants are chosen arbitrarily as 0.1, 0.3, and 0.5, which is equivalent to 10, 30, and 50% of the original p_T of individual charged particle, respectively. It can be seen that the resulting R_{AA} can describe the rising trend up to 2 GeV/c, above which R_{AA} starts decreasing.

The same p_T broadening is applied to the charged particles in the 200 GeV PYTHIA MC sample produced in the same way as previously described. The result is compared to the STAR R_{AA} measurement [104] for charged hadrons (Fig. 8.1(a) right). It can be clearly seen that resulting model- R_{AA} is also larger for $\sqrt{s_{NN}} = 0.2$ TeV as in the measurement. Since the magnitude of the broadening is fixed at the two center-of-mass energies, the difference of the model- R_{AA} is attributed to the difference of the shape of original p_T distribution, which is more sharply falling at $\sqrt{s_{NN}} = 0.2$ TeV.

While this study is not meant to verify or constrain different models used to explain the Cronin effect, it supports that the rising trend of R_{AA} , which is universally seen across different center-of-mass energies, can be described if the original p_T distribution is smeared with the momentum broadening. It is interesting in particular to see that the momentum broadening explains naturally why the R_{AA} at $\sqrt{s_{NN}} = 0.2$ TeV is larger than at $\sqrt{s_{NN}} = 2.76$ TeV for the p_T range below 2–3 GeV/c.

8.2. Constraining Energy Loss Models

A set of different energy loss models are tested by applying the the energy loss models to the jets (or partons) generated by the PYTHIA MC and convoluting the modified jet energy spectrum with the ‘vacuum-like’ PYTHIA fragmentation functions. While the way fragmentation happens may be altered as well in the presence of hot and dense medium, the assumption of ‘vacuum-like’ fragmentation is well supported by the measurement of the fragmentation functions in PbPb collisions [191] as well as the recent theoretical development [192] for the high- p_T charged particles, which dominate the inclusive charged particle spectra in the high- p_T region. As mentioned earlier, there is no assumption and modeling of heavy-ion geometry made in this toy model study. However, by comparing to the measurements in different centrality bins, centrality dependence of parton energy loss is studied, which can be linked to the system size dependence and/or the path length dependence once the collision geometry is properly modeled. Furthermore, the correlations between the measured R_{AA} and v_2 in the high- p_T region are checked, which can further help constraining the path length dependence of the parton energy loss in medium.

8.2.1. Convolution Method

The production of high- p_T charged particles are dominated by the hadrons originating from parton fragmentation, which is well understood in the factorized-QCD as discussed in Sec. 2.4.3.1. In the pQCD framework, any of the following observables can be independently obtained from the (de-)convolution of the other two: the inclusive jet spectrum, the fragmentation functions of inclusive jets, and the inclusive charged particle spectrum, as can be seen from the formulation of the inclusive cross section (Eq 2.17). A detailed convolution technique can be found in Ref. [193], where it was used to cross check the measured charged particle spectrum based on the measured jet spectrum with a number of different model fragmentation functions.

Figure 8.2(a) shows the transverse momentum spectra ($d\sigma/dp_T$) constructed by merging different samples with different (non-overlapping) \hat{p}_T ranges after the cross section weighting. To see whether the spectrum of all charged particles can be reproduced by the charged particle spectrum constructed from the convolution of the jet spectrum² with the fragmentation functions, the ratio of the convoluted one to the spectrum of all charged particles is checked and shown in Fig. 8.2(b), which shows that the inclusive all charged particle spectrum can be reproduced well down to $p_T \sim 5$ GeV/c with the convolution method.

Here, for the purpose of studying phenomenological consequence of parton energy loss, we first modify the PYTHIA jet energy spectrum based on a few different energy loss scenarios and then convolute the modified jet energy spectrum with the un-modified (i.e., vacuum-like) fragmentation function to produce ‘modified’ charged particle spec-

²Iterative Cone jet finding algorithm with a cone radius of $R = 0.5$ is used to define jet at the generator level.

8. Model Studies

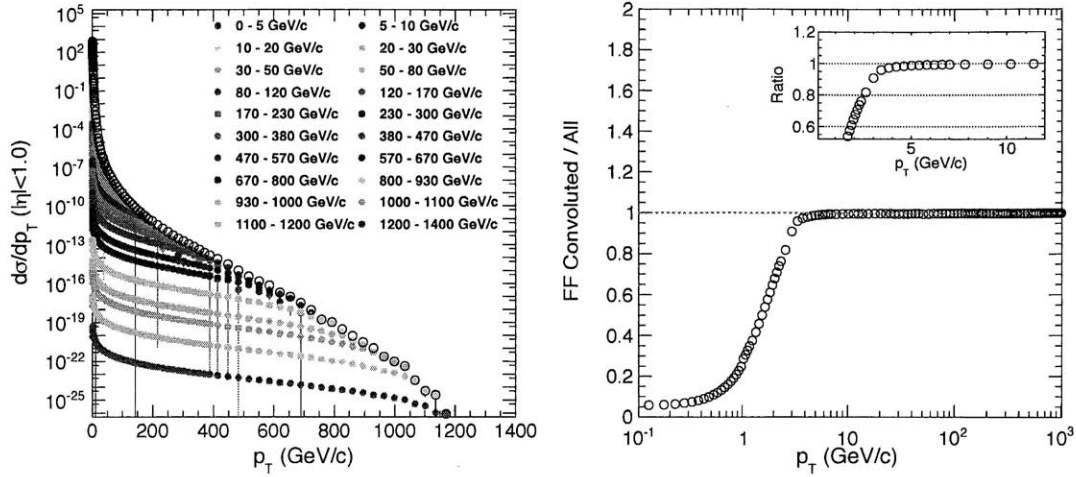


Figure 8.2.: (Left) Inclusive charged particle spectra from the PROQ20 PYTHIA. (Right) Comparison between the inclusive spectra of all charged particles in events with the inclusive spectra of all charged particles obtained from the convolution.

tra, mimicking the modified charged particle spectra in PbPb collisions. As in the previous section (Sec. 8.1), the resulting, modified p_T spectrum is divided by the original, unmodified p_T spectrum and the ratio, i.e., $(dN/dp_T)_{\text{modified}}/(dN/dp_T)_{\text{unmodified}}$ is compared to the measured R_{AA} .

8.2.2. Energy Loss Scenarios

The following energy loss scenarios (i.e., models) are studied in the modeling of the modified charged particle spectra in PbPb collisions for the case where outgoing parton with initial energy E_i loses its energy and carries final energy of E_f .

- Constant E-loss: $E_f = E_i - \Delta E$, where ΔE is constant.
- Constant fractional E-loss: $E_f = E_i \times (1 - f)$, where f is constant.
- Fractional E-loss with logarithmic energy dependence: $E_f = E_i \times (1 - f)$, where f is $c \times \ln E_i/E_f$ with a constant c .

Note that the third one, the fractional energy loss with logarithmic energy dependence is motivated³ by some of the pQCD energy loss calculations [81–83] as discussed in Sec. 2.4.2.2. Figure 8.3 shows an example of the amount of energy lost as an absolute loss (ΔE) and as a fractional loss ($\Delta E/E$), both as a function of E for the three distinctive scenarios.

³The constant energy loss is also motivated by some of the pQCD energy loss calculations that have no energy-dependence.

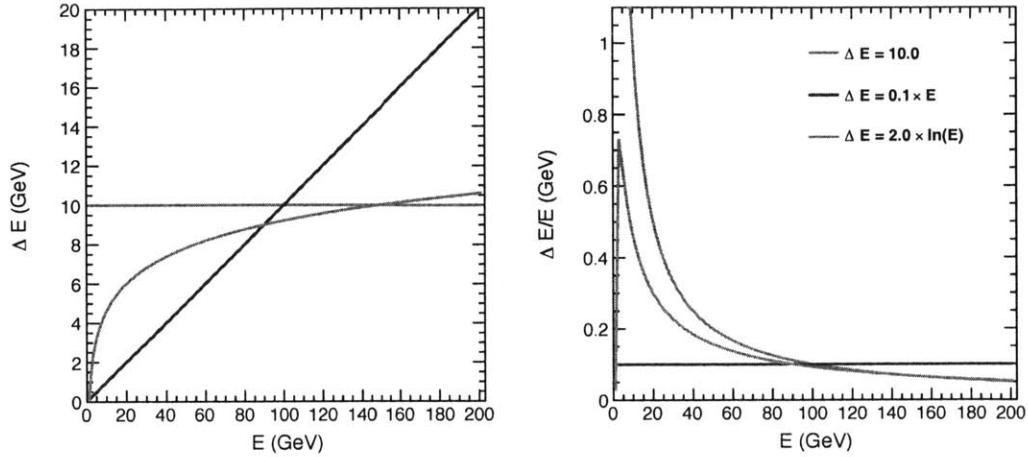


Figure 8.3.: Different energy loss scenarios

It can be seen that the constant energy loss and the fractional energy loss with logarithmic energy dependence become close above 100 GeV in energy while they are wildly different in the lower energy towards the minimum energy. Therefore, in order to distinguish the two scenarios, it is suggested to look at low jet energy region of any jet quenching observables.

The modified p_T spectrum of jet and charged particles in turn is obtained by applying these energy loss models to the original jet spectrum, i.e., the original energy is reduced according to the formula in each scenario (e.g., $E_f = E_i - \Delta E$).

8.2.3. Modeled R_{AA}

An example set of parameters in each energy loss scenario is chosen as follows in order to study the implication of each energy loss scenario in the charged particle p_T spectra.

- $\Delta E = 10, 20,$ and 30 GeV for the constant E-loss.
- $f = 0.1, 0.2,$ and 0.3 for the constant fractional E-loss.
- $c = 1, 2,$ and 3 for the fractional E-loss with logarithmic energy dependence

With each energy loss scenario applied to all the jets produced in the PYTHIA MC samples, the ratio of the modified jet spectrum to the unmodified spectrum is obtained. As mentioned earlier, there is no assumption on any geometrical quantities such as a impact parameter b , N_{coll} , and etc, as the spectrum is obtained from the simulation of pp events. Nonetheless, the ratio of the modified spectrum to the unmodified spectrum can tell us about the implication of different parton energy loss scenarios as the nuclear modification factor R_{AA} of jet or charged particle does. It is noted that while the system

8. Model Studies

size or the path length dependence of the parton energy loss is averaged in the definition of R_{AA} of jet and charged particle for a given centrality bin, the average system size and the average path length are different in different centrality bins. Therefore, the free parameter introduced in the model- R_{AA} can be thought of as a parameter to account for the system size and path length dependence which is not modeled in this study.

The modified jet energy spectra⁴ along with the unmodified one are shown for each energy loss scenario with the respective example parameters in the left panel of Fig. 8.4(a) 8.5(a) 8.6(a). Also shown in the right panel of the same figures are their ratios, i.e., jet R_{AA} defined as the same as the charged particle R_{AA} but for jet.

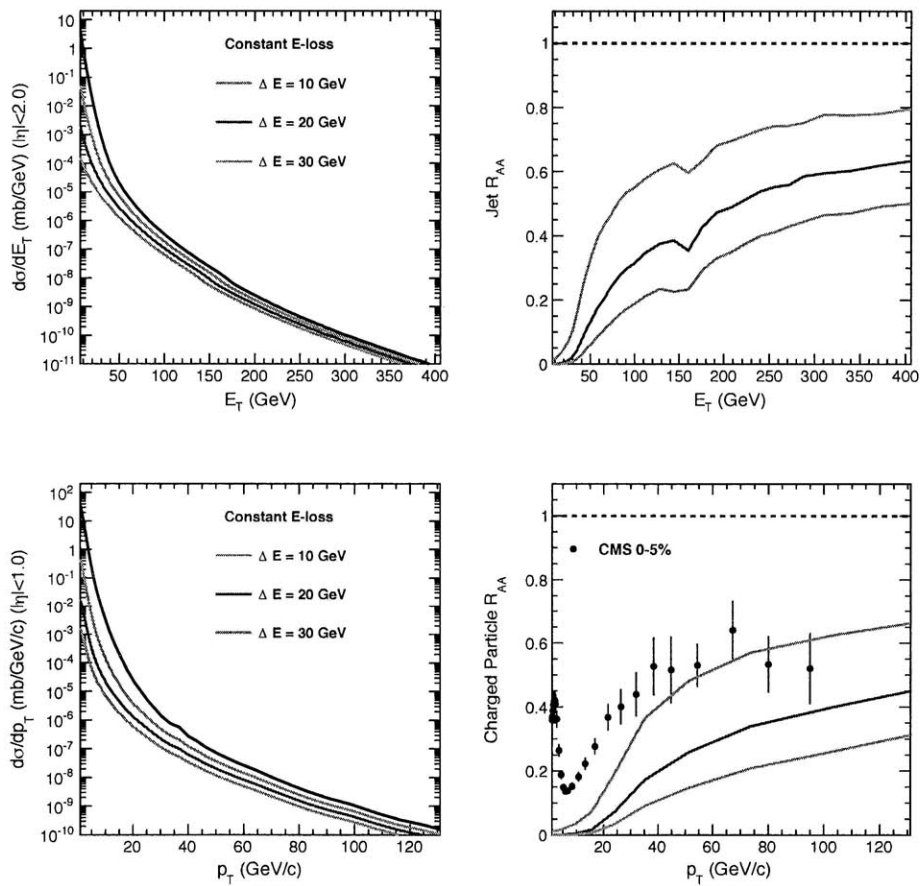


Figure 8.4.: Energy and momentum spectra of jets and charged particles with and without the modification due to the constant parton energy loss and resulting model- R_{AA} of jet and charged particle compared to the measured R_{AA} in 0-5%.

⁴Transverse energy (E_T) was chosen in this study to directly compare with the experimental observables that are typically made as a function of E_T .

8.2. Constraining Energy Loss Models

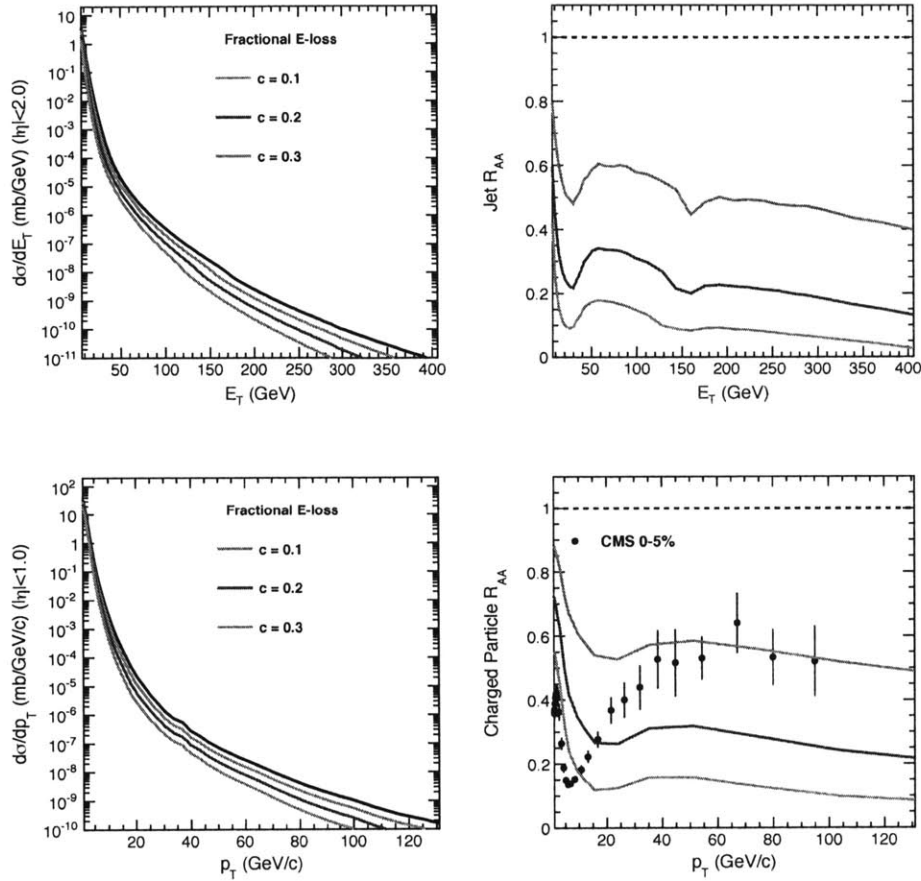


Figure 8.5.: Energy and momentum spectra of jets and charged particles with and without the modification due to the constant fractional parton energy loss and resulting model- R_{AA} of jet and charged particle compared to the measured R_{AA} in 0–5%.

Now with the modified jet spectra, the modified charged particle spectra are obtained by convoluting the modified spectra with the vacuum-like fragmentation functions as described in the previous sections. Fig. 8.4(b) 8.5(b) 8.6(b) show the charged particle spectra before and after the modification and the ratio of the modified spectra to the unmodified spectra. Also shown in the R_{AA} figure is the measured charged particle R_{AA} in 0–5% centrality bin for comparisons.

The comparisons to the measured R_{AA} show that the pQCD-motivated fractional energy loss with logarithmic energy dependence gives a best description of the measurement. The constant energy loss can describe the fast rise of the R_{AA} above 10 GeV/c or so if the loss of energy is smaller than 10 GeV, i.e., $\Delta E < 10$ GeV. However, it fails to describe the shape of R_{AA} below 10 GeV/c because the constant energy loss implies that a large fraction of the jet cross section below ΔE essentially diminishes, and does the charged

8. Model Studies

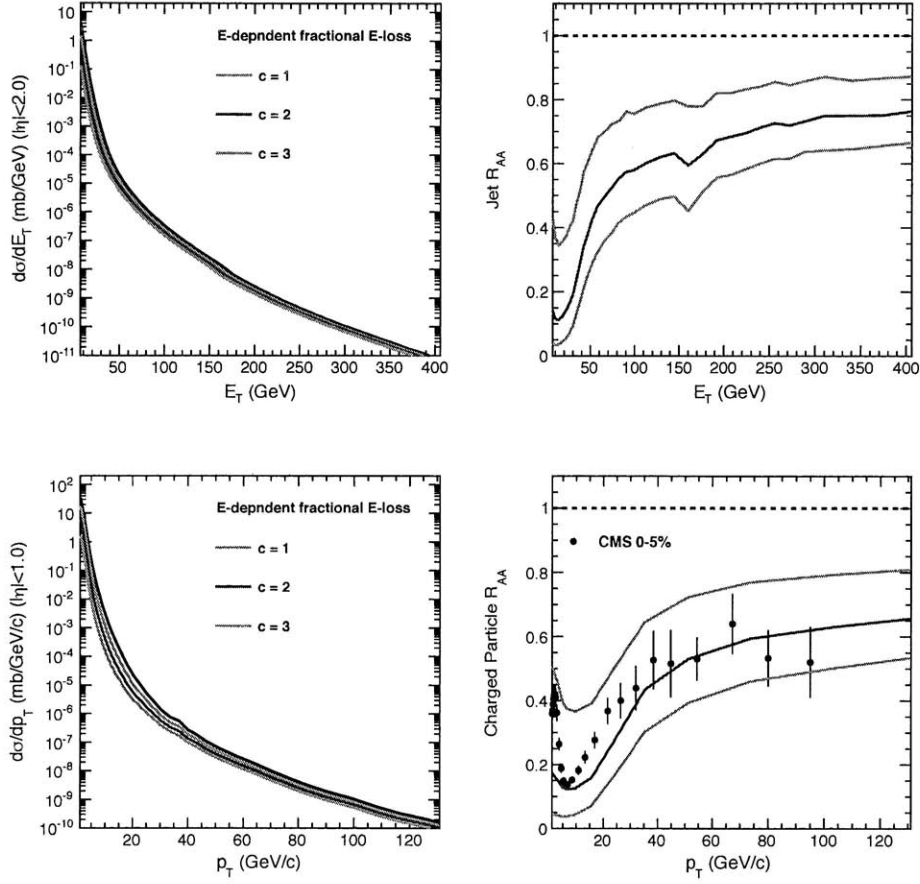


Figure 8.6.: Energy and momentum spectra of jets and charged particles with and without the modification due to the fractional energy loss with logarithmic energy dependence and resulting model- R_{AA} of jet and charged particle compared to the measured R_{AA} in 0–5%.

particle cross section in turn. The constant fractional energy loss results in decreasing R_{AA} in general. It can give a reasonable description of the high- p_T part of the measured R_{AA} ($p_T > 40$ GeV/c), but fails largely toward the lower p_T . Lastly, the fractional energy loss with logarithmic energy dependence describes both the low- and high- p_T regions. It is interesting to see that while this energy loss model results in fast-rising R_{AA} in the high p_T region, it also describes the turn-around (i.e., change of slope) of the R_{AA} around $p_T = 5\text{--}10$ GeV/c.

8.2.3.1. Centrality Dependence

In the comparisons of different energy loss models made in the previous section, the system size or the path length dependence of the parton energy loss could not be di-

rectly studied, such dependence, however, can be studied by comparing the resulting model- R_{AA} to the measured R_{AA} in different centrality bins and determining a best value for the free ‘quenching’ parameter (e.g., the constant c) in a given centrality bin. The best value is determined based on the χ^2 minimization of the difference between the measurements and the model. The free parameter encodes the path length (or the system size) dependence⁵. While it is not straightforward to extract specific physical meanings out of this free parameter in the following study, provided that the collisions geometry is modeled properly, it can further be used to study the other jet quenching observable that are dependent on the collision geometry.

Figure 8.2.3.1 shows the modeled R_{AA} with the parameter c varying from 0.4 to 2.6 with a step of either 0.1 or 0.2 in comparison to the measured R_{AA} in 0–5, 0–10, 10–30, 30–50, 70–90% centrality bins and the normalized χ^2 between the modeled and measured R_{AA} as a function of c . From the found minimum of the normalized χ^2 in each centrality bin, the correlation of the quenching parameter and the centrality as well as the N_{coll} can be plotted, which is shown in Fig. 8.8.

8.2.4. R_{AA} and v_2 Correlation

While the low- p_T region ($<1-2$ GeV/ c) of the elliptic flow v_2 is believed to arise from the hydrodynamical nature of the thermalized system, i.e., the pressure gradient built during an early stage of the system expansion, an azimuthal isotropy characterized by v_2 in the high- p_T region is thought to be a manifestation of the path length dependence of parton energy loss, i.e., jet quenching *per se* [194–196]. v_2 with the jet quenching origin, can be related to R_{AA} as follows [195],

$$v_2 \equiv \int R_{AA}(\phi_r) \cos(2\phi_r) d\phi_r / \int R_{AA}(\phi_r) d\phi_r, \quad (8.1)$$

where ϕ_r is defined as the azimuthal angle with respect to the reaction plane (Ψ_{RP})⁶, i.e., $\phi_r \equiv \phi - \Psi_{RP}$. Therefore, the high- p_T v_2 measurement can probe the ϕ -dependent jet quenching. Given the path length a highly energetic parton has to travel is dependent on the azimuthal direction defined with respect to the reaction plane due to the geometric consideration, it implies that the high- p_T v_2 measurement probes the path length dependence of jet quenching.

The R_{AA} measurement presented in this thesis are plotted along with the CMS high- p_T v_2 measurement [197] as a function of p_T up to 65 GeV/ c , the maximum p_T reach in the high- p_T v_2 measurement, which is shown in Fig. 8.10. The error bar represents the quadratic sum of the statistical and systematic errors. In order to compare the two measurements in the same centrality bins, 0–5% and 5–10% bins of the R_{AA} measurements are combined and 10–20 (30–40)% and 20–30 (40–50)% bins of the high- p_T v_2 measurements are combined. As the most peripheral centrality bin in the high- p_T v_2

⁵One can associate the determined constant with the known formulation of parton energy loss, e.g.,

$$\Delta E \approx \frac{C_R \alpha_s}{N(E)} \frac{L^2 \mu^2}{\lambda_g} \log \frac{E}{\mu} \quad [81].$$

⁶The reaction plane is further defined by the beam direction and the short direction of the lenticular region created in the overlap region of the colliding nuclei.

rectly studied, such dependence, however, can be studied by comparing the resulting model- R_{AA} to the measured R_{AA} in different centrality bins and determining a best value for the free ‘quenching’ parameter (e.g., the constant c) in a given centrality bin. The best value is determined based on the χ^2 minimization of the difference between the measurements and the model. The free parameter encodes the path length (or the system size) dependence⁵. While it is not straightforward to extract specific physical meanings out of this free parameter in the following study, provided that the collisions geometry is modeled properly, it can further be used to study the other jet quenching observable that are dependent on the collision geometry.

Figure 8.2.3.1 shows the modeled R_{AA} with the parameter c varying from 0.4 to 2.6 with a step of either 0.1 or 0.2 in comparison to the measured R_{AA} in 0–5, 0–10, 10–30, 30–50, 70–90% centrality bins and the normalized χ^2 between the modeled and measured R_{AA} as a function of c . From the found minimum of the normalized χ^2 in each centrality bin, the correlation of the quenching parameter and the centrality as well as the N_{coll} can be plotted, which is shown in Fig. 8.8.

8.2.4. R_{AA} and v_2 Correlation

While the low- p_T region (<1 -2 GeV/ c) of the elliptic flow v_2 is believed to arise from the hydrodynamical nature of the thermalized system, i.e., the pressure gradient built during an early stage of the system expansion, an azimuthal isotropy characterized by v_2 in the high- p_T region is thought to be a manifestation of the path length dependence of parton energy loss, i.e., jet quenching *per se* [194–196]. v_2 with the jet quenching origin, can be related to R_{AA} as follows [195],

$$v_2 \equiv \int R_{AA}(\phi_r) \cos(2\phi_r) d\phi_r / \int R_{AA}(\phi_r) d\phi_r, \quad (8.1)$$

where ϕ_r is defined as the azimuthal angle with respect to the reaction plane (Ψ_{RP})⁶, i.e., $\phi_r \equiv \phi - \Psi_{RP}$. Therefore, the high- p_T v_2 measurement can probe the ϕ -dependent jet quenching. Given the path length a highly energetic parton has to travel is dependent on the azimuthal direction defined with respect to the reaction plane due to the geometric consideration, it implies that the high- p_T v_2 measurement probes the path length dependence of jet quenching.

The R_{AA} measurement presented in this thesis are plotted along with the CMS high- p_T v_2 measurement [197] as a function of p_T up to 65 GeV/ c , the maximum p_T reach in the high- p_T v_2 measurement, which is shown in Fig. 8.10. The error bar represents the quadratic sum of the statistical and systematic errors. In order to compare the two measurements in the same centrality bins, 0–5% and 5–10% bins of the R_{AA} measurements are combined and 10–20 (30–40)% and 20–30 (40–50)% bins of the high- p_T v_2 measurements are combined. As the most peripheral centrality bin in the high- p_T v_2

⁵One can associate the determined constant with the known formulation of parton energy loss, e.g., $\Delta E \approx \frac{C_R \alpha_s}{N(E)} \frac{L^2 \mu^2}{\lambda_g} \log \frac{E}{\mu}$ [81].

⁶The reaction plane is further defined by the beam direction and the short direction of the lenticular region created in the overlap region of the colliding nuclei.

8. Model Studies

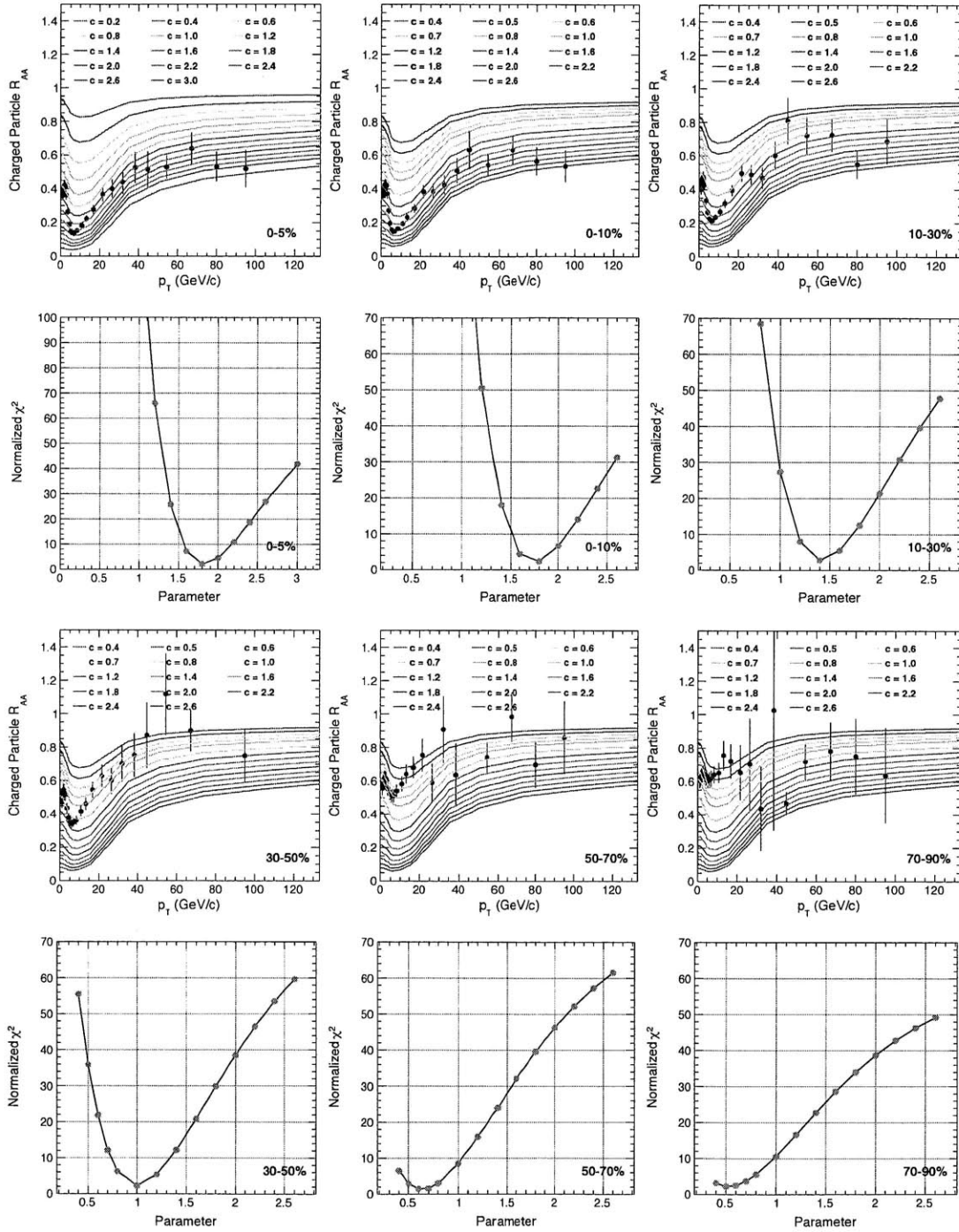


Figure 8.7.: Comparison between the modeled R_{AA} with varying quenching parameter and the measured R_{AA} in different centrality bins.

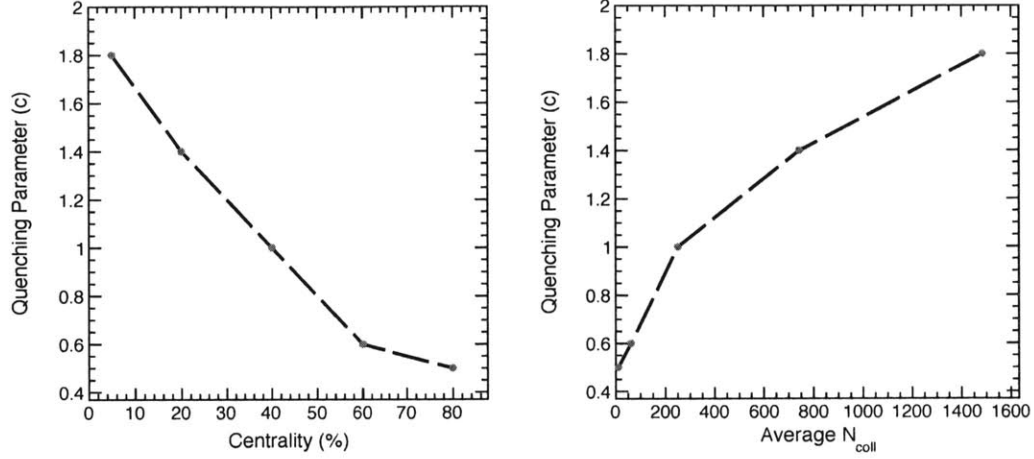


Figure 8.8.: Correlation between the quenching parameter c with the event centrality and the average N_{coll} .

measurement is between 50–60%, it is compared to the most peripheral bin of the R_{AA} measurement, i.e., 50–70%. Also shown in the figure are the theoretical predictions for the selected centrality bins made in Ref. [198]. The correlation between the two measurements are directly plotted as a function of v_2 in the x -axis and R_{AA} in the y -axis and shown in Fig. 8.2.3.1. In a similar way, the theoretical prediction made for R_{AA} (0–5%) and v_2 (0–10%) are correlated and shown as filled circle (red) in the figure. There are two distinctive regions in the correlation plot: In the low- p_T region around 4 GeV/ c both R_{AA} and v_2 decrease as a function of p_T . In the higher p_T region between 10 and 60 GeV/ c , R_{AA} increases but v_2 decreases showing an anti-correlation, which is not as prominent in the 0–10% bin as the other centrality bins since v_2 in the 0–10% bin flattens starting from 20 GeV/ c in p_T . It is subject further studies. In particular, by comparing this correlation to the jet quenching models, it will help constraining the path length dependence of the parton energy loss (i.e., $dE/dx \propto L^2$ or L^3), as first studied in the limited p_T range in Ref. [194, 195].

8. Model Studies

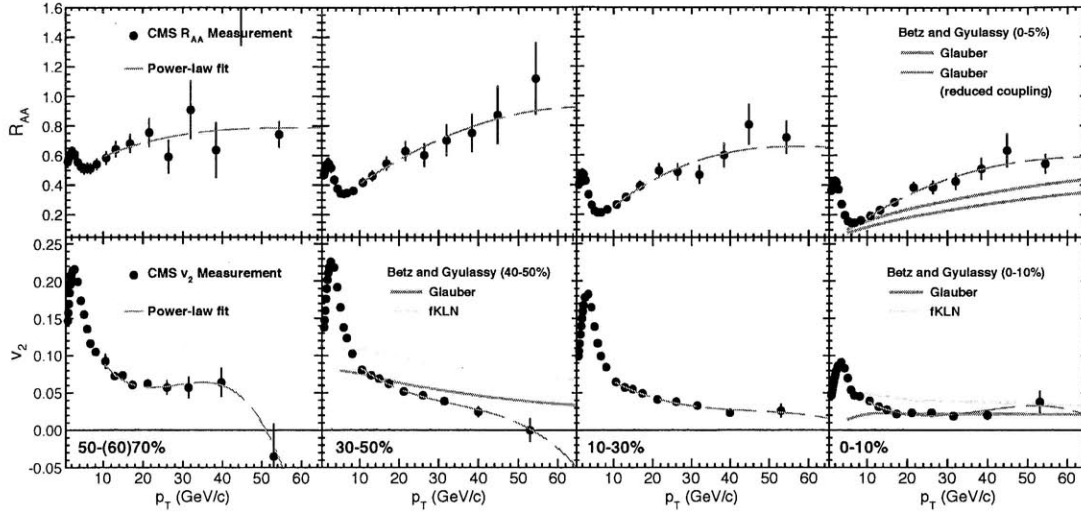


Figure 8.9.: R_{AA} and v_2 measurements as a function of p_T in bins of four centralities along with the theoretical predictions made for the selected centrality ranges [198].

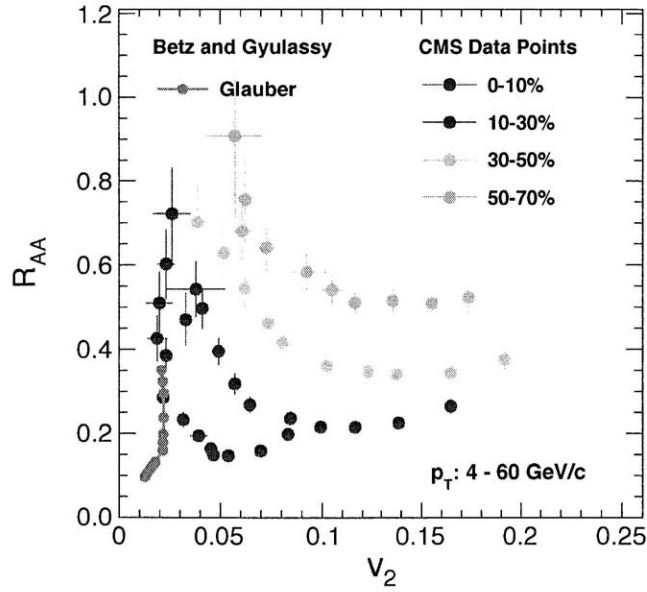


Figure 8.10.: Correlation between R_{AA} and v_2 measurements in the range $p_T = 5-60$ GeV/c in difference centrality bins. The theoretical prediction is based on the 0-5% R_{AA} with 0-10% v_2 from Ref. [198].

9. Conclusions

The energy loss of energetic parton, known as jet quenching, as a probe of the hot, dense medium created in heavy-ion collisions has been studied experimentally via the observation of high transverse momentum charged particle suppression with the CMS detector at the LHC. Details of the analyses of the transverse momentum spectra in pp and PbPb collisions as well as the construction of R_{AA} are presented in this thesis.

The charged particle transverse momentum distributions in the form of the invariant differential yield $E d^3N_{ch}/dp^3$ in pp collisions at $\sqrt{s} = 0.9, 2.76, 7$ TeV and in PbPb collisions at $\sqrt{s_{NN}} = 2.76$ TeV have been measured. Calorimeter-based high-transverse-energy triggers are employed to enhance the statistical reach of the high- p_T measurements. The calorimeter information is also explicitly used to suppress the fake tracks in the case of PbPb spectra measurements.

The pp results have been compared to both leading-order (LO) and next-to-leading-order (NLO) QCD calculations. The LO calculations obtained from the generator-level PYTHIA MC with various tunes show reasonable agreement with the measurements. The 7 TeV data are most consistent with PYTHIA8, which agrees at the 10% level over the full p_T range of the measurement. In contrast, the 0.9 TeV and 2.76 TeV data are considerably better described by the ProQ20 tune. The NLO calculations, on the other hand, over-predict the measured cross sections by almost a factor of two at all collision energies, possibly suggesting that the fragmentation functions used in the calculations are not well tuned for LHC energies.

Additionally, the consistency of the 0.9, 2.76, and 7 TeV spectra has been demonstrated with an empirical x_T scaling that unifies the differential cross sections from a wide range of collision energies onto a common curve. Furthermore, within the theoretical uncertainties of the NLO calculations, the residual breaking of x_T scaling above $p_T \approx 8$ GeV/c is found to be consistent between the measured cross sections and the NLO calculations.

Overall, the detailed comparisons have testified our understanding of the high- p_T charged particle production in the framework of factorized pQCD at a wide range of the collisions energies, providing an important theoretical and empirical ground for the study of jet quenching with high- p_T charged particle production.

The nuclear modification factors R_{AA} in different centrality bins have been constructed by dividing the p_T spectrum in PbPb collisions for a given centrality by the charged particle p_T spectrum in pp collisions scaled by the corresponding number of incoherent nucleon-nucleon collisions. It was observed via R_{AA} that the high- p_T yields in central PbPb collisions are significantly suppressed when compared to peripheral PbPb and pp collisions, reaching about a factor of 7 suppression. This deviation of the measured PbPb spectra (i.e. high- p_T particles in QCD medium) from the pp reference

9. Conclusions

spectrum (i.e. high- p_T particles in QCD vacuum) at the same center of mass energy is understood as a consequence of the energy loss of highly energetic parton traversing the hot, dense medium created in the heavy-ion collisions at unprecedentedly high collision energy.

In the range $p_T = 5\text{--}10$ GeV/ c , the suppression is stronger than that seen at RHIC. Beyond 10 GeV/ c , both R_{AA} and R_{CP} show a rising trend, as already suggested by the early measurement, limited to $p_T = 20$ GeV/ c . The measurement presented in this thesis, with improved statistical precision, clearly shows that this rise continues at higher p_T , approaching a suppression factor $R_{AA} \approx 0.5\text{--}0.6$ in the range 40–100 GeV/ c . The overall p_T dependence of the suppression can be described by a number of phenomenological predictions. The detailed evolution of the R_{AA} rise from 6 to 100 GeV/ c , however, varies significantly between the models, exhibiting large theoretical uncertainties. Because of the wildly varying details in different modeling of parton energy loss and the medium, it is not straightforward to draw definitive conclusions solely based on the presented model comparisons. Therefore, it is subject to further systematic studies.

The simple toy model studies of Cronin effect and parton energy loss provide insight into how the characteristic shape of the measured R_{AA} can be understood: The low- p_T region $p_T = 1\text{--}2$ GeV/ c , where R_{AA} initially increases as a function of p_T , can be described when the transverse momentum broadening is introduced in the charged particle spectrum. The transverse momentum broadening also gives a natural explanation why the measured R_{AA} at $\sqrt{s_{NN}} = 200$ GeV is higher than at $\sqrt{s_{NN}} = 2.76$ TeV. The high- p_T region above 5 GeV/ c , on the other hand, can be described when the energy degradation is introduced in the parton energy spectrum before fragmenting into charged particles. The comparison of different parton energy loss models reveals that while the shape of the measured R_{AA} in the high- p_T region ($p_T \gtrsim 35$ GeV/ c) can be described by all the energy loss models, the entire p_T range is highly preferred by the logarithmic fractional energy loss over the constant- or constant-fractional energy loss models. The intermediate region ($2 < p_T < 5$) was not directly studied with the toy model. However, it can be inferred that the parton energy loss gradually dominates over the effect of transverse momentum broadening in this region.

Overall, we have learned from the study of high transverse momentum charged particles suppression that an unambiguously large final-state medium effect is present over a large transverse momentum range in the PbPb collisions at the LHC and that the measured shape of R_{AA} in the high- p_T region can be best understood by the fractional energy loss with logarithmic energy dependence, which is supported by some of the pQCD energy loss calculations. However, the magnitude of the overall suppression and the slope of rising R_{AA} are subject to further studies to draw more quantitative conclusions. While R_{AA} does not measure differentially the azimuthal angle of charged particle with respect to the event plane, which can be linked to the path-length dependence of parton energy loss, studying correlations of the presented R_{AA} measurement with various observables such as high- p_T charged particle azimuthal anisotropy, inclusive jet spectra, and dijet transverse energy balance, will further elucidate the detailed mechanism of jet quenching such as path-length dependence and the properties of the medium produced in heavy-ion collisions at collider energies.

A. QCD Lagrangian

The QCD Lagrangian is given by

$$\mathcal{L}_{QCD} = -\frac{1}{4} F_{\mu\nu}^{(a)} F^{(a)\mu\nu} + i \sum_q \bar{\psi}_{qi} (\gamma^\mu (D_\mu)_j^i - m_q \delta_j^i) \psi_q^j, \quad (\text{A.1})$$

where the ψ_q^j are the fermion fields representing a quark of flavor q and mass m_q with a color index j , which transforms in the fundamental representation of the color $SU(3)$ gauge group. D_μ is the covariant derivative

$$(D_\mu)_j^i = \delta_j^i \partial_\mu + i g_s \sum_a \frac{(\lambda^a)_j^i}{2} A_\mu^a, \quad (\text{A.2})$$

where λ^a ($a = 1, \dots, 8$) are the $SU(3)$ Gell-Mann matrices, A_μ^a are the gluon fields, and g_s is the dimensionless strong coupling constant. λ^a encodes the fact that a gluon's interaction with a quark rotates the quark color in $SU(3)$ space. Lastly, $F_{\mu\nu}^{(a)}$ is the gluon field-strength tensor

$$F_{\mu\nu}^{(a)} = \partial_\mu A_\nu^a - \partial_\nu A_\mu^a - g_s f_{abc} A_\mu^b A_\nu^c, \quad (\text{A.3})$$

where the constants f_{abc} are the $SU(3)$ structure constants, which can be expressed as

$$f_{abc} = (4i)^{-1} \text{tr}(\lambda^c [\lambda^a, \lambda^b]) \quad (\text{A.4})$$

since λ^a satisfies the following commutation relations.

$$[\lambda^a, \lambda^b] = 2i f_{abc} \lambda^c \quad (\text{A.5})$$

The non-vanishing structure constants in Eq. A.4 is what distinguishes QCD from Quantum Electrodynamics (QED); QCD is a non-Abelian (i.e. non-commutative) gauge theory.

B. Track Quality Distributions

The distribution of the track quality distributions are shown differentially in bins of p_T and centrality. From the top left, it is N_{hits}^{valid} , $\sigma(p_T)/p_T$, $(\chi^2/N_{d.o.f})/N_{layers}$, $d_0/\sqrt{\sigma(d_0^2)+\sigma(v_0)}$, and $d_z/\sqrt{\sigma(d_z^2)+\sigma(v_z)}$.

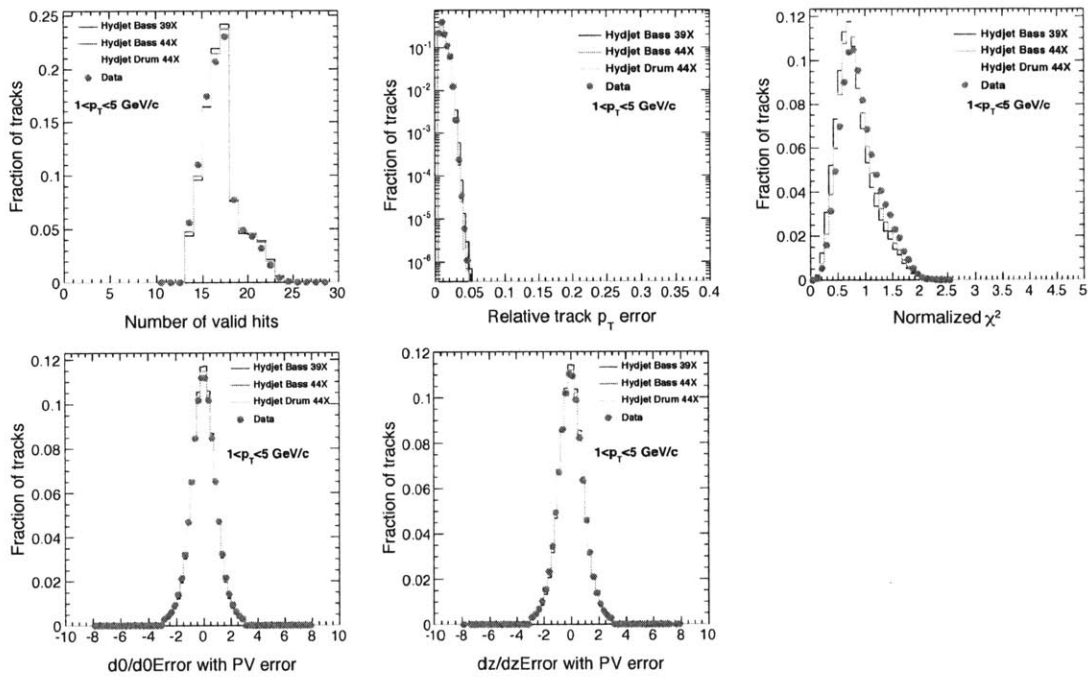


Figure B.1.: Track quality distributions. 1–5 GeV/c

B. Track Quality Distributions

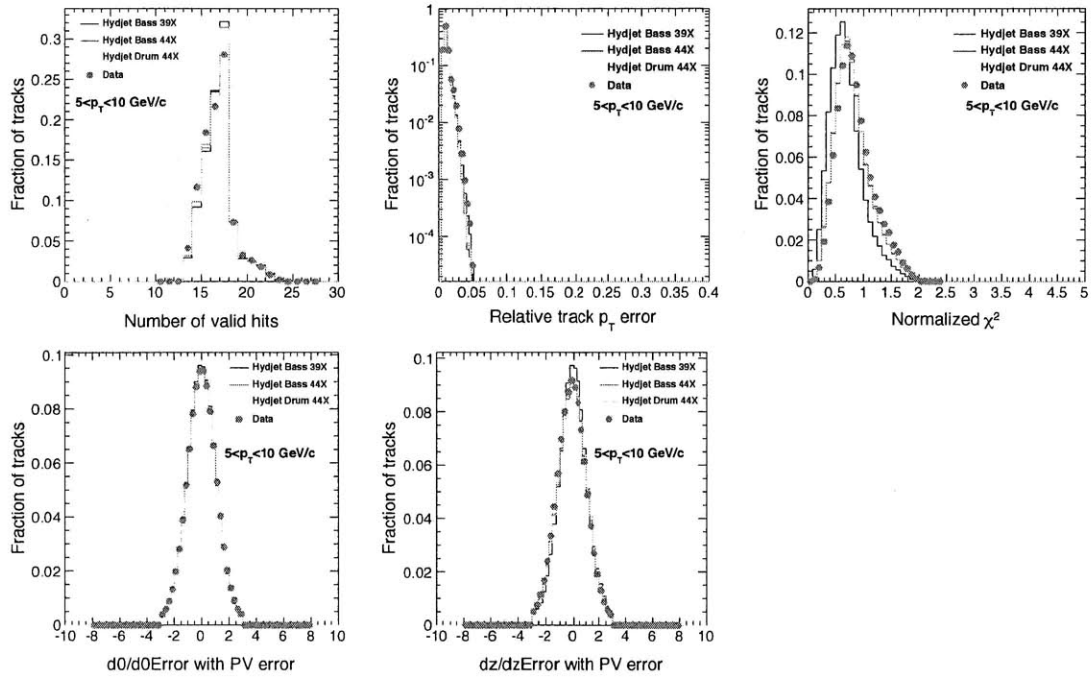


Figure B.2.: Track quality distributions. 5–10 GeV/c

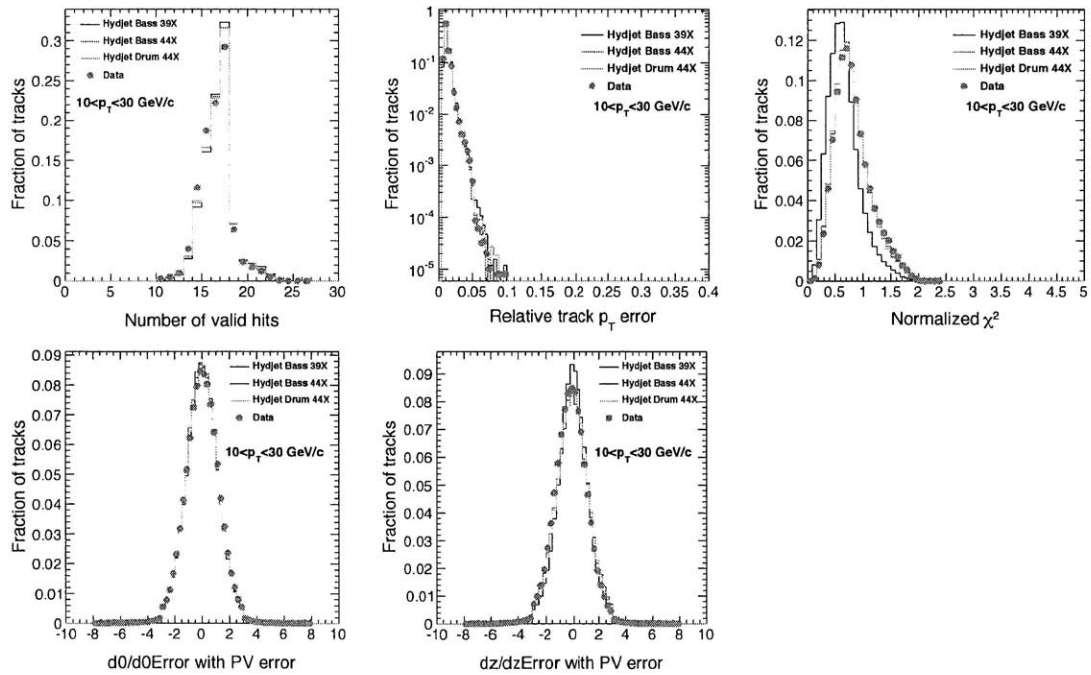


Figure B.3.: Track quality distributions. 10–30 GeV/c

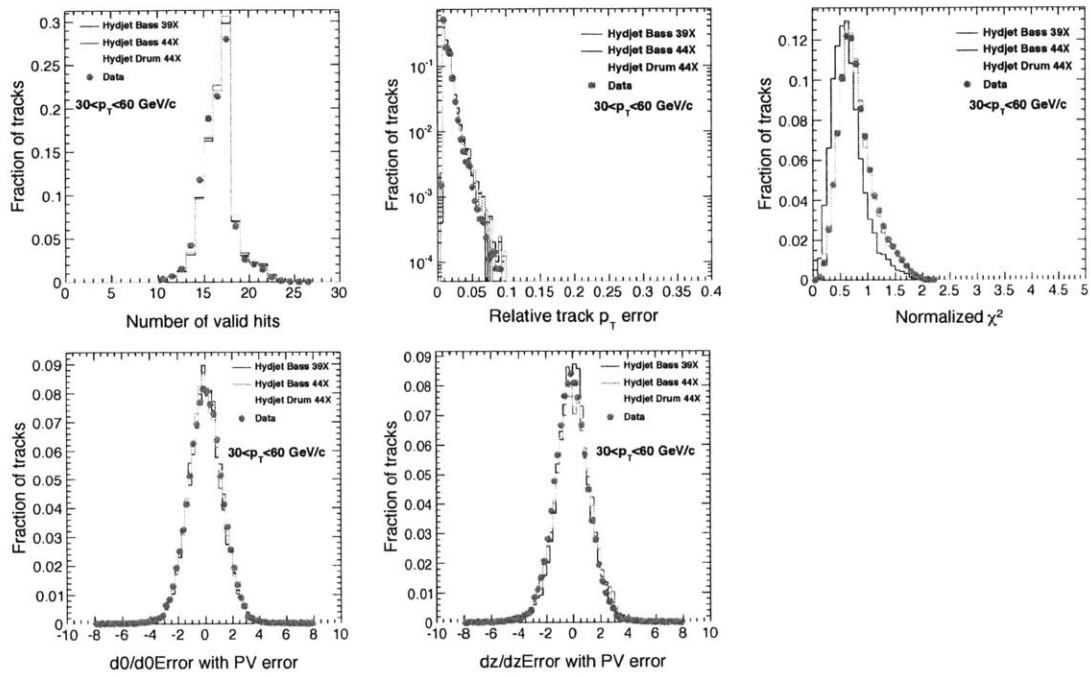


Figure B.4.: Track quality distributions. 30–60 GeV/c

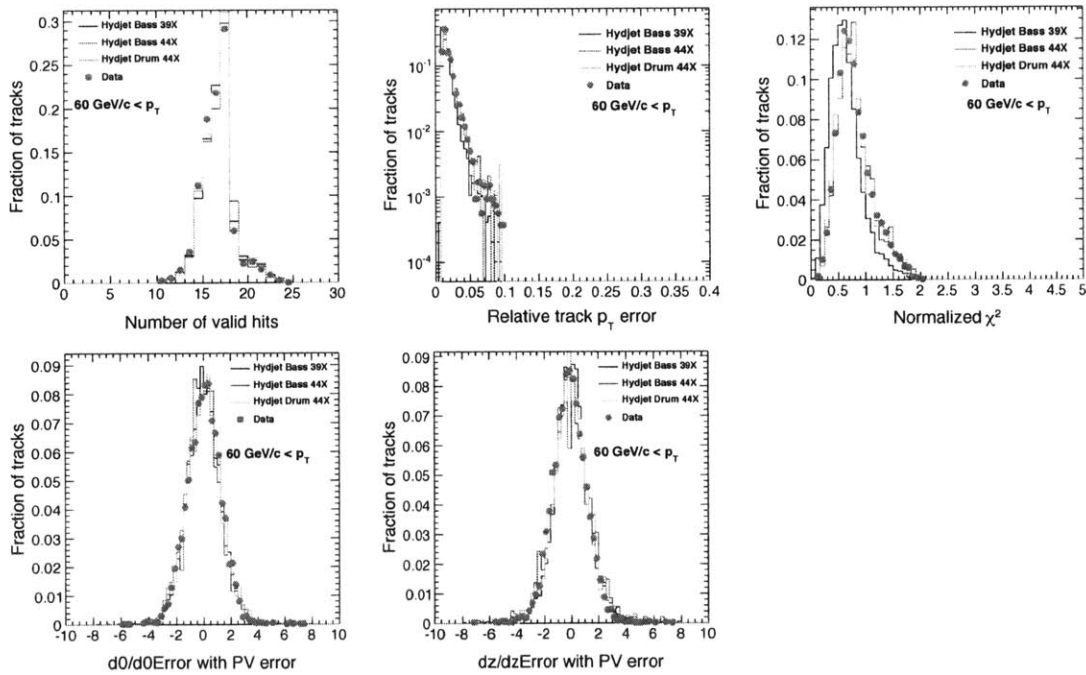


Figure B.5.: Track quality distributions. 60– ∞ GeV/c

B. Track Quality Distributions

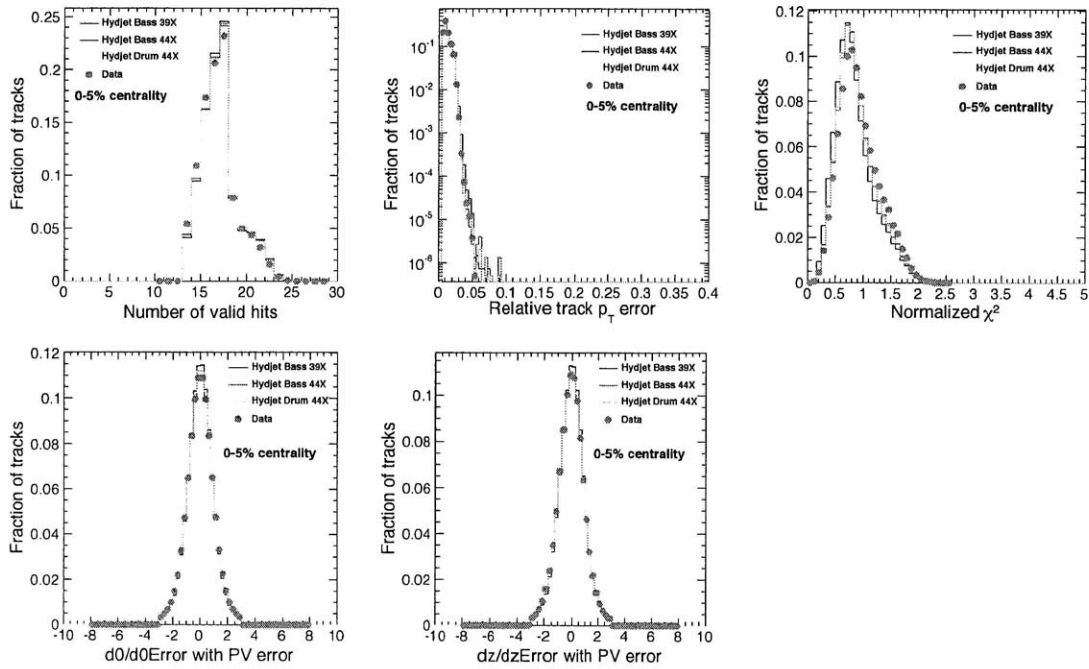


Figure B.6.: Track quality distributions. 0–5%

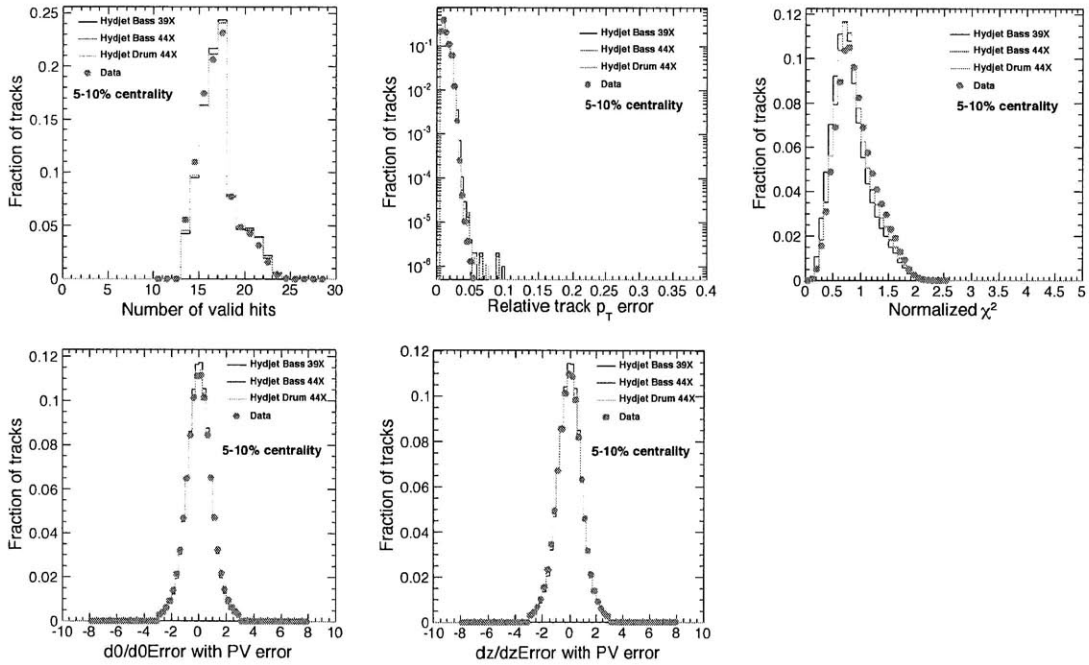


Figure B.7.: Track quality distributions. 5–10%

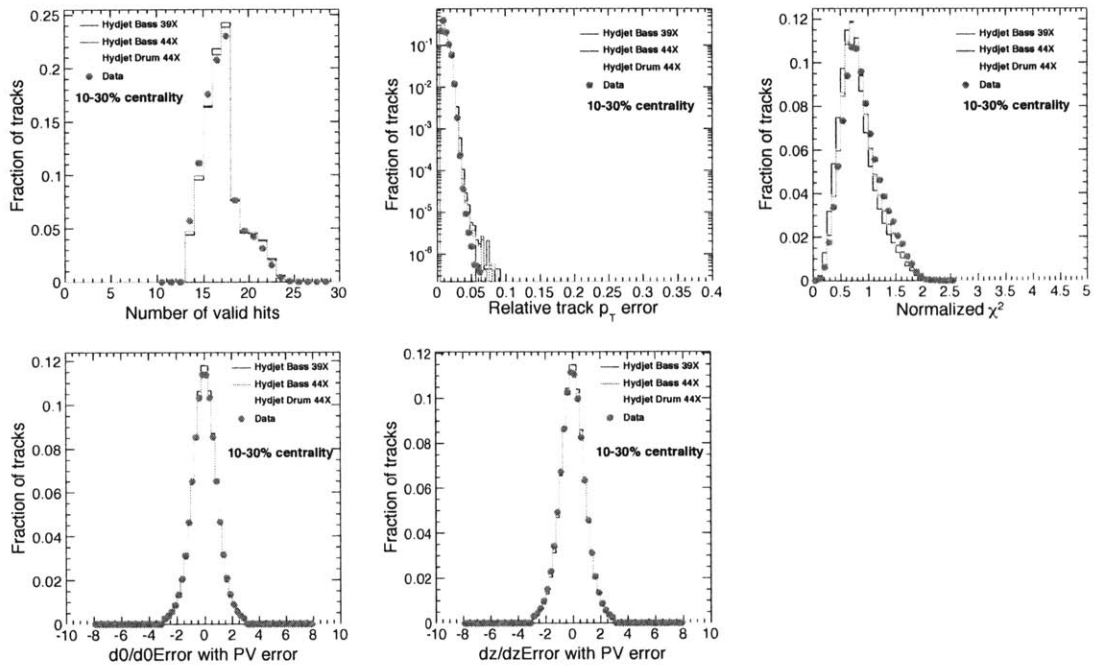


Figure B.8.: Track quality distributions. 10–30%

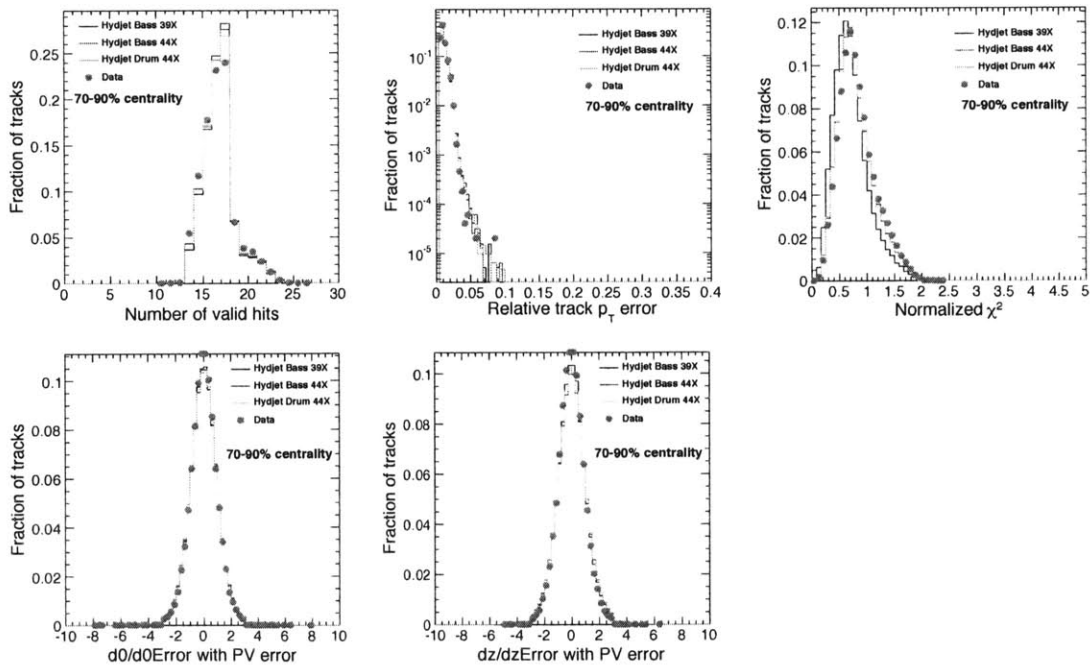


Figure B.9.: Track quality distributions. 70–90%

C. Tabulated Results

Table C.1.: Tabulated result of Fig. 7.2(a)

p_T low edge	p_T up edge	Yield	Statistical Error (\pm)	Systematic Error (\pm)
4.000e-01	6.000e-01	1.12039e+00	2.2e-04	4.814e-02
6.000e-01	8.000e-01	4.3415e-01	1.1e-04	1.866e-02
8.000e-01	1.000e+00	1.84944e-01	6.3e-05	7.952e-03
1.000e+00	1.200e+00	8.5811e-02	3.9e-05	3.691e-03
1.200e+00	1.600e+00	3.0526e-02	1.4e-05	1.313e-03
1.600e+00	2.000e+00	9.1459e-03	6.8e-06	3.938e-04
2.000e+00	2.400e+00	3.1714e-03	3.6e-06	1.366e-04
2.400e+00	3.200e+00	7.9086e-04	1.11e-06	3.409e-05
3.200e+00	4.000e+00	1.62026e-04	4.46e-07	6.991e-06
4.000e+00	4.800e+00	4.2808e-05	2.10e-07	1.849e-06
4.800e+00	5.600e+00	1.36076e-05	1.095e-07	5.880e-07
5.600e+00	6.400e+00	5.0980e-06	6.38e-08	2.204e-07
6.400e+00	7.200e+00	2.09996e-06	3.959e-08	9.084e-08
7.200e+00	9.200e+00	5.8109e-07	1.171e-08	2.515e-08
9.200e+00	1.120e+01	1.19391e-07	4.539e-09	5.171e-09
1.120e+01	1.320e+01	3.3481e-08	2.165e-09	1.451e-09
1.320e+01	1.720e+01	7.9256e-09	6.624e-10	3.436e-10
1.720e+01	2.120e+01	1.5183e-09	2.592e-10	6.59e-11
2.120e+01	2.520e+01	4.632e-10	1.335e-10	2.02e-11
2.520e+01	3.720e+01	4.601e-11	1.889e-11	2.04e-12

C. Tabulated Results

Table C.2.: Tabulated result of Fig. 7.2(b)

p_T low edge	p_T up edge	Yield	Statistical Error (\pm)	Systematic Error (\pm)
4.000e-01	6.000e-01	1.68022e+00	1.9e-04	7.961e-02
6.000e-01	8.000e-01	7.1916e-01	1.0e-04	3.401e-02
8.000e-01	1.000e+00	3.3621e-01	6e-05	1.588e-02
1.000e+00	1.200e+00	1.71979e-01	3.7e-05	8.113e-03
1.200e+00	1.600e+00	7.0213e-02	1.5e-05	3.308e-03
1.600e+00	2.000e+00	2.4796e-02	8e-06	1.167e-03
2.000e+00	2.400e+00	9.9366e-03	4.4e-06	4.670e-04
2.400e+00	3.200e+00	2.9975e-03	1.5e-06	1.407e-04
3.200e+00	4.000e+00	7.7056e-04	6.7e-07	3.612e-05
4.000e+00	4.800e+00	2.4402e-04	3.5e-07	1.143e-05
4.800e+00	5.600e+00	9.0609e-05	1.94e-07	4.240e-06
5.600e+00	6.400e+00	3.8438e-05	1.17e-07	1.798e-06
6.400e+00	7.200e+00	1.78328e-05	7.48e-08	8.335e-07
7.200e+00	9.200e+00	5.7719e-06	2.38e-08	2.696e-07
9.200e+00	1.120e+01	1.52171e-06	1.092e-08	7.104e-08
1.120e+01	1.320e+01	5.1369e-07	5.76e-09	2.398e-08
1.320e+01	1.720e+01	1.35670e-07	1.745e-09	6.342e-09
1.720e+01	2.120e+01	3.3087e-08	7.49e-10	1.555e-09
2.120e+01	2.520e+01	1.01372e-08	3.236e-10	4.826e-10
2.520e+01	3.720e+01	1.68816e-09	5.201e-11	8.607e-11
3.720e+01	4.920e+01	2.2497e-10	8.75e-12	1.375e-11
4.920e+01	6.120e+01	4.4431e-11	1.845e-12	2.965e-12
6.120e+01	8.120e+01	8.4116e-12	4.517e-13	5.853e-13
8.120e+01	1.012e+02	1.5299e-12	7.32e-14	1.102e-13
1.012e+02	1.212e+02	3.9626e-13	1.039e-14	2.937e-14
1.212e+02	1.612e+02	8.1866e-14	2.959e-15	6.296e-15
1.612e+02	2.012e+02	1.2708e-14	1.097e-15	1.018e-15

Table C.3.: Tabulated result of Fig. 7.3

p_T low edge	p_T up edge	Yield	Statistical Error (\pm)	Systematic Error (\pm)
4.500e-01	6.000e-01	1.25693e+00	2.3e-04	5.892e-02
6.000e-01	7.500e-01	6.5225e-01	1.4e-04	3.058e-02
7.500e-01	9.000e-01	3.5477e-01	9e-05	1.663e-02
9.000e-01	1.050e+00	2.04273e-01	6.6e-05	9.577e-03
1.050e+00	1.200e+00	1.22879e-01	4.8e-05	5.761e-03
1.200e+00	1.500e+00	6.0767e-02	2.1e-05	2.849e-03
1.500e+00	1.800e+00	2.6044e-02	1.3e-05	1.221e-03
1.800e+00	2.100e+00	1.20503e-02	8.0e-06	5.651e-04
2.100e+00	2.400e+00	5.9672e-03	5.2e-06	2.799e-04
2.400e+00	3.600e+00	1.27945e-03	9.8e-07	6.002e-05
3.600e+00	4.800e+00	1.74135e-04	3.11e-07	8.172e-06
4.800e+00	6.000e+00	3.6943e-05	1.29e-07	1.734e-06
6.000e+00	7.200e+00	9.9927e-06	6.07e-08	4.693e-07
7.200e+00	1.080e+01	1.34959e-06	9.84e-09	6.344e-08
1.080e+01	1.440e+01	1.49549e-07	2.734e-09	7.041e-09
1.440e+01	2.160e+01	1.45113e-08	4.021e-10	6.851e-10
2.160e+01	2.880e+01	1.74160e-09	9.326e-11	8.275e-11
2.880e+01	3.840e+01	2.7965e-10	1.916e-11	1.432e-11
3.840e+01	4.800e+01	4.7389e-11	1.436e-12	3.257e-12
4.800e+01	6.720e+01	6.7976e-12	2.236e-13	5.545e-13
6.720e+01	8.640e+01	1.08078e-12	7.396e-14	9.018e-14
8.640e+01	1.122e+02	1.8676e-13	2.447e-14	1.592e-14

C. Tabulated Results

Table C.4.: Tabulated result of Fig. 7.4(a) (0.9 TeV)

x_T	Yield	Statistical Error (\pm)	Systematic Error (\pm)
1.111e-03	6.4390e+15	1.8e+12	2.766e+14
1.556e-03	2.5380e+15	1.0e+12	1.091e+14
2.000e-03	1.09935e+15	5.5e+11	4.727e+13
2.444e-03	5.1757e+14	3.4e+11	2.226e+13
3.111e-03	1.88388e+14	1.25e+11	8.106e+12
4.000e-03	5.7626e+13	6.1e+10	2.481e+12
4.889e-03	2.02005e+13	3.29e+10	8.702e+11
6.222e-03	5.1279e+12	1.01e+10	2.211e+11
8.000e-03	1.06549e+12	4.12e+09	4.598e+10
9.778e-03	2.8379e+11	1.93e+09	1.226e+10
1.156e-02	9.0134e+10	1.012e+09	3.895e+09
1.333e-02	3.4017e+10	5.88e+08	1.471e+09
1.511e-02	1.38212e+10	3.516e+08	5.979e+08
1.822e-02	3.7508e+09	1.039e+08	1.624e+08
2.267e-02	8.4807e+08	4.350e+07	3.673e+07
2.711e-02	2.3716e+08	2.075e+07	1.028e+07
3.378e-02	5.3622e+07	6.173e+06	2.325e+06
4.267e-02	1.2794e+07	2.670e+06	5.56e+05
5.156e-02	5.171e+06	1.634e+06	2.25e+05
6.933e-02	1.738e+05	1.222e+05	7.7e+03

Table C.5.: Tabulated result of Fig. 7.4(a) (7 TeV)

x_T	Yield	Statistical Error (\pm)	Systematic Error (\pm)
1.429e-04	3.2736e+20	5e+16	1.535e+19
2.000e-04	1.42773e+20	2.9e+16	6.693e+18
2.571e-04	6.7233e+19	1.7e+16	3.152e+18
3.143e-04	3.4795e+19	1.1e+16	1.631e+18
4.000e-04	1.43962e+19	4.4e+15	6.750e+17
5.143e-04	5.1468e+18	2.3e+15	2.414e+17
6.286e-04	2.07754e+18	1.34e+15	9.744e+16
8.000e-04	6.3199e+17	4.6e+14	2.965e+16
1.029e-03	1.64095e+17	2.07e+14	7.699e+15
1.257e-03	5.2119e+16	1.06e+14	2.446e+15
1.486e-03	1.94493e+16	5.97e+13	9.130e+14
1.714e-03	8.2818e+15	3.62e+13	3.889e+14
1.943e-03	3.8485e+15	2.31e+13	1.808e+14
2.343e-03	1.24309e+15	7.31e+12	5.842e+13
2.914e-03	3.2959e+14	3.35e+12	1.550e+13
3.486e-03	1.12857e+14	1.776e+12	5.312e+12
4.343e-03	2.9957e+13	5.45e+11	1.412e+12
5.486e-03	7.6190e+12	2.414e+11	3.600e+11
6.629e-03	2.02985e+12	9.326e+10	9.624e+10
8.914e-03	3.7213e+11	1.609e+10	1.860e+10
1.234e-02	5.2573e+10	3.321e+09	3.218e+09
1.577e-02	9.0289e+09	5.157e+08	5.917e+08
2.034e-02	1.8813e+09	1.252e+08	1.316e+08
2.606e-02	3.5532e+08	2.236e+07	2.549e+07
3.177e-02	9.2168e+07	3.113e+06	6.810e+06
4.034e-02	2.0643e+07	9.61e+05	1.613e+06
5.177e-02	3.5401e+06	3.751e+05	2.816e+05

C. Tabulated Results

Table C.6.: Tabulated result of Fig. 7.4(b) (2.76 TeV)

x_T	Yield	Statistical Error (\pm)	Systematic Error (\pm)
3.804e-04	2.2410e+18	4e+14	1.706e+17
4.891e-04	1.16289e+18	2.6e+14	8.855e+16
5.978e-04	6.3252e+17	1.7e+14	4.816e+16
7.065e-04	3.6420e+17	1.2e+14	2.773e+16
8.152e-04	2.1908e+17	8e+13	1.668e+16
9.783e-04	1.08340e+17	3.8e+13	8.250e+15
1.196e-03	4.6435e+16	2.3e+13	3.536e+15
1.413e-03	2.1484e+16	1.4e+13	1.636e+15
1.630e-03	1.06389e+16	9.3e+12	8.102e+14
2.174e-03	2.2811e+15	1.7e+12	1.737e+14
3.043e-03	3.1046e+14	5.6e+11	2.365e+13
3.913e-03	6.5866e+13	2.31e+11	5.018e+12
4.783e-03	1.7816e+13	1.08e+11	1.357e+12
6.522e-03	2.4062e+12	1.75e+10	1.834e+11
9.130e-03	2.6663e+11	4.88e+09	2.033e+10
1.304e-02	2.5872e+10	7.17e+08	1.975e+09
1.826e-02	3.1051e+09	1.663e+08	2.376e+08
2.435e-02	4.9858e+08	3.416e+07	3.933e+07
3.130e-02	8.4488e+07	2.560e+06	7.708e+06
4.174e-02	1.2119e+07	3.99e+05	1.227e+06
5.565e-02	1.9269e+06	1.319e+05	1.980e+05
7.196e-02	3.3297e+05	4.363e+04	3.471e+04

Table C.7.: Tabulated result of Fig. 7.6 (0–5%)

p_T low edge	p_T up edge	Yield	Statistical Error (\pm)	Systematic Error (\pm)
1.000e+00	1.100e+00	7.4455e+01	5.1e-02	4.486e+00
1.100e+00	1.200e+00	5.5077e+01	4.0e-02	3.319e+00
1.200e+00	1.400e+00	3.6124e+01	2.1e-02	2.177e+00
1.400e+00	1.600e+00	2.1042e+01	1.5e-02	1.268e+00
1.600e+00	1.800e+00	1.25377e+01	1.06e-02	7.560e-01
1.800e+00	2.000e+00	7.5417e+00	7.6e-03	4.549e-01
2.000e+00	2.200e+00	4.6527e+00	5.6e-03	2.807e-01
2.200e+00	2.400e+00	2.8806e+00	4.1e-03	1.738e-01
2.400e+00	3.200e+00	8.9319e-01	9.8e-04	5.393e-02
3.200e+00	4.000e+00	1.52717e-01	3.07e-04	9.235e-03
4.000e+00	4.800e+00	3.2371e-02	1.12e-04	1.960e-03
4.800e+00	5.600e+00	9.1762e-03	5.01e-05	5.567e-04
5.600e+00	6.400e+00	3.3036e-03	2.70e-05	2.008e-04
6.400e+00	7.200e+00	1.51319e-03	1.714e-05	9.228e-05
7.200e+00	9.600e+00	4.2152e-04	4.34e-06	2.587e-05
9.600e+00	1.200e+01	1.00386e-04	1.765e-06	6.308e-06
1.200e+01	1.440e+01	3.2573e-05	9.09e-07	2.095e-06
1.440e+01	1.920e+01	8.4063e-06	2.739e-07	5.750e-07
1.920e+01	2.400e+01	2.1867e-06	1.152e-07	1.615e-07
2.400e+01	2.880e+01	7.0724e-07	5.618e-08	5.461e-08
2.880e+01	3.520e+01	2.2789e-07	2.254e-08	1.850e-08
3.520e+01	4.160e+01	7.399e-08	1.001e-08	6.28e-09
4.160e+01	4.800e+01	2.5626e-08	4.247e-09	2.270e-09
4.800e+01	6.080e+01	7.0247e-09	2.914e-10	6.287e-10
6.080e+01	7.360e+01	2.0528e-09	1.073e-10	1.863e-10
7.360e+01	8.640e+01	6.4064e-10	3.937e-11	5.813e-11
8.640e+01	1.036e+02	1.6811e-10	1.544e-11	1.526e-11

C. Tabulated Results

Table C.8.: Tabulated result of Fig. 7.6 (5–10%)

p_T low edge	p_T up edge	Yield	Statistical Error (\pm)	Systematic Error (\pm)
1.000e+00	1.100e+00	6.0360e+04	4.6e+01	3.637e+03
1.100e+00	1.200e+00	4.4651e+04	3.7e+01	2.691e+03
1.200e+00	1.400e+00	2.9412e+04	2.0e+01	1.773e+03
1.400e+00	1.600e+00	1.7138e+04	1.4e+01	1.033e+03
1.600e+00	1.800e+00	1.02051e+04	9.9e+00	6.153e+02
1.800e+00	2.000e+00	6.1853e+03	7.2e+00	3.730e+02
2.000e+00	2.200e+00	3.8072e+03	5.3e+00	2.297e+02
2.200e+00	2.400e+00	2.3814e+03	4.0e+00	1.437e+02
2.400e+00	3.200e+00	7.4920e+02	9.6e-01	4.524e+01
3.200e+00	4.000e+00	1.29434e+02	2.89e-01	7.827e+00
4.000e+00	4.800e+00	2.8669e+01	1.08e-01	1.736e+00
4.800e+00	5.600e+00	8.3739e+00	4.94e-02	5.081e-01
5.600e+00	6.400e+00	3.1018e+00	2.70e-02	1.886e-01
6.400e+00	7.200e+00	1.41059e+00	1.699e-02	8.602e-02
7.200e+00	9.600e+00	3.9280e-01	4.29e-03	2.410e-02
9.600e+00	1.200e+01	9.1679e-02	1.689e-03	5.761e-03
1.200e+01	1.440e+01	2.8430e-02	8.37e-04	1.828e-03
1.440e+01	1.920e+01	7.1000e-03	2.520e-04	4.856e-04
1.920e+01	2.400e+01	1.9130e-03	1.091e-04	1.413e-04
2.400e+01	2.880e+01	5.1509e-04	4.626e-05	3.978e-05
2.880e+01	3.520e+01	1.6754e-04	1.877e-05	1.360e-05
3.520e+01	4.160e+01	5.4194e-05	7.940e-06	4.599e-06
4.160e+01	4.800e+01	3.0623e-05	6.473e-06	2.712e-06
4.800e+01	6.080e+01	5.8419e-06	2.949e-07	5.228e-07
6.080e+01	7.360e+01	1.5767e-06	1.403e-07	1.431e-07
7.360e+01	8.640e+01	5.7708e-07	4.329e-08	5.237e-08
8.640e+01	1.036e+02	1.4198e-07	1.345e-08	1.289e-08

Table C.9.: Tabulated result of Fig. 7.6 (10–30%)

p_T low edge	p_T up edge	Yield	Statistical Error (\pm)	Systematic Error (\pm)
1.000e+00	1.100e+00	3.7213e+07	1.8e+04	2.150e+06
1.100e+00	1.200e+00	2.7611e+07	1.4e+04	1.596e+06
1.200e+00	1.400e+00	1.8122e+07	8e+03	1.047e+06
1.400e+00	1.600e+00	1.05596e+07	5.5e+03	6.103e+05
1.600e+00	1.800e+00	6.2890e+06	3.9e+03	3.635e+05
1.800e+00	2.000e+00	3.8090e+06	2.9e+03	2.202e+05
2.000e+00	2.200e+00	2.3592e+06	2.1e+03	1.364e+05
2.200e+00	2.400e+00	1.47821e+06	1.58e+03	8.549e+04
2.400e+00	3.200e+00	4.7478e+05	3.8e+02	2.747e+04
3.200e+00	4.000e+00	8.6932e+04	1.20e+02	5.033e+03
4.000e+00	4.800e+00	2.0429e+04	4.6e+01	1.184e+03
4.800e+00	5.600e+00	6.2377e+03	2.16e+01	3.618e+02
5.600e+00	6.400e+00	2.3407e+03	1.15e+01	1.359e+02
6.400e+00	7.200e+00	1.05925e+03	7.18e+00	6.160e+01
7.200e+00	9.600e+00	2.9362e+02	1.81e+00	1.713e+01
9.600e+00	1.200e+01	6.6409e+01	7.03e-01	3.907e+00
1.200e+01	1.440e+01	2.0856e+01	3.51e-01	1.237e+00
1.440e+01	1.920e+01	5.3843e+00	1.066e-01	3.304e-01
1.920e+01	2.400e+01	1.32597e+00	4.437e-02	8.496e-02
2.400e+01	2.880e+01	3.8802e-01	2.047e-02	2.580e-02
2.880e+01	3.520e+01	1.09441e-01	7.563e-03	7.587e-03
3.520e+01	4.160e+01	3.7957e-02	3.655e-03	2.778e-03
4.160e+01	4.800e+01	1.7996e-02	2.341e-03	1.387e-03
4.800e+01	6.080e+01	4.2895e-03	4.553e-04	3.349e-04
6.080e+01	7.360e+01	1.04244e-03	3.652e-05	8.281e-05
7.360e+01	8.640e+01	2.9651e-04	1.308e-05	2.356e-05
8.640e+01	1.036e+02	9.9705e-05	5.646e-06	7.924e-06

C. Tabulated Results

Table C.10.: Tabulated result of Fig. 7.6 (30–50%)

p_T low edge	p_T up edge	Yield	Statistical Error (\pm)	Systematic Error (\pm)
1.000e+00	1.100e+00	1.47598e+10	1.14e+07	8.529e+08
1.100e+00	1.200e+00	1.08916e+10	9.2e+06	6.294e+08
1.200e+00	1.400e+00	7.1252e+09	5.0e+06	4.118e+08
1.400e+00	1.600e+00	4.1202e+09	3.6e+06	2.381e+08
1.600e+00	1.800e+00	2.4447e+09	2.6e+06	1.413e+08
1.800e+00	2.000e+00	1.47583e+09	1.88e+06	8.533e+07
2.000e+00	2.200e+00	9.1621e+08	1.39e+06	5.298e+07
2.200e+00	2.400e+00	5.7531e+08	1.02e+06	3.327e+07
2.400e+00	3.200e+00	1.9273e+08	2.5e+05	1.115e+07
3.200e+00	4.000e+00	3.8095e+07	8.1e+04	2.206e+06
4.000e+00	4.800e+00	9.7941e+06	3.22e+04	5.675e+05
4.800e+00	5.600e+00	3.2164e+06	1.58e+04	1.866e+05
5.600e+00	6.400e+00	1.25326e+06	8.53e+03	7.277e+04
6.400e+00	7.200e+00	5.7481e+05	5.37e+03	3.343e+04
7.200e+00	9.600e+00	1.51574e+05	1.243e+03	8.841e+03
9.600e+00	1.200e+01	3.4735e+04	4.98e+02	2.043e+03
1.200e+01	1.440e+01	1.02189e+04	2.410e+02	6.063e+02
1.440e+01	1.920e+01	2.5033e+03	7.10e+01	1.536e+02
1.920e+01	2.400e+01	5.6536e+02	2.876e+01	3.622e+01
2.400e+01	2.880e+01	1.6076e+02	1.316e+01	1.069e+01
2.880e+01	3.520e+01	5.5060e+01	5.594e+00	3.817e+00
3.520e+01	4.160e+01	1.5967e+01	2.275e+00	1.169e+00
4.160e+01	4.800e+01	6.545e+00	1.288e+00	5.04e-01
4.800e+01	6.080e+01	2.2400e+00	4.242e-01	1.749e-01
6.080e+01	7.360e+01	4.3615e-01	1.974e-02	3.465e-02
7.360e+01	8.640e+01	3.023e-01	1.820e-01	2.40e-02
8.640e+01	1.036e+02	3.6643e-02	3.306e-03	2.912e-03

Table C.11.: Tabulated result of Fig. 7.6 (50–70%)

p_T low edge	p_T up edge	Yield	Statistical Error (\pm)	Systematic Error (\pm)
1.000e+00	1.100e+00	4.3724e+12	6.3e+09	2.527e+11
1.100e+00	1.200e+00	3.1988e+12	5.1e+09	1.849e+11
1.200e+00	1.400e+00	2.0567e+12	2.7e+09	1.189e+11
1.400e+00	1.600e+00	1.17881e+12	1.93e+09	6.814e+10
1.600e+00	1.800e+00	6.9015e+11	1.35e+09	3.990e+10
1.800e+00	2.000e+00	4.1713e+11	9.6e+08	2.412e+10
2.000e+00	2.200e+00	2.5860e+11	6.9e+08	1.495e+10
2.200e+00	2.400e+00	1.64170e+11	5.05e+08	9.494e+09
2.400e+00	3.200e+00	5.6862e+10	1.21e+08	3.290e+09
3.200e+00	4.000e+00	1.21470e+10	3.96e+07	7.033e+08
4.000e+00	4.800e+00	3.4104e+09	1.71e+07	1.976e+08
4.800e+00	5.600e+00	1.19186e+09	8.76e+06	6.913e+07
5.600e+00	6.400e+00	4.7390e+08	4.92e+06	2.752e+07
6.400e+00	7.200e+00	2.1239e+08	2.99e+06	1.235e+07
7.200e+00	9.600e+00	5.6873e+07	7.26e+05	3.317e+06
9.600e+00	1.200e+01	1.21848e+07	2.896e+05	7.168e+05
1.200e+01	1.440e+01	3.5570e+06	1.398e+05	2.110e+05
1.440e+01	1.920e+01	7.8271e+05	3.898e+04	4.803e+04
1.920e+01	2.400e+01	1.6991e+05	1.572e+04	1.089e+04
2.400e+01	2.880e+01	3.9459e+04	6.353e+03	2.624e+03
2.880e+01	3.520e+01	1.7839e+04	3.312e+03	1.237e+03
3.520e+01	4.160e+01	3.3818e+03	9.443e+02	2.475e+02
4.160e+01	4.800e+01	3.968e+03	1.380e+03	3.06e+02
4.800e+01	6.080e+01	3.7207e+02	1.674e+01	2.905e+01
6.080e+01	7.360e+01	1.19531e+02	8.703e+00	9.496e+00
7.360e+01	8.640e+01	3.1781e+01	4.148e+00	2.525e+00
8.640e+01	1.036e+02	1.0529e+01	1.774e+00	8.37e-01

C. Tabulated Results

Table C.12.: Tabulated result of Fig. 7.6 (70–90%)

p_T low edge	p_T up edge	Yield	Statistical Error (\pm)	Systematic Error (\pm)
1.000e+00	1.100e+00	8.2255e+14	2.28e+12	4.753e+13
1.100e+00	1.200e+00	5.9519e+14	1.79e+12	3.439e+13
1.200e+00	1.400e+00	3.7489e+14	9.1e+11	2.167e+13
1.400e+00	1.600e+00	2.1234e+14	6.1e+11	1.227e+13
1.600e+00	1.800e+00	1.23777e+14	4.07e+11	7.155e+12
1.800e+00	2.000e+00	7.4566e+13	2.83e+11	4.311e+12
2.000e+00	2.200e+00	4.6485e+13	2.04e+11	2.688e+12
2.200e+00	2.400e+00	2.9699e+13	1.49e+11	1.718e+12
2.400e+00	3.200e+00	1.04937e+13	3.64e+10	6.071e+11
3.200e+00	4.000e+00	2.4229e+12	1.39e+10	1.403e+11
4.000e+00	4.800e+00	7.0518e+11	6.51e+09	4.086e+10
4.800e+00	5.600e+00	2.4501e+11	3.48e+09	1.421e+10
5.600e+00	6.400e+00	9.7200e+10	1.995e+09	5.644e+09
6.400e+00	7.200e+00	4.4443e+10	1.264e+09	2.584e+09
7.200e+00	9.600e+00	1.16725e+10	3.158e+08	6.808e+08
9.600e+00	1.200e+01	2.3578e+09	1.262e+08	1.387e+08
1.200e+01	1.440e+01	7.2490e+08	6.305e+07	4.301e+07
1.440e+01	1.920e+01	1.4370e+08	1.646e+07	8.82e+06
1.920e+01	2.400e+01	2.5531e+07	5.938e+06	1.636e+06
2.400e+01	2.880e+01	8.170e+06	3.030e+06	5.43e+05
2.880e+01	3.520e+01	1.4856e+06	8.400e+05	1.030e+05
3.520e+01	4.160e+01	9.441e+05	6.563e+05	6.91e+04
4.160e+01	4.800e+01	1.5265e+05	1.539e+04	1.176e+04
4.800e+01	6.080e+01	6.2593e+04	6.572e+03	4.887e+03
6.080e+01	7.360e+01	1.6416e+04	2.931e+03	1.304e+03
7.360e+01	8.640e+01	5.918e+03	1.543e+03	4.70e+02
8.640e+01	1.036e+02	1.3467e+03	5.512e+02	1.070e+02

Table C.13.: Tabulated result of Fig. 7.7 (0–5%)

p_T low edge	p_T up edge	R_{AA}	Statistical Error (\pm)	Systematic Error (\pm)
1.000e+00	1.100e+00	3.5912e-01	2.9e-04	2.622e-02
1.100e+00	1.200e+00	3.7009e-01	3.3e-04	2.702e-02
1.200e+00	1.400e+00	3.8869e-01	2.8e-04	2.838e-02
1.400e+00	1.600e+00	4.0592e-01	3.6e-04	2.964e-02
1.600e+00	1.800e+00	4.1808e-01	4.4e-04	3.054e-02
1.800e+00	2.000e+00	4.2038e-01	5.3e-04	3.071e-02
2.000e+00	2.200e+00	4.2023e-01	6.4e-04	3.071e-02
2.200e+00	2.400e+00	4.1042e-01	7.5e-04	2.999e-02
2.400e+00	3.200e+00	3.6221e-01	5.0e-04	2.648e-02
3.200e+00	4.000e+00	2.6398e-01	6.7e-04	1.932e-02
4.000e+00	4.800e+00	1.8823e-01	8.1e-04	1.379e-02
4.800e+00	5.600e+00	1.4869e-01	1.00e-03	1.091e-02
5.600e+00	6.400e+00	1.36037e-01	1.363e-03	9.997e-03
6.400e+00	7.200e+00	1.3803e-01	1.93e-03	1.017e-02
7.200e+00	9.600e+00	1.5191e-01	1.97e-03	1.124e-02
9.600e+00	1.200e+01	1.8199e-01	4.26e-03	1.369e-02
1.200e+01	1.440e+01	2.2265e-01	8.47e-03	1.703e-02
1.440e+01	1.920e+01	2.7680e-01	1.226e-02	2.216e-02
1.920e+01	2.400e+01	3.6784e-01	2.703e-02	3.120e-02
2.400e+01	2.880e+01	4.0027e-01	4.232e-02	3.533e-02
2.880e+01	3.520e+01	4.3947e-01	5.587e-02	4.056e-02
3.520e+01	4.160e+01	5.2699e-01	7.328e-02	5.352e-02
4.160e+01	4.800e+01	5.1609e-01	8.782e-02	5.718e-02
4.800e+01	6.080e+01	5.3031e-01	2.897e-02	6.102e-02
6.080e+01	7.360e+01	6.4004e-01	5.405e-02	7.729e-02
7.360e+01	8.640e+01	5.3311e-01	5.980e-02	6.474e-02
8.640e+01	1.036e+02	5.2017e-01	9.059e-02	6.358e-02

C. Tabulated Results

Table C.14.: Tabulated result of Fig. 7.7 (5–10%)

p_T low edge	p_T up edge	R_{AA}	Statistical Error (\pm)	Systematic Error (\pm)
1.000e+00	1.100e+00	3.6831e-01	3.2e-04	2.689e-02
1.100e+00	1.200e+00	3.7956e-01	3.6e-04	2.771e-02
1.200e+00	1.400e+00	4.0036e-01	3.2e-04	2.923e-02
1.400e+00	1.600e+00	4.1825e-01	4.0e-04	3.054e-02
1.600e+00	1.800e+00	4.3051e-01	5.0e-04	3.144e-02
1.800e+00	2.000e+00	4.3617e-01	6.1e-04	3.186e-02
2.000e+00	2.200e+00	4.3503e-01	7.3e-04	3.179e-02
2.200e+00	2.400e+00	4.2924e-01	8.6e-04	3.137e-02
2.400e+00	3.200e+00	3.8436e-01	5.8e-04	2.810e-02
3.200e+00	4.000e+00	2.8304e-01	7.7e-04	2.072e-02
4.000e+00	4.800e+00	2.1090e-01	9.6e-04	1.545e-02
4.800e+00	5.600e+00	1.7166e-01	1.22e-03	1.260e-02
5.600e+00	6.400e+00	1.6158e-01	1.69e-03	1.187e-02
6.400e+00	7.200e+00	1.6278e-01	2.37e-03	1.199e-02
7.200e+00	9.600e+00	1.7908e-01	2.41e-03	1.325e-02
9.600e+00	1.200e+01	2.1027e-01	5.06e-03	1.582e-02
1.200e+01	1.440e+01	2.4585e-01	9.63e-03	1.881e-02
1.440e+01	1.920e+01	2.9576e-01	1.375e-02	2.368e-02
1.920e+01	2.400e+01	4.0711e-01	3.120e-02	3.453e-02
2.400e+01	2.880e+01	3.6879e-01	4.194e-02	3.255e-02
2.880e+01	3.520e+01	4.0874e-01	5.624e-02	3.772e-02
3.520e+01	4.160e+01	4.8835e-01	7.321e-02	4.959e-02
4.160e+01	4.800e+01	7.802e-01	1.676e-01	8.64e-02
4.800e+01	6.080e+01	5.5792e-01	3.445e-02	6.420e-02
6.080e+01	7.360e+01	6.2191e-01	6.904e-02	7.510e-02
7.360e+01	8.640e+01	6.0752e-01	7.299e-02	7.378e-02
8.640e+01	1.036e+02	5.5576e-01	9.764e-02	6.793e-02

Table C.15.: Tabulated result of Fig. 7.7 (10–30%)

p_T low edge	p_T up edge	R_{AA}	Statistical Error (\pm)	Systematic Error (\pm)
1.000e+00	1.100e+00	3.9991e-01	2.6e-04	2.838e-02
1.100e+00	1.200e+00	4.1337e-01	3.0e-04	2.934e-02
1.200e+00	1.400e+00	4.3445e-01	2.6e-04	3.084e-02
1.400e+00	1.600e+00	4.5387e-01	3.3e-04	3.222e-02
1.600e+00	1.800e+00	4.6725e-01	4.2e-04	3.317e-02
1.800e+00	2.000e+00	4.7306e-01	5.1e-04	3.359e-02
2.000e+00	2.200e+00	4.7477e-01	6.2e-04	3.372e-02
2.200e+00	2.400e+00	4.6925e-01	7.3e-04	3.333e-02
2.400e+00	3.200e+00	4.2899e-01	5.0e-04	3.048e-02
3.200e+00	4.000e+00	3.3480e-01	6.9e-04	2.380e-02
4.000e+00	4.800e+00	2.6467e-01	9.0e-04	1.883e-02
4.800e+00	5.600e+00	2.2520e-01	1.18e-03	1.603e-02
5.600e+00	6.400e+00	2.1475e-01	1.63e-03	1.530e-02
6.400e+00	7.200e+00	2.1528e-01	2.30e-03	1.536e-02
7.200e+00	9.600e+00	2.3577e-01	2.36e-03	1.685e-02
9.600e+00	1.200e+01	2.6825e-01	5.02e-03	1.929e-02
1.200e+01	1.440e+01	3.1763e-01	9.80e-03	2.299e-02
1.440e+01	1.920e+01	3.9502e-01	1.421e-02	2.928e-02
1.920e+01	2.400e+01	4.9698e-01	3.041e-02	3.800e-02
2.400e+01	2.880e+01	4.8929e-01	4.280e-02	3.868e-02
2.880e+01	3.520e+01	4.7024e-01	4.967e-02	3.859e-02
3.520e+01	4.160e+01	6.0240e-01	6.109e-02	5.539e-02
4.160e+01	4.800e+01	8.075e-01	1.096e-01	8.22e-02
4.800e+01	6.080e+01	7.2151e-01	8.076e-02	7.677e-02
6.080e+01	7.360e+01	7.2416e-01	5.433e-02	8.149e-02
7.360e+01	8.640e+01	5.4977e-01	5.700e-02	6.226e-02
8.640e+01	1.036e+02	6.874e-01	1.089e-01	7.84e-02

C. Tabulated Results

Table C.16.: Tabulated result of Fig. 7.7 (30–50%)

p_T low edge	p_T up edge	R_{AA}	Statistical Error (\pm)	Systematic Error (\pm)
1.000e+00	1.100e+00	4.7082e-01	4.2e-04	3.342e-02
1.100e+00	1.200e+00	4.8401e-01	4.7e-04	3.435e-02
1.200e+00	1.400e+00	5.0703e-01	4.1e-04	3.599e-02
1.400e+00	1.600e+00	5.2565e-01	5.3e-04	3.732e-02
1.600e+00	1.800e+00	5.3912e-01	6.6e-04	3.828e-02
1.800e+00	2.000e+00	5.4405e-01	8.1e-04	3.863e-02
2.000e+00	2.200e+00	5.4728e-01	9.8e-04	3.886e-02
2.200e+00	2.400e+00	5.4209e-01	1.14e-03	3.850e-02
2.400e+00	3.200e+00	5.1688e-01	8.0e-04	3.672e-02
3.200e+00	4.000e+00	4.3548e-01	1.14e-03	3.096e-02
4.000e+00	4.800e+00	3.7664e-01	1.57e-03	2.679e-02
4.800e+00	5.600e+00	3.4467e-01	2.17e-03	2.454e-02
5.600e+00	6.400e+00	3.4130e-01	3.05e-03	2.432e-02
6.400e+00	7.200e+00	3.4675e-01	4.32e-03	2.473e-02
7.200e+00	9.600e+00	3.6126e-01	4.10e-03	2.583e-02
9.600e+00	1.200e+01	4.1646e-01	8.78e-03	2.996e-02
1.200e+01	1.440e+01	4.6195e-01	1.617e-02	3.343e-02
1.440e+01	1.920e+01	5.4513e-01	2.251e-02	4.041e-02
1.920e+01	2.400e+01	6.2896e-01	4.541e-02	4.809e-02
2.400e+01	2.880e+01	6.0171e-01	6.472e-02	4.756e-02
2.880e+01	3.520e+01	7.0221e-01	9.076e-02	5.763e-02
3.520e+01	4.160e+01	7.522e-01	1.098e-01	6.92e-02
4.160e+01	4.800e+01	8.717e-01	1.749e-01	8.88e-02
4.800e+01	6.080e+01	1.1183e+00	2.155e-01	1.190e-01
6.080e+01	7.360e+01	8.993e-01	7.22e-02	1.012e-01
7.360e+01	8.640e+01	1.664e+00	1.014e+00	1.88e-01
8.640e+01	1.036e+02	7.498e-01	1.299e-01	8.56e-02

Table C.17.: Tabulated result of Fig. 7.7 (50–70%)

p_T low edge	p_T up edge	R_{AA}	Statistical Error (\pm)	Systematic Error (\pm)
1.000e+00	1.100e+00	5.5681e-01	8.3e-04	3.952e-02
1.100e+00	1.200e+00	5.6750e-01	9.4e-04	4.028e-02
1.200e+00	1.400e+00	5.8428e-01	8.1e-04	4.147e-02
1.400e+00	1.600e+00	6.0041e-01	1.03e-03	4.262e-02
1.600e+00	1.800e+00	6.0761e-01	1.25e-03	4.314e-02
1.800e+00	2.000e+00	6.1389e-01	1.49e-03	4.359e-02
2.000e+00	2.200e+00	6.1669e-01	1.74e-03	4.379e-02
2.200e+00	2.400e+00	6.1756e-01	2.02e-03	4.386e-02
2.400e+00	3.200e+00	6.0882e-01	1.39e-03	4.325e-02
3.200e+00	4.000e+00	5.5436e-01	2.00e-03	3.941e-02
4.000e+00	4.800e+00	5.2358e-01	2.94e-03	3.724e-02
4.800e+00	5.600e+00	5.0990e-01	4.26e-03	3.630e-02
5.600e+00	6.400e+00	5.1522e-01	6.13e-03	3.671e-02
6.400e+00	7.200e+00	5.1149e-01	8.35e-03	3.648e-02
7.200e+00	9.600e+00	5.4115e-01	8.11e-03	3.869e-02
9.600e+00	1.200e+01	5.8323e-01	1.653e-02	4.195e-02
1.200e+01	1.440e+01	6.4193e-01	3.021e-02	4.646e-02
1.440e+01	1.920e+01	6.8048e-01	3.957e-02	5.044e-02
1.920e+01	2.400e+01	7.5462e-01	7.981e-02	5.769e-02
2.400e+01	2.880e+01	5.896e-01	1.035e-01	4.66e-02
2.880e+01	3.520e+01	9.083e-01	1.836e-01	7.45e-02
3.520e+01	4.160e+01	6.360e-01	1.787e-01	5.85e-02
4.160e+01	4.800e+01	2.1100e+00	7.384e-01	2.148e-01
4.800e+01	6.080e+01	7.4161e-01	4.252e-02	7.891e-02
6.080e+01	7.360e+01	9.840e-01	9.69e-02	1.107e-01
7.360e+01	8.640e+01	6.983e-01	1.122e-01	7.91e-02
8.640e+01	1.036e+02	8.602e-01	1.929e-01	9.81e-02

C. Tabulated Results

Table C.18.: Tabulated result of Fig. 7.7 (70–90%)

p_T low edge	p_T up edge	R_{AA}	Statistical Error (\pm)	Systematic Error (\pm)
1.000e+00	1.100e+00	6.0530e-01	1.70e-03	4.296e-02
1.100e+00	1.200e+00	6.1017e-01	1.86e-03	4.331e-02
1.200e+00	1.400e+00	6.1542e-01	1.51e-03	4.368e-02
1.400e+00	1.600e+00	6.2495e-01	1.82e-03	4.437e-02
1.600e+00	1.800e+00	6.2971e-01	2.11e-03	4.471e-02
1.800e+00	2.000e+00	6.3412e-01	2.46e-03	4.503e-02
2.000e+00	2.200e+00	6.4056e-01	2.88e-03	4.549e-02
2.200e+00	2.400e+00	6.4558e-01	3.33e-03	4.585e-02
2.400e+00	3.200e+00	6.4924e-01	2.32e-03	4.613e-02
3.200e+00	4.000e+00	6.3895e-01	3.80e-03	4.542e-02
4.000e+00	4.800e+00	6.2560e-01	5.99e-03	4.450e-02
4.800e+00	5.600e+00	6.0571e-01	8.92e-03	4.312e-02
5.600e+00	6.400e+00	6.1066e-01	1.302e-02	4.351e-02
6.400e+00	7.200e+00	6.1849e-01	1.831e-02	4.412e-02
7.200e+00	9.600e+00	6.4180e-01	1.808e-02	4.588e-02
9.600e+00	1.200e+01	6.5216e-01	3.634e-02	4.691e-02
1.200e+01	1.440e+01	7.5596e-01	6.860e-02	5.471e-02
1.440e+01	1.920e+01	7.2189e-01	8.549e-02	5.351e-02
1.920e+01	2.400e+01	6.553e-01	1.560e-01	5.01e-02
2.400e+01	2.880e+01	7.055e-01	2.662e-01	5.58e-02
2.880e+01	3.520e+01	4.371e-01	2.496e-01	3.59e-02
3.520e+01	4.160e+01	1.0260e+00	7.140e-01	9.43e-02
4.160e+01	4.800e+01	4.6901e-01	5.063e-02	4.776e-02
4.800e+01	6.080e+01	7.2093e-01	7.992e-02	7.671e-02
6.080e+01	7.360e+01	7.809e-01	1.487e-01	8.79e-02
7.360e+01	8.640e+01	7.514e-01	2.082e-01	8.51e-02
8.640e+01	1.036e+02	6.358e-01	2.767e-01	7.25e-02

Table C.19.: Tabulated result of Fig. 7.8 (0–5%/50–90%)

p_T low edge	p_T up edge	R_{CP}	Statistical Error (\pm)	Systematic Error (\pm)
1.000e+00	1.100e+00	6.3923e-01	9.2e-04	3.852e-02
1.100e+00	1.200e+00	6.4726e-01	1.02e-03	3.900e-02
1.200e+00	1.400e+00	6.6280e-01	8.6e-04	3.995e-02
1.400e+00	1.600e+00	6.7427e-01	1.06e-03	4.065e-02
1.600e+00	1.800e+00	6.8656e-01	1.27e-03	4.140e-02
1.800e+00	2.000e+00	6.8410e-01	1.48e-03	4.126e-02
2.000e+00	2.200e+00	6.7869e-01	1.71e-03	4.094e-02
2.200e+00	2.400e+00	6.6157e-01	1.92e-03	3.992e-02
2.400e+00	3.200e+00	5.9224e-01	1.21e-03	3.576e-02
3.200e+00	4.000e+00	4.6554e-01	1.57e-03	2.815e-02
4.000e+00	4.800e+00	3.4973e-01	1.91e-03	2.118e-02
4.800e+00	5.600e+00	2.8383e-01	2.37e-03	1.722e-02
5.600e+00	6.400e+00	2.5787e-01	3.13e-03	1.568e-02
6.400e+00	7.200e+00	2.6133e-01	4.37e-03	1.594e-02
7.200e+00	9.600e+00	2.7428e-01	4.21e-03	1.683e-02
9.600e+00	1.200e+01	3.0683e-01	8.55e-03	1.928e-02
1.200e+01	1.440e+01	3.3727e-01	1.529e-02	2.169e-02
1.440e+01	1.920e+01	4.0189e-01	2.249e-02	2.749e-02
1.920e+01	2.400e+01	4.9486e-01	4.979e-02	3.654e-02
2.400e+01	2.880e+01	6.557e-01	1.096e-01	5.06e-02
2.880e+01	3.520e+01	5.199e-01	1.051e-01	4.22e-02
3.520e+01	4.160e+01	7.400e-01	2.197e-01	6.28e-02
4.160e+01	4.800e+01	2.750e-01	1.006e-01	2.44e-02
4.800e+01	6.080e+01	6.9264e-01	4.050e-02	6.199e-02
6.080e+01	7.360e+01	6.5900e-01	5.608e-02	5.979e-02
7.360e+01	8.640e+01	7.4798e-01	9.723e-02	6.788e-02
8.640e+01	1.036e+02	6.378e-01	1.152e-01	5.79e-02

C. Tabulated Results

Table C.20.: Tabulated result of Fig. 7.8 (5–10%/50–90%)

p_T low edge	p_T up edge	R_{CP}	Statistical Error (\pm)	Systematic Error (\pm)
1.000e+00	1.100e+00	6.5559e-01	9.7e-04	3.950e-02
1.100e+00	1.200e+00	6.6383e-01	1.08e-03	4.000e-02
1.200e+00	1.400e+00	6.8269e-01	9.1e-04	4.115e-02
1.400e+00	1.600e+00	6.9473e-01	1.12e-03	4.188e-02
1.600e+00	1.800e+00	7.0697e-01	1.35e-03	4.263e-02
1.800e+00	2.000e+00	7.0979e-01	1.59e-03	4.281e-02
2.000e+00	2.200e+00	7.0258e-01	1.83e-03	4.238e-02
2.200e+00	2.400e+00	6.9190e-01	2.09e-03	4.175e-02
2.400e+00	3.200e+00	6.2846e-01	1.35e-03	3.795e-02
3.200e+00	4.000e+00	4.9916e-01	1.76e-03	3.018e-02
4.000e+00	4.800e+00	3.9184e-01	2.21e-03	2.373e-02
4.800e+00	5.600e+00	3.2768e-01	2.83e-03	1.988e-02
5.600e+00	6.400e+00	3.0629e-01	3.83e-03	1.862e-02
6.400e+00	7.200e+00	3.0819e-01	5.31e-03	1.879e-02
7.200e+00	9.600e+00	3.2335e-01	5.10e-03	1.984e-02
9.600e+00	1.200e+01	3.5450e-01	1.007e-02	2.228e-02
1.200e+01	1.440e+01	3.7242e-01	1.724e-02	2.395e-02
1.440e+01	1.920e+01	4.2942e-01	2.478e-02	2.937e-02
1.920e+01	2.400e+01	5.4769e-01	5.638e-02	4.044e-02
2.400e+01	2.880e+01	6.041e-01	1.041e-01	4.67e-02
2.880e+01	3.520e+01	4.836e-01	1.010e-01	3.92e-02
3.520e+01	4.160e+01	6.857e-01	2.072e-01	5.82e-02
4.160e+01	4.800e+01	4.157e-01	1.616e-01	3.68e-02
4.800e+01	6.080e+01	7.2871e-01	4.749e-02	6.522e-02
6.080e+01	7.360e+01	6.4033e-01	7.140e-02	5.810e-02
7.360e+01	8.640e+01	8.524e-01	1.167e-01	7.73e-02
8.640e+01	1.036e+02	6.815e-01	1.240e-01	6.19e-02

Table C.21.: Tabulated result of Fig. 7.8 (10–30%/50–90%)

p_T low edge	p_T up edge	R_{CP}	Statistical Error (\pm)	Systematic Error (\pm)
1.000e+00	1.100e+00	7.1184e-01	9.6e-04	4.113e-02
1.100e+00	1.200e+00	7.2297e-01	1.08e-03	4.178e-02
1.200e+00	1.400e+00	7.4082e-01	9.1e-04	4.281e-02
1.400e+00	1.600e+00	7.5391e-01	1.13e-03	4.358e-02
1.600e+00	1.800e+00	7.6732e-01	1.35e-03	4.436e-02
1.800e+00	2.000e+00	7.6983e-01	1.58e-03	4.451e-02
2.000e+00	2.200e+00	7.6677e-01	1.82e-03	4.434e-02
2.200e+00	2.400e+00	7.5640e-01	2.07e-03	4.374e-02
2.400e+00	3.200e+00	7.0143e-01	1.34e-03	4.058e-02
3.200e+00	4.000e+00	5.9044e-01	1.80e-03	3.419e-02
4.000e+00	4.800e+00	4.9175e-01	2.36e-03	2.849e-02
4.800e+00	5.600e+00	4.2989e-01	3.09e-03	2.494e-02
5.600e+00	6.400e+00	4.0707e-01	4.17e-03	2.364e-02
6.400e+00	7.200e+00	4.0759e-01	5.73e-03	2.370e-02
7.200e+00	9.600e+00	4.2569e-01	5.51e-03	2.483e-02
9.600e+00	1.200e+01	4.5225e-01	1.089e-02	2.660e-02
1.200e+01	1.440e+01	4.8116e-01	1.900e-02	2.855e-02
1.440e+01	1.920e+01	5.7354e-01	2.847e-02	3.519e-02
1.920e+01	2.400e+01	6.6859e-01	6.152e-02	4.284e-02
2.400e+01	2.880e+01	8.015e-01	1.252e-01	5.33e-02
2.880e+01	3.520e+01	5.563e-01	1.053e-01	3.86e-02
3.520e+01	4.160e+01	8.459e-01	2.379e-01	6.19e-02
4.160e+01	4.800e+01	4.303e-01	1.511e-01	3.31e-02
4.800e+01	6.080e+01	9.424e-01	1.073e-01	7.36e-02
6.080e+01	7.360e+01	7.4561e-01	5.648e-02	5.923e-02
7.360e+01	8.640e+01	7.7134e-01	9.468e-02	6.129e-02
8.640e+01	1.036e+02	8.428e-01	1.394e-01	6.70e-02

C. Tabulated Results

Table C.22.: Tabulated result of Fig. 7.8 (30–50%/50–90%)

p_T low edge	p_T up edge	R_{CP}	Statistical Error (\pm)	Systematic Error (\pm)
1.000e+00	1.100e+00	8.3805e-01	1.24e-03	4.843e-02
1.100e+00	1.200e+00	8.4650e-01	1.38e-03	4.892e-02
1.200e+00	1.400e+00	8.6459e-01	1.17e-03	4.997e-02
1.400e+00	1.600e+00	8.7314e-01	1.44e-03	5.047e-02
1.600e+00	1.800e+00	8.8534e-01	1.73e-03	5.118e-02
1.800e+00	2.000e+00	8.8535e-01	2.03e-03	5.119e-02
2.000e+00	2.200e+00	8.8388e-01	2.37e-03	5.111e-02
2.200e+00	2.400e+00	8.7381e-01	2.70e-03	5.053e-02
2.400e+00	3.200e+00	8.4514e-01	1.83e-03	4.890e-02
3.200e+00	4.000e+00	7.6800e-01	2.65e-03	4.447e-02
4.000e+00	4.800e+00	6.9979e-01	3.75e-03	4.055e-02
4.800e+00	5.600e+00	6.5795e-01	5.25e-03	3.816e-02
5.600e+00	6.400e+00	6.4695e-01	7.29e-03	3.756e-02
6.400e+00	7.200e+00	6.5652e-01	1.015e-02	3.818e-02
7.200e+00	9.600e+00	6.5228e-01	9.15e-03	3.804e-02
9.600e+00	1.200e+01	7.0212e-01	1.823e-02	4.130e-02
1.200e+01	1.440e+01	6.9977e-01	2.996e-02	4.152e-02
1.440e+01	1.920e+01	7.9148e-01	4.244e-02	4.857e-02
1.920e+01	2.400e+01	8.4615e-01	8.434e-02	5.421e-02
2.400e+01	2.880e+01	9.857e-01	1.659e-01	6.55e-02
2.880e+01	3.520e+01	8.308e-01	1.690e-01	5.76e-02
3.520e+01	4.160e+01	1.0562e+00	3.170e-01	7.73e-02
4.160e+01	4.800e+01	4.644e-01	1.769e-01	3.58e-02
4.800e+01	6.080e+01	1.4607e+00	2.831e-01	1.140e-01
6.080e+01	7.360e+01	9.2596e-01	7.499e-02	7.356e-02
7.360e+01	8.640e+01	2.334e+00	1.430e+00	1.85e-01
8.640e+01	1.036e+02	9.194e-01	1.652e-01	7.31e-02

Bibliography

- [1] A. Pich. Quantum chromodynamics. 1995. [arXiv:hep-ph/9505231].
- [2] Andreas S. Kronfeld and Chris Quigg. Resource Letter: Quantum Chromodynamics. *Am.J.Phys.*, 78:1081–1116, 2010. doi: 10.1119/1.3454865.
- [3] J. C. Collins and M. J. Perry. Superdense matter: Neutrons or asymptotically free quarks? *Phys. Rev. Lett.*, 34:1353–1356, May 1975. doi: 10.1103/PhysRevLett.34.1353. URL <http://link.aps.org/doi/10.1103/PhysRevLett.34.1353>.
- [4] N Cabibbo and G Parisi. Exponential hadronic spectrum and quark liberation. *Phys. Lett.*, B59:67–69, 1975. doi: 10.1016/0370-2693(75)90158-6.
- [5] Edward V. Shuryak. Quantum Chromodynamics and the Theory of Superdense Matter. *Phys. Rept.*, 61:71–158, 1980. doi: 10.1016/0370-1573(80)90105-2.
- [6] Torbjorn Sjöstrand, Stephen Mrenna, and Peter Z. Skands. A Brief Introduction to PYTHIA 8.1. *Comput. Phys. Commun.*, 178:852, 2008. doi: 10.1016/j.cpc.2008.01.036.
- [7] Simon Hands. The Phase Diagram of QCD. *Contemp. Phys.*, 42:209–225, 2001. doi: 10.1080/00107510110063843.
- [8] K. Nakamura et al. Review of particle physics. *J. Phys.*, G37:075021, 2010. doi: 10.1088/0954-3899/37/7A/075021.
- [9] R. Sekhar Chivukula. The Origin of mass in QCD. *eConf*, C040802:L010, 2004.
- [10] David J Griffiths. *Introduction to elementary particles*. John Wiley & Sons, Inc., 1987.
- [11] G.M. Prosperi, M. Raciti, and C. Simolo. On the running coupling constant in QCD. *Prog.Part.Nucl.Phys.*, 58:387–438, 2007. doi: 10.1016/j.pnnp.2006.09.001.
- [12] Siegfried Bethke. Experimental tests of asymptotic freedom. *Prog.Part.Nucl.Phys.*, 58:351–386, 2007. doi: 10.1016/j.pnnp.2006.06.001.
- [13] Siegfried Bethke. α_s at Zinnowitz 2004. *Nucl.Phys.Proc.Suppl.*, 135:345–352, 2004. doi: 10.1016/j.nuclphysbps.2004.09.020.

Bibliography

- [14] Vernon D. Barger and Roger J.N. Phillips. *Collider Physics*. Addison-Wesley Publishing Company, 1987.
- [15] Wei Li. Clustering phenomena from two-particle angular correlations in proton-proton and heavy ion collisions. <http://hdl.handle.net/1721.1/53207>. PhD thesis, Massachusetts Institute of Technology, 2009.
- [16] S Chakrabarty. On the possibility of nuclear liquid-gas phase transition. *Journal of Physics G: Nuclear and Particle Physics*, 20(3):469, 1994. URL <http://stacks.iop.org/0954-3899/20/i=3/a=008>.
- [17] Bertrand C. and Barrois. Superconducting quark matter. *Nuclear Physics B*, 129(3):390 – 396, 1977. ISSN 0550-3213. doi: 10.1016/0550-3213(77)90123-7. URL <http://www.sciencedirect.com/science/article/pii/0550321377901237>.
- [18] Leon N. Cooper. Bound electron pairs in a degenerate fermi gas. *Phys. Rev.*, 104: 1189–1190, Nov 1956. doi: 10.1103/PhysRev.104.1189. URL <http://link.aps.org/doi/10.1103/PhysRev.104.1189>.
- [19] Mark G. Alford, Andreas Schmitt, Krishna Rajagopal, and Thomas Schafer. Color superconductivity in dense quark matter. *Rev.Mod.Phys.*, 80:1455–1515, 2008. doi: 10.1103/RevModPhys.80.1455.
- [20] P. Braun-Munzinger and J. Wambach. The Phase Diagram of Strongly-Interacting Matter. *Rev.Mod.Phys.*, 2008.
- [21] Igor A. Shovkovy. Two lectures on color superconductivity. *Found.Phys.*, 35:1309–1358, 2005. doi: 10.1007/s10701-005-6440-x.
- [22] Edward Shuryak. Toward the theory of strongly coupled quark-gluon plasma. *Nucl.Phys.*, A774:387–396, 2006. doi: 10.1016/j.nuclphysa.2006.06.058.
- [23] Y. Aoki, Z. Fodor, S.D. Katz, and K.K. Szabo. The QCD transition temperature: Results with physical masses in the continuum limit. *Phys.Lett.*, B643:46–54, 2006. doi: 10.1016/j.physletb.2006.10.021.
- [24] Y. Aoki, G. Endrodi, Z. Fodor, S.D. Katz, and K.K. Szabo. The order of the quantum chromodynamics transition predicted by the standard model of particle physics. *Nature*, 443:675–678, 2006. doi: 10.1038/nature05120.
- [25] Philippe de Forcrand and Owe Philipsen. The Chiral critical line of $N(f) = 2+1$ QCD at zero and non-zero baryon density. *JHEP*, 0701:077, 2007. doi: 10.1088/1126-6708/2007/01/077.
- [26] F. Karsch and E. Laermann. Thermodynamics and in medium hadron properties from lattice QCD. 2003. Prepared for Quark-Gluon Plasma III, R. Hwa (ed.).

- [27] F. Karsch, E. Laermann, and A. Peikert. The pressure in 2, 2+1 and 3 flavour QCD. *Phys. Lett.*, B478:447–455, 2000. doi: 10.1016/S0370-2693(00)00292-6.
- [28] M. Cheng, N.H. Christ, S. Datta, J. van der Heide, C. Jung, et al. The Transition temperature in QCD. *Phys.Rev.*, D74:054507, 2006. doi: 10.1103/PhysRevD.74.054507.
- [29] Szabolcs Borsanyi, Zoltan Fodor, Christian Hoelbling, Sandor D. Katz, Stefan Krieg, et al. QCD transition temperature: full staggered result. 2010.
- [30] Umut Gürsoy, Elias Kiritsis, Liuba Mazzanti, and Francesco Nitti. Deconfinement and gluon plasma dynamics in improved holographic qcd. *Phys. Rev. Lett.*, 101:181601, Oct 2008. doi: 10.1103/PhysRevLett.101.181601. URL <http://link.aps.org/doi/10.1103/PhysRevLett.101.181601>.
- [31] Marco Panero. Thermodynamics of the qcd plasma and the large- n limit. *Phys. Rev. Lett.*, 103:232001, Dec 2009. doi: 10.1103/PhysRevLett.103.232001. URL <http://link.aps.org/doi/10.1103/PhysRevLett.103.232001>.
- [32] J. D. Bjorken. Highly relativistic nucleus-nucleus collisions: The central rapidity region. *Phys. Rev. D*, 27:140–151, Jan 1983. doi: 10.1103/PhysRevD.27.140. URL <http://link.aps.org/doi/10.1103/PhysRevD.27.140>.
- [33] CMS Collaboration. Centrality determination for heavy ion data 2010. CMS Analysis Note, CMS-NOTE-AN-10-412, 2010.
- [34] Krisztian Krajczar. Charged hadron multiplicity and transverse energy densities in Pb Pb collisions from CMS. *J. Phys.*, G38:124041, 2011. doi: 10.1088/0954-3899/38/12/124041.
- [35] Jean Letessier and Johann Rafelski. *Hadrons and Quark-Gluon Plasma*. Cambridge University Press, 2002.
- [36] Kohsuke. Yagi and Miake Yasuo. Hatsuda, Tetsuo. *Quark-Gluon plasma: from big bang to little bang*. Cambridge University Press, 2008.
- [37] Edward Wenger. Studies of High Transverse Momentum Phenomena in Heavy Ion Collisions Using the PHOBOS Detector. <http://dspace.mit.edu/handle/1721.1/45164>. PhD thesis, Massachusetts Institute of Technology, 2008.
- [38] A. Adare et al. Enhanced production of direct photons in Au+Au collisions at $\sqrt{s_{NN}}=200$ GeV and implications for the initial temperature. *Phys.Rev.Lett.*, 104:132301, 2010. doi: 10.1103/PhysRevLett.104.132301.
- [39] Larry McLerran. What have we learned from RHIC? *Pramana*, 60:765–786, 2003. doi: 10.1007/BF02705174.

Bibliography

- [40] Larry McLerran and Thomas Ludlam. What Have We Learned From the Relativistic Heavy Ion Collider? Oct 2003. *Physics Today*.
- [41] Paul M. Chesler and Laurence G. Yaffe. Horizon formation and far-from-equilibrium isotropization in supersymmetric Yang-Mills plasma. *Phys.Rev.Lett.*, 102:211601, 2009. doi: 10.1103/PhysRevLett.102.211601.
- [42] P.F. Kolb, P. Huovinen, Ulrich W. Heinz, and H. Heiselberg. Elliptic flow at SPS and RHIC: From kinetic transport to hydrodynamics. *Phys.Lett.*, B500:232–240, 2001. doi: 10.1016/S0370-2693(01)00079-X.
- [43] Peter F. Kolb and Ulrich W. Heinz. Hydrodynamic description of ultrarelativistic heavy ion collisions. 2003. Invited review for 'Quark Gluon Plasma 3'. Editors: R.C. Hwa and X.N. Wang, World Scientific, Singapore.
- [44] Ulrich W. Heinz. Thermalization at RHIC. *AIP Conf.Proc.*, 739:163–180, 2005. doi: 10.1063/1.1843595.
- [45] S. S. Adler et al. Elliptic flow of identified hadrons in Au + Au collisions at $s(NN)^{1/2} = 200$ -GeV. *Phys. Rev. Lett.*, 91:182301, 2003. doi: 10.1103/PhysRevLett.91.182301.
- [46] John Adams et al. Particle type dependence of azimuthal anisotropy and nuclear modification of particle production in Au + Au collisions at $s(NN)^{1/2} = 200$ -GeV. *Phys.Rev.Lett.*, 92:052302, 2004. doi: 10.1103/PhysRevLett.92.052302.
- [47] (ed.) Ritter, H. G. and (ed.) Wang, X. N. Ultra-relativistic nucleus-nucleus collisions. Proceedings, 17th International Conference, Quark Matter 2004, Oakland, USA, January 11-17, 2004. Prepared for 17th International Conference on Ultra Relativistic Nucleus-Nucleus Collisions (Quark Matter 2004), Oakland, California, 11-17 Jan 2004.
- [48] (ed.) Csörgő, T., (ed.) Lévai, P., (ed.) David, G., and (ed.) Papp, G. Quark matter. Proceedings, 18th International Conference on Ultra-Relativistic Nucleus-Nucleus Collisions, QM'05, Budapest, Hungary, August 4-9, 2005. Prepared for 18th International Conference on Ultrarelativistic Nucleus-Nucleus Collisions: Quark Matter 2005 (QM 2005), Budapest, Hungary, 4-9 Aug 2005.
- [49] (ed.) Ma, Yu-Gang et al. Ultra-relativistic nucleus-nucleus collisions. Proceedings, 19th International Conference, Quark Matter 2006, Shanghai, P.R. China, November 14-20, 2006. Prepared for 19th International Conference on Ultra-Relativistic Nucleus-Nucleus Collisions: Quark Matter 2006 (QM2006), Shanghai, China, 14-20 Nov 2006.
- [50] (ed.) Alam, J., (ed.) Chattopadhyay, S., (ed.) Nayak, T., (ed.) Sinha, B., and (ed.) Bristol, Y. Ultra-relativistic nucleus-nucleus collisions. Proceedings, 20th International Conference, Quark Matter 2008, Japur, India, February 4-10, 2008. Pre-

- pared for 20th International Conference on Ultra- Relativistic Nucleus-Nucleus Collisions: Quark Matter 2008 (QM2008), Japur, India, 4-10 Feb 2008.
- [51] Soren Sorensen Paul Stankus, David Silvermyr and Victoria Greene. Ultra-relativistic nucleus-nucleus collisions. Proceedings, 21st International Conference, Quark Matter 2009, Knoxville, TN, U.S.A. Volume 830, Issues 1–4, Pages 1c-985c.
- [52] John Adams et al. Experimental and theoretical challenges in the search for the quark gluon plasma: The STAR collaboration's critical assessment of the evidence from RHIC collisions. *Nucl. Phys.*, A757:102, 2005. doi: 10.1016/j.nuclphysa.2005.03.085.
- [53] K. Adcox et al. Formation of dense partonic matter in relativistic nucleus nucleus collisions at RHIC: Experimental evaluation by the PHENIX collaboration. *Nucl. Phys.*, A757:184, 2005. doi: 10.1016/j.nuclphysa.2005.03.086.
- [54] I. Arsene et al. Quark Gluon Plasma and Color Glass Condensate at RHIC? The perspective from the BRAHMS experiment. *Nucl. Phys.*, A757:1, 2005. doi: 10.1016/j.nuclphysa.2005.02.130.
- [55] B. B. Back et al. The PHOBOS perspective on discoveries at RHIC. *Nucl. Phys.*, A757:28, 2005. doi: 10.1016/j.nuclphysa.2005.03.084.
- [56] D d'Enterria, M Ballintijn, M Bedjidian, D Hoffman, Olga Kodolova, C Loizides, I P Lokhtin, C Lourenco, C Mironov, S V Petrushanko, C Roland, G Roland, F Sikler, and G Veres. *CMS Physics: Technical Design Report v.2: Addendum on High Density QCD with Heavy Ions*, volume 34 of *Technical Design Report CMS*. CERN, Geneva, 2007. revised version submitted on 2007-03-15 12:08:08.
- [57] Dariusz Prorok. Thermal freeze-out versus chemical freeze-out revised. *Acta Phys.Polon.*, B40:2825–2842, 2009.
- [58] Serguei Chatrchyan et al. Measurement of the pseudorapidity and centrality dependence of the transverse energy density in PbPb collisions at $\sqrt{s(NN)} = 2.76$ TeV. 2012. [arXiv:1205.2488].
- [59] A. Bazilevsky. Charge particle multiplicity and transverse energy measurements in Au - Au collisions in PHENIX at RHIC. *Nucl.Phys.*, A715:486, 2003.
- [60] T. Abbott et al. Systematics of midrapidity transverse energy distributions in limited apertures from p+Be to Au+Au collisions at relativistic energies. *Phys. Rev.*, C63:064602, 2001. doi: 10.1103/PhysRevC.63.064602. [Erratum-ibid.C64:029901,2001].
- [61] J. D. Bjorken. Energy Loss of Energetic Partons in Quark - Gluon Plasma: Possible Extinction of High p(t) Jets in Hadron - Hadron Collisions. FERMILAB-PUB-82-059-THY.

Bibliography

- [62] J. P. Blaizot and Larry D. McLerran. Jets in Expanding Quark - Gluon Plasmas. *Phys. Rev.*, D34:2739, 1986. doi: 10.1103/PhysRevD.34.2739.
- [63] David A. Appel. JETS AS A PROBE OF QUARK - GLUON PLASMAS. *Phys. Rev.*, D33:717, 1986. doi: 10.1103/PhysRevD.33.717.
- [64] David d'Enterria. Jet quenching. 2009. Springer Verlag. Landolt-Boernstein Vol. 1-23A. 49 pages. 36 figures., [arXiv:0902.2011].
- [65] Jorge Casalderrey-Solana and Carlos A. Salgado. Introductory lectures on jet quenching in heavy ion collisions. *Acta Phys.Polon.*, B38:3731–3794, 2007.
- [66] R. Baier, D. Schiff, and B. G. Zakharov. Energy loss in perturbative QCD. *Ann. Rev. Nucl. Part. Sci.*, 50:37–69, 2000. doi: 10.1146/annurev.nucl.50.1.37.
- [67] Markus H. Thoma. Collisional energy loss of high-energy jets in the quark gluon plasma. *Phys. Lett.*, B273:128–132, 1991. doi: 10.1016/0370-2693(91)90565-8.
- [68] Markus H. Thoma. Applications of high temperature field theory to heavy ion collisions. 1995. [arXiv:hep-ph/9503400].
- [69] Abhee K. Dutt-Mazumder, Jan-e Alam, Pradip Roy, and Bikash Sinha. Stopping power of hot QCD plasma. *Phys.Rev.*, D71:094016, 2005. doi: 10.1103/PhysRevD.71.094016.
- [70] B.Z. Kopeliovich, H.-J. Pirner, I.K. Potashnikova, and Ivan Schmidt. Jet lag effect and leading hadron production. *Phys.Lett.*, B662:117–122, 2008. doi: 10.1016/j.physletb.2008.02.061.
- [71] Pradip Roy, Jan-e Alam, and Abhee K. Dutt-Mazumder. Quenching of light hadrons at RHIC in a collisional energy loss scenario. *J.Phys.G*, G35:104047, 2008. doi: 10.1088/0954-3899/35/10/104047.
- [72] Pradip Roy, Abhee K. Dutt-Mazumder, and Jan-e Alam. Energy loss and dynamical evolution of quark p_T spectra. *Phys. Rev. C*, 73:044911, Apr 2006. doi: 10.1103/PhysRevC.73.044911. URL <http://link.aps.org/doi/10.1103/PhysRevC.73.044911>.
- [73] Magdalena Djordjevic. Collisional energy loss in a finite size qcd matter. *Phys. Rev. C*, 74:064907, Dec 2006. doi: 10.1103/PhysRevC.74.064907. URL <http://link.aps.org/doi/10.1103/PhysRevC.74.064907>.
- [74] A. Peshier. Qcd collisional energy loss reexamined. *Phys. Rev. Lett.*, 97:212301, Nov 2006. doi: 10.1103/PhysRevLett.97.212301. URL <http://link.aps.org/doi/10.1103/PhysRevLett.97.212301>.
- [75] B.G. Zakharov. Parton energy loss in an expanding quark-gluon plasma: Radiative versus collisional. *JETP Lett.*, 86:444–450, 2007. doi: 10.1134/S0021364007190034. 13 pages, 3 figures.

- [76] Urs Achim Wiedemann. Jet Quenching in Heavy Ion Collisions. 2009. Landolt-Boernstein Handbook of Physics, ed. R. Stock. 41 pages, [arXiv:0908.2306].
- [77] R. Baier, Yuri L. Dokshitzer, S. Peigne, and D. Schiff. Induced gluon radiation in a QCD medium. *Phys. Lett.*, B345:277–286, 1995. doi: 10.1016/0370-2693(94)01617-L.
- [78] R. Baier, Yuri L. Dokshitzer, Alfred H. Mueller, S. Peigne, and D. Schiff. Radiative energy loss of high-energy quarks and gluons in a finite volume quark - gluon plasma. *Nucl.Phys.*, B483:291–320, 1997. doi: 10.1016/S0550-3213(96)00553-6.
- [79] R. Baier, Yuri L. Dokshitzer, Alfred H. Mueller, S. Peigne, and D. Schiff. Radiative energy loss and p(T) broadening of high-energy partons in nuclei. *Nucl.Phys.*, B484:265–282, 1997. doi: 10.1016/S0550-3213(96)00581-0.
- [80] R. Baier, Yuri L. Dokshitzer, Alfred H. Mueller, and D. Schiff. Medium induced radiative energy loss: Equivalence between the BDMPS and Zakharov formalisms. *Nucl.Phys.*, B531:403–425, 1998. doi: 10.1016/S0550-3213(98)00546-X.
- [81] Miklos Gyulassy, Peter Levai, and Ivan Vitev. Jet quenching in thin quark gluon plasmas. 1. Formalism. *Nucl.Phys.*, B571:197–233, 2000. doi: 10.1016/S0550-3213(99)00713-0.
- [82] M. Gyulassy, P. Levai, and I. Vitev. NonAbelian energy loss at finite opacity. *Phys.Rev.Lett.*, 85:5535–5538, 2000. doi: 10.1103/PhysRevLett.85.5535.
- [83] M. Gyulassy, P. Levai, and I. Vitev. Reaction operator approach to nonAbelian energy loss. *Nucl.Phys.*, B594:371–419, 2001. doi: 10.1016/S0550-3213(00)00652-0.
- [84] Enke Wang and Xin-Nian Wang. Parton energy loss with detailed balance. *Phys.Rev.Lett.*, 87:142301, 2001. doi: 10.1103/PhysRevLett.87.142301.
- [85] Urs Wiedemann. Selected Topics in the Physics of Heavy Ion Collisions. <http://indico.cern.ch/conferenceDisplay.py?confId=116338>, 2011. CERN Academic Training Lecture Regular Programme.
- [86] B. Alver et al. Importance of correlations and fluctuations on the initial source eccentricity in high-energy nucleus-nucleus collisions. *Phys. Rev. C*, 77:014906, 2008. doi: 10.1103/PhysRevC.77.014906.
- [87] S.S. Adler et al. Absence of suppression in particle production at large transverse momentum in $S(NN)^{1/2} = 200$ -GeV d + Au collisions. *Phys.Rev.Lett.*, 91:072303, 2003. doi: 10.1103/PhysRevLett.91.072303.
- [88] Serguei Chatrchyan et al. Study of Z boson production in PbPb collisions at nucleon-nucleon centre of mass energy = 2.76 TeV. *Phys.Rev.Lett.*, 106:212301, 2011. doi: 10.1103/PhysRevLett.106.212301.

Bibliography

- [89] CMS Collaboration. Study of W boson production in PbPb collisions. CMS Physics Analysis Summary, CMS-PAS-HIN-11-008, 2011.
- [90] CMS Collaboration. Measurement of isolated photon production in pp and PbPb collisions at $\sqrt{s_{NN}} = 2.76$ TeV. 2012. [arXiv:1201.3093].
- [91] E. Leader and E. Predazzi. *An introduction to gauge theories and modern particle physics Volume 2 (CP-violation, QCD and hard processes)*, volume 2. Cambridge Monographs on Particle Physics, Nuclear Physics and Cosmology, 1996.
- [92] J. F. Owens, E. Reya, and M. Gluck. Detailed Quantum Chromodynamic Predictions for High p(T) Processes. *Phys. Rev.*, D18:1501, 1978. doi: 10.1103/PhysRevD.18.1501.
- [93] A. Breakstone et al. Inclusive charged particle cross-sections in full phase space from proton proton interactions at ISR energies. *Z. Phys.*, C69:55–66, 1995. doi: 10.1007/s002880050005.
- [94] J. Adams et al. Transverse momentum and collision energy dependence of high p(T) hadron suppression in Au+Au collisions at ultrarelativistic energies. *Phys.Rev.Lett.*, 91:172302, 2003. doi: 10.1103/PhysRevLett.91.172302.
- [95] C. Albajar et al. A Study of the General Characteristics of Proton - anti- Proton Collisions at $s^{**}(1/2) = 0.2$ -TeV to 0.9-TeV. *Nucl. Phys.*, B335:261, 1990. doi: 10.1016/0550-3213(90)90493-W.
- [96] F. Abe et al. Transverse Momentum Distributions of Charged Particles Produced in anti-p p Interactions at $s^{**}(1/2) = 630$ -GeV and 1800-GeV. *Phys. Rev. Lett.*, 61: 1819, 1988. doi: 10.1103/PhysRevLett.61.1819.
- [97] T. Aaltonen et al. Measurement of Particle Production and Inclusive Differential Cross Sections in p anti-p Collisions at $s^{**}(1/2) = 1.96$ -TeV. *Phys.Rev.*, D79:112005, 2009. doi: 10.1103/PhysRevD.79.112005,10.1103/PhysRevD.82.119903,10.1103/PhysRevD.79.112005,10.1103/PhysRevD.82.119903.
- [98] Vardan Khachatryan et al. Transverse momentum and pseudorapidity distributions of charged hadrons in pp collisions at $\sqrt{s} = 0.9$ and 2.36 TeV. *JHEP*, 1002: 041, 2010. doi: 10.1007/JHEP02(2010)041.
- [99] G. Aad et al. Charged-particle multiplicities in pp interactions at $\sqrt{s} = 900$ GeV measured with the ATLAS detector at the LHC. *Phys.Lett.*, B688:21–42, 2010. doi: 10.1016/j.physletb.2010.03.064.
- [100] K. Aamodt et al. Suppression of Charged Particle Production at Large Transverse Momentum in Central Pb–Pb Collisions at $\sqrt{s_{NN}} = 2.76$ TeV. *Phys. Lett.*, B696:30, 2011. doi: 10.1016/j.physletb.2010.12.020.

Bibliography

- [113] D. Antreasyan et al. Production of Hadrons at Large Transverse Momentum in 200- GeV, 300-GeV and 400-GeV p p and p n Collisions. *Phys. Rev.*, D19:764–778, 1979. doi: 10.1103/PhysRevD.19.764.
- [114] A.L.S. Angelis et al. LARGE TRANSVERSE MOMENTUM π^0 PRODUCTION IN alpha alpha d d AND p p COLLISIONS AT THE CERN ISR. *Phys.Lett.*, B185:213, 1987. doi: 10.1016/0370-2693(87)91557-7.
- [115] A. Accardi, F. Arleo, W. K. Brooks, David D’Enterria, and V. Muccifora. Parton Propagation and Fragmentation in QCD Matter. *Riv. Nuovo Cim.*, 32:439–553, 2010. doi: 10.1393/ncr/i2009-10048-0.
- [116] M. Lamont. LHC Commissioning. <http://lhc-commissioning.web.cern.ch/lhc-commissioning/>, 2009.
- [117] CERN Press Release. LHC to run at 4 TeV per beam in 2012. <http://press.web.cern.ch/press/PressReleases/Releases2012/PR01.12E.html>, 2012.
- [118] Lyndon Evans and Philip Bryant. LHC Machine . *JINST*, 3:S08001, 2008. doi: 10.1088/1748-0221/3/08/S08001.
- [119] Cid R. and Cid-Vidal X. Taking A Closer Look At LHC. <http://www.lhc-closer.es/php/index.php?i=1&s=3&p=4&e=0>.
- [120] CERN Communication Group. Frequently asked questions. <http://homepage.mac.com/fishbone1pc/CERN/public.web.cern.ch/Public/Content/Chapters/AskAnExpert/LHC-en.html>, 2006.
- [121] K. Schindl. The Injector Chain for the LHC. <http://sl-div.web.cern.ch/sl-div/>, 1999. Chamonix IX workshop.
- [122] C Lefevre. LHC: the guide. <http://cdsweb.cern.ch/record/1092437>, 2008.
- [123] R. Scrivens et al, editor. *Proceedings of IPAC2011, San Sebastián, Spain*, 2011.
- [124] R. Adolphi et al. The CMS experiment at the CERN LHC. *JINST*, 03:S08004, 2008. doi: 10.1088/1748-0221/3/08/S08004.
- [125] Vardan Khachatryan et al. CMS Tracking Performance Results from early LHC Operation. *Eur. Phys. J.*, C70:1165–1192, 2010. doi: 10.1140/epjc/s10052-010-1491-3.
- [126] Serguei Chatrchyan et al. Alignment of the CMS Silicon Tracker during Commissioning with Cosmic Rays. *JINST*, 5:T03009, 2010. doi: 10.1088/1748-0221/5/03/T03009.

- [101] M.M. Aggarwal et al. Transverse mass distributions of neutral pions from Pb-208 induced reactions at 158-A-GeV. *Eur. Phys. J.*, C23:225, 2002. doi: 10.1007/s100520100886.
- [102] David G. d'Enterria. Indications of suppressed high p_T hadron production in nucleus-nucleus collisions at CERN-SPS. *Phys. Lett.*, B596:32, 2004. doi: 10.1016/j.physletb.2004.06.071.
- [103] A. Adare et al. Suppression pattern of neutral pions at high transverse momentum in Au + Au collisions at $\sqrt{s_{NN}} = 200$ GeV and constraints on medium transport coefficients. *Phys. Rev. Lett.*, 101:232301, 2008. doi: 10.1103/PhysRevLett.101.232301.
- [104] John Adams et al. Transverse momentum and collision energy dependence of high p_T hadron suppression in Au+Au collisions at ultrarelativistic energies. *Phys. Rev. Lett.*, 91:172302, 2003. doi: 10.1103/PhysRevLett.91.172302.
- [105] A. Dainese, C. Loizides, and G. Paic. Leading-particle suppression in high energy nucleus-nucleus collisions. *Eur. Phys. J.*, C38:461, 2005. doi: 10.1140/epjc/s2004-02077-x.
- [106] Ivan Vitev and Miklos Gyulassy. High p_T tomography of $d + Au$ and Au+Au at SPS, RHIC, and LHC. *Phys. Rev. Lett.*, 89:252301, 2002. doi: 10.1103/PhysRevLett.89.252301.
- [107] Ivan Vitev. Jet tomography. *J. Phys.*, G30:S791, 2004. doi: 10.1088/0954-3899/30/8/019.
- [108] Carlos A. Salgado and Urs Achim Wiedemann. Calculating quenching weights. *Phys.Rev.*, D68:014008, 2003. doi: 10.1103/PhysRevD.68.014008.
- [109] Nestor Armesto, Andrea Dainese, Carlos A. Salgado, and Urs Achim Wiedemann. Testing the color charge and mass dependence of parton energy loss with heavy-to-light ratios at RHIC and CERN LHC. *Phys.Rev.*, D71:054027, 2005. doi: 10.1103/PhysRevD.71.054027.
- [110] Thorsten Renk et al. Systematics of the charged-hadron p_T spectrum and the nuclear suppression factor in heavy-ion collisions from $\sqrt{s} = 200$ GeV to $\sqrt{s} = 2.76$ TeV. *Phys. Rev.*, C84:014906, 2011. doi: 10.1103/PhysRevC.84.014906.
- [111] B.I. Abelev et al. Identified baryon and meson distributions at large transverse momenta from Au+Au collisions at $\sqrt{s_{NN}} = 200$ GeV. *Phys. Rev. Lett.*, 97:152301, 2006. doi: 10.1103/PhysRevLett.97.152301.
- [112] J.W. Cronin, Henry J. Frisch, M.J. Shochet, J.P. Boymond, R. Mermod, et al. Production of Hadrons with Large Transverse Momentum at 200-GeV, 300-GeV, and 400-GeV. *Phys.Rev.*, D11:3105, 1975. doi: 10.1103/PhysRevD.11.3105.

- [127] V Karimäki. *The CMS tracker system project: Technical Design Report*. Technical Design Report CMS. CERN, Geneva, 1997.
- [128] Aaron and Dominguez. The cms pixel detector. *Nuclear Instruments and Methods in Physics Research Section A: Accelerators, Spectrometers, Detectors and Associated Equipment*, 581:343 – 346, 2007. doi: 10.1016/j.nima.2007.07.156. URL <http://www.sciencedirect.com/science/article/pii/S016890020701635X>. Proceedings of the 11th International Vienna Conference on Instrumentation.
- [129] CMS Collaboration. Silicon Strips. <http://cms.web.cern.ch/news/silicon-strips>, 2008-2012. Public CMS Website.
- [130] F Hartmann. Silicon tracking detectors in high-energy physics. *Nuclear Instruments and Methods in Physics Research A*, 666:25–46, February 2012. doi: 10.1016/j.nima.2011.11.005.
- [131] Laura Borrello, Alberto Messineo, Ettore Focardi, and Anna Macchiolo. Sensor design for the cms silicon strip tracker. Technical Report CMS-NOTE-2003-020, CERN, Geneva, Aug 2003.
- [132] Y-J Lee. Measurement of the charged-hadron multiplicity in proton-proton collisions at LHC with the CMS detector. <http://hdl.handle.net/1721.1/68876>. PhD thesis, Massachusetts Institute of Technology, 2011.
- [133] M. Raymond et al. The CMS Tracker APV250.25 μ m CMOS readout chip. <http://hdl.handle.net/1721.1/68876>, 2000. Proceedings of the 6th Workshop on Electronics for LHC Experiments, Cracow Poland.
- [134] R.M. Brown and D.J.A. Cockerill. Electromagnetic calorimetry. *Nuclear Instruments and Methods in Physics Research Section A: Accelerators, Spectrometers, Detectors and Associated Equipment*, 666(0):47–79, 2012. ISSN 0168-9002. doi: 10.1016/j.nima.2011.03.017. URL <http://www.sciencedirect.com/science/article/pii/S0168900211005572>. Advanced Instrumentation.
- [135] D. Bailleux, I. Britvitch, K. Deiters, R. Egeland, B. Gilbert, J. Grahl, Q. Ingram, A. Kuznetsov, E. Lester, Y. Musienko, D. Renker, S. Reucroft, R. Rusack, T. Sakhelashvili, A. Singovski, and J. Swain. Hamamatsu apd for cms ecal: quality insurance. *Nuclear Instruments and Methods in Physics Research Section A: Accelerators, Spectrometers, Detectors and Associated Equipment*, 518(1-2):622–625, 2004. ISSN 0168-9002. doi: 10.1016/j.nima.2003.11.102. URL <http://www.sciencedirect.com/science/article/pii/S0168900203029735>. Frontier Detectors for Frontier Physics: Proceeding.

Bibliography

- [136] D. Acosta et al. CMS Physics Technical Design Report Volume I: Detector Performance and Software. 2006. Technical Design Report CMS.
- [137] Allen Bell. Design and Construction of the Beam Scintillation Counter for CMS. <http://hdl.handle.net/10092/1588>. Master thesis, University of Canterbury, 2008.
- [138] CMS Collaboration. BSC Triggers. <https://twiki.cern.ch/twiki/bin/viewauth/CMS/BSCTrigger>, 2011.
- [139] CMS Collaboration. The CMS Beam Conditions and Radiation Monitoring System. <https://twiki.cern.ch/twiki/bin/view/CMS/BrmWikiHome>, 2011.
- [140] CMS Collaboration. Evaluation of oscilloscopes for the bptx read-out system - tests in the atlas trigger electronics lab. CMS Internal Note CMS-IN-2007-000, 2007. URL <https://twiki.cern.ch/twiki/pub/CMS/BrmBptx/cmspaper.pdf>.
- [141] V M Ghete and CMS Collaboration. The cms ll trigger emulation software. *Journal of Physics: Conference Series*, 219(3):032009, 2010. URL <http://stacks.iop.org/1742-6596/219/i=3/a=032009>.
- [142] Sergio Cittolin, Attila Racz, and Paris Sphicas. *CMS trigger and data-acquisition project: Technical Design Report*. Technical Design Report CMS. CERN, Geneva, 2002.
- [143] S. Agostinelli et al. GEANT4: a simulation toolkit. *Nucl. Instrum. and Methods*, A506:250, 2003. doi: 10.1016/S0168-9002(03)01368-8.
- [144] CMS Collaboration. The cms offline sw guide. <https://twiki.cern.ch/twiki/bin/view/CMSPublic/SWGuide>, 2011.
- [145] Olga Kodolova, I. Vardanian, A. Nikitenko, and A. Oulianov. The performance of the jet identification and reconstruction in heavy ions collisions with CMS detector. *Eur. Phys. J. C*, 50:117, 2007. doi: 10.1140/epjc/s10052-007-0223-9.
- [146] CMS Collaboration. Centrality dependence of dijet energy balance distributions in pbb collisions at 2.76 tev. CMS Analysis Note CMS-AN-10-399, 2010. URL http://cms.cern.ch/iCMS/jsp/openfile.jsp?tp=draft&files=AN2010_399_v8.pdf.
- [147] Roy J. Glauber. Quantum Optics and Heavy Ion Physics. *Nucl. Phys.*, A774:3-13, 2006. doi: 10.1016/j.nuclphysa.2006.06.009.
- [148] Michael L. Miller, Klaus Reygers, Stephen J. Sanders, and Peter Steinberg. Glauber modeling in high energy nuclear collisions. *Ann.Rev.Nucl.Part.Sci.*, 57:205-243, 2007. doi: 10.1146/annurev.nucl.57.090506.123020.

- [149] C.W. deJager et al. Atomic Data and Nuclear Data Tables 14 485, 1974.
- [150] David G. d'Enterria. Hard scattering cross-sections at LHC in the Glauber approach: From pp to pA and AA collisions. 2003. Contribution to the CERN Yellow Report on Hard Probes in Heavy Ion Collisions at the LHC.
- [151] I. P. Lokhtin and A. M. Snigirev. A model of jet quenching in ultrarelativistic heavy ion collisions and high- p_T hadron spectra at RHIC. *Eur. Phys. J. C*, 45:211, 2006. doi: 10.1140/epjc/s2005-02426-3.
- [152] Serguei Chatrchyan et al. Observation and studies of jet quenching in PbPb collisions at $\sqrt{s_{NN}} = 2.76\text{TeV}$. *Phys. Rev. C*, 84:024906, 2011. doi: 10.1103/PhysRevC.84.024906.
- [153] E. Yumiceva T. Miao, H. Wenzel and N. Leioatts. Beam position determination using tracks. *CMS Note*, [2007/021], 2007.
- [154] CMS Collaboration. Tracking and vertexing results from first collisions. *CMS Physics Analysis Summary*, CMS-PAS-TRK-10-001, 2010. URL <http://cdsweb.cern.ch/record/1258204>.
- [155] Wolfgang Adam. Track and vertex reconstruction in CMS. *Nucl. Instrum. Meth.*, A582:781, 2007. doi: 10.1016/j.nima.2007.07.091.
- [156] W. Adam, B. Mangano, Th. Speer, and T. Todorov. Track reconstruction in the cms tracker. *CMS Note*, [2006/041], 2006.
- [157] D. Kotliński S. Cucciarelli, M. Konecki and T. Todorov. Track reconstruction, primary vertex finding and seed generation with the pixel detector. *CMS Note*, [2006/026], 2006.
- [158] D. Kotliński S. Cucciarelli and T. Todorov. Position determination of the pixel hits. *CMS Note*, [2002/049], 2002.
- [159] D. Kotliński S. Cucciarelli, M. Konecki and T. Todorov. Track reconstruction, primary vertex finding and seed generation with the pixel detector. *CMS Note*, [2006/026], 2006.
- [160] Rand . Fréhwith T. Speer, K. Prokofiev. Vertex fitting with the kalman filter formalism in the orca reconstruction program. *CMS Internal Note*, 2003.
- [161] Greg Welch and Gary Bishop. An introduction to the kalman filter. *TR 95-041*, , 2007. University of North Carolina at Chapel Hill, Department of Computer Science.
- [162] Wolfgang Adam for the CMS Collaboration. A model of jet quenching in ultrarelativistic heavy ion collisions and high- p_T hadron spectra at RHIC. *Nuclear Instruments and Methods in Physics Research Section A: Accelerators, Spectrometers,*

Bibliography

- Detectors and Associated Equipment*, 582:781–784, 2007. doi: 10.1016/j.nima.2007.07.091.
- [163] Susanna Cucciarelli. Track and vertex reconstruction with the cms detector. *BEAUTY 2005 10th International Conference in B-Physics at Hadron Machines*, , 2005.
- [164] CMS Collaboration. Track reconstruction in the CMS Tracker. CMS Physics Analysis Summary CMS-PAS-TRK-09-0011, 2009.
- [165] CMS Collaboration. Iterative Tracking. <https://twiki.cern.ch/twiki/bin/view/CMSPublic/SWGuideIterativeTracking>, 2011.
- [166] Serguei Chatrchyan et al. Dependence on pseudorapidity and centrality of charged hadron production in PbPb collisions at a nucleon-nucleon centre-of-mass energy of 2.76 TeV. *JHEP*, 1108:141, 2011. doi: 10.1007/JHEP08(2011)141.
- [167] CMS Collaboration. Transverse-momentum and pseudorapidity distributions of charged hadrons in pp collisions at $\sqrt{s} = 0.9$ and 2.36 tev. *JHEP*, 02:041, 2010. doi: 10.1007/JHEP02(2010)041.
- [168] ALICE Collaboration. Charged-particle multiplicity density at mid-rapidity in central pb-pb collisions at $\sqrt{s_{NN}} = 2.76$ tev. *Phys. Rev. Lett.*, 105:252301, 2010. doi: 10.1103/PhysRevLett.105.252301.
- [169] Christof Roland. Track reconstruction in heavy ion events using the cms tracker. Technical Report CMS-NOTE-2006-031, CERN, Geneva, Jan 2006.
- [170] I. P. Lokhtin. Hydjet event generator. <http://lokhtin.web.cern.ch/lokhtin/hydro/hydjet.html>, 2011.
- [171] CMS Collaboration. Measurement of CMS luminosity. CMS Physics Analysis Summary CMS-PAS-EWK-10-004, 2010. URL <http://cdsweb.cern.ch/record/1279145>.
- [172] CMS Collaboration. Absolute calibration of the CMS luminosity measurement: Summer 2011 update. CMS Physics Analysis Summary CMS-PAS-EWK-11-001, 2011. URL <http://cdsweb.cern.ch/record/1376102>.
- [173] Serguei Chatrchyan et al. Charged particle transverse momentum spectra in pp collisions at $\sqrt{s} = 0.9$ and 7 TeV. *JHEP*, 08:086, 2011. doi: 10.1007/JHEP08(2011)086.
- [174] Vardan Khachatryan et al. Transverse-momentum and pseudorapidity distributions of charged hadrons in pp collisions at $\sqrt{s} = 7$ TeV. *Phys. Rev. Lett.*, 105:022002, 2010. doi: 10.1103/PhysRevLett.105.022002.

- [175] Constantino Tsallis. Possible generalization of boltzmann-gibbs statistics. *Journal of Statistical Physics*, 52:479, 1988. ISSN 0022-4715. doi: 10.1007/BF01016429.
- [176] P. Bartalini and L. Fanó, editors. *Proceedings of the First Workshop on Multiple Partonic Interactions at the LHC, Perugia, Italy, October 27-31, 2008*, 2009. [arXiv:1003.4220].
- [177] Peter Z. Skands. The Perugia Tunes. page (2009). [arXiv:0905.3418].
- [178] Andy Buckley et al. Systematic event generator tuning for the LHC. *Eur. Phys. J.*, C65:331, 2010. doi: 10.1140/epjc/s10052-009-1196-7.
- [179] P et. al. Abreu. Tuning and test of fragmentation models based on identified particles and precision event shape data. oai:cds.cern.ch:309559. *Z. Phys. C*, 73(CERN-PPE-96-120):11–60, 1996.
- [180] Francois Arleo, Stanley J. Brodsky, Dae Sung Hwang, and Anne M. Sickles. Higher-Twist Dynamics in Large Transverse Momentum Hadron Production. *Phys. Rev. Lett.*, 105:062002, 2010. doi: 10.1103/PhysRevLett.105.062002.
- [181] Francois Arleo, David d’Enterria, and Andre S. Yoon. Single-inclusive production of large- p_T charged particles in hadronic collisions at TeV energies and perturbative QCD predictions. *JHEP*, 06:035, 2010. doi: 10.1007/JHEP06(2010)035.
- [182] Serguei Chatrchyan et al. Measurement of the Inclusive Jet Cross Section in pp Collisions at $\sqrt{s} = 7$ TeV. 2011. [arXiv:1106.0208].
- [183] Georges Aad et al. Measurement of inclusive jet and dijet cross sections in proton-proton collisions at 7 TeV centre-of-mass energy with the ATLAS detector. *Eur. Phys. J.*, C71:1512, 2011. doi: 10.1140/epjc/s10052-010-1512-2.
- [184] M. Stratmann, R. Sassot, and P. Zurita. Inclusive Hadron Production in the CERN-LHC Era. 2010. [arXiv:1008.0540].
- [185] T. Aaltonen et al. Erratum: Measurement of particle production and inclusive differential cross sections in $p\bar{p}$ collisions at $\sqrt{s} = 1.96$ *te v* [*Phys. Rev.* **D79** (2009) 112005]. *Phys. Rev.*, D82:119903, 2010. doi: 10.1103/PhysRevD.82.119903.
- [186] Pavel M. Nadolsky et al. Implications of CTEQ global analysis for collider observables. *Phys. Rev.*, D78:013004, 2008. doi: 10.1103/PhysRevD.78.013004.
- [187] Daniel de Florian, Rodolfo Sassot, and Marco Stratmann. Global analysis of fragmentation functions for pions and kaons and their uncertainties. *Phys. Rev.*, D75: 114010, 2007. doi: 10.1103/PhysRevD.75.114010.
- [188] TECHQM Main Page. Partonic Energy Loss. https://wiki.bnl.gov/TECHQM/index.php/Main_Page, 2010.

Bibliography

- [189] TECHQM. Partonic Energy Loss. https://wiki.bnl.gov/TECHQM/index.php/Partonic_Energy_Loss, 2010.
- [190] Constantin Loizides. High transverse momentum suppression and surface effects in Cu+Cu and Au+Au collisions within the PQM model. *Eur.Phys.J.*, C49:339–345, 2007. doi: 10.1140/epjc/s10052-006-0059-8.
- [191] CMS Collaboration. Measurement of the hard component of jet fragmentation functions in PbPb collisions at 2.76 TeV. (CMS-PAS-HIN-11-004), 2011. URL <http://cdsweb.cern.ch/record/1354531?ln=en>.
- [192] A. Beraudo, J.G. Milhano, and U.A. Wiedemann. The contribution of medium-modified color flow to jet quenching. 2012. [arXiv:1204.4342].
- [193] Andre S. Yoon, Edward Wenger, and Gunther Roland. Convoluting jet spectra with fragmentation functions: a cross-check of the charged particle p_T spectrum. 2010. [arXiv:1003.5928].
- [194] A. Adare et al. Azimuthal anisotropy of neutral pion production in Au+Au collisions at $\sqrt{s_{NN}} = 200$ GeV: Path-length dependence of jet quenching and the role of initial geometry. *Phys.Rev.Lett.*, 105:142301, 2010. doi: 10.1103/PhysRevLett.105.142301.
- [195] Jianguo Jia, W.A. Horowitz, and Jinfeng Liao. A study of the correlations between jet quenching observables at RHIC. *Phys.Rev.*, C84:034904, 2011. doi: 10.1103/PhysRevC.84.034904.
- [196] Roy A. Lacey, N.N. Ajitanand, J.M. Alexander, J. Jia, and A. Taranenko. Scaling patterns for azimuthal anisotropy in Pb+Pb collisions at $\sqrt{s_{NN}} = 2.76$ TeV: Further constraints on transport coefficients. 2012.
- [197] Serguei Chatrchyan et al. Azimuthal anisotropy of charged particles at high transverse momenta in PbPb collisions at $\sqrt{s_{NN}} = 2.76$ TeV. 2012. [arXiv:1204.1850].
- [198] Barbara Betz and Miklos Gyulassy. Reduced Jet-Medium Coupling in Pb+Pb Collisions at the LHC? 2012. [arXiv:1201.0281].

List of Figures

2.1.	Feynman diagrams of quark-gluon and gluon-gluon interaction vertices. .	12
2.2.	Summary of the measurements of $\alpha_s(Q)$ in comparison with the QCD predictions shown as a function of the energy scale Q [12]. Also shown is the α_s at a fixed, standard energy scale of Z boson mass, i.e., $Q = M_Z$	14
2.3.	Schematic phase diagram of nuclear matter as a function of temperature and baryon chemical potential [15]. (see text)	15
2.4.	LQCD calculation of ϵ/T^4 as a function of T with different number of quark flavors up to three (u, d, s) with equal mass and two equal and one heavier mass scenarios [26, 27]. Also shown is the energy density estimated based on the Bjorken formula [32] (see also Sec. 2.3.2) in the initial stage of heavy-ion collisions at the SPS, RHIC, and LHC.	18
2.5.	Schematic light-cone diagram of the (longitudinal) evolution of hot and dense system created in the collision of heavy ions [36]. The hyperbolic lines represent the contours of constant proper time τ	21
2.6.	Schematic diagram of collisional and radiative energy loss for a quark with energy E traversing a medium [64]. Note the second diagram takes place in the absence of any medium as well (c.f. the QCD radiation probability which follows the Dokshitzer-Gribov-Lipatov-Altarelli-Parisi (DGALP) evolution equation [8] in vacuum.)	23
2.7.	The collisional energy loss of a quark propagating a medium of temperature $T = 250$ MeV with an initial energy E [69]. The prime ($'$) denotes different quark flavors.	25
2.8.	A schematic of a typical gluon radiation diagrams in the presence of the medium (courtesy of M. van Leeuwen). The blue circle represents the scattering center and the red wiggled-line represents the radiated gluon. .	26
2.9.	The radiative energy loss of a quark and a gluon propagating a medium with an initial energy E [69].	28
2.10.	(Left) R_{AA} of π^0 and η in dAu collisions at RHIC [87]. (Right) R_{AA} of the 'colorless' probes: Z^0 , W and isolated photon.	30
2.11.	Measurements of the nuclear modification factor R_{AA} in central heavy-ion collisions at three different center-of-mass energies, as a function of p_T , for neutral pions (π^0), charged hadrons (h^\pm), and charged particles [100–104], compared to several theoretical predictions [105–110].	32
3.1.	Schematic layout of the CERN accelerator complex [120]	36
3.2.	Overall layout of the CMS detector [124]	37

List of Figures

3.3.	Overall layout of the CMS tracker [124]. A detector module is represented a line with double line indicating modules mounted back-to-back. Also shown is the η coverage of each detector module.	38
3.4.	Schematic view of the CMS pixel system. The forward pixel detectors (FPix) are in turbine-like geometry tilted by 20° [127].	39
3.5.	Photos of four pixel cells used in the barrel (left) and in the forward (right) [124]	40
3.6.	Schematic of the SST viewed in the plane perpendicular to the beam direction [129].	41
3.7.	Schematic layout of the ECAL system [134].	43
3.8.	Schematic longitudinal view of the CMS detector with the HCAL subsystems, HB, HF, and HO shown with their η (dotted-lines) coverages.	44
3.9.	Schematic longitudinal view of the CMS detector with the muon subsystems, DT, CSC, and RPC shown with their η (dotted-lines) coverages [136].	45
3.10.	Schematic layout and the illustration of the segmentation of the BSC detector system [138]	46
3.11.	Schematic of the CMS DAQ system architecture [136].	47
4.1.	(Left panel) Correlation for 60k minimum bias events in one collision run between the number of pixel hits and the total energy deposited by the HF. Good collisions (colored points) have a tight correlation, while events firing the BSC halo bits, displaying beam-scraping event-like features, or lacking a valid reconstructed vertex are off-diagonal (black points). (Right panel) The same correlation for only those events passing all selection cuts described in the text.	50
4.2.	Trigger efficiency of HLT jet-trigger with (un-corrected)energy threshold of 50 GeV.	51
4.3.	Illustration of high energy nucleus-nucleus collision viewed transversely (left) and sideways (right).	52
4.4.	A cartoon that illustrates how a measured charged particle multiplicity is related to the collision geometry and centrality variables [148].	54
4.5.	(a) Probability distribution of the total HF energy for minimum bias events (black line), Jet65-triggered (blue-shaded region), and Jet80-triggered (red-shaded region) events. (b) Distribution of the events in bins of fractional cross section for minimum bias (black line), Jet65-triggered (blue-shaded region), and Jet80-triggered (red-shaded region) events.	55
4.6.	Distributions of pixel cluster size along the beam as a function of z with the red lines to illustrate at which z position the highest number of compatible pixel clusters are found. In this event, the most compatible z position is found to be around -4 cm.	56
4.7.	rz distributions of reconstructed vertices in data and MC for different centrality bins	57
4.8.	Vertex resolution and pull size in x, y, z directions as a function of the number of associated tracks.	58

5.1. Distribution of the cluster charge in the pixel barrel (left) and in the end-cap (right) [125]. The same figure with the semi-log scale is shown in the inset.	60
5.2. Possible pixel layer and disk combinations for finding pixel pairs.	61
5.3. Possible pixel layer and disk combinations for finding pixel triplets.	61
5.4. Tracker occupancy in pp minimum bias event (Left). Tracker occupancy in PbPb 0–5% event (Right).	66
5.5. Distribution of the ADC counts for each strip and the illustration of the Zero-Suppression	67
5.6. Correlation between the calorimeter energy deposit and the track momentum.	68
5.7. Track quality distributions. From the top left, it is N_{hits}^{valid} , $\sigma(p_T)/p_T$, $(\chi^2/N_{d.o.f})/N_{layers}$, $d_0/\sqrt{\sigma(d_0^2) + \sigma(v_0)}$, and $d_z/\sqrt{\sigma(d_z^2) + \sigma(v_z)}$	70
5.8. Track η and ϕ distribution between data and MC.	71
5.9. Global tracking efficiency and fake rate evaluated from MinBias sample and HYDJET embedded dijet sample with hard-scattering scales of 50, 80, 170 GeV/c.	72
5.10. Secondary fraction and multiple reconstruction fraction evaluated from the HYDJET embedded dijet sample with hard-scattering scales of 170 GeV/c.	73
6.1. Closure test of MC-based tracking corrections applied to reconstructed MC (HYDJET), MC (HYDJET + PYTHIA QCD $\hat{p}_T > 80$ and 170 GeV/c) events and compared to the generator-level truth for different centralities	77
6.2. (a) E_T distributions and the efficiency turn-on (b) Combined charged particle dN/dp_T with each trigger contribution explicitly shown	78
6.3. The same plot as in Fig 6.2(b) made for other centrality bins as well.	78
6.4. 2D scatter plot of reconstructed track p_T versus simulated track p_T from the MB mixed with QCD sample with a hard-scattering scale of 170 GeV/c.	80
6.5. (Right) Momentum resolution $(p_T^{reco} - p_T^{true})/p_T^{reco}$ determined from various MC samples: minimum bias, hard-scattering scales of 30, 50, 80, 110, and 170 GeV (Left) Momentum resolution determined from MC sample with the hard-scattering scale of 170 GeV for different centralities.	80
6.6. The ratio of the momentum resolution smeared dN/dp_T to dN/dp_T before smearing in different centrality bins with a four-component power-law fitted to the ratio.	81
6.7. Magnitude of binning correction alone (open red circles) and binning + momentum smearing corrections (open blue circles) in the original narrow bins of the analysis (i.e. before re-binning) After re-binning, the same quantities are shown as filled triangles.	82

List of Figures

6.8.	The fully corrected (including binning correction) differential invariant yield in the original narrow bins (open circles) and in the final wider bins (solid circles) is compared to a common fit. The bottom panel shows the ratio of the yield to the fit.	83
6.9.	The systematic uncertainties assigned to each corrections and the combined one.	84
6.10.	Comparison between the tracking efficiency obtained based on the MC sample mixed with real data and the tracking efficiency obtained based on the pure MC sample.	85
6.11.	Fake estimation based on the sideband method in comparison to the fake rate estimated based on the MC samples.	86
7.1.	Upper panel: the invariant charged particle differential yield from the present analysis (solid circles) and the previous CMS measurements (stars) at $\sqrt{s} = 0.9$ TeV (Left) and 7 TeV (Right) over the limited p_T range of the earlier result. Lower panel: the ratio of the new (solid circles) and previous (stars) CMS results to a Tsallis fit of the earlier measurement. . . .	90
7.2.	Upper panel: the invariant charged particle differential yield at $\sqrt{s} = 0.9$ TeV (Left), and 7 TeV (Right) compared with the predictions of four tunes of the PYTHIA MC generator. Lower panel: the ratio of the new CMS measurement to the four PYTHIA tunes. Tabulated result can be found in Table C.1 and C.2.	91
7.3.	Upper panel: the invariant charged particle differential yield at $\sqrt{s} = 2.76$ TeV for $ \eta < 1.0$ compared with the predictions of four tunes of the PYTHIA MC generator. Lower panel: the ratio of the new CMS measurement to the four PYTHIA tunes as well as to the interpolated spectra, which is explained in Sec. 7.0.9. Tabulated result can be found in Table C.3.	92
7.4.	(a) Inclusive charged particle invariant differential cross sections, scaled by $\sqrt{s}^{4.9}$, for $ \eta < 1.0$ as a function of x_T for the measurements at various center-of-mass energies with the ratios of differential cross sections measured at 0.9, 1.96, and 7 TeV to those predicted by NLO calculations for factorisation scales ranging from 0.5–2.0 p_T in the lower panel. (b) The same cross sections for CMS data only including the measurement at 2.76 TeV with the NLO calculations in the lower lower panel. Tabulated result can be found in Table C.6.	93
7.5.	(a) Interpolations between measured charged particle differential cross sections at different \sqrt{s} for the two example values of $p_T = 3$ and 9 GeV/c. (b) Upper panel: ratios of the scaled differential cross sections to the global power-law x_T fit described in the text (coloured markers) and fits to these ratios (similarly coloured thin lines). The upper axis translates x_T to p_T for $\sqrt{s} = 2.76$ TeV. Lower panel: ratios of the NLO-calculated cross sections at three different energies, scaled by $\sqrt{s}^{4.9}$, to the cross section calculated at $\sqrt{s} = 2.75$ TeV.	94

7.6. Upper panel: Invariant charged particle differential yield in PbPb collisions at 2.76 TeV in bins of collision centrality (symbols), compared to that of pp at 2.76 TeV, normalized by the corresponding pp invariant cross sections scaled by the nuclear overlap function (dashed lines). Tabulated results can be found in Table C.7– C.12.	97
7.7. Nuclear modification factor R_{AA} (filled circles) as a function of p_T for six PbPb centralities. The error bars represent the statistical uncertainties and the yellow boxes represent the p_T -dependent systematic uncertainties. An additional systematic uncertainty from the normalization of T_{AA} and the pp integrated luminosity, common to all points, is shown as the shaded band around unity in each plot. Tabulated results can be found in Table C.13– C.18.	98
7.8. T_{AA} -scaled ratio of p_T spectra in central and peripheral bins, R_{CP} , as a function of p_T for four PbPb centralities. The error bars represent the statistical uncertainties and the yellow boxes the p_T -dependent systematic uncertainties. An additional systematic uncertainty from the normalization of T_{AA} , common to all points, is shown as the shaded band around unity in each plot. Tabulated results can be found in Table C.19– C.22.	99
7.9. Measurements of the nuclear modification factor R_{AA} in central heavy-ion collisions at three different center-of-mass energies, as a function of p_T , for neutral pions (π^0), charged hadrons (h^\pm), and charged particles [100–104], including the measurement presented here compared to several theoretical predictions [105–110] (see text).	100
8.1. R_{AA} in 0–5% bin compared to the PYTHIA-based modeled ' R_{AA} ' with different choices of the Gaussian broadening parameter for $\sqrt{s_{NN}} = 2.76$ TeV (Left) and for $\sqrt{s_{NN}} = 0.2$ TeV (Right).	104
8.2. (Left) Inclusive charged particle spectra from the PROQ20 PYTHIA. (Right) Comparison between the inclusive spectra of all charged particles in events with the inclusive spectra of all charged particles obtained from the convolution.	106
8.3. Different energy loss scenarios	107
8.4. Energy and momentum spectra of jets and charged particles with and without the modification due to the constant parton energy loss and resulting model- R_{AA} of jet and charged particle compared to the measured R_{AA} in 0–5%.	108
8.5. Energy and momentum spectra of jets and charged particles with and without the modification due to the constant fractional parton energy loss and resulting model- R_{AA} of jet and charged particle compared to the measured R_{AA} in 0–5%.	109
8.6. Energy and momentum spectra of jets and charged particles with and without the modification due to the fractional energy loss with logarithmic energy dependence and resulting model- R_{AA} of jet and charged particle compared to the measured R_{AA} in 0–5%.	110

List of Figures

8.7. Comparison between the modeled R_{AA} with varying quenching parameter and the measured R_{AA} in different centrality bins.	112
8.8. Correlation between the quenching parameter c with the event centrality and the average N_{coll}	113
8.9. R_{AA} and v_2 measurements as a function of p_T in bins of four centrality along with the theoretical predictions made for the selected centrality ranges [198].	114
8.10. Correlation between R_{AA} and v_2 measurements in the range $p_T = 5-60$ GeV/ c in difference centrality bins. The theoretical prediction is based on the 0–5% R_{AA} with 0–10% v_2 from Ref. [198].	114
B.1. Track quality distributions. 1–5 GeV/ c	119
B.2. Track quality distributions. 5–10 GeV/ c	120
B.3. Track quality distributions. 10–30 GeV/ c	120
B.4. Track quality distributions. 30–60 GeV/ c	121
B.5. Track quality distributions. 60– ∞ GeV/ c	121
B.6. Track quality distributions. 0–5%	122
B.7. Track quality distributions. 5–10%	122
B.8. Track quality distributions. 10–30%	123
B.9. Track quality distributions. 70–90%	123

List of Tables

3.1. Resolution of the pixel system	39
3.2. Specification of each subsystem in the SST. For the barrel systems, the mean pitch is shown separately for inner and outer rings with the number of layers. (e.g., for TIB, first two layers have $80\mu\text{m}$ and the second two layers have $120\mu\text{m}$.)	42
4.1. Centrality Tables	56
5.1. Setting for each iteration in the iterative tracking. The p_T cut and impact parameter cuts are applied during the seeding. d_z is calculated with respect to the center of the CMS detector except the 1 st iteration where it's calculated with respect to the reconstructed vertex, noted by the symbol *.	64
6.1. Summary of the various contributions to the systematic uncertainties affecting the PbPb and pp p_T spectra, and the nuclear modification factors R_{AA} and R_{CP}	87
C.1. Tabulated result of Fig. 7.2(a)	125
C.2. Tabulated result of Fig. 7.2(b)	126
C.3. Tabulated result of Fig. 7.3	127
C.4. Tabulated result of Fig. 7.4(a) (0.9 TeV)	128
C.5. Tabulated result of Fig. 7.4(a) (7 TeV)	129
C.6. Tabulated result of Fig. 7.4(b) (2.76 TeV)	130
C.7. Tabulated result of Fig. 7.6 (0–5%)	131
C.8. Tabulated result of Fig. 7.6 (5–10%)	132
C.9. Tabulated result of Fig. 7.6 (10–30%)	133
C.10. Tabulated result of Fig. 7.6 (30–50%)	134
C.11. Tabulated result of Fig. 7.6 (50–70%)	135
C.12. Tabulated result of Fig. 7.6 (70–90%)	136
C.13. Tabulated result of Fig. 7.7 (0–5%)	137
C.14. Tabulated result of Fig. 7.7 (5–10%)	138
C.15. Tabulated result of Fig. 7.7 (10–30%)	139
C.16. Tabulated result of Fig. 7.7 (30–50%)	140
C.17. Tabulated result of Fig. 7.7 (50–70%)	141
C.18. Tabulated result of Fig. 7.7 (70–90%)	142
C.19. Tabulated result of Fig. 7.8 (0–5%/50–90%)	143
C.20. Tabulated result of Fig. 7.8 (5–10%/50–90%)	144

C.21. Tabulated result of Fig. 7.8 (10–30%/50–90%)	145
C.22. Tabulated result of Fig. 7.8 (30–50%/50–90%)	146

Acknowledgments

It has been almost six years since I came to MIT for a Ph.D. program in the Physics department. I still vividly remember the day when I first came to Cambridge with my father after more than a day of driving from Urbana-Champaign in Illinois. Time has flown by unbelievably quickly since then and now it is time to graduate. It has been truly an invaluable experience to pursue my Ph.D. degree at MIT, in particular, in the MIT Relativistic Heavy Ion Group. This thesis and the works presented therein would not have been possible without guidances, assistances, and supports of many people. I would like to make the best use of this opportunity to thank those people.

First and foremost, I would like to thank my advisor, Wit Busza, who has guided me through my entire Ph.D. program. I chose Wit as my advisor because I thought I would be able to learn not only physics but also wisdoms. It did not take long to realize that such choice was indeed right. He has taught me many interesting aspects of heavy-ion physics, but at the same time he has shown his wisdoms. Wit was always very supportive, and he encouraged me all the time to ponder upon the meanings and the implications of what I am working on. I was always very surprised and impressed by how Wit makes physics (not only in the field of heavy-ion) very intriguing, in particular those that many people overlook and take it for granted.

I would like to thank the other members of my thesis committees, Richard Milner and Gunther Roland. I would especially like to thank our new group leader, Gunther Roland, who has supervised me through in almost all the major works I (and all the other students!) have been involved. Gunther has shown keen and quantitative insight, which I put it as 'great insight', into many different analyses and physics results, and it has inspired me to learn closely from him by taking his advices, suggestions, and comments very seriously.

It has been a pleasure working with the MIT Relativistic Heavy Ion Group. I would first like to thank Bolek Wyslouch, who has helped tremendously not only myself but also other students as well as the other members of the Heavy Ion group in CMS. He has shown very strong leadership during the heavy-ion runs in 2010 and 2011. Christof Roland guided Frank and myself so that we could get involved in the HLT validation work. He has also shared his expertise in the CMS tracking. Ivan Cali has shared his expertise in the detailed hardware and firmware level CMS tracking. I would like to thank in particular Bolek, Christof, and Ivan for helping me to carry out the HLT on-call expert role by driving me to the point 5 (where the CMS detector and control room are located) every morning during the heavy-ion run in 2011. I would like to thank George Stephans for his help with the pp spectra analysis and the language editing of the R_{AA} paper. Wei Li has helped me a lot when I seriously struggled with the use of the MIT Tier2 computing facility. Also as a senior graduate student Wei had provided help and guidance when

we had bi-weekly heavy-ion physics journal club. I wish I had more time to work with Yue Shi Lai, but as I left the CERN early 2012, I lost the chance. Siarhei Vaurynovich has shown his great endurance with the ϕ analysis. Also, Constantin Loizides, Burak Alver, and Edward Wenger, who are no longer in our group, had shown their tremendous expertises in the heavy-ion physics and detector analyses. I would especially like to thank Edward Wenger, who had guided and helped me most closely to carry out major part of the analyses presented in this thesis. Ed has been an excellent role model. He always completed given tasks very effectively in a neat way, which I always wanted to learn. I wish the best of luck to the newly joined students, Dragos Velicanu, Doga Gulhan, Alex Barbieri, and a new post-doc, Krisztian Krajczar. Last but not least, I owe many thanks to my fellow students, Frank Ma, YenJie-Lee, Yetkin Yilmaz, and Yongsun Kim. We have been through many challenges, successes, and frustrations together. I cannot imagine how hard and dry the last six years would have been without them.

I spent more than four years in Geneva working on the data analyses as well as so-called 'service' work for the CMS collaboration. There I met more than a handful of skilful people with expertise. Among those, I would like to thank Emilio Meschi, Marco Zanetti, and Andrea Petrucci, who have been always very happy to lend their expertise in the CMS Data Acquisition and Trigger system. It also has been a pleasure working with Gabor Veres, Krisztian Krajczar, Matthew Nguyen, and Victoria Zhukova within the CMS Heavy Ion group. I would like to thank David d'Enterria and Francois Arleo for allowing me to work with them on the high- p_T phenomenology and for having in-depth discussions on the related subjects. I would also like to thank Thomas Ferguson, Joanne Cole, and Leandar Litov for reviewing the spectra papers very carefully as the CMS Analysis Review Committee and being very supportive and helpful.

In Boston and in Geneva I have met many great friends. In particular, I would like to thank Dong Hyun Kim, Hyowon Gweon, Sejoong Kim, and Taesin Kwak at MIT, and Garam Hahn, Dong Ho Moon, JiHyun Kim, Hyunchul Kim, JunGyu Yi, Sanghyun Song, Minwoo Kim and Mihee Jo at CERN for making and sharing good memories that I will cherish forever. I would also like to thank several professors from Korea whom I met during my stay at CERN, which includes Prof. Kwang Suk Sim (Korean Univ.), InKyu Park (Univ. of Seoul) and Prof. In-Kwon Yoo (Pusan Natl. Univ.). Lastly, a special thanks is given to Hwa Lee, who has given me enormous mental support throughout. She always has been by my side and continuously cheered me up.

Finally, I owe everything to my family. Without their support and understanding, none of this would have been possible. Thank you and I love you!

Published papers

The *arXiv* version of the following papers are reprinted in the next pages.

- Single-inclusive production of large- p_T charged particles in hadronic collisions at TeV energies and perturbative QCD predictions, JHEP 06 (2010) 035, 2010
- Convoluting jet spectra with fragmentation functions: a cross-check of the charged particle p_T spectrum, arXiv:1003.5928, 2010 (not published)
- Charged particle transverse momentum spectra in pp collisions at $\sqrt{s} = 0.9$ and 7 TeV, JHEP 08 (2011) 086, 2011
- Study of high- p_T charged particle suppression in PbPb compared to pp collisions at $\sqrt{s_{NN}} = 2.76$ TeV, Eur. Phys. J. C (2012) 72:1945, 2012

Single-inclusive production of large- p_T charged particles in hadronic collisions at TeV energies and perturbative QCD predictions

François Arleo

LAPTH, Université de Savoie, CNRS, BP 110, 74941 Annecy-le-Vieux cedex, France*

David d'Enterria

ICREA & Institut Ciències del Cosmos, Univ. Barcelona, 08028 Barcelona, Catalonia

Andre S. Yoon

Laboratory for Nuclear Science, MIT, Cambridge, MA 02139-4307, USA

ABSTRACT: The single inclusive spectrum of charged particles with transverse momenta $p_T = 3 - 150$ GeV/ c measured at midrapidity by the CDF experiment in proton-antiproton ($p\bar{p}$) collisions at $\sqrt{s} = 1.96$ TeV is compared to next-to-leading order (NLO) perturbative QCD calculations using the most recent parametrizations of the parton distributions and parton-to-hadron fragmentation functions. Above $p_T \approx 20$ GeV/ c , there is a very sizeable disagreement of the Tevatron data compared to the NLO predictions and to x_T -scaling expectations, suggesting a problem in the experimental data. We also present the predictions for the p_T -differential charged hadron spectra and the associated theoretical uncertainties for proton-proton ($p-p$) collisions at LHC energies ($\sqrt{s} = 0.9 - 14$ TeV). Two procedures to estimate the charged hadron spectra at LHC heavy-ion collision energies ($\sqrt{s} = 2.76, 5.5$ TeV) from $p-p$ measurements are suggested.

KEYWORDS: PACS: 12.38.-t 12.38.Bx 13.85.-t 13.87.Fh.

*Laboratoire d'Annecy-le-Vieux de Physique Théorique, UMR5108

Contents

1. Introduction	1
2. Hadroproduction in factorised pQCD	3
3. Tevatron data versus perturbative QCD	4
3.1 Data versus INCNLO	4
3.2 Data versus PYTHIA	7
3.3 Data versus x_T -scaling	10
3.4 Discussion	11
4. Inclusive charged hadron spectra at the LHC	14
4.1 INCNLO predictions	15
4.2 Interpolation of measured charged-hadron spectra at $\sqrt{s} = 5.5$ TeV	17
4.2.1 Centre-of-mass energy rescaling	17
4.2.2 x_T -scaling	19
5. Summary	20

1. Introduction

Hadron production at large transverse momenta ($p_T \gg \Lambda_{\text{QCD}} \approx 0.2$ GeV) in hadronic interactions originates from the fragmentation of the hard scattered partons produced in the collision. The presence of a hard scale in the process allows one to employ the powerful theoretical machinery of collinear factorisation [1] to compute the corresponding production cross sections. High- p_T hadron cross sections can be thus obtained as a convolution of (i) long-distance universal pieces representing the structure of the initial hadrons (parton distribution functions, PDFs) as well as the fragmentation of a final-state quark or gluon into the observed hadron (fragmentation functions, FFs), and (ii) short-distance parts that describe the hard partonic interactions calculable as a perturbative expansion in terms of the strong running coupling α_s . The measurement of high- p_T hadroproduction in p - p and p - \bar{p} collisions provides, thus, a valuable testing ground of the perturbative regime of Quantum Chromodynamics (pQCD) and of the non-perturbative objects (PDFs, FFs) needed to compute a large variety of cross sections at hadronic colliders.

Theoretically, lowest-order (LO) calculations of the inclusive hadron cross sections were performed in the late 70s [2], later improved at next-to-leading order (NLO) [3–5] and more recently at next-to-leading-log (including soft gluon resummation) [6, 7] accuracies. The latest phenomenological developments in this field have focused on constraints of the

proton PDFs (in particular the polarised ones [7, 8]), on improvements of the parton-to-hadron (in particular, gluon-to-hadron) FFs [9], as well as on baseline measurements of relevance for high-energy heavy-ions collisions [10]. On the experimental side, inclusive unidentified charged hadron production – i.e. $pp, p\bar{p} \rightarrow h^\pm X$, where $h^\pm = (h^+ + h^-)$ is effectively the sum of pions (about 60% of all hadrons), kaons (about 20% of the total) and protons (about 10% of all hadrons) and their antiparticles – have been measured above $p_T \approx 1$ GeV/c at the ISR ($\sqrt{s} = 31, 44, 63$ GeV) [11], at RHIC ($\sqrt{s} = 200$ GeV) [12], SpS ($\sqrt{s} = 0.2, 0.5, 0.9$ TeV) [13], and Tevatron ($\sqrt{s} = 0.63, 1.8, 1.96$ TeV) [14–16] energies. Except at Tevatron, the rest of measurements are unfortunately in a moderate p_T range ($p_T \approx 12$ GeV/c at most). The latest comparisons of the available charged hadron spectra, at RHIC energies [8,12], to NLO calculations [6] show a good data–theory agreement above $p_T \approx 1.5$ GeV/c for central and forward rapidities [10].

In this paper, we compare NLO pQCD calculations to the latest charged particle spectrum measured at Tevatron and we present predictions with their theoretical uncertainties for the high- p_T hadron spectra expected at LHC energies. The motivation is two-fold. First, the most recent CDF charged particle spectrum [16] covers a very large p_T range, up to $p_T = 150$ GeV/c where pQCD predictions are reliable and can be confronted to the data. Similarly, comparable “minimum bias” measurements are expected to be available in the early running of the LHC [17]. CMS has already measured a first, yet mostly low- p_T , charged hadron spectrum at $\sqrt{s} = 2.36$ TeV [18]. Secondly, at the LHC, a p - p reference hadron spectrum will be needed at the *same* centre-of-mass (c.m.) energy as that of heavy-ion (Pb–Pb) collisions to study the high- p_T suppression observed in nucleus-nucleus reactions at RHIC [19]. Since the Pb–Pb results will be nominally obtained at $\sqrt{s_{NN}} = 5.5$ TeV a pQCD-based interpolation between the results recorded at Tevatron ($\sqrt{s} = 1.96$ TeV) and during the first LHC p - p run ($\sqrt{s} = 7$ TeV) will be needed.

The paper is organized as follows. In Section 2 we succinctly remind the theoretical framework of our study based on the next-to-leading-order pQCD Monte Carlo (MC) code INCNLO [20]. In Section 3, we compare the charged particle spectra measured at mid-rapidity in p - \bar{p} collisions at $\sqrt{s} = 1.96$ TeV [16] to the NLO calculations INCNLO and to the LO parton shower MC PYTHIA, as well as to simple x_T -scaling expectations. We find that the *maximum* theoretical uncertainties of the NLO prediction – associated to the PDF, FF and scale variations added in quadrature – are $\pm 40\%$. For increasing transverse momenta, the data is a factor up to 3 orders of magnitude larger than the perturbative predictions. We conclude that above $p_T \approx 20$ GeV/c, there is no possibility to accommodate the data–theory discrepancy even accounting for possible additional contributions to the charged particle yield coming e.g. from heavy-quarks or vector-boson (plus jet) production. The fact that the parent jet p_T -differential spectrum is, on the contrary, well reproduced by NLO calculations and that the single particle data also violate simple x_T -scaling expectations, suggest a problem in the experimental results at the highest p_T values. Finally, in Section 4 we present the charged hadron spectra and associated uncertainties predicted by INCNLO in p - p collisions in the range of energies covered by the LHC ($\sqrt{s} = 0.9 - 14$ TeV), and propose two methods to determine the p - p spectra at intermediate LHC energies of relevance for heavy-ion running.

2. Hadroproduction in factorised pQCD

The inclusive cross section for the production of a single hadron, differential in transverse momentum p_T and rapidity y , takes the following form at next-to-leading order in α_s [21]:

$$\frac{d\sigma}{d\mathbf{p}_T dy} = \sum_{i,j,k=q,g} \int dx_1 dx_2 F_{i/p}(x_1, \mu_F) F_{j/p}(x_2, \mu_F) \frac{dz}{z^2} D_k^h(z, \mu_{FF}) \times \left[\left(\frac{\alpha_s(\mu_R)}{2\pi} \right)^2 \frac{d\hat{\sigma}_{ij,k}}{d\mathbf{p}_T dy} + \left(\frac{\alpha_s(\mu_R)}{2\pi} \right)^3 K_{ij,k}(\mu_R, \mu_F, \mu_{FF}) \right]. \quad (2.1)$$

Here $F_{i/p}(x_1, \mu_F)$ are the PDFs of the incoming protons p at parton momentum fraction x , $D_k^h(z, \mu_{FF})$ are the parton-to-hadron FFs describing the transition of the parton k into an unidentified hadron h carrying a fraction z of its momentum, $d\hat{\sigma}_{ij,k}/d\mathbf{p}_T dy$ is the Born cross section of the subprocess $i + j \rightarrow k + X$, and $K_{ij,k}$ is the corresponding higher-order term (the full kinematic dependence is omitted for clarity). In this paper, we use the INCNLO programme [20] to compute the cross sections, supplemented with various PDFs and FFs sets (see below). The truncation of the perturbative series at next-to-leading order accuracy in α_s introduces an artificial dependence with magnitude $\mathcal{O}(\alpha_s^3)$, of the cross section on initial-state (μ_F) and final-state (μ_{FF}) factorization scales, as well as on the renormalization scale μ_R . The choice of scales is arbitrary but the standard procedure is to choose a value around the natural physical scale of the hard scattering process, here given by the p_T of the produced hadron. We consider below scale variations $\mu_R, \mu_F, \mu_{FF} = \kappa p_T$, with $\kappa = 0.5 - 2$ to gauge the theoretical uncertainty linked to the neglected higher-order terms. Hereafter, whenever the scales μ_R, μ_F and μ_{FF} , are given a common value, the latter is denoted μ .

The two non-perturbative inputs of Eq. (2.1) are the parton densities and the fragmentation functions. The former are mostly obtained from global-fit analyses of HERA proton structure function data, the latter from hadron production results in e^+e^- collisions. We use here the three latest PDFs parametrisations available: CTEQ6.6 [22], MSTW08 [23] and NNPDF1.2 [24], included in the LHAPDF (version 5.7.1) package [25], which take into account the most up-to-date data from deep-inelastic lepton-proton scattering and hadronic collisions as well as various theoretical improvements. For the fragmentation functions into hadrons, we use and compare the three more recent FF sets available: DSS [26], AKK08 [27] and HKNS [28], which, except for the latter, include for the first time also hadron-hadron collision data in their global analyses. These new FF fits cover a larger z range and are more sensitive to the gluon fragmentation which dominates high- p_T hadron production in p - p collisions [9].

For transverse momenta close to the phase space boundary where the p_T of the hadron is about half of the partonic centre-of-mass energy ($x_T = 2p_T/\sqrt{s} \approx 0.1 - 1$), the coefficients of the perturbative expansion are enhanced by extra powers of logarithmic terms of the form $\alpha_s^n \ln^{2n-1}(1 - x_T)/(1 - x_T)$ [29]. Resummation to all orders of such ‘‘threshold’’ terms – which appear when the initial partons have just enough energy to produce the high- p_T hadron – have been carried out at next-to-leading logarithmic (NLL) accuracy

in [6, 7]. Interestingly, the NLL results provide a much reduced scale-dependence than the NLO approximation. The presently used fixed-order calculations (INCNLO) do not include threshold resummations but their effect in the final spectrum is expected to be less important since the typical charged hadron p_T range covered by the Tevatron and LHC experiments, $x_T \equiv 2p_T/\sqrt{s} \approx 10^{-4} - 10^{-1}$, is far away from the region where such effects start to play a role.

3. Tevatron data versus perturbative QCD

In this Section we compare the high- p_T charged particle spectrum measured by the CDF collaboration [16] in the pseudorapidity range $|\eta| < 1$ to the predictions of INCNLO [20] and PYTHIA [30] MCs and to simple perturbative expectations based on x_T -scaling [31]. The measured spectrum covers the range $p_T = 0.4 - 150$ GeV/ c , but a comparison to pQCD predictions is only meaningful at high enough p_T ; therefore we impose a minimal cut of $p_T = 3$ GeV/ c . For the NLO analysis, we study separately the effects on the spectrum of varying in the calculations the three theoretical scales ($\mu = p_T/2, p_T, 2p_T$), PDFs (MSTW08; CTEQ6.6 and NNPDF1.2) and FFs (AKK08, DSS and HKNS). We use PYTHIA to determine possible extra contributions to the measured high- p_T tracks spectrum coming from heavy-quark fragmentation as well as from real and virtual vector-boson production, either single-inclusive or in association with a jet.

3.1 Data versus INCNLO

The measured CDF charged particle $p\bar{p}$ single inclusive distribution is compared to the INCNLO predictions for charged hadrons in Fig. 1. First, we note that the measured primary track spectrum is not corrected for contributions from charged particles other than hadrons. Possible contamination from stable leptons (electrons, positrons and muons) are not in principle removed from the measured spectrum. As we discuss *a posteriori* in Section 3.2, those amount however only to a small fraction (a few percents) of the total charged particle tracks coming from quark and gluon jet fragmentation according to our PYTHIA simulations. The INCNLO prediction shown in Fig. 1 is that which best fits the (low p_T range of) the experimental results. We see that below $p_T \approx 20$ GeV/ c data and theory agree well for the choice of scales $\mu = 2p_T$, CTEQ6.6 parton densities, and AKK08 parton-to-hadron fragmentation functions. Above this p_T value, the CDF spectrum starts to rapidly deviate from the theoretical predictions. At the highest transverse momenta the data is up to a factor 800 above the NLO calculations. A very conservative quadratic sum of all uncertainties discussed hereafter – amounting to $\pm 30\%$ for the scales, $\pm 10\%$ for the PDFs, and $\pm 25\%$ for the FFs choices – would result in a maximum theoretical uncertainty of $\pm 40\%$ in the yields (dashed lines around the data/theory ratio).

Scale uncertainty: First, in the INCNLO calculations we have fixed the PDFs and FFs to the CTEQ6.6 and DSS sets respectively¹, and computed the corresponding spectra

¹The choice is in principle arbitrary, other PDF and FF combinations yield similar results for the scale dependence.

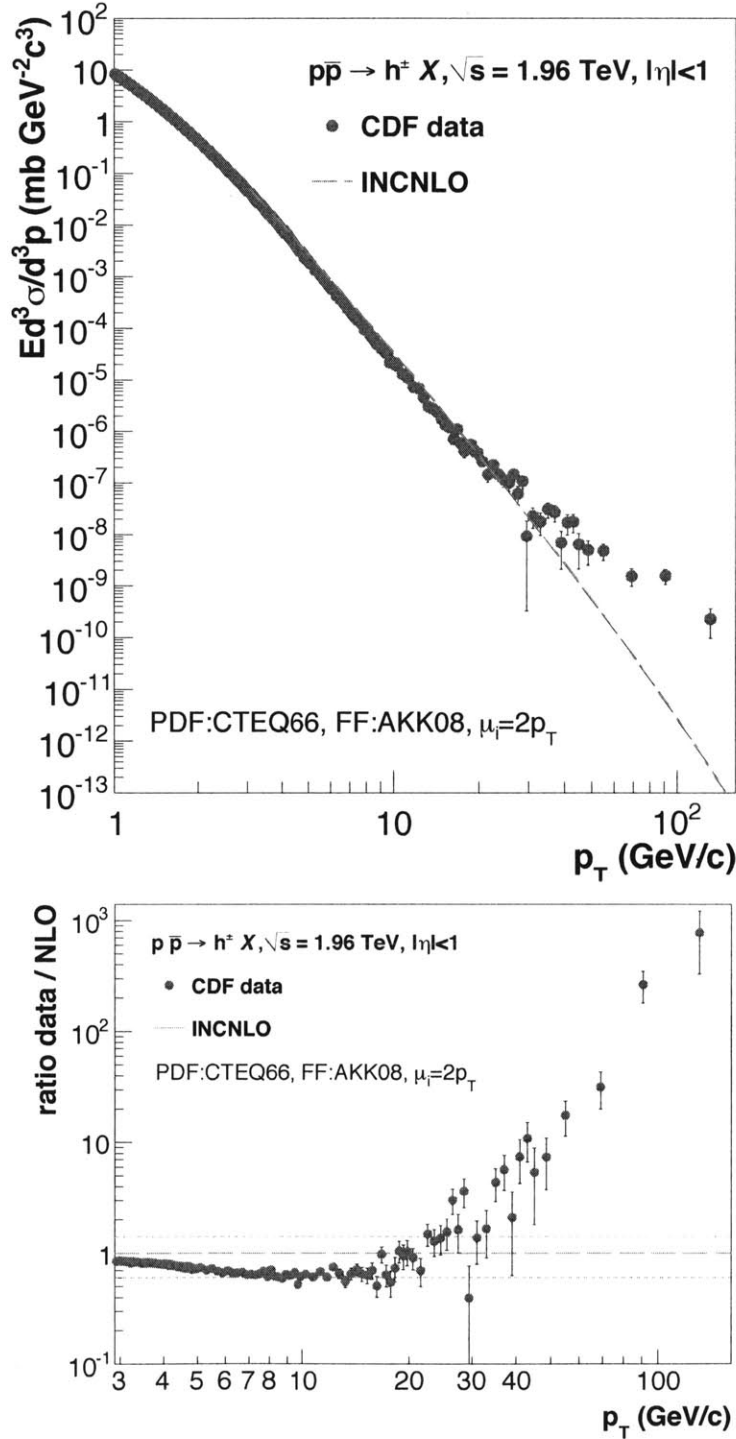


Figure 1: Top: Comparison of the charged particle p_T spectrum measured by CDF in $p\bar{p}$ collisions at $\sqrt{s} = 1.96$ TeV [16] to NLO pQCD predictions with PDFs fixed to CTEQ6.6, scales to $\mu = 2p_T$, and FFs to AKK08. Bottom: Corresponding ratio of CDF data over theory. The dashed lines indicate the maximum $\pm 40\%$ theoretical uncertainty of the calculations (see text).

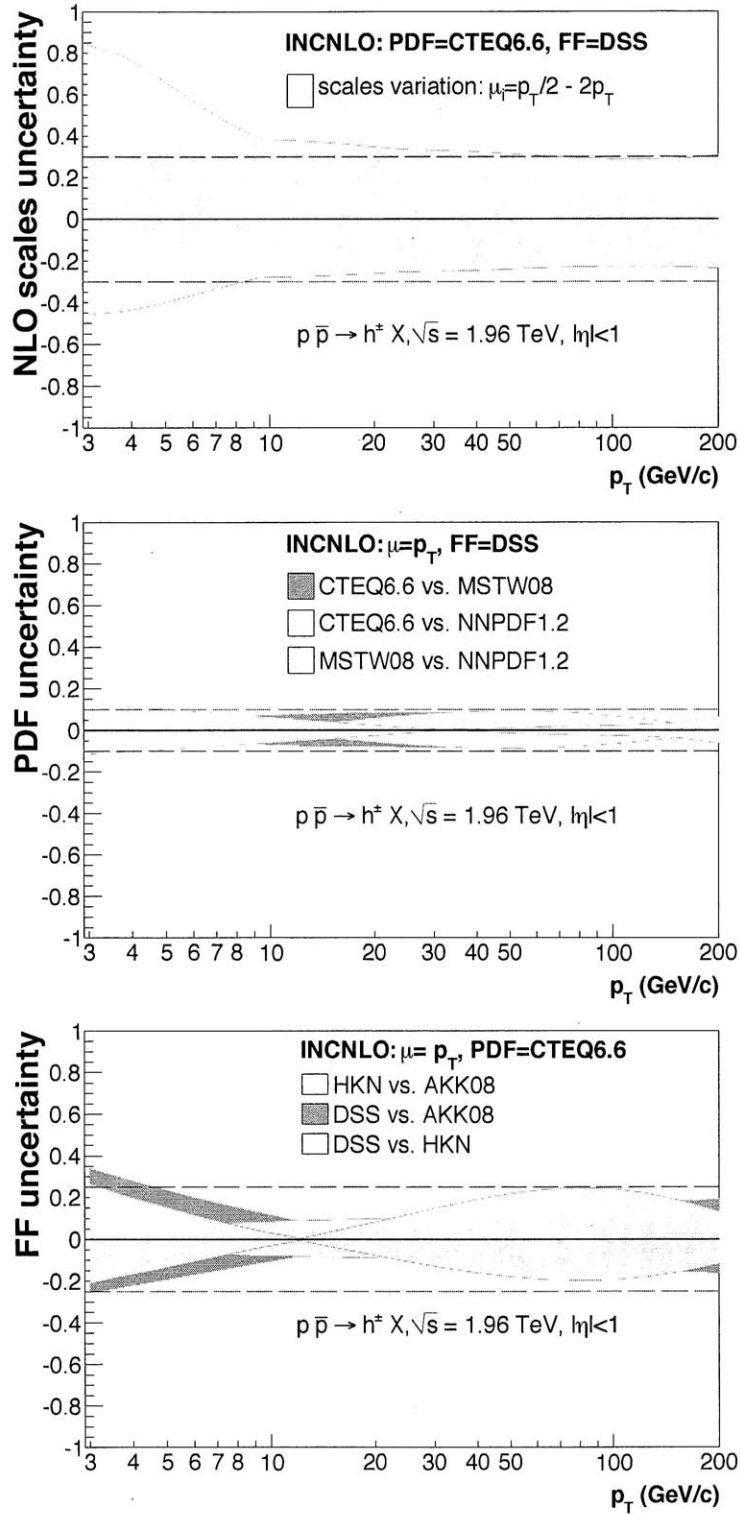


Figure 2: Fractional differences between the INCNLO charged hadron spectra in $p\bar{p}$ at $\sqrt{s} = 1.96$ TeV for varying scales μ_i , PDF and FF. Top: Scale uncertainty obtained for fixed PDF (CTEQ6.6) and FF (DSS) varying all three scales within $\mu_i = p_T/2 - 2p_T$ (the dashed lines indicate a $\pm 30\%$ uncertainty). Middle: PDF uncertainty obtained for fixed $\mu = p_T$ and FF (DSS) with three PDFs: CTEQ6.6, MSTW08, NNPDF1.2 (the dashed lines indicate $\pm 10\%$ differences). Bottom: FF uncertainty obtained for fixed scales ($\mu = p_T$) and PDF (CTEQ6.6) with three FFs: AKK08, DSS, HKNS (the dashed lines represent $\pm 25\%$).

setting the three theoretical scales to three different values $\mu_{F,M,FF} = p_T/2, p_T, 2p_T$ in all possible 27 combinations. The corresponding range of predictions is shown in Fig. 2 (top) where we plot a shaded band covering the whole range of fractional differences between the spectra obtained for any choice of scales. The “closest-to-the-average” spectrum is obtained setting all scales to $\mu = p_T$. The largest (resp. lowest) charged hadron yield predictions are obtained with mostly all three scale values set to $\mu_i = p_T/2$ (resp. $\mu_i = 2p_T$). At low p_T the scale uncertainty is quite large (indicating as expected larger higher-order corrections) but otherwise above $p_T = 10$ GeV/ c it stays roughly constant at around $\pm 30\%$ up to the highest momenta considered (dashed lines in the figure).

PDF uncertainty: Second, in the middle panel of Fig. 2 we show as a function of p_T the theoretical uncertainty associated to the PDF choice. It has been obtained with INCNLO comparing the fractional differences between the single charged hadron spectra at $\sqrt{s} = 1.96$ TeV for fixed scales ($\mu = p_T$) and FF (DSS) and three different PDFs. The dashed bands plotted cover the range of maximum relative differences in the theoretical spectra obtained with MSTW08, CTEQ6.6 and NNPDF1.2. Those differences are small, below 10% and mostly p_T -independent (dashed lines).

FF uncertainty: Last, we have used INCNLO complemented with the three latest FFs available in the market: AKK08, DSS and HKNS, to compute the charged hadron spectrum for the CDF kinematics, with scales ($\mu = p_T$) and PDFs (CTEQ6.6) fixed. The main differences between FF sets concern the fractional π^\pm , K^\pm and p/\bar{p} compositions as a function of p_T . Yet, the total² hadron yield predicted by the three FFs for $p\bar{p}$ at 1.96 TeV is quite similar as can be seen in the bottom panel of Fig. 2 where we plot the relative differences between the spectra computed for varying FFs. The maximum theoretical uncertainty linked to the FF choice amounts to about $\pm 25\%$ of the charged hadron yield at any p_T (dashed lines), although the differences between FFs appear to be smaller at intermediate hadron $p_T \approx 10 - 25$ GeV/ c .

A conservative quadratic sum of the fractional uncertainties linked to the NLO scales, PDFs and FFs choices results in a total theoretical uncertainty of order $\pm 40\%$ whereas the maximum difference between the data and the calculations amounts to much larger factors, up to $\mathcal{O}(10^3)$ at $p_T \gtrsim 100$ GeV/ c (Fig. 1).

3.2 Data versus PYTHIA

Given the large discrepancy between the experimental and NLO predictions for the charged particle spectrum at high- p_T one may wonder whether other charged particles – apart from $\pi^\pm, K^\pm, p/\bar{p}$ coming from the fragmentation of quarks and gluons – may contribute in any way to the experimentally measured distribution beyond $p_T \approx 20$ GeV/ c . A first possibility that we have considered is whether other charged products from charm and bottom jets (with relative increasing importance at large transverse momentum) play any

²As a cross check, for all FF sets we have confirmed that the NLO spectrum obtained from the sum of the spectra individually obtained with the pions, kaons and protons FFs is indeed equal to the one obtained with the non-identified charged hadron FFs.

role. Although the inclusive hadron FFs used in our NLO calculations contain *all* pion, kaons and (anti)protons issuing from light- as well as heavy-quark fragmentation, charm and bottom hadrons decay also into charged leptons³ which are not included in INCNLO. Thus as a independent theoretical check, we have computed the inclusive yield of *all* charged particles with the PYTHIA MC (v6.420) [30] with the D6T [33] tuning⁴ in the “minimum bias” and QCD-jets modes (MSEL = 1 with low- p_T production, ISUB = 95, switched on to correctly simulate the low- p_T region). The chosen processes produce not only light-quarks and gluons but also heavy-quarks⁵ including flavour excitation, $Qg \rightarrow Qg$, and gluon splitting, $g \rightarrow Q\bar{Q}$.

To obtain enough statistics at high- p_T , we have run with up to 12 different ranges for the minimum and maximum parton momenta in the 2→2 scatterings ($\hat{p}_T = 0 - 10, 10 - 15, 15 - 20, 20 - 50$ GeV/ c , ... and $\hat{p}_T > 470$ GeV/ c) weighted by their corresponding cross sections. We have then explicitly separated the contributions coming from the fragmentation of high- p_T light-flavours (u, d, s and gluon) from those coming from charm and bottom quarks. As done in CDF, we take all charged particles⁶ exactly as defined in their analysis (i.e. all primary particles with mean lifetimes $\tau > 0.3 \cdot 10^{-10}$ s and the decay products of those particles with shorter τ). The results of our studies are shown in Fig. 3. The inclusive charged products of c -quark and b -quark fragmentation represent a very small (less than 5%) fraction of the total yield of particles measured at high- p_T by CDF.

A second possibility that we have explored is whether the charged products of real and virtual vector-boson ($\gamma^{(*)}$, W^\pm , and Z^0) production – either single-inclusive or in association with a jet – which start to play a role at increasing transverse momenta, could partially account for the data–theory discrepancy. We have run prompt photon production in PYTHIA including the Born-level γ -jet Compton and annihilation diagrams (ISUB = 29, 14 respectively). The W^\pm , Z^0 and DY production (ISUB = 1, 2, 15, 16, 30, 31), includes single-inclusive ($2 \rightarrow 1$) as well as double-inclusive ($2 \rightarrow 2$) W^\pm -, Z^0 -, DY-jet channels with $\hat{p}_T > 20$ GeV/ c . The W^\pm and Z^0 contributions produce a (local) Jacobian peak in the charged-particle p_T distribution at about half the vector-boson mass, $p_T \approx 40$ GeV/ c . All those contributions, shown added up in Fig. 3, increase the charged particle yield by up to 10% in the range above $p_T \approx 40$ GeV/ c . This number is consistent with a simple order of magnitude estimate based on the ratio of electroweak and strong coupling constants valid when $p_T \gg M_W/2$: $(\alpha_{EW}/\alpha_s)^2 = (0.034/0.12)^2 = \mathcal{O}(10^{-1})$. Clearly, those processes contribute little to the total yield of charged particles and therefore cannot justify the observed large discrepancy between data and theory.

³As a cross check, we have confirmed that the PYTHIA spectrum of single leptons from c and b production agrees relatively well (within a factor of two) with more involved fixed-order NLL calculations [32].

⁴Tune D6T uses the CTEQ6LL PDF and describes the underlying event and the Drell-Yan data at Tevatron.

⁵PYTHIA settings: PARP(91)=2.1 GeV/ c (intrinsic k_T), PMAS(4,1)=1.5 GeV/ c^2 (m_c mass), PMAS(5,1)=4.8 GeV/ c^2 (m_b mass), MSTP(33)=1 (K -factor). Alternative running of *standalone* heavy-quark production (with MSEL = 4 and 5) would require K -factors of 2 – 4 in order to reproduce the heavy flavour p_T spectra measured at various colliders [34].

⁶PYTHIA settings: MSTJ(22)=2, PARJ(71)=10.

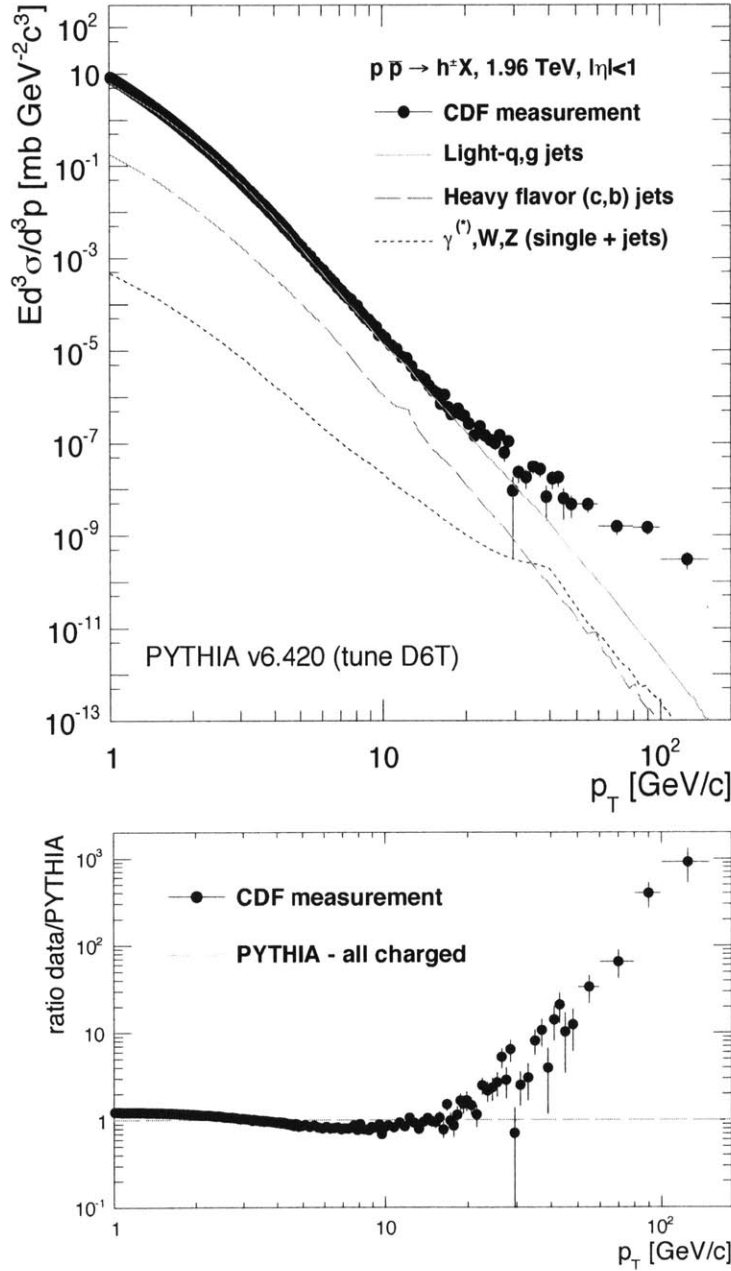


Figure 3: Top: Comparison of the CDF data (symbols) to PYTHIA (v6.420, D6T tuning) p_T distribution of charged particles in $p\bar{p}$ collisions at $\sqrt{s} = 1.96$ TeV coming from the fragmentation of (i) light-quarks and gluons and (ii) heavy-quarks, and (iii) from processes involving the production of vector bosons ($\gamma^{(*)}, W^\pm, Z^0$). Bottom: Ratio of the CDF data to the sum of all PYTHIA charged particle contributions.

3.3 Data versus x_T -scaling

A robust pQCD prediction for hard processes $A B \rightarrow C X$ in hadronic collisions is the power-law scaling of the inclusive invariant cross section,

$$E d^3\sigma/d^3p = F(x_T)/p_T^{n(x_T, \sqrt{s})} = F'(x_T)/\sqrt{s}^{n(x_T, \sqrt{s})}. \quad (3.1)$$

In the original parton model the power-law fall-off of the spectrum is simply $n = 4$ since the underlying $2 \rightarrow 2$ subprocess amplitude for point-like partons is scale invariant. In QCD, small scaling violations appear due to the running of α_s and the evolution of PDFs and FFs. At midrapidity and at fixed $p_T = 10 \text{ GeV}/c$, the power-law exponent computed at NLO accuracy increases slowly from $n \simeq 5$ at small values of x_T ($x_T = 10^{-2}$) up to $n \simeq 6$ at $x_T = 0.5$, with a very small dependence on the specific hadron species [35].

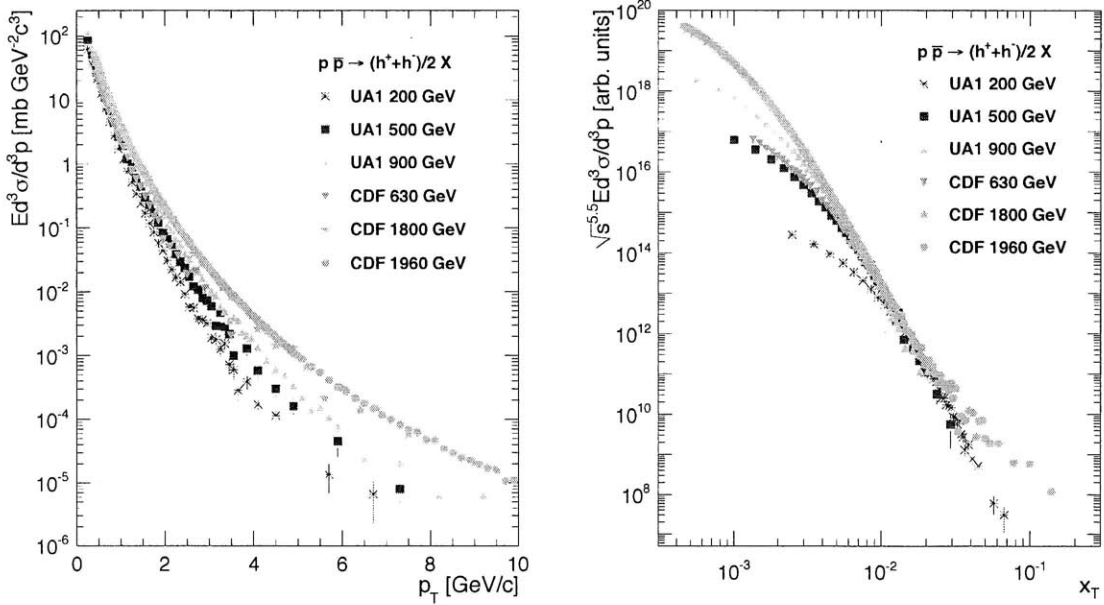


Figure 4: Compiled charged particle cross-sections measured in $p\bar{p}$ collisions at five different c.m. energies from 0.2 TeV to 1.96 TeV plotted as a function of p_T (left) and as a function of x_T (right) scaled with an effective common exponent of $n = 5.5$ (see text).

Except for the latest CDF data, the theoretical expectation, Eq. (3.1), is indeed well fulfilled by the experimental charged particle spectra measured so far in $p\bar{p}$ collisions⁷ at different centre-of-mass energies at the CERN Sp \bar{p} S ($\sqrt{s} = 0.2, 0.5, 0.9 \text{ TeV}$) [13] and Tevatron ($\sqrt{s} = 0.63, 1.8, 1.96 \text{ TeV}$) [14,16] colliders. All the p_T spectra feature power-law behaviours above $p_T \approx 2 \text{ GeV}/c$ (the higher the c.m. energy the smaller the exponent of the fall-off, see Fig. 4 left). Following the expectation Eq. (3.1), in order to extract a common n value from these different data sets, the measurements are plotted as a function

⁷A factor of 1/2 is applied hereafter to the CDF Run II spectrum as they measured $(h^+ + h^-)$ instead of the average $0.5 \times (h^+ + h^-)$ for all other measurements.

of x_T , multiplied by \sqrt{s}^n and fitted with the following 3-parameter functional form

$$\sqrt{s}^n \frac{E d^3 \sigma}{d^3 p} \Big|_{y=0} = p_0 \cdot [1 + (x_T/p_1)]^{p_2}. \quad (3.2)$$

In the data fitting, a minimum p_T of 2 GeV/ c is applied to exclude the region where soft particle production (which does not follow x_T -scaling) is dominant, which is consistent with what is used in [35]. We also exclude the CDF Run-II data from the global fit since, as we see *a posteriori*, there is no possibility to get an agreement with the lower energy measurements. With the obtained $\{p_i\}$ -parameters, using $n_{\text{NLO}} \approx 5$ as a guidance, the exponent n is varied from 4 to 7 in incremental steps in order to minimize the following χ^2 function with MINUIT [36]

$$\chi^2(n, \{p_i\}) = \sum_{j=1}^{n_{\text{dat}}} \left[\frac{\frac{E d^3 \sigma}{d^3 p} \Big|_{y=0} - \left(\frac{p_0 [1 + (x_T/p_1)]^{p_2}}{\sqrt{s}^n} \right)}{\sigma_j} \right]^2, \quad (3.3)$$

where σ_j are the quadratic sum of the statistical and systematic experimental uncertainties. In Fig. 4 (right) we show the experimental charged particle spectra scaled by \sqrt{s}^n as a function of x_T with the best value of n obtained from the fit, $n = 5.5$. We note that all measurements spanning a range of one order-of-magnitude in centre-of-mass energies follow a universal curve after rescaling up to the highest $x_T \sim 0.03$ measured at lower energy. A deviation of the CDF measurement at $\sqrt{s} = 1.96$ TeV from the trend established by the lower \sqrt{s} measurements is prominent above $x_T \sim 0.03$ ($p_T \sim 30$ GeV/ c).

In order to better assess the amount of deviation of the CDF data to the x_T -scaling expectation we show in Fig. 5 (top) the x_T -scaled fit obtained from all lower-energy data extrapolated to an expected p_T spectrum at $\sqrt{s} = 1.96$ TeV compared with the CDF Run II measurement and with the PYTHIA prediction shown in Fig. 3. As observed before, beyond $p_T \approx 20$ GeV/ c the latest CDF data clearly fail to follow the x_T -scaling expectation fulfilled by the rest of charged hadron measurements.

3.4 Discussion

The fact that no combination of PDF, FF and/or theoretical scales in the NLO calculations is able to reproduce the Tevatron experimental data above $p_T \approx 20$ GeV/ c by such a large factor is totally unexpected. Indeed, similar calculations based on FASTNLO/NLOJET++ [37, 38], reproduce perfectly well the inclusive jet spectrum measured in $p\bar{p}$ collisions at $\sqrt{s} = 1.96$ TeV in the range $p_T^{jet} \approx 50 - 600$ GeV/ c . The shape and magnitude of the CDF jet measurement is well reproduced using CTEQ6.1M PDFs and renormalization and factorization scales⁸ set to $\mu_R = \mu_F = p_T^{jet}/2$ [39]. Likewise, the $D\emptyset$ jet measurement agrees well with the same NLO predictions with CTEQ6.5M parton densities and $\mu_R = \mu_F = p_T^{jet}$ scales [40]. Variations of PDF and/or scales in the jet calculations, result in differences typically of order 10% – 15% for both measurements [39, 40].

⁸Note that in the inclusive jet calculation there is one scale less, the fragmentation one μ_F .

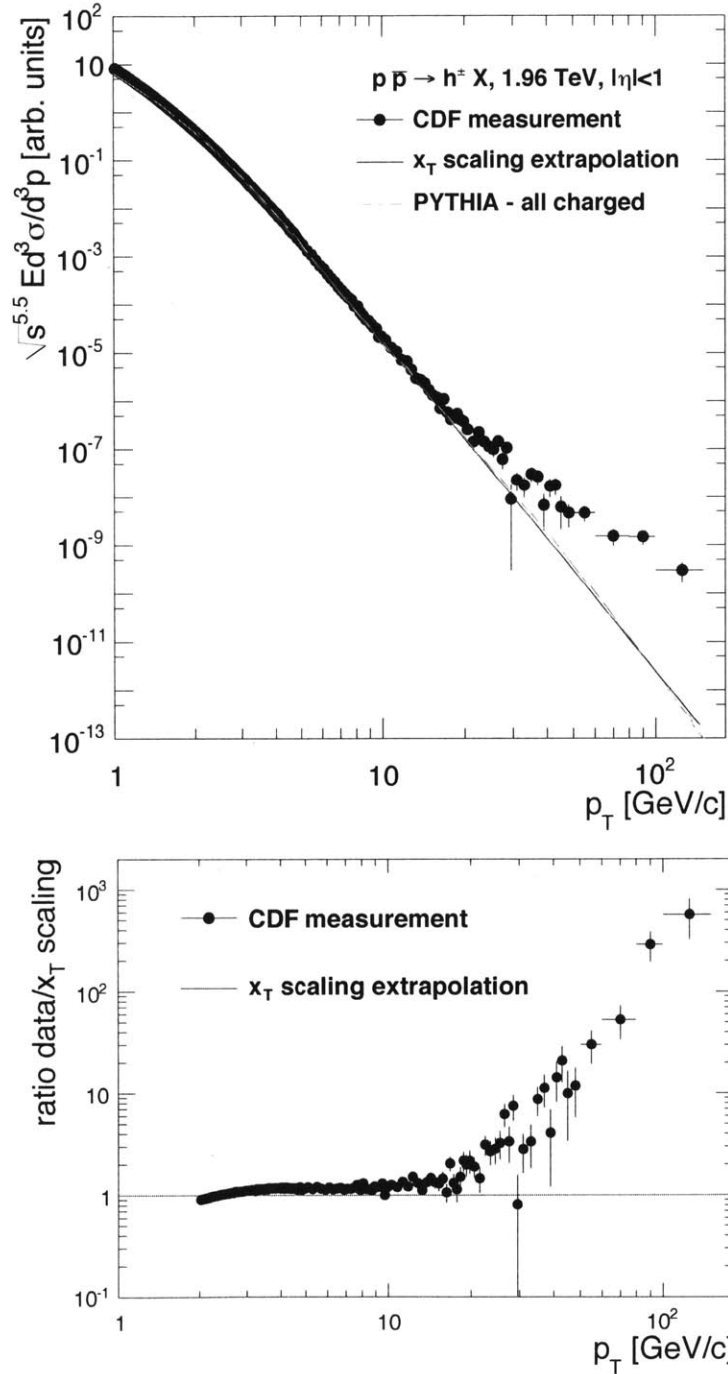


Figure 5: Top: Inclusive CDF Run-II charged hadron spectrum (filled circles) compared to the x_T -scaled extrapolation of lower energy $p\bar{p}$ data (blue solid line), as well as to the total PYTHIA prediction (dashed red line) of Fig. 3. Bottom: Corresponding ratio of CDF data over x_T -scaling expectation.

Given the agreement between the jet data and the fixed-order calculations⁹, it is somehow difficult to conceive a strong disagreement in the hadron production channel since the single high- p_T charged particle spectrum is dominated by leading hadrons carrying out a large fraction, $\langle z \rangle \approx 0.6$ – 0.7 , of the parent parton energy. Quite naively, the distribution of charged hadrons above $p_T \sim \langle z \rangle p_T^{jet} \gtrsim 30$ GeV/ c should be also perfectly consistent with the theoretical predictions within the additional uncertainty introduced by the fragmentation functions which is at most of the order $\pm 25\%$ as seen in Fig. 2 (bottom). Let us give a rough estimate of the expected invariant hadron production cross section based on the jet data. At leading order accuracy and assuming that one partonic channel dominates jet and hadron production (e.g. $u\bar{u} \rightarrow u\bar{u}$ scattering at large x_T), the hadron production cross section Eq. (2.1) is roughly given by

$$\frac{d^3\sigma^h}{d^3p}(p_T) \sim \frac{d^3\sigma^{jet}}{d^3p}\left(\frac{p_T}{z}\right) \times D_u^{h^++h^-}(z, p_T) \times \Delta z \simeq 10^{-2} \times \frac{d^3\sigma^{jet}}{d^3p}\left(\frac{p_T}{z}\right)$$

with $z \simeq 0.7$, the typical range $\Delta z \simeq 10^{-1}$ which contributes to the hadron production cross section, and $D_u^{h^++h^-}(z, p_T) \simeq 10^{-1}$ the u -quark-to-hadron FF (see e.g. [42]). Using the DØ jet measurement of $d^2\sigma^{jet}/dp_T dy \simeq 200$ pb/(GeV/ c) at $p_T = 100/z \simeq 140$ GeV/ c and $|y| < 1$ [40], one gets for the hadron production cross section a value of $d^3\sigma^h/d^3p \simeq 2 \times 10^{-12}$ mb/(GeV/ c)² which is the right order of magnitude estimate expected in QCD (see the LO PYTHIA curve in Fig. 3). The inconsistency between jet and the CDF large- p_T hadron spectrum is also discussed in detail in [43, 44].

Of course the above argument relies on the factorization assumption that large- p_T hadron production can be expressed as a convolution of hard matrix elements with parton-to-hadron fragmentation functions. Should the FFs – mostly based on fits of e^+e^- data – be non-universal one could imagine that the recent CDF measurement actually reflects dramatic modifications of fragmentation functions in hadronic collisions. This however seems unlikely given the success of the DSS [26] and AKK08 [27] global fits of fragmentation functions which consistently use e^+e^- data together with RHIC measurements in p - p collisions at $\sqrt{s} = 200$ GeV. It is in particular unclear how possible factorization breaking effects could enhance hadron production cross sections by up to 3 orders of magnitude at transverse momenta as large as $p_T = 150$ GeV/ c .

There exist even more general arguments why the large- p_T CDF data cannot be understood as coming from hadron production in perturbative QCD. As discussed in the previous section (Sect. 3.3), the recent CDF spectrum departs from the x_T -scaling behaviour observed in the lower-energy data which can all be described assuming a scaling exponent $n \simeq 5.5$. We find on the contrary that the scaling exponent obtained from the comparison of the large- p_T CDF measurement with the UA1 data at $\sqrt{s} = 200$ GeV is roughly¹⁰ $n \simeq 4$ – 4.7 . This value is extremely close to what is expected in the conformal limit ($n = 4$), i.e. assuming no scaling violations at all in QCD. It is in particular smaller than the exponents

⁹Prompt photon data at the Tevatron are also very well reproduced at large p_T by NLO pQCD calculations [41].

¹⁰The precise value is difficult to obtain since the x_T -spectra at the two c.m. energies have a different slope, already indicating a non-conventional behaviour in one of the two data sets.

expected for jet and prompt photon production [35], despite the fact that scaling violations are expected to be stronger in the hadron production channel because of the additional fragmentation process. What is more, the scaling exponent n obtained at fixed x_T reflects the p_T -dependence of the hard partonic cross section $\hat{\sigma} \sim p_T^{-n}$. Because of the fast variation of the parton densities with x_T , the p_T -slope, α , of the invariant production cross section at fixed \sqrt{s} is expected to be somehow larger than the scale dependence of the partonic cross section, i.e. $\alpha > n$. Surprisingly the value α obtained from a fit of CDF data alone above $p_T = 22 \text{ GeV}/c$ is as small as $\alpha \simeq 3.9$, that is *smaller* than the combined UA1-CDF scaling exponent $n \simeq 4\text{--}4.7$ (and even lower than the smallest scaling exponent $n = 4$!). This clearly indicates that it is not possible to describe the Run-II CDF measurement as coming from hadron production in perturbative QCD. Hence factorization breaking effects in the fragmentation channel cannot be at the origin of the present discrepancy between data and NLO theory.

We conclude from this Section that the facts that (i) the NLO calculations largely fail to reproduce the measured single-hadron spectrum at large p_T while reproducing well the single jet p_T -differential cross sections, and (ii) that the measurement violates simple phenomenological expectations such as x_T -scaling confirmed empirically in all hadronic collisions so far, point to a possible experimental problem in the data above $p_T \approx 20 \text{ GeV}/c$ – or from unknown sources of charged particles – rather than from a sudden breakdown of QCD perturbation theory in the hadron production channel.

After we finished this work, other analyses appeared [43–46] that point out to the same discrepancy between the CDF data [16] and NLO calculations. In [45], Albino, Kniehl and Krämer point out the disagreement between data and NLO theory and question the validity of factorization theorems for large- p_T hadron production, a possibility which we exclude (see discussion above). In [43] it is shown on general grounds that the spectrum measured by CDF is inconsistent with existing Tevatron data on the inclusive jet production cross section and the distribution of hadrons inside jets (a similar argument is given in [44]). This observation allows the authors to exclude, as well, the breakdown of factorization as a possible explanation of the data. They also conclude that new physics scenarios explaining the CDF excess are unlikely, yet they cannot be fully eliminated. Finally, it has been claimed in [46] that weak boson decays into hadrons might explain the CDF data. This possibility is however excluded as shown in Section 3.2, either from the detailed PYTHIA calculations or from the order of magnitude estimate¹¹.

4. Inclusive charged hadron spectra at the LHC

In this last Section of the paper we present first the INCNLO predictions for the charged

¹¹We believe that the calculations in [46] is incorrect partly because of the use of fragmentation functions which are two orders of magnitude larger than the usual fits from e^+e^- data, at large z . We also note that the Jacobian peak in the p_T -spectrum is located at $\sim m_W$ instead of $\sim m_W/2$. Finally it is difficult to conceive why the invariant cross section scales as $\sim s/p_T^6$ instead of conventional behaviour $\sim 1/p_T^4$ (we thank S. Brodsky for pointing this out), which might lead to another two order of magnitude, $\mathcal{O}(s/p_T^2)$, overestimate in [46].

hadron p_T -differential cross sections at mid-rapidity ($|\eta| < 1$) in p - p collisions in the range of CERN LHC energies ($\sqrt{s} = 0.9 - 14$ TeV) including their expected theoretical uncertainties. Second, we discuss two interpolation methods, based on pQCD-ratios and x_T -scaling, that can be used to obtain a baseline charged hadron p - p spectrum at intermediate LHC energies ($\sqrt{s} = 2.76, 5.5$ TeV) needed to compare against similar measurements to be carried out in Pb-Pb collisions.

4.1 INCNLO predictions

Figure 6 (left) shows the INCNLO p_T -differential cross sections in $pp \rightarrow h^\pm X$ at six different c.m. energies (expected to be) reached at the LHC at various stages of the collider programme. The spectra have been obtained with CTEQ6.6 PDFs, DSS FFs and theoretical scales set to $\mu = p_T$. Whereas at p_T below about 10 GeV/c all calculations converge, with increasing c.m. energies (and thus phase-space for hard parton-parton scatterings), the spectra become increasingly flatter. For example, the charged hadron yield at $p_T \approx 100$ GeV/c, increases by a factor of 10 between $\sqrt{s} = 2.76$ TeV and $\sqrt{s} = 7$ TeV and yet by another factor of 5 between the latter and the top LHC energy of 14 TeV. As shown in Fig. 6 (right), for this particular choice of scales/PDFs/FFs, a common power-law exponent of $n = 4.9$ allows one to scale all NLO spectra in the range $\sqrt{s} = 0.9 - 14$ TeV to a universal curve, using the x_T prescription given by Eq. (3.1). This value is slightly smaller than what has been obtained in Section 3.3 from Tevatron and Sp̄S measurements ($n = 5.5$), indicating as expected smaller scaling violations at larger c.m. energy [35].

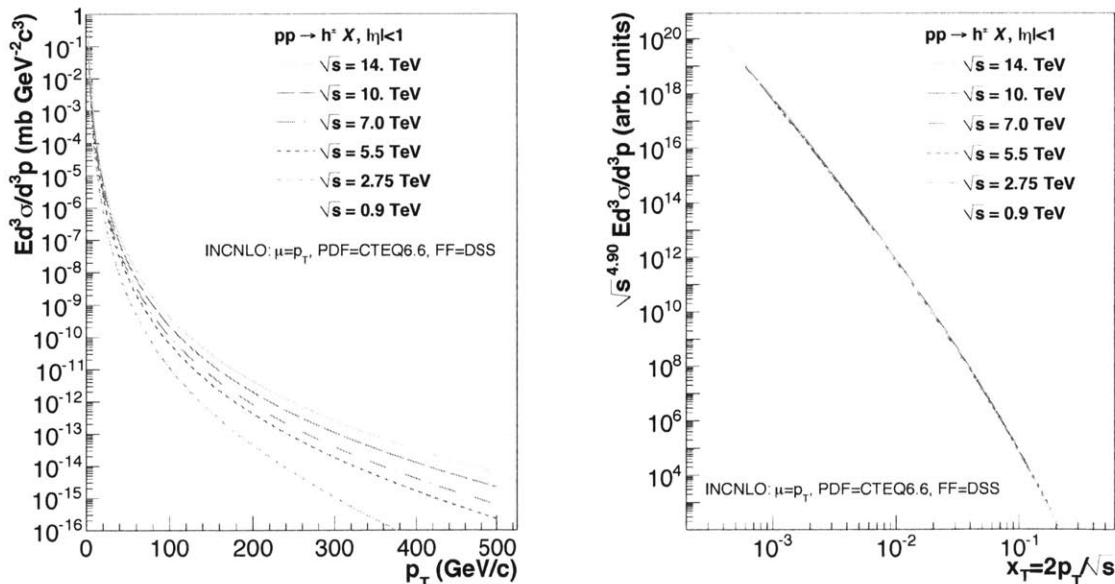


Figure 6: Charged hadron spectra in p - p collisions at $\sqrt{s} = 0.9, 2.76, 5.5, 7, 10$ and 14 TeV predicted by NLO pQCD calculations with CTEQ6.6 parton distribution functions, DSS fragmentation functions, and scales set to $\mu = p_T$: p_T -differential (left) and x_T -scaled with exponent $n = 4.9$ (right).

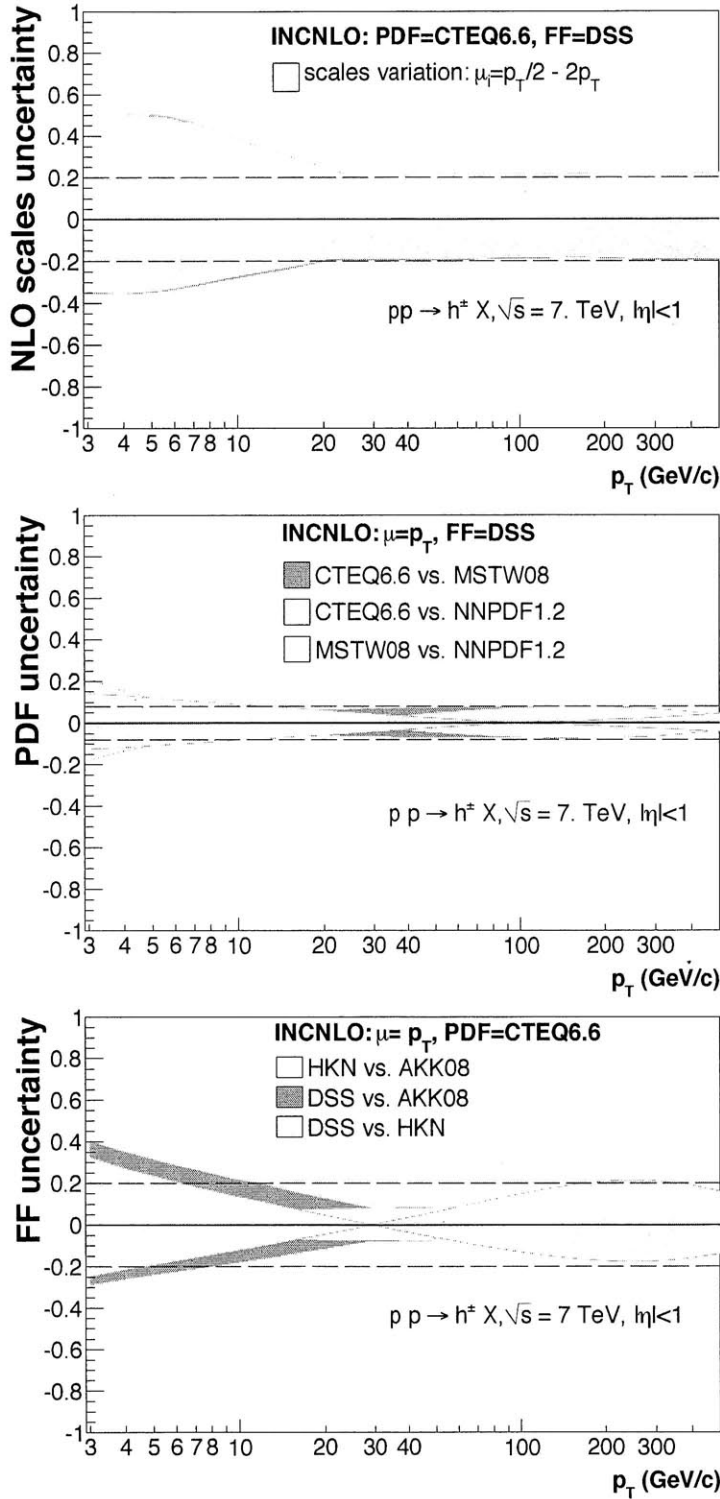


Figure 7: Fractional differences between the INCNLO charged hadron spectra in p - p at $\sqrt{s} = 7$ TeV for varying scales μ_i , PDF and FF. Top: Scale uncertainty obtained for fixed PDF (CTEQ6.6) and FF (DSS) varying all three scales within $\mu_i = p_T/2 - 2p_T$ (the dashed lines indicate a $\pm 20\%$ uncertainty). Middle: PDF uncertainty obtained for fixed $\mu = p_T$ and FF (DSS) with three PDFs: CTEQ6.6, MSTW08, NNPDF1.2 (the dashed lines indicate $\pm 8\%$ differences). Bottom: FF uncertainty obtained for fixed scales ($\mu = p_T$) and PDF (CTEQ6.6) with three FFs: AKK08, DSS, HKNS (the dashed lines represent $\pm 20\%$). - 16 -

To assess the uncertainties linked to the choice of PDFs, FFs and scales μ in the domain of energies covered by the LHC, we have computed $pp \rightarrow h^\pm X$ at a fixed $\sqrt{s} = 7$ TeV for various combinations of the theoretical ingredients as done for the Tevatron prediction (see Section 3.1). Figure 7 (top) shows that the scale uncertainty is smaller ($\pm 20\%$ above $p_T \approx 10$ GeV/ c) than found at lower (Tevatron) energies (see Fig. 2 top). The middle plot of Fig. 7 shows that the uncertainty linked to the PDF choice is also slightly smaller than found at Tevatron, of the order of $\pm 8\%$. Finally, the bottom panel shows that the fractional FF uncertainty is at most of $\pm 20\%$ above $p_T \approx 10$ GeV/ c , whereas below that transverse momentum the uncertainties increase up to $\pm 40\%$. In the range $p_T \approx 30 - 60$ GeV/ c the FF choice has uncertainties of only 10 percent. Those results point again to a somehow smaller FF uncertainty than found at Tevatron (see Fig. 2 bottom). A simple quadrature addition of the fractional uncertainties linked to the scales, PDF and FF choices results in a total theoretical uncertainty of around $\pm 35\%$ for the NLO single inclusive charged hadron spectrum in p - p collisions at LHC energies.

4.2 Interpolation of measured charged-hadron spectra at $\sqrt{s} = 5.5$ TeV

One of the assets of the successful RHIC physics program has been the ability to study the production of hard processes in p - p and nucleus-nucleus (A-A) collisions at the *same* centre-of-mass energy. At the LHC, protons and ions have to travel in the same magnetic lattice¹² i.e. the two beams are required to have the same charge-to-mass ratio Z/A . This limits the beam momentum of a given species to $p = 7$ TeV $\times Z/A$ for the nominal 8.3 T dipole bending field. The nominal nucleon-nucleon c.m. energy for Pb-Pb collisions at the LHC is thus $\sqrt{s_{NN}} = 5.5$ TeV for lead ions with $A = 208$ and $Z = 82$. Since the maximum c.m. energy in the first LHC p - p runs is half of the nominal value, $\sqrt{s} = 7$ TeV in lieu of $\sqrt{s} = 14$ TeV, the first Pb-Pb runs are actually expected at a maximum $\sqrt{s_{NN}} = 2.76$ TeV. In order to correctly normalize the yields measured in Pb-Pb collisions at $\sqrt{s_{NN}} = 2.76, 5.5$ TeV, it will be crucial to get reliable estimates of the corresponding cross sections in p - p collisions at the same c.m. energy. Ideally the predictions in p - p collisions should take advantage of the data accumulated at the LHC at nearby energies and be obtained with the smallest model-dependence possible to avoid any theoretical prejudice. In the following we present two methods for rescaling experimental p - p charged hadron spectra, measured at different c.m. energies than those expected for heavy-ion collisions, based respectively on pQCD yield ratios and x_T -scaling.

4.2.1 Centre-of-mass energy rescaling

As seen in the previous section, at a given c.m. energy there are combined uncertainties of the order of $\pm 35\%$ in the NLO predictions for the *absolute* p_T -differential cross sections of charged hadrons at LHC energies. Most of these uncertainties – in particular the largest scale dependence – however cancel out when taking *ratios* of the predicted perturbative

¹²The magnetic rigidity is defined as $p/Z = Br$ for an ion with momentum p and charge Z that would have a bending radius r in a magnetic field B .

yields at different, yet close, c.m. energies. One can, thus, rescale the p - p spectrum measured at a given $\sqrt{s} = X$ TeV (say, 7 TeV) to a $\sqrt{s} = 2.76, 5.5$ TeV reference value with a simple prescription:

$$\frac{d\sigma_{\text{ref}}(\sqrt{s} = 2.76, 5.5 \text{ TeV})}{dp_T} = \left(\frac{d\sigma_{\text{NLO}}/dp_T(\sqrt{s} = 2.76, 5.5 \text{ TeV})}{d\sigma_{\text{NLO}}/dp_T(\sqrt{s} = X \text{ TeV})} \right) \times \frac{d\sigma_{\text{exp}}(\sqrt{s} = X \text{ TeV})}{dp_T}. \quad (4.1)$$

As an example, we plot in Fig. 8 the scaling factors as a function of p_T obtained from the ratios of 2.76-TeV/7-TeV and 5.5-TeV/7-TeV pQCD yields. They have been obtained with up to 14 combinations of the different theoretical ingredients (scales, PDFs and FFs). The important scale dependence (Fig. 7, top) largely cancels out and only residual differences arise from the slightly different parton x and hadron z momentum fractions probed at different energies (of course, the closer the c.m. energies the smaller the uncertainty in the yield ratios). The maximum theoretical uncertainties of the rescaling factors amount to a small $\pm 5\%$ (resp. $\pm 12\%$) for $\sqrt{s} = 5.5$ TeV (resp. 2.76 TeV), which will be likely below the expected uncertainties in the 7-TeV p - p experimental spectrum alone.

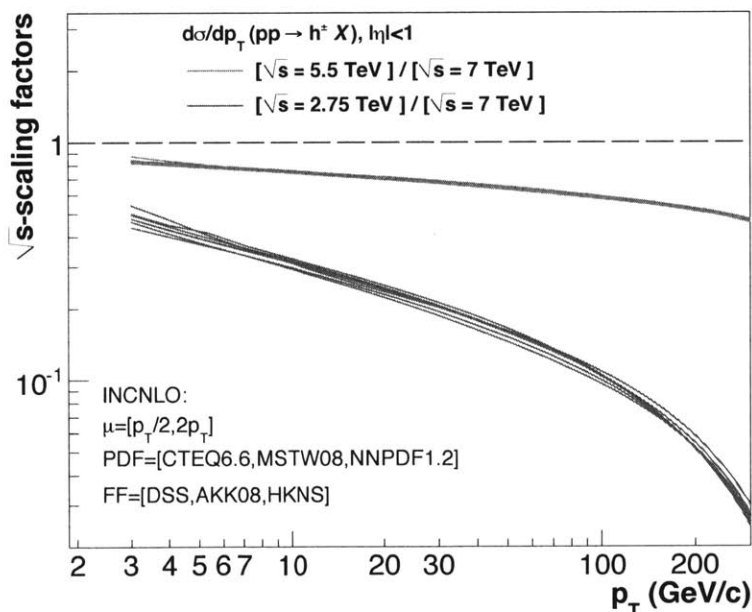


Figure 8: Rescaling factors of the p_T -differential charged hadron cross-sections in p - p at $\sqrt{s} = 7$ TeV down to lower $\sqrt{s} = 2.76, 5.5$ TeV values, obtained from the ratio of the corresponding NLO calculations, Eq. (4.1). The various curves show the small residual differences arising from different scale/PDF/FF choices.

4.2.2 x_T -scaling

In this last section, we suggest to use the x_T -scaling of particle production in high-energy scattering discussed in Sect. 3.3 in order to predict the large- p_T hadron production cross sections in p - p collisions at $\sqrt{s} = 2.76$ and 5.5 TeV from the interpolation of Tevatron ($\sqrt{s} = 1.96$ TeV) and LHC ($\sqrt{s} = 7$ TeV) data.

Assuming that Eq. (3.1) holds from Tevatron to LHC¹³, it is straightforward to deduce the invariant cross section at a given \sqrt{s} and x_T from previous measurements performed at Tevatron and LHC. Using the power-law interpolation¹⁴, Eq. (3.1), the invariant cross section $\sigma^{\text{inv}} \equiv E d^3\sigma/d^3p$ reads

$$\sigma^{\text{inv}}(\sqrt{s}, x_T) = \sigma^{\text{inv}}(\sqrt{s}, p_T = x_T \frac{\sqrt{s}}{2}) = \sigma^{\text{inv}}(1.96 \text{ TeV}, x_T) \times \left[\frac{\sigma^{\text{inv}}(7 \text{ TeV}, x_T)}{\sigma^{\text{inv}}(1.96 \text{ TeV}, x_T)} \right]^\alpha \quad (4.2)$$

where we define $\alpha \equiv \ln(\sqrt{s}/1.96)/\ln(7/1.96)$. The relative uncertainty on the cross section at \sqrt{s} resulting from the power-law interpolation from the data at 7 and 1.96 TeV is thus simply given by

$$\frac{\delta\sigma^{\text{inv}}(\sqrt{s}, x_T)}{\sigma^{\text{inv}}(\sqrt{s}, x_T)} = \sqrt{(1 - \alpha)^2 \left(\frac{\delta\sigma^{\text{inv}}(1.96 \text{ TeV}, x_T)}{\sigma^{\text{inv}}(1.96 \text{ TeV}, x_T)} \right)^2 + \alpha^2 \left(\frac{\delta\sigma^{\text{inv}}(7 \text{ TeV}, x_T)}{\sigma^{\text{inv}}(7 \text{ TeV}, x_T)} \right)^2} \quad (4.3)$$

where $\delta\sigma^{\text{inv}}(1.96 \text{ TeV}, x_T)$ and $\delta\sigma^{\text{inv}}(7 \text{ TeV}, x_T)$ are the uncertainties of spectra measured at Tevatron and LHC, respectively. Let us suppose for simplicity that the experimental relative uncertainty $\delta\sigma^{\text{inv}}/\sigma^{\text{inv}}$ on the hadron spectrum is identical at Tevatron and LHC, thus the relative uncertainty on the interpolated cross section at \sqrt{s} will be $\sqrt{\alpha^2 + (1 - \alpha)^2} \times \delta\sigma/\sigma$, i.e. 0.83 $\delta\sigma^{\text{inv}}/\sigma^{\text{inv}}$ at both $\sqrt{s} = 2.76$ and 5.5 TeV. Therefore, if the measurements at Tevatron and LHC used for the interpolation are precise enough, this procedure would allow for predictions whose uncertainties become possibly smaller than the usual theoretical uncertainties of NLO QCD calculations. Note however that the uncertainty Eq. (4.3) only reflects the propagation of errors in the power-law interpolation and does not account for the systematic uncertainty of the procedure currently used.

Since the invariant cross sections are compared at a given x_T , the p_T range reached at the lower (Tevatron) and upper (LHC) limits of the interpolation domain is crucial. The currently “reliable” Tevatron data extend up to $p_T \simeq 20$ GeV/ c which allows for a prediction up to $p_T \simeq 30$ (60) GeV/ c at $\sqrt{s} = 2.76$ (5.5) TeV. Conversely, the upper limit at $\sqrt{s} = 2.76$ (5.5) TeV is 40% (80%) of the highest p_T to be reached at $\sqrt{s} = 7$ TeV.

In order to check this procedure, the p_T -spectrum of mid-rapidity charged hadrons at $\sqrt{s} = 5.5$ TeV has been estimated from the PYTHIA spectra at $\sqrt{s} = 1.96$ and at 7 TeV using the interpolation Eq. (4.2) with $\alpha = 0.81$, within the range $x_T \approx 2 \cdot 10^{-3} - 0.2$. The

¹³We note that the Tevatron data are measured in p - \bar{p} collisions unlike the p - p collisions at the LHC. The differences between both systems on unidentified hadron production at midrapidity is very small (especially, far away from the valence quark region, i.e. for $x_T \ll 1$).

¹⁴Note that the exponent n depends in principle on p_T (and thus x_T) from the scaling violations in QCD and should approach $n = 4$ in the Bjorken limit. However this dependence is expected to be logarithmic and can be safely neglected in the p_T -range being considered here.

result is plotted in Fig. 9 and compared to the direct PYTHIA calculation of the hadron spectrum at $\sqrt{s} = 5.5$ TeV. As it can be seen, the x_T -interpolated cross section reproduces nicely the MC result at $\sqrt{s} = 5.5$ TeV above $p_T \approx 5$ GeV/ c .

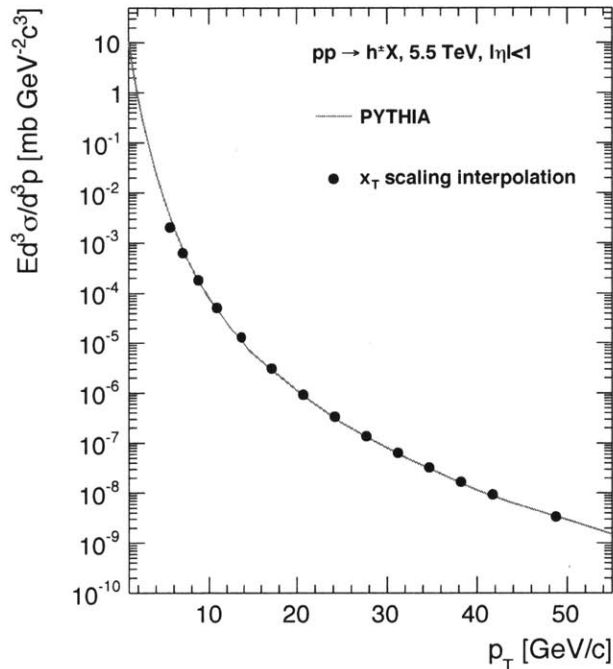


Figure 9: Comparison of the PYTHIA charged hadron spectrum in p - p collisions at $\sqrt{s} = 5.5$ TeV to the x_T -scaling interpolation obtained via Eq. (4.2) from the corresponding PYTHIA spectra at $\sqrt{s} = 1.96$ TeV (p - \bar{p}) and 7 TeV (p - p).

5. Summary

We have compared the latest high- p_T charged particle spectrum measured by CDF in proton-antiproton collisions at $\sqrt{s} = 1.96$ TeV to various perturbative QCD expectations based on next-to-leading-order calculations (INCNLO), parton-shower Monte Carlo (PYTHIA), and x_T -scaling respectively. The NLO calculations employ the latest sets of parton distribution functions (PDFs) and fragmentation functions (FFs). The Tevatron data can be well reproduced below $p_T \approx 20$ GeV/ c for the choice of scales $\mu = 2p_T$, CTEQ6.6 parton densities, and AKK08 parton-to-hadron fragmentation functions. Above this p_T value, the CDF spectrum starts to rapidly deviate, by up to three orders of magnitude, from the predictions. The most important source of theoretical uncertainty, of order $\pm 30\%$, is related to the choice of the factorization, fragmentation and normalization scales. The maximum uncertainties linked to the choice of the PDFs and FFs are $\pm 10\%$ and $\pm 25\%$ respectively. A conservative quadratic addition of all these differences results in a maximum $\pm 40\%$ uncertainty in the NLO calculations which cannot by any means explain

the important data–theory disagreement above $p_T \approx 20$ GeV/ c .

We have next determined with the PYTHIA MC the possible extra contributions of high- p_T charged particles, including leptons, coming from heavy-quark fragmentation as well as from real and virtual vector-boson production either single-inclusive or in association with a jet. The addition of such processes, which amount to about an additional ten percent of the charged particle yield above $p_T \approx 40$ GeV/ c , does not help to reduce the large data–theory deviation. The CDF spectrum also fails to fulfill simple x_T scaling expectations which are empirically confirmed by all other high- p_T hadron spectra measured so far in $p\bar{p}$ collisions in the range $\sqrt{s} = 0.2 - 1.8$ TeV. Moreover, the power-law exponent of the CDF data above $x_T \approx 0.02$, is below the $n = 4$ limit expected from simple dimensional arguments for pure $2 \rightarrow 2$ parton scattering in QCD.

We conclude that the fact that the NLO calculations largely fail to reproduce the measured CDF single hadron spectrum at large p_T while simultaneously reproducing correctly the single jet p_T -differential cross sections, and that the measurement violates simple phenomenological expectations such as x_T -scaling, point to a possible experimental problem in the Tevatron data above $p_T \approx 20$ GeV/ c (or to unknown sources of charged particles not considered here, a possibility disfavoured in [43]).

The NLO predictions of charged hadron spectra at LHC energies $\sqrt{s} = 0.9\text{--}14$ TeV, have also been provided. Finally, we have proposed two simple interpolation procedures, based on a pQCD-rescaling and an x_T -scaling of (future) experimental p - p transverse momentum spectra, in order to obtain the nuclear modification factors of high- p_T charged hadron production in nucleus-nucleus collisions at intermediate ($\sqrt{s_{NN}} = 2.76, 5.5$ TeV) LHC energies.

Acknowledgments

FA thanks J.-P. Guillet and É. Pilon for discussions and the hospitality of CERN PH-TH department where part of this work has been completed. DdE acknowledges support by the 7th EU Framework Programme (contract FP7-ERG-2008-235071). A.S Yoon acknowledges support by U.S DOE grant DE-FG02-94ER40818.

References

- [1] J. C. Collins, D. E. Soper and G. Sterman, Nucl. Phys. B **261** (1985) 104.
- [2] J. F. Owens, E. Reya and M. Gluck, Phys. Rev. D **18** (1978) 1501.
- [3] F. Aversa, P. Chiappetta, M. Greco and J. P. Guillet, Nucl. Phys. B **327** (1989) 105.
- [4] D. de Florian, Phys. Rev. **D67**, 054004 (2003)
- [5] B. Jäger, A. Schäfer, M. Stratmann, and W. Vogelsang, Phys. Rev. **D67**, 054005 (2003)
- [6] D. de Florian and W. Vogelsang, Phys. Rev. D **71** (2005) 114004; W. Vogelsang, private communication.

- [7] D. de Florian, W. Vogelsang and F. Wagner, Phys. Rev. D **76**, 094021 (2007).
- [8] S. S. Adler *et al.* [PHENIX Collab.], Phys. Rev. Lett. **95** (2005) 202001.
- [9] S. Albino, arXiv:0810.4255 [hep-ph]; F. Arleo, Eur. Phys. J. C **61** (2009) 603.
- [10] See e.g. D. d'Enterria and B. Betz, Lect. Notes Phys. **785** (2010) 285.
- [11] A. Breakstone *et al.* [CDHW Collab.] Z. Phys. C **69** (1995) 55; T. Akesson *et al.* [AFS Collab.], Nucl. Phys. B **209** (1982) 309.
- [12] J. Adams *et al.* [STAR Collab.], Phys. Rev. Lett. **91** (2003) 172302; I. Arsene *et al.* [BRAHMS Collab.], Phys. Rev. Lett. **93** (2004) 242303.
- [13] C. Albajar *et al.* [UA1 Collab.], Nucl. Phys. B **335** (1990) 261.
- [14] F. Abe *et al.* [CDF Collab.], Phys. Rev. Lett. **61** (1988) 1819.
- [15] D. E. Acosta *et al.* [CDF Collab.], Phys. Rev. D **65** (2002) 072005.
- [16] T. Aaltonen *et al.* [CDF Collab.], Phys. Rev. D **79** (2009) 112005.
- [17] F. Sikler, PoS High- p_T -LHC (2008) 011; J. P. Revol, Nucl. Phys. Proc. Suppl. **177-178** (2008) 60; W. H. Bell [ATLAS Collab.], in MPI'08, Perugia, DESY-Proceeds.
- [18] V. Khachatryan *et al.* [CMS Collaboration], arXiv:1002.0621 [hep-ex].
- [19] K. Adcox *et al.* [PHENIX Collab.], Nucl. Phys. A **757** (2005) 184; J. Adams *et al.* [STAR Collab.], Nucl. Phys. A **757** (2005) 102.
- [20] P. Aurenche, M. Fontannaz, J.-P. Guillet, B. A. Kniehl and M. Werlen, Eur. Phys. J. C **13**, 347 (2000); P. Aurenche, T. Binoth, M. Fontannaz, J.-P. Guillet, G. Heinrich, É. Pilon and M. Werlen, http://lappweb.in2p3.fr/lapth/PHOX_FAMILY/readme_inc.html
- [21] P. Aurenche, M. Fontannaz, J. P. Guillet, B. A. Kniehl and M. Werlen, Eur. Phys. J. C **13**, 347 (2000)
- [22] P. M. Nadolsky *et al.*, Phys. Rev. D **78** (2008) 013004.
- [23] A. D. Martin, W. J. Stirling, R. S. Thorne and G. Watt, Eur. Phys. J. C **63** (2009) 189; A. D. Martin, W. J. Stirling, R. S. Thorne and G. Watt, arXiv:0905.3531 [hep-ph].
- [24] R. D. Ball *et al.* [NNPDF Collab.], Nucl. Phys. B **809**, 1 (2009) [Erratum-ibid. B **816**, 293 (2009)].
- [25] M. R. Whalley, D. Bourilkov, R. C. Group, hep-ph/0508110; <http://hepforge.cedar.ac.uk/lhapdf/>
- [26] D. de Florian, R. Sassot and M. Stratmann, Phys. Rev. D **75**, 114010 (2007).
- [27] S. Albino, B. A. Kniehl and G. Kramer, Nucl. Phys. B **803** (2008) 42.
- [28] M. Hirai, S. Kumano, T. H. Nagai and K. Sudoh, Phys. Rev. D **75** (2007) 094009.
- [29] G. Sterman, Nucl. Phys. B **281**, 310 (1987); S. Catani and L. Trentadue, Nucl. Phys. B **327**, 323 (1989); Nucl. Phys. B **353**, 183 (1991).
- [30] T. Sjöstrand, S. Mrenna and P. Skands, JHEP 0605 (2006) 026 [PYTHIA v6.411 is used].
- [31] S. J. Brodsky, G. R. Farrar, Phys. Rev. Lett. **31** (1973) 1153; D. W. Sivers, S. J. Brodsky, R. Blankenbecler, Phys. Rept. **23** (1976) 1; R. Blankenbecler, S. J. Brodsky, J. F. Gunion, Phys. Rev. D **18** (1978) 900; M. J. Tannenbaum, arXiv:0904.4363 [nucl-ex]

- [32] M. Cacciari, S. Frixione, M. L. Mangano, P. Nason and G. Ridolfi, JHEP **0407** (2004) 033; M. Cacciari, private communication.
- [33] MPI'08 Workshop Proceeds, Perugia, Italy, Oct. 2008. DESY-PROC-2009-06; arXiv:1003.4220.
- [34] C. Lourenço and H. K. Wöhri, Phys. Rept. **433** (2006) 127.
- [35] F. Arleo, S. J. Brodsky, D. S. Hwang and A. M. Sickles, arXiv:0911.4604 [hep-ph].
- [36] F. James and M. Roos, Comput. Phys. Commun. **10** (1975) 343.
- [37] T. Kluge, K. Rabbertz and M. Wobisch, arXiv:hep-ph/0609285;
- [38] Z. Nagy, Phys. Rev. D **68** (2003) 094002.
- [39] T. Aaltonen *et al.* [CDF Collab.], Phys. Rev. D **78**, 052006 (2008) [Erratum-ibid. D **79**, 119902 (2009)]
- [40] V. M. Abazov *et al.* [D0 Collab.], Phys. Rev. Lett. **101** (2008) 062001.
- [41] P. Aurenche, M. Fontannaz, J. P. Guillet, É. Pilon and M. Werlen, Phys. Rev. D **73** (2006) 094007
- [42] Fragmentation Function Generator, <http://lappweb.in2p3.fr/lapth/generators>
- [43] M. Cacciari, G. P. Salam and M. J. Strassler, arXiv:1003.3433 [hep-ph].
- [44] A. S. Yoon, E. Wenger and G. Roland, arXiv:1003.5928 [hep-ph].
- [45] S. Albino, B. A. Kniehl and G. Kramer, arXiv:1003.1854 [hep-ph].
- [46] B. L. Ioffe, arXiv:1005.1078.

Convoluting jet spectra with fragmentation functions: a cross-check of the charged particle p_T spectrum

Andre S. Yoon, Edward Wenger, and Gunther Roland

Laboratory for Nuclear Science, MIT, Cambridge, MA 02139-4307, USA

Abstract

Motivated by the excellent agreement between next-to-leading-order pQCD calculations and the inclusive jet spectra measured by CDF, we cross-check PYTHIA fragmentation functions. The convolution of the measured jet spectra with unmodified PYTHIA fragmentation functions results in reasonable agreement with the PYTHIA charged particle spectrum over the entire p_T range of interest, while there is a sizable disagreement with the measured charged particle spectrum above $p_T = 30$ GeV/c. In an attempt to understand the source of this discrepancy, we introduce a number of increasingly different toy-model fragmentation functions for the convolution. However, even the most extreme fragmentation functions result in an underestimate of the high- p_T CDF spectrum, which remains irreconcilable with the measured jet spectra.

1 Introduction

After an intense period of commissioning and a short period of collisions at 0.9 and 2.36 TeV in 2009 [1], the continuous operation of the Large Hadron Collider (LHC) at multi-TeV collision energies looms just around the corner. Among the first measurements at the LHC will be the inclusive production of single charged particles (or hadrons), i.e. $pp \rightarrow h + X$, measured differentially in pseudorapidity (η) and transverse momentum (p_T) [2]. While both distributions are the subject of Quantum Chromodynamics (QCD), the former is generally modeled phenomenologically due to the non-perturbative nature of low- p_T bulk production, while the latter, which involves hard processes, is generally described by the perturbative theory of QCD (pQCD). Hard production of high transverse momenta particles ($p_T \geq 2$ GeV/c) originates from the fragmentation of hard-scattered partons [3]. The fragmentation of hard-scattered partons into hadrons is described by the probability of finding a hadron carrying a specific fraction of the parton momentum, known as the fragmentation function (FF). In hadronic collisions, a full description also requires knowledge of the distribution of the initial partons within the colliding hadrons, known as the parton distribution function (PDF). The measurement of the inclusive charged particle p_T spectrum at large transverse momentum, therefore, measures in essence the convolution of three pieces: the hard-parton scattering cross section, the PDFs and the FFs.

Especially at LHC energies, where a large fraction of the total cross section is comprised of the underlying QCD dynamics, a precise understanding of the QCD background rates is not only important for understanding Standard Model particle production (W^\pm , Z, Higgs), but also for rare processes beyond the Standard Model [4, 5]. In addition, the inclusive charged particle p_T spectrum in pp collisions is an important reference for studying high- p_T particle suppression in the dense QCD medium produced in high energy nucleus-nucleus (AA) collisions [6, 7]. The suppression (or enhancement) of high- p_T particles is typically quantified by the ratio of charged particle p_T spectra in AA collisions to those in pp collisions scaled by the number of binary nucleon-nucleon collisions, known as the nuclear modification factor R_{AA} [7]. At RHIC, the factor of 5 suppression seen in R_{AA} [8, 9, 10, 11] was an early indication of strong final-state medium effects on particle production. It is similarly expected to be one of the first measurements performed by the heavy ion programs at the LHC [12].

Experimentally, the inclusive charged particle p_T spectra have been measured in pp and $p\bar{p}$ over a wide range of center-of-mass energies from 31 GeV to 1.96 TeV [13, 14, 15, 16, 17], and recently at 2.36 TeV at LHC [18, 19]. While the measurements up to $\sqrt{s}=1.8$ TeV (and $\sqrt{s}=2.36$ TeV) are limited to $p_T < 20$ GeV/c, the latest CDF measurement [17] at $\sqrt{s}=1.96$ TeV, based on an integrated luminosity of 506 pb^{-1} , extended the p_T reach up to about 140 GeV/c for the first time. However, the measurement shows that the high- p_T region cannot be described by the power-law modeling established in their earlier measurement at $\sqrt{s}=1.8$ TeV [16]. The incompatibility between the new measurement and the power-law modeling grows from 50% at $p_T = 20$ GeV/c up to a factor of 1000 at $p_T = 125$ GeV/c. In order to fit the entire p_T range, a more sophisticated parameterization was introduced [16], namely another power law term was added to the previous fit. With the new parameterization, the normalized chi-square (χ^2/ndf) is reduced from 258/182 to 80/223, albeit with a factor of 5-7 discrepancy remaining above ~ 90 GeV/c. The similarity between the spectra observed at both collision energies up to $p_T = 9$ GeV/c (the range measured at 1.8 TeV) suggests that the incompatibility cannot be accounted for by the 9% increase in center-of-mass energy.

A disagreement of similar magnitude is observed when the measured high- p_T spectra are compared to leading-order (LO) and next-to-leading-order (NLO) pQCD calculations, as well as a simple extrapolation based on x_T scaling [20, 21]. The validity of the factorization theorem is even questioned in [21], as a response to the huge discrepancy seen at high p_T – the regime where their NLO pQCD calculation should be most reliable. While the CDF paper [17] offers no possible physics origin for the exceptionally large measured cross section at high p_T , the sizable incompatibility with not only their former power-law modeling but also (N)LO pQCD calculations and x_T scaling suggests that further study might be necessary.

At the LHC, the nominal heavy ion collisions ($PbPb$) will take place at a center-of-mass energy of 5.5 TeV per nucleon pair, corresponding to the nominal pp collision energy of 14 TeV for the same magnetic rigidity ¹. For the first year, however, as the center-of-mass energy of pp collisions will be limited to 7 TeV [1], the corresponding $PbPb$ center-of-mass energy will be limited to 2.76 TeV per nucleon pair. Since the R_{AA} measurement requires a pp reference at the same collision energy as $PbPb$, the first-year heavy ion measurements at 2.76 TeV will rely on a combination of theory predictions and interpolations between lower energy measurements and those performed at 7 TeV. In this perspective, the CDF measurement is unique in two regards. First, the center-of-mass energy of 1.96 TeV is closest to that planned for the first-year heavy ion run (except for the measurement at 2.36 TeV which is limited in p_T reach). Second, the reach to high p_T far exceeds any previous measurements. Thus, understanding the observed discrepancy with the pQCD prediction is crucial.

In contrast to the observed discrepancy in the charged hadron spectra, the CDF inclusive jet spectrum are in fact well described by NLO pQCD calculations [22, 23, 24, 25]. This is of particular interest, as high- p_T charged particles are understood in pQCD to be predominantly ² the fragmentation products of hard-scattered partons from the collision, i.e. “jets”. In fact, NLO pQCD calculations carried out for charged particle spectra differ only from those for jet spectra by the addition of a parameterization of jet fragmentation. It is shown in [20] that the uncertainties related to different parameterizations of fragmentation functions (FF) and parton distribution functions (PDF) only amount to 10% and 25%, respectively. In this case, the only possible explanations for the exceptionally large measured cross section are either that the current modeling of fragmentation is dramatically incorrect (by a factor of 1000!), or there is a flaw in the measurement, or there is a breakdown in the QCD factorization theorem as suggested in [21].

In this paper, we attempt to reconcile the apparent discrepancy in the CDF inclusive charged particle spectrum by convoluting the CDF inclusive jet spectra measurement with a set of increasingly different fragmentation functions. We start with the PYTHIA fragmentation functions to see what the CDF jet spectra imply for the charged hadron spectra absent any surprises in the fragmentation. Then, we modify the fragmentation functions arbitrarily within the bounds of energy and momentum conservation to see if the measured hadron spectrum can be recreated. Finally, by using the hardest imaginable fragmentation function – each jet fragments into a single charged hadron – we rule out the possibility that unexpectedly hard fragmentation is responsible

¹For the same magnetic rigidity of the LHC machine, the center-of-mass energy per nucleon pair in heavy ion collisions is just defined as the center-of-mass energy in pp scaled by the charge-to-mass ratio of the lead ion: 82/208.

²There is a contribution from the leptonic decays of weak gauge bosons, but this sub-leading processes is negligible in the inclusive spectrum. In PYTHIA it amounts to only 10% at most [20]. It is also possible for high- p_T hadrons to originate in the absence of a jet in a higher-twist (HT) picture. However, as the production of hadrons in HT is power-law-suppressed in p_T , that contribution should be negligible as well [26].

for the exceptionally large measured cross section.

The rest of the paper is organized as follows. In section 2, we introduce the technical details of the convolution method. We then describe the measured inclusive jet spectra and the PYTHIA inclusive jet spectra in section 3. In section 4, we argue that the convolution method can effectively reproduce the charged particle spectra within PYTHIA, i.e. by convoluting the PYTHIA jet spectrum with the PYTHIA fragmentation functions. We then show that the CDF jet spectra convoluted with the same PYTHIA fragmentation functions gives a similar result. In section 5, we compare to the CDF charged hadron spectrum the results of convoluting the CDF jet spectra with an arbitrary set of increasingly unrealistic fragmentation functions. The final section contains our conclusions and a further discussion on how this convolution method may be used to cross-check charged particle cross sections.

2 Convolution Method

In the QCD factorization scheme of hadron-hadron collisions [3, 27], the invariant cross section for inclusive high- p_T hadron production is given by:

$$E_C \frac{d^3\sigma(AB \rightarrow CX)}{d^3p_C} = \frac{1}{\pi} \sum \int_0^1 dx_a \int_0^1 dx_b q_a^A(x_a; Q^2) q_b^B(x_b; Q^2) \frac{1}{z} D_C^c(z; Q^2) \frac{d\hat{\sigma}(ab \rightarrow cd)}{d\hat{t}}, \quad (1)$$

where the parton distribution function $q_a^A(x_a)$ describes the number density of constituents a within hadron A with longitudinal momentum fraction x_a (in the range $x_a \rightarrow x_a + dx_a$). The fragmentation function $D_C^c(z)$ represents the probability that parton c hadronizes into C carrying a fraction z of the parton energy. Q^2 is the characteristic energy scale of the hard scattering. The LO cross section for the hard scattering of partons a and b at short distance is denoted by $\hat{\sigma}$. The summation is over all partons a, b, c , and d . The hadronization of parton d is implicit in the summation. A direct calculation of Eq. 1 is possible up to a certain order in α_s provided that $q_a^A(x_a)$ and $D_C^c(z)$ are given.

Similarly, the related cross section for inclusive jet production ($AB \rightarrow Jet + X$) can be given by the same equation, but with the term $(1/z)D_C^c(z; Q^2)$ replaced by $\delta(1-z)$, since $\sum_C D_C^c(z) = \delta(1-z)$. The convolution method is essentially equivalent to evaluating Eq. 1 but based on measurements of the inclusive jet cross section and the fragmentation functions, provided that both are measured:

$$\begin{aligned} \sigma_{had} &= PDF_{a/A} \otimes PDF_{b/B} \otimes \hat{\sigma}(\text{hard parton scattering}) \otimes \text{FF} \\ &= \sigma_{jet} \otimes \text{FF}. \end{aligned} \quad (2)$$

In this case, it is clear that a knowledge of the inclusive jet cross section and the fragmentation functions associated by jet- p_T are enough to reproduce the hadron spectra. The convolution of the jet cross section weighted in each jet- p_T bin by the associated fragmentation function can be cast into the following simple differential form:

$$\frac{d\sigma_{had}}{dp_T dy_{had}} \simeq \sum_{i=0} \frac{d\sigma_{jet}}{dp_{T,jet} dy_{jet}} \Big|_{p_{T,jet}=p_{T,jet}^i} \times \Delta p_{T,jet}^i \Delta y_{jet} \times FF_i(p_T, p_{T,jet}^i), \quad (3)$$

where the summation is over all jet- p_T bins, and the custom-built fragmentation function FF_i is defined as:

$$FF_i(p_T, p_{T,jet}^i) \equiv \frac{\Delta(\frac{d\sigma_{had}}{dp_T dy_{had}})}{\Delta\sigma_{jet}} \Big|_{p_{T,jet}=p_{T,jet}^i} \quad (4)$$

The quantity FF_i is just the transverse momentum differential cross section of charged particles per jet cross section at a certain jet- p_T with finite bin size.

The first term in Eq. 3 is well known not only from theoretical calculations but also from measurements of the inclusive jet cross section. However, the fragmentation functions are not known from any measurement in the exact form that they are needed (i.e. Eq. 4). In particular, the convolution requires that FF_i be measured in the same bins of jet- p_T as the inclusive jet cross section measurement.

3 Inclusive Jet Spectra (Data vs PYTHIA)

The inclusive jet cross sections have been reported on numerous occasions by the CDF collaboration, showing good agreement with NLO pQCD predictions for different jet algorithms³ [22, 23, 24, 25]. In particular, their latest measurement of the jet cross section [22], which used a mid-point cone algorithm on 1.13 fb^{-1} of $p\bar{p}$ collision data, agrees over a large range of jet- p_T and rapidity not only with the NLO pQCD prediction within the respective experimental and theoretical uncertainties, but also with the previous CDF measurements using different jet-finding algorithms. Good agreement with NLO pQCD predictions is also seen by the $D\emptyset$ measurement over a similar jet- p_T range [28]. While a direct comparison of the inclusive jet measurements between the two experiments is not possible due to different rapidity binning, systematic data-theory comparisons for the determination of LO, NLO, and NNLO pQCD PDFs show no significant inconsistency between the measurements [29]. In order to test whether the disagreement [17, 20] in the charged particle spectra between CDF and PYTHIA might originate from a difference in the respective jet cross sections, we compare the latest inclusive jet cross section measurement with that from PYTHIA.

To maintain similar statistics over a large range of jet- p_T , several QCD jets samples⁴ were generated in bins of the hard parton momentum transfer ($\hat{p}_T = 0\text{-}15, 15\text{-}20, 20\text{-}30 \text{ GeV}/c$, etc.) using the D6T [30] tune of PYTHIA 6.41 (or 6.42) [31]. The different \hat{p}_T bins were then combined after properly weighting each sample by its corresponding cross section⁵. Several different jet finding algorithms⁶ were used at MC level to test for possible algorithmic dependences of the jet

³ k_T [32] and midpoint cone [33] algorithms are used.

⁴(MSEL = 1) with *low* p_T process (ISUB = 95) added for $\hat{p}_T \rightarrow 0$ to avoid a divergent jet cross section.

⁵The cross section for the first \hat{p}_T bin was obtained by taking the difference of the minimum bias cross section with the sum of the cross sections for all other \hat{p}_T bins.

⁶Iterative cone, k_T , and SIS cone were used with a cone radius $R \equiv \sqrt{\Delta\phi^2 + \Delta y^2} = 0.7$

cross section. The variation was observed to be smaller than the uncertainties in the measurement over the entire jet- p_T range.

Figure 1(a) shows the inclusive jet cross sections from CDF data and PYTHIA, where the different rapidity (y) intervals have been scaled by arbitrary factors for clarity of comparison. In Fig. 1(b), where the different y bins have been plotted on the same scale, it is clear that the jet cross section decreases towards more forward rapidities. In the bottom of the figure, the ratio of the CDF jet cross section to the PYTHIA cross section is shown for each y bin. The inclusive jet cross section obtained from the PYTHIA D6T samples tends to underestimate the measured jet cross section. We note, however, that the default K -factor of $\sigma_{NLO}/\sigma_{LO} = 1$ was used in the generation of our PYTHIA samples. Therefore, one may claim that the difference would be reduced by applying a greater-than-unity K -factor to account for the known difference between σ_{NLO} and σ_{LO} .⁷ Other than the underestimation of the overall scale, PYTHIA describes the rapidity dependence of the jet spectra quite well for a wide range of jet- p_T . This study shows that the inclusive charged particle p_T spectra should not differ by more than a factor of 3 due to differences in the measured and PYTHIA jet cross sections (see lower panel of Fig. 1(b)).

4 Convolution with PYTHIA fragmentation functions

4.1 PYTHIA fragmentation functions

The fragmentation functions defined in Eq. 4 are obtained from the same PYTHIA samples described in the previous section for the jet cross sections. Since these samples were generated in a series of \hat{p}_T bins, some care must be taken to ensure that the contributions from each \hat{p}_T sample are properly accounted for in both the numerator and the denominator of Eq. 4. Specifically, the fragmentation functions are determined via the following sum:

$$\begin{aligned}
 FF_i(p_T, p_{T,jet}^i) &= \left. \frac{\Delta(\frac{d\sigma_{had}}{dp_T dy_{had}}|_{|y_{had}|<1.0})}{\Delta\sigma_{jet}|_{|y_{jet}|<y'_{jet}}} \right|_{p_{T,jet}=p_{T,jet}^i} \\
 &= \sum_j \left[\frac{\Delta(dN_{had}^j/dp_T dy_{had})}{N_{event}^j/\sigma_{event}^j} \right] / \sum_k \left[\frac{\Delta N_{jet}^k}{N_{event}^k/\sigma_{event}^k} \right], \quad (5)
 \end{aligned}$$

where N_{event}^j and σ_{event}^j are the number of events and the cross section for the j^{th} \hat{p}_T bin, respectively. Each fragmentation function is evaluated at $p_{T,jet} = p_{T,jet}^i$ with a width of $\Delta p_{T,jet}^i$ for the i^{th} jet- p_T bin. N_{had} and N_{jet} are the number of charged particles and the number of jets in $|y_{had}| < 1.0$ and $|y_{jet}| < y'_{jet}$, respectively. (Note that y_{had} and y_{jet} are not necessarily the same.)

The PYTHIA fragmentation functions $FF_i(p_T, p_{T,jet}^i)$ for $|y_{had}| < 1.0$ and $|y_{jet}| < 1.0$ are shown in Fig. 2(a) for $p_T < 140$ GeV/c and bins of $p_{T,jet}^i$ corresponding to the CDF jet cross-section measurement. The hardening of the fragmentation function with increasing jet- p_T is apparent. The same fragmentation functions are shown in Fig. 2(b), where each has been weighted by the associated jet cross section in order to compare their relative contributions to the charged

⁷For example, the K -factor for the inclusive charged particle spectra at Tevatron energy ($\sqrt{s} = 1.8$ TeV) is found phenomenologically to be slightly above unity (1.28) [34]

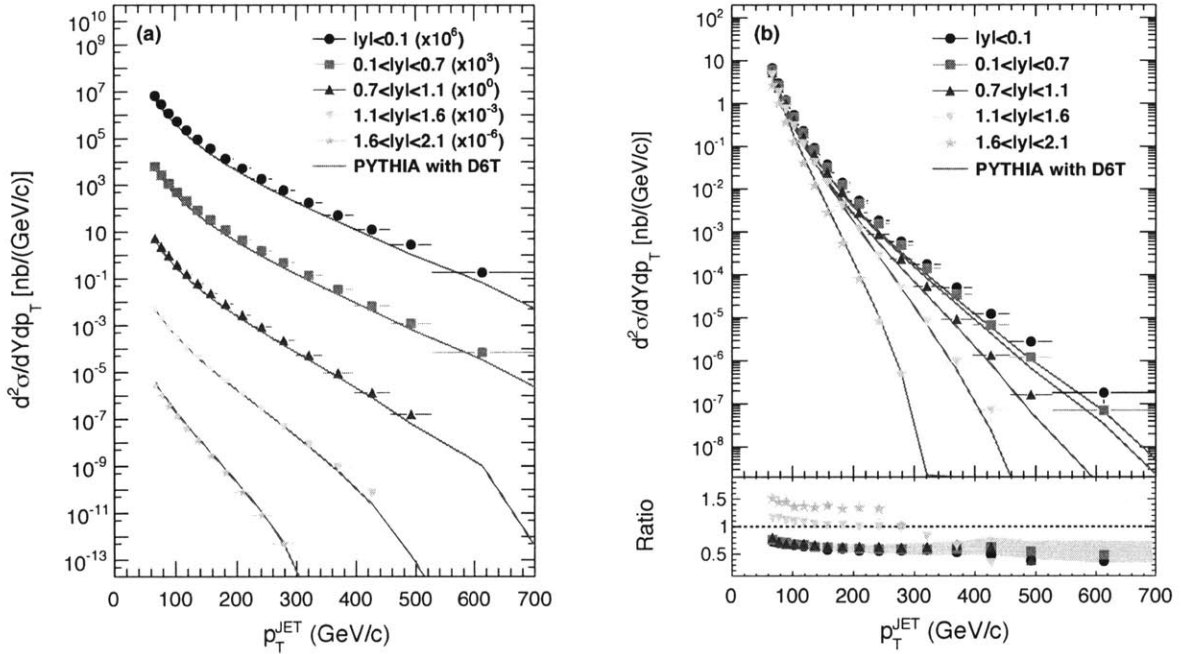


Figure 1: (a) The inclusive jet cross sections in different rapidity intervals. CDF values (filled markers) measured at hadron level using the midpoint algorithm (cone radius=0.7); error bar is statistical only. PYTHIA generated with D6T tune (solid lines) using an iterative cone algorithm (radius=0.7). An arbitrary factor of 10^3 separates the different rapidity intervals as in the CDF paper for clarity. (b) The same distributions as in (a), but with all rapidity bins on the same scale. The ratios of the PYTHIA jet cross sections to the measured values are plotted in the lower panel with systematic uncertainties drawn for the measurement in $0.1 < |y| < 0.7$ to illustrate the size of the uncertainties involved in the measurement.

particle spectra. Due to the steeply falling nature of the jet cross section, the vast majority of charged particles in the region of interest ($30 \text{ GeV}/c < p_T < 140 \text{ GeV}/c$) are from jets with $p_T < 400 \text{ GeV}/c$. The contribution from higher p_T jets is less than 0.1%.

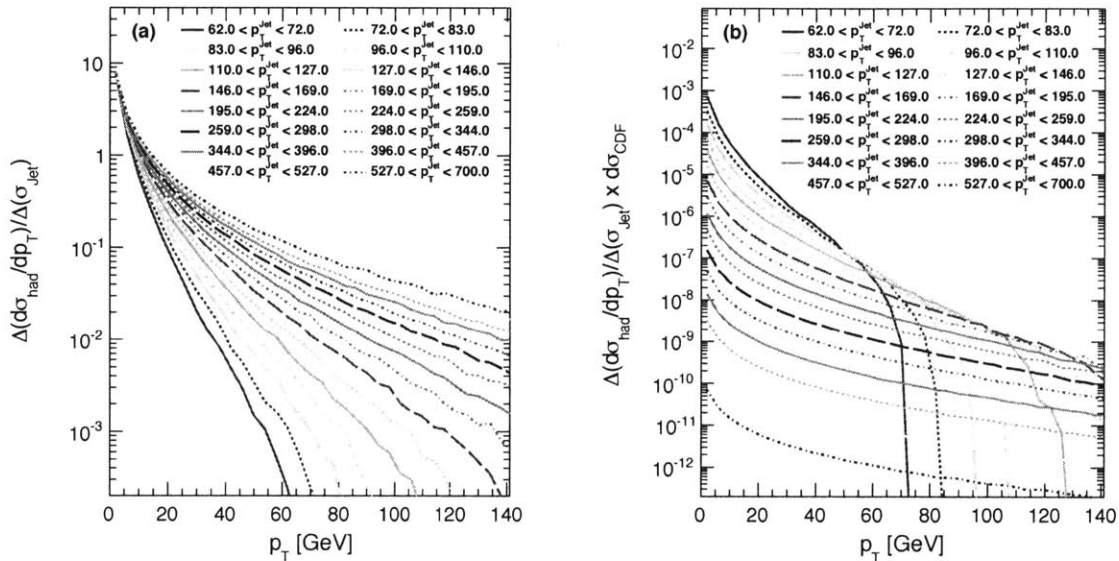


Figure 2: (a) PYTHIA D6T fragmentation function in each jet- p_T bin. (b) The same fragmentation functions weighted by the associated jet cross section measured by CDF. $d\sigma_{\text{CDF}}$ corresponds to $d\sigma_{\text{jet}}/dp_T dy$ in Eq. 3.

Although a direct verification of the PYTHIA fragmentation functions in Fig. 2 is not possible in the absence of the same measurement on 1.96 TeV data, reasonable (and sometime very good) agreement⁸ has been seen between PYTHIA and a variety of fragmentation-related measurements [35, 36, 37, 38]. For example, detailed CDF studies of inclusive jet shapes at $\sqrt{s}=1.96 \text{ TeV}$ [38] show that the integrated and differential jet shapes are well described by PYTHIA Tune A for jet- p_T up to 380 GeV/c. Furthermore, the fact that PYTHIA and NLO charged particle spectra are in reasonable agreement [20], where the latter uses fragmentation functions based on global data fits (AKK [39], DSS [40], HKNS [41]), implies that PYTHIA fragmentation should be comparable to these global fits. In this case, the fragmentation functions obtained from PYTHIA should be a reliable proxy for the global understanding of fragmentation from data. Regardless, this paper investigates discrepancies significantly larger than 50%, so the detailed matching of the PYTHIA fragmentation model to measurement is not our primary concern. Moreover, model-independent fragmentation functions will be introduced later in Section 5.

⁸There is some indication that the fragmentation properties of quark jets are rather poorly described by PYTHIA when quark and gluon jet are investigated separately [35].

4.2 Convolution of PYTHIA jet spectrum with PYTHIA fragmentation functions

To test the effectiveness of the convolution technique put forth in Section 2, we first attempt to retrieve the known PYTHIA charged particle p_T spectrum from a convolution of the PYTHIA jet spectra with the PYTHIA fragmentation functions calculated in Eq. 5 and plotted in Fig. 2. We perform the convolution separately for each of the five jet rapidity intervals (see Fig. 1), in order to quantify their relative contributions to the single particle spectra. The results of this test are shown in Fig. 3, where the PYTHIA charged particle spectrum (solid line) is compared to the output of the convolution for charged particles with $|\eta| < 1.0$. The relative contribution of jets in different y ranges to $|\eta| < 1.0$ charged particles can be seen in Fig. 3(a), where the rapidity ranges are indicated by the same symbols as in Fig. 1. As expected from the measured jet shapes⁹ [38], the large majority of particles fragment from jets within $|y| < 1.1$. In Fig. 3(b), the contributions from all rapidity intervals are summed and compared to the true charged particle spectrum. In the bottom of that figure, the ratio of the convoluted spectra to the true charged particle spectra is shown. Except at low p_T (below a few GeV/c) where non-perturbative particle production and jet reconstruction inefficiency become relevant, the convolution method reproduces the true spectra almost exactly (well within 0.01% for $p_T \geq 6$ GeV/c).

4.3 Convolution of measured jet spectrum with PYTHIA fragmentation functions

With the robustness of the convolution technique verified on PYTHIA, the next step is to introduce the CDF measurement of the jet spectrum in the convolution. Given the level of agreement already demonstrated in Section 3 between PYTHIA and the measured jet spectra, one should expect the convolution based on the measured jet spectra to result in quite similar charged particle spectra as already seen for PYTHIA in Fig. 3. However, there is an additional complication involved in using the measured jet spectra in the convolution instead of the generated PYTHIA events.

Unlike for PYTHIA where the jet cross section is available down to very low p_T , the jet cross section measured by CDF has only been published between 62 and 700 GeV/c. The effect on the charged particle spectrum from excluding the fragmentation products of jets below 62 GeV/c is shown for PYTHIA in Fig. 3(b) represented by empty squares. These low- p_T jets contribute significantly to the charged particle spectrum up to around 40 GeV/c. As expected, the contribution completely vanishes at $p_T = 62$ GeV/c, since a jet cannot fragment into a more energetic charged particle. Since the disagreement with (N)LO pQCD calculations is most prominent above $p_T \geq 50$ GeV/c, a detailed understanding of the low- p_T contributions is not central to this investigation. Hereafter, whenever the measured jet cross section is used in the convolution, we use the PYTHIA value for $p_T < 62$ GeV/c.

In Fig. 4(a), the charged particle p_T spectra are shown for the convolutions based on the measured jet cross sections, again using the same symbol conventions for the rapidity ranges as in Fig. 1. In Fig. 4(b), the contributions from all rapidity intervals are summed as it is done in 3(b). To see the variation of the obtained spectrum due to the uncertainties in the CDF jet measurement, a conservative choice of 82%, which is the largest systematic uncertainty from the measurements in the first three rapidity intervals for jet- p_T below 457 GeV is applied to the obtained charged particle spectrum, which is shown as a grey band. Also, a grey band is

⁹From measured jet shapes, we know that the majority of the energy in a jet is concentrated around jet axis. So, the rapidity of the leading tracks should correlate quite closely with the rapidity of the jet.

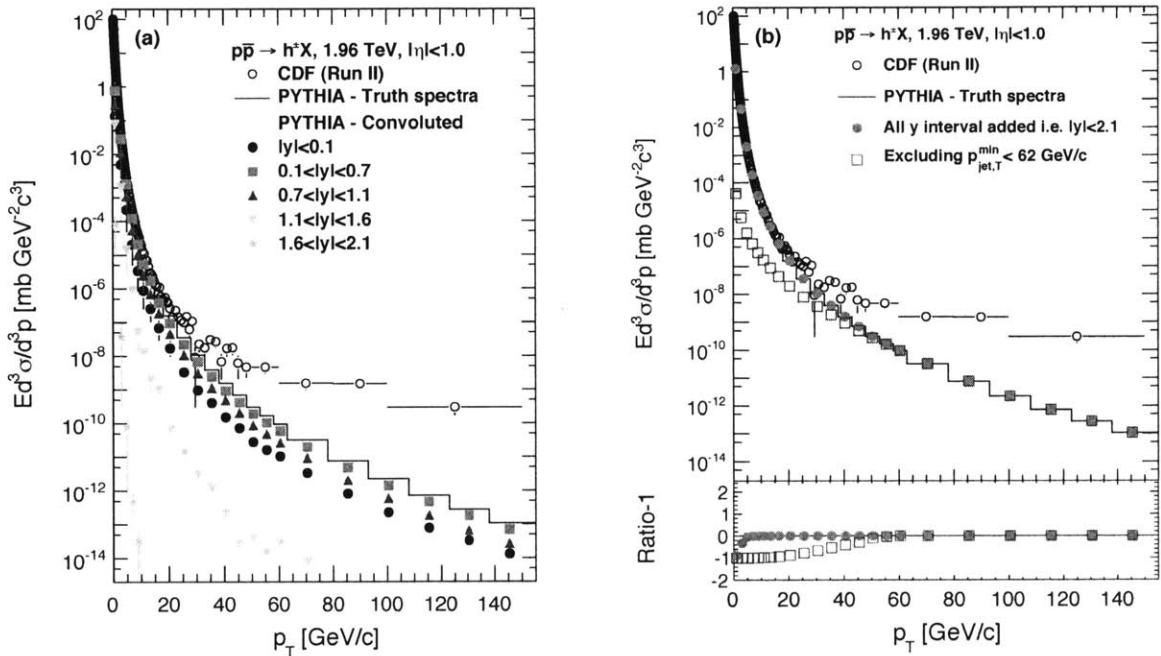


Figure 3: (a) PYTHIA charged particle cross section obtained from the convolution of the PYTHIA inclusive jet cross sections in different jet y ranges with PYTHIA fragmentation functions (filled markers) compared to the “true” charged particle cross section from PYTHIA (solid line). (b) The convoluted spectra after summing the contributions from all jet y ranges (filled circles), and the same after excluding the contribution from jets with $p_T < 62$ GeV/c (open squares). In both figures, the CDF measured cross sections are also shown (empty circles) for comparison.

drawn for the measured charged particle spectrum to indicate the size of the uncertainties in the measurement ¹⁰. The spectra from the PYTHIA-only convolution is drawn as black lines for comparison in both 4(a) and 4(b). In the bottom of the figure, the ratio of the resulting spectrum from the convolution of PYTHIA jet spectra to that of CDF jet spectra is shown. As expected from the agreement between the CDF measured jet spectra and PYTHIA (better than $\pm 50\%$ below 400 GeV), the convoluted charged particle spectra are in similar agreement.

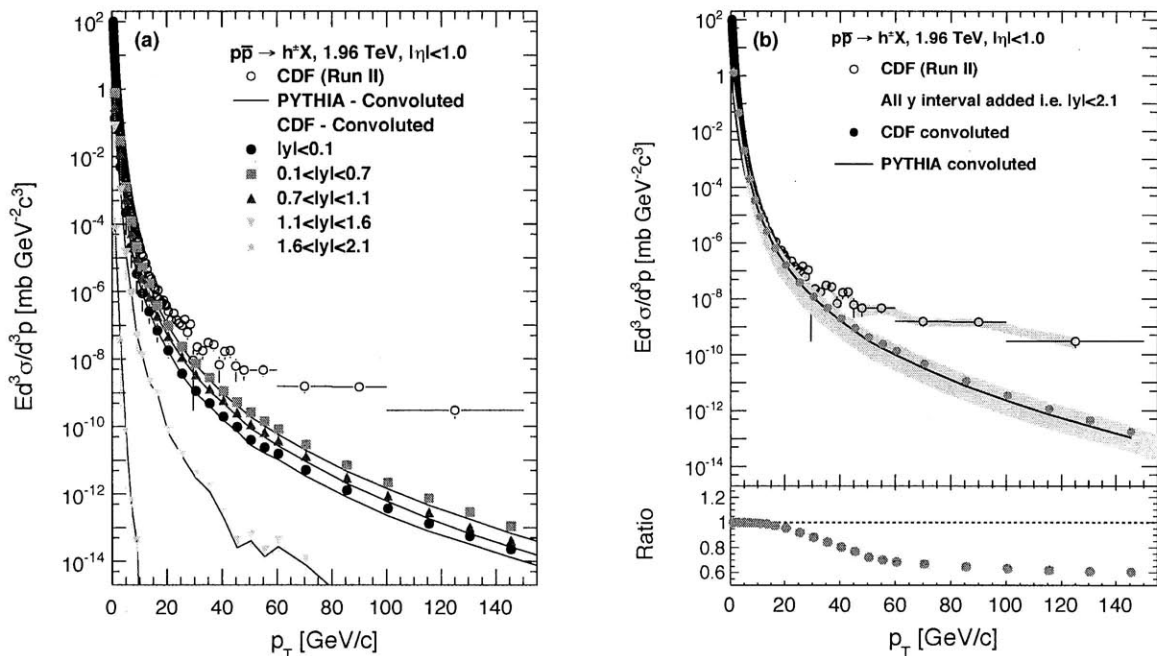


Figure 4: (a) Charged particle p_T differential cross section obtained from the convolution of the CDF jet cross sections measured in five rapidity intervals with the PYTHIA fragmentation functions (filled markers). Same cross sections obtained from the PYTHIA-only convolution are also shown in comparison (black line). (b) The convoluted spectra after summing the contributions from all jet y ranges (filled circle), and the same from the PYTHIA-only convolution (black line). The ratio of the two resulting charged particle spectra (from convolution with either the CDF or PYTHIA jet spectra) is shown in the lower panel.

5 Convolution with toy-model fragmentation functions

Knowing that the charged particle spectra from the convolution of the measured jet spectra with PYTHIA fragmentation functions still vastly undershoot the measured spectrum, it is interesting to know how sensitive the charged particle spectra are to arbitrary changes in the fragmentation

¹⁰Statistical uncertainty only, although the statistical uncertainties are comparable to the total uncertainties for $p_T \geq 50$ GeV/c [17]

function; or rather, how large a change in the fragmentation functions would be required to reproduce the measured spectrum? We address this question by convoluting the measured jet spectra with the fragmentation functions obtained based on the following two toy fragmentation models:

1. Harder fragmentation – modified shapes
2. Hardest possible fragmentation – one charged particle per jet

The modified fragmentation functions are obtained in the same manner as for the default PYTHIA (see Eq. 3).

5.1 Harder fragmentation

We make the default PYTHIA fragmentation functions harder by modifying the shape of the fragmentation functions. Of course, there are arbitrarily many imaginable functional forms one could use for “hardening” the fragmentation functions. Here we have chosen to harden the fragmentation functions by bending the p_T -shape with a simple power-law functional weight:

$$f(p_T) = 1 + c(p_T - p_T^{min})^n \text{ for } p_T > p_T^{min}, \quad (6)$$

The shape of the modification is governed by the constant c and the exponent n , while p_T^{min} determines the p_T value where the modification begins. To maximize the effect in this study, we bend the shape of the fragmentation function to the extent that the energy sum of the fragmented charged particles equals the energy of the corresponding jet. In this fashion, the fragmentation function can be maximally hardened for any choice of two parameters: c and p_T^{min} . We try four different combinations of c and p_T^{min} , which are presented in Fig. 5. The values of c (0.005 and 0.0005) were selected to ensure the bending is not unrealistically abrupt. Since the spectrum from the convolution already describes the CDF measurement rather well up to 20 GeV/c, we pick p_T^{min} accordingly (10 and 20 GeV/c) to maintain this agreement. With these choices of c and p_T^{min} , the exponent n that fulfills the maximum hardening ranges from 1 to 4 for the various jet- p_T bins. The modified fragmentation functions from jets within a range of $0.1 < |y| < 0.7$ are shown in Fig. 5 for the different values of c and p_T^{min} . Here, we only show the fragmentation functions for jets with p_T up to 400 GeV/c, as the fragmentation functions with higher jet p_T have a negligible contribution to the inclusive spectrum (see Fig. 2(b)). When compared to Fig. 2(a), the hardening of the fragmentation functions is immediately apparent. Despite an attempt to maintain smooth functions, the fragmentation functions in the first few jet- p_T bins are if anything unrealistically hard, as they contain regions with positive slopes.

For each of the four scenarios, the convolution of the hardened fragmentation functions with the CDF jet measurement is performed for the three dominant rapidity intervals ($|y| < 0.1$, $0.1 < |y| < 0.7$, $0.7 < |y| < 1.1$), which are then summed. In Fig 6(a), the resulting charged particle spectra are compared to the CDF measured charged particle spectrum. The harder fragmentation functions are reflected in a hardening of the inclusive spectrum. The disagreement between the measurement and the resulting spectra is less pronounced between 30 and 60 GeV/c. However, a disagreement of up to two orders of magnitude remains at the highest measured transverse momentum.

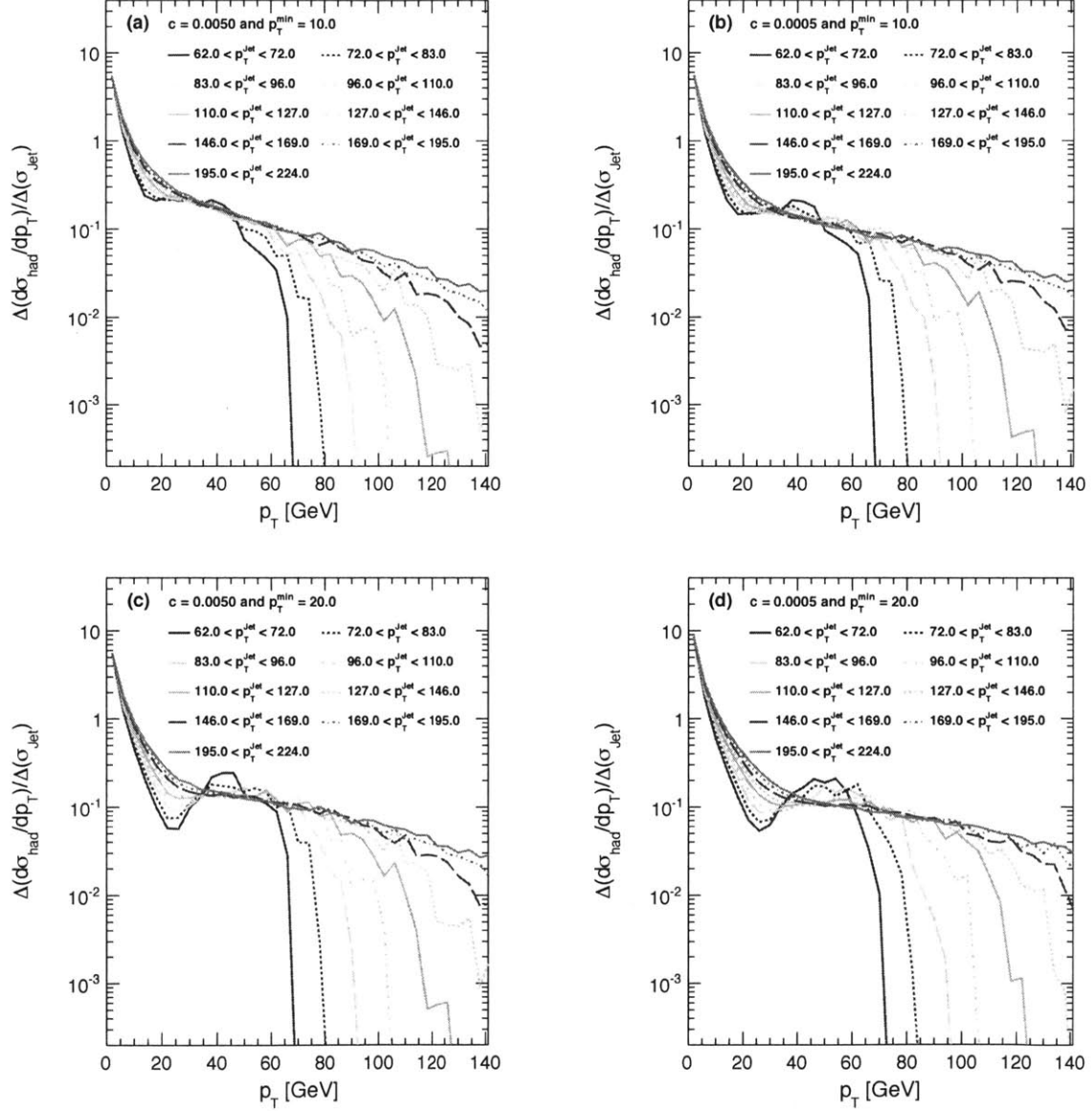


Figure 5: (a-d) PYTHIA (with D6T) fragmentation function in each jet- p_T bin modified by the power-law function (see Eq. 6) for different choices of the “hardening parameters”, c and p_T^{min} . The same color and line style conventions are used from Fig. 2.

5.2 Hardest possible fragmentation

Finally, we assume the extreme case of hard fragmentation, for which each hard-scattered parton fragments into a single charged particle. This is the hardest possible fragmentation ($z = 1$) that still conserves energy (though not necessarily other conserved quantities). Unlike the previous fragmentation functions, which are still model-dependent to some extent, the $z = 1$ scenario is model-independent.

In Fig 6(b), the result of applying the $z = 1$ fragmentation to the measured jet spectrum is shown. Again, the contributions from the three dominant rapidity intervals are summed to obtain the inclusive charged particle spectrum for $|\eta| < 1$. Both the shape as well as the overall magnitude are dramatically changed, enhancing the cross section by a few orders of magnitude. In the same figure, the jet spectra for the three y intervals ($|y| < 0.1$, $0.1 < |y| < 0.7$, $0.7 < |y| < 1.1$) are averaged and plotted in the form of an invariant yield for comparison. However, the charged particle spectrum measured by CDF at the highest p_T actually exceeds their measured jet spectra with $z = 1$ fragmentation. Furthermore, the level of underestimation is beyond the level of systematic uncertainties shown in the CDF jet measurement, which range from 10 to 80% depending on jet- p_T [22].

6 Summary and discussion

The latest CDF measurement of the inclusive charged particle p_T spectrum up to very high p_T is cross-checked against the convolution of the measured inclusive jet spectra with a set of different fragmentation functions. The inclusive charged particle spectrum obtained from the PYTHIA fragmentation functions convoluted with the measured jet cross section fails to reproduce the measured spectrum, despite matching (N)LO predictions reasonably well. PYTHIA fragmentation functions modified by a simple toy model result in quite different spectra shapes. However, despite an improved agreement at intermediate p_T , the convolutions still underestimate the measured charged particle spectrum at high p_T . Finally, we show that even the most extreme case of each jet fragmenting into a single charged particle fails to reconcile the measured jet and charged particle spectrum. Based on these studies, we rule out the possibility that the disagreement of the NLO pQCD calculations with the measured charged particle spectrum (but not the measured jet spectra) is due to an unexpectedly hard fragmentation of jets. Thus, we conclude that the CDF charged particle spectrum cannot be reconciled with the present understanding of factorized pQCD ¹¹.

This work was originally motivated for the purpose of cross-checking the CDF charged particle p_T spectrum measurement, but this convolution technique can be extended for use in future measurements without relying on input from PYTHIA at all. Any of the following three measurements can be independently obtained from the (de)convolution of the other two: the inclusive jet spectrum, the fragmentation functions of inclusive jets, and the inclusive charged particle spectrum. We expect that such a cross-check of future single particle p_T spectra measurements against the available calorimetric information will be very helpful for understanding the tracking-related systematic uncertainties in the high- p_T regime.

¹¹This doesn't rule out the possibility discussed in [39] that the factorization breaks down, since this investigation with the convolution method relies upon the validity of the factorization theorem.

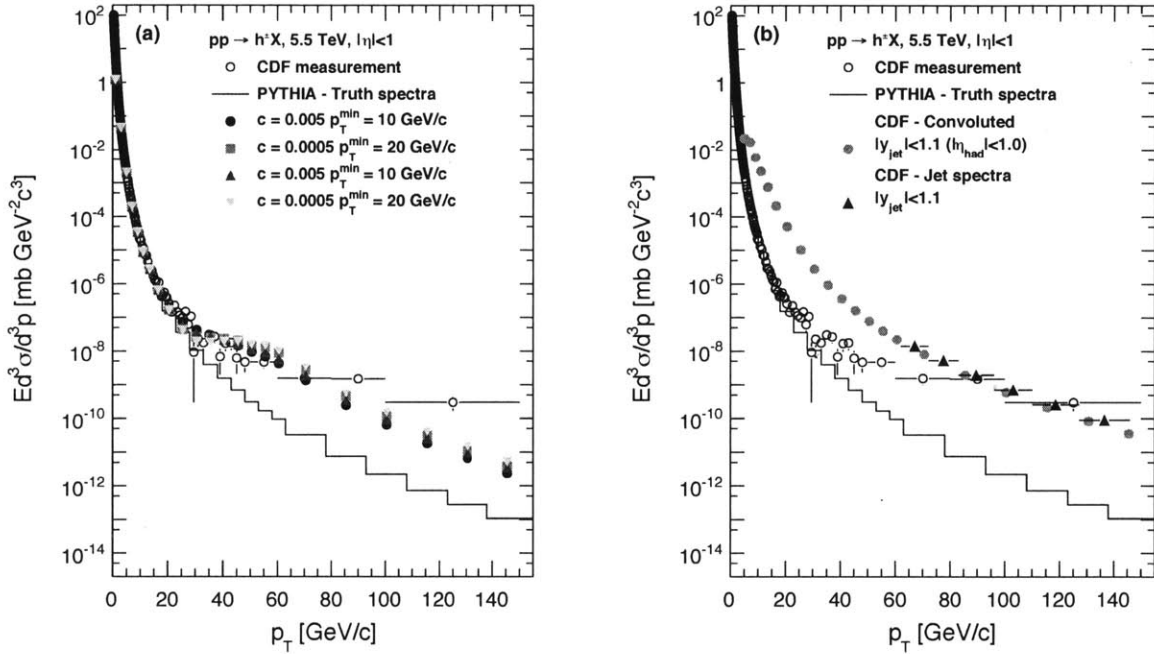


Figure 6: (a) Charged particle p_T differential cross sections obtained from the convolution of the measured jet cross sections with PYTHIA fragmentation functions modified according to Eq. 6. Different symbols show the spectra obtained with the modified fragmentation functions based on different sets of hardening parameters. (b) The same cross sections obtained from the convolution of measured jet cross sections ($|y| < 1.1$) with the hardest possible fragmentation (filled circles) compared to PYTHIA (solid line). The CDF combined jet spectra averaged over $|y| < 1.1$ (filled triangle) and the CDF charged particle spectrum (open circle) are plotted for comparison.

Note added: Another analysis reaching similar conclusions [42] was submitted for publication during the finalization of this paper.

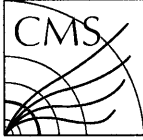
7 Acknowledgment

ASY thanks David d'Enterria and Francois Arleo for discussions.

References

- [1] M. Lamont, *LHC Commissioning*,
<http://lhc-commissioning.web.cern.ch/lhc-commissioning/>.
- [2] A. Hoecker, arXiv:1002.2891 [hep-ex].
- [3] E. Leader and E. Predazzi, *An introduction to gauge theories and modern particle physics Volume 2 (CP-violation, QCD and hard processes)*, Cambridge Monographs on Particle Physics, Nuclear Physics and Cosmology.
- [4] S. Moch, J. Phys. G: Nucl. Part. Phys. **35** (2008) 073001.
- [5] J. M. Campbell, J. W. Huston, W. J. Stirling, Rept. Prog. Phys. **70**:89,2007
- [6] D. d'Enterria, arXiv:0902.2011 [nucl-ex].
- [7] K. Yagi, T. Hatsuda, and Y. Miake, *Quark-Gluon Plasma*, Cambridge University Press.
- [8] I. Arsene *et al.* (BRAHMS Collaboration), Nucl. Phys. A **757** (2005) 1-27.
- [9] K. Adcox, *et al.* (PHENIX Collaboration), Nucl. Phys. A **757** (2005) 184-283.
- [10] B. B. Back *et al.* (PHOBOS Collaboration), Nucl. Phys. A **757** (2005) 184-283.
- [11] J. Adams, *et al.* (STAR Collaboration), Nucl. Phys. A **757** (2005) 102-183.
- [12] D d'Enterria *et al.* (CMS Collaboration), J. Phys. G **34** (2007) 2307-2455.
- [13] A. Breakstone *et al.* (CDHW Collaboration), Z. Phys. C **69** (1995) 55.
- [14] J. Adams *et al.* (STAR Collaboration), Phys. Rev. Lett. **91** (2003) 172302.
I. Arsene *et al.* (BRAHMS Collaboration), Phys. Rev. Lett. **93** (2004) 242303.
- [15] C. Albajar *et al.* (UA1 Collaboration), Nucl. Phys. B **335** (1990) 261.
- [16] F. Abe *et al.* (CDF Collaboration), Phys. Rev. Lett. **61** (1988) 1819.
- [17] T. Aaltonen *et al.* (CDF Collaboration) Phys. Rev. D **79** (2009) 112005.
- [18] CMS Collaboration, JHEP **02** (2010) 041.

- [19] G. Aad *et al.* (ATLAS Collaboration), arXiv:1003.3124 [hep-ex].
- [20] F. Arleo, D. d’Enterria, and A. S. Yoon, arXiv:1003.2963 [hep-ph].
- [21] S. Albino, B. A. Kniehl and G. Kramer, arXiv:1003.1854 [hep-ph].
- [22] T. Aaltonen *et al.* (CDF Collaboration), Phys. Rev. D **78** (2008) 052006.
- [23] A. Abulencia *et al.* (CDF Collaboration), Phys. Rev. D **75** (2007) 092006.
- [24] A. Abulencia *et al.* (CDF Collaboration), Phys. Rev. D **74** (2006) 071103(R).
- [25] A. Abulencia *et al.* (CDF Collaboration), Phys. Rev. Lett. **96** (2006) 122001.
- [26] F. Arleo, S. J. Brodsky, D. S. Hwang and A. M. Sickles, arXiv:0911.4604 [hep-ph], (Private communication with F. Arleo)
- [27] J. F. Owens, E. Reya and M. Gluck, Phys. Rev. D **18** (1978) 1501.
- [28] V. M. Abazov *et al.* (D0 Collaboration), Phys. Rev. Lett. **101** (2008) 062001.
- [29] A. D. Martin *et al.* arXiv:0901.0002v3 [hep-ph].
- [30] Multiple Parton Interactions at the LHC. Proceedings, 1st Workshop, Perugia, Italy, October 27-31, 2008. DESY-PROC-2009-06.
- [31] T. Sjöstrand, S. Mrenna, and P. Skands, JHEP **05** (2006) 026, arXiv:hep-ph/0603175.
- [32] S. Catani *et al.* Nucl. Phys. B **406** (1993) 187.
- [33] S. D. Ellis, *et al.* arXiv:hep-ph/0111434.
- [34] K. J. Eskola and H. Honkanen, arXiv:0205048v1 [hep-ph].
- [35] A. Pronko, (for the CDF Collaboration), Acta. Phy. Pol. B **36** (2005).
- [36] H. Caines (for the STAR Collaboration), Nucl. Phys. A **830** (2009) 263c-266c.
- [37] M. Heinz (for the STAR Collaboration), Eur. Phys. J. C **61** (2009) 769773.
- [38] D. Acosta *et al.* (CDF Collaboration), Phys. Rev. D **71** (2005) 112002.
- [39] S. Albino, B. A. Kniehl and G. Kramer, Nucl. Phys. B **803** (2008) 42.
- [40] D. de Florian, R. Sassot and M. Stratmann, Phys. Rev. D **75** (2007) 114010.
- [41] M. Hirai, S. Kumano, T. H. Nagai and K. Sudoh, Phys. Rev. D **75** (2007) 094009.
- [42] M. Cacciari, G. P. Salam, M. J. Strassler, arXiv:1003.3433 [hep-ph].



CMS-QCD-10-008

Charged particle transverse momentum spectra in pp collisions at $\sqrt{s} = 0.9$ and 7 TeV

The CMS Collaboration*

Abstract

The charged particle transverse momentum (p_T) spectra are presented for pp collisions at $\sqrt{s} = 0.9$ and 7 TeV. The data samples were collected with the CMS detector at the LHC and correspond to integrated luminosities of $231 \mu\text{b}^{-1}$ and 2.96pb^{-1} , respectively. Calorimeter-based high-transverse-energy triggers are employed to enhance the statistical reach of the high- p_T measurements. The results are compared with leading and next-to-leading order QCD and with an empirical scaling of measurements at different collision energies using the scaling variable $x_T \equiv 2p_T/\sqrt{s}$ over the p_T range up to $200 \text{GeV}/c$. Using a combination of x_T scaling and direct interpolation at fixed p_T , a reference transverse momentum spectrum at $\sqrt{s} = 2.76 \text{TeV}$ is constructed, which can be used for studying high- p_T particle suppression in the dense QCD medium produced in heavy-ion collisions at that centre-of-mass energy.

Submitted to the Journal of High Energy Physics

arXiv:1104.3547v2 [hep-ex] 29 Sep 2011

*See Appendix A for the list of collaboration members

1 Introduction

The charged particle transverse momentum (p_T) spectrum is an important observable for understanding the fundamental quantum chromodynamic (QCD) interactions involved in proton-proton collisions. While the energy dependence of the bulk of particle production with p_T below a few GeV/ c is typically described either empirically or with phenomenological models, the rest of the spectrum can be well described by a convolution of parton distribution functions, the hard-scattering cross section from perturbative calculations, and fragmentation functions. Such a prescription has been generally successful over a large range of lower energy pp and p \bar{p} collisions [1–7]. Along with measurements of the jet production cross section and fragmentation functions, measurements of high- p_T spectra provide a test of factorised perturbative QCD (pQCD) [8] at the highest collision energy to date.

In addition to its relevance to the understanding of pQCD, the charged particle spectrum in pp collisions will be an important reference for measurements of high- p_T particle suppression in the dense QCD medium produced in heavy-ion collisions. At the Relativistic Heavy Ion Collider (RHIC), the sizable suppression of high- p_T particle production, compared to the spectrum expected from a superposition of a corresponding number of pp collisions, was one of the first indications of strong final-state medium effects [9–12]. A similar measurement of nuclear modification to charged particle p_T spectra has been one of the first heavy-ion results at the Large Hadron Collider (LHC) [13]. The reference spectrum for the PbPb collisions at $\sqrt{s_{NN}} = 2.76$ TeV per nucleon can be constrained by interpolating between the pp spectra measured at $\sqrt{s} = 0.9$ and 7 TeV.

In this paper, the phase-space-invariant differential yield $E d^3N_{ch}/dp^3$ is presented for primary charged particles with energy (E) and momentum (p), averaged over the pseudorapidity acceptance of the Compact Muon Solenoid (CMS) tracking system ($|\eta| < 2.4$). The pseudorapidity is defined as $-\ln[\tan(\theta/2)]$, with θ being the polar angle of the charged particle with respect to the counterclockwise beam direction. The number of primary charged particles (N_{ch}) is defined to include decay products of particles with proper lifetimes less than 1 cm. Using the integrated luminosities calculated in Refs. [14, 15] with an estimated uncertainty of 11% and 4% at $\sqrt{s} = 0.9$ and 7 TeV, respectively, the differential cross sections are constructed and compared to a scaling with the variable $x_T \equiv 2p_T/\sqrt{s}$. Such a scaling has already been observed for p \bar{p} measurements at lower collision energies [4, 5, 16, 17]. For consistency with the CDF measurements at $\sqrt{s} = 0.63, 1.8,$ and 1.96 TeV, the pseudorapidity range of the x_T distributions has been restricted to $|\eta| < 1.0$.

Finally, using the new measurements presented in this paper, as well as previously measured pp and p \bar{p} cross sections, an estimate of the differential transverse momentum cross section is constructed at the interpolated energy of $\sqrt{s} = 2.76$ TeV, corresponding to the nucleon-nucleon centre-of-mass energy of PbPb collisions recorded at the LHC.

The paper is organised as follows: Section 2 contains a description of the CMS detector; Section 3 describes the trigger and event selection; Sections 4 and 5 detail the reconstruction and selection of primary vertices and tracks; Section 6 explains the characterisation of events based on the leading-jet transverse energy; Section 7 describes the various applied corrections and systematic uncertainties; Section 8 presents the final invariant differential yields and comparisons to data and simulation; and Section 9 discusses the interpolation procedures used to construct a reference spectrum at $\sqrt{s} = 2.76$ TeV.

2 The CMS Detector

A detailed description of the CMS experiment can be found in Ref. [18]. The central feature of the CMS apparatus is a superconducting solenoid of 6 m internal diameter, providing an axial magnetic field of 3.8 T. Immersed in the magnetic field are the pixel tracker, the silicon strip tracker, the lead tungstate crystal electromagnetic calorimeter (ECAL), and the brass/scintillator hadron calorimeter (HCAL). Muons are measured in gas ionisation detectors embedded in the steel return yoke.

The CMS experiment uses a right-handed coordinate system, with the origin at the nominal interaction point, the x axis pointing to the centre of the LHC ring, the y axis pointing up perpendicular to the plane of the LHC, and the z axis along the counterclockwise beam direction. The azimuthal angle, ϕ , is measured in the (x, y) plane.

The tracker consists of 1440 silicon pixel and 15 148 silicon strip detector modules and measures charged particle trajectories within the nominal pseudorapidity range $|\eta| < 2.4$. The pixel tracker consists of three 53.3 cm-long barrel layers and two endcap disks on each side of the barrel section. The innermost barrel layer has a radius of 4.4 cm, while for the second and third layers the radii are 7.3 cm and 10.2 cm, respectively. The tracker is designed to provide an impact parameter resolution of about $100 \mu\text{m}$ and a transverse momentum resolution of about 0.7% for 1 GeV/ c charged particles at normal incidence ($\eta = 0$) [19].

The tracker was aligned as described in Ref. [20] using cosmic ray data prior to the LHC commissioning. The precision achieved for the positions of the detector modules with respect to particle trajectories is 3–4 μm in the barrel for the coordinate in the bending plane (ϕ).

Two elements of the CMS detector monitoring system, the beam scintillator counters (BSC) [18, 21] and the beam pick-up timing for the experiments devices (BPTX) [18, 22], were used to trigger the detector readout. The BSCs are located at a distance of 10.86 m from the nominal interaction point (IP), one on each side, and are sensitive in the $|\eta|$ range from 3.23 to 4.65. Each BSC is a set of 16 scintillator tiles. The BSC elements have a time resolution of 3 ns, an average minimum ionising particle detection efficiency of 95.7%, and are designed to provide hit and coincidence rates. The two BPTX devices, located around the beam pipe at a position of $z = \pm 175$ m from the IP, are designed to provide precise information on the bunch structure and timing of the incoming beam, with better than 0.2 ns time resolution.

The two steel/quartz-fibre forward calorimeters (HF), which extend the calorimetric coverage beyond the barrel and endcap detectors to the $|\eta|$ region between 2.9 and 5.2, were used for further offline selection of collision events.

The detailed Monte Carlo (MC) simulation of the CMS detector response is based on GEANT4 [23]. Simulated events were processed and reconstructed in the same manner as collision data.

3 Event Selection

This analysis uses data samples collected from 0.9 and 7 TeV pp collisions in the first months of the 2010 LHC running, corresponding to integrated luminosities of $(231 \pm 25) \mu\text{b}^{-1}$ and $(2.96 \pm 0.12) \text{pb}^{-1}$, respectively [14, 15]. This section gives a brief description of the requirements imposed to select good events for this analysis. A more detailed description of the CMS trigger selections can be found in Ref. [24].

First, a minimum bias trigger was used to select events with a signal in any of the BSC tiles, coincident with a signal from either of the two BPTX detectors, indicating the presence of at

least one proton bunch crossing the interaction point. From this sample, collision events were selected offline by requiring a coincidence of BPTX signals, indicating the presence of both beams.

To select preferentially non-single-diffractive (NSD) events, at least one forward calorimeter (HF) tower with energy deposition $E > 3\text{ GeV}$ in each of the forward and backward hemispheres was required. Events with beam-halo muons crossing the detector were identified and rejected based on the time difference between BSC hits on either side of the interaction point. Beam-induced background events, producing anomalous numbers of low-quality tracks, were rejected by requiring that at least 25% of the charged particles reconstructed in the pixel-silicon tracking system satisfied the *highPurity* criterion. This criterion, described in Ref. [25], consists of numerous selections on the properties of the tracks, including the normalised χ^2 , the compatibility with the beamline and primary vertices, the number of hit layers, the number of ‘3D’ layers, and the number of lost layers. The selection on the fraction of *highPurity* tracks was only applied to events with more than 10 tracks, providing a clean separation between real pp collisions and beam backgrounds. The remaining non-collision event fraction, determined by applying the same selections to events where only a single beam was crossing the interaction point, is estimated to be less than 2×10^{-5} . Events were required to have at least one primary vertex, reconstructed according to the description in the following section from triplets of pixel hits. A further requirement, namely at least one vertex found from fully reconstructed tracks (see next section for details) with number of degrees of freedom (*Ndof*) greater than four, was imposed to improve the robustness against triggered events containing multiple pp collisions, i.e., “event pileup”. The loss in event selection efficiency from the fully-reconstructed-track vertex compared to the pixel vertex alone was determined entirely from data, based on a subset of early runs with negligible event pileup. The percentage of events remaining after each selection step is presented in Table 1.

For a large part of the 7 TeV data collection, the minimum bias trigger paths had to be prescaled by large factors because of the increasing instantaneous luminosity of the LHC. In order to maximise the p_T reach of the charged particle transverse momentum measurement at this centre-of-mass energy, two high-level trigger (HLT) paths were used that selected events with minimum uncorrected transverse jet energies (E_T) of 15 and 50 GeV, based only on information from the calorimeters. While the higher threshold path was not prescaled during the 7 TeV data-taking period corresponding to the 2.96 pb^{-1} used in this analysis, the lower threshold path had to be prescaled for a significant fraction of this sample. The 0.9 TeV data sample consists of 6.8 million minimum bias triggered events, while the 7 TeV sample is composed of 18.7 million minimum bias events, and 1.4 (5.6) million events selected with the HLT minimum- E_T values of 15 (50) GeV.

The selection efficiency for NSD events was determined based on simulated events from the PYTHIA [26] event generator (version 6.420, tune D6T [27]) that were subsequently passed through a Monte Carlo simulation of the CMS detector response. The resulting event selection efficiency as a function of the multiplicity of reconstructed charged particles is shown for 7 TeV collisions in Fig. 1a. The corresponding event selection efficiency is calculated by the same technique for the 0.9 TeV data (not shown). Based on events simulated with PHOJET [28, 29] and PYTHIA, the remaining fraction of single-diffractive (SD) events in the selected sample was estimated to be $(5 \pm 1)\%$ and $(6 \pm 1)\%$ for the 0.9 and 7 TeV data, respectively.

Table 1: Summary of event selection steps applied to the 0.9 and 7 TeV collision data sets and the percentage of events from the original minimum bias samples that remain after each step.

Collision energy	0.9 TeV	7 TeV
Selection	Percentage passing each selection cut	
One BSC + one BPTX	100.0	100.0
BPTX coincidence	94.49	90.05
Beam halo rejection	94.08	89.83
HF coincidence	73.27	83.32
Beam background rejection	73.26	83.32
Valid pixel-track vertex	70.14	82.48
Quality full-track vertex	64.04	77.35

4 Primary Vertex

In this analysis, two separate algorithms are employed to determine the primary vertex position. The first is a highly efficient algorithm based on pixel triplet tracks that requires a minimum of just a single track consistent with the beam-spot position. The position of the beam-spot, taken as the centre of the region where the LHC beams collide, is calculated for each LHC fill based on the average over many events of the three-dimensional fitted vertex positions [25]. The second vertex-finding algorithm, based on fully reconstructed tracks with hits also in the silicon strip tracker, is less efficient in selecting low-multiplicity events, but more robust in discriminating against event pileup. Since pileup is significant over the majority of the analysed data sample, only the fully-reconstructed-track vertex is used to construct the raw charged particle momentum spectra. The raw spectra are subsequently corrected for the fraction of events with fewer than four tracks (and the fraction of tracks in such low-multiplicity events), based on a subset of the event sample selected with the more efficient pixel-track vertex requirement during collision runs with negligible event pileup.

To determine the z position of the pixel vertex in each event, tracks consisting of three pixel hits are constructed with a minimum p_T of 75 MeV/ c from a region within a transverse distance of 0.2 cm from the beam axis. The x and y positions of the pixel vertex are taken from the transverse position of the beam axis. Fitted tracks are selected based on the requirement that the transverse impact parameter is less than three times the quadratic sum of the transverse errors on the track impact parameter and the beam axis position. The selected tracks are then passed to an agglomerative algorithm [30], which iteratively clusters the tracks into vertex-candidates. The procedure is halted when the distance between nearest clusters, normalised by their respective position uncertainties, reaches 12. Only vertices consisting of at least two tracks are kept, except when the event contains a single reconstructed track, which occurs in 1.67% (0.99%) of the events at $\sqrt{s} = 0.9$ (7) TeV. In the case of multiple vertex-candidates, only the vertex with the most associated tracks is kept. While this occurs in as many as 20% of events, the rejected vertex typically has very few associated tracks and is highly correlated in z position to the vertex with the most associated tracks. These characteristics imply that the rejected vertices are not from event pileup, but rather from tracks in the tails of the impact parameter distribution that are not agglomerated into the primary vertex.

The fully-reconstructed-track vertex algorithm begins from a set of tracks selected according to their transverse impact parameter to the beam-spot (< 2 cm), number of hits (> 6), and normalised χ^2 (< 20). These tracks are passed to an adaptive vertex fitter, in which tracks are as-

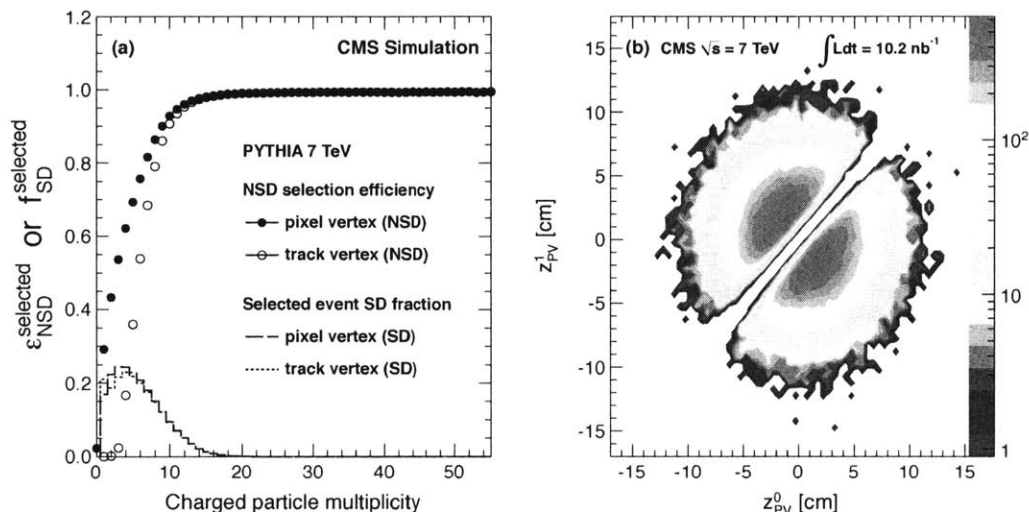


Figure 1: (a) The efficiency ($\epsilon_{\text{NSD}}^{\text{selected}}$ in Eq. (2)) for selecting non-single-diffractive (NSD) events as a function of the multiplicity of reconstructed charged particles in the tracker acceptance ($|\eta| < 2.4$) after applying the full event selection described in the text, including a single pixel-track vertex (filled circles) and additionally requiring a fully-reconstructed-track vertex with $Ndof > 4$ (open circles) as described in Section 4. Also, the remaining single-diffractive (SD) fraction ($f_{\text{SD}}^{\text{selected}}$ in Eq. (2)) as a function of charged particle multiplicity for the same selections (solid and dashed lines). (b) Correlation between the z positions, z_{PV}^0 and z_{PV}^1 , of the two vertices with the most associated tracks for measured events with more than one fully-reconstructed-track vertex satisfying the quality selections.

signed a weight between 0 and 1 according to their compatibility with the common vertex [25]. Quality vertices are further required to have more than four degrees of freedom ($Ndof$), corresponding to at least four tracks with weights of approximately one. For events with multiple reconstructed vertices passing the quality selection, the correlation between the z positions of the two vertices with the most associated tracks is shown in Fig. 1b. Other than the diagonal region without multiple vertices, expected from the algorithmic parameter of at least a 1 cm separation, the uncorrelated positions of the two vertices are indicative of random event pileup.

The event pileup rate is estimated from the fraction of events with multiple reconstructed vertices, after correcting for vertices that are not found because of their proximity. The beam conditions varied over the analysed minimum bias data samples, such that the corrected fraction of pileup events is in the range (0.4–7.5)%. The uncertainty on the event pileup fraction, determined from the largest correction to the multiple-vertex fraction, is a constant factor of 0.2% and 1.2% for the 0.9 and 7 TeV data, respectively.

5 Track Selection

This analysis uses tracks from the standard CMS reconstruction algorithm, which consists of multiple iterations of a combinatorial track finder based on various seeding layer patterns [31]. After each iteration, hits belonging unambiguously to tracks in the previous step are removed from consideration for subsequent steps.

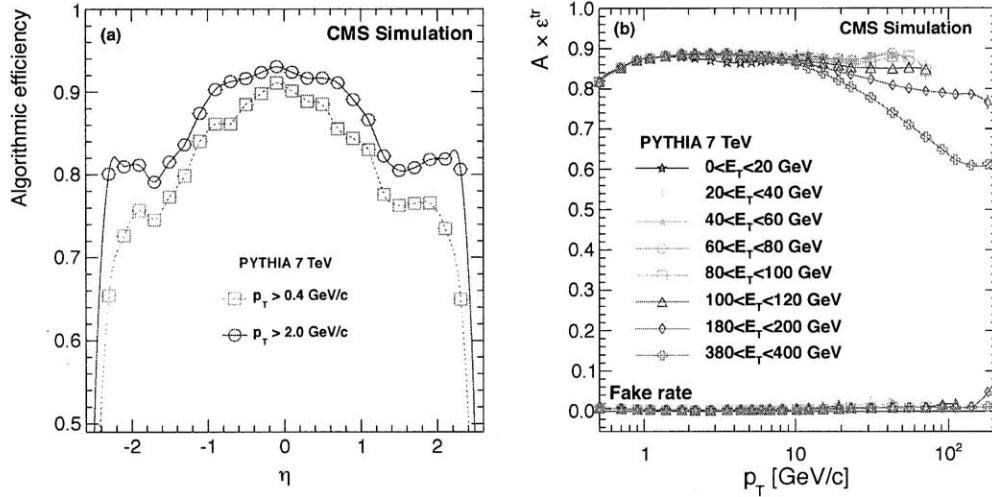


Figure 2: (a) The algorithmic tracking efficiency for two different momentum ranges as a function of η . (b) The product of geometrical acceptance (A) with tracking efficiency (ϵ^{tr}) (upper points) and the misidentification (“fake”) rate (lower points) as a function of transverse momentum for tracks with $|\eta| < 1$ in bins of corrected leading-jet transverse energy.

In order to minimise the contribution from misidentified tracks and tracks with poor momentum resolution, a number of quality selections are applied. These include the *highPurity* selection mentioned in Section 3, the requirement of at least five hits on the track, the normalized χ^2 per degree of freedom divided by the number of tracker layers used in the fit less than a maximum value which varies from 0.48 and 0.07 depending on η and p_T , and a relative momentum uncertainty of less than 20%. Furthermore, to reject non-primary tracks (i.e., the products of weak decays and secondary interactions with detector material), only the pixel-seeded tracking iterations are used, and selections are placed on the impact parameter of the tracks with respect to the primary vertex position. Specifically, the transverse and longitudinal impact parameters are required to be less than 0.2 cm and also less than 3 times the sum in quadrature of the uncertainties on the impact parameter and the corresponding vertex position. In the case of multiple quality reconstructed vertices in the minimum bias event samples, tracks that pass the impact parameter selections with respect to any vertex are used in the analysis. The number of events, by which the track p_T distribution is normalised, is then scaled by a factor to account for the event pileup fraction. In contrast, for the jet-triggered samples, tracks are selected based on the impact parameter with respect to the single vertex responsible for the trigger. The primary vertex of the hard-scattering process is identified as the vertex with the largest value of $\sum p_T^2$ for the associated fitted tracks.

With the above-mentioned selections applied to the reconstructed tracks, the algorithmic efficiency determined from simulated PYTHIA events is greater than 85% (80%) for tracks with transverse momentum above 2.0 (0.4) GeV/c averaged over $|\eta| < 2.4$ (Fig. 2a). In the same kinematic region, misidentified and non-primary tracks are each below 1%, while multiple reconstruction occurs for less than 0.01% of tracks.

6 Event Classification by Leading-Jet Energy

All events in this analysis are classified according to the transverse energy of the most energetic reconstructed jet, defined as the leading jet. Jets are reconstructed from calorimeter deposits alone using the anti- k_T algorithm [32] with cone radius $R = \sqrt{(\Delta\phi)^2 + (\Delta\eta)^2} = 0.5$. The measured energy of the jet is adjusted according to corrections based on a MC description of the CMS calorimeter response with a 3–6% uncertainty on the jet energy scale [33].

The motivation for classifying events according to the leading-jet transverse energy is twofold. First, the degrading effect of the local-track density on the high- p_T tracking performance (e.g., inside a jet) can be parametrised according to this variable. Based on events simulated with PYTHIA in minimum bias and QCD samples with various thresholds on the hard-scattering scale (\hat{p}_T), the efficiency and misidentification rates of the selected tracks are estimated as a function of transverse momentum in bins of leading-jet transverse energy (see Fig. 2b). Second, as discussed in Section 3, calorimeter-based triggers with leading-jet transverse energy thresholds of 15 GeV (Jet15U) and 50 GeV (Jet50U) were used to extend the p_T reach of the 7 TeV measurement.

To avoid potential biases from the jet-trigger selection, it is desirable to operate in a region where the trigger is fully efficient. The region above which the jet trigger with an uncorrected energy threshold of 15 GeV becomes fully efficient is determined by first plotting the leading-jet E_T distribution for a sample of events selected with the prescaled minimum bias trigger and the offline selections described in Section 3. This distribution is then compared to the subset of those events which also fire the 15 GeV jet trigger as a function of corrected transverse energy. The resulting ratio is the trigger efficiency curve presented in the lower panel of Fig. 3a. The 15 GeV jet trigger achieves more than 99% efficiency at a corrected energy of $E_T = 45$ GeV. The analogous procedure is repeated on a sample of events selected by the 15 GeV jet trigger to determine that the 50 GeV jet trigger becomes fully efficient above $E_T = 95$ GeV. For the trigger efficiency study, an early subset of the data (10.2 nb^{-1}) was used, because the minimum bias and lower-threshold jet triggers were highly prescaled in the later runs. In the upper panel of Fig. 3a, the E_T distributions from the jet-triggered sample are normalised per equivalent minimum bias event by matching their integrals in the regions where the triggers are fully efficient.

For the 7 TeV analysis, events are divided into three classes based on leading-jet E_T : below 60 GeV, between 60 and 120 GeV, and above 120 GeV. Since each event is uniquely assigned to one such leading-jet E_T range, the overall dN_{ch}/dp_T distribution is simply the sum of the spectra from the three ranges, each corresponding to a fully-efficient HLT selection (i.e., minimum bias, 15 GeV jet trigger, and 50 GeV jet trigger). The contributions to the spectra from the jet-triggered events are normalised per selected minimum bias event; the fraction of minimum bias events containing a leading jet with greater than either 60 or 120 GeV is calculated as shown in Fig. 3a by matching the fully-efficient regions of the leading-jet E_T distributions. The three contributions to the combined charged particle transverse momentum spectrum are shown in Fig. 3b. The lower panel of that figure compares the combined spectrum first to the minimum bias spectrum alone and then to a spectrum constructed with the addition of only the lower-threshold jet trigger. These are all in good agreement within their respective statistical uncertainties. A p_T -dependent systematic uncertainty of 0–4% is attributed to the normalisation of the contributions from the triggered samples. This value is determined by changing the leading-jet E_T ranges that separate the three samples (e.g., to $E_T = 40$ and 100 GeV), by basing the normalisation directly on the HLT prescale values, and by comparing the normalisations determined from different subsets of the full data sample.

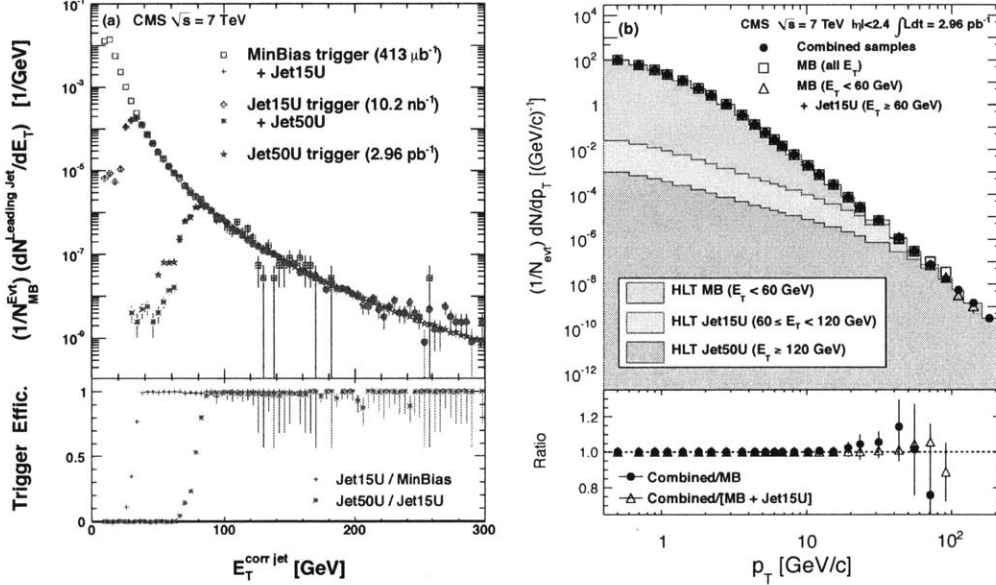


Figure 3: (a) Upper panel: distributions of the corrected transverse energy of leading jets normalised by the number of selected minimum bias events $N_{\text{MB}}^{\text{Evt}}$. Lower panel: the efficiency turn-on curves for the jet triggers with uncorrected energy thresholds of 15 and 50 GeV. (b) Upper panel: the three contributions to the charged particle transverse momentum spectrum and their sum (solid circles). Open squares show the minimum bias spectrum for all values of leading-jet E_T ; open triangles show the spectrum with the addition of only the lower threshold jet trigger. Lower panel: the ratio of the combined spectrum to minimum bias only (solid circles) and with the addition of only the lower threshold jet trigger (open triangles).

7 Corrections and Systematic Uncertainties

To obtain the final phase-space-invariant charged particle differential momentum distribution, a number of corrections must be applied to the raw distributions of reconstructed charged particles, according to the following equation:

$$E \frac{d^3 N_{\text{ch}}}{d p^3}(p_T, \eta) = \frac{\sum_{M, E_T^{\text{jet}}} N_{\text{track}}^{\text{raw}}(M, E_T^{\text{jet}}, p_T, \eta) \cdot w_{\text{tr}}(p_T, \eta, E_T^{\text{jet}}) \cdot w_{\text{ev}}(M)}{2\pi p_T \cdot \Delta p_T \cdot \Delta \eta \cdot \sum_M N^{\text{selected}}(M) \cdot (1 - f_{\text{NSD}}^0)^{-1} \cdot (1 + f^{\text{pileup}}) \cdot w_{\text{ev}}(M)}, \quad (1)$$

where $N_{\text{track}}^{\text{raw}}$ is the raw number of tracks in a bin with transverse momentum width Δp_T and pseudorapidity width $\Delta \eta$, and N^{selected} is the number of selected events. An event weight w_{ev} (see Eq. (2)) is applied as a function of the multiplicity of reconstructed charged particles (M), while a track weight w_{tr} (see Eq. (3)) is applied for each M and leading-jet transverse energy (E_T^{jet}), as a function of p_T ; the final results are summed over M and E_T^{jet} . The number of selected events is corrected for the fraction of NSD events (f_{NSD}^0) that have zero reconstructed tracks in the tracker acceptance of $|\eta| < 2.4$ (about 5%) and for the pileup event fraction (f^{pileup}).

The multiplicity-dependent event weight w_{ev} accounts for the efficiency of the event selection for accepting NSD events ($f_{\text{NSD}}^{\text{selected}}$) and for the fraction of SD events ($f_{\text{SD}}^{\text{selected}}$) that contaminate

Table 2: Summary of the various contributions to the estimated systematic uncertainty.

Source	Uncertainty [%]	
	0.9 TeV	7 TeV
Collision energy		
Event selection	3.2	3.5
Pileup effect on vertexing	0.2	1.2
Acceptance	1.5	1.5
Reconstruction efficiency	2.2	2.2
Occupancy effect on efficiency	0.0–0.5	0.0–2.8
Misidentified track rate	0.3–1.0	0.3–3.0
Correction for secondary particles	1.0	1.0
Momentum resolution and binning	0.3–1.5	0.3–2.7
Normalisation of jet-triggered spectra	–	0.0–4.0
Total	4.3–4.7	4.7–7.9
Total excluding event selection uncertainty	2.9–3.4	3.1–7.1
Total including luminosity uncertainty	11.4–11.6	5.1–8.1

the selected sample (about 5% overall):

$$w_{\text{ev}}(M) = \frac{1}{\epsilon_{\text{NSD}}^{\text{selected}}} (1 - f_{\text{SD}}^{\text{selected}}). \quad (2)$$

The correction factor w_{tr} , by which each track is weighted, is calculated for each bin in transverse momentum, pseudorapidity, and leading-jet transverse energy. This factor accounts for the geometric detector acceptance (A) and algorithmic tracking efficiency (ϵ^{tr}), as well as the fraction of tracks corresponding to the same, multiply reconstructed charged particle (D), the fraction of tracks corresponding to a non-primary charged particle (S), and the fraction of misidentified ('fake') tracks that do not correspond to any charged particle (F):

$$w_{\text{tr}}(p_{\text{T}}, \eta, E_{\text{T}}^{\text{jet}}) = \frac{(1 - F) \cdot (1 - S)}{A \cdot \epsilon^{\text{tr}} \cdot (1 + D)}. \quad (3)$$

The common uncertainty related to the triggering and event selection efficiency is discussed in detail in Ref. [34]. Contributions from uncertain diffractive-event fractions and detector inefficiencies in the BSC and HF combine to contribute a scale error of $\pm 3.5\%$ to the total systematic uncertainty at $\sqrt{s} = 7$ TeV (see Table 2). At $\sqrt{s} = 0.9$ TeV, the diffractive fractions are slightly better constrained, hence an uncertainty of $\pm 3.2\%$ is assigned.

Using simulated events generated with PYTHIA tune D6T, the various terms in Eq. (3) are estimated by matching selected reconstructed tracks to simulated tracks based on the requirement that they share 75% of their hits. As an example, the algorithmic efficiency (ϵ^{tr}) versus η is presented in Fig. 2a. The slight asymmetry between the positive and negative hemispheres is attributed to a slightly displaced beam-spot and the distribution of dead channels in the tracker. The systematic uncertainties assigned to the various tracking corrections are discussed below and are summarised, along with the total systematic uncertainty, in Table 2.

The uncertainty on the geometrical acceptance of the tracker was estimated from three sources. First, the efficiency of the pixel hit reconstruction was estimated from a data-driven technique

involving the projection of two-hit combinations (called tracklets) onto the third layer in search of a compatible hit. The observed efficiency of $(99.0 \pm 0.5)\%$ leads to a 0.3% uncertainty on the acceptance of pixel-seeded tracks. Second, the variation of the geometrical acceptance was estimated for a variety of generator tunes including PYTHIA8 [35] and the Perugia0 [36] tune of PYTHIA. Third, the variation was estimated after shifting the generated beam-spot and modifying the width of the generated z vertex distribution. The latter two effects each contribute a 1% shift in the acceptance.

In a similar fashion, using the different generator tunes results in a 2% shift in the reconstruction efficiency. An additional series of checks was performed by varying the cuts imposed during the track selection and in the determination of the corresponding MC-based corrections. The resulting variation in the corrected results contributes another 1% to the reconstruction efficiency uncertainty.

Since the dependence of the reconstruction efficiency on local hit density has been parametrised in terms of leading-jet transverse energy, both the uncertainty on the jet energy scale and the accuracy of the jet-fragmentation description become relevant. The former contribution is estimated by convolving the dependence of the tracking efficiency on the leading-jet transverse energy (see Fig. 2b) with a 4% uncertainty in the jet energy scale [33]. The latter contribution is estimated by comparing the PYTHIA-based corrections to HERWIG++ [37]. The resulting p_T -dependent uncertainty on the occupancy is in the range (0.0–2.8)%.

Based on studies of different generator tunes and MC samples with different hard-scattering scales, the assigned uncertainty to the misidentified-track correction grows linearly as a function of p_T from 0.3 to 3.0%. An additional check was performed for tracks with p_T above 10 GeV/ c to correlate the reconstructed track momentum with the deposited energy in the projected ECAL and HCAL cells. For the selected tracks in this analysis, there is no evidence of any excess of high- p_T misidentified tracks characterised by atypically little energy deposited in the calorimeters. The correction for secondaries and feed-down from weak decays is assigned a 1% systematic uncertainty, which is large compared to the scale of the contributions, but intended to account for the uncertainties in the K_S^0 and Λ fractions [38].

The tendency for finite bin widths (up to 40 GeV/ c) and a finite transverse momentum resolution (rising from 1 to 5% in the range $p_T = 10$ –150 GeV/ c) to deform a steeply falling spectrum is corrected based on the shape of the p_T spectrum and the MC-based p_T response matrix. The effect of momentum resolution alone is 0.5–2.5%, while the wide binning results in an additional correction ranging from a fraction of a percent up to approximately 20% in the widest high- p_T bins. The correction for the two effects is determined by fitting an empirical function to the differential yield, smearing it with the MC-based momentum resolution, re-binning into the bins of the final invariant yield, and dividing by the original fitted form. The quoted systematic uncertainty of 0.3–2.7% is estimated by varying the fitted form of the spectrum and by performing multiple iterations of the unsmearing with successively more accurate input spectra.

In addition to the uncertainties from the event selection efficiency weighting and the tracking corrections described above, the total systematic uncertainty contains a contribution from the uncertainty on the estimation of the event pileup fraction of 0.2 and 1.2% for the 0.9 and 7 TeV data, respectively. In the cases where the total integrated luminosity is used to normalise the results, this contributes an additional 4% (11%) scale uncertainty [14, 15] for $\sqrt{s} = 7$ (0.9) TeV. Assuming that the various p_T -dependent contributions are uncorrelated, the total systematic uncertainty is determined from their sum in quadrature, as indicated in Table 2.

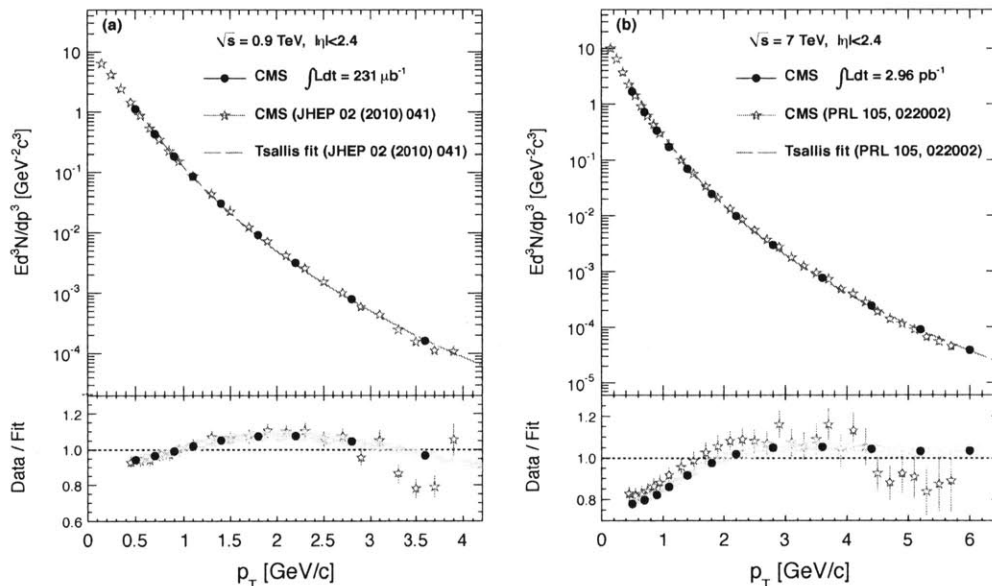


Figure 4: (a) Upper panel: the invariant charged particle differential yield from the present analysis (solid circles) and the previous CMS measurements at $\sqrt{s} = 0.9$ TeV (stars) over the limited p_T range of the earlier result. Lower panel: the ratio of the new (solid circles) and previous (stars) CMS results to a Tsallis fit of the earlier measurement. Error bars on the earlier measurement are the statistical plus systematic uncertainties added in quadrature. The systematic uncertainty band around the new measurement consists of all contributions, except for the common event selection uncertainty. (b) The same for $\sqrt{s} = 7$ TeV.

8 Results

After applying the corrections described in the previous section, the resulting invariant differential yields for charged particles within $|\eta| < 2.4$ are shown for a limited p_T range in Figs. 4a and 4b in order to quantify the agreement with previous CMS measurements at $\sqrt{s} = 0.9$ and 7 TeV [24, 34]. At each energy, both CMS measurements are divided by a Tsallis fit [39] to the earlier measurement and the ratios compared in the lower panels. For the earlier measurements, the error bars indicate the statistical plus systematic uncertainties added in quadrature. The bands around the new measurements represent all contributions to the systematic uncertainty, except the contribution from the common event selection. Statistical uncertainties are negligible on the new measurements in this p_T range. Below $p_T = 4$ GeV/ c for the 0.9 TeV sample and below $p_T = 6$ GeV/ c at $\sqrt{s} = 7$ TeV, which are the limits of the previously published CMS spectra, the new results are in reasonable agreement with the earlier measurements. However, the measured spectra do deviate from the Tsallis fits in the earlier papers by as much as 20% at low p_T . The origin of the small difference between the two CMS measurements at $\sqrt{s} = 7$ TeV is attributed to the different tracking algorithms used in the two measurements, as well as the different PYTHIA tunes used to determine the tracking corrections.

In the upper plots of Figs. 5a and 5b, the charged particle differential transverse momentum yields from this analysis are displayed for $\sqrt{s} = 0.9$ and 7 TeV, respectively. The latter distribution covers the p_T range up to 200 GeV/ c , the largest range ever measured in a colliding beam

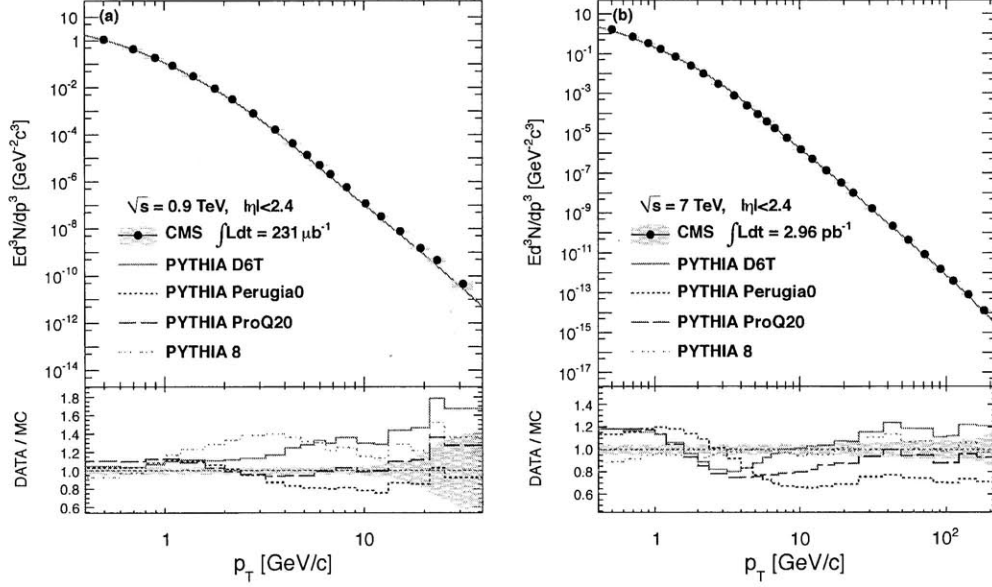


Figure 5: (a) Upper panel: the invariant charged particle differential yield at $\sqrt{s} = 0.9$ TeV compared with the predictions of four tunes of the PYTHIA MC generator. Lower panel: the ratio of the new CMS measurement to the four PYTHIA tunes. The grey band corresponds to the statistical and systematic uncertainties added in quadrature. (b) The same for $\sqrt{s} = 7$ TeV.

experiment. Also shown in the figures are various generator-level MC predictions for the yields [27, 35, 36, 40]. The lower plots of Figs. 5a and 5b show the ratios of the data to the various MC predictions. As already observed in Ref. [34], there is a deficit of $p_T < 1$ GeV/c particles in the predicted 7 TeV spectra for several of the popular PYTHIA tunes. For the whole p_T range above 1 GeV/c, PYTHIA8 is the most consistent with the new 7 TeV result (within 10%). This provides an important constraint on the different generator parameters responsible for sizable variations among the tunes. A similar but slightly larger spread is observed in Fig. 5a for different generator parameters at $\sqrt{s} = 0.9$ TeV, where the CMS measurement is most consistently described by the ProQ20 tune.

As discussed in Ref. [41, 42], a robust prediction of pQCD hard processes is the power-law scaling of the inclusive charged particle invariant differential cross section with the variable x_T :

$$E \frac{d^3\sigma}{dp^3} = F(x_T) / p_T^{n(x_T, \sqrt{s})} = F'(x_T) / \sqrt{s}^{n(x_T, \sqrt{s})}, \quad (4)$$

where F and F' are independent of \sqrt{s} , and the slow evolution of the power-law exponent n with x_T and \sqrt{s} ($n \simeq 5-6$) is due to the running of α_s and changes in the parton distribution and fragmentation functions. In the upper plot of Fig. 6a, the 0.9 and 7 TeV pp measurements from this analysis are compared to the empirical scaling observed from measurements over a range of lower pp collision energies by plotting $\sqrt{s}^n E d^3\sigma/dp^3$. For the purpose of reporting the CMS results as differential cross sections, the integrated luminosities for the analysed data samples were measured according to the descriptions in Ref. [14, 15]. Also, to compare with the published results from the CDF experiment at $\sqrt{s} = 0.63, 1.8,$ and 1.96 TeV, the pseudorapidity

range has been restricted to $|\eta| < 1.0$. Whereas an exponent $n = 5.5$ was found in Ref. [42] from a global fit to only the previous $p\bar{p}$ measurements from $\sqrt{s} = 0.2$ to 1.96 TeV, the x_T scaling presented in this paper is optimised for use in an interpolation between the CDF and CMS measurements from $\sqrt{s} = 0.9$ to 7 TeV. Within this range, the best scaling is achieved with an exponent of $n = 4.9 \pm 0.1$. This is consistent with the predictions of next-to-leading-order (NLO) calculations, where the scaling is also found to be optimised for this value of the exponent [42]. From the lower panel of Fig. 6a, it is apparent that the NLO calculations over-predict the measured cross sections by almost a factor of two at all collision energies. This is in spite of the relatively good agreement in the inclusive jet spectrum [43, 44], which suggests that the fragmentation functions are not well tuned for LHC energies.

The CMS results are consistent over the accessible x_T range with the empirical x_T scaling given by Eq. (4) and established at lower energies. This quality of the scaling is more easily seen in the upper panel of Fig. 6b, where the points show the ratio of the various differential cross sections, scaled by $\sqrt{s}^{4.9}$, to the result of a global power-law fit to the CDF and CMS data from Fig. 6a. The fitting function is of the form $F'(x_T) = p_0 \cdot [1 + (x_T/p_1)]^{p_2}$, where p_0 , p_1 , and p_2 are free parameters, and the region below $p_T = 3.5$ GeV/c has been excluded to avoid complications from soft-particle production. Considering the somewhat naïve power-law function and the expected non-scaling effects [45], the new measurement is in reasonable agreement with the global power-law fit result (within roughly 50%) over its full x_T range.

9 Interpolation to 2.76 TeV

In order to construct a predicted reference charged particle differential cross section at $\sqrt{s} = 2.76$ TeV for comparison with the measured PbPb heavy-ion spectrum, two different techniques are used in partially overlapping transverse momentum regimes. In the high- p_T range from 5.0–200 GeV/c, where approximate x_T scaling is expected to hold, the estimated 2.76 TeV cross section is derived from a common x_T -scaling curve, based on the CDF and CMS measurements shown in Fig. 6a. In the low- p_T range from 1.0–20 GeV/c, it is possible to interpolate directly between the several measured cross section values as a function of \sqrt{s} at each fixed p_T value.

As discussed in the previous section, the upper panel of Fig. 6b shows the residual difference from perfect x_T scaling with exponent $n = 4.9$ for the 0.9 and 7 TeV CMS measurements and for the 1.96 TeV CDF measurement [4, 5]. The \sqrt{s} and x_T dependence of the residuals are not unexpected, since this behaviour is predicted by NLO calculations. This can be seen in the lower panel of Fig. 6b, which shows the predicted deviation from perfect x_T scaling for calculated NLO cross sections at several collision energies with respect to a reference centre-of-mass energy of 2.75 TeV [42]. The calculations were performed using the CTEQ66 parton distribution functions [46], DSS fragmentation [47], and a factorisation scale $\mu = p_T$ [42]. Taking the magnitude of the x_T -scaling violation from NLO (ranging from 0–20%), each of the three measurements in data (i.e., 0.9, 1.96, and 7 TeV) can be corrected separately to arrive at an expectation for the 2.76 TeV cross section. The three independent interpolations based on NLO-corrected x_T scaling are shown as solid blue lines in the upper panel of Fig. 6b. The combined ‘best estimate’ (shown as a shaded band) has an associated uncertainty that covers the deviations of up to 12% observed by varying the factorisation scale from $\mu = 0.5 p_T$ to $\mu = 2.0 p_T$ for each of the three collision energies. The error band is expanded below $p_T \approx 8$ GeV/c to include the full difference between the 1.96 and 7 TeV results, since the evolution of the spectra below this value — corresponding to $x_T = 0.0023$ (7 TeV), 0.0082 (1.96 TeV), and 0.018 (0.9 TeV) — is no longer consistently described by x_T scaling and the NLO-based corrections. In addition to the 12% contribution from the uncertainty on the NLO-based correction, the final uncertainty on

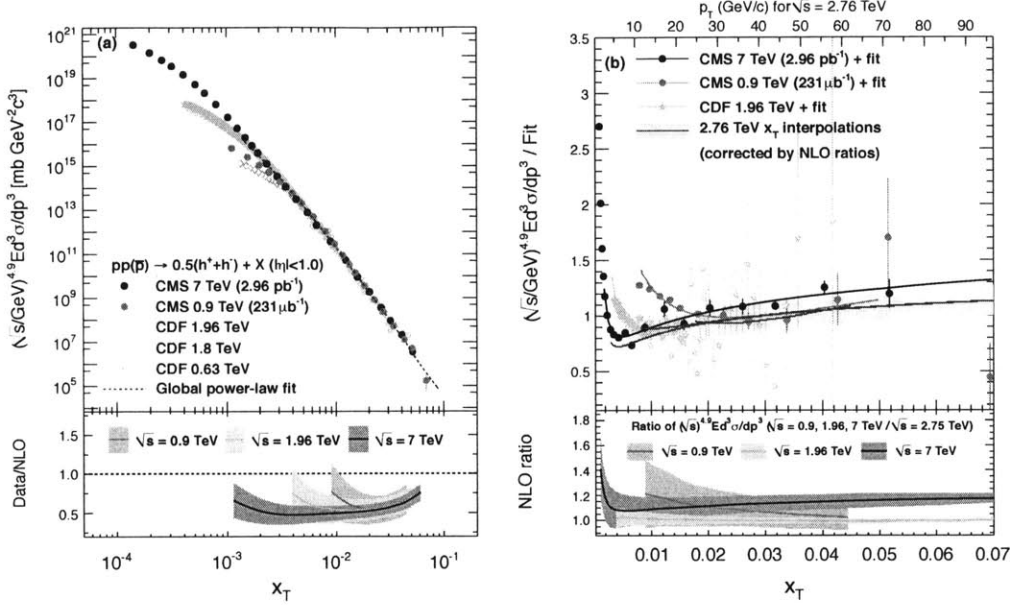


Figure 6: (a) Upper panel: inclusive charged particle invariant differential cross sections, scaled by $\sqrt{s}^{4.9}$, for $|\eta| < 1.0$ as a function of the scaling parameter x_T . The result is the average of the positive and negative charged particles. Lower panel: ratios of differential cross sections measured at 0.9, 1.96, and 7 TeV to those predicted by NLO calculations for factorisation scales ranging from 0.5–2.0 p_T . (b) Upper panel: ratios of the scaled differential cross sections to the global power-law x_T fit described in the text (coloured markers) and fits to these ratios (similarly coloured thin lines). The expected ratio for $\sqrt{s} = 2.76$ TeV after applying NLO-based corrections to each of the three measurements as described in the text (solid blue lines). The uncertainty from the NLO parameters is represented by the shaded band. The upper axis translates x_T to p_T for $\sqrt{s} = 2.76$ TeV. Lower panel: ratios of the NLO-calculated cross sections at three different energies, scaled by $\sqrt{s}^{4.9}$, to the cross section calculated at $\sqrt{s} = 2.75$ TeV. The width of the bands represents the variation of the factorisation scale by a factor of two.

the interpolated cross section has an additional component to account for possible correlations in the luminosity uncertainty between the three measurements. This term, taken as equal to the smallest individual uncertainty (4%), is added in quadrature.

The direct interpolation of cross sections at a fixed value of p_T is done using CDF measurements at $\sqrt{s} = 0.63, 1.8$ and 1.96 TeV [4, 5, 17], the new CMS measurements at $\sqrt{s} = 0.9$ and 7 TeV, as well as an earlier result at $\sqrt{s} = 2.36$ TeV [24]. The latter measurement is converted to a differential cross section assuming the total inelastic cross section of 60.52 mb from PYTHIA. At each energy, an empirical fit to the p_T distribution is first constructed to provide a continuous estimation independent of different binning. Then, in arbitrarily small p_T bins, these empirical fits are evaluated and the evolution of the cross section with \sqrt{s} is parametrised by a second-order polynomial. Two examples of these fits are shown in Fig. 7a for $p_T = 3$ and 9 GeV/c. The uncertainty on the value of the fit evaluated at $\sqrt{s} = 2.76$ TeV is taken from the covariance matrix of the fit terms, with an additional 4% added in quadrature to account conservatively for any correlation in the luminosity uncertainty between the different measurements.

To arrive at a single interpolated spectrum over the full p_T range, a linear combination of the two techniques is used with weights that vary linearly across the overlap range from $p_T = 5 \text{ GeV}/c$ (only direct interpolation at fixed p_T) to $p_T = 20 \text{ GeV}/c$ (only x_T scaling with NLO-based residual correction). In the p_T range where the two techniques overlap, the different methods agree to within their respective systematic uncertainties. (The fixed- p_T interpolation value is typically around 8% lower than the x_T interpolation.) The resulting predicted 2.76 TeV differential cross section is shown in the upper panel of Fig. 7b, and its ratio with respect to various PYTHIA tunes at that centre-of-mass energy in the lower panel. The uncertainty on the predicted cross section, shown by the grey band in the lower panel, is the weighted sum (where applicable) of the uncertainties derived from the two methods described in the preceding paragraphs. Also shown in the lower panel of Fig. 7b is the ratio of the predicted 2.76 TeV cross section to that found by simply scaling the CMS measured 7 TeV result by the expected 2.75 TeV to 7 TeV ratio from NLO calculations [42]. The interpolation used in the recent ALICE publication [13] is a few percent lower than the result quoted in this paper, but consistent within the respective systematic uncertainties. The behavior of the various generators compared to the interpolated 2.76 TeV cross section is broadly similar to the 0.9 TeV invariant yields presented in Fig. 7b. The ProQ20 tune agrees most closely (within 15%) with the interpolated cross section above 2 GeV/ c . Future analysis of a recently recorded 2.76 TeV pp collision sample will provide verification of this result and a reduction in the systematic uncertainties.

10 Summary

In this paper, measurements of the phase-space-invariant differential yield $E d^3 N_{\text{ch}}/dp^3$ at $\sqrt{s} = 0.9$ and 7 TeV have been presented for primary charged particles, averaged over the pseudorapidity acceptance of the CMS tracking system ($|\eta| < 2.4$). The results have been shown to be in reasonable agreement with the previously published CMS measurements at $\sqrt{s} = 0.9$ and 7 TeV [24, 34] and, except for the surplus of tracks at very low transverse momentum, with PYTHIA leading-order pQCD. The 7 TeV data are most consistent with PYTHIA8, which agrees at the 10% level over the full p_T range of the measurement. In contrast, the 0.9 TeV data are considerably better described by the ProQ20 tune. Additionally, the consistency of the 0.9 and 7 TeV spectra has been demonstrated with an empirical x_T scaling that unifies the differential cross sections from a wide range of collision energies onto a common curve. Furthermore, within the theoretical uncertainties of the NLO calculations, the residual breaking of x_T scaling above $p_T \approx 8 \text{ GeV}/c$ is consistent between the measured cross sections and the NLO calculations.

This result has removed a large uncertainty from an important ingredient of existing and future PbPb measurements, namely the pp reference spectrum corresponding to the energy of the 2010 PbPb run: 2.76 TeV per nucleon. By employing a combination of techniques to interpolate between the results presented here at $\sqrt{s} = 0.9$ and 7 TeV, including information from existing CDF measurements at $\sqrt{s} = 0.63, 1.8,$ and 1.96 TeV , a pp reference at $\sqrt{s} = 2.76 \text{ TeV}$ has been constructed over a large range of transverse momentum ($p_T = 1\text{--}100 \text{ GeV}/c$) with systematic uncertainties of less than 13%.

Acknowledgements

We wish to congratulate our colleagues in the CERN accelerator departments for the excellent performance of the LHC machine. We thank the technical and administrative staff at CERN and other CMS institutes, and acknowledge support from: FMSR (Austria); FNRS and FWO (Belgium); CNPq, CAPES, FAPERJ, and FAPESP (Brazil); MES (Bulgaria); CERN; CAS, MoST, and

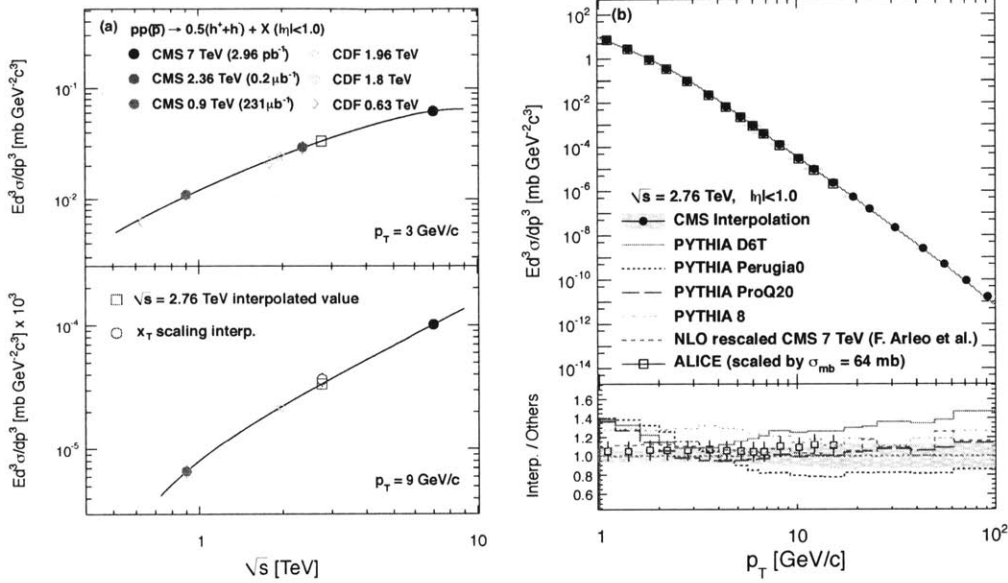


Figure 7: (a) Interpolations between measured charged particle differential cross sections at different \sqrt{s} for the two example values of $p_T = 3$ and $9 \text{ GeV}/c$. Second-order polynomial fits to the measured data are shown by the solid lines. The open squares show the resulting interpolated cross sections for $\sqrt{s} = 2.76 \text{ TeV}$. The open circle on the lower panel represents the corresponding estimate from the x_T -scaling approach in the overlap region where both can be estimated. (b) Upper panel: the predicted 2.76 TeV charged particle differential transverse momentum cross section, based on the combined direct p_T interpolation and NLO-corrected x_T -scaling techniques described in the text. Lower panel: ratios of combined interpolation to predictions from several PYTHIA tunes, an NLO-based rescaling approach [42], and the ALICE interpolation used in Ref. [13].

NSFC (China); COLCIENCIAS (Colombia); MSES (Croatia); RPF (Cyprus); Academy of Sciences and NICPB (Estonia); Academy of Finland, MEC, and HIP (Finland); CEA and CNRS/IN2P3 (France); BMBF, DFG, and HGF (Germany); GSRT (Greece); OTKA and NKTH (Hungary); DAE and DST (India); IPM (Iran); SFI (Ireland); INFN (Italy); NRF and WCU (Korea); LAS (Lithuania); CINVESTAV, CONACYT, SEP, and UASLP-FAI (Mexico); PAEC (Pakistan); SCSR (Poland); FCT (Portugal); JINR (Armenia, Belarus, Georgia, Ukraine, Uzbekistan); MST and MAE (Russia); MSTD (Serbia); MICINN and CPAN (Spain); Swiss Funding Agencies (Switzerland); NSC (Taipei); TUBITAK and TAEK (Turkey); STFC (United Kingdom); DOE and NSF (USA). Individuals have received support from the Marie-Curie programme and the European Research Council (European Union); the Leventis Foundation; the A. P. Sloan Foundation; the Alexander von Humboldt Foundation; the Associazione per lo Sviluppo Scientifico e Tecnologico del Piemonte (Italy); the Belgian Federal Science Policy Office; the Fonds pour la Formation à la Recherche dans l'Industrie et dans l'Agriculture (FRIA-Belgium); and the Agentschap voor Innovatie door Wetenschap en Technologie (IWT-Belgium).

References

- [1] F. Arleo and D. d’Enterria, “Single inclusive pion p_T -spectra in proton-proton collisions at $\sqrt{s} = 22.4$ GeV: data versus perturbative QCD calculations”, *Phys. Rev.* **D78** (2008) 094004, arXiv:0807.1252. doi:10.1103/PhysRevD.78.094004.
- [2] PHENIX Collaboration, “Inclusive cross section and double helicity asymmetry for π^0 production in $p + p$ collisions at $\sqrt{s} = 200$ GeV: Implications for the polarized gluon distribution in the proton”, *Phys. Rev.* **D76** (2007) 051106, arXiv:0704.3599. doi:10.1103/PhysRevD.76.051106.
- [3] PHENIX Collaboration, “Inclusive cross section and double helicity asymmetry for π^0 production in $p + p$ collisions at $\sqrt{s} = 62.4$ GeV”, *Phys. Rev.* **D79** (2009) 012003, arXiv:0810.0701. doi:10.1103/PhysRevD.79.012003.
- [4] CDF Collaboration, “Measurement of Particle Production and Inclusive Differential Cross Sections in $p\bar{p}$ Collisions at $\sqrt{s} = 1.96$ TeV”, *Phys. Rev.* **D79** (2009) 112005, arXiv:0904.1098. doi:10.1103/PhysRevD.79.112005.
- [5] CDF Collaboration, “Erratum: Measurement of particle production and inclusive differential cross sections in $p\bar{p}$ collisions at $\sqrt{s} = 1.96$ TeV [*Phys. Rev.* **D79** (2009) 112005]”, *Phys. Rev.* **D82** (2010) 119903, arXiv:0904.1098. doi:10.1103/PhysRevD.82.119903.
- [6] ATLAS Collaboration, “Charged-particle multiplicities in pp interactions measured with the ATLAS detector at the LHC”, arXiv:1012.5104.
- [7] ALICE Collaboration, “Transverse momentum spectra of charged particles in proton-proton collisions at $\sqrt{s} = 900$ GeV with ALICE at the LHC”, *Phys. Lett.* **B693** (2010) 53, arXiv:1007.0719. doi:10.1016/j.physletb.2010.08.026.
- [8] A. S. Yoon, E. Wenger, and G. Roland, “Convoluting jet spectra with fragmentation functions: a cross-check of the charged particle p_T spectrum”, arXiv:1003.5928.
- [9] B. B. Back et al., “The PHOBOS perspective on discoveries at RHIC”, *Nucl. Phys.* **A757** (2005) 28. doi:10.1016/j.nuclphysa.2005.03.084.
- [10] STAR Collaboration, “Experimental and theoretical challenges in the search for the quark gluon plasma: The STAR collaboration’s critical assessment of the evidence from RHIC collisions”, *Nucl. Phys.* **A757** (2005) 102. doi:10.1016/j.nuclphysa.2005.03.085.
- [11] PHENIX Collaboration, “Formation of dense partonic matter in relativistic nucleus nucleus collisions at RHIC: Experimental evaluation by the PHENIX collaboration”, *Nucl. Phys.* **A757** (2005) 184. doi:10.1016/j.nuclphysa.2005.03.086.
- [12] BRAHMS Collaboration, “Quark gluon plasma and color glass condensate at RHIC? The perspective from the BRAHMS experiment”, *Nucl. Phys.* **A757** (2005) 1. doi:10.1016/j.nuclphysa.2005.02.130.
- [13] ALICE Collaboration, “Suppression of Charged Particle Production at Large Transverse Momentum in Central Pb–Pb Collisions at $\sqrt{s_{NN}} = 2.76$ TeV”, *Phys. Lett.* **B696** (2011) 30, arXiv:1012.1004. doi:10.1016/j.physletb.2010.12.020.

- [14] CMS Collaboration, "Measurement of CMS Luminosity", *CMS Physics Analysis Summary CMS-PAS-EWK-10-004* (2010).
- [15] CMS Collaboration, "Absolute luminosity normalization", *CMS Detector Performance Summary CMS-DP-2011-002* (2011).
- [16] UA1 Collaboration, "A Study of the General Characteristics of Proton-Antiproton Collisions at $\sqrt{s} = 0.2$ to 0.9 TeV", *Nucl. Phys.* **B335** (1990) 261.
doi:10.1016/0550-3213(90)90493-W.
- [17] CDF Collaboration, "Transverse momentum distributions of charged particles produced in $\bar{p}p$ interactions at $\sqrt{s} = 630$ GeV and 1800 GeV", *Phys. Rev. Lett.* **61** (1988) 1819.
doi:10.1103/PhysRevLett.61.1819.
- [18] CMS Collaboration, "The CMS experiment at the CERN LHC", *JINST* **3** (2008) S08004.
doi:10.1088/1748-0221/3/08/S08004.
- [19] CMS Collaboration, "CMS Physics TDR: Volume I, Detector Performance and Software", *CERN-LHCC* **2006-001** (2006).
- [20] CMS Collaboration, "Alignment of the CMS Silicon Tracker during Commissioning with Cosmic Rays", *JINST* **5** (2010) T03009, arXiv:0910.2505.
doi:10.1088/1748-0221/5/03/T03009.
- [21] A. J. Bell, "Design and Construction of the Beam Scintillation Counter for CMS", Master's thesis, University of Canterbury, Christchurch, New Zealand, 2008.
- [22] T. Aumeyr, "Beam Phase and Intensity Monitoring for the Compact Muon Solenoid Experiment", Master's thesis, Vienna University of Technology, Austria, 2008.
- [23] GEANT4 Collaboration, "GEANT4: a simulation toolkit", *Nucl. Instrum. and Methods* **A506** (2003) 250. doi:10.1016/S0168-9002(03)01368-8.
- [24] CMS Collaboration, "Transverse momentum and pseudorapidity distributions of charged hadrons in pp collisions at $\sqrt{s} = 0.9$ and 2.36 TeV", *JHEP* **02** (2010) 041, arXiv:1002.0621. doi:10.1007/JHEP02(2010)041.
- [25] CMS Collaboration, "Tracking and Vertexing Results from First Collisions", *CMS Physics Analysis Summary CMS-PAS-TRK-10-001* (2010).
- [26] T. Sjöstrand, S. Mrenna, and P. Z. Skands, "PYTHIA 6.4 Physics and Manual", *JHEP* **05** (2006) 026, arXiv:hep-ph/0603175.
- [27] P. Bartalini and L. Fanó, eds., "Proceedings of the First Workshop on Multiple Partonic Interactions at the LHC, Perugia, Italy, October 27-31, 2008". (2009).
arXiv:1003.4220.
- [28] F. W. Bopp, R. Engel, and J. Ranft, "Rapidity gaps and the PHOJET Monte Carlo", arXiv:hep-ph/9803437.
- [29] R. Engel, J. Ranft, and S. Roesler, "Hard diffraction in hadron-hadron interactions and in photoproduction", *Phys. Rev.* **D52** (1995) 1459, arXiv:hep-ph/9502319.
doi:10.1103/PhysRevD.52.1459.

-
- [30] F. Siklér, "Study of clustering methods to improve primary vertex finding for collider detectors", *Nucl. Instrum. Meth.* **A621** (2010) 526, arXiv:0911.2767.
doi:10.1016/j.nima.2010.04.058.
- [31] CMS Collaboration, "Track and vertex reconstruction in CMS", *Nucl. Instrum. Meth.* **A582** (2007) 781. doi:10.1016/j.nima.2007.07.091.
- [32] M. Cacciari, G. P. Salam, and G. Soyez, "The anti- k_t jet clustering algorithm", *JHEP* **04** (2008) 063, arXiv:0802.1189. doi:10.1088/1126-6708/2008/04/063.
- [33] CMS Collaboration, "Determination of the Jet Energy Scale in CMS with pp Collisions at $\sqrt{s} = 7$ TeV", *CMS Physics Analysis Summary CMS-PAS-JME-10-010* (2010).
- [34] CMS Collaboration, "Transverse-momentum and pseudorapidity distributions of charged hadrons in pp collisions at $\sqrt{s} = 7$ TeV", *Phys. Rev. Lett.* **105** (2010) 022002, arXiv:1005.3299. doi:10.1103/PhysRevLett.105.022002.
- [35] T. Sjöstrand, S. Mrenna, and P. Z. Skands, "A Brief Introduction to PYTHIA 8.1", *Comput. Phys. Commun.* **178** (2008) 852, arXiv:0710.3820.
doi:10.1016/j.cpc.2008.01.036.
- [36] P. Z. Skands, "The Perugia Tunes", (2009). arXiv:0905.3418.
- [37] M. Bähr et al., "Herwig++ Physics and Manual", *Eur. Phys. J.* **C58** (2008) 639, arXiv:0803.0883. doi:10.1140/epjc/s10052-008-0798-9.
- [38] CMS Collaboration, "Strange Particle Production in pp Collisions at $\sqrt{s} = 0.9$ and 7 TeV", (2011). arXiv:1102.4282. Submitted to *JHEP*.
- [39] C. Tsallis, "Possible generalization of Boltzmann-Gibbs statistics", *Journal of Statistical Physics* **52** (1988) 479. doi:10.1007/BF01016429.
- [40] A. Buckley et al., "Systematic event generator tuning for the LHC", *Eur. Phys. J.* **C65** (2010) 331, arXiv:0907.2973. doi:10.1140/epjc/s10052-009-1196-7.
- [41] F. Arleo, S. J. Brodsky, D. S. Hwang et al., "Higher-Twist Dynamics in Large Transverse Momentum Hadron Production", *Phys. Rev. Lett.* **105** (2010) 062002, arXiv:0911.4604. doi:10.1103/PhysRevLett.105.062002.
- [42] F. Arleo, D. d'Enterria, and A. S. Yoon, "Single-inclusive production of large-pT charged particles in hadronic collisions at TeV energies and perturbative QCD predictions", *JHEP* **06** (2010) 035, arXiv:1003.2963. doi:10.1007/JHEP06(2010)035.
- [43] CMS Collaboration, "Measurement of the Inclusive Jet Cross Section in pp Collisions at $\sqrt{s} = 7$ TeV", arXiv:1106.0208.
- [44] ATLAS Collaboration, "Measurement of inclusive jet and dijet cross sections in proton-proton collisions at 7 TeV centre-of-mass energy with the ATLAS detector", *Eur. Phys. J.* **C71** (2011) 1512, arXiv:1009.5908.
doi:10.1140/epjc/s10052-010-1512-2.
- [45] M. Stratmann, R. Sassot, and P. Zurita, "Inclusive Hadron Production in the CERN-LHC Era", arXiv:1008.0540.

-
- [46] P. M. Nadolsky et al., "Implications of CTEQ global analysis for collider observables", *Phys. Rev.* **D78** (2008) 013004, arXiv:0802.0007.
doi:10.1103/PhysRevD.78.013004.
- [47] D. de Florian, R. Sassot, and M. Stratmann, "Global analysis of fragmentation functions for pions and kaons and their uncertainties", *Phys. Rev.* **D75** (2007) 114010,
arXiv:hep-ph/0703242. doi:10.1103/PhysRevD.75.114010.

A The CMS Collaboration

Yerevan Physics Institute, Yerevan, Armenia

S. Chatrchyan, V. Khachatryan, A.M. Sirunyan, A. Tumasyan

Institut für Hochenergiephysik der OeAW, Wien, Austria

W. Adam, T. Bergauer, M. Dragicevic, J. Erö, C. Fabjan, M. Friedl, R. Frühwirth, V.M. Ghete, J. Hammer¹, S. Häsnel, M. Hoch, N. Hörmann, J. Hrubec, M. Jeitler, W. Kiesenhofer, M. Krammer, D. Liko, I. Mikulec, M. Pernicka, H. Rohringer, R. Schöfbeck, J. Strauss, A. Taurok, F. Teischinger, P. Wagner, W. Waltenberger, G. Walzel, E. Widl, C.-E. Wulz

National Centre for Particle and High Energy Physics, Minsk, Belarus

V. Mossolov, N. Shumeiko, J. Suarez Gonzalez

Universiteit Antwerpen, Antwerpen, Belgium

L. Benucci, E.A. De Wolf, X. Janssen, J. Maes, T. Maes, L. Mucibello, S. Ochesanu, B. Roland, R. Rougny, M. Selvaggi, H. Van Haevermaet, P. Van Mechelen, N. Van Remortel

Vrije Universiteit Brussel, Brussel, Belgium

F. Blekman, S. Blyweert, J. D'Hondt, O. Devroede, R. Gonzalez Suarez, A. Kalogeropoulos, M. Maes, W. Van Doninck, P. Van Mulders, G.P. Van Onsem, I. Villella

Université Libre de Bruxelles, Bruxelles, Belgium

O. Charaf, B. Clerbaux, G. De Lentdecker, V. Dero, A.P.R. Gay, G.H. Hammad, T. Hreus, P.E. Marage, L. Thomas, C. Vander Velde, P. Vanlaer

Ghent University, Ghent, Belgium

V. Adler, A. Cimmino, S. Costantini, M. Grunewald, B. Klein, J. Lellouch, A. Marinov, J. Mccartin, D. Ryckbosch, F. Thyssen, M. Tytgat, L. Vanelderen, P. Verwilligen, S. Walsh, N. Zaganidis

Université Catholique de Louvain, Louvain-la-Neuve, Belgium

S. Basegmez, G. Bruno, J. Caudron, L. Ceard, E. Cortina Gil, J. De Favereau De Jeneret, C. Delaere¹, D. Favart, A. Giammanco, G. Grégoire, J. Hollar, V. Lemaitre, J. Liao, O. Militaru, S. Ovyn, D. Pagano, A. Pin, K. Piotrkowski, N. Schul

Université de Mons, Mons, Belgium

N. Belyi, T. Caebergs, E. Daubie

Centro Brasileiro de Pesquisas Físicas, Rio de Janeiro, Brazil

G.A. Alves, D. De Jesus Damiao, M.E. Pol, M.H.G. Souza

Universidade do Estado do Rio de Janeiro, Rio de Janeiro, Brazil

W. Carvalho, E.M. Da Costa, C. De Oliveira Martins, S. Fonseca De Souza, L. Mundim, H. Nogima, V. Oguri, W.L. Prado Da Silva, A. Santoro, S.M. Silva Do Amaral, A. Sznajder, F. Torres Da Silva De Araujo

Instituto de Física Teórica, Universidade Estadual Paulista, Sao Paulo, Brazil

F.A. Dias, T.R. Fernandez Perez Tomei, E. M. Gregores², C. Lagana, F. Marinho, P.G. Mercadante², S.F. Novaes, Sandra S. Padula

Institute for Nuclear Research and Nuclear Energy, Sofia, Bulgaria

N. Darnenov¹, L. Dimitrov, V. Genchev¹, P. Iaydjiev¹, S. Piperov, M. Rodozov, S. Stoykova, G. Sultanov, V. Tcholakov, R. Trayanov, I. Vankov

University of Sofia, Sofia, Bulgaria

A. Dimitrov, R. Hadjiiska, A. Karadzhinova, V. Kozhuharov, L. Litov, M. Mateev, B. Pavlov, P. Petkov

Institute of High Energy Physics, Beijing, China

J.G. Bian, G.M. Chen, H.S. Chen, C.H. Jiang, D. Liang, S. Liang, X. Meng, J. Tao, J. Wang, J. Wang, X. Wang, Z. Wang, H. Xiao, M. Xu, J. Zang, Z. Zhang

State Key Lab. of Nucl. Phys. and Tech., Peking University, Beijing, China

Y. Ban, S. Guo, Y. Guo, W. Li, Y. Mao, S.J. Qian, H. Teng, L. Zhang, B. Zhu, W. Zou

Universidad de Los Andes, Bogota, Colombia

A. Cabrera, B. Gomez Moreno, A.A. Ocampo Rios, A.F. Osorio Oliveros, J.C. Sanabria

Technical University of Split, Split, Croatia

N. Godinovic, D. Lelas, K. Lelas, R. Plestina³, D. Polic, I. Puljak

University of Split, Split, Croatia

Z. Antunovic, M. Dzelalija

Institute Rudjer Boskovic, Zagreb, Croatia

V. Brigljevic, S. Duric, K. Kadija, S. Morovic

University of Cyprus, Nicosia, Cyprus

A. Attikis, M. Galanti, J. Mousa, C. Nicolaou, F. Ptochos, P.A. Razis

Charles University, Prague, Czech Republic

M. Finger, M. Finger Jr.

Academy of Scientific Research and Technology of the Arab Republic of Egypt, Egyptian Network of High Energy Physics, Cairo, Egypt

Y. Assran⁴, S. Khalil⁵, M.A. Mahmoud⁶

National Institute of Chemical Physics and Biophysics, Tallinn, Estonia

A. Hektor, M. Kadastik, M. Müntel, M. Raidal, L. Rebane

Department of Physics, University of Helsinki, Helsinki, Finland

V. Azzolini, P. Eerola, G. Fedi

Helsinki Institute of Physics, Helsinki, Finland

S. Czellar, J. Härkönen, A. Heikkinen, V. Karimäki, R. Kinnunen, M.J. Kortelainen, T. Lampén, K. Lassila-Perini, S. Lehti, T. Lindén, P. Luukka, T. Mäenpää, E. Tuominen, J. Tuominiemi, E. Tuovinen, D. Ungaro, L. Wendland

Lappeenranta University of Technology, Lappeenranta, Finland

K. Banzuzi, A. Korpela, T. Tuuva

Laboratoire d'Annecy-le-Vieux de Physique des Particules, IN2P3-CNRS, Annecy-le-Vieux, France

D. Sillou

DSM/IRFU, CEA/Saclay, Gif-sur-Yvette, France

M. Besancon, S. Choudhury, M. Dejardin, D. Denegri, B. Fabbro, J.L. Faure, F. Ferri, S. Ganjour, F.X. Gentit, A. Givernaud, P. Gras, G. Hamel de Monchenault, P. Jarry, E. Locci, J. Malcles, M. Marionneau, L. Millischer, J. Rander, A. Rosowsky, I. Shreyber, M. Titov, P. Verrecchia

Laboratoire Leprince-Ringuet, Ecole Polytechnique, IN2P3-CNRS, Palaiseau, France

S. Baffioni, F. Beaudette, L. Benhabib, L. Bianchini, M. Bluj⁷, C. Broutin, P. Busson, C. Charlot, T. Dahms, L. Dobrzynski, S. Elgammal, R. Granier de Cassagnac, M. Haguenaer, P. Miné, C. Mironov, C. Ochando, P. Paganini, D. Sabes, R. Salerno, Y. Sirois, C. Thiebaut, B. Wyslouch⁸, A. Zabi

Institut Pluridisciplinaire Hubert Curien, Université de Strasbourg, Université de Haute Alsace Mulhouse, CNRS/IN2P3, Strasbourg, France

J.-L. Agram⁹, J. Andrea, D. Bloch, D. Bodin, J.-M. Brom, M. Cardaci, E.C. Chabert, C. Collard, E. Conte⁹, F. Drouhin⁹, C. Ferro, J.-C. Fontaine⁹, D. Gelé, U. Goerlach, S. Greder, P. Juillot, M. Karim⁹, A.-C. Le Bihan, Y. Mikami, P. Van Hove

Centre de Calcul de l'Institut National de Physique Nucleaire et de Physique des Particules (IN2P3), Villeurbanne, France

F. Fassi, D. Mercier

Université de Lyon, Université Claude Bernard Lyon 1, CNRS-IN2P3, Institut de Physique Nucléaire de Lyon, Villeurbanne, France

C. Baty, S. Beauceron, N. Beaupere, M. Bedjidian, O. Bondu, G. Boudoul, D. Boumediene, H. Brun, J. Chasserat, R. Chierici, D. Contardo, P. Depasse, H. El Mamouni, J. Fay, S. Gascon, B. Ille, T. Kurca, T. Le Grand, M. Lethuillier, L. Mirabito, S. Perries, V. Sordini, S. Tosi, Y. Tschudi, P. Verdier

Institute of High Energy Physics and Informatization, Tbilisi State University, Tbilisi, Georgia

D. Lomidze

RWTH Aachen University, I. Physikalisches Institut, Aachen, Germany

G. Anagnostou, M. Edelhoff, L. Feld, N. Heracleous, O. Hindrichs, R. Jussen, K. Klein, J. Merz, N. Mohr, A. Ostapchuk, A. Perieanu, F. Raupach, J. Sammet, S. Schael, D. Sprenger, H. Weber, M. Weber, B. Wittmer

RWTH Aachen University, III. Physikalisches Institut A, Aachen, Germany

M. Ata, W. Bender, E. Dietz-Laursonn, M. Erdmann, J. Frangenheim, T. Hebbeker, A. Hinzmann, K. Hoepfner, T. Klimkovich, D. Klingebiel, P. Kreuzer, D. Lanske[†], C. Magass, M. Merschmeyer, A. Meyer, P. Papacz, H. Pieta, H. Reithler, S.A. Schmitz, L. Sonnenschein, J. Steggemann, D. Teyssier

RWTH Aachen University, III. Physikalisches Institut B, Aachen, Germany

M. Bontenackels, M. Davids, M. Duda, G. Flügge, H. Geenen, M. Giffels, W. Haj Ahmad, D. Heydhausen, T. Kress, Y. Kuessel, A. Linn, A. Nowack, L. Perchalla, O. Pooth, J. Rennefeld, P. Sauerland, A. Stahl, M. Thomas, D. Tornier, M.H. Zoeller

Deutsches Elektronen-Synchrotron, Hamburg, Germany

M. Aldaya Martin, W. Behrenhoff, U. Behrens, M. Bergholz¹⁰, A. Bethani, K. Borras, A. Cakir, A. Campbell, E. Castro, D. Dammann, G. Eckerlin, D. Eckstein, A. Flossdorf, G. Flucke, A. Geiser, J. Hauk, H. Jung¹, M. Kasemann, I. Katkov¹¹, P. Katsas, C. Kleinwort, H. Kluge, A. Knutsson, M. Krämer, D. Krücker, E. Kuznetsova, W. Lange, W. Lohmann¹⁰, R. Mankel, M. Marienfeld, I.-A. Melzer-Pellmann, A.B. Meyer, J. Mnich, A. Mussgiller, J. Olzem, D. Pitzl, A. Raspereza, A. Raval, M. Rosin, R. Schmidt¹⁰, T. Schoerner-Sadenius, N. Sen, A. Spiridonov, M. Stein, J. Tomaszewska, R. Walsh, C. Wissing

University of Hamburg, Hamburg, Germany

C. Autermann, V. Blobel, S. Bobrovskiy, J. Draeger, H. Enderle, U. Gebbert, K. Kaschube,

G. Kaussen, R. Klanner, J. Lange, B. Mura, S. Naumann-Emme, F. Nowak, N. Pietsch, C. Sander, H. Schettler, P. Schleper, M. Schröder, T. Schum, J. Schwandt, H. Stadie, G. Steinbrück, J. Thomsen

Institut für Experimentelle Kernphysik, Karlsruhe, Germany

C. Barth, J. Bauer, V. Buege, T. Chwalek, W. De Boer, A. Dierlamm, G. Dirkes, M. Feindt, J. Gruschke, C. Hackstein, F. Hartmann, M. Heinrich, H. Held, K.H. Hoffmann, S. Honc, J.R. Komaragiri, T. Kuhr, D. Martschei, S. Mueller, Th. Müller, M. Niegel, O. Oberst, A. Oehler, J. Ott, T. Peiffer, G. Quast, K. Rabbertz, F. Ratnikov, N. Ratnikova, M. Renz, C. Saout, A. Scheurer, P. Schieferdecker, F.-P. Schilling, M. Schmanau, G. Schott, H.J. Simonis, F.M. Stober, D. Troendle, J. Wagner-Kuhr, T. Weiler, M. Zeise, V. Zhukov¹¹, E.B. Ziebarth

Institute of Nuclear Physics "Demokritos", Aghia Paraskevi, Greece

G. Daskalakis, T. Gerasis, S. Kesisoglou, A. Kyriakis, D. Loukas, I. Manolakos, A. Markou, C. Markou, C. Mavrommatis, E. Ntomari, E. Petrakou

University of Athens, Athens, Greece

L. Gouskos, T.J. Mertzimekis, A. Panagiotou, E. Stiliaris

University of Ioánnina, Ioánnina, Greece

I. Evangelou, C. Foudas, P. Kokkas, N. Manthos, I. Papadopoulos, V. Patras, F.A. Triantis

KFKI Research Institute for Particle and Nuclear Physics, Budapest, Hungary

A. Aranyi, G. Bencze, L. Boldizsar, C. Hajdu¹, P. Hidas, D. Horvath¹², A. Kapusi, K. Krajczar¹³, F. Sikler¹, G.I. Veres¹³, G. Vesztergombi¹³

Institute of Nuclear Research ATOMKI, Debrecen, Hungary

N. Beni, J. Molnar, J. Palinkas, Z. Szillasi, V. Veszpremi

University of Debrecen, Debrecen, Hungary

P. Raics, Z.L. Trocsanyi, B. Ujvari

Panjab University, Chandigarh, India

S. Bansal, S.B. Beri, V. Bhatnagar, N. Dhingra, R. Gupta, M. Jindal, M. Kaur, J.M. Kohli, M.Z. Mehta, N. Nishu, L.K. Saini, A. Sharma, A.P. Singh, J.B. Singh, S.P. Singh

University of Delhi, Delhi, India

S. Ahuja, S. Bhattacharya, B.C. Choudhary, B. Gomber, P. Gupta, S. Jain, S. Jain, R. Khurana, A. Kumar, K. Ranjan, R.K. Shivpuri

Bhabha Atomic Research Centre, Mumbai, India

R.K. Choudhury, D. Dutta, S. Kailas, V. Kumar, A.K. Mohanty¹, L.M. Pant, P. Shukla

Tata Institute of Fundamental Research - EHEP, Mumbai, India

T. Aziz, M. Guchait¹⁴, A. Gurtu, M. Maity¹⁵, D. Majumder, G. Majumder, K. Mazumdar, G.B. Mohanty, A. Saha, K. Sudhakar, N. Wickramage

Tata Institute of Fundamental Research - HECR, Mumbai, India

S. Banerjee, S. Dugad, N.K. Mondal

Institute for Research and Fundamental Sciences (IPM), Tehran, Iran

H. Arfaei, H. Bakhshiansohi¹⁶, S.M. Etesami, A. Fahim¹⁶, M. Hashemi, A. Jafari¹⁶, M. Khakzad, A. Mohammadi¹⁷, M. Mohammadi Najafabadi, S. Paktinat Mehdiabadi, B. Safarzadeh, M. Zeinali¹⁸

INFN Sezione di Bari ^a, Università di Bari ^b, Politecnico di Bari ^c, Bari, Italy

M. Abbrescia^{a,b}, L. Barbone^{a,b}, C. Calabria^{a,b}, A. Colaleo^a, D. Creanza^{a,c}, N. De Filippis^{a,c,1}, M. De Palma^{a,b}, L. Fiore^a, G. Iaselli^{a,c}, L. Lusito^{a,b}, G. Maggi^{a,c}, M. Maggi^a, N. Manna^{a,b}, B. Marangelli^{a,b}, S. My^{a,c}, S. Nuzzo^{a,b}, N. Pacifico^{a,b}, G.A. Pierro^a, A. Pompili^{a,b}, G. Pugliese^{a,c}, F. Romano^{a,c}, G. Roselli^{a,b}, G. Selvaggi^{a,b}, L. Silvestris^a, R. Trentadue^a, S. Tupputi^{a,b}, G. Zito^a

INFN Sezione di Bologna ^a, Università di Bologna ^b, Bologna, Italy

G. Abbiendi^a, A.C. Benvenuti^a, D. Bonacorsi^a, S. Braibant-Giacomelli^{a,b}, L. Brigliadori^a, P. Capiluppi^{a,b}, A. Castro^{a,b}, F.R. Cavallo^a, M. Cuffiani^{a,b}, G.M. Dallavalle^a, F. Fabbri^a, A. Fanfani^{a,b}, D. Fasanella^a, P. Giacomelli^a, M. Giunta^a, C. Grandi^a, S. Marcellini^a, G. Masetti^b, M. Meneghelli^{a,b}, A. Montanari^a, F.L. Navarria^{a,b}, F. Odorici^a, A. Perrotta^a, F. Primavera^a, A.M. Rossi^{a,b}, T. Rovelli^{a,b}, G. Siroli^{a,b}, R. Travaglini^{a,b}

INFN Sezione di Catania ^a, Università di Catania ^b, Catania, Italy

S. Albergo^{a,b}, G. Cappello^{a,b}, M. Chiorboli^{a,b,1}, S. Costa^{a,b}, A. Tricomi^{a,b}, C. Tuve^a

INFN Sezione di Firenze ^a, Università di Firenze ^b, Firenze, Italy

G. Barbagli^a, V. Ciulli^{a,b}, C. Civinini^a, R. D'Alessandro^{a,b}, E. Focardi^{a,b}, S. Frosali^{a,b}, E. Gallo^a, S. Gozzi^{a,b}, P. Lenzi^{a,b}, M. Meschini^a, S. Paoletti^a, G. Sguazzoni^a, A. Tropiano^{a,1}

INFN Laboratori Nazionali di Frascati, Frascati, Italy

L. Benussi, S. Bianco, S. Colafranceschi¹⁹, F. Fabbri, D. Piccolo

INFN Sezione di Genova, Genova, Italy

P. Fabbricatore, R. Musenich

INFN Sezione di Milano-Bicocca ^a, Università di Milano-Bicocca ^b, Milano, Italy

A. Benaglia^{a,b}, F. De Guio^{a,b,1}, L. Di Matteo^{a,b}, S. Gennai¹, A. Ghezzi^{a,b}, S. Malvezzi^a, A. Martelli^{a,b}, A. Massironi^{a,b}, D. Menasce^a, L. Moroni^a, M. Paganoni^{a,b}, D. Pedrini^a, S. Ragazzi^{a,b}, N. Redaelli^a, S. Sala^a, T. Tabarelli de Fatis^{a,b}

INFN Sezione di Napoli ^a, Università di Napoli "Federico II" ^b, Napoli, Italy

S. Buontempo^a, C.A. Carrillo Montoya^{a,1}, N. Cavallo^{a,20}, A. De Cosa^{a,b}, F. Fabozzi^{a,20}, A.O.M. Iorio^{a,1}, L. Lista^a, M. Merola^{a,b}, P. Paolucci^a

INFN Sezione di Padova ^a, Università di Padova ^b, Università di Trento (Trento) ^c, Padova, Italy

P. Azzi^a, N. Bacchetta^a, P. Bellan^{a,b}, D. Bisello^{a,b}, A. Branca^a, R. Carlin^{a,b}, P. Checchia^a, M. De Mattia^{a,b}, T. Dorigo^a, U. Dosselli^a, F. Fanzago^a, F. Gasparini^{a,b}, U. Gasparini^{a,b}, A. Gozzelino, S. Lacaprara^{a,21}, I. Lazzizzera^{a,c}, M. Margoni^{a,b}, M. Mazzucato^a, A.T. Meneguzzo^{a,b}, M. Nespolo^{a,1}, L. Perrozzi^{a,1}, N. Pozzobon^{a,b}, P. Ronchese^{a,b}, F. Simonetto^{a,b}, E. Torassa^a, M. Tosi^{a,b}, S. Vanini^{a,b}, P. Zotto^{a,b}, G. Zumerle^{a,b}

INFN Sezione di Pavia ^a, Università di Pavia ^b, Pavia, Italy

P. Baesso^{a,b}, U. Berzano^a, S.P. Ratti^{a,b}, C. Riccardi^{a,b}, P. Torre^{a,b}, P. Vitulo^{a,b}, C. Viviani^{a,b}

INFN Sezione di Perugia ^a, Università di Perugia ^b, Perugia, Italy

M. Biasini^{a,b}, G.M. Bilei^a, B. Caponeri^{a,b}, L. Fanò^{a,b}, P. Lariccia^{a,b}, A. Lucaroni^{a,b,1}, G. Mantovani^{a,b}, M. Menichelli^a, A. Nappi^{a,b}, F. Romeo^{a,b}, A. Santocchia^{a,b}, S. Taroni^{a,b,1}, M. Valdata^{a,b}

INFN Sezione di Pisa ^a, Università di Pisa ^b, Scuola Normale Superiore di Pisa ^c, Pisa, Italy

P. Azzurri^{a,c}, G. Bagliesi^a, J. Bernardini^{a,b}, T. Boccali^{a,1}, G. Broccolo^{a,c}, R. Castaldi^a, R.T. D'Agnolo^{a,c}, R. Dell'Orso^a, F. Fiori^{a,b}, L. Foà^{a,c}, A. Giassi^a, A. Kraan^a, F. Ligabue^{a,c}

T. Lomtadze^a, L. Martini^{a,22}, A. Messineo^{a,b}, F. Palla^a, G. Segneri^a, A.T. Serban^a, P. Spagnolo^a, R. Tenchini^a, G. Tonelli^{a,b,1}, A. Venturi^{a,1}, P.G. Verdini^a

INFN Sezione di Roma ^a, Università di Roma "La Sapienza" ^b, Roma, Italy

L. Barone^{a,b}, F. Cavallari^a, D. Del Re^{a,b}, E. Di Marco^{a,b}, M. Diemoz^a, D. Franci^{a,b}, M. Grassi^{a,1}, E. Longo^{a,b}, S. Nourbakhsh^a, G. Organtini^{a,b}, F. Pandolfi^{a,b,1}, R. Paramatti^a, S. Rahatlou^{a,b}, C. Rovelli¹

INFN Sezione di Torino ^a, Università di Torino ^b, Università del Piemonte Orientale (Novara) ^c, Torino, Italy

N. Amapane^{a,b}, R. Arcidiacono^{a,c}, S. Argiro^{a,b}, M. Arneodo^{a,c}, C. Biino^a, C. Botta^{a,b,1}, N. Cartiglia^a, R. Castello^{a,b}, M. Costa^{a,b}, N. Demaria^a, A. Graziano^{a,b,1}, C. Mariotti^a, M. Marone^{a,b}, S. Maselli^a, E. Migliore^{a,b}, G. Mila^{a,b}, V. Monaco^{a,b}, M. Musich^{a,b}, M.M. Obertino^{a,c}, N. Pastrone^a, M. Pelliccioni^{a,b}, A. Romero^{a,b}, M. Ruspa^{a,c}, R. Sacchi^{a,b}, V. Sola^{a,b}, A. Solano^{a,b}, A. Staiano^a, A. Vilela Pereira^a

INFN Sezione di Trieste ^a, Università di Trieste ^b, Trieste, Italy

S. Belforte^a, F. Cossutti^a, G. Della Ricca^{a,b}, B. Gobbo^a, D. Montanino^{a,b}, A. Penzo^a

Kangwon National University, Chunchon, Korea

S.G. Heo, S.K. Nam

Kyungpook National University, Daegu, Korea

S. Chang, J. Chung, D.H. Kim, G.N. Kim, J.E. Kim, D.J. Kong, H. Park, S.R. Ro, D. Son, D.C. Son, T. Son

Chonnam National University, Institute for Universe and Elementary Particles, Kwangju, Korea

Zero Kim, J.Y. Kim, S. Song

Korea University, Seoul, Korea

S. Choi, B. Hong, M.S. Jeong, M. Jo, H. Kim, J.H. Kim, T.J. Kim, K.S. Lee, D.H. Moon, S.K. Park, H.B. Rhee, E. Seo, S. Shin, K.S. Sim

University of Seoul, Seoul, Korea

M. Choi, S. Kang, H. Kim, C. Park, I.C. Park, S. Park, G. Ryu

Sungkyunkwan University, Suwon, Korea

Y. Choi, Y.K. Choi, J. Goh, M.S. Kim, E. Kwon, J. Lee, S. Lee, H. Seo, I. Yu

Vilnius University, Vilnius, Lithuania

M.J. Bilinskas, I. Grigelionis, M. Janulis, D. Martisiute, P. Petrov, T. Sabonis

Centro de Investigacion y de Estudios Avanzados del IPN, Mexico City, Mexico

H. Castilla-Valdez, E. De La Cruz-Burelo, I. Heredia-de La Cruz, R. Lopez-Fernandez, R. Magaña Villalba, A. Sánchez-Hernández, L.M. Villasenor-Cendejas

Universidad Iberoamericana, Mexico City, Mexico

S. Carrillo Moreno, F. Vazquez Valencia

Benemerita Universidad Autonoma de Puebla, Puebla, Mexico

H.A. Salazar Ibarguen

Universidad Autónoma de San Luis Potosí, San Luis Potosí, Mexico

E. Casimiro Linares, A. Morelos Pineda, M.A. Reyes-Santos

University of Auckland, Auckland, New Zealand

D. Krofcheck, J. Tam, C.H. Yiu

University of Canterbury, Christchurch, New Zealand

P.H. Butler, R. Doesburg, H. Silverwood

National Centre for Physics, Quaid-I-Azam University, Islamabad, Pakistan

M. Ahmad, I. Ahmed, M.I. Asghar, H.R. Hoorani, W.A. Khan, T. Khurshid, S. Qazi

Institute of Experimental Physics, Faculty of Physics, University of Warsaw, Warsaw, Poland

G. Brona, M. Cwiok, W. Dominik, K. Doroba, A. Kalinowski, M. Konecki, J. Krolikowski

Soltan Institute for Nuclear Studies, Warsaw, Poland

T. Frueboes, R. Gokieli, M. Górski, M. Kazana, K. Nawrocki, K. Romanowska-Rybinska, M. Szeleper, G. Wrochna, P. Zalewski

Laboratório de Instrumentação e Física Experimental de Partículas, Lisboa, Portugal

N. Almeida, P. Bargassa, A. David, P. Faccioli, P.G. Ferreira Parracho, M. Gallinaro, P. Musella, A. Nayak, P.Q. Ribeiro, J. Seixas, J. Varela

Joint Institute for Nuclear Research, Dubna, Russia

S. Afanasiev, I. Belotelov, P. Bunin, I. Golutvin, A. Kamenev, V. Karjavin, G. Kozlov, A. Lanev, P. Moisenz, V. Palichik, V. Perelygin, S. Shmatov, V. Smirnov, A. Volodko, A. Zarubin

Petersburg Nuclear Physics Institute, Gatchina (St Petersburg), Russia

V. Golovtsov, Y. Ivanov, V. Kim, P. Levchenko, V. Murzin, V. Oreshkin, I. Smirnov, V. Sulimov, L. Uvarov, S. Vavilov, A. Vorobyev, A. Vorobyev

Institute for Nuclear Research, Moscow, Russia

Yu. Andreev, A. Dermenev, S. Gninenko, N. Golubev, M. Kirsanov, N. Krasnikov, V. Matveev, A. Pashenkov, A. Toropin, S. Troitsky

Institute for Theoretical and Experimental Physics, Moscow, RussiaV. Epshteyn, V. Gavrilov, V. Kaftanov[†], M. Kossov¹, A. Krokhotin, N. Lychkovskaya, V. Popov, G. Safronov, S. Semenov, V. Stolin, E. Vlasov, A. Zhokin**Moscow State University, Moscow, Russia**E. Boos, M. Dubinin²³, L. Dudko, A. Ershov, O. Kodolova, V. Korotkikh, I. Lokhtin, A. Markina, S. Obraztsov, M. Perfilov, S. Petrushanko, L. Sarycheva, V. Savrin, A. Snigirev**P.N. Lebedev Physical Institute, Moscow, Russia**

V. Andreev, M. Azarkin, I. Dremin, M. Kirakosyan, A. Leonidov, S.V. Rusakov, A. Vinogradov

State Research Center of Russian Federation, Institute for High Energy Physics, Protvino, RussiaI. Azhgirey, S. Bitioukov, V. Grishin¹, V. Kachanov, D. Konstantinov, A. Korablev, V. Krychkine, V. Petrov, R. Ryutin, S. Slabospitsky, A. Sobol, L. Tourtchanovitch, S. Troshin, N. Tyurin, A. Uzunian, A. Volkov**University of Belgrade, Faculty of Physics and Vinca Institute of Nuclear Sciences, Belgrade, Serbia**P. Adzic²⁴, M. Djordjevic, D. Krpic²⁴, J. Milosevic**Centro de Investigaciones Energéticas Medioambientales y Tecnológicas (CIEMAT), Madrid, Spain**

M. Aguilar-Benitez, J. Alcaraz Maestre, P. Arce, C. Battilana, E. Calvo, M. Cepeda, M. Cerrada,

M. Chamizo Llatas, N. Colino, B. De La Cruz, A. Delgado Peris, C. Diez Pardos, D. Domínguez Vázquez, C. Fernandez Bedoya, J.P. Fernández Ramos, A. Ferrando, J. Flix, M.C. Fouz, P. Garcia-Abia, O. Gonzalez Lopez, S. Goy Lopez, J.M. Hernandez, M.I. Josa, G. Merino, J. Puerta Pelayo, I. Redondo, L. Romero, J. Santaolalla, M.S. Soares, C. Willmott

Universidad Autónoma de Madrid, Madrid, Spain

C. Albajar, G. Codispoti, J.F. de Trocóniz

Universidad de Oviedo, Oviedo, Spain

J. Cuevas, J. Fernandez Menendez, S. Folgueras, I. Gonzalez Caballero, L. Lloret Iglesias, J.M. Vizán García

Instituto de Física de Cantabria (IFCA), CSIC-Universidad de Cantabria, Santander, Spain

J.A. Brochero Cifuentes, I.J. Cabrillo, A. Calderon, S.H. Chuang, J. Duarte Campderros, M. Felcini²⁵, M. Fernandez, G. Gomez, J. Gonzalez Sanchez, C. Jorda, P. Lobelle Pardo, A. Lopez Virto, J. Marco, R. Marco, C. Martinez Rivero, F. Matorras, F.J. Munoz Sanchez, J. Piedra Gomez²⁶, T. Rodrigo, A.Y. Rodríguez-Marrero, A. Ruiz-Jimeno, L. Scodellaro, M. Sobron Sanudo, I. Vila, R. Vilar Cortabitarte

CERN, European Organization for Nuclear Research, Geneva, Switzerland

D. Abbaneo, E. Auffray, G. Auzinger, P. Baillon, A.H. Ball, D. Barney, A.J. Bell²⁷, D. Benedetti, C. Bernet³, W. Bialas, P. Bloch, A. Bocci, S. Bolognesi, M. Bona, H. Breuker, K. Bunkowski, T. Camporesi, G. Cerminara, J.A. Coarasa Perez, B. Curé, D. D'Enterria, A. De Roeck, S. Di Guida, N. Dupont-Sagorin, A. Elliott-Peisert, B. Frisch, W. Funk, A. Gaddi, G. Georgiou, H. Gerwig, D. Gigi, K. Gill, D. Giordano, F. Glege, R. Gomez-Reino Garrido, M. Gouzevitch, P. Govoni, S. Gowdy, L. Guiducci, M. Hansen, C. Hartl, J. Harvey, J. Hegeman, B. Hegner, H.F. Hoffmann, A. Honma, V. Innocente, P. Janot, K. Kaadze, E. Karavakis, P. Lecoq, C. Lourenço, T. Mäki, M. Malberti, L. Malgeri, M. Mannelli, L. Masetti, A. Maurisset, F. Meijers, S. Mersi, E. Meschi, R. Moser, M.U. Mozer, M. Mulders, E. Nesvold¹, M. Nguyen, T. Orimoto, L. Orsini, E. Perez, A. Petrilli, A. Pfeiffer, M. Pierini, M. Pimiä, D. Piparo, G. Polese, A. Racz, J. Rodrigues Antunes, G. Rolandi²⁸, T. Rommerskirchen, M. Rovere, H. Sakulin, C. Schäfer, C. Schwick, I. Segoni, A. Sharma, P. Siegrist, M. Simon, P. Sphicas²⁹, M. Spiropulu²³, M. Stoye, M. Tadel, P. Tropea, A. Tsiros, P. Vichoudis, M. Voutilainen, W.D. Zeuner

Paul Scherrer Institut, Villigen, Switzerland

W. Bertl, K. Deiters, W. Erdmann, K. Gabathuler, R. Horisberger, Q. Ingram, H.C. Kaestli, S. König, D. Kotlinski, U. Langenegger, F. Meier, D. Renker, T. Rohe, J. Sibille³⁰, A. Starodumov³¹

Institute for Particle Physics, ETH Zurich, Zurich, Switzerland

P. Bortignon, L. Caminada³², N. Chanon, Z. Chen, S. Cittolin, G. Dissertori, M. Dittmar, J. Eugster, K. Freudenreich, C. Grab, A. Hervé, W. Hintz, P. Lecomte, W. Luster, C. Marchica³², P. Martinez Ruiz del Arbol, P. Meridiani, P. Milenovic³³, F. Moortgat, C. Nägeli³², P. Nef, F. Nessi-Tedaldi, L. Pape, F. Pauss, T. Punz, A. Rizzi, F.J. Ronga, M. Rossini, L. Sala, A.K. Sanchez, M.-C. Sawley, B. Stieger, L. Tauscher[†], A. Thea, K. Theofilatos, D. Treille, C. Urscheler, R. Wallny, M. Weber, L. Wehrli, J. Weng

Universität Zürich, Zurich, Switzerland

E. Aguiló, C. Amsler, V. Chiochia, S. De Visscher, C. Favaro, M. Ivova Rikova, B. Millan Mejias, P. Otiougov, C. Regenfur, P. Robmann, A. Schmidt, H. Snoek

National Central University, Chung-Li, Taiwan

Y.H. Chang, K.H. Chen, S. Dutta, C.M. Kuo, S.W. Li, W. Lin, Z.K. Liu, Y.J. Lu, D. Mekterovic, R. Volpe, J.H. Wu, S.S. Yu

National Taiwan University (NTU), Taipei, Taiwan

P. Bartalini, P. Chang, Y.H. Chang, Y.W. Chang, Y. Chao, K.F. Chen, W.-S. Hou, Y. Hsiung, K.Y. Kao, Y.J. Lei, R.-S. Lu, J.G. Shiu, Y.M. Tzeng, M. Wang

Cukurova University, Adana, Turkey

A. Adiguzel, M.N. Bakirci³⁴, S. Cerci³⁵, C. Dozen, I. Dumanoglu, E. Eskut, S. Girgis, G. Gokbulut, I. Hos, E.E. Kangal, A. Kayis Topaksu, G. Onengut, K. Ozdemir, S. Ozturk, A. Polatoz, K. Sogut³⁶, D. Sunar Cerci³⁵, B. Tali³⁵, H. Topakli³⁴, D. Uzun, L.N. Vergili, M. Vergili

Middle East Technical University, Physics Department, Ankara, Turkey

I.V. Akin, T. Aliev, S. Bilmis, M. Deniz, H. Gamsizkan, A.M. Guler, K. Ocalan, A. Ozpineci, M. Serin, R. Sever, U.E. Surat, E. Yildirim, M. Zeyrek

Bogazici University, Istanbul, Turkey

M. Deliomeroğlu, D. Demir³⁷, E. Gülmez, B. Isildak, M. Kaya³⁸, O. Kaya³⁸, S. Ozkorucuklu³⁹, N. Sonmez⁴⁰

National Scientific Center, Kharkov Institute of Physics and Technology, Kharkov, Ukraine

L. Levchuk

University of Bristol, Bristol, United Kingdom

F. Bostock, J.J. Brooke, T.L. Cheng, E. Clement, D. Cussans, R. Frazier, J. Goldstein, M. Grimes, M. Hansen, D. Hartley, G.P. Heath, H.F. Heath, L. Kreczko, S. Metson, D.M. Newbold⁴¹, K. Nirunpong, A. Poll, S. Senkin, V.J. Smith, S. Ward

Rutherford Appleton Laboratory, Didcot, United Kingdom

L. Basso⁴², K.W. Bell, A. Belyaev⁴², C. Brew, R.M. Brown, B. Camanzi, D.J.A. Cockerill, J.A. Coughlan, K. Harder, S. Harper, J. Jackson, B.W. Kennedy, E. Olaiya, D. Petyt, B.C. Radburn-Smith, C.H. Shepherd-Themistocleous, I.R. Tomalin, W.J. Womersley, S.D. Worm

Imperial College, London, United Kingdom

R. Bainbridge, G. Ball, J. Ballin, R. Beuselinck, O. Buchmuller, D. Colling, N. Cripps, M. Cutajar, G. Davies, M. Della Negra, W. Ferguson, J. Fulcher, D. Futyan, A. Gilbert, A. Guneratne Bryer, G. Hall, Z. Hatherell, J. Hays, G. Iles, M. Jarvis, G. Karapostoli, L. Lyons, B.C. MacEvoy, A.-M. Magnan, J. Marrouche, B. Mathias, R. Nandi, J. Nash, A. Nikitenko³¹, A. Papageorgiou, M. Pesaresi, K. Petridis, M. Pioppi⁴³, D.M. Raymond, S. Rogerson, N. Rompotis, A. Rose, M.J. Ryan, C. Seez, P. Sharp, A. Sparrow, A. Tapper, S. Tourneur, M. Vazquez Acosta, T. Virdee, S. Wakefield, N. Wardle, D. Wardrope, T. Whyntie

Brunel University, Uxbridge, United Kingdom

M. Barrett, M. Chadwick, J.E. Cole, P.R. Hobson, A. Khan, P. Kyberd, D. Leslie, W. Martin, I.D. Reid, L. Teodorescu

Baylor University, Waco, USA

K. Hatakeyama, H. Liu

Boston University, Boston, USA

T. Bose, E. Carrera Jarrin, C. Fantasia, A. Heister, J. St. John, P. Lawson, D. Lazic, J. Rohlf, D. Sperka, L. Sulak

Brown University, Providence, USA

A. Avetisyan, S. Bhattacharya, J.P. Chou, D. Cutts, A. Ferapontov, U. Heintz, S. Jabeen,

G. Kukartsev, G. Landsberg, M. Luk, M. Narain, D. Nguyen, M. Segala, T. Sinthuprasith, T. Speer, K.V. Tsang

University of California, Davis, Davis, USA

R. Breedon, M. Calderon De La Barca Sanchez, S. Chauhan, M. Chertok, J. Conway, P.T. Cox, J. Dolen, R. Erbacher, E. Friis, W. Ko, A. Kopecky, R. Lander, H. Liu, S. Maruyama, T. Miceli, M. Nikolic, D. Pellett, J. Robles, S. Salur, T. Schwarz, M. Searle, J. Smith, M. Squires, M. Tripathi, R. Vasquez Sierra, C. Veelken

University of California, Los Angeles, Los Angeles, USA

V. Andreev, K. Arisaka, D. Cline, R. Cousins, A. Deisher, J. Duris, S. Erhan, C. Farrell, J. Hauser, M. Ignatenko, C. Jarvis, C. Plager, G. Rakness, P. Schlein[†], J. Tucker, V. Valuev

University of California, Riverside, Riverside, USA

J. Babb, A. Chandra, R. Clare, J. Ellison, J.W. Gary, F. Giordano, G. Hanson, G.Y. Jeng, S.C. Kao, F. Liu, H. Liu, O.R. Long, A. Luthra, H. Nguyen, B.C. Shen[†], R. Stringer, J. Sturdy, S. Sumowidagdo, R. Wilken, S. Wimpenny

University of California, San Diego, La Jolla, USA

W. Andrews, J.G. Branson, G.B. Cerati, E. Dusinger, D. Evans, F. Golf, A. Holzner, R. Kelley, M. Lebourgeois, J. Letts, B. Mangano, S. Padhi, C. Palmer, G. Petrucciani, H. Pi, M. Pieri, R. Ranieri, M. Sani, V. Sharma, S. Simon, Y. Tu, A. Vartak, S. Wasserbaech⁴⁴, F. Würthwein, A. Yagil, J. Yoo

University of California, Santa Barbara, Santa Barbara, USA

D. Barge, R. Bellan, C. Campagnari, M. D'Alfonso, T. Danielson, K. Flowers, P. Geffert, J. Incandela, C. Justus, P. Kalavase, S.A. Koay, D. Kovalskyi, V. Krutelyov, S. Lowette, N. Mccoll, V. Pavlunin, F. Rebassoo, J. Ribnik, J. Richman, R. Rossin, D. Stuart, W. To, J.R. Vlimant

California Institute of Technology, Pasadena, USA

A. Apresyan, A. Bornheim, J. Bunn, Y. Chen, M. Gataullin, Y. Ma, A. Mott, H.B. Newman, C. Rogan, K. Shin, V. Timciuc, P. Traczyk, J. Veverka, R. Wilkinson, Y. Yang, R.Y. Zhu

Carnegie Mellon University, Pittsburgh, USA

B. Akgun, R. Carroll, T. Ferguson, Y. Iiyama, D.W. Jang, S.Y. Jun, Y.F. Liu, M. Paulini, J. Russ, H. Vogel, I. Vorobiev

University of Colorado at Boulder, Boulder, USA

J.P. Cumalat, M.E. Dinardo, B.R. Drell, C.J. Edlmaier, W.T. Ford, A. Gaz, B. Heyburn, E. Luiggi Lopez, U. Nauenberg, J.G. Smith, K. Stenson, K.A. Ulmer, S.R. Wagner, S.L. Zang

Cornell University, Ithaca, USA

L. Agostino, J. Alexander, D. Cassel, A. Chatterjee, S. Das, N. Eggert, L.K. Gibbons, B. Heltsley, W. Hopkins, A. Khukhunaishvili, B. Kreis, G. Nicolas Kaufman, J.R. Patterson, D. Puigh, A. Ryd, E. Salvati, X. Shi, W. Sun, W.D. Teo, J. Thom, J. Thompson, J. Vaughan, Y. Weng, L. Winstrom, P. Wittich

Fairfield University, Fairfield, USA

A. Biselli, G. Cirino, D. Winn

Fermi National Accelerator Laboratory, Batavia, USA

S. Abdullin, M. Albrow, J. Anderson, G. Apollinari, M. Atac, J.A. Bakken, S. Banerjee, L.A.T. Bauerdick, A. Beretvas, J. Berryhill, P.C. Bhat, I. Bloch, F. Borchering, K. Burkett, J.N. Butler, V. Chetluru, H.W.K. Cheung, F. Chlebana, S. Cihangir, W. Cooper, D.P. Eartly, V.D. Elvira, S. Esen, I. Fisk, J. Freeman, Y. Gao, E. Gottschalk, D. Green, K. Gunthoti,

O. Gutsche, J. Hanlon, R.M. Harris, J. Hirschauer, B. Hooberman, H. Jensen, M. Johnson, U. Joshi, R. Khatiwada, B. Klima, K. Kousouris, S. Kunori, S. Kwan, C. Leonidopoulos, P. Limon, D. Lincoln, R. Lipton, J. Lykken, K. Maeshima, J.M. Marraffino, D. Mason, P. McBride, T. Miao, K. Mishra, S. Mrenna, Y. Musienko⁴⁵, C. Newman-Holmes, V. O'Dell, R. Pordes, O. Prokofyev, N. Saoulidou, E. Sexton-Kennedy, S. Sharma, W.J. Spalding, L. Spiegel, P. Tan, L. Taylor, S. Tkaczyk, L. Uplegger, E.W. Vaandering, R. Vidal, J. Whitmore, W. Wu, F. Yang, F. Yumiceva, J.C. Yun

University of Florida, Gainesville, USA

D. Acosta, P. Avery, D. Bourilkov, M. Chen, M. De Gruttola, G.P. Di Giovanni, D. Dobur, A. Drozdetskiy, R.D. Field, M. Fisher, Y. Fu, I.K. Furic, J. Gartner, B. Kim, J. Konigsberg, A. Korytov, A. Kropivnitskaya, T. Kypreos, K. Matchev, G. Mitselmakher, L. Muniz, C. Prescott, R. Remington, M. Schmitt, B. Scurlock, P. Sellers, N. Skhirtladze, M. Snowball, D. Wang, J. Yelton, M. Zakaria

Florida International University, Miami, USA

C. Ceron, V. Gaultney, L. Kramer, L.M. Lebolo, S. Linn, P. Markowitz, G. Martinez, D. Mesa, J.L. Rodriguez

Florida State University, Tallahassee, USA

T. Adams, A. Askew, J. Bochenek, J. Chen, B. Diamond, S.V. Gleyzer, J. Haas, S. Hagopian, V. Hagopian, M. Jenkins, K.F. Johnson, H. Prosper, L. Quertenmont, S. Sekmen, V. Veeraraghavan

Florida Institute of Technology, Melbourne, USA

M.M. Baarmand, B. Dorney, S. Guragain, M. Hohlmann, H. Kalakhety, R. Ralich, I. Vodopyanov

University of Illinois at Chicago (UIC), Chicago, USA

M.R. Adams, I.M. Anghel, L. Apanasevich, Y. Bai, V.E. Bazterra, R.R. Betts, J. Callner, R. Cavanaugh, C. Dragoiu, L. Gauthier, C.E. Gerber, S. Hamdan, D.J. Hofman, S. Khalatyan, G.J. Kunde⁴⁶, F. Lacroix, M. Malek, C. O'Brien, C. Silvestre, A. Smoron, D. Strom, N. Varelas

The University of Iowa, Iowa City, USA

U. Akgun, E.A. Albayrak, B. Bilki, W. Clarida, F. Duru, C.K. Lae, E. McCliment, J.-P. Merlo, H. Mermerkaya⁴⁷, A. Mestvirishvili, A. Moeller, J. Nachtman, C.R. Newsom, E. Norbeck, J. Olson, Y. Onel, F. Ozok, S. Sen, J. Wetzell, T. Yetkin, K. Yi

Johns Hopkins University, Baltimore, USA

B.A. Barnett, B. Blumenfeld, A. Bonato, C. Eskew, D. Fehling, G. Giurgiu, A.V. Gritsan, Z.J. Guo, G. Hu, P. Maksimovic, S. Rappoccio, M. Swartz, N.V. Tran, A. Whitbeck

The University of Kansas, Lawrence, USA

P. Baringer, A. Bean, G. Benelli, O. Grachov, R.P. Kenny III, M. Murray, D. Noonan, S. Sanders, J.S. Wood, V. Zhukova

Kansas State University, Manhattan, USA

A.f. Barfuss, T. Bolton, I. Chakaberia, A. Ivanov, S. Khalil, M. Makouski, Y. Maravin, S. Shrestha, I. Svintradze, Z. Wan

Lawrence Livermore National Laboratory, Livermore, USA

J. Gronberg, D. Lange, D. Wright

University of Maryland, College Park, USA

A. Baden, M. Boutemour, S.C. Eno, D. Ferencek, J.A. Gomez, N.J. Hadley, R.G. Kellogg, M. Kirn,

Y. Lu, A.C. Mignerey, K. Rossato, P. Rumerio, F. Santanastasio, A. Skuja, J. Temple, M.B. Tonjes, S.C. Tonwar, E. Twedt

Massachusetts Institute of Technology, Cambridge, USA

B. Alver, G. Bauer, J. Bendavid, W. Busza, E. Butz, I.A. Cali, M. Chan, V. Dutta, P. Everaerts, G. Gomez Ceballos, M. Goncharov, K.A. Hahn, P. Harris, Y. Kim, M. Klute, Y.-J. Lee, W. Li, C. Loizides, P.D. Luckey, T. Ma, S. Nahn, C. Paus, D. Ralph, C. Roland, G. Roland, M. Rudolph, G.S.F. Stephans, F. Stöckli, K. Sumorok, K. Sung, E.A. Wenger, S. Xie, M. Yang, Y. Yilmaz, A.S. Yoon, M. Zanetti

University of Minnesota, Minneapolis, USA

S.I. Cooper, P. Cushman, B. Dahmes, A. De Benedetti, P.R. Duderø, G. Franzoni, J. Haupt, K. Klappoetke, Y. Kubota, J. Mans, V. Rekovic, R. Rusack, M. Sasseville, A. Singovsky

University of Mississippi, University, USA

L.M. Cremaldi, R. Godang, R. Kroeger, L. Perera, R. Rahmat, D.A. Sanders, D. Summers

University of Nebraska-Lincoln, Lincoln, USA

K. Bloom, S. Bose, J. Butt, D.R. Claes, A. Dominguez, M. Eads, J. Keller, T. Kelly, I. Kravchenko, J. Lazo-Flores, H. Malbouisson, S. Malik, G.R. Snow

State University of New York at Buffalo, Buffalo, USA

U. Baur, A. Godshalk, I. Iashvili, S. Jain, A. Kharchilava, A. Kumar, S.P. Shipkowski, K. Smith

Northeastern University, Boston, USA

G. Alverson, E. Barberis, D. Baumgartel, O. Boeriu, M. Chasco, S. Reucroft, J. Swain, D. Trocino, D. Wood, J. Zhang

Northwestern University, Evanston, USA

A. Anastassov, A. Kubik, N. Odell, R.A. Ofierzynski, B. Pollack, A. Pozdnyakov, M. Schmitt, S. Stoynev, M. Velasco, S. Won

University of Notre Dame, Notre Dame, USA

L. Antonelli, D. Berry, M. Hildreth, C. Jessop, D.J. Karmgard, J. Kolb, T. Kolberg, K. Lannon, W. Luo, S. Lynch, N. Marinelli, D.M. Morse, T. Pearson, R. Ruchti, J. Slaunwhite, N. Valls, M. Wayne, J. Ziegler

The Ohio State University, Columbus, USA

B. Bylsma, L.S. Durkin, J. Gu, C. Hill, P. Killewald, K. Kotov, T.Y. Ling, M. Rodenburg, G. Williams

Princeton University, Princeton, USA

N. Adam, E. Berry, P. Elmer, D. Gerbaudo, V. Halyo, P. Hebda, A. Hunt, J. Jones, E. Laird, D. Lopes Pegna, D. Marlow, T. Medvedeva, M. Mooney, J. Olsen, P. Piroué, X. Quan, H. Saka, D. Stickland, C. Tully, J.S. Werner, A. Zuranski

University of Puerto Rico, Mayaguez, USA

J.G. Acosta, X.T. Huang, A. Lopez, H. Mendez, S. Oliveros, J.E. Ramirez Vargas, A. Zatserklyaniy

Purdue University, West Lafayette, USA

E. Alagoz, V.E. Barnes, G. Bolla, L. Borrello, D. Bortoletto, A. Everett, A.F. Garfinkel, L. Gutay, Z. Hu, M. Jones, O. Koybasi, M. Kress, A.T. Laasanen, N. Leonardo, C. Liu, V. Maroussov, P. Merkel, D.H. Miller, N. Neumeister, I. Shipsey, D. Silvers, A. Svyatkovskiy, H.D. Yoo, J. Zablocki, Y. Zheng

Purdue University Calumet, Hammond, USA

P. Jindal, N. Parashar

Rice University, Houston, USA

C. Boulahouache, V. Cuplov, K.M. Ecklund, F.J.M. Geurts, B.P. Padley, R. Redjimi, J. Roberts, J. Zabel

University of Rochester, Rochester, USA

B. Betchart, A. Bodek, Y.S. Chung, R. Covarelli, P. de Barbaro, R. Demina, Y. Eshaq, H. Flacher, A. Garcia-Bellido, P. Goldenzweig, Y. Gotra, J. Han, A. Harel, D.C. Miner, D. Orbaker, G. Petrillo, D. Vishnevskiy, M. Zielinski

The Rockefeller University, New York, USA

A. Bhatti, R. Ciesielski, L. Demortier, K. Goulianos, G. Lungu, S. Malik, C. Mesropian, M. Yan

Rutgers, the State University of New Jersey, Piscataway, USA

O. Atramentov, A. Barker, D. Duggan, Y. Gershtein, R. Gray, E. Halkiadakis, D. Hidas, D. Hits, A. Lath, S. Panwalkar, R. Patel, A. Richards, K. Rose, S. Schnetzer, S. Somalwar, R. Stone, S. Thomas

University of Tennessee, Knoxville, USA

G. Cerizza, M. Hollingsworth, S. Spanier, Z.C. Yang, A. York

Texas A&M University, College Station, USA

R. Eusebi, J. Gilmore, A. Gurrola, T. Kamon, V. Khotilovich, R. Montalvo, I. Osipenkov, Y. Pakhotin, J. Pivarski, A. Safonov, S. Sengupta, A. Tatarinov, D. Toback, M. Weinberger

Texas Tech University, Lubbock, USA

N. Akchurin, C. Bardak, J. Damgov, C. Jeong, K. Kovitangoon, S.W. Lee, P. Mane, Y. Roh, A. Sill, I. Volobouev, R. Wigmans, E. Yazgan

Vanderbilt University, Nashville, USA

E. Appelt, E. Brownson, D. Engh, C. Florez, W. Gabella, M. Issah, W. Johns, P. Kurt, C. Maguire, A. Melo, P. Sheldon, B. Snook, S. Tuo, J. Velkovska

University of Virginia, Charlottesville, USA

M.W. Arenton, M. Balazs, S. Boutle, B. Cox, B. Francis, R. Hirosky, A. Ledovskoy, C. Lin, C. Neu, R. Yohay

Wayne State University, Detroit, USA

S. Gollapinni, R. Harr, P.E. Karchin, P. Lamichhane, M. Mattson, C. Milstène, A. Sakharov

University of Wisconsin, Madison, USA

M. Anderson, M. Bachtis, J.N. Bellinger, D. Carlsmith, S. Dasu, J. Efron, K. Flood, L. Gray, K.S. Grogg, M. Grothe, R. Hall-Wilton, M. Herndon, P. Klabbers, J. Klukas, A. Lanaro, C. Lazaridis, J. Leonard, R. Loveless, A. Mohapatra, F. Palmonari, D. Reeder, I. Ross, A. Savin, W.H. Smith, J. Swanson, M. Weinberg

†: Deceased

1: Also at CERN, European Organization for Nuclear Research, Geneva, Switzerland

2: Also at Universidade Federal do ABC, Santo Andre, Brazil

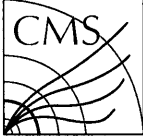
3: Also at Laboratoire Leprince-Ringuet, Ecole Polytechnique, IN2P3-CNRS, Palaiseau, France

4: Also at Suez Canal University, Suez, Egypt

5: Also at British University, Cairo, Egypt

6: Also at Fayoum University, El-Fayoum, Egypt

- 7: Also at Soltan Institute for Nuclear Studies, Warsaw, Poland
- 8: Also at Massachusetts Institute of Technology, Cambridge, USA
- 9: Also at Université de Haute-Alsace, Mulhouse, France
- 10: Also at Brandenburg University of Technology, Cottbus, Germany
- 11: Also at Moscow State University, Moscow, Russia
- 12: Also at Institute of Nuclear Research ATOMKI, Debrecen, Hungary
- 13: Also at Eötvös Loránd University, Budapest, Hungary
- 14: Also at Tata Institute of Fundamental Research - HECR, Mumbai, India
- 15: Also at University of Visva-Bharati, Santiniketan, India
- 16: Also at Sharif University of Technology, Tehran, Iran
- 17: Also at Shiraz University, Shiraz, Iran
- 18: Also at Isfahan University of Technology, Isfahan, Iran
- 19: Also at Facoltà Ingegneria Università di Roma "La Sapienza", Roma, Italy
- 20: Also at Università della Basilicata, Potenza, Italy
- 21: Also at Laboratori Nazionali di Legnaro dell' INFN, Legnaro, Italy
- 22: Also at Università degli studi di Siena, Siena, Italy
- 23: Also at California Institute of Technology, Pasadena, USA
- 24: Also at Faculty of Physics of University of Belgrade, Belgrade, Serbia
- 25: Also at University of California, Los Angeles, Los Angeles, USA
- 26: Also at University of Florida, Gainesville, USA
- 27: Also at Université de Genève, Geneva, Switzerland
- 28: Also at Scuola Normale e Sezione dell' INFN, Pisa, Italy
- 29: Also at University of Athens, Athens, Greece
- 30: Also at The University of Kansas, Lawrence, USA
- 31: Also at Institute for Theoretical and Experimental Physics, Moscow, Russia
- 32: Also at Paul Scherrer Institut, Villigen, Switzerland
- 33: Also at University of Belgrade, Faculty of Physics and Vinca Institute of Nuclear Sciences, Belgrade, Serbia
- 34: Also at Gaziosmanpasa University, Tokat, Turkey
- 35: Also at Adiyaman University, Adiyaman, Turkey
- 36: Also at Mersin University, Mersin, Turkey
- 37: Also at Izmir Institute of Technology, Izmir, Turkey
- 38: Also at Kafkas University, Kars, Turkey
- 39: Also at Suleyman Demirel University, Isparta, Turkey
- 40: Also at Ege University, Izmir, Turkey
- 41: Also at Rutherford Appleton Laboratory, Didcot, United Kingdom
- 42: Also at School of Physics and Astronomy, University of Southampton, Southampton, United Kingdom
- 43: Also at INFN Sezione di Perugia; Università di Perugia, Perugia, Italy
- 44: Also at Utah Valley University, Orem, USA
- 45: Also at Institute for Nuclear Research, Moscow, Russia
- 46: Also at Los Alamos National Laboratory, Los Alamos, USA
- 47: Also at Erzincan University, Erzincan, Turkey



CMS-HIN-10-005

Study of high- p_T charged particle suppression in PbPb compared to pp collisions at $\sqrt{s_{NN}} = 2.76$ TeV

The CMS Collaboration*

Abstract

The transverse momentum spectra of charged particles have been measured in pp and PbPb collisions at $\sqrt{s_{NN}} = 2.76$ TeV by the CMS experiment at the LHC. In the transverse momentum range $p_T = 5\text{--}10$ GeV/ c , the charged particle yield in the most central PbPb collisions is suppressed by up to a factor of 7 compared to the pp yield scaled by the number of incoherent nucleon-nucleon collisions. At higher p_T , this suppression is significantly reduced, approaching roughly a factor of 2 for particles with p_T in the range $p_T = 40\text{--}100$ GeV/ c .

Submitted to the European Physical Journal C

arXiv:1202.2554v2 [nucl-ex] 3 May 2012

*See Appendix A for the list of collaboration members

1 Introduction

The charged particle spectrum at large transverse momentum (p_T), dominated by hadrons originating from parton fragmentation, is an important observable for studying the properties of the hot, dense medium produced in high-energy heavy-ion collisions. The study of the modifications of the p_T spectrum in PbPb compared to pp collisions at the same collision energy can shed light on the detailed mechanism by which hard partons lose energy traversing the medium [1, 2], complementing recent studies of jet quenching and fragmentation properties using fully reconstructed jets [3, 4].

Using data collected by the Compact Muon Solenoid (CMS) experiment at the LHC, this paper presents measurements of charged particle yields as a function of p_T and event centrality in PbPb collisions at a center-of-mass energy per nucleon pair $\sqrt{s_{NN}} = 2.76$ TeV. The PbPb charged particle spectra are compared to the corresponding p_T -differential cross sections measured in pp collisions at the same center-of-mass energy, a measurement that follows closely the analysis described in Ref. [5]. Charged tracks are measured in the pseudorapidity range $|\eta| < 1$, where $\eta = -\ln[\tan(\theta/2)]$, with θ the polar angle of the track with respect to the counterclockwise beam direction.

The measurements are motivated by lower-energy results [6–9] from the Relativistic Heavy Ion Collider (RHIC), where high- p_T particle production was found to be strongly suppressed relative to expectations from an independent superposition of nucleon-nucleon collisions. This observation is typically expressed in terms of the nuclear modification factor,

$$R_{AA}(p_T) = \frac{d^2 N_{ch}^{AA} / dp_T d\eta}{\langle T_{AA} \rangle d^2 \sigma_{ch}^{pp} / dp_T d\eta}, \quad (1)$$

where N_{ch}^{AA} and σ_{ch}^{pp} represent the charged particle yield per event in nucleus-nucleus (AA) collisions and the charged particle cross section in pp collisions, respectively. In order to compare the yield of high- p_T charged particles produced in PbPb and pp collisions, a scaling factor, the nuclear overlap function T_{AA} , is needed to provide a proper normalization at a given PbPb centrality. This factor is computed as the ratio between the number of binary nucleon-nucleon collisions N_{coll} , calculated from the Glauber model of the nuclear collision geometry [10], and the inelastic nucleon-nucleon (NN) cross section $\sigma_{inel}^{NN} = 64 \pm 5$ mb at $\sqrt{s} = 2.76$ TeV [11]. It can be interpreted as the NN-equivalent integrated luminosity per collision at any given PbPb centrality. The mean of the nuclear overlap function $\langle T_{AA} \rangle$, averaged over a given centrality bin, is used to determine the nuclear modification factor at that PbPb centrality.

In addition, the centrality dependence of the PbPb spectrum can also be examined through the T_{AA} -scaled ratio of spectra in central and peripheral bins,

$$R_{CP}(p_T) = \frac{(d^2 N_{ch}^{AA} / dp_T d\eta) / \langle T_{AA} \rangle [\text{central}]}{(d^2 N_{ch}^{AA} / dp_T d\eta) / \langle T_{AA} \rangle [\text{peripheral}]}. \quad (2)$$

In the absence of initial- and/or final-state effects on the PbPb p_T spectrum, the factors R_{AA} and R_{CP} at high p_T are unity by construction. However, as observed first at RHIC in 200 GeV AuAu collisions [6–9] and later by ALICE in 2.76 TeV PbPb collisions [12], the yield of $p_T \sim 5$ –10 GeV/ c charged particles is suppressed in the most central heavy-ion collisions by up to a factor of five compared to that in pp collisions. The CMS measurement presented in this paper confirms these results with improved experimental uncertainties and extends the measured transverse momentum range to 100 GeV/ c .

2 Data sample and analysis procedures

This measurement is based on $\sqrt{s_{NN}} = 2.76$ TeV PbPb data samples corresponding to integrated luminosities of $7 \mu\text{b}^{-1}$ and $150 \mu\text{b}^{-1}$, collected by the CMS experiment in 2010 and 2011, respectively. The pp reference measurement uses a data sample collected in $\sqrt{s} = 2.76$ TeV collisions in the 2011 LHC run, corresponding to an integrated luminosity of 230nb^{-1} .

A detailed description of the CMS detector can be found in Ref. [13]. The central feature of the CMS apparatus is a superconducting solenoid of 6 m internal diameter, providing an axial magnetic field of 3.8 T. Immersed in the magnetic field are the pixel tracker, the silicon strip tracker, the lead-tungstate crystal electromagnetic calorimeter (ECAL), and the brass/scintillator hadron calorimeter (HCAL). Muons are measured in gas ionization detectors embedded in the steel return yoke. The tracker consists of 1440 silicon pixel and 15 148 silicon strip detector modules and measures charged particle trajectories within the nominal pseudorapidity range $|\eta| < 2.4$. The pixel tracker consists of three 53.3 cm long barrel layers and two endcap disks on each side of the barrel section. The innermost barrel layer has a radius of 4.4 cm, while for the second and third layers the radii are 7.3 cm and 10.2 cm, respectively. The tracker is designed to provide a track impact parameter resolution of about $100 \mu\text{m}$ and a transverse momentum resolution of about 0.7 (2.0)% for 1 (100) GeV/ c charged particles at normal incidence ($\eta = 0$) [14]. The beam scintillator counters (BSCs) are located at a distance of 10.86 m from the nominal interaction point (IP), one on each side, and cover the $|\eta|$ range from 3.23 to 4.65. Each BSC is a set of 16 scintillator tiles. The BSC elements provide hit and coincidence rates with a time resolution of 3 ns and an average minimum ionising particle detection efficiency of 95.7%. The two steel/quartz-fibre hadron forward calorimeters (HF), which extend the calorimetric coverage beyond the barrel and endcap detectors to the $|\eta|$ region between 2.9 and 5.2, are used for further offline selection of collision events. For online event selection, CMS uses a two-level trigger system: a hardware level (L1) and a software-based higher level (HLT).

A sample of minimum bias events from PbPb collisions was collected, based on a trigger requiring a coincidence between signals in the opposite sides of either the HF or the BSCs. To ensure a pure sample of inelastic hadronic collision events, additional offline selections were performed. These include a beam-halo veto, based on the BSC timing, an offline requirement of at least 3 towers on each HF with an energy deposit of more than 3 GeV per tower, a reconstructed vertex, based on at least two pixel tracks with $p_T > 75 \text{MeV}/c$, and a rejection of beam-scraping events, based on the compatibility of pixel cluster shapes with the reconstructed primary vertex. Further details can be found in Ref. [4].

The collision event centrality is determined from the event-by-event total energy deposition in both HF calorimeters. The distribution of this observable in minimum bias events from the 2010 data sample, shown in Fig. 1 (a), is used to divide the event sample into 40 centrality bins, each corresponding to 2.5% of the total inelastic cross section. Figure 1 (b) shows the distribution of events according to centrality bin, which is flat by construction for the minimum bias selection, except in the most peripheral events where the trigger and offline event selection are no longer fully efficient. Figure 1 also shows the distributions of the total HF energy and of the cross-section fraction for the events selected by single-jet triggers with calibrated transverse energy thresholds of $E_T = 65 \text{GeV}$ (Jet65) and 80GeV (Jet80) from the 2011 data samples. The reconstruction of calorimeter-based jets in heavy-ion collisions in the online trigger as well as in the offline analysis is performed with an iterative cone algorithm modified to subtract the soft underlying event on an event-by-event basis [15]. The overall selection efficiency is estimated to be $(97 \pm 3)\%$ based on Monte Carlo (MC) simulations [4]. For the pp analysis, there is an uncertainty from the estimated number of additional collision interactions in a given beam

crossing (i.e. “event pile-up”) in addition to the uncertainties from the event selection efficiency. For the PbPb analysis, the uncertainty due to the event pile-up fraction is negligible ($< 0.1\%$).

For this analysis, the events are analyzed in six centrality bins: 0–5% (most central), 5–10%, 10–30%, 30–50%, 50–70%, and 70–90% (most peripheral). Details of the centrality determination are described in Ref. [4].

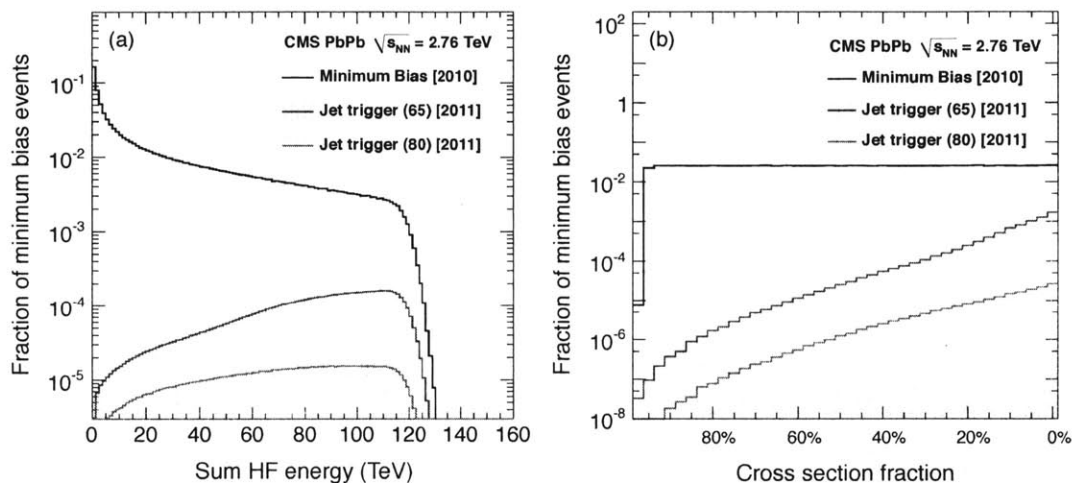


Figure 1: (a) Probability distribution of the total HF energy for minimum bias events (black line), Jet65-triggered (blue-shaded region), and Jet80-triggered (red-shaded region) events. (b) Distribution of the events in bins of fractional cross section for minimum bias (black line), Jet65-triggered (blue-shaded region), and Jet80-triggered (red-shaded region) events. By convention, 0% denotes the most central events and 100% the most peripheral.

The event centrality, specified as a fraction of the total inelastic cross section, can be related to properties of the PbPb collisions such as the number of nucleons undergoing at least one inelastic collision (N_{part}) and the total number of binary nucleon-nucleon collisions (N_{coll}). The calculation of these properties is based on a Glauber model of the incoming nuclei [10] and studies of bin-to-bin smearing, caused by finite resolution effects and evaluated using fully simulated and reconstructed MC events [4]. The mean and r.m.s. of the N_{part} , N_{coll} , and T_{AA} distributions, along with their corresponding systematic uncertainties, are listed in Table 1 for the six centrality bins used in this analysis. The uncertainties on the centrality variables are derived from propagating the uncertainties on the event selection efficiency and on the parameters of the Glauber model.

In order to extend the statistical reach of the p_T spectra in the highly prescaled minimum bias sample, data recorded in 2011 by unprescaled single-jet triggers, Jet65 and Jet80, are included in the analysis. The jet E_T thresholds in the trigger are applied after subtracting the contribution from the underlying event and correcting for the calorimeter response. Transverse energy distributions of the most energetic reconstructed jet with $|\eta| < 2$, referred to as the leading jet, are shown in the upper panel of Fig. 2 (a) for the three samples (minimum bias, Jet65, and Jet80) as a function of corrected E_T , and normalized per minimum bias event. The distribution for the Jet80 trigger has a peak in the low- E_T region as a consequence of stricter ECAL and HCAL noise elimination, as well as a tighter pseudorapidity requirement in the offline leading-jet selection than in the trigger. This feature is less prominent in the lower threshold Jet65 jet trigger because the rate of noise triggers relative to the rate of true jet triggers is smaller at lower jet E_T . The lower panel in Fig. 2 (a) shows the trigger efficiency given by the ratio of each jet-triggered

Table 1: The average number of participating nucleons (N_{part}), number of binary nucleon-nucleon collisions (N_{coll}), and nuclear overlap function (T_{AA}) for the centrality bins used in this analysis. The r.m.s. values give the spread over the centrality bins, which are expressed as fractions of the total inelastic PbPb cross section.

Centrality bin	$\langle N_{\text{part}} \rangle$	r.m.s.	$\langle N_{\text{coll}} \rangle$	r.m.s.	$\langle T_{\text{AA}} \rangle$ (mb^{-1})	r.m.s.
0–5%	381 ± 2	19.2	1660 ± 130	166	25.9 ± 1.06	2.60
5–10%	329 ± 3	22.5	1310 ± 110	168	20.5 ± 0.94	2.62
10–30%	224 ± 4	45.9	745 ± 67	240	11.6 ± 0.67	3.75
30–50%	108 ± 4	27.1	251 ± 28	101	3.92 ± 0.37	1.58
50–70%	42.0 ± 3.5	14.4	62.8 ± 9.4	33.4	0.98 ± 0.14	0.52
70–90%	11.4 ± 1.5	5.73	10.8 ± 2.0	7.29	0.17 ± 0.03	0.11
50–90%	26.7 ± 2.5	18.84	36.9 ± 5.7	35.5	0.58 ± 0.09	0.56

distribution to that from the immediately looser selection. The Jet65 (Jet80) trigger becomes fully efficient above $E_T = 80$ (100) GeV. Following the procedure introduced in the analogous measurement of the charged particle spectra in 0.9 and 7 TeV pp collisions [5], the spectra for $|\eta| < 1.0$ are calculated separately in three ranges of leading-jet E_T , below 80 GeV, between 80 and 100 GeV, and above 100 GeV, each corresponding to a fully efficient trigger path, and then combined to obtain the final result. Figure 2 (b) shows the contributions from the three ranges to the combined spectrum. The lower panel of the figure compares the combined spectrum to the minimum bias spectrum alone, which is in good agreement within statistical uncertainties. As in the previous analysis [5], a p_T -dependent normalization uncertainty of 0–4% is assigned to this procedure of matching the spectra from the different triggered samples.

The reconstruction of charged particles in PbPb collisions, based on hits in the silicon pixel and strip detectors, is performed similarly to what is done in pp collisions [5, 16]. However, some criteria have been fine-tuned to cope with the challenges presented by the much higher hit density in central PbPb collisions. First, prior to track reconstruction, the three-dimensional primary vertex position is fitted from a collection of pixel-only tracks reconstructed with three hits in the pixel detector and extrapolating back to a region around the beam spot. Next, to reduce the random combinatorial background, track candidates are built from triplet seeds alone, consisting of hits in three layers of the pixel barrel and endcap detectors. The seeds from a restricted region within 2 mm of the primary vertex are constructed with a minimum p_T of 0.9 GeV/c. Further selections are made on the normalized goodness-of-fit (i.e. χ^2) of the track fit and on the compatibility of the fitted triplet seeds with the primary vertex, before propagating the seed trajectories through the strip tracker to build fully reconstructed tracks.

To improve the track reconstruction efficiency, two more iterations of the tracking are performed after removing hits unambiguously belonging to the tracks found in the first iteration. This procedure is based on the standard pp iterative tracking [16]. More efficient pp-based pixel-pair and triplet-track seedings are used in the second and third iterations, respectively. The tracks found in the later iterations are merged with the first-iteration tracks after removing any duplicate tracks, based on the fraction of shared hits. Lastly, the calorimeter (ECAL and HCAL) information is used to improve tracking efficiency at high p_T ($\gtrsim 30$ GeV/c) by requiring looser quality criteria for tracks that are determined to be calorimeter compatible. This is possible because genuine charged hadron tracks with high p_T are expected to leave large energy deposits in the calorimeter. Tracks are matched to the closest calorimeter cell in (η, ϕ) , where ϕ

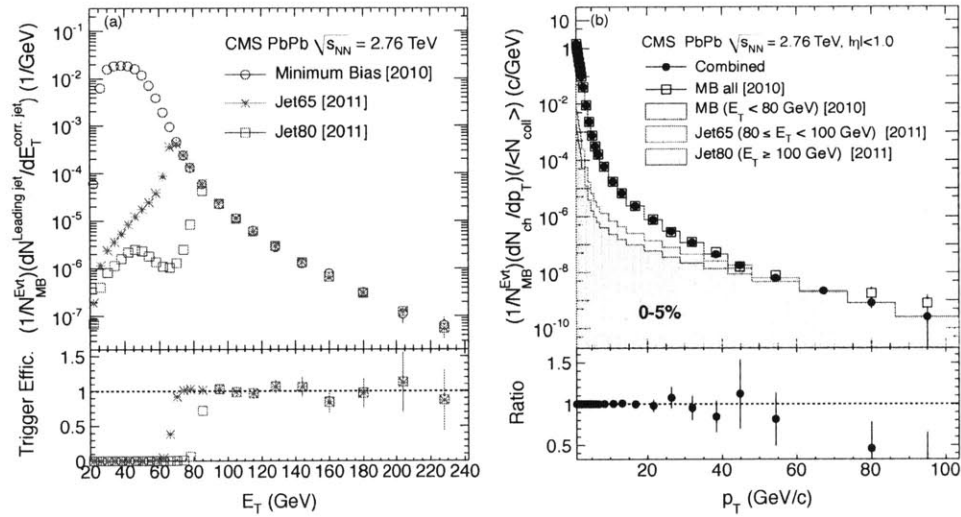


Figure 2: (a) Upper panel: Corrected transverse energy E_T of leading jets with $|\eta| < 2$ for a minimum bias trigger and two jet triggers normalized to the number of selected minimum bias events N_{MB}^{Evt} . Lower panel: efficiency curves for the jet triggers with corrected energy thresholds of 65 and 80 GeV. (b) Upper panel: The three trigger contributions to the charged particle transverse momentum spectrum and their sum (filled circles) for the 0–5% most central events. Open squares show the minimum bias spectrum for all values of leading-jet E_T . Lower panel: the ratio of the combined spectrum to the minimum bias spectrum.

is the azimuthal angle of the track. A track is determined to be compatible with the matched calorimeter cell if the sum of the transverse energy measured by the ECAL and HCAL cells is above a minimum fraction (30%) of the track transverse momentum. Finally, tight quality criteria are imposed for tracks that are incompatible with their matched calorimeter cell energy. These include requirements of at least 13 hits on the track (counting stereo strip layers separately), a relative momentum resolution of less than 5%, a normalized χ^2 of less than 0.15 times the number of hits, and transverse and longitudinal impact parameters of less than three times the sum in quadrature of the uncertainties on the impact parameter and the corresponding vertex position.

Each track is weighted by a factor that accounts for the geometrical acceptance of the detector, the efficiency of the reconstruction algorithm, the fraction of the tracks for which a single charged particle is reconstructed as more than one track, the fraction of tracks corresponding to non-primary charged particles, and the fraction of misidentified tracks that do not correspond to any charged particle. These correction factors are applied differentially as functions of pseudorapidity, transverse momentum, transverse energy of the leading jet, and event centrality. The various correction terms are estimated based on simulated minimum bias PbPb events from the HYDJET [17] generator. To improve the statistical precision of the correction factors at high p_T , HYDJET MC samples are also mixed at the level of simulated hits with dijet events generated with different settings of the hard-scattering scale ($\hat{p}_T=30, 50, 80, 110, \text{ and } 170 \text{ GeV}/c$) from PYQUEN [17], a generator for the simulation of rescattering as well as radiative and collisional energy loss of hard partons in heavy-ion collisions.

Before applying the tight quality selections on the reconstructed tracks, the charged particle reconstruction efficiency is studied by inserting simulated pion tracks or PYQUEN dijet events into two different background samples: (i) simulated minimum bias HYDJET events by mixing GEANT4 [18] detector hits, and (ii) PbPb data events by combining the raw digitized detector signals. The efficiencies estimated by these two methods agree within 3.0–5.7% in the range $1 < p_T < 100 \text{ GeV}/c$. Due to limitations in the data-mixing technique, the two cannot be compared on an equal footing after applying all of the quality cuts, in particular those involving the consistency of a track with the primary vertex. However, it is possible to ensure that the distributions on which the selections are made (i.e. the χ^2 of the track fit, the distance of closest approach between track and vertex, the number of hits in the silicon pixel and strip detectors) are consistent between the data and the MC simulations, both as a function of p_T and event centrality. To this end, an additional series of checks is performed by varying the requirements imposed during the track selection and in the determination of the corresponding MC-based corrections. The resulting variations in the corrected results are within the quoted systematic uncertainties.

The fraction of misidentified tracks estimated from simulated events for each leading-jet E_T sample as a function of track p_T is checked against an estimate from data that uses the sidebands of the impact parameter distributions. Studies of simulated events reveal that, at low p_T and in peripheral events (e.g. 50–90%), the sidebands are dominated by secondaries and products of weak decays because of their displaced vertex positions. However, in central events (e.g. 0–5%) and at high p_T they are mostly misidentified tracks. Based on varying the functional form of the sideband extrapolation under the peak from correctly reconstructed primary tracks, a 2.5–4.0% systematic uncertainty is quoted for the fraction of misidentified tracks remaining after all selection cuts. An additional check is performed for tracks with p_T above $10 \text{ GeV}/c$ to correlate the reconstructed track momentum with the energy deposited in the ECAL and HCAL. The fraction of high- p_T tracks with an atypically small amount of energy deposited in the calorimeters is consistent with the quoted uncertainty on the misidentification rate.

The tendency for finite bin widths and finite transverse-momentum resolution to deform a steeply falling p_T spectrum is corrected for in the analysis of the pp spectrum [5]. The higher occupancy in PbPb events than in pp events has negligible effect on the momentum resolution. The resulting 3.0% systematic uncertainty is dominated by the uncertain shape of the momentum spectrum at high p_T . For the R_{AA} and R_{CP} measurements, a 2.0% systematic uncertainty is quoted after subtracting the correlated uncertainty between the PbPb and pp p_T spectra, or between the central and peripheral PbPb p_T spectra. A summary of all the contributions to the systematic uncertainty affecting the PbPb and pp p_T spectra, and the resulting R_{AA} and R_{CP} values, is given in Table 2.

Table 2: Summary of the various contributions to the systematic uncertainties affecting the PbPb and pp p_T spectra, and the nuclear modification factors R_{AA} and R_{CP} .

Source	Uncertainty [%]	
	PbPb	pp
Track reconstruction efficiency	3.0–5.7	2.2–3.6
Non-primary and misidentified tracks	2.5–4.0	1.0–3.2
Momentum resolution and binning	3.0	0.3–2.7
Normalization of jet-triggered spectra	0.0–4.0	0.0–6.0
Event selection	3.0	3.5
Pile-up estimation	<0.1	1.2
Total for p_T spectra	5.8–9.1	4.4–9.0
Luminosity	–	6.0
T_{AA} determination	4.1–18.0	–
Total for R_{CP}	6.7–20.0	–
Total for R_{AA}	9.9–23.0	–

3 Results

The charged particle invariant differential yield ($E d^3N_{ch}/dp^3$) averaged over the pseudorapidity $|\eta| < 1.0$ in pp collisions is shown in Fig. 3 (a). The invariant and p_T -differential pp cross section is obtained by normalizing the corresponding yield by the integrated luminosities described in Refs. [19, 20]. Also shown in Fig. 3 (a) are various generator-level predictions from the PYTHIA MC [21] for different tunes [22–25], and the ratios of the data to the various MC predictions. The pp measurement is also compared to the empirical global power-law scaling prediction [26] with an exponent $n = 4.9$ determined from the previous CMS measurements [5] by plotting $(\sqrt{s})^{n=4.9} E d^3\sigma/dp^3$ versus the scaling variable $x_T = 2p_T/\sqrt{s}$, as shown in Fig. 3 (b).

The pp measurement at $\sqrt{s} = 2.76$ TeV is consistent with the global power-law fit established in Ref. [5]. The next-to-leading-order (NLO) prediction [26] for $\sqrt{s} = 2.75$ TeV overestimates the measured cross section by almost a factor of two, as shown in Fig. 3 (b).

The PbPb spectrum is shown for six centrality bins and compared to the measured pp reference spectrum, scaled by the nuclear overlap function, in Fig. 4. For easier viewing, several sets of points have been scaled by the arbitrary factors given in the figure. By comparing the PbPb measurements to the dashed lines representing the scaled pp reference spectrum, it is clear that the charged particle spectrum is strongly suppressed in central PbPb events compared to pp, with the most pronounced suppression at around 5–10 GeV/c.

The tendency for finite bin widths and finite transverse-momentum resolution to deform a steeply falling p_T spectrum is corrected for in the analysis of the pp spectrum [5]. The higher occupancy in PbPb events than in pp events has negligible effect on the momentum resolution. The resulting 3.0% systematic uncertainty is dominated by the uncertain shape of the momentum spectrum at high p_T . For the R_{AA} and R_{CP} measurements, a 2.0% systematic uncertainty is quoted after subtracting the correlated uncertainty between the PbPb and pp p_T spectra, or between the central and peripheral PbPb p_T spectra. A summary of all the contributions to the systematic uncertainty affecting the PbPb and pp p_T spectra, and the resulting R_{AA} and R_{CP} values, is given in Table 2.

Table 2: Summary of the various contributions to the systematic uncertainties affecting the PbPb and pp p_T spectra, and the nuclear modification factors R_{AA} and R_{CP} .

Source	Uncertainty [%]	
	PbPb	pp
Track reconstruction efficiency	3.0–5.7	2.2–3.6
Non-primary and misidentified tracks	2.5–4.0	1.0–3.2
Momentum resolution and binning	3.0	0.3–2.7
Normalization of jet-triggered spectra	0.0–4.0	0.0–6.0
Event selection	3.0	3.5
Pile-up estimation	<0.1	1.2
Total for p_T spectra	5.8–9.1	4.4–9.0
Luminosity	–	6.0
T_{AA} determination	4.1–18.0	–
Total for R_{CP}	6.7–20.0	–
Total for R_{AA}	9.9–23.0	–

3 Results

The charged particle invariant differential yield ($E d^3N_{ch}/dp^3$) averaged over the pseudorapidity $|\eta| < 1.0$ in pp collisions is shown in Fig. 3 (a). The invariant and p_T -differential pp cross section is obtained by normalizing the corresponding yield by the integrated luminosities described in Refs. [19, 20]. Also shown in Fig. 3 (a) are various generator-level predictions from the PYTHIA MC [21] for different tunes [22–25], and the ratios of the data to the various MC predictions. The pp measurement is also compared to the empirical global power-law scaling prediction [26] with an exponent $n = 4.9$ determined from the previous CMS measurements [5] by plotting $(\sqrt{s})^{n=4.9} E d^3\sigma/dp^3$ versus the scaling variable $x_T = 2p_T/\sqrt{s}$, as shown in Fig. 3 (b).

The pp measurement at $\sqrt{s} = 2.76$ TeV is consistent with the global power-law fit established in Ref. [5]. The next-to-leading-order (NLO) prediction [26] for $\sqrt{s} = 2.75$ TeV overestimates the measured cross section by almost a factor of two, as shown in Fig. 3 (b).

The PbPb spectrum is shown for six centrality bins and compared to the measured pp reference spectrum, scaled by the nuclear overlap function, in Fig. 4. For easier viewing, several sets of points have been scaled by the arbitrary factors given in the figure. By comparing the PbPb measurements to the dashed lines representing the scaled pp reference spectrum, it is clear that the charged particle spectrum is strongly suppressed in central PbPb events compared to pp, with the most pronounced suppression at around 5–10 GeV/c.

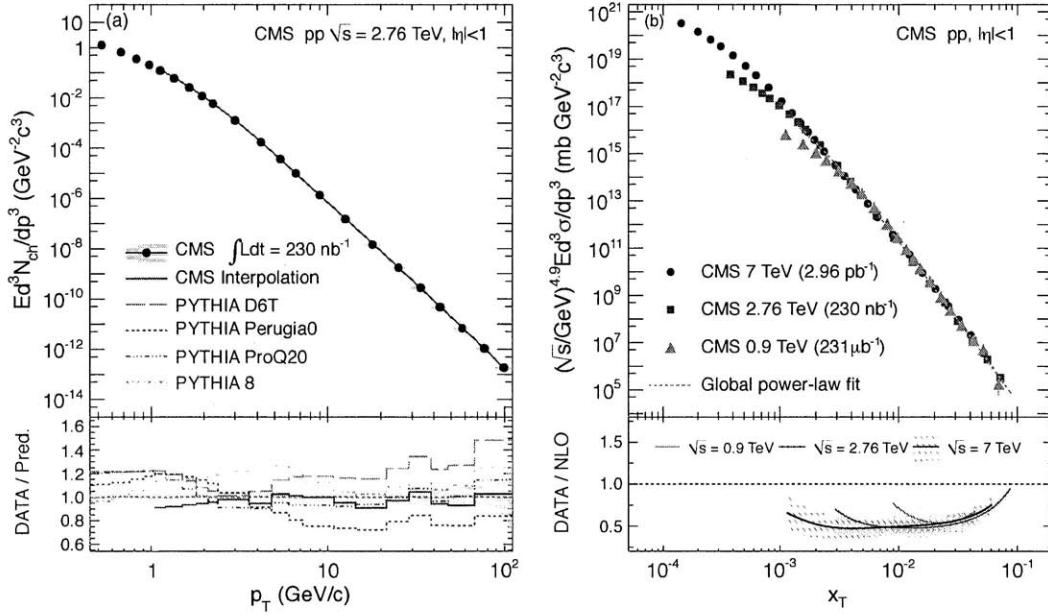


Figure 3: (a) Upper panel: Invariant charged particle differential yield for $|\eta| < 1.0$ in pp collisions at $\sqrt{s} = 2.76$ TeV compared with the predictions of four tunes [22–25] of the PYTHIA MC generator and with the CMS interpolated spectrum using data at 0.9 and 7 TeV [5]. Lower panel: the ratio of the measured spectrum to the predictions of the four PYTHIA tunes and to the interpolated spectrum. The grey band corresponds to the statistical and systematic uncertainties of the measurement added in quadrature. (b) Upper panel: Inclusive charged particle invariant differential cross sections, scaled by $(\sqrt{s})^{4.9}$, for $|\eta| < 1.0$ as a function of the scaling parameter x_T for CMS data at 0.9 and 7 TeV [5] and this analysis at 2.76 TeV. The result is the average of the positive and negative charged particles. Lower panel: ratios of the differential cross sections measured at 0.9, 2.76, and 7 TeV to those predicted by NLO calculations [26]. The bands show the variations in the predictions when changing the factorization scales from 0.5 to 2.0 p_T .

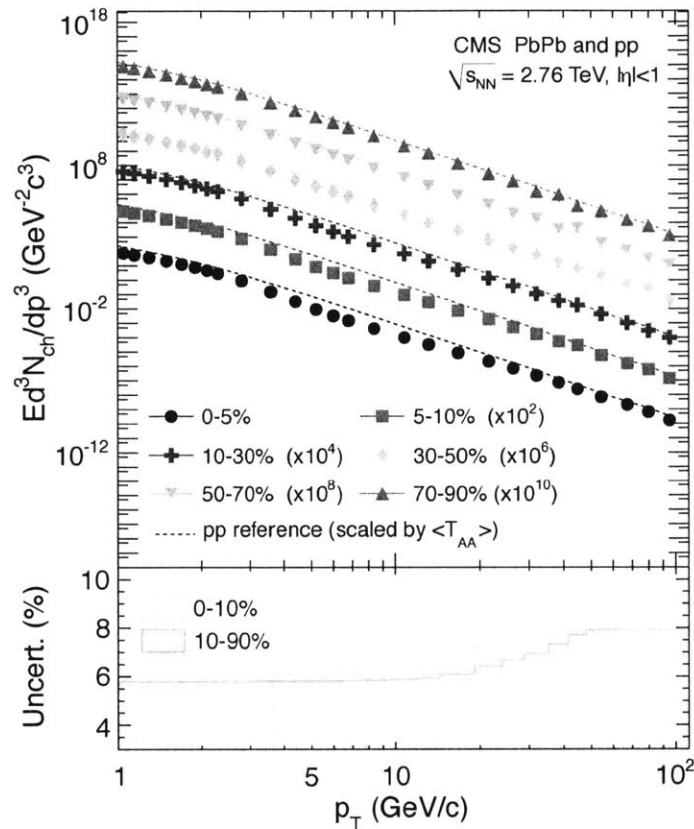


Figure 4: Upper panel: Invariant charged particle differential yield in PbPb collisions at 2.76 TeV in bins of collision centrality (symbols), compared to that of pp at 2.76 TeV, normalized by the corresponding pp invariant cross sections scaled by the nuclear overlap function (dashed lines). The spectra for different centrality bins have been scaled by the arbitrary factors shown in the figure, for easier viewing. The statistical uncertainty is smaller than the marker size for most of the points. Lower panel: The average relative systematic uncertainties of the PbPb differential yields for the 0–10% and 10–90% centrality intervals, as a function of p_T .

The nuclear modification factor R_{AA} is constructed according to Eq. (1) by dividing the PbPb p_T spectrum for each centrality range by the scaled pp reference spectrum (i.e. the filled points by the dashed lines in Fig. 4). It is presented as a function of p_T in Fig. 5 for each of the six centrality bins. The yellow boxes around the points show the systematic uncertainties, including those from the pp reference spectrum, listed in Table 2. An additional systematic uncertainty from the T_{AA} normalization, common to all points and also listed in Table 2, is displayed as the shaded band around unity in each plot. The statistical uncertainties do not increase monotonically as a function of p_T , as seen most prominently in the peripheral bins, as a consequence of combining the highly prescaled minimum bias sample with the two unprescaled jet triggers, as discussed in Section 2. In the most peripheral events (70–90%), a moderate suppression of about a factor of 2 ($R_{AA} \approx 0.6$) is observed at low p_T , with R_{AA} rising slightly with increasing transverse momentum. The suppression becomes more pronounced in the more central collisions, as expected from the increasingly dense final-state system and longer average path-

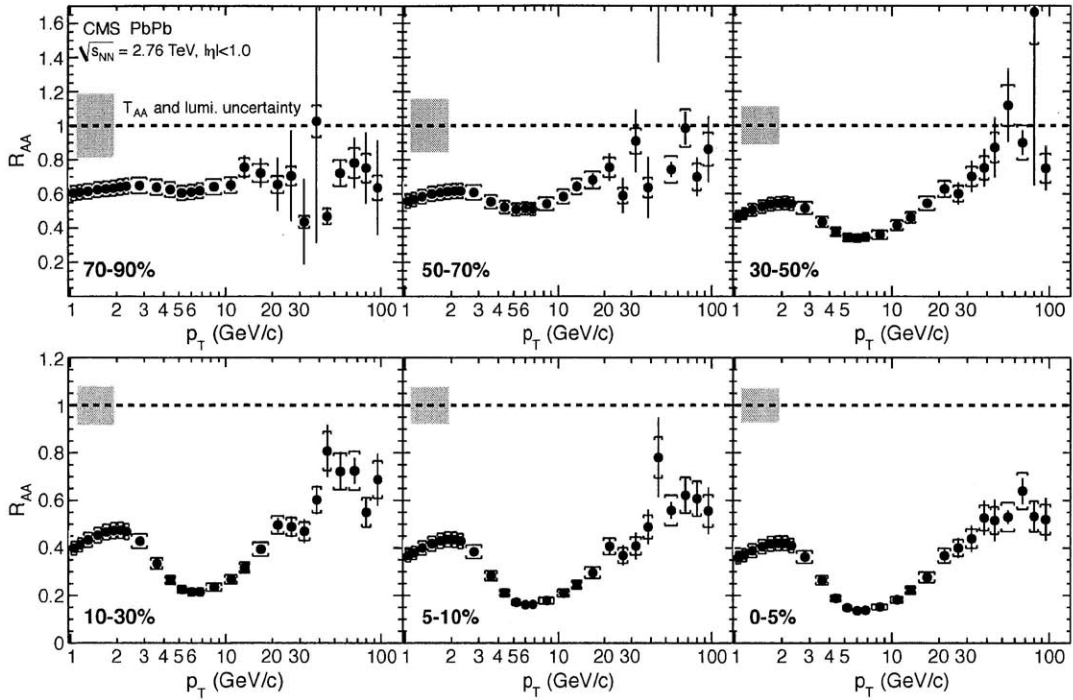


Figure 5: Nuclear modification factor R_{AA} (filled circles) as a function of p_T for six PbPb centralities. The error bars represent the statistical uncertainties and the yellow boxes represent the p_T -dependent systematic uncertainties. An additional systematic uncertainty from the normalization of T_{AA} and the pp integrated luminosity, common to all points, is shown as the shaded band around unity in each plot.

lengths traversed by hard-scattered partons before fragmenting into final hadrons. In the 0–5% centrality bin, R_{AA} reaches a minimum value of about 0.13 at $p_T = 6\text{--}7\text{ GeV}/c$. At higher p_T , the value of R_{AA} rises and levels off above 40 GeV/c at approximately 0.5. A rising R_{AA} may simply reflect the flattening of the unquenched nucleon-nucleon spectrum at high p_T if one assumes a constant fractional energy loss, although the magnitude of the rise varies among the different theoretical models.

The T_{AA} -scaled ratio of spectra in central and peripheral bins, R_{CP} , is constructed according to Eq. (2). The peripheral interval used for the normalization is chosen as the combined 50–90% centrality bin to improve the statistical precision at high p_T . This approach removes the 4.4–9.0% systematic uncertainty from the pp reference. Also part of the T_{AA} uncertainties is correlated between centrality bins and cancels out in the R_{CP} ratio. The resulting values of R_{CP} for the four most central bins are shown in Fig. 6. The statistical uncertainty of R_{CP} does not increase monotonically with p_T for the same reasons as mentioned for R_{AA} . As in the measurement of R_{AA} , the R_{CP} results show that the p_T spectra in central PbPb collisions are significantly suppressed compared to peripheral collisions.

The evolution of the nuclear modification factor with center-of-mass energy, from the SPS [27, 28] to RHIC [29, 30] and then to the LHC [12], is presented in Fig. 7. Note that RHIC results are shown for both neutral pions and charged hadrons, the latter being less suppressed below $p_T \approx 8\text{ GeV}/c$ [29, 30] possibly due to parton recombination processes that enhance proton

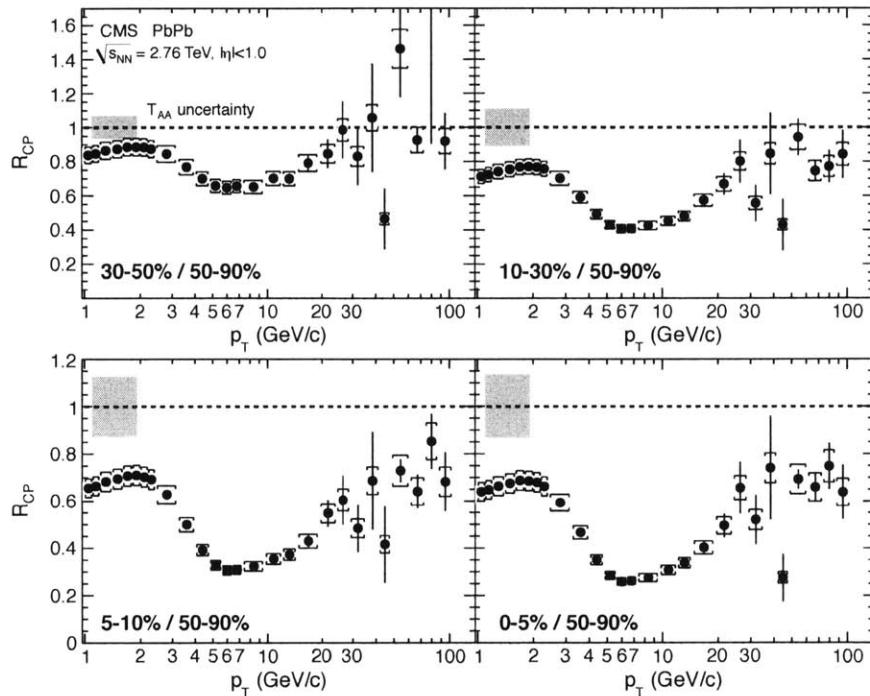


Figure 6: T_{AA} -scaled ratio of p_T spectra in central and peripheral bins, R_{CP} , as a function of p_T for four PbPb centralities. The error bars represent the statistical uncertainties and the yellow boxes the p_T -dependent systematic uncertainties. An additional systematic uncertainty from the normalization of T_{AA} , common to all points, is shown as the shaded band around unity in each plot.

production and thus the overall yield of charged hadrons [31]. Below $p_T \approx 10$ GeV/c, charged hadron production at the LHC is found to be about 50% more suppressed than at RHIC, and has a similar suppression value as for neutral pions measured by PHENIX [29].

The CMS measurement of R_{AA} presented in this paper for the 0–5% centrality interval is compared to the ALICE result [12] in Fig. 7. Note that the pp spectrum measured by CMS at $\sqrt{s} = 2.76$ TeV is roughly 5–15% higher than the ALICE spectrum obtained by interpolating their 0.9 and 7 TeV spectra [12]. The two R_{AA} results are in agreement within their respective statistical and systematic uncertainties.

The high- p_T measurement of R_{AA} from this analysis, up to $p_T = 100$ GeV/c, is also compared to a number of theoretical predictions, for the LHC design energy of $\sqrt{s_{NN}} = 5.5$ TeV (PQM [32] with medium transport-coefficient $\langle \hat{q} \rangle = 30\text{--}80$ GeV²/fm and GLV [33, 34] for various values of the medium gluon pseudorapidity density dN_g/dy) and for the actual collision energy of $\sqrt{s_{NN}} = 2.76$ TeV (ASW [35, 36] and YaJEM [37] including a model for elastic energy loss parameterized with the P_{esc} variable). While most models predict the generally rising behavior of R_{AA} that is observed in the data at high p_T , the magnitude of the predicted slope varies greatly between models, depending on the assumptions for the jet-quenching mechanism. The new CMS measurement presented here should help in constraining the quenching parameters used in these models and improve the understanding of parton energy loss in a hot and dense medium.

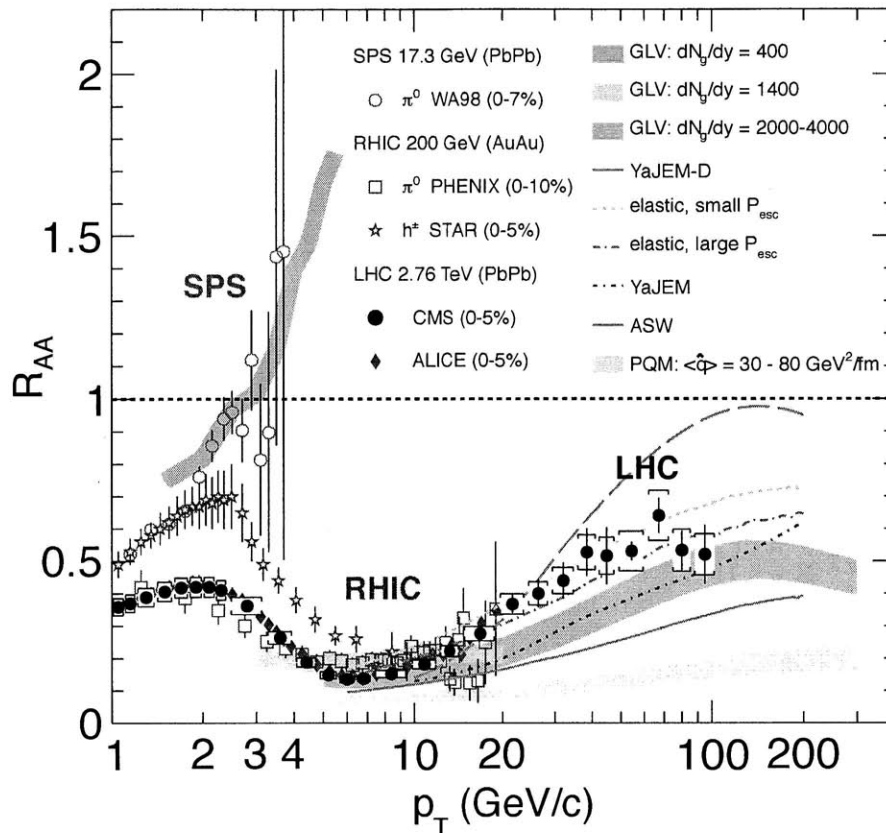


Figure 7: Measurements of the nuclear modification factor R_{AA} in central heavy-ion collisions at three different center-of-mass energies, as a function of p_T , for neutral pions (π^0), charged hadrons (h^\pm), and charged particles [12, 27–30], compared to several theoretical predictions [32–37] (see text). The error bars on the points are the statistical uncertainties, and the yellow boxes around the CMS points are the systematic uncertainties. Additional absolute T_{AA} uncertainties of order $\pm 5\%$ are not plotted. The bands for several of the theoretical calculations represent their uncertainties.

4 Summary

Measurements of the charged particle transverse momentum spectra have been presented for $\sqrt{s_{NN}} = 2.76 \text{ TeV}$ pp and PbPb collisions. The results for the PbPb collisions have been compared to the measured pp p_T spectrum scaled by the corresponding number of incoherent nucleon-nucleon collisions. The high- p_T yields in central PbPb collisions are significantly suppressed when compared to peripheral PbPb and pp collisions. In the range $p_T = 5\text{--}10 \text{ GeV}/c$, the suppression is stronger than that seen at RHIC. Beyond $10 \text{ GeV}/c$, both R_{AA} and R_{CP} show a rising trend, as already suggested by data from the ALICE experiment, limited to $p_T = 20 \text{ GeV}/c$. The CMS measurement, with improved statistical precision, clearly shows that this rise continues at higher p_T , approaching a suppression factor $R_{AA} \approx 0.5\text{--}0.6$ in the range $40\text{--}100 \text{ GeV}/c$. The overall p_T dependence of the suppression can be described by a number of phenomenological predictions. The detailed evolution of the R_{AA} rise from 6 to $100 \text{ GeV}/c$ depends on the details of the models. Together with measurements of high- p_T charged hadron azimuthal anisotropies, inclusive jet spectra, fragmentation functions, and dijet transverse energy balance,

this measurement of the nuclear modification factors as a function of p_T and collision centrality should help elucidate the mechanism of jet quenching and the properties of the medium produced in heavy-ion collisions at collider energies.

Acknowledgements

We wish to congratulate our colleagues in the CERN accelerator departments for the excellent performance of the LHC machine. We thank the technical and administrative staff at CERN and other CMS institutes. This work was supported by the Austrian Federal Ministry of Science and Research; the Belgium Fonds de la Recherche Scientifique, and Fonds voor Wetenschappelijk Onderzoek; the Brazilian Funding Agencies (CNPq, CAPES, FAPERJ, and FAPESP); the Bulgarian Ministry of Education and Science; CERN; the Chinese Academy of Sciences, Ministry of Science and Technology, and National Natural Science Foundation of China; the Colombian Funding Agency (COLCIENCIAS); the Croatian Ministry of Science, Education and Sport; the Research Promotion Foundation, Cyprus; the Ministry of Education and Research, Recurrent financing contract SF0690030s09 and European Regional Development Fund, Estonia; the Academy of Finland, Finnish Ministry of Education and Culture, and Helsinki Institute of Physics; the Institut National de Physique Nucléaire et de Physique des Particules / CNRS, and Commissariat à l'Énergie Atomique et aux Énergies Alternatives / CEA, France; the Bundesministerium für Bildung und Forschung, Deutsche Forschungsgemeinschaft, and Helmholtz-Gemeinschaft Deutscher Forschungszentren, Germany; the General Secretariat for Research and Technology, Greece; the National Scientific Research Foundation, and National Office for Research and Technology, Hungary; the Department of Atomic Energy and the Department of Science and Technology, India; the Institute for Studies in Theoretical Physics and Mathematics, Iran; the Science Foundation, Ireland; the Istituto Nazionale di Fisica Nucleare, Italy; the Korean Ministry of Education, Science and Technology and the World Class University program of NRF, Korea; the Lithuanian Academy of Sciences; the Mexican Funding Agencies (CINVESTAV, CONACYT, SEP, and UASLP-FAI); the Ministry of Science and Innovation, New Zealand; the Pakistan Atomic Energy Commission; the Ministry of Science and Higher Education and the National Science Centre, Poland; the Fundação para a Ciência e a Tecnologia, Portugal; JINR (Armenia, Belarus, Georgia, Ukraine, Uzbekistan); the Ministry of Education and Science of the Russian Federation, the Federal Agency of Atomic Energy of the Russian Federation, Russian Academy of Sciences, and the Russian Foundation for Basic Research; the Ministry of Science and Technological Development of Serbia; the Ministerio de Ciencia e Innovación, and Programa Consolider-Ingenio 2010, Spain; the Swiss Funding Agencies (ETH Board, ETH Zurich, PSI, SNF, UniZH, Canton Zurich, and SER); the National Science Council, Taipei; the Scientific and Technical Research Council of Turkey, and Turkish Atomic Energy Authority; the Science and Technology Facilities Council, UK; the US Department of Energy, and the US National Science Foundation.

Individuals have received support from the Marie-Curie programme and the European Research Council (European Union); the Leventis Foundation; the A. P. Sloan Foundation; the Alexander von Humboldt Foundation; the Belgian Federal Science Policy Office; the Fonds pour la Formation à la Recherche dans l'Industrie et dans l'Agriculture (FRIA-Belgium); the Agentschap voor Innovatie door Wetenschap en Technologie (IWT-Belgium); the Council of Science and Industrial Research, India; and the HOMING PLUS programme of Foundation for Polish Science, cofinanced from European Union, Regional Development Fund.

References

- [1] D. d’Enterria, “Jet quenching”, volume 23: Relativistic Heavy Ion Physics of *Springer Materials - The Landolt-Börnstein Database*, ch. 6.4. Springer-Verlag, 2010.
arXiv:0902.2011. doi:10.1007/978-3-642-01539-7_16.
- [2] J. Casalderrey-Solana and C. A. Salgado, “Introductory lectures on jet quenching in heavy ion collisions”, *Acta Phys. Polon. B* **38** (2007) 3731–3794, arXiv:0712.3443.
- [3] ATLAS Collaboration, “Observation of a Centrality-Dependent Dijet Asymmetry in Lead-Lead Collisions at $\sqrt{s_{NN}} = 2.76$ TeV with the ATLAS Detector at the LHC”, *Phys. Rev. Lett.* **105** (2010) 252303, doi:10.1103/PhysRevLett.105.252303, arXiv:1011.6182.
- [4] CMS Collaboration, “Observation and studies of jet quenching in PbPb collisions at $\sqrt{s_{NN}} = 2.76$ TeV”, *Phys. Rev. C* **84** (2011) 024906, doi:10.1103/PhysRevC.84.024906, arXiv:1102.1957.
- [5] CMS Collaboration, “Charged particle transverse momentum spectra in pp collisions at $\sqrt{s} = 0.9$ and 7 TeV”, *JHEP* **08** (2011) 086, doi:10.1007/JHEP08(2011)086, arXiv:1104.3547.
- [6] STAR Collaboration, “Experimental and theoretical challenges in the search for the quark–gluon plasma: The STAR Collaboration’s critical assessment of the evidence from RHIC collisions”, *Nucl. Phys. A* **757** (2005) 102, doi:10.1016/j.nuclphysa.2005.03.085, arXiv:nucl-ex/0501009.
- [7] PHENIX Collaboration, “Formation of dense partonic matter in relativistic nucleus nucleus collisions at RHIC: Experimental evaluation by the PHENIX Collaboration”, *Nucl. Phys. A* **757** (2005) 184, doi:10.1016/j.nuclphysa.2005.03.086, arXiv:nucl-ex/0410003.
- [8] BRAHMS Collaboration, “Quark–gluon plasma and color glass condensate at RHIC? The perspective from the BRAHMS experiment”, *Nucl. Phys. A* **757** (2005) 1, doi:10.1016/j.nuclphysa.2005.02.130, arXiv:nucl-ex/0410020.
- [9] PHOBOS Collaboration, “The PHOBOS perspective on discoveries at RHIC”, *Nucl. Phys. A* **757** (2005) 28, doi:10.1016/j.nuclphysa.2005.03.084, arXiv:nucl-ex/0410022.
- [10] B. Alver et al., “Importance of correlations and fluctuations on the initial source eccentricity in high-energy nucleus-nucleus collisions”, *Phys. Rev. C* **77** (2008) 014906, doi:10.1103/PhysRevC.77.014906, arXiv:0711.3724.
- [11] Particle Data Group Collaboration, “Review of particle physics”, *J. Phys. G* **37** (2010) 075021, doi:10.1088/0954-3899/37/7A/075021.
- [12] ALICE Collaboration, “Suppression of charged particle production at large transverse momentum in central Pb–Pb collisions at $\sqrt{s_{NN}} = 2.76$ TeV”, *Phys. Lett. B* **696** (2011) 30, doi:10.1016/j.physletb.2010.12.020, arXiv:1012.1004.
- [13] CMS Collaboration, “The CMS experiment at the CERN LHC”, *JINST* **3** (2008) S08004, doi:10.1088/1748-0221/3/08/S08004.

-
- [14] CMS Collaboration, "CMS Physics TDR: Volume I, Detector Performance and Software", CERN-LHCC 2006-001, (2006).
- [15] O. Kodolova, I. Vardanian, A. Nikitenko et al., "The performance of the jet identification and reconstruction in heavy ions collisions with CMS detector", *Eur. Phys. J. C* **50** (2007) 117, doi:10.1140/epjc/s10052-007-0223-9.
- [16] CMS Collaboration, "Tracking and Vertexing Results from First Collisions", CMS Physics Analysis Summary CMS-PAS-TRK-10-001, (2010).
- [17] I. P. Lokhtin and A. M. Snigirev, "A model of jet quenching in ultrarelativistic heavy ion collisions and high- p_T hadron spectra at RHIC", *Eur. Phys. J. C* **45** (2006) 211, doi:10.1140/epjc/s2005-02426-3, arXiv:hep-ph/0506189.
- [18] GEANT4 Collaboration, "GEANT4: a simulation toolkit", *Nucl. Instrum. and Methods A* **506** (2003) 250, doi:10.1016/S0168-9002(03)01368-8.
- [19] CMS Collaboration, "Measurement of CMS Luminosity", CMS Physics Analysis Summary CMS-PAS-EWK-10-004, (2010).
- [20] CMS Collaboration, "Absolute Calibration of the CMS Luminosity Measurement: Summer 2011 Update", CMS Physics Analysis Summary CMS-PAS-EWK-11-001, (2011).
- [21] T. Sjöstrand, S. Mrenna, and P. Z. Skands, "PYTHIA 6.4 Physics and Manual", *JHEP* **05** (2006) 026, doi:10.1088/1126-6708/2006/05/026, arXiv:hep-ph/0603175.
- [22] P. Bartalini and L. Fanó, eds., "Proceedings of the First Workshop on Multiple Partonic Interactions at the LHC". (2009). arXiv:1003.4220.
- [23] T. Sjöstrand, S. Mrenna, and P. Z. Skands, "A Brief Introduction to PYTHIA 8.1", *Comput. Phys. Commun.* **178** (2008) 852, doi:10.1016/j.cpc.2008.01.036, arXiv:0710.3820.
- [24] P. Z. Skands, "The Perugia Tunes", (2009). arXiv:0905.3418.
- [25] A. Buckley, H. Hoeth, H. Lacker et al., "Systematic event generator tuning for the LHC", *Eur. Phys. J. C* **65** (2010) 331, doi:10.1140/epjc/s10052-009-1196-7, arXiv:0907.2973.
- [26] F. Arleo, D. d'Enterria, and A. S. Yoon, "Single-inclusive production of large- p_T charged particles in hadronic collisions at TeV energies and perturbative QCD predictions", *JHEP* **06** (2010) 035, doi:10.1007/JHEP06(2010)035, arXiv:1003.2963.
- [27] WA98 Collaboration, "Transverse mass distributions of neutral pions from Pb^{208} induced reactions at $158 \cdot A$ GeV", *Eur. Phys. J. C* **23** (2002) 225, doi:10.1007/s100520100886, arXiv:nucl-ex/0108006.
- [28] D. d'Enterria, "Indications of suppressed high p_T hadron production in nucleus-nucleus collisions at CERN-SPS", *Phys. Lett. B* **596** (2004) 32, doi:10.1016/j.physletb.2004.06.071, arXiv:nucl-ex/0403055.
- [29] PHENIX Collaboration, "Suppression pattern of neutral pions at high transverse momentum in Au + Au collisions at $\sqrt{s_{NN}} = 200$ GeV and constraints on medium transport coefficients", *Phys. Rev. Lett.* **101** (2008) 232301, doi:10.1103/PhysRevLett.101.232301, arXiv:0801.4020.

- [30] STAR Collaboration, "Transverse momentum and collision energy dependence of high p_T hadron suppression in Au+Au collisions at ultrarelativistic energies", *Phys. Rev. Lett.* **91** (2003) 172302, doi:10.1103/PhysRevLett.91.172302, arXiv:nucl-ex/0305015.
- [31] STAR Collaboration, "Identified baryon and meson distributions at large transverse momenta from Au+Au collisions at $\sqrt{s_{NN}} = 200$ GeV", *Phys. Rev. Lett.* **97** (2006) 152301, doi:10.1103/PhysRevLett.97.152301, arXiv:nucl-ex/0606003.
- [32] A. Dainese, C. Loizides, and G. Paic, "Leading-particle suppression in high energy nucleus-nucleus collisions", *Eur. Phys. J. C* **38** (2005) 461, doi:10.1140/epjc/s2004-02077-x, arXiv:hep-ph/0406201.
- [33] I. Vitev and M. Gyulassy, "High p_T tomography of $d + Au$ and Au+Au at SPS, RHIC, and LHC", *Phys. Rev. Lett.* **89** (2002) 252301, doi:10.1103/PhysRevLett.89.252301, arXiv:hep-ph/0209161.
- [34] I. Vitev, "Jet tomography", *J. Phys. G* **30** (2004) S791, doi:10.1088/0954-3899/30/8/019, arXiv:hep-ph/0403089.
- [35] C. A. Salgado and U. A. Wiedemann, "Calculating quenching weights", *Phys. Rev. D* **68** (2003) 014008, doi:10.1103/PhysRevD.68.014008, arXiv:hep-ph/0302184.
- [36] N. Armesto, A. Dainese, C. A. Salgado et al., "Testing the color charge and mass dependence of parton energy loss with heavy-to-light ratios at BNL RHIC and CERN LHC", *Phys. Rev. D* **71** (2005) 054027, doi:10.1103/PhysRevD.71.054027, arXiv:hep-ph/0501225.
- [37] T. Renk et al., "Systematics of the charged-hadron p_T spectrum and the nuclear suppression factor in heavy-ion collisions from $\sqrt{s} = 200$ GeV to $\sqrt{s} = 2.76$ TeV", *Phys. Rev. C* **84** (2011) 014906, doi:10.1103/PhysRevC.84.014906, arXiv:1103.5308.

A The CMS Collaboration

Yerevan Physics Institute, Yerevan, Armenia

S. Chatrchyan, V. Khachatryan, A.M. Sirunyan, A. Tumasyan

Institut für Hochenergiephysik der OeAW, Wien, Austria

W. Adam, T. Bergauer, M. Dragicevic, J. Erö, C. Fabjan, M. Friedl, R. Frühwirth, V.M. Ghete, J. Hammer¹, M. Hoch, N. Hörmann, J. Hrubec, M. Jeitler, W. Kiesenhofer, M. Krammer, D. Liko, I. Mikulec, M. Pernicka[†], B. Rahbaran, C. Rohringer, H. Rohringer, R. Schöfbeck, J. Strauss, A. Taurok, F. Teischinger, P. Wagner, W. Waltenberger, G. Walzel, E. Widl, C.-E. Wulz

National Centre for Particle and High Energy Physics, Minsk, Belarus

V. Mossolov, N. Shumeiko, J. Suarez Gonzalez

Universiteit Antwerpen, Antwerpen, Belgium

S. Bansal, L. Benucci, T. Cornelis, E.A. De Wolf, X. Janssen, S. Luyckx, T. Maes, L. Mucibello, S. Ochesanu, B. Roland, R. Rougny, M. Selvaggi, H. Van Haevermaet, P. Van Mechelen, N. Van Remortel, A. Van Spilbeeck

Vrije Universiteit Brussel, Brussel, Belgium

F. Blekman, S. Blyweert, J. D'Hondt, R. Gonzalez Suarez, A. Kalogeropoulos, M. Maes, A. Olbrechts, W. Van Doninck, P. Van Mulders, G.P. Van Onsem, I. Villella

Université Libre de Bruxelles, Bruxelles, Belgium

O. Charaf, B. Clerbaux, G. De Lentdecker, V. Dero, A.P.R. Gay, G.H. Hammad, T. Hreus, A. Léonard, P.E. Marage, L. Thomas, C. Vander Velde, P. Vanlaer, J. Wickens

Ghent University, Ghent, Belgium

V. Adler, K. Beernaert, A. Cimmino, S. Costantini, G. Garcia, M. Grunewald, B. Klein, J. Lellouch, A. Marinov, J. Mccartin, A.A. Ocampo Rios, D. Ryckbosch, N. Strobbe, F. Thyssen, M. Tytgat, L. Vanelderen, P. Verwilligen, S. Walsh, E. Yazgan, N. Zaganidis

Université Catholique de Louvain, Louvain-la-Neuve, Belgium

S. Basegmez, G. Bruno, L. Ceard, J. De Favereau De Jeneret, C. Delaere, T. du Pree, D. Favart, L. Forthomme, A. Giammanco², G. Grégoire, J. Hollar, V. Lemaitre, J. Liao, O. Militaru, C. Nuttens, D. Pagano, A. Pin, K. Piotrkowski, N. Schul

Université de Mons, Mons, Belgium

N. Belyi, T. Caebegs, E. Daubie

Centro Brasileiro de Pesquisas Físicas, Rio de Janeiro, Brazil

G.A. Alves, D. De Jesus Damiao, T. Martins, M.E. Pol, M.H.G. Souza

Universidade do Estado do Rio de Janeiro, Rio de Janeiro, Brazil

W.L. Aldá Júnior, W. Carvalho, A. Custódio, E.M. Da Costa, C. De Oliveira Martins, S. Fonseca De Souza, D. Matos Figueiredo, L. Mundim, H. Nogima, V. Oguri, W.L. Prado Da Silva, A. Santoro, S.M. Silva Do Amaral, L. Soares Jorge, A. Sznajder

Instituto de Física Teórica, Universidade Estadual Paulista, Sao Paulo, Brazil

T.S. Anjos³, C.A. Bernardes³, F.A. Dias⁴, T.R. Fernandez Perez Tomei, E. M. Gregores³, C. Lagana, F. Marinho, P.G. Mercadante³, S.F. Novaes, Sandra S. Padula

Institute for Nuclear Research and Nuclear Energy, Sofia, Bulgaria

V. Genchev¹, P. Iaydjiev¹, S. Piperov, M. Rodozov, S. Stoykova, G. Sultanov, V. Tcholakov, R. Trayanov, M. Vutova

University of Sofia, Sofia, Bulgaria

A. Dimitrov, R. Hadjiiska, A. Karadzhinova, V. Kozhuharov, L. Litov, B. Pavlov, P. Petkov

Institute of High Energy Physics, Beijing, China

J.G. Bian, G.M. Chen, H.S. Chen, C.H. Jiang, D. Liang, S. Liang, X. Meng, J. Tao, J. Wang, J. Wang, X. Wang, Z. Wang, H. Xiao, M. Xu, J. Zang, Z. Zhang

State Key Lab. of Nucl. Phys. and Tech., Peking University, Beijing, China

C. Asawatangtrakuldee, Y. Ban, S. Guo, Y. Guo, W. Li, S. Liu, Y. Mao, S.J. Qian, H. Teng, S. Wang, B. Zhu, W. Zou

Universidad de Los Andes, Bogota, Colombia

A. Cabrera, B. Gomez Moreno, A.F. Osorio Oliveros, J.C. Sanabria

Technical University of Split, Split, Croatia

N. Godinovic, D. Lelas, R. Plestina⁵, D. Polic, I. Puljak¹

University of Split, Split, Croatia

Z. Antunovic, M. Dzelalija, M. Kovac

Institute Rudjer Boskovic, Zagreb, Croatia

V. Brigljevic, S. Duric, K. Kadija, J. Luetic, S. Morovic

University of Cyprus, Nicosia, Cyprus

A. Attikis, M. Galanti, J. Mousa, C. Nicolaou, F. Ptochos, P.A. Razis

Charles University, Prague, Czech Republic

M. Finger, M. Finger Jr.

Academy of Scientific Research and Technology of the Arab Republic of Egypt, Egyptian Network of High Energy Physics, Cairo, Egypt

Y. Assran⁶, A. Ellithi Kamel⁷, S. Khalil⁸, M.A. Mahmoud⁹, A. Radi^{8,10}

National Institute of Chemical Physics and Biophysics, Tallinn, Estonia

A. Hektor, M. Kadastik, M. Müntel, M. Raidal, L. Rebane, A. Tiko

Department of Physics, University of Helsinki, Helsinki, Finland

V. Azzolini, P. Eerola, G. Fedi, M. Voutilainen

Helsinki Institute of Physics, Helsinki, Finland

S. Czellar, J. Härkönen, A. Heikkinen, V. Karimäki, R. Kinnunen, M.J. Kortelainen, T. Lampén, K. Lassila-Perini, S. Lehti, T. Lindén, P. Luukka, T. Mäenpää, T. Peltola, E. Tuominen, J. Tuominiemi, E. Tuovinen, D. Ungaro, L. Wendland

Lappeenranta University of Technology, Lappeenranta, Finland

K. Banzuzi, A. Korpela, T. Tuuva

Laboratoire d'Annecy-le-Vieux de Physique des Particules, IN2P3-CNRS, Annecy-le-Vieux, France

D. Sillou

DSM/IRFU, CEA/Saclay, Gif-sur-Yvette, France

M. Besancon, S. Choudhury, M. Dejardin, D. Denegri, B. Fabbro, J.L. Faure, F. Ferri, S. Ganjour, A. Givernaud, P. Gras, G. Hamel de Monchenault, P. Jarry, E. Locci, J. Malcles, M. Marionneau, L. Millischer, J. Rander, A. Rosowsky, I. Shreyber, M. Titov

Laboratoire Leprince-Ringuet, Ecole Polytechnique, IN2P3-CNRS, Palaiseau, France

S. Baffioni, F. Beaudette, L. Benhabib, L. Bianchini, M. Bluj¹¹, C. Broutin, P. Busson, C. Charlot, N. Daci, T. Dahms, L. Dobrzynski, S. Elgammal, R. Granier de Cassagnac, M. Haguenaue, P. Miné, C. Mironov, C. Ochando, P. Paganini, D. Sabes, R. Salerno, Y. Sirois, C. Thiebaux, C. Veelken, A. Zabi

Institut Pluridisciplinaire Hubert Curien, Université de Strasbourg, Université de Haute Alsace Mulhouse, CNRS/IN2P3, Strasbourg, France

J.-L. Agram¹², J. Andrea, D. Bloch, D. Bodin, J.-M. Brom, M. Cardaci, E.C. Chabert, C. Collard, E. Conte¹², F. Drouhin¹², C. Ferro, J.-C. Fontaine¹², D. Gelé, U. Goerlach, S. Greder, P. Juillot, M. Karim¹², A.-C. Le Bihan, P. Van Hove

Centre de Calcul de l'Institut National de Physique Nucleaire et de Physique des Particules (IN2P3), Villeurbanne, France

F. Fassi, D. Mercier

Université de Lyon, Université Claude Bernard Lyon 1, CNRS-IN2P3, Institut de Physique Nucléaire de Lyon, Villeurbanne, France

C. Baty, S. Beauceron, N. Beaupere, M. Bedjidian, O. Bondu, G. Boudoul, D. Boumediene, H. Brun, J. Chasserat, R. Chierici¹, D. Contardo, P. Depasse, H. El Mamouni, A. Falkiewicz, J. Fay, S. Gascon, M. Gouzevitch, B. Ille, T. Kurca, T. Le Grand, M. Lethuillier, L. Mirabito, S. Perries, V. Sordini, S. Tosi, Y. Tschudi, P. Verdier, S. Viret

Institute of High Energy Physics and Informatization, Tbilisi State University, Tbilisi, Georgia

D. Lomidze

RWTH Aachen University, I. Physikalisches Institut, Aachen, Germany

G. Anagnostou, S. Beranek, M. Edelhoff, L. Feld, N. Heracleous, O. Hindrichs, R. Jussen, K. Klein, J. Merz, A. Ostapchuk, A. Perieanu, F. Raupach, J. Sammet, S. Schael, D. Sprenger, H. Weber, B. Wittmer, V. Zhukov¹³

RWTH Aachen University, III. Physikalisches Institut A, Aachen, Germany

M. Ata, J. Caudron, E. Dietz-Laursonn, M. Erdmann, A. Güth, T. Hebbeker, C. Heidemann, K. Hoepfner, T. Klimovich, D. Klingebiel, P. Kreuzer, D. Lanske[†], J. Lingemann, C. Magass, M. Merschmeyer, A. Meyer, M. Olschewski, P. Papacz, H. Pieta, H. Reithler, S.A. Schmitz, L. Sonnenschein, J. Steggemann, D. Teysier, M. Weber

RWTH Aachen University, III. Physikalisches Institut B, Aachen, Germany

M. Bontenackels, V. Cherepanov, M. Davids, G. Flügge, H. Geenen, M. Geisler, W. Haj Ahmad, F. Hoehle, B. Kargoll, T. Kress, Y. Kuessel, A. Linn, A. Nowack, L. Perchalla, O. Pooth, J. Rennefeld, P. Sauerland, A. Stahl, M.H. Zoeller

Deutsches Elektronen-Synchrotron, Hamburg, Germany

M. Aldaya Martin, W. Behrenhoff, U. Behrens, M. Bergholz¹⁴, A. Bethani, K. Borras, A. Cakir, A. Campbell, E. Castro, D. Dammann, G. Eckerlin, D. Eckstein, A. Flossdorf, G. Flucke, A. Geiser, J. Hauk, H. Jung¹, M. Kasemann, P. Katsas, C. Kleinwort, H. Kluge, A. Knutsson, M. Krämer, D. Krücker, E. Kuznetsova, W. Lange, W. Lohmann¹⁴, B. Lutz, R. Mankel, I. Marfin, M. Marienfeld, I.-A. Melzer-Pellmann, A.B. Meyer, J. Mnich, A. Mussgiller, S. Naumann-Emme, J. Olzem, A. Petrukhin, D. Pitzl, A. Raspereza, P.M. Ribeiro Cipriano, M. Rosin, J. Salfeld-Nebgen, R. Schmidt¹⁴, T. Schoerner-Sadenius, N. Sen, A. Spiridonov, M. Stein, J. Tomaszewska, R. Walsh, C. Wissing

University of Hamburg, Hamburg, Germany

C. Autermann, V. Blobel, S. Bobrovskyi, J. Draeger, H. Enderle, J. Erfle, U. Gebbert, M. Görner, T. Hermanns, R.S. Höing, K. Kaschube, G. Kaussen, H. Kirschenmann, R. Klanner, J. Lange, B. Mura, F. Nowak, N. Pietsch, C. Sander, H. Schettler, P. Schleper, E. Schlieckau, A. Schmidt, M. Schröder, T. Schum, H. Stadie, G. Steinbrück, J. Thomsen

Institut für Experimentelle Kernphysik, Karlsruhe, Germany

C. Barth, J. Berger, T. Chwalek, W. De Boer, A. Dierlamm, G. Dirkes, M. Feindt, J. Gruschke, M. Guthoff¹, C. Hackstein, F. Hartmann, M. Heinrich, H. Held, K.H. Hoffmann, S. Honc, I. Katkov¹³, J.R. Komaragiri, T. Kuhr, D. Martschei, S. Mueller, Th. Müller, M. Niegel, O. Oberst, A. Oehler, J. Ott, T. Peiffer, G. Quast, K. Rabbertz, F. Ratnikov, N. Ratnikova, M. Renz, S. Röcker, C. Saout, A. Scheurer, P. Schieferdecker, F.-P. Schilling, M. Schmanau, G. Schott, H.J. Simonis, F.M. Stober, D. Troendle, J. Wagner-Kuhr, T. Weiler, M. Zeise, E.B. Ziebarth

Institute of Nuclear Physics "Demokritos", Aghia Paraskevi, Greece

G. Daskalakis, T. Geralis, S. Kesisoglou, A. Kyriakis, D. Loukas, I. Manolakos, A. Markou, C. Markou, C. Mavrommatis, E. Ntomari

University of Athens, Athens, Greece

L. Gouskos, T.J. Mertzimekis, A. Panagiotou, N. Saoulidou, E. Stiliaris

University of Ioánnina, Ioánnina, Greece

I. Evangelou, C. Foudas¹, P. Kokkas, N. Manthos, I. Papadopoulos, V. Patras, F.A. Triantis

KFKI Research Institute for Particle and Nuclear Physics, Budapest, Hungary

A. Aranyi, G. Bencze, L. Boldizsar, C. Hajdu¹, P. Hidas, D. Horvath¹⁵, A. Kapusi, K. Krajczar¹⁶, F. Sikler¹, G. Vesztergombi¹⁶

Institute of Nuclear Research ATOMKI, Debrecen, Hungary

N. Beni, J. Molnar, J. Palinkas, Z. Szillasi, V. Veszpremi

University of Debrecen, Debrecen, Hungary

J. Karancsi, P. Raics, Z.L. Trocsanyi, B. Ujvari

Panjab University, Chandigarh, India

S.B. Beri, V. Bhatnagar, N. Dhingra, R. Gupta, M. Jindal, M. Kaur, J.M. Kohli, M.Z. Mehta, N. Nishu, L.K. Saini, A. Sharma, A.P. Singh, J. Singh, S.P. Singh

University of Delhi, Delhi, India

S. Ahuja, B.C. Choudhary, A. Kumar, A. Kumar, S. Malhotra, M. Naimuddin, K. Ranjan, V. Sharma, R.K. Shivpuri

Saha Institute of Nuclear Physics, Kolkata, India

S. Banerjee, S. Bhattacharya, S. Dutta, B. Gomber, S. Jain, S. Jain, R. Khurana, S. Sarkar

Bhabha Atomic Research Centre, Mumbai, India

R.K. Choudhury, D. Dutta, S. Kailas, V. Kumar, A.K. Mohanty¹, L.M. Pant, P. Shukla

Tata Institute of Fundamental Research - EHEP, Mumbai, India

T. Aziz, S. Ganguly, M. Guchait¹⁷, A. Gurtu¹⁸, M. Maity¹⁹, G. Majumder, K. Mazumdar, G.B. Mohanty, B. Parida, A. Saha, K. Sudhakar, N. Wickramage

Tata Institute of Fundamental Research - HECR, Mumbai, India

S. Banerjee, S. Dugad, N.K. Mondal

Institute for Research in Fundamental Sciences (IPM), Tehran, Iran

H. Arfaei, H. Bakhshiansohi²⁰, S.M. Etesami²¹, A. Fahim²⁰, M. Hashemi, H. Hesari, A. Jafari²⁰, M. Khakzad, A. Mohammadi²², M. Mohammadi Najafabadi, S. Paktinat Mehdiabadi, B. Safarzadeh²³, M. Zeinali²¹

INFN Sezione di Bari ^a, Università di Bari ^b, Politecnico di Bari ^c, Bari, Italy

M. Abbrescia^{a,b}, L. Barbone^{a,b}, C. Calabria^{a,b}, S.S. Chhibra^{a,b}, A. Colaleo^a, D. Creanza^{a,c}, N. De Filippis^{a,c,1}, M. De Palma^{a,b}, L. Fiore^a, G. Iaselli^{a,c}, L. Lusito^{a,b}, G. Maggi^{a,c}, M. Maggi^a, N. Manna^{a,b}, B. Marangelli^{a,b}, S. My^{a,c}, S. Nuzzo^{a,b}, N. Pacifico^{a,b}, A. Pompili^{a,b}, G. Pugliese^{a,c}, F. Romano^{a,c}, G. Selvaggi^{a,b}, L. Silvestris^a, G. Singh^{a,b}, S. Tuppiti^{a,b}, G. Zito^a

INFN Sezione di Bologna ^a, Università di Bologna ^b, Bologna, Italy

G. Abbiendi^a, A.C. Benvenuti^a, D. Bonacorsi^a, S. Braibant-Giacomelli^{a,b}, L. Brigliadori^a, P. Capiluppi^{a,b}, A. Castro^{a,b}, F.R. Cavallo^a, M. Cuffiani^{a,b}, G.M. Dallavalle^a, F. Fabbri^a, A. Fanfani^{a,b}, D. Fasanella^{a,1}, P. Giacomelli^a, C. Grandi^a, S. Marcellini^a, G. Masetti^a, M. Meneghelli^{a,b}, A. Montanari^a, F.L. Navarria^{a,b}, F. Odorici^a, A. Perrotta^a, F. Primavera^a, A.M. Rossi^{a,b}, T. Rovelli^{a,b}, G. Siroli^{a,b}, R. Travaglini^{a,b}

INFN Sezione di Catania ^a, Università di Catania ^b, Catania, Italy

S. Albergò^{a,b}, G. Cappello^{a,b}, M. Chiorboli^{a,b}, S. Costa^{a,b}, R. Potenza^{a,b}, A. Tricomi^{a,b}, C. Tuve^{a,b}

INFN Sezione di Firenze ^a, Università di Firenze ^b, Firenze, Italy

G. Barbagli^a, V. Ciulli^{a,b}, C. Civinini^a, R. D'Alessandro^{a,b}, E. Focardi^{a,b}, S. Frosali^{a,b}, E. Gallo^a, S. Gozzi^{a,b}, M. Meschini^a, S. Paoletti^a, G. Sguazzoni^a, A. Tropiano^{a,1}

INFN Laboratori Nazionali di Frascati, Frascati, Italy

L. Benussi, S. Bianco, S. Colafranceschi²⁴, F. Fabbri, D. Piccolo

INFN Sezione di Genova, Genova, Italy

P. Fabbriatore, R. Musenich

INFN Sezione di Milano-Bicocca ^a, Università di Milano-Bicocca ^b, Milano, Italy

A. Benaglia^{a,b,1}, F. De Guio^{a,b}, L. Di Matteo^{a,b}, S. Fiorendi^{a,b}, S. Gennai^{a,1}, A. Ghezzi^{a,b}, S. Malvezzi^a, R.A. Manzoni^{a,b}, A. Martelli^{a,b}, A. Massironi^{a,b,1}, D. Menasce^a, L. Moroni^a, M. Paganoni^{a,b}, D. Pedrini^a, S. Ragazzi^{a,b}, N. Redaelli^a, S. Sala^a, T. Tabarelli de Fatis^{a,b}

INFN Sezione di Napoli ^a, Università di Napoli "Federico II" ^b, Napoli, Italy

S. Buontempo^a, C.A. Carrillo Montoya^{a,1}, N. Cavallo^{a,25}, A. De Cosa^{a,b}, O. Dogangun^{a,b}, F. Fabozzi^{a,25}, A.O.M. Iorio^{a,1}, L. Lista^a, M. Merola^{a,b}, P. Paolucci^a

INFN Sezione di Padova ^a, Università di Padova ^b, Università di Trento (Trento) ^c, Padova, Italy

P. Azzi^a, N. Bacchetta^{a,1}, P. Bellan^{a,b}, D. Bisello^{a,b}, A. Branca^a, R. Carlin^{a,b}, P. Checchia^a, T. Dorigo^a, U. Dosselli^a, F. Gasparini^{a,b}, U. Gasparini^{a,b}, A. Gozzelino^a, K. Kanishchev, S. Lacaprara^{a,26}, I. Lazzizzera^{a,c}, M. Margoni^{a,b}, M. Mazzucato^a, A.T. Meneguzzo^{a,b}, M. Michelotto^a, M. Nespolo^{a,1}, L. Perrozzi^a, N. Pozzobon^{a,b}, P. Ronchese^{a,b}, F. Simonetto^{a,b}, E. Torassa^a, M. Tosi^{a,b,1}, S. Vanini^{a,b}, P. Zotto^{a,b}, G. Zumerle^{a,b}

INFN Sezione di Pavia ^a, Università di Pavia ^b, Pavia, Italy

P. Baesso^{a,b}, U. Berzano^a, S.P. Ratti^{a,b}, C. Riccardi^{a,b}, P. Torre^{a,b}, P. Vitulo^{a,b}, C. Viviani^{a,b}

INFN Sezione di Perugia ^a, Università di Perugia ^b, Perugia, Italy

M. Biasini^{a,b}, G.M. Bilei^a, B. Caponeri^{a,b}, L. Fanò^{a,b}, P. Lariccia^{a,b}, A. Lucaroni^{a,b,1}, G. Mantovani^{a,b}, M. Menichelli^a, A. Nappi^{a,b}, F. Romeo^{a,b}, A. Santocchia^{a,b}, S. Taroni^{a,b,1}, M. Valdata^{a,b}

INFN Sezione di Pisa ^a, Università di Pisa ^b, Scuola Normale Superiore di Pisa ^c, Pisa, Italy
 P. Azzurri^{a,c}, G. Bagliesi^a, T. Boccali^a, G. Broccolo^{a,c}, R. Castaldi^a, R.T. D’Agnolo^{a,c},
 R. Dell’Orso^a, F. Fiori^{a,b}, L. Foà^{a,c}, A. Giassi^a, A. Kraan^a, F. Ligabue^{a,c}, T. Lomtadze^a,
 L. Martini^{a,27}, A. Messineo^{a,b}, F. Palla^a, F. Palmonari^a, A. Rizzi, A.T. Serban^a, P. Spagnolo^a,
 R. Tenchini^a, G. Tonelli^{a,b,1}, A. Venturi^{a,1}, P.G. Verdini^a

INFN Sezione di Roma ^a, Università di Roma “La Sapienza” ^b, Roma, Italy
 L. Barone^{a,b}, F. Cavallari^a, D. Del Re^{a,b,1}, M. Diemoz^a, C. Fanelli, D. Franci^{a,b}, M. Grassi^{a,1},
 E. Longo^{a,b}, P. Meridiani^a, F. Micheli, S. Nourbakhsh^a, G. Organtini^{a,b}, F. Pandolfi^{a,b},
 R. Paramatti^a, S. Rahatlou^{a,b}, M. Sigamani^a, L. Soffi

**INFN Sezione di Torino ^a, Università di Torino ^b, Università del Piemonte Orientale (No-
 vara) ^c, Torino, Italy**
 N. Amapane^{a,b}, R. Arcidiacono^{a,c}, S. Argiro^{a,b}, M. Arneodo^{a,c}, C. Biino^a, C. Botta^{a,b},
 N. Cartiglia^a, R. Castello^{a,b}, M. Costa^{a,b}, N. Demaria^a, A. Graziano^{a,b}, C. Mariotti^{a,1}, S. Maselli^a,
 E. Migliore^{a,b}, V. Monaco^{a,b}, M. Musich^a, M.M. Obertino^{a,c}, N. Pastrone^a, M. Pelliccioni^a,
 A. Potenza^{a,b}, A. Romero^{a,b}, M. Ruspa^{a,c}, R. Sacchi^{a,b}, V. Sola^{a,b}, A. Solano^{a,b}, A. Staiano^a,
 A. Vilela Pereira^a

INFN Sezione di Trieste ^a, Università di Trieste ^b, Trieste, Italy
 S. Belforte^a, F. Cossutti^a, G. Della Ricca^{a,b}, B. Gobbo^a, M. Marone^{a,b}, D. Montanino^{a,b,1},
 A. Penzo^a

Kangwon National University, Chunchon, Korea
 S.G. Heo, S.K. Nam

Kyungpook National University, Daegu, Korea
 S. Chang, J. Chung, D.H. Kim, G.N. Kim, J.E. Kim, D.J. Kong, H. Park, S.R. Ro, D.C. Son

**Chonnam National University, Institute for Universe and Elementary Particles, Kwangju,
 Korea**
 J.Y. Kim, Zero J. Kim, S. Song

Konkuk University, Seoul, Korea
 H.Y. Jo

Korea University, Seoul, Korea
 S. Choi, D. Gyun, B. Hong, M. Jo, H. Kim, T.J. Kim, K.S. Lee, D.H. Moon, S.K. Park, E. Seo,
 K.S. Sim

University of Seoul, Seoul, Korea
 M. Choi, S. Kang, H. Kim, J.H. Kim, C. Park, I.C. Park, S. Park, G. Ryu

Sungkyunkwan University, Suwon, Korea
 Y. Cho, Y. Choi, Y.K. Choi, J. Goh, M.S. Kim, B. Lee, J. Lee, S. Lee, H. Seo, I. Yu

Vilnius University, Vilnius, Lithuania
 M.J. Bilinskas, I. Grigelionis, M. Janulis

Centro de Investigacion y de Estudios Avanzados del IPN, Mexico City, Mexico
 H. Castilla-Valdez, E. De La Cruz-Burelo, I. Heredia-de La Cruz, R. Lopez-Fernandez,
 R. Magaña Villalba, J. Martínez-Ortega, A. Sánchez-Hernández, L.M. Villasenor-Cendejas

Universidad Iberoamericana, Mexico City, Mexico
 S. Carrillo Moreno, F. Vazquez Valencia

Benemerita Universidad Autonoma de Puebla, Puebla, Mexico

H.A. Salazar Ibarguen

Universidad Autónoma de San Luis Potosí, San Luis Potosí, Mexico

E. Casimiro Linares, A. Morelos Pineda, M.A. Reyes-Santos

University of Auckland, Auckland, New Zealand

D. Krofcheck

University of Canterbury, Christchurch, New Zealand

A.J. Bell, P.H. Butler, R. Doesburg, S. Reucroft, H. Silverwood

National Centre for Physics, Quaid-I-Azam University, Islamabad, Pakistan

M. Ahmad, M.I. Asghar, H.R. Hoorani, S. Khalid, W.A. Khan, T. Khurshid, S. Qazi, M.A. Shah, M. Shoaib

Institute of Experimental Physics, Faculty of Physics, University of Warsaw, Warsaw, Poland

G. Brona, M. Cwiok, W. Dominik, K. Doroba, A. Kalinowski, M. Konecki, J. Krolikowski

Soltan Institute for Nuclear Studies, Warsaw, Poland

H. Bialkowska, B. Boimska, T. Frueboes, R. Gokieli, M. Górski, M. Kazana, K. Nawrocki, K. Romanowska-Rybinska, M. Szeleper, G. Wrochna, P. Zalewski

Laboratório de Instrumentação e Física Experimental de Partículas, Lisboa, Portugal

N. Almeida, P. Bargassa, A. David, P. Faccioli, P.G. Ferreira Parracho, M. Gallinaro, P. Musella, A. Nayak, J. Pela¹, P.Q. Ribeiro, J. Seixas, J. Varela, P. Vischia

Joint Institute for Nuclear Research, Dubna, Russia

S. Afanasiev, I. Belotelov, P. Bunin, M. Gavrilenko, I. Golutvin, I. Gorbunov, A. Kamenev, V. Karjavin, G. Kozlov, A. Lanev, P. Moisezen, V. Palichik, V. Perelygin, S. Shmatov, V. Smirnov, A. Volodko, A. Zarubin

Petersburg Nuclear Physics Institute, Gatchina (St Petersburg), Russia

S. Evstyukhin, V. Golovtsov, Y. Ivanov, V. Kim, P. Levchenko, V. Murzin, V. Oreshkin, I. Smirnov, V. Sulimov, L. Uvarov, S. Vavilov, A. Vorobyev, An. Vorobyev

Institute for Nuclear Research, Moscow, Russia

Yu. Andreev, A. Dermenev, S. Gninenko, N. Golubev, M. Kirsanov, N. Krasnikov, V. Matveev, A. Pashenkov, A. Toropin, S. Troitsky

Institute for Theoretical and Experimental Physics, Moscow, Russia

V. Epshteyn, M. Erofeeva, V. Gavrilov, M. Kossov¹, A. Krokhotin, N. Lychkovskaya, V. Popov, G. Safronov, S. Semenov, V. Stolin, E. Vlasov, A. Zhokin

Moscow State University, Moscow, Russia

A. Belyaev, E. Boos, A. Ershov, A. Gribushin, O. Kodolova, V. Korotkikh, I. Lokhtin, A. Markina, S. Obraztsov, M. Perfilov, S. Petrushanko, L. Sarycheva[†], V. Savrin, A. Snigirev, I. Vardanyan

P.N. Lebedev Physical Institute, Moscow, Russia

V. Andreev, M. Azarkin, I. Dremin, M. Kirakosyan, A. Leonidov, G. Mesyats, S.V. Rusakov, A. Vinogradov

State Research Center of Russian Federation, Institute for High Energy Physics, Protvino, Russia

I. Azhgirey, I. Bayshev, S. Bitioukov, V. Grishin¹, V. Kachanov, D. Konstantinov, A. Korablev,

V. Krychkin, V. Petrov, R. Ryutin, A. Sobol, L. Tourtchanovitch, S. Troshin, N. Tyurin, A. Uzunian, A. Volkov

University of Belgrade, Faculty of Physics and Vinca Institute of Nuclear Sciences, Belgrade, Serbia

P. Adzic²⁸, M. Djordjevic, M. Ekmedzic, D. Krpic²⁸, J. Milosevic

Centro de Investigaciones Energéticas Medioambientales y Tecnológicas (CIEMAT), Madrid, Spain

M. Aguilar-Benitez, J. Alcaraz Maestre, P. Arce, C. Battilana, E. Calvo, M. Cerrada, M. Chamizo Llatas, N. Colino, B. De La Cruz, A. Delgado Peris, C. Diez Pardos, D. Domínguez Vázquez, C. Fernandez Bedoya, J.P. Fernández Ramos, A. Ferrando, J. Flix, M.C. Fouz, P. Garcia-Abia, O. Gonzalez Lopez, S. Goy Lopez, J.M. Hernandez, M.I. Josa, G. Merino, J. Puerta Pelayo, I. Redondo, L. Romero, J. Santaolalla, M.S. Soares, C. Willmott

Universidad Autónoma de Madrid, Madrid, Spain

C. Albajar, G. Codispoti, J.F. de Trocóniz

Universidad de Oviedo, Oviedo, Spain

J. Cuevas, J. Fernandez Menendez, S. Folgueras, I. Gonzalez Caballero, L. Lloret Iglesias, J.M. Vizán García

Instituto de Física de Cantabria (IFCA), CSIC-Universidad de Cantabria, Santander, Spain

J.A. Brochero Cifuentes, I.J. Cabrillo, A. Calderon, S.H. Chuang, J. Duarte Campderros, M. Felcini²⁹, M. Fernandez, G. Gomez, J. Gonzalez Sanchez, C. Jorda, P. Lobelle Pardo, A. Lopez Virto, J. Marco, R. Marco, C. Martinez Rivero, F. Matorras, F.J. Muñoz Sanchez, J. Piedra Gomez³⁰, T. Rodrigo, A.Y. Rodríguez-Marrero, A. Ruiz-Jimeno, L. Scodellaro, M. Sobron Sanudo, I. Vila, R. Vilar Cortabitarte

CERN, European Organization for Nuclear Research, Geneva, Switzerland

D. Abbaneo, E. Auffray, G. Auzinger, P. Baillon, A.H. Ball, D. Barney, C. Bernet⁵, W. Bialas, G. Bianchi, P. Bloch, A. Bocci, H. Breuker, K. Bunkowski, T. Camporesi, G. Cerminara, T. Christiansen, J.A. Coarasa Perez, B. Curé, D. D'Enterria, A. De Roeck, S. Di Guida, M. Dobson, N. Dupont-Sagorin, A. Elliott-Peisert, B. Frisch, W. Funk, A. Gaddi, G. Georgiou, H. Gerwig, M. Giffels, D. Gigi, K. Gill, D. Giordano, M. Giunta, F. Glege, R. Gomez-Reino Garrido, P. Govoni, S. Gowdy, R. Guida, L. Guiducci, M. Hansen, P. Harris, C. Hartl, J. Harvey, B. Hegner, A. Hinzmann, H.F. Hoffmann, V. Innocente, P. Janot, K. Kaadze, E. Karavakis, K. Kousouris, P. Lecoq, P. Lenzi, C. Lourenço, T. Mäki, M. Malberti, L. Malgeri, M. Mannelli, L. Masetti, G. Mavromanolakis, F. Meijers, S. Mersi, E. Meschi, R. Moser, M.U. Mozer, M. Mulders, E. Nesvold, M. Nguyen, T. Orimoto, L. Orsini, E. Palencia Cortezon, E. Perez, A. Petrilli, A. Pfeiffer, M. Pierini, M. Pimiä, D. Piparo, G. Polese, L. Quertenmont, A. Racz, W. Reece, J. Rodrigues Antunes, G. Rolandi³¹, T. Rommerskirchen, C. Rovelli³², M. Rovere, H. Sakulin, F. Santanastasio, C. Schäfer, C. Schwick, I. Segoni, A. Sharma, P. Siegrist, P. Silva, M. Simon, P. Sphicas³³, D. Spiga, M. Spiropulu⁴, M. Stoye, A. Tsirou, G.I. Veres¹⁶, P. Vichoudis, H.K. Wöhri, S.D. Worm³⁴, W.D. Zeuner

Paul Scherrer Institut, Villigen, Switzerland

W. Bertl, K. Deiters, W. Erdmann, K. Gabathuler, R. Horisberger, Q. Ingram, H.C. Kaestli, S. König, D. Kotlinski, U. Langenegger, F. Meier, D. Renker, T. Rohe, J. Sibille³⁵

Institute for Particle Physics, ETH Zurich, Zurich, Switzerland

L. Bäni, P. Bortignon, M.A. Buchmann, B. Casal, N. Chanon, Z. Chen, A. Deisher, G. Dissertori, M. Dittmar, M. Dünser, J. Eugster, K. Freudenreich, C. Grab, P. Lecomte, W. Lustermann,

P. Martinez Ruiz del Arbol, N. Mohr, F. Moortgat, C. Nägeli³⁶, P. Nef, F. Nessi-Tedaldi, L. Pape, F. Pauss, M. Peruzzi, F.J. Ronga, M. Rossini, L. Sala, A.K. Sanchez, M.-C. Sawley, A. Starodumov³⁷, B. Stieger, M. Takahashi, L. Tauscher[†], A. Thea, K. Theofilatos, D. Treille, C. Urscheler, R. Wallny, H.A. Weber, L. Wehrli, J. Weng

Universität Zürich, Zurich, Switzerland

E. Aguilo, C. AMSler, V. Chiochia, S. De Visscher, C. Favaro, M. Ivova Rikova, B. Millan Mejias, P. Otiougova, P. Robmann, H. Snoek, M. Verzetti

National Central University, Chung-Li, Taiwan

Y.H. Chang, K.H. Chen, C.M. Kuo, S.W. Li, W. Lin, Z.K. Liu, Y.J. Lu, D. Mekterovic, R. Volpe, S.S. Yu

National Taiwan University (NTU), Taipei, Taiwan

P. Bartalini, P. Chang, Y.H. Chang, Y.W. Chang, Y. Chao, K.F. Chen, C. Dietz, U. Grundler, W.-S. Hou, Y. Hsiung, K.Y. Kao, Y.J. Lei, R.-S. Lu, D. Majumder, E. Petrakou, X. Shi, J.G. Shiu, Y.M. Tzeng, X. Wan, M. Wang

Cukurova University, Adana, Turkey

A. Adiguzel, M.N. Bakirci³⁸, S. Cerci³⁹, C. Dozen, I. Dumanoglu, E. Eskut, S. Girgis, G. Gokbulut, I. Hos, E.E. Kangal, G. Karapinar, A. Kayis Topaksu, G. Onengut, K. Ozdemir, S. Ozturk⁴⁰, A. Polatoz, K. Sogut⁴¹, D. Sunar Cerci³⁹, B. Tali³⁹, H. Topakli³⁸, D. Uzun, L.N. Vergili, M. Vergili

Middle East Technical University, Physics Department, Ankara, Turkey

I.V. Akin, T. Aliev, B. Bilin, S. Bilmis, M. Deniz, H. Gamsizkan, A.M. Guler, K. Ocalan, A. Ozpineci, M. Serin, R. Sever, U.E. Surat, M. Yalvac, E. Yildirim, M. Zeyrek

Bogazici University, Istanbul, Turkey

M. Deliomeroglu, E. Gülmez, B. Isildak, M. Kaya⁴², O. Kaya⁴², S. Ozkorucuklu⁴³, N. Sonmez⁴⁴

National Scientific Center, Kharkov Institute of Physics and Technology, Kharkov, Ukraine

L. Levchuk

University of Bristol, Bristol, United Kingdom

F. Bostock, J.J. Brooke, E. Clement, D. Cussans, H. Flacher, R. Frazier, J. Goldstein, M. Grimes, G.P. Heath, H.F. Heath, L. Kreczko, S. Metson, D.M. Newbold³⁴, K. Nirunpong, A. Poll, S. Senkin, V.J. Smith, T. Williams

Rutherford Appleton Laboratory, Didcot, United Kingdom

L. Basso⁴⁵, A. Belyaev⁴⁵, C. Brew, R.M. Brown, D.J.A. Cockerill, J.A. Coughlan, K. Harder, S. Harper, J. Jackson, B.W. Kennedy, E. Olaiya, D. Petyt, B.C. Radburn-Smith, C.H. Shepherd-Themistocleous, I.R. Tomalin, W.J. Womersley

Imperial College, London, United Kingdom

R. Bainbridge, G. Ball, R. Beuselinck, O. Buchmuller, D. Colling, N. Cripps, M. Cutajar, P. Dauncey, G. Davies, M. Della Negra, W. Ferguson, J. Fulcher, D. Futyan, A. Gilbert, A. Guneratne Bryer, G. Hall, Z. Hatherell, J. Hays, G. Iles, M. Jarvis, G. Karapostoli, L. Lyons, A.-M. Magnan, J. Marrouche, B. Mathias, R. Nandi, J. Nash, A. Nikitenko³⁷, A. Papageorgiou, M. Pesaresi, K. Petridis, M. Pioppi⁴⁶, D.M. Raymond, S. Rogerson, N. Rompotis, A. Rose, M.J. Ryan, C. Seez, P. Sharp, A. Sparrow, A. Tapper, S. Tourneur, M. Vazquez Acosta, T. Virdee, S. Wakefield, N. Wardle, D. Wardrope, T. Whyntie

Brunel University, Uxbridge, United Kingdom

M. Barrett, M. Chadwick, J.E. Cole, P.R. Hobson, A. Khan, P. Kyberd, D. Leslie, W. Martin, I.D. Reid, P. Symonds, L. Teodorescu, M. Turner

Baylor University, Waco, USA

K. Hatakeyama, H. Liu, T. Scarborough

The University of Alabama, Tuscaloosa, USA

C. Henderson

Boston University, Boston, USA

A. Avetisyan, T. Bose, E. Carrera Jarrin, C. Fantasia, A. Heister, J. St. John, P. Lawson, D. Lazic, J. Rohlf, D. Sperka, L. Sulak

Brown University, Providence, USA

S. Bhattacharya, D. Cutts, A. Ferapontov, U. Heintz, S. Jabeen, G. Kukartsev, G. Landsberg, M. Luk, M. Narain, D. Nguyen, M. Segala, T. Sinthuprasith, T. Speer, K.V. Tsang

University of California, Davis, Davis, USA

R. Breedon, G. Breto, M. Calderon De La Barca Sanchez, M. Caulfield, S. Chauhan, M. Chertok, J. Conway, R. Conway, P.T. Cox, J. Dolen, R. Erbacher, M. Gardner, R. Houtz, W. Ko, A. Kopecky, R. Lander, O. Mall, T. Miceli, R. Nelson, D. Pellett, J. Robles, B. Rutherford, M. Searle, J. Smith, M. Squires, M. Tripathi, R. Vasquez Sierra

University of California, Los Angeles, Los Angeles, USA

V. Andreev, K. Arisaka, D. Cline, R. Cousins, J. Duris, S. Erhan, P. Everaerts, C. Farrell, J. Hauser, M. Ignatenko, C. Jarvis, C. Plager, G. Rakness, P. Schlein[†], J. Tucker, V. Valuev, M. Weber

University of California, Riverside, Riverside, USA

J. Babb, R. Clare, J. Ellison, J.W. Gary, F. Giordano, G. Hanson, G.Y. Jeng, H. Liu, O.R. Long, A. Luthra, H. Nguyen, S. Paramesvaran, J. Sturdy, S. Sumowidagdo, R. Wilken, S. Wimpenny

University of California, San Diego, La Jolla, USA

W. Andrews, J.G. Branson, G.B. Cerati, S. Cittolin, D. Evans, F. Golf, A. Holzner, R. Kelley, M. Lebourgeois, J. Letts, I. Macneill, B. Mangano, S. Padhi, C. Palmer, G. Petrucciani, H. Pi, M. Pieri, R. Ranieri, M. Sani, I. Sfiligoi, V. Sharma, S. Simon, E. Sudano, M. Tadel, Y. Tu, A. Vartak, S. Wasserbaech⁴⁷, F. Würthwein, A. Yagil, J. Yoo

University of California, Santa Barbara, Santa Barbara, USA

D. Barge, R. Bellan, C. Campagnari, M. D'Alfonso, T. Danielson, K. Flowers, P. Geffert, J. Incandela, C. Justus, P. Kalavase, S.A. Koay, D. Kovalskyi¹, V. Krutelyov, S. Lowette, N. Mccoll, V. Pavlunin, F. Rebassoo, J. Ribnik, J. Richman, R. Rossin, D. Stuart, W. To, J.R. Vlimant, C. West

California Institute of Technology, Pasadena, USA

A. Apresyan, A. Bornheim, J. Bunn, Y. Chen, E. Di Marco, J. Duarte, M. Gataullin, Y. Ma, A. Mott, H.B. Newman, C. Rogan, V. Timciuc, P. Traczyk, J. Veverka, R. Wilkinson, Y. Yang, R.Y. Zhu

Carnegie Mellon University, Pittsburgh, USA

B. Akgun, R. Carroll, T. Ferguson, Y. Iiyama, D.W. Jang, S.Y. Jun, Y.F. Liu, M. Paulini, J. Russ, H. Vogel, I. Vorobiev

University of Colorado at Boulder, Boulder, USA

J.P. Cumalat, M.E. Dinardo, B.R. Drell, C.J. Edelmaier, W.T. Ford, A. Gaz, B. Heyburn, E. Luiggi Lopez, U. Nauenberg, J.G. Smith, K. Stenson, K.A. Ulmer, S.R. Wagner, S.L. Zang

Cornell University, Ithaca, USA

L. Agostino, J. Alexander, A. Chatterjee, N. Eggert, L.K. Gibbons, B. Heltsley, W. Hopkins, A. Khukhunaishvili, B. Kreis, N. Mirman, G. Nicolas Kaufman, J.R. Patterson, D. Puigh, A. Ryd, E. Salvati, W. Sun, W.D. Teo, J. Thom, J. Thompson, J. Vaughan, Y. Weng, L. Winstrom, P. Wittich

Fairfield University, Fairfield, USA

A. Biselli, G. Cirino, D. Winn

Fermi National Accelerator Laboratory, Batavia, USA

S. Abdullin, M. Albrow, J. Anderson, G. Apollinari, M. Atac, J.A. Bakken, L.A.T. Bauerdick, A. Beretvas, J. Berryhill, P.C. Bhat, I. Bloch, K. Burkett, J.N. Butler, V. Chetluru, H.W.K. Cheung, F. Chlebana, S. Cihangir, W. Cooper, D.P. Eartly, V.D. Elvira, S. Esen, I. Fisk, J. Freeman, Y. Gao, E. Gottschalk, D. Green, O. Gutsche, J. Hanlon, R.M. Harris, J. Hirschauer, B. Hooberman, H. Jensen, S. Jindariani, M. Johnson, U. Joshi, B. Klima, S. Kunori, S. Kwan, C. Leonidopoulos, D. Lincoln, R. Lipton, J. Lykken, K. Maeshima, J.M. Marraffino, S. Maruyama, D. Mason, P. McBride, T. Miao, K. Mishra, S. Mrenna, Y. Musienko⁴⁸, C. Newman-Holmes, V. O'Dell, J. Pivarski, R. Pordes, O. Prokofyev, T. Schwarz, E. Sexton-Kennedy, S. Sharma, W.J. Spalding, L. Spiegel, P. Tan, L. Taylor, S. Tkaczyk, L. Uplegger, E.W. Vaandering, R. Vidal, J. Whitmore, W. Wu, F. Yang, F. Yumiceva, J.C. Yun

University of Florida, Gainesville, USA

D. Acosta, P. Avery, D. Bourilkov, M. Chen, S. Das, M. De Gruttola, G.P. Di Giovanni, D. Dobur, A. Drozdetskiy, R.D. Field, M. Fisher, Y. Fu, I.K. Furic, J. Gartner, S. Goldberg, J. Hugon, B. Kim, J. Konigsberg, A. Korytov, A. Kropivnitskaya, T. Kypreos, J.F. Low, K. Matchev, P. Milenovic⁴⁹, G. Mitselmakher, L. Muniz, R. Remington, A. Rinkevicius, M. Schmitt, B. Scurlock, P. Sellers, N. Skhirtladze, M. Snowball, D. Wang, J. Yelton, M. Zakaria

Florida International University, Miami, USA

V. Gaultney, L.M. Lebolo, S. Linn, P. Markowitz, G. Martinez, J.L. Rodriguez

Florida State University, Tallahassee, USA

T. Adams, A. Askew, J. Bochenek, J. Chen, B. Diamond, S.V. Gleyzer, J. Haas, S. Hagopian, V. Hagopian, M. Jenkins, K.F. Johnson, H. Prosper, S. Sekmen, V. Veeraraghavan, M. Weinberg

Florida Institute of Technology, Melbourne, USA

M.M. Baarmand, B. Dorney, M. Hohlmann, H. Kalakhety, I. Vodopiyanov

University of Illinois at Chicago (UIC), Chicago, USA

M.R. Adams, I.M. Anghel, L. Apanasevich, Y. Bai, V.E. Bazterra, R.R. Betts, J. Callner, R. Cavanaugh, C. Dragoiu, L. Gauthier, C.E. Gerber, D.J. Hofman, S. Khalatyan, G.J. Kunde⁵⁰, F. Lacroix, M. Malek, C. O'Brien, C. Silkworth, C. Silvestre, D. Strom, N. Varelas

The University of Iowa, Iowa City, USA

U. Akgun, E.A. Albayrak, B. Bilki⁵¹, W. Clarida, F. Duru, S. Griffiths, C.K. Lae, E. McCliment, J.-P. Merlo, H. Mermerkaya⁵², A. Mestvirishvili, A. Moeller, J. Nachtman, C.R. Newsom, E. Norbeck, J. Olson, Y. Onel, F. Ozok, S. Sen, E. Tiras, J. Wetzel, T. Yetkin, K. Yi

Johns Hopkins University, Baltimore, USA

B.A. Barnett, B. Blumenfeld, S. Bolognesi, A. Bonato, C. Eskew, D. Fehling, G. Giurgiu, A.V. Gritsan, Z.J. Guo, G. Hu, P. Maksimovic, S. Rappoccio, M. Swartz, N.V. Tran, A. Whitbeck

The University of Kansas, Lawrence, USA

P. Baringer, A. Bean, G. Benelli, O. Grachov, R.P. Kenny Iii, M. Murray, D. Noonan, S. Sanders, R. Stringer, G. Tinti, J.S. Wood, V. Zhukova

Kansas State University, Manhattan, USA

A.F. Barfuss, T. Bolton, I. Chakaberia, A. Ivanov, S. Khalil, M. Makouski, Y. Maravin, S. Shrestha, I. Svintradze

Lawrence Livermore National Laboratory, Livermore, USA

J. Gronberg, D. Lange, D. Wright

University of Maryland, College Park, USA

A. Baden, M. Boutemur, B. Calvert, S.C. Eno, J.A. Gomez, N.J. Hadley, R.G. Kellogg, M. Kirn, T. Kolberg, Y. Lu, A.C. Mignerey, A. Peterman, K. Rossato, P. Rumerio, A. Skuja, J. Temple, M.B. Tonjes, S.C. Tonwar, E. Twedt

Massachusetts Institute of Technology, Cambridge, USA

B. Alver, G. Bauer, J. Bendavid, W. Busza, E. Butz, I.A. Cali, M. Chan, V. Dutta, G. Gomez Ceballos, M. Goncharov, K.A. Hahn, Y. Kim, M. Klute, Y.-J. Lee, W. Li, P.D. Luckey, T. Ma, S. Nahn, C. Paus, D. Ralph, C. Roland, G. Roland, M. Rudolph, G.S.F. Stephans, F. Stöckli, K. Sumorok, K. Sung, D. Velicanu, E.A. Wenger, R. Wolf, B. Wyslouch, S. Xie, M. Yang, Y. Yilmaz, A.S. Yoon, M. Zanetti

University of Minnesota, Minneapolis, USA

S.I. Cooper, P. Cushman, B. Dahmes, A. De Benedetti, G. Franzoni, A. Gude, J. Haupt, S.C. Kao, K. Klapoetke, Y. Kubota, J. Mans, N. Pastika, V. Rekovic, R. Rusack, M. Sasseville, A. Singovsky, N. Tambe, J. Turkewitz

University of Mississippi, University, USA

L.M. Cremaldi, R. Godang, R. Kroeger, L. Perera, R. Rahmat, D.A. Sanders, D. Summers

University of Nebraska-Lincoln, Lincoln, USA

E. Avdeeva, K. Bloom, S. Bose, J. Butt, D.R. Claes, A. Dominguez, M. Eads, P. Jindal, J. Keller, I. Kravchenko, J. Lazo-Flores, H. Malbouisson, S. Malik, G.R. Snow

State University of New York at Buffalo, Buffalo, USA

U. Baur, A. Godshalk, I. Iashvili, S. Jain, A. Kharchilava, A. Kumar, S.P. Shipkowski, K. Smith, Z. Wan

Northeastern University, Boston, USA

G. Alverson, E. Barberis, D. Baumgartel, M. Chasco, D. Trocino, D. Wood, J. Zhang

Northwestern University, Evanston, USA

A. Anastassov, A. Kubik, N. Mucia, N. Odell, R.A. Ofierzynski, B. Pollack, A. Pozdnyakov, M. Schmitt, S. Stoynev, M. Velasco, S. Won

University of Notre Dame, Notre Dame, USA

L. Antonelli, D. Berry, A. Brinkerhoff, M. Hildreth, C. Jessop, D.J. Karmgard, J. Kolb, K. Lannon, W. Luo, S. Lynch, N. Marinelli, D.M. Morse, T. Pearson, R. Ruchti, J. Slaunwhite, N. Valls, M. Wayne, M. Wolf, J. Ziegler

The Ohio State University, Columbus, USA

B. Bylsma, L.S. Durkin, C. Hill, P. Killewald, K. Kotov, T.Y. Ling, M. Rodenburg, C. Vuosalo, G. Williams

Princeton University, Princeton, USA

N. Adam, E. Berry, P. Elmer, D. Gerbaudo, V. Halyo, P. Hebda, J. Hegeman, A. Hunt, E. Laird, D. Lopes Pegna, P. Lujan, D. Marlow, T. Medvedeva, M. Mooney, J. Olsen, P. Piroué, X. Quan, A. Raval, H. Saka, D. Stickland, C. Tully, J.S. Werner, A. Zuranski

University of Puerto Rico, Mayaguez, USA

J.G. Acosta, X.T. Huang, A. Lopez, H. Mendez, S. Oliveros, J.E. Ramirez Vargas, A. Zatserklyaniy

Purdue University, West Lafayette, USA

E. Alagoz, V.E. Barnes, D. Benedetti, G. Bolla, L. Borrello, D. Bortoletto, M. De Mattia, A. Everett, L. Gutay, Z. Hu, M. Jones, O. Koybasi, M. Kress, A.T. Laasanen, N. Leonardo, V. Maroussov, P. Merkel, D.H. Miller, N. Neumeister, I. Shipsey, D. Silvers, A. Svyatkovskiy, M. Vidal Marono, H.D. Yoo, J. Zablocki, Y. Zheng

Purdue University Calumet, Hammond, USA

S. Guragain, N. Parashar

Rice University, Houston, USA

A. Adair, C. Boulahouache, V. Cuplov, K.M. Ecklund, F.J.M. Geurts, B.P. Padley, R. Redjimi, J. Roberts, J. Zabel

University of Rochester, Rochester, USA

B. Betchart, A. Bodek, Y.S. Chung, R. Covarelli, P. de Barbaro, R. Demina, Y. Eshaq, A. Garcia-Bellido, P. Goldenzweig, Y. Gotra, J. Han, A. Harel, D.C. Miner, G. Petrillo, W. Sakumoto, D. Vishnevskiy, M. Zielinski

The Rockefeller University, New York, USA

A. Bhatti, R. Ciesielski, L. Demortier, K. Goulianos, G. Lungu, S. Malik, C. Mesropian

Rutgers, the State University of New Jersey, Piscataway, USA

S. Arora, O. Atramentov, A. Barker, J.P. Chou, C. Contreras-Campana, E. Contreras-Campana, D. Duggan, D. Ferencek, Y. Gershtein, R. Gray, E. Halkiadakis, D. Hidas, D. Hits, A. Lath, S. Panwalkar, M. Park, R. Patel, A. Richards, K. Rose, S. Salur, S. Schnetzer, C. Seitz, S. Somalwar, R. Stone, S. Thomas

University of Tennessee, Knoxville, USA

G. Cerizza, M. Hollingsworth, S. Spanier, Z.C. Yang, A. York

Texas A&M University, College Station, USA

R. Eusebi, W. Flanagan, J. Gilmore, T. Kamon⁵³, V. Khotilovich, R. Montalvo, I. Osipenkov, Y. Pakhotin, A. Perloff, J. Roe, A. Safonov, T. Sakuma, S. Sengupta, I. Suarez, A. Tatarinov, D. Toback

Texas Tech University, Lubbock, USA

N. Akchurin, C. Bardak, J. Damgov, P.R. Duderov, C. Jeong, K. Kovitanggoon, S.W. Lee, T. Libeiro, P. Mane, Y. Roh, A. Sill, I. Volobouev, R. Wigmans

Vanderbilt University, Nashville, USA

E. Appelt, E. Brownson, D. Engh, C. Florez, W. Gabella, A. Gurrola, M. Issah, W. Johns, P. Kurt, C. Maguire, A. Melo, P. Sheldon, B. Snook, S. Tuo, J. Velkovska

University of Virginia, Charlottesville, USA

M.W. Arenton, M. Balazs, S. Boutle, S. Conetti, B. Cox, B. Francis, S. Goadhouse, J. Goodell, R. Hirosky, A. Ledovskoy, C. Lin, C. Neu, J. Wood, R. Yohay

Wayne State University, Detroit, USA

S. Gollapinni, R. Harr, P.E. Karchin, C. Kottachchi Kankanamge Don, P. Lamichhane, M. Mattson, C. Milstène, A. Sakharov

University of Wisconsin, Madison, USA

M. Anderson, M. Bachtis, D. Belknap, J.N. Bellinger, J. Bernardini, D. Carlsmith, M. Cepeda, S. Dasu, J. Efron, E. Friis, L. Gray, K.S. Grogg, M. Grothe, R. Hall-Wilton, M. Herndon, A. Hervé, P. Klabbers, J. Klukas, A. Lanaro, C. Lazaridis, J. Leonard, R. Loveless, A. Mohapatra, I. Ojalvo, G.A. Pierro, I. Ross, A. Savin, W.H. Smith, J. Swanson

†: Deceased

- 1: Also at CERN, European Organization for Nuclear Research, Geneva, Switzerland
- 2: Also at National Institute of Chemical Physics and Biophysics, Tallinn, Estonia
- 3: Also at Universidade Federal do ABC, Santo Andre, Brazil
- 4: Also at California Institute of Technology, Pasadena, USA
- 5: Also at Laboratoire Leprince-Ringuet, Ecole Polytechnique, IN2P3-CNRS, Palaiseau, France
- 6: Also at Suez Canal University, Suez, Egypt
- 7: Also at Cairo University, Cairo, Egypt
- 8: Also at British University, Cairo, Egypt
- 9: Also at Fayoum University, El-Fayoum, Egypt
- 10: Now at Ain Shams University, Cairo, Egypt
- 11: Also at Soltan Institute for Nuclear Studies, Warsaw, Poland
- 12: Also at Université de Haute-Alsace, Mulhouse, France
- 13: Also at Moscow State University, Moscow, Russia
- 14: Also at Brandenburg University of Technology, Cottbus, Germany
- 15: Also at Institute of Nuclear Research ATOMKI, Debrecen, Hungary
- 16: Also at Eötvös Loránd University, Budapest, Hungary
- 17: Also at Tata Institute of Fundamental Research - HECR, Mumbai, India
- 18: Now at King Abdulaziz University, Jeddah, Saudi Arabia
- 19: Also at University of Visva-Bharati, Santiniketan, India
- 20: Also at Sharif University of Technology, Tehran, Iran
- 21: Also at Isfahan University of Technology, Isfahan, Iran
- 22: Also at Shiraz University, Shiraz, Iran
- 23: Also at Plasma Physics Research Center, Science and Research Branch, Islamic Azad University, Teheran, Iran
- 24: Also at Facoltà Ingegneria Università di Roma, Roma, Italy
- 25: Also at Università della Basilicata, Potenza, Italy
- 26: Also at Laboratori Nazionali di Legnaro dell' INFN, Legnaro, Italy
- 27: Also at Università degli studi di Siena, Siena, Italy
- 28: Also at Faculty of Physics of University of Belgrade, Belgrade, Serbia
- 29: Also at University of California, Los Angeles, Los Angeles, USA
- 30: Also at University of Florida, Gainesville, USA
- 31: Also at Scuola Normale e Sezione dell' INFN, Pisa, Italy
- 32: Also at INFN Sezione di Roma; Università di Roma "La Sapienza", Roma, Italy
- 33: Also at University of Athens, Athens, Greece
- 34: Also at Rutherford Appleton Laboratory, Didcot, United Kingdom
- 35: Also at The University of Kansas, Lawrence, USA
- 36: Also at Paul Scherrer Institut, Villigen, Switzerland
- 37: Also at Institute for Theoretical and Experimental Physics, Moscow, Russia
- 38: Also at Gaziosmanpasa University, Tokat, Turkey

- 39: Also at Adiyaman University, Adiyaman, Turkey
- 40: Also at The University of Iowa, Iowa City, USA
- 41: Also at Mersin University, Mersin, Turkey
- 42: Also at Kafkas University, Kars, Turkey
- 43: Also at Suleyman Demirel University, Isparta, Turkey
- 44: Also at Ege University, Izmir, Turkey
- 45: Also at School of Physics and Astronomy, University of Southampton, Southampton, United Kingdom
- 46: Also at INFN Sezione di Perugia; Università di Perugia, Perugia, Italy
- 47: Also at Utah Valley University, Orem, USA
- 48: Also at Institute for Nuclear Research, Moscow, Russia
- 49: Also at University of Belgrade, Faculty of Physics and Vinca Institute of Nuclear Sciences, Belgrade, Serbia
- 50: Also at Los Alamos National Laboratory, Los Alamos, USA
- 51: Also at Argonne National Laboratory, Argonne, USA
- 52: Also at Erzincan University, Erzincan, Turkey
- 53: Also at Kyungpook National University, Daegu, Korea